ELEMENTS OF OIL AND GAS WELL TUBULAR DESIGN

P.D. PATTILLO

GPP

ELEMENTS OF OIL AND GAS WELL TUBULAR DESIGN

ELEMENTS OF OIL AND GAS WELL TUBULAR DESIGN

P.D. PATTILLO

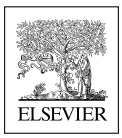

Gulf Professional Publishing
An imprint of Elsevier

Gulf Professional Publishing is an imprint of Elsevier
50 Hampshire Street, 5th Floor, Cambridge, MA 02139, United States
The Boulevard, Langford Lane, Kidlington, Oxford, OX5 1GB, United Kingdom

Notices

Knowledge and best practice in this field are constantly changing. As new research and experience broaden our understanding, changes in research methods, professional practices, or medical treatment may become necessary.

Practitioners and researchers must always rely on their own experience and knowledge in evaluating and using any information, methods, compounds, or experiments described herein. In using such information or methods they should be mindful of their own safety and the safety of others, including parties for whom they have a professional responsibility.

To the fullest extent of the law, neither the Publisher nor the authors, contributors, or editors, assume any liability for any injury and/or damage to persons or property as a matter of products liability, negligence or otherwise, or from any use or operation of any methods, products, instructions, or ideas contained in the material herein.

Library of Congress Cataloging-in-Publication Data
A catalog record for this book is available from the Library of Congress

British Library Cataloguing-in-Publication Data
A catalogue record for this book is available from the British Library

ISBN: 978-0-12-811769-9

Publishing Director: Joe Hayton
Senior Acquisition Editor: Katie Hammon
Senior Editorial Project Manager: Kattie Washington
Production Project Manager: Vijayaraj Purushothaman
Designer: Greg Harris

Typeset by VTeX

To Linda

Her husband is known in the gates, when he sits among the elders of the land. Proverbs 31:23

ABOUT THE AUTHOR

Phillip D. Pattillo has received a BS degree in Mechanical Engineering and an MS degree in Engineering Science from Louisiana State University, and also both MS and PhD degrees in Engineering Science from the University of Notre Dame. He has authored or coauthored over 40 refereed technical publications. He served as an SPE Distinguished Lecturer in 2006–2007 and was the recipient of the SPE Drilling Engineering award in 2009. Prior to retirement, he worked for 42 years for Amoco Production Company and BP America in the areas of tubular design, wellbore stability and multiphase flow. He is currently an independent contractor residing in Cypress, Texas, USA.

PREFACE

SCOPE

This book offers one engineer's insight into the complexities of oil well casing and tubing design. The book's intent is to be sufficiently detailed on the tubular-oriented application of principles of solid mechanics to serve as a stand-alone reference, while at the same time providing the reader with ready access to the key equations pertinent to design.

It will be apparent from the outset that the presentation is equation-rich. An objective of this work is to offer the reader a unified treatment of the current state of tubular design starting with the fundamentals of continuum theory and then applying those relations to a loaded tubular structure. New concepts are reinforced by example calculations. The interrelation between, and differentiation of, various limit states is clearly defined.

Organization

Mechanical design involves two competing considerations—load and resistance. Due to its geometry and material, a structure has the potential for a certain level of resistance. That potential is evidenced when the structure is subjected to a load. The object of design is to ensure that the structure retains integrity by some reasonable margin for all foreseeable loads, i.e.,

$$Resistance \geq Load,$$

where the placement of the margin will be discussed later. The current treatment of the above equation begins with a discussion of resistance. Assuming the presence of internal pressure, external pressure and axial load from some unknown origin, the resistance of a tubular or tubular string to those loads, singly or in combination, is examined.

Chapters 3–6 review the concepts of deformation, stress and elastic and inelastic behavior in sufficient detail to provide reference for the discussions to follow. Chapter 3 begins with the position of a point within the tubular and, introducing displacement, then proceeds to examine the consequences of differential displacement in the structure. This leads to the consideration of three measures of differential displacement—Lagrangian, Eulerian and logarithmic strain. The chapter concludes with a number of special cases of strain applicable to investigations in later chapters.

Chapter 4 examines the internal stresses associated with applied surface tractions and distributed body force (gravity). Natural consequences of the discussion of traction

include the equations of motion and principal stresses. The general concepts are then simplified for certain special load cases.

The two material-independent concepts of strain and stress are then related through the introduction of two models of material constitution—elastic (Chapter 5) and plastic (Chapter 6) behavior. Chapter 5 includes derivations of the essential equations of tubular design applicable to elastic response, including thermoelastic response. Introduced here are the Lamé equations and the general relations for a tubular when viewed as a beam. Chapter 6 addresses the all-important boundary between elasticity and plasticity, the yield criterion. Several alternatives for expressing yield are offered, depending on the investigation to be performed. Further, sufficient material is included to address post-yield behavior associated with the ductile rupture limit state and expandable tubulars.

In addition to yield (Chapter 6), limit states associated with loads dominated by internal (Chapter 7) and external (Chapter 8) pressure are addressed. A separate chapter is devoted to the unique considerations surrounding structural behavior and resistance of threaded connections (Chapter 9).

Anticipating the discussion of loads, two transition subjects—column stability (Chapter 10) and environmental change (Chapter 11)—receive attention. Chapter 10 includes a discussion of the concept of effective force and constrained post-buckling behavior leading to sinusoidal and helical configurations of the tubular.

The discussion of Chapter 11 is key to subsequent well design calculations. Here, the importance of environmental change is discussed inasmuch as surrounding pressure and temperature changes not only effect change in axial load but also, through the altered axial load, impact the tubular's resistance to the environmental load change.

Following the discussion of the transition topics, the origin of the imposed loads—pressure, temperature, axial force—is examined in Chapter 12. Typical design loads for each limit state, and for each tubular type (Chapter 1), are presented as conjectures of reasonable worst-case environments to which the tubular might be subjected. A closing design discussion in Chapter 13 addresses the topic of tubular geometry—to what depth should each tubular string be run and what is its appropriate diameter.

Finally, the two concepts—resistance and load—are combined in an example design in Chapter 14. Design calculations incorporating all previous knowledge are detailed. The discussion closes with selected special topics (Chapter 15), addressing such issues as annular pressure build-up and wear.

Appendix A addresses vector and tensor notation and operations. A review of this chapter, even for the advanced reader, is recommended for familiarity with the notation used throughout the book. Derivations in earlier material make frequent reference to this appendix. Appendix B discusses the relations necessary to describe a space curve, which for current purposes will be the centerline of the wellbore. Detailing one aspect of the discussion of casing seat selection (Chapter 13), Appendix C presents the fundamental relations governing determination of mechanical wellbore stability. Appendix D

contains tubing and casing property tables pertinent to calculations in the main body of text.

The above organizational scheme encompasses the bulk of the text. This entire exposition is preceded by two important chapters—an introduction setting forth the conceptual aspects of tubular design (Chapter 1) and a design summary (Chapter 2). The latter is of particular importance for the practitioner. Whereas the bulk of the text is arranged in an order that flows from the general to the specific in terms of *developing* the equations of design, the design summary is arranged in an order suitable for *using* the equations of design. The design summary is a narrative focusing on a (design-oriented) chronological presentation of the final equations, with appropriate cross references to their details in the later chapters of the book.

AUDIENCE

The book has as its intended audience:

- upper-class undergraduate petroleum engineers, particularly those leaning toward the drilling and completion disciplines;
- graduates from other engineering fields desiring an in-depth discussion of tubular structural design;
- practicing engineers desiring a reference for mechanical[1] well tubular design;
- research or technology-oriented engineers desiring a unified treatment of tubular design, including pertinent background references for major tubular topics.

HOW TO READ THE CONTENTS

The contents of this book can be digested in different orders depending on one's tubular focus.

Petroleum engineering student or graduate from another discipline

Begin your study by at least scanning Appendix A to review both the concepts of tensor analysis and the nomenclature dominating derivations in the main text. Then, beginning with Chapter 3, read the main text sequentially through Chapter 15. This path begins with deformation (Chapter 3) and load (Chapter 4) concepts, then relates the two through mechanical constitutive equations for elastic (Chapter 5) and inelastic (Chapter 6) behavior. Subsequent chapters specialize the opening developments to the specific task of designing an oil or gas well tubular string. These topical chapters are then followed by an example design (Chapter 14) that illustrates the concerted use of

[1] The terms "solid mechanics" and "mechanical design" are used here to emphasize that this book has little to say of the metallurgical aspects of tubular design. The interested reader is referred to [1].

previous material in practice. The survey closes with a chapter (Chapter 15) on subjects of specialized interest to particular areas such as deepwater and viscous oil.

Practicing drilling or completion engineer

If your need inclines toward a ready reference of design principles for actual design, use Chapter 2 as a base from which all other queries originate. Chapter 2 presents a step-by-step procedure—starting with the minimum input data requirements—for designing a well's tubulars. The procedure of Chapter 2 is heavily documented with references to other chapters in case a refresher on a particular concept is in order. Particularly useful for the practitioner is the example design. This scenario can be input into existing commercial software packages and then used to better understand the software tools' calculations and sensitivities to input variables.

Research engineer

The material of this book can also be useful to the technology branch of an enterprise as a reference source. Not all papers on any subjects have been included, but hopefully the reference list is sufficient to aid a technologist in his or her personal study. The attempt herein to present a unified treatment of tubular design principles is especially directed at such individuals.

P.D. Pattillo
Cypress, TX, USA
December 2, 2017

ACKNOWLEDGMENT

This book has a coauthor, P. David Pattillo II. Dr. Pattillo not only rederived the vast majority of the equations, but also edited the text. In addition, he offered invaluable advice on communicating the material to the reader in the most friendly and understandable manner. The manuscript is much better for his effort.

I am also fortunate in having had the opportunity to work with Katie Hammon and Kattie Washington at Elsevier. Both ladies smoothed my path through the foreign world of book publication. I particularly appreciate their availability and patience with schedule adjustments and with maneuvering the complicated process of obtaining third-party permissions. The entire experience with Katie and Kattie was a pleasure.

A special thanks to Suresh Kumar for the many times he saved this project from the author's lack of knowledge of the powerful LaTeX document preparation tool. His responses to my queries were always on target and speedily supplied.

The references cited in the text only suggest the number of industry sources and co-workers whose accomplishments are summarized in these pages. I offer an apology to anyone whose contribution has been missed, hoping such oversights can be corrected in any future revision. The drilling and completion community within our industry is a fine group with whom to associate.

Finally, a thanks to my wife, Linda, who did everything she could to minimize distractions, usually by assuming responsibility for a task in my place. I owe her a long trip on a slow train.

P.D. Pattillo

March 12, 2018

SYMBOLS

The units following the definition of each symbol are in a generic system where the base units include mass (M), length (L), time (T), temperature (Θ) and amount of substance (N). If no units are supplied the quantity is dimensionless or has variable dimensions.

The symbols are arranged in alphabetical order with upper case first. The same pattern is used in sorting symbols by superscript or subscript.

In some cases the same symbol is used for more than one quantity. The assignment at a particular point in the text should be clear from the context.

A	area, $[L^2]$
$\mathbf{A}$	material area vector, $[L^2]$
A_c	empirical constant in historical API collapse formulation
A_{cr}	connection critical cross-sectional area, $[L^2]$
A_i	cross-sectional area based on inside diameter, $A_i = \frac{\pi}{4} d^2$, $[L^2]$
A_{ia}	cross-sectional area based on outer boundary of annulus exposed to external fluid flow, $[L^2]$
A_o	cross-sectional area based on outside diameter, $A_o = \frac{\pi}{4} D^2$, $[L^2]$
A_{oa}	cross-sectional area of annulus, $[L^2]$
A_S	surface area, $[L^2]$
A_s	cross-sectional area of tube, $A_s = A_o - A_i$, $[L^2]$
$\mathbf{a}$	acceleration, $[LT^{-2}]$
$\mathbf{a}$	spatial area vector, $[L^2]$
a_N	inspection threshold corresponding t the maximum depth of a crack-like imperfection that could be undetected by the tube inspection system, [L]
B	a configuration of the body $\mathcal{B}$
$\mathcal{B}$	a collection of particles
B_c	empirical constant in historical API collapse formulation
b	property per unit mass
$\mathbf{b}$	unit binormal vector
$\mathbf{b}_f$	body force per unit mass, $[LT^{-2}]$
$\mathbf{C}$	Green deformation tensor
$\check{\mathbf{C}}$	Cauchy deformation tensor
C_{BHA}	annular capacity opposite bottomhole assembly, $[L^2]$
C_c	empirical constant in historical API collapse formulation, $[ML^{-1}T^{-2}]$
C_{DP}	annular capacity opposite drill pipe, $[L^2]$
C_f	compressibility of fluid, $[M^{-1}LT^2]$
C_i	circumference based on inside diameter, $C_i = \pi d$, [L]
C_{ia}	circumference of outer boundary of annulus exposed to external fluid flow, [L]
C_o	circumference based on outside diameter, $C_o = \pi D$, [L]
c	cohesion, intercept of Mohr–Coulomb failure envelope with Σ'_s axis, $[ML^{-1}T^{-2}]$
$\mathbf{c}$	moment per length, $[MLT^{-2}]$
c_0	wave speed, $[LT^{-1}]$
D	specified outside diameter, [L]

$\bar{D}$	mean diameter, $\bar{D} = \frac{D+d}{2}$, [L]
D_l	"lower" outside diameter at a cross-over, [L]
D_{max}	maximum value of D around cross section, [L]
D_{min}	minimum value of D around cross section, [L]
D_{TJ}	outside diameter of tool joint, [L]
D_u	"upper" outside diameter at a cross-over, [L]
d	inside diameter, $d = D - 2t$, [L]
d_l	"lower" inside diameter at a cross-over, [L]
d_u	"upper" inside diameter at a cross-over, [L]
d_{wall}	inside diameter including factor to account for the manufacturing tolerance of the tube wall thickness, $d_{wall} = D - 2k_{wall}t$, [L]
$DF_{Collapse}$	collapse design factor
$DF_{Triaxial}$	triaxial design factor
$\left(\frac{D}{t}\right)_{yp}$	D/t boundary between API minimum yield and plastic collapse
$\left(\frac{D}{t}\right)_{pt}$	D/t boundary between API minimum plastic and transition collapse
$\left(\frac{D}{t}\right)_{te}$	D/t boundary between API minimum transition and elastic collapse
E	Young's modulus, $[\mathrm{ML}^{-1}\mathrm{T}^{-2}]$
$\mathbf{E}$	Lagrangian strain tensor
$\check{\mathbf{E}}$	Eulerian strain tensor
$\check{\mathbf{E}}^{(e)}$	elastic part of Eulerian strain tensor
$\check{\mathbf{E}}^{(p)}$	plastic part of Eulerian strain tensor
$\tilde{\mathbf{E}}$	logarithmic strain tensor
$\tilde{\mathbf{E}}^{(e)}$	elastic part of logarithmic strain tensor
$\tilde{\mathbf{E}}^{(p)}$	plastic part of logarithmic strain tensor
$\check{E}_e^{(p)}$	equivalent plastic strain
E_{IJ}	component of Lagrangian strain tensor
$\check{E}_{ij}$	component of Eulerian strain tensor
E_{jt}	joint efficiency, [%]
E_L	local slope of Ludwik stress–strain model, $[\mathrm{ML}^{-1}\mathrm{T}^{-2}]$
E_s	secant modulus, $[\mathrm{ML}^{-1}\mathrm{T}^{-2}]$
E_t	tangent modulus, $[\mathrm{ML}^{-1}\mathrm{T}^{-2}]$
E_1	thread pitch diameter at hand-tight plane for API round thread, [L]
e	base of the natural logarithm, $\ln e = 1$
$\mathbf{e}_K$	unit base vector associated with Kth material coordinate axis, $K = 1, 2, 3$ or $K = R, \Theta, Z$
$\mathbf{F}$	deformation gradient
F_c	empirical constant in historical API collapse formulation
$\hat{f}()$	function describing yield surface, $[\mathrm{M}^2\mathrm{L}^{-2}\mathrm{T}^{-4}]$
$\mathbf{f}$	force, $[\mathrm{MLT}^{-2}]$
$\tilde{\mathbf{f}}$	pseudo-force related to Piola–Kirchhoff stress of second kind, $[\mathrm{MLT}^{-2}]$
f_b	shear force along $\mathbf{b}$ in $\mathbf{t}$–$\mathbf{n}$–$\mathbf{b}$ coordinate system, $[\mathrm{MLT}^{-2}]$
$\mathbf{f}_b$	bending force distribution, $[\mathrm{MLT}^{-2}]$
f_c	critical effective force for buckling, $[\mathrm{MLT}^{-2}]$
f_{ch}	critical effective force for helical buckling, $[\mathrm{MLT}^{-2}]$
f_{cs}	critical effective force for sinusoidal buckling, $[\mathrm{MLT}^{-2}]$
f_{eff}	effective force, $[\mathrm{MLT}^{-2}]$
$\mathbf{f}_f$	resultant force on fluid, $[\mathrm{MLT}^{-2}]$
f_h	axial force (f_t) in helix, $[\mathrm{MLT}^{-2}]$

f_n	shear force along **n** in **t**–**n**–**b** coordinate system, [MLT^{-2}]
$\mathbf{f}_{(\mathbf{n})-res}$	resultant force on surface with normal **n**, [MLT^{-2}]
$\mathbf{f}_{S-res}$	resultant force on surface area A_S, [MLT^{-2}]
f_t	axial force in **t**–**n**–**b** coordinate system, [MLT^{-2}]
f_y	yield stress, [ML^{-1}T^{-2}]
f_{ycom}	yield stress adjusted for the presence of axial stress and internal pressure, [ML^{-1}T^{-2}]
f_{ymn}	specified minimum yield stress, [ML^{-1}T^{-2}]
f_u	ultimate stress, [ML^{-1}T^{-2}]
f_{umn}	specified minimum ultimate stress, [ML^{-1}T^{-2}]
f_{uts}	axial force scaling factor in API ductile rupture calculation, [MLT^{-2}]
f_{WOB}	axial force associated with weight on bit, [MLT^{-2}]
f_w	wear factor, [M^{-1}LT^2]
f_z	axial force, [MLT^{-2}]
$\mathbf{f}_z$	axial force in API ductile rupture calculation, [MLT^{-2}]
G	shear modulus, $G = \mu_E$, [ML^{-1}T^{-2}]
$\hat{G}$	limit state equation
$\mathbf{G}$	matrix transforming tensors from the **X** coordinate system to the $\mathbf{x}_w$ coordinate system
G_c	empirical constant in historical API collapse formulation
g	acceleration of gravity, [LT^{-2}]
g_c	gravitational constant
$\mathbf{g}_{hyd}$	unit vector along hydrostatic state of stress
$\mathbf{g}_k$	unit base vector associated with kth spatial coordinate axis, $k = 1, 2, 3$ or $k = r, \theta, z$, or $k = t, n, b$
$\mathbf{g}_k^p$	unit base vector associated with kth spatial coordinate axis, $k = 1, 2, 3$
$H(x)$	Heaviside step function
h	height, [L]
h_c	height of wear groove segment in casing, [L]
h_{LC}	height of lost circulation fluid column, [L]
h_{TJ}	height of wear groove segment in tool joint, [L]
h_w	wall thickness loss due to wear, $h_w = h_{TJ} - h_c$, [L]
I	moment of inertia of cross section ($I = \frac{\pi}{64}\left(D^4 - d^4\right)$ for a tube), [L^4]
$\mathbf{I}$	identity tensor
I_1	first invariant of a second order tensor, trace
I_2	second invariant of a second order tensor
I_3	third invariant of a second order tensor
$\mathcal{J}$	Jacobian, or determinant of **F**
J_1	first invariant of the deviatoric stress tensor, [ML^{-1}T^{-2}]
J_2	second invariant of the deviatoric stress tensor, [M^{2}L^{-2}T^{-4}]
J_3	third invariant of the deviatoric stress tensor, [M^{3}L^{-3}T^{-6}]
K_b	bulk modulus of a porous medium, [ML^{-1}T^{-2}]
K_s	bulk modulus of a solid medium, [ML^{-1}T^{-2}]
k_a	burst strength factor—1.0 for quenched and temperated tubes with a martensitic grain structure or grades with minimum 13% chromium and 2.0 for as-rolled and normalized tubes—which offers a measure (which may optionally be determined experimentally) of the ductility of the tube material
k_{BR}	bias factor for necking and rupture in ductile rupture calculation
$k_{bc\gamma}$	buoyancy factor, $k_{bc\gamma} = 1 - \rho_f/\rho_s = 1 - \gamma_f/\gamma_s$
k_{ch}	constant multiplier for helical buckling in an inclined wellbore
k_{corr}	design factor multiplying factor to account for loss of specified wall thickness due to corrosion
k_{DR}	ratio of $\Sigma_{\underline{eff}}$ to $\Sigma_{\theta\theta} - \Sigma_{rr}$ in ductile rupture calculation

k_M	factor in API ductile rupture calculation, [L^2]
k_R	factor in API ductile rupture calculation
k_{scc}	design factor multiplying factor to account for a sour environment
k_{wall}	factor to account for the manufacturing tolerance of the tube wall thickness
k_{wear}	design factor multiplying factor design factor to account loss of specified wall thickness due to wear
L	length, [L]
$\mathbf{L}$	coordinate transformation matrix
L_c	length of contact in tool joint wear calculation, [L]
L_c	length of helix along its (straight) tubular centerline at incipient buckling, [L]
$(L_c)_{TJ}$	residence length per tool joint at a casing location, [L]
L_{dp}	length of a joint of drill pipe, [L]
L_{dr}	length of drilled interval, [L]
L_h	length of helix measured along its (curved) tubular centerline, [L]
L_{TJ}	length of tool joint, [L]
L_1	length from end of pin to hand-tight plane for API round thread, [L]
L_2	length of effective threads for API round thread, [L]
ΔL	length change, [L]
ΔL_B	length change due to ballooning, [L]
ΔL_{Bu}	length change due to column buckling, [L]
ΔL_S	length change due to force change on exposed shoulder, [L]
ΔL_T	length change due to temperature change, [L]
ΔL_{Total}	total length change, [L]
ΔL_W	length change due to self-weight, [L]
$\mathcal{M}$	molecular mass
m	mass, [M]
$\mathbf{m}$	moment, [ML^2T^{-2}]
m_b	bending moment in **t**–**n**–**b** coordinate system, [ML^2T^{-2}]
m_t	torsion in **t**–**n**–**b** coordinate system, [ML^2T^{-2}]
n	Needleman's parameter
$\mathbf{n}$	unit normal vector, coordinate unit base vector in **t**–**n**–**b** coordinate system
$\check{\mathbf{n}}$	unit normal vector to control surface
n_{NR}	Ludwik's parameter
$\mathbf{o}$	offset between origins of global material and spatial coordinate systems, [L]
$\mathbf{P}$	matrix transforming tensors from the $\mathbf{X}_p$ coordinate system to the $\mathbf{X}$ coordinate system
p	pressure, [$ML^{-1}T^{-2}$]
$\mathbf{p}$	path, position vector, [L]
$\tilde{p}_c$	collapse pressure measured at tube mid-surface, [$ML^{-1}T^{-2}$]
Δp_c	collapse differential pressure, [$ML^{-1}T^{-2}$]
p_{cn}	characteristic magnitude of nonuniform pressure, [$ML^{-1}T^{-2}$]
p_{co}	confining pressure, [$ML^{-1}T^{-2}$]
p_{cr}	pressure of a fluid at its critical point, [$ML^{-1}T^{-2}$]
p_{DF}	design factor pressure for kick tolerance calculation, [$ML^{-1}T^{-2}$]
p_{dr}	internal ductile rupture pressure, [$ML^{-1}T^{-2}$]
p_{ds}	differential sticking pressure, [$ML^{-1}T^{-2}$]
p_f	pressure in fluid column, [$ML^{-1}T^{-2}$]
p_{fr}	fracture pressure, [$ML^{-1}T^{-2}$]
p_h	pitch of helix, [L]
p_i	internal pressure, [$ML^{-1}T^{-2}$]

p_{is}	static component of internal pressure, $[\mathrm{ML}^{-1}\mathrm{T}^{-2}]$
p_M	internal pressure at rupture from von Mises yield criterion in API ductile rupture calculation, $[\mathrm{ML}^{-1}\mathrm{T}^{-2}]$
p_{max}	maximum pressure, $[\mathrm{ML}^{-1}\mathrm{T}^{-2}]$
p_o	external pressure, $[\mathrm{ML}^{-1}\mathrm{T}^{-2}]$
p_{oc}	collapse pressure measured at outside diameter, $[\mathrm{ML}^{-1}\mathrm{T}^{-2}]$
p_{of}	frictional component of external pressure, $[\mathrm{ML}^{-1}\mathrm{T}^{-2}]$
p_{os}	static component of external pressure, $[\mathrm{ML}^{-1}\mathrm{T}^{-2}]$
p_p	pore pressure, $[\mathrm{ML}^{-1}\mathrm{T}^{-2}]$
p_{pc}	pseudocritical pressure of a fluid, $[\mathrm{ML}^{-1}\mathrm{T}^{-2}]$
p_{pr}	pseudoreduced pressure
p_{pt}	characteristic magnitude of nonuniform line load, $[\mathrm{MT}^{-2}]$
p_{refM}	capped-end design rupture pressure from von Mises yield criterion in API ductile rupture calculation, $[\mathrm{ML}^{-1}\mathrm{T}^{-2}]$
p_{refT}	capped-end design rupture pressure from Tresca yield criterion in API ductile rupture calculation, $[\mathrm{ML}^{-1}\mathrm{T}^{-2}]$
p_{uts}	pressure scaling factor in API ductile rupture calculation, $[\mathrm{ML}^{-1}\mathrm{T}^{-2}]$
Q	fluid volumetric flow rate, $[\mathrm{L}^3\mathrm{T}^{-1}]$
Q_a	fluid volumetric flow rate in annulus, $[\mathrm{L}^3\mathrm{T}^{-1}]$
Q_h	heat flow into system, $[\mathrm{ML}^2\mathrm{T}^{-2}]$
$\mathbf{q}$	(total) force per length, $[\mathrm{MT}^{-2}]$
$\mathbf{q}_c$	force per length due to contact with confining hole, $[\mathrm{MT}^{-2}]$
$(\mathbf{q}_c)_{pipe}$	force per length on drill pipe body due to contact with confining hole, $[\mathrm{MT}^{-2}]$
$(\mathbf{q}_c)_{TJ}$	force per length on tool joint due to contact with confining hole, $[\mathrm{MT}^{-2}]$
$\mathbf{q}_f$	force per length due to the presence of fluids and pressure, $[\mathrm{MT}^{-2}]$
$\mathbf{q}_{fr}$	force per length due to friction from contact with confining hole, $[\mathrm{MT}^{-2}]$
q_t	component of $\mathbf{q}$ along t, $q_t = \mathbf{q} \cdot \mathbf{t}$, $[\mathrm{MT}^{-2}]$
R	material radial coordinate, [L]
$\bar{R}$	mean radius, $\bar{R} = \frac{D+d}{4}$, [L]
$\mathcal{R}$	individual gas constant, $[\mathrm{L}^2\mathrm{T}^{-2}\Theta^{-1}]$
R_{jt}	connection joint strength, $\mathrm{MLT}^{-2}]$
R_{jt-API}	API casing connection joint strength based on f_{umn}, $\mathrm{MLT}^{-2}]$
$R_{jt-yield}$	API casing connection joint strength based on f_{ymn}, $\mathrm{MLT}^{-2}]$
R_{ta}	tube body strength, $\mathrm{MLT}^{-2}]$
$\mathcal{R}_u$	universal gas constant, $[\mathrm{ML}^2\mathrm{T}^{-2}\Theta^{-1}\mathrm{N}^{-1}]$
r	spatial radial coordinate, radius, [L]
r_c	radial clearance, [L]
r_{S-max}	maximum radius of bounding surface S, [L]
S	surface, control surface, $[\mathrm{L}^2]$
$\mathbf{S}$	Piola–Kirchhoff stress of first kind, $[\mathrm{ML}^{-1}\mathrm{T}^{-2}]$
$\mathbf{S}^e$	rock mechanical effective Piola–Kirchhoff stress of first kind, $[\mathrm{ML}^{-1}\mathrm{T}^{-2}]$
$\mathbf{S}'$	Piola–Kirchhoff deviatoric stress of first kind, $[\mathrm{ML}^{-1}\mathrm{T}^{-2}]$
$\tilde{\mathbf{S}}$	Piola–Kirchhoff stress of second kind, $[\mathrm{ML}^{-1}\mathrm{T}^{-2}]$
S^{H1}	(algebraically) larger horizontal (total) stress or closure stress, $[\mathrm{ML}^{-1}\mathrm{T}^{-2}]$
S^{H2}	(algebraically) smaller horizontal (total) stress, $[\mathrm{ML}^{-1}\mathrm{T}^{-2}]$
S_{IJ}	component of Piola–Kirchhoff stress tensor, $[\mathrm{ML}^{-1}\mathrm{T}^{-2}]$
S^V	overburden (total) stress, $[\mathrm{ML}^{-1}\mathrm{T}^{-2}]$

S_a	axial Piola–Kirchhoff stress in the absence of bending, $[\mathrm{ML}^{-1}\mathrm{T}^{-2}]$
S_c	confining Piola–Kirchhoff stress, $[\mathrm{ML}^{-1}\mathrm{T}^{-2}]$
S_i	surface of tube exposed to internal fluid flow, $[\mathrm{L}^2]$
S_{ia}	surface of outer boundary of annulus exposed to external fluid flow, $[\mathrm{L}^2]$
S_n	normal Piola–Kirchhoff stress on a plane, $[\mathrm{ML}^{-1}\mathrm{T}^{-2}]$
S_o	surface of tube exposed to external fluid flow, $[\mathrm{L}^2]$
S_I^p	principal Piola–Kirchhoff stress of first kind, $S_1^p \geq S_2^p \geq S_3^p$, $[\mathrm{ML}^{-1}\mathrm{T}^{-2}]$
S_s	shear Piola–Kirchhoff stress on a plane, $[\mathrm{ML}^{-1}\mathrm{T}^{-2}]$
s	length along path, [L]
s	spatial surface, $[\mathrm{L}^2]$
$\mathbf{s}$	surface unit vector perpendicular to $\mathbf{n}$
s_h	length along helically buckled path measured from either the neutral point (vertical well) or from the transition from a sinusoidal to a helical configuration, [L]
s_n	(negative) distance along helically buckled path to the neutral point from a location where f_{eff} is known, [L]
SF_{Axial}	axial safety factor
$SF_{Collapse}$	collapse safety factor
$SF_{Triaxial}$	triaxial safety factor
SG	specific gravity
T	temperature, $[\Theta]$
T_{cr}	temperature of a fluid at its critical point, $[\Theta]$
$\mathbf{T_{(N)}}$	local traction on material surface with local normal $\mathbf{N}$, $[\mathrm{ML}^{-1}\mathrm{T}^{-2}]$
T_{pc}	pseudocritical temperature of a fluid, $[\Theta]$
T_{pr}	pseudoreduced temperature
T_0	initial temperature, $[\Theta]$
t	specified wall thickness, [L]
$\mathbf{t}$	unit tangent vector
$\mathbf{t}_b$	bending traction, $[\mathrm{ML}^{-1}\mathrm{T}^{-2}]$
t_{DR}	design wall thickness for ductile rupture calculations, $t_{DR} = k_{wall}t - k_a a_N$, [L]
$\mathbf{t_{(n)}}$	local traction on spatial surface with local normal $\mathbf{n}$, $[\mathrm{ML}^{-1}\mathrm{T}^{-2}]$
$\mathbf{t}_{(\mathbf{n})-ave}$	average traction on surface with normal $\mathbf{n}$, $[\mathrm{ML}^{-1}\mathrm{T}^{-2}]$
$\left(\mathbf{t_{(n)}}\right)_n$	component of $\mathbf{t_{(n)}}$ normal to surface, $[\mathrm{ML}^{-1}\mathrm{T}^{-2}]$
$\left(\mathbf{t_{(n)}}\right)_s$	component of $\mathbf{t_{(n)}}$ in plane of surface, $[\mathrm{ML}^{-1}\mathrm{T}^{-2}]$
$\hat{\mathbf{U}}$	displacement function in global material coordinate system, $\mathbf{u} = \hat{\mathbf{U}}(\mathbf{X}, \tau)$, [L]
U_i	internal energy of system, $[\mathrm{ML}^2\mathrm{T}^{-2}]$
U_{ia}	internal energy due to axial force, $[\mathrm{ML}^2\mathrm{T}^{-2}]$
U_{ib}	internal energy due to bending, $[\mathrm{ML}^2\mathrm{T}^{-2}]$
$\mathbf{u}$	displacement, [L]
$\hat{\mathbf{u}}$	displacement function in spatial coordinate system, $\mathbf{u} = \hat{\mathbf{u}}(\mathbf{x}, \tau)$, [L]
V	volume, $[\mathrm{L}^3]$
V_{bit}	volume of gas influx at bit, $[\mathrm{L}^3]$
V_f	fluid volume, $[\mathrm{L}^3]$
V_e	total potential energy of external forces, $[\mathrm{ML}^2\mathrm{T}^{-2}]$
V_k	total kinetic energy of system, $[\mathrm{ML}^2\mathrm{T}^{-2}]$
V_O	volume of oil constituent in mixture, $[\mathrm{L}^3]$
V_p	total potential energy of system, $[\mathrm{ML}^2\mathrm{T}^{-2}]$
V_S	volume of solid constituent in mixture, $[\mathrm{L}^3]$
V_W	volume of water constituent in mixture, $[\mathrm{L}^3]$
V_w	volume of wear per length, $[\mathrm{L}^2]$

V_{wp}	volume of gas influx at open hole section weak point, $[\mathrm{L}^3]$
$V_{wp}\|_{bit}$	volume of gas influx at open hole section weak point corrected to bit depth, $[\mathrm{L}^3]$
v	speed, $v = \sqrt{\mathbf{v} \cdot \mathbf{v}}$, $[\mathrm{LT}^{-1}]$
v	spatial volume, $[\mathrm{L}^3]$
v	specific volume, $v = 1/\rho$, $[\mathrm{M}^{-1}\mathrm{L}^3]$
$\mathbf{v}$	velocity, $[\mathrm{LT}^{-1}]$
v_{TJ}	forward velocity of tool joint/rate of penetration, $[\mathrm{LT}^{-1}]$
W	total work done on system, $[\mathrm{ML}^2\mathrm{T}^{-2}]$
W'	virtual work done on system, $[\mathrm{ML}^2\mathrm{T}^{-2}]$
W^e	elastic work done on system, $\dot{W} = \dot{W}^e + \dot{W}^p$, $[\mathrm{ML}^2\mathrm{T}^{-2}]$
W^p	plastic work done on system, $\dot{W} = \dot{W}^e + \dot{W}^p$, $[\mathrm{ML}^2\mathrm{T}^{-2}]$
W_e	work done by external forces on system, $W = W_e + W_i$, $[\mathrm{ML}^2\mathrm{T}^{-2}]$
W_i	work done by internal forces in system, $W = W_e + W_i$, $[\mathrm{ML}^2\mathrm{T}^{-2}]$
w_a	"air" weight per length, $[\mathrm{MT}^{-2}]$
w_{eff}	effective weight per length, $[\mathrm{MT}^{-2}]$
$\mathbf{X}$	material (initial) position, [L]
$\mathbf{X}_p$	position in a coordinate system aligned with the global principal stresses, [L]
X_1	material coordinate aligned with North, [L]
X_2	material coordinate aligned with East, [L]
X_3	material coordinate aligned with vertical depth, [L]
x	spatial coordinate, [L]
$\mathbf{x}$	spatial position, [L]
x_i	spatial coordinate, $i = 1, 2, 3$, [L]
y	spatial coordinate, [L]
Z	material axial coordinate, vertical depth, $Z = X_3$, [L]
Z_{bit}	vertical depth to bit, [L]
Z_c	compressibility factor
Z_{MSL}	vertical depth to mean sea level, [L]
Z_{wh}	vertical depth to subsea wellhead, [L]
Z_{wp}	vertical depth to open hole section weak point, [L]
Z_0	vertical depth datum, [L]
z	spatial axial coordinate, [L]
$\mathbf{A}$	translation of center of initial yield surface, $[\mathrm{ML}^{-1}\mathrm{T}^{-2}]$
α	Biot parameter, $0 \leq \alpha \leq 1$
α_T	linear coefficient of thermal expansion, $[\Theta^{-1}]$
α_{Tf}	linear coefficient of linear thermal expansion of fluid, $[\Theta^{-1}]$
$\mathbf{B}_T$	coefficient of linear thermal stress tensor, $[\mathrm{ML}^{-1}\mathrm{T}^{-2}\Theta^{-1}]$
β_T	coefficient of linear thermal stress, $[\mathrm{ML}^{-1}\mathrm{T}^{-2}\Theta^{-1}]$
γ	weight density, $[\mathrm{ML}^{-2}\mathrm{T}^{-2}]$
γ_{ds}	differential sticking limit gradient, $[\mathrm{ML}^{-2}\mathrm{T}^{-2}]$
γ_f	weight density of fluid, $[\mathrm{ML}^{-2}\mathrm{T}^{-2}]$
γ_{fr}	fracture pressure gradient, $[\mathrm{ML}^{-2}\mathrm{T}^{-2}]$
γ_i	weight density of internal fluid, $[\mathrm{ML}^{-2}\mathrm{T}^{-2}]$
γ_g	weight density of gas, $[\mathrm{ML}^{-2}\mathrm{T}^{-2}]$
γ_o	weight density of external fluid, $[\mathrm{ML}^{-2}\mathrm{T}^{-2}]$
γ_p	pore pressure gradient, $[\mathrm{ML}^{-2}\mathrm{T}^{-2}]$
γ_{rm}	riser margin, $[\mathrm{ML}^{-2}\mathrm{T}^{-2}]$
γ_s	weight density of solid, $[\mathrm{ML}^{-2}\mathrm{T}^{-2}]$

γ_{sb} swab margin, $[\mathrm{ML}^{-2}\mathrm{T}^{-2}]$
γ_{su} surge margin, $[\mathrm{ML}^{-2}\mathrm{T}^{-2}]$
γ_{sw} weight density of sea water, $[\mathrm{ML}^{-2}\mathrm{T}^{-2}]$
γ_T temperature gradient, $[\Theta\mathrm{L}^{-1}]$
γ_{wn} minimum drilling fluid density for wellbore stability, $[\mathrm{ML}^{-2}\mathrm{T}^{-2}]$
γ_{wx} maximum drilling fluid density for wellbore stability, $[\mathrm{ML}^{-2}\mathrm{T}^{-2}]$
δ_{Kj}, δkJ component of shifter tensor, $\delta_{Kj} = \mathbf{e}_K \cdot \mathbf{g}_j$, $\delta_{kJ} = \mathbf{g}_k \cdot \mathbf{e}_J$
δ_{mn} Kronecker delta, $\delta_{mn} = 1$ if $m = n$, $\delta_{mn} = 0$ otherwise
ε_{ijk} Levi-Civita (permutation) symbol, see Section A.3.1.4 in Appendix A
ε_w specific wear energy, $[\mathrm{ML}^{-1}\mathrm{T}^{-2}]$
ε_y yield strain
η_c central angle in casing spanning wear groove, [rad]
η_{TJ} central angle in tool joint spanning wear groove, [rad]
Θ material angular coordinate measured from the X_1 axis, [rad]
θ spatial angular coordinate measured from the x_1 axis or inclination, [rad]
θ angle between tangent to wellbore trajectory and downward vertical, [rad]
κ curvature of space curve, $[\mathrm{L}^{-1}]$
κ_w work hardening parameter
Λ scalar function that relates $\dot{\hat{\mathbf{E}}}^{(p)}$ to $\frac{\partial \hat{f}}{\partial \boldsymbol{\Sigma}}$
$\Lambda_{(\mathbf{N})}$ stretch ratio in direction of unit vector $\mathbf{N}$
λ arbitrary constant
λ characteristic value or eigenvalue
λ_E Lamé constant, $[\mathrm{ML}^{-1}\mathrm{T}^{-2}]$
M parameter in Ziegler's kinematic hardening rule
μ tangent of angle of internal friction in Mohr–Coulomb model
μ_E Lamé constant, $[\mathrm{ML}^{-1}\mathrm{T}^{-2}]$
μ_k kinetic coefficient of friction
μ_s static coefficient of friction
ν Poisson's ratio
π_k Coordinate system associated with π-plane.
ρ mass density, $[\mathrm{ML}^{-3}]$
ρ_f mass density of fluid, $[\mathrm{ML}^{-3}]$
ρ_i mass density of internal fluid, $[\mathrm{ML}^{-3}]$
ρ_{Of} final mass density of oil constituent in mixture, $[\mathrm{ML}^{-3}]$
ρ_o mass density of external fluid, $[\mathrm{ML}^{-3}]$
ρ_{PF} mass density of packer fluid, $[\mathrm{ML}^{-3}]$
ρ_{Sf} final mass density of solid constituent in mixture, $[\mathrm{ML}^{-3}]$
ρ_s mass density of steel, $[\mathrm{ML}^{-3}]$
ρ_{Wf} final mass density of water constituent in mixture, $[\mathrm{ML}^{-3}]$
$\boldsymbol{\Sigma}$ Cauchy stress tensor, $[\mathrm{ML}^{-1}\mathrm{T}^{-2}]$
$\check{\boldsymbol{\Sigma}}$ elastic stiffness tensor, $[\mathrm{ML}^{-1}\mathrm{T}^{-2}]$
$\boldsymbol{\Sigma}'$ Cauchy deviatoric stress tensor, $\boldsymbol{\Sigma}' = \boldsymbol{\Sigma} - \Sigma_m \mathbf{I}$, $[\mathrm{ML}^{-1}\mathrm{T}^{-2}]$
Σ_a portion of axial Cauchy stress not due to bending, $[\mathrm{ML}^{-1}\mathrm{T}^{-2}]$
Σ_b portion of axial Cauchy stress due to bending, $[\mathrm{ML}^{-1}\mathrm{T}^{-2}]$
Σ_e von Mises equivalent stress, $[\mathrm{ML}^{-1}\mathrm{T}^{-2}]$
$\boldsymbol{\Sigma}^e$ rock mechanical effective stress, $[\mathrm{ML}^{-1}\mathrm{T}^{-2}]$
Σ_{eff} effective stress, $[\mathrm{ML}^{-1}\mathrm{T}^{-2}]$
Σ_{ffi} wall shear stress on tube due to internal fluid flow, $[\mathrm{ML}^{-1}\mathrm{T}^{-2}]$

Σ_{ffo}	wall shear stress on annulus outer boundary due to external/annular fluid flow, $[\mathrm{ML}^{-1}\mathrm{T}^{-2}]$
Σ_{ffoa}	wall shear stress on tube due to external/annular fluid flow, $[\mathrm{ML}^{-1}\mathrm{T}^{-2}]$
Σ_m	mean Cauchy stress, $[\mathrm{ML}^{-1}\mathrm{T}^{-2}]$
Σ_i^p	principal Cauchy stress, $\Sigma_1^p \geq \Sigma_2^p \geq \Sigma_3^p$, $[\mathrm{ML}^{-1}\mathrm{T}^{-2}]$
Σ_s	shear stress magnitude, $[\mathrm{ML}^{-1}\mathrm{T}^{-2}]$
Σ_{smax}	maximum shear stress magnitude, $[\mathrm{ML}^{-1}\mathrm{T}^{-2}]$
$\boldsymbol{\Sigma}^w$	Cauchy far field stress tensor, $[\mathrm{ML}^{-1}\mathrm{T}^{-2}]$
Σ^{we}	rock mechanical far field effective stress tensor, $[\mathrm{ML}^{-1}\mathrm{T}^{-2}]$
τ	time, [T]
τ	torsion of space curve, $[\mathrm{L}^{-1}]$
τ_{TJ}	residence time per tool joint at a casing location, [T]
υ	polar angle of helix, [rad]
ϕ	internal angle of friction in Mohr–Coulomb failure envelope or azimuth, [rad]
ϕ	azimuth angle between horizontal projection of tangent to wellbore trajectory ($\sin\theta$) and North, [rad]
χ	vector of variables in limit state equation
χ_L	portion of χ that defines the load
χ_{Oi}	initial fractional percentage of oil constituent in mixture
χ_R	extension of χ_R to the limit state
χ_{Si}	initial fractional percentage of solid constituent in mixture
χ_{Wi}	initial fractional percentage of water constituent in mixture
Ω	rotary speed of drill string, $[\mathrm{T}^{-1}]$
ω	ovality
$\widehat{(\ldots)}$	functional form of quantity $(\ldots)$
$\overline{(\ldots)}$	average of quantity $(\ldots)$
$(\ldots)_{bot}$	value of quantity $(\ldots)$ at bottom of tubular string
$(\ldots)^e$	rock mechanical effective counterpart of stress quantity $(\ldots)$
$(\ldots)_{rup}$	value of quantity $(\ldots)$ at ductile rupture condition
$(\ldots)^T$	transpose of quantity $(\ldots)$
$\mathrm{tr}(\ldots)$	trace of quantity $(\ldots)$
$(\ldots)_{TOC}$	value of quantity $(\ldots)$ at top of cement
$(\ldots)_{top}$	value of quantity $(\ldots)$ at top of tubular string
$\lvert\mathbf{v}\rvert$	magnitude of vector $\mathbf{v}$
$\Delta(\ldots)$	change in quantity $(\ldots)$
$\delta(\ldots)$	increment (not necessarily infinitesimal) in quantity $(\ldots)$
$\frac{D(\ldots)}{D\tau}$	material derivative, $\frac{D(\ldots)}{D\tau} = \frac{\partial(\ldots)}{\partial \mathbf{x}} \cdot \mathbf{v}(\mathbf{X}, \tau) + \frac{\partial(\ldots)}{\partial \tau}$
∇	del operator, $\nabla = \frac{\partial}{\partial X_1}\mathbf{e}_1 + \frac{\partial}{\partial X_2}\mathbf{e}_2 + \frac{\partial}{\partial X_3}\mathbf{e}_3$, $[\mathrm{L}^{-1}]$

CHAPTER 1

Introduction

1.1. THE PLACE OF WELL TUBULARS

Well tubulars—combinations of a circular cylindrical tube and the associated threaded connections with which it is joined to its neighbors—constitute major pressure containing components of an oil or gas well. Some tubulars, such as the intermediate casing string(s) used to penetrate the overburden layers above a hydrocarbon reservoir (see Section 1.3.1.3), serve a temporary function. The outermost (structural) and innermost (pressurized conduit) tubulars, however, are permanent, active components of the well structure.

As detailed in Chapter 13 (see especially Section 13.2.1), an underlying function of all casing and tubing is to remedy the inability of subsurface rock formations to provide the fluid isolation and mechanical integrity crucial to protection of the local environment. Depending on the subsurface climate, an individual well can contain from two (onshore, benign subsurface) to eight or more (deepwater high pressure, high temperature environment) tubular strings, with each successive string sized to fit within its previously installed neighbor.

Almost all well tubulars are composed of steel. Although applications can be found that favor alternative materials, particularly in corrosive environments [2], to date steel, perhaps lined with a less corrosive susceptible material, remains the well construction product of choice.[1]

Well schematics have become increasingly detailed, reflecting the current state of interactive graphics software. In this book we will use simple stick figures to discuss the particulars of a well design. Examples of typical well components discussed below and analyzed in the remainder of the book are shown in Fig. 1.1. Unlike the schematics in Fig. 1.1, the cement sheath may be shown in a wellbore sketch. When cement is included it is usually indicated by a patterned or shaded area.

1.2. CASING AND TUBING AS WELL BARRIERS

The intent of well construction is to provide a controlled means of transporting reservoir fluids to the surface. A well barrier, on the other hand, has as its objective the prevention of unintended flow of fluids. This flow may either be from one subsur-

[1] In this regard, the entirety of this book assumes the tubular to be composed of a crystalline solid having elastic, plastic and creep behavior governed by the classic mathematical models of metals.

Elements of Oil and Gas Well Tubular Design
DOI: 10.1016/B978-0-12-811769-9.00001-3

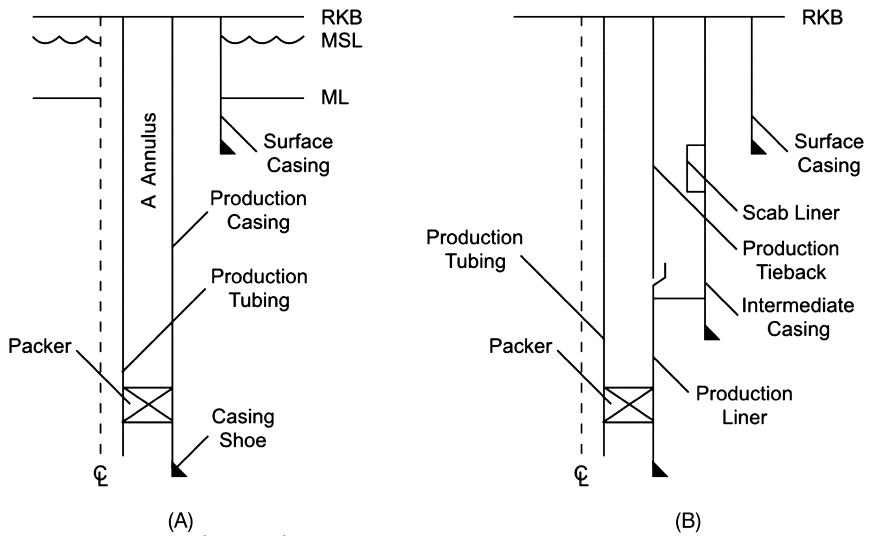

Figure 1.1 ***Sample wellbore schematics.*** (A) Diagram depicts an offshore well with surface casing, production casing and production tubing (intermediate strings are omitted), with the production tubing annulus, the so-called A annulus, sealed by a packer. (B) Diagram depicts an onshore well with one intermediate casing string containing a scab liner, perhaps to protect against a mobile salt. The production casing in this diagram consists of a liner and tieback.

face location to another—for example, cross flow between formations—or it may be between a subsurface source and the surface [3].

A well barrier is an envelope of one or more barrier elements that, together with their neighbors, form a continuous boundary against flow. A barrier element may be any one of a number of well components—fluid column, cement sheath, valve—including a casing or tubing string. While some barrier elements may be temporary (for example, a fluid column), under normal[2] operating conditions, tubular strings are usually considered to be permanent barrier elements.

1.3. TYPES OF TUBULAR

Well tubulars can be categorized in a number of ways depending on the context of the discussion. We begin with the most common determinant—function—and then discuss a second classification system—interval.

1.3.1 Differentiation by function

Starting with the shallowest tubulars, typical designations are as follows:

[2] We insert "normal" to accommodate those instances when, for example, a tubing string is pulled for repair of itself or an associated accessory.

1.3.1.1 Conductor casing

Conductor casing is usually the primary structural component of the well and supports the wellhead, into which many or all of the subsequent casing and tubing strings are landed during installation, depending on the type of installation:

- Onshore wells. For onshore developments all casings and the production tubing usually have their upper terminus in a profile in the surface wellhead (except for liners).
- Offshore platform wells. If an offshore development is based on a fixed offshore structure, usually all of the casings will terminate in a wellhead located in the well bay of the structure. In some instances, in order to decrease the weight that must be supported by the platform, some casing may be landed in a hanger at the mudline and then tied back to the platform with a tubular string termed a riser. The conductor extends up to the well bay and supports the wellhead.
- Offshore floating structures (TLP,[3] spar[4]). For these deepwater structures only the production tubing extends to the surface. It is possible to extend the A (production tubing) and B (production casing) annuli to the platform, but the extension is accomplished with risers, design of which, especially for fatigue, is outside the bounds of conventional casing and tubing design. The conductor terminates a few feet/meters above the mudline and supports those casings which are terminated at that point. The conductor supports a wellhead at the mudline into which subsequent strings are landed in profiles.
- Offshore subsea completions. In subsea completions the gathering system for produced fluids is usually a manifold setting on the sea floor. The conductor supports a subsea wellhead and all casings and tubing which are extended to the mudline.

Particularly in offshore locations the conductor is exposed to environmental loads that are the purview of the structural engineering team designing the platform and risers—essentially from the mudline upward.

Often the conductor casing is preceded by a structural casing string intended to stabilize loose or weak near-surface formations and provide a means of circulating drilling fluid.

The conductor can be driven, or it can be drilled and cemented. In the latter case it is usually cemented to the surface or mudline. In either case, it serves as a receptacle for the surface casing, including the wellhead to which the surface casing is attached.[5]

1.3.1.2 Surface casing

The surface casing serves several purposes:

[3] Tension-leg platform.

[4] A moored offshore structure similar in shape to a large buoy.

[5] In subsea completions a low pressure wellhead is normally attached to the conductor casing. The surface casing is attached to the high pressure wellhead.

- acting in concert with the conductor to provide both axial and lateral structural integrity;
- supporting the wellhead to which it is usually attached;
- isolating shallow fresh water aquifers;
- isolating shallow formations which may be weak or overpressured.

The surface casing is the string to which the blowout preventer (BOP) is attached. If more than one string of surface casing is necessary, the second string is often landed in a supplemental adaptor installed in the first string, to preserve profile and seal room in the wellhead for the casing strings to follow. The surface casing is often cemented to the surface or mudline.

1.3.1.3 Intermediate casing

Intermediate (sometimes called drilling) casing refers to all strings between the surface casing and production casing and is therefore the primary casing used to penetrate the reservoir overburden. Multiple intermediate strings may be necessary to allow adjusting drilling fluid density when drilling subsequent hole sections. Intermediate casing serves as a barrier to both weak (both mechanically and chemically) formation rock and abnormally (either high or low) pressured zones, and is particularly important in traversing a transition between pressure gradients (see Section 13.2 of Chapter 13).

1.3.1.4 Production casing

Depending on the type of completion in the reservoir, production casing will penetrate, and may traverse, the reservoir formation. To the degree that the production casing penetrates the reservoir, the casing, along with a cement sheath in the production casing annulus, serves to isolate the reservoir fluids from the results of drilling.

Perforations—post-installation holes in the production casing—provide communication between the reservoir and the interior of the wellbore, particularly the production tubing. A short distance above the perforations, the lower end of the tubing receives the produced fluids, the annulus of the production tubing being sealed with a packer.

The production casing also serves as an integral contributor to well completion. Temperature and pressure gauges, control lines, gas lift mandrels and other artificial lift equipment all may reside in the annulus between the production tubing and casing. The production casing also serves as an anchor for packers and may, if a packer is not present, constitute the primary path of hydrocarbons to the surface.

In a typical well the production casing serves as one element of the secondary well barrier during production [3].

1.3.1.5 Production tubing

In most wells the production tubing is the conduit for fluids from the reservoir to the surface or mudline. It is the most important tubular to size (see Section 13.4 of Chapter 13), as inefficiency in flow will affect the economics of the well and its parent project.

Because of its proximity to reservoir hydrocarbons the tubing may require special metallurgy or, as a minimum, a corrosion-resistant lining. Further, as it serves as an element of the primary well barrier during production, the tubing should be machined with a threaded connection that has sufficient leak integrity in service to avoid the exposure of other, less metallurgically robust tubulars.

Although remedial action, such as removing and replacing a portion of a tubing string, can be costly, the tubing is the one tubular string in the well installed with the knowledge that it may be removed in the future. Wear (sucker rod pumps), corrosion and low-cycle fatigue from repeatedly producing and shutting-in a well all serve to lower the desired life of a tubing string.

It is possible for a well to have no tubing string, or for the production tubing and production casing to be the same string [4]. A number of fields in the mid-continental United States use so-called tubingless completions in the recovery of gas from low permeability formations. Using a size range (3.500–4.500 in. or 88.9–114.3 mm) such a wellbore can provide sufficient cross-section for massive hydraulic fracturing and, following, accommodate the produced gas.

1.3.2 Differentiation by interval

In addition to function, tubular strings can also be characterized by their top and bottom locations.

1.3.2.1 Long string

The term "long string" simply refers to a single tubular string run from the bottom of the current hole section up to the wellhead. This construction technique results in a simple well design but, depending on the clearance with the previous casing, may have collateral effects associated with the hydrodynamic pressure required to cement such a long annulus.

1.3.2.2 Liner

A liner is a casing string that, rather than extending back to the wellhead, is landed with its top inside a previous casing and its bottom still reaching into the next hole section. Liners are connected to the previous casing by slips which penetrate the wall of that casing. Further a liner top packer can be run to better assure isolation of pressure and fluids in the annulus.

Table 1.1 Comparison of long string with liner/tieback solutions

Issue	Long string	Liner/Tieback
Cost		Less expensive (if no tieback is necessary)
Rig hook load capacity	Entire string is run at once	Tubulars are run in two "parts"
Cementing	A long, continuous fluid column may be difficult to achieve	Cementing the tieback, when performed, avoids any open hole issues
Component reliability	Primary concern is connections	Liner hanger, liner top packer and receptacle for tieback are additional components A trapped, inaccessible annulus may be created (a) adjacent to the polished bore in the tieback and (b) below the hanger in the liner
Collateral design issues	String is in greater tension	
	All previous strings are isolated	Previous strings are subject to additional loads until a tieback is run[a]

[a] See discussions in Sections 12.7.1.1, 12.7.1.2, 12.7.1.3 and 12.8.1.1 of Chapter 12.

1.3.2.3 Tieback

A tieback extends a previously run liner to the wellhead. The tieback may or not be cemented although it is typically sealed at its lower end to provide a continuous conduit with the liner it extends.

The liner/tieback combination is a viable alternative to a long string. Both choices, however, possess favorable and unfavorable aspects as listed in Table 1.1.

1.3.2.4 Scab liner

A scab liner is a liner which is installed completely within previously run casing. A scab liner might be run as a remediation on a previously damaged tubular, or it might be run as an aid in preventing damage. An example of the latter application is to create a concentric configuration to counter nonuniform loading opposite a mobile formation (see Section 8.3 of Chapter 8).

Of concern with a scab liner is the associated reduction in hole size. This reduction may affect access to the wellbore below the liner and, depending on whether the scabbed string is the production casing, the ability to implement artificial lift or other completion practices associated with the production tubing annulus.

Table 1.2 Base units for USC and SI unit systems[a]

Quantity	USC unit	SI unit	Unit designator[b]
Length	foot (ft)	meter (m)	L
Mass	pound mass (lb_m)	kilogram (kg)	M
Time	second (s)	second (s)	T
Temperature	rankine (R)	kelvin (K)	Θ
Amount	lb_m mole	mole (mol)	N

[a] HYB units are a mixture of USC and SI.
[b] See Symbols section in front matter of the book.

1.4. UNIT SYSTEMS

Within petroleum-based tubular mechanics three unit systems are popular:

1. US Customary (USC). This unit system is primarily used in the United States.
2. International System (SI[6]). This modern version of the metric system is used extensively throughout a large portion of the world, but less so in petroleum applications.
3. Hybrid (HYB). The name and abbreviation are of this author. A hybrid mixture of USC with SI units for length and possibly pressure gradient is common in both Europe, South America and the Middle East.

A starting point for defining a unit system is the collection of base units. In the SI system base units are defined for length, mass, time, temperature, electric current, luminous intensity and amount of substance [5]. All other units are derived from these base units. The base units pertinent to this book for the USC and SI unit systems are summarized in Table 1.2.

The last column of Table 1.2 lists designators for the base units. The Symbols section in the front matter preceding this chapter uses these designators to indicate the base units comprising the derived units used in this book.

Conversion factors between quantities in the three unit systems follow in Tables 1.3–1.16. In using the tables:

- Multiply a USC quality in the first column times the number in the second column to arrive at the equivalent SI quantity in the third column. Example using Table 1.3: 9.625 in. × 25.4 = 244.475 mm.
- Multiply an SI quality in the third column times the number in the fourth column to arrive at the equivalent USC quantity in the fifth column. Example using Table 1.3: 30 m × 3.28084 = 98.4252 ft.
- The lower sections of some tables include conversion factors for units in the same unit system. These rows may be used as described in the above bullets by simply ignoring the column headings referring to USC and SI units. Example using Table 1.3: 24 in. × (1/12) = 2 ft.

[6] Système international d'unités.

Table 1.3 Unit conversions for the base unit length[a]

USC unit	×[b]	SI unit	×[c]	USC unit
inch (in.)	25.4	millimeter (mm)	0.039 370 08	inch
inch (in.)	2.54	centimeter (cm)	0.393 700 8	inch
inch (in.)	0.0254	meter (m)	39.370 08	inch
foot (ft)	0.3048	meter (m)	3.280 84	foot
USC units to USC units				
inch (in.)	$\frac{1}{12}$	foot (ft)	12	inch
SI units to SI units				
millimeter (mm)	0.001	meter (m)	1000	millimeter
centimeter (cm)	0.01	meter (m)	100	centimeter

[a] Underlined conversion factors are exact.
[b] Example: 1 inch = 25.4 millimeters.
[c] Example: 1 millimeter = 0.03937008 inches.

Table 1.4 Unit conversions for the derived unit area[a]

USC unit	×[b]	SI unit	×[c]	USC unit
square inch (in^2)	645.16	square millimeter (mm^2)	0.001 550 003 1	square inch
square inch (in^2)	6.4516	square centimeter (cm^2)	0.155 000 31	square inch
square foot (ft^2)	0.092 903 04	square meter (m^2)	10.763 910 417	square foot
USC units to USC units				
square inch (in^2)	$\frac{1}{144}$	square foot (ft^2)	144	square inch
SI units to SI units				
square millimeter (mm^2)	1×10^{-6}	square meter (m^2)	1×10^{6}	square millimeter
square centimeter (cm^2)	1×10^{-4}	square meter (m^2)	1×10^{4}	square centimeter

[a] Underlined conversion factors are exact.
[b] Example: 1 square inch = 645.16 square millimeters.
[c] Example: 1 square millimeter = 0.001 550 003 1 square inches.

1.4.1 Force and mass

Confusion sometimes exists over the conversion between force f and mass m. In the context of unit systems, mass, the quantity of substance, is the more primitive quantity and is related to force through the equation

$$f \propto ma, \tag{1.1}$$

where acceleration a is defined in terms of the length and time primitives, $a = L/\tau^2$. This implies that the units of force in the USC unit system are pound mass ×

Table 1.5 Unit conversions for the derived unit dry volume[a]

USC unit	×[b]	SI unit	×[c]	USC unit
cubic foot (ft^3)	0.028 316 85	cubic meter (m^3)	35.314 666 721	cubic foot
USC units to USC units				
cubic inch (in^3)	$\frac{1}{1728}$	square foot (ft^3)	1728	cubic inch
SI units to SI units				
cubic millimeter (mm^3)	1×10^{-9}	cubic meter (m^3)	1×10^{9}	cubic millimeter
cubic centimeter (cm^3)	1×10^{-6}	cubic meter (m^3)	1×10^{6}	cubic centimeter

[a] Underlined conversion factors are exact.
[b] Example: 1 cubic foot = 0.028 316 85 cubic meters.
[c] Example: 1 cubic meter = 35.314 666 721 cubic feet.

Table 1.6 Unit conversions for the derived unit wet volume[a]

USC unit	×[b]	SI unit	×[c]	USC unit
gallon (gal)	0.003 785 411 784	cubic meter (m^3)	264.172 052 36	gallon
gallon (gal)	3.785 411 784	liter (L)	0.264 172 052 36	gallon
barrel (bbl)	0.158 987 3	cubic meter (m^3)	6.289 810 770 4	barrel
barrel (bbl)	158.9873	liter (L)	0.006 289 810 770 4	barrel
USC units to USC units				
gallon (gal)	$\frac{1}{42}$	barrel (bbl)	42	gallon
gallon (gal)	0.133 680 555 56	cubic foot (ft^3)	7.480 519 480 5	gallon
barrel (bbl)	5.614 583 333 4	cubic foot (ft^3)	0.178 107 606 68	barrel
SI units to SI units				
liter (L)	0.001	cubic meter (m^3)	1000	liter

[a] Underlined conversion factors are exact.
[b] Example: 1 gallon = 0.003 785 411 784 cubic meters.
[c] Example: 1 cubic meter = 264.172 052 36 gallons.

foot/second^2 ($\frac{lb_m\,ft}{s^2}$). Similarly, in the SI system the units for force would be kilogram × meter/second^2 ($\frac{kg\,m}{s^2}$). We prefer, however, to have unique units for force, examples being pound force (lb_f, USC system) and newton N (N, SI system). To accommodate this preference, we may do the following:

- Define the force unit. In the USC system, for example, the pound force is defined as the force of gravitational attraction of the earth on a pound mass (lb_m) of material, where the acceleration of gravity is taken to be 32.1740 feet per second squared ($\frac{ft}{s^2}$). A newton, however, is defined at the force necessary accelerate a kilogram of mass at the rate of one meter per second squared ($\frac{m}{s^2}$).
- Introduce a proportionality constant into Equation (1.1).

Table 1.7 Unit conversions for the derived unit velocity[a]

USC unit	×[b]	SI unit	×[c]	USC unit
inch per second ($\frac{\text{in}}{\text{s}}$)	2.54	centimeter per second ($\frac{\text{cm}}{\text{s}}$)	0.3937008	inch per second
inch per second ($\frac{\text{in}}{\text{s}}$)	0.0254	meter per second ($\frac{\text{m}}{\text{s}}$)	39.37008	inch per second
foot per second ($\frac{\text{ft}}{\text{s}}$)	0.3048	meter per second ($\frac{\text{m}}{\text{s}}$)	3.28084	foot per second
USC units to USC units				
inch per second ($\frac{\text{in}}{\text{s}}$)	$\frac{1}{12}$	foot per second ($\frac{\text{ft}}{\text{s}}$)	12	inch per second
SI units to SI units				
centimeter per second ($\frac{\text{cm}}{\text{s}}$)	0.01	meter per second ($\frac{\text{m}}{\text{s}}$)	100	centimeter per second

[a] Underlined conversion factors are exact.
[b] Example: 1 inch per second = 2.54 centimeters per second.
[c] Example: 1 centimeter per second = 0.3937008 inches per second.

Table 1.8 Unit conversions for the derived unit acceleration[a]

USC unit	×[b]	SI unit	×[c]	USC unit
inch per second squared ($\frac{\text{in}}{\text{s}^2}$)	2.54	centimeter per second squared ($\frac{\text{cm}}{\text{s}^2}$)	0.3937008	inch per second squared
inch per second squared ($\frac{\text{in}}{\text{s}^2}$)	0.0254	meter per second squared ($\frac{\text{m}}{\text{s}^2}$)	39.37008	inch per second squared
foot per second squared ($\frac{\text{ft}}{\text{s}^2}$)	0.3048	meter per second squared ($\frac{\text{m}}{\text{s}^2}$)	3.28084	foot per second squared
USC units to USC units				
inch per second squared ($\frac{\text{in}}{\text{s}^2}$)	$\frac{1}{12}$	foot per second squared ($\frac{\text{ft}}{\text{s}^2}$)	12	inch per second squared
SI units to SI units				
centimeter per second squared ($\frac{\text{cm}}{\text{s}}$)	0.01	meter per second squared($\frac{\text{m}}{\text{s}^2}$)	100	centimeter per second squared

[a] Underlined conversion factors are exact.
[b] Example: 1 inch per second squared = 2.54 centimeters per second squared.
[c] Example: 1 centimeter per second squared = 0.3937008 inches per second squared.

In the USC system, Eq. (1.1) becomes

$$1\ \text{lb}_\text{f} = \frac{1}{g_c} \times 1\ \text{lb}_\text{m} \times 32.1740\ \frac{\text{ft}}{\text{s}^2}. \tag{1.2}$$

From Eq. (1.2)

$$g_c = 32.1740\ \frac{\text{lb}_\text{m}\,\text{ft}}{\text{lb}_\text{f}\,\text{s}^2}. \tag{1.3}$$

Table 1.9 Unit conversions for the derived unit volumetric flow rate[a]

USC unit	×[b]	SI unit	×[c]	USC unit
gallon per minute (gpm)[d]	0.000 063 090 2	cubic meter per second ($\frac{m^3}{s}$)	15 850.3	gallon per minute
gallon per minute (gpm)[d]	0.063 090 2	liter per second ($\frac{L}{s}$)	15.8503	gallon per minute
barrel per minute (bpm)[e]	0.002 649 788 2	cubic meter per second ($\frac{m^3}{s}$)	377.3886	barrel per minute
barrel per minute (bpm)[e]	2.649 788 2	liter per second ($\frac{L}{s}$)	0.377 388 6	barrel per minute
USC units to USC units				
gallon per minute (gpm)[d]	$\underline{\frac{1}{42}}$	barrel per minute (bpm)[e]	$\underline{42}$	gallon per minute
gallon per minute (gpm)[d]	34.2857	barrel per day (bpd)[e]	0.029 166 7	gallon per minute
SI units to SI units				
liter per second ($\frac{L}{s}$)	$\underline{0.001}$	cubic meter per second ($\frac{m^3}{s}$)	$\underline{1000}$	liter per second

[a] Underlined conversion factors are exact.
[b] Example: 1 gallon per minute = 0.000 063 090 2 cubic meters per second.
[c] Example: 1 cubic meter per second = 15 850.3 gallons per minute.
[d] 1 gpm = 1 $\frac{gal}{min}$.
[e] 1 bpm = 1 $\frac{bbl}{min}$; 1bpd = 1 $\frac{bbl}{d}$.

Table 1.10 Unit conversions for the derived unit curvature[a]

USC unit	×[b]	SI unit	×[c]	USC unit
radian per foot ($\frac{rad}{ft}$)	$\underline{3.280\,84}$	radian per meter ($\frac{rad}{m}$)	$\underline{0.3048}$	radian per foot
degree per foot ($\frac{°}{ft}$)	$\underline{3.280\,84}$	degree per meter ($\frac{°}{m}$)	$\underline{0.3048}$	degree per foot
degree per 100 foot ($\frac{°}{100\ ft}$)	0.984 252	degree per 30 meter ($\frac{°}{30\ m}$)	1.016	degree per 100 foot
USC units to USC units				
degree per 100 foot ($\frac{°}{100\ ft}$)	$1.745\,329 \times 10^{-4}$	radian per foot ($\frac{rad}{ft}$)	5729.578	degree per 100 foot
SI units to SI units				
degree per 30 meter ($\frac{°}{30\ m}$)	$5.817\,764 \times 10^{-4}$	radian per meter ($\frac{rad}{m}$)	1718.873	degree per 30 meter

[a] Underlined conversion factors are exact.
[b] Example: 1 radian per foot = 3.280 84 radians per meter.
[c] Example: 1 radian per meter = 0.3048 radians per foot.

Table 1.11 Unit conversions for the base unit mass[a]

USC unit	×[b]	SI unit	×[c]	USC unit
pound mass (lb_m)	453.592 37	gram (g)	0.002 204 623	pound mass
pound mass (lb_m)	0.453 592 37	kilogram (kg)	2.204 623	pound mass

[a] Underlined conversion factors are exact.
[b] Example: 1 pound mass = 453.592 37 grams.
[c] Example: 1 kilogram = 2.204 623 pounds mass.

Table 1.12 Unit conversions for the derived unit mass density[a]

USC unit	×[b]	SI unit	×[c]	USC unit
pound mass per gallon ($p_m pg$)[d]	119.8264	kilogram per cubic meter ($\frac{kg}{m^3}$)	0.008 345 405	pound mass per gallon
pound mass per gallon ($p_m pg$)[d]	0.119 826 4	gram per cubic centimeter ($\frac{g}{cm^3}$)	8.345 405	pound mass per gallon
pound mass per gallon ($p_m pg$)[d]	0.119 826 4	specific gravity (SG)[e]	8.345 405	pound mass per gallon

[a] Underlined conversion factors are exact.
[b] Example: 1 pound mass per gallon = 119.8264 kilograms per cubic meter.
[c] Example: 1 kilogram per cubic meter = 0.008 345 405 pounds mass per gallon.
[d] 1 $p_m pg = 1\ \frac{lb_m}{gal}$.
[e] 1 SG = 1 $\frac{g}{cm^3}$ at standard temperature (273.15 K) and pressure (100 kPa).

Table 1.13 Unit conversions for the derived unit force[a]

USC unit	×[b]	SI unit	×[c]	USC unit
pound force (lb_f)	4.448 222	newton (N)	0.224 808 9	pound force

[a] Underlined conversion factors are exact.
[b] Example: 1 pound force = 4.448 222 newtons.
[c] Example: 1 newton = 0.224 808 9 pounds mass.

In the SI system, Eq. (1.1) becomes

$$1\,\mathrm{N} = \frac{1}{g_c} \times 1\,\mathrm{kg} \times 1\,\frac{\mathrm{m}}{\mathrm{s}^2}, \tag{1.4}$$

and from Eq. (1.4)

$$g_c = 1\,\frac{\mathrm{kg\,m}}{\mathrm{N\,s}^2}. \tag{1.5}$$

Each new unit system that we investigate will require a new definition of g_c.

In the remainder of this book we will continually use the constant g_c when necessary to properly convert between units of force and mass.

Finally, consider the difference between Eq. (1.1) when applied to converting mass to weight for the two instances considered in this example. For the USC system, the

Table 1.14 Unit conversions for the derived unit pressure[a]

USC unit	×[b]	SI unit	×[c]	USC unit
pound force per square inch (psi)	6894.757	newton per square meter ($\frac{N}{m^2}$)	0.000 145 037 7	pound force per square inch
pound force per square inch (psi)	6894.757	pascal (Pa)	0.000 145 037 7	pound force per square inch
pound force per square inch (psi)	6.894 757	kilopascal (kPa)	0.145 037 7	pound force per square inch
pound force per square inch (psi)	0.006 894 757	megapascal (MPa)	145.0377	pound force per square inch
pound force per square inch (psi)	0.068 947 57	bar (bar)	14.503 77	pound force per square inch
SI units to SI units				
pascal (Pa)	1	newton per square meter ($\frac{N}{m^2}$)	1	pascal
kilopascal (kPa)	1000	pascal (Pa)	0.001	kilopascal
megapascal (MPa)	10^6	pascal (Pa)	10^{-6}	megapascal
bar (bar)	10^5	pascal (Pa)	10^{-5}	bar

[a] Underlined conversion factors are exact.
[b] Example: 1 pound force per square inch = 6894.757 Newtons per square meter.
[c] Example: 1 Newton per square meter = 0.000 145 037 7 pounds force per square inch.

weight of 1 lb_m is

$$\frac{1}{32.1740\ \frac{lb_m\ ft}{lb_f\ s^2}} \times 1\ lb_m \times 32.1740\ \frac{ft}{s^2} = 1\ lb_f, \tag{1.6}$$

whereas in the SI system, the weight of 1 kg is

$$\frac{1}{1\ \frac{kg\ m}{N\ s^2}} \times 1\,kg \times 9.806\,64\ \frac{m}{s^2} = 9.806\,64\,N. \tag{1.7}$$

1.4.1.1 Example problem—compute g_c using inch for length in a USC system

Often commercial software has no inherent unit system but expects the user to input data in "consistent" units, that is, values that use only the base units. For example, one might work a finite element problem for a tubular with such a code. If so, it is often the case for tubular problems that inches are a better length choice than feet. Assuming that is the case, compute g_c for working problems in a system where the base unit for length is inches.

Table 1.15 Unit conversions for the derived unit pressure gradient[a]

USC unit	×[b]	SI unit	×[c]	USC unit
pound force per square inch per foot ($\frac{\text{psi}}{\text{ft}}$)	$2.262\,059 \times 10^4$	newton per square meter per meter ($\frac{\text{N}}{\text{m}^2\,\text{m}}$)	$4.420\,749 \times 10^{-5}$	pound force per square inch per foot
pound force per square inch per foot ($\frac{\text{psi}}{\text{ft}}$)	$2.262\,059 \times 10^4$	pascal per meter ($\frac{\text{Pa}}{\text{m}}$)	$4.420\,749 \times 10^{-5}$	pound force per square inch per foot
pound force per square inch per foot ($\frac{\text{psi}}{\text{ft}}$)	22.620 59	kilopascal per meter ($\frac{\text{kPa}}{\text{m}}$)	0.044 207 49	pound force per square inch per foot
pound force per square inch per foot ($\frac{\text{psi}}{\text{ft}}$)	0.022 620 59	megapascal per meter ($\frac{\text{MPa}}{\text{m}}$)	44.207 49	pound force per square inch per foot
USC units to USC units				
pound force per square inch per foot ($\frac{\text{psi}}{\text{ft}}$)	0.051 948 05	pound force per gallon (ppg)	19.250 00	pound force per square inch per foot
SI units to SI units				
pascal per meter ($\frac{\text{Pa}}{\text{m}}$)	1	newton per square meter per meter ($\frac{\text{N}}{\text{m}^2\,\text{m}}$)	1	pascal per meter
kilopascal per meter ($\frac{\text{kPa}}{\text{m}}$)	1000	pascal per meter ($\frac{\text{Pa}}{\text{m}}$)	0.001	kilopascal per meter
megapascal per meter ($\frac{\text{MPa}}{\text{m}}$)	10^6	pascal per meter ($\frac{\text{Pa}}{\text{m}}$)	10^{-6}	megapascal per meter

[a] Underlined conversion factors are exact.
[b] Example: 1 pound force per square inch per foot = $2.262\,059 \times 10^4$ Newtons per square meter per meter.
[c] Example: 1 Newton per square meter per meter = $4.420\,749 \times 10^{-5}$ pounds force per square inch per foot.

Table 1.16 Unit conversions for the base unit temperature[a]

USC unit	×[b]	SI unit	×[c]	USC unit
Rankine	0.555 555 56	Kelvin	1.8	Rankine

[a] Underlined conversion factors are exact.
[b] Example: 1 Rankine =0.555 555 56 Kelvin.
[c] Example: 1 Kelvin = 1.8 Rankine.

Returning to Eq. (1.2) and using Table 1.3 to convert the acceleration of gravity to inches per second squared

$$1\ \text{lb}_\text{f} = \frac{1}{g_c} \times 1\ \text{lb}_\text{m} \times 32.1740\ \frac{\text{ft}}{\text{s}^2} \times 12\ \frac{\text{in}}{\text{ft}}$$
$$= 386.088 \frac{1}{g_c} \frac{\text{lb}_\text{m}\,\text{in}}{\text{s}^2}, \tag{1.8}$$

or $g_c = 386.088\ \frac{\text{lb}_\text{m}\,\text{in}}{\text{lb}_\text{f}\,\text{s}^2}$.

1.4.1.2 Example problem—compute g_c using slug for mass in a USC system

An alternate mass unit for USC unit systems is the slug, which is defined as the mass that accelerates 1 $\frac{\text{ft}}{\text{s}^2}$ when acted on by a force of 1 lb_f. Compute g_c for working problems in a system where the base unit for mass is a slug.

In a manner similar to Eq. (1.2), from the definition of a slug we may write

$$1\ \text{lb}_\text{f} = \frac{1}{g_c} \times 1\ \text{slug} \times 1\ \frac{\text{ft}}{\text{s}^2}. \tag{1.9}$$

or $g_c = 1\ \frac{\text{slug}\,\text{ft}}{\text{lb}_\text{f}\,\text{s}^2}$. The weight of 1 slug is

$$\frac{1}{1\ \frac{\text{slug}\,\text{ft}}{\text{lb}_\text{f}\,\text{s}^2}} \times 1\ \text{slug} \times 32.1740\ \frac{\text{ft}}{\text{s}^2} = 32.1740\ \text{lb}_\text{f}. \tag{1.10}$$

1.4.2 Conversion of temperature units

Conversion of the standard temperature units does not lend itself to the tabular format used above for other quantities. Let [°F] be the temperature value in degrees Fahrenheit, [°C] be the temperature value in degrees Celsius, [R] be the temperature value in Rankine and [K] be the temperature value in Kelvin. Then absolute zero is [R] = [K] = 0 and

$$[\text{R}] = [^\circ\text{F}] + 459.67, \tag{1.11}$$
$$[\text{K}] = [^\circ\text{C}] + 273.15, \tag{1.12}$$
$$[^\circ\text{C}] = ([^\circ\text{F}] - 32) \times \frac{5}{9}, \tag{1.13}$$
$$[^\circ\text{F}] = [^\circ\text{C}] \times \frac{9}{5} + 32. \tag{1.14}$$

1.4.3 The gas constants

Calculations involving gas constituents can include either the universal gas constant $\mathcal{R}_u$ or the constant of an individual gas $\mathcal{R}$. The two are related by

$$\mathcal{R} = \frac{\mathcal{R}_u}{\mathcal{M}}, \tag{1.15}$$

where $\mathcal{M}$ is the molecular mass of the gas. A few comments are in order:

- $\mathcal{R}_u$ is truly universal (applicable to all gases), its value depending only on the unit system. For USC units, $\mathcal{R}_u = 1545.349\ \frac{\text{lb}_\text{f}\,\text{ft}}{\text{lb}_\text{m}\,\text{mol}\,\text{R}}$; for SI units, $\mathcal{R}_u = 8.314472\ \frac{\text{N}\,\text{m}}{\text{g}\,\text{mol}\,\text{K}}$.
- The mol appearing in the above constants is not actually a unit—it is an amount. A mol is the amount of a substance that contains as many particles as there are atoms in carbon-12 that, by definition, has an atomic mass of 12. That number is Avogadro's constant, $6.022\,140\,857 \times 10^{23}\ \frac{1}{\text{mol}}$. As an example, since the molecular mass of methane is 16.04, 16.04 lb_m of methane has the same number of molecules (Avogadro's constant) as 12 lb_m of carbon-12, and 16.04 g of methane has the same number of molecules as 12 g of carbon-12.
- Although the lb_m mol is still used in USC units, the term g mol has now been replaced with simply mol.
- The conversion from $\mathcal{R}_u$ to $\mathcal{R}$ involves dividing by the atomic mass of the gas (or gas mixture) in question. Using USC units as an example, since we are dividing "per lb_m mol" by molecular mass, this is the same as multiplying by the conversion factor $\frac{1}{\mathcal{M}}$ with units $\frac{\text{lb}_\text{m}\,\text{mol}}{\text{lb}_\text{m}}$. Following the conversion, we are no longer dealing with Avogadro's constant amount of substance, but rather the amount of substance that has a mass of 1 lb_m. That is, again using methane, $\mathcal{R}$ (with units $\frac{\text{lb}_\text{f}\,\text{ft}}{\text{lb}_\text{m}\,\text{R}}$ is addressing 1/16.04 as many molecules as $\mathcal{R}_u$, and that amount of substance has a mass of 1 lb_m.

1.5. NOTATION

Throughout the book use is made of three orders of tensors:

- Zeroth order tensors. Scalars such as temperature T and hydrostatic pressure p are denoted by lightface letters.
- First order tensors. Vectors such as displacement $\mathbf{u}$ and force $\mathbf{f}$ are denoted by lowercase boldface letters. Exception is the initial position vector of a material point in the global coordinate system, which is $\mathbf{X}$.
- Second order tensors. Stress $\mathbf{S}$, strain $\mathbf{E}$ and deformation gradient $\mathbf{F}$ are denoted by uppercase boldface letters.

The term "tensor" is proper for all of the above quantities. In use, however, tensor operations often resemble those of matrix algebra. The term "matrix" must be avoided in general because all matrices are not tensors. In math, a matrix is simply a rectangular array of numbers, whereas a tensor obeys certain transformation rules. Appendix A provides a more detailed discussion of zeroth, first and second order tensors and the tensor operations employed in this book. Even the seasoned reader should at least scan this appendix to view the manipulations common to the discussion to follow.

Whenever possible, equations will contain two forms—direct (coordinate-independent) and index notation. As an example, Newton's second law of motion

can be written in the alternate forms

$$\mathbf{f} = \frac{m}{g_c}\mathbf{a}, \quad f_i = \frac{m}{g_c}a_i, \tag{1.16}$$

where $\mathbf{f}$ is the force vector, m is mass (a scalar) and $\mathbf{a}$ is the acceleration vector. The left form of Newton's second law in Eq. (1.16) is written in direct notation. This equation is independent of the coordinate system with which one might be working. The right form of the law is written in index notation and shows the relation between the ith components of force and acceleration in a particular coordinate system. Appendix A contains a number of examples worked using these alternate expressions.

1.6. EXAMPLE PROBLEM CALCULATIONS

The book contains a number of worked examples, many involving floating point calculations. Some of these calculations have been worked using a hand calculator; other calculations employ a commercial spreadsheet; still others depend on a small computer program. If a reader employs a different tool(s) in attempting to match the book's values, it may be difficult to match every significant figure in an example, particularly for intermediate numerical results. Almost all calculations, however, should be the same to at least two, and often three significant digits.

CHAPTER 2

Design Summary

2.1. INTRODUCTION

Subsequent chapters detail the origin and development of the equations used in casing and tubing design. In those chapters the material is presented deliberately and with a view to unifying the variety of historical studies which have led to the current state-of-the-art. The fundamental concepts of kinematics and loads are combined via material constitution into low level, and fairly general, behavior of tubulars as solid mechanical components of the oil well. Specific limit states associated with internal and external pressure, axial loading and possible column buckling, and operational factors such as wear are then treated as applications of the fundamental concepts. A similar treatment is given to design loads. The presentation is from the general to the specific.

In this chapter the emphasis is on design. Here the governing equations are identical to those in the chapters to follow, but the presentation is a narrative that walks through the chronological implementation of the equations in a well design. Only the final forms of pertinent relations are presented, and these are limited to the relations actually used by the designing engineer. The remainder of the book is for the reader who requires a deeper discussion, either because of the uniqueness of the well's loads and/or resistance requirements, or in order to apply the principles covered to a new type of problem.

One's first exposure to this chapter should be accompanied by a coordinated review of Chapter 14. The current chapter is formal, presenting concepts and procedures in abbreviated form; Chapter 14 is intended to add flesh to the skeleton summary presented here.

2.2. INPUT DATA

As a minimum, a well design will begin with the following input data[1]:

- a distribution of pore pressure versus vertical depth;
- a distribution of fracture pressure versus vertical depth;
- a distribution of undisturbed temperature versus depth;
- a wellbore trajectory from the surface to the well target.

[1] The actual data package accompanying the initiation of a well will, in general, include a number of additional pieces of information—the reason for drilling the well, offset well (if available) experience, expected risks, etc.—all of which are important to the drilling engineer. The list provided here relates to the physical design of the well.

Elements of Oil and Gas Well Tubular Design
DOI: 10.1016/B978-0-12-811769-9.00002-5

Table 2.1 Design status following initial data collection

Task[a]	Calculations	Chapters	Knowns
Initial data collection	N/A[b]	N/A	Pore and fracture pressure distributions, temperature distribution, trajectory

[a] Completed rows highlighted in gray.
[b] Abandonment pressure and some estimate of reservoir fluid properties are useful when available.

Table 2.1 summarizes the status of the design following initial data collection. This is the first of several such tables indicating what should have been accomplished and what data should be available at each stage in the design. The design process is rarely this linear and can involve repeated visits to previous work. The general flow, however, is important and provides an overview of when specific data should be available for future design steps.

2.3. CASING SEAT DETERMINATION (SEE SECTION 13.3 OF CHAPTER 13)

Given the distributions of pore pressure and fracture pressure with vertical depth, plot the data with pressure gradient as the abscissa and vertical depth as the (axis pointing downward) ordinate. Adjust both curves inward for the effects of surge and swab pressure and uncertainty in the pressure distributions. Using this plot as a starting point, consider additional adjustments to the acceptable range of drilling fluid density by consideration of the following:

- differential sticking (Section 13.3.2.3 of Chapter 13);
- wellbore stability (Section 13.3.2.4 of Chapter 13);
- riser margin (Section 13.3.2.5 of Chapter 13).

All of the above should limit the acceptable drilling fluid density at each vertical depth according to the formula (Eq. (13.15)) reproduced here (see also Fig. 2.1)

$$\max \begin{Bmatrix} \gamma_p(Z) + \gamma_{sb}(Z) \\ \gamma_{wn}(Z) \\ \gamma_p(Z) + \gamma_{rm}(Z) \end{Bmatrix} \leq \gamma_f(Z) \leq \min \begin{Bmatrix} \gamma_{fr}(Z) - \gamma_{su}(Z) \\ \gamma_{ds}(Z) \\ \gamma_{wx}(Z) \end{Bmatrix}, \quad \begin{matrix} \text{base constraint} \\ + \text{ surge and swab margins} \\ + \text{ differential sticking limit} \\ + \text{ wellbore stability} \\ + \text{ riser margin} \end{matrix} . \tag{2.1}$$

In addition, the following considerations—formation mobility and/or chemical sensitivity (see Section 13.3.2.6 of Chapter 13) and government regulations (see Section 13.3.2.7 of Chapter 13)—may dictate that casing be set at a specific depth.

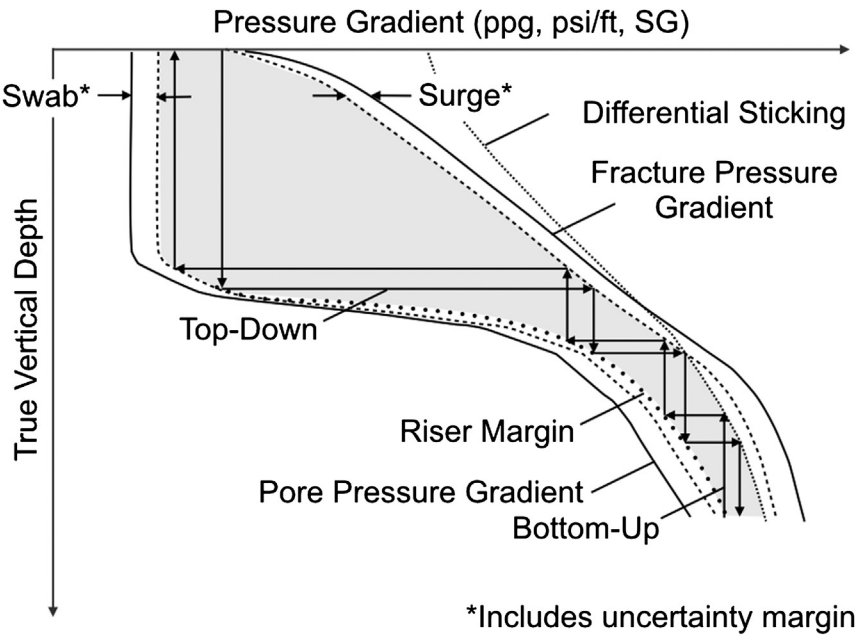

Figure 2.1 ***Casing seat selection—illustration of limitations on the acceptable range of drilling fluid density provided by Eq. (2.1).*** Either the "bottom-up" or the "top-down" method, or a combination of the two, can be used to determine casing seats.

With the above constraints, either the "bottom-up" or "top-down" method of casing seat selection (see Section 13.3.3 of Chapter 13) may be used.

Check each casing seat for its kick tolerance—see Section 13.3.4 of Chapter 13.

2.4. TUBULAR SIZING (SEE SECTION 13.4 OF CHAPTER 13)

The following are guidelines for sizing the production tubing and casing:

- Size the production tubing first, as it is the most important tubular determinant of well production rate. For tubing sizing considerations see Section 13.4.1 of Chapter 13. This task is usually the responsibility of production and completions engineers and is heavily tied to flow assurance considerations.
- Size the production casing. For production casing sizing considerations see Section 13.4.2 of Chapter 13.
- Size the intermediate and surface casing. Sizing of these strings follows the discussion (see Section 13.4.3 of Chapter 13) surrounding Table 13.4, reproduced here (see Table 2.2).

Table 2.3 summarizes the status of the design following casing seat selection and sizing.

Table 2.2 Casing diametric sizing—selection chart.[a, b] See Table 13.4 in Section 13.4.3 of Chapter 13 for details

Casing[c]	Bit or confining open hole size (in.)															
	4-3/4	5-7/8	6-1/8	6-1/2	7-7/8	8-1/2	8-3/4	9-1/2	10-5/8	12-1/4	14-3/4	17-1/2	20	22	26	33
3-1/2	C															
4	SC	C														
4-1/2		SC	C													
5			SC	C												
5-1/2	SB			SC	C											
6-5/8	B	SB			SC	C										
7		B	SB			C	C									
7-5/8			B	B		SC	SC	C								
7-3/4			B	B		SC	SC	C								
8-5/8				B	SB			SC	C							
9-5/8					B	B	SB		SC	C						
9-7/8					B	B	SB		SC	C						
10-3/4							B	B		SC	C					
11-3/4									B		C					
11-7/8									B		C					
13-3/8										B	SC	C				
13-5/8										B	SC	C				
14										B	SC	C				
16											B	SC	C	C	C	
18-5/8													SC	SC	C	
20												B			C	
24													B	B	C	
26																C
30															B	C
36																B

[a] C = standard clearance for running and cementing casing, SC = non-standard casing clearance, B = standard bit inside casing, SB = thinner casing wall to accommodate bit.

[b] Starting with the production casing size, search horizontally for a "C" or "SC", according to the desired annular clearance between the casing and its confining open hole. Then read the corresponding column heading to determine the bit/confining open hole size for this casing. Search vertically in this same column for previous casing sizes that can accommodate this bit, with either popular wall thicknesses ("B") or thinner walls ("SB"). Having selected a previous casing size, repeat the process to determine its bit/hole size. Continue until all casing sizes have been determined.

[c] Label 1 designation or outside diameter in inches.

Table 2.3 Design status following casing seat selection and tubular sizing

Task[a]	Calculations	Chapters	Knowns
Initial data collection	N/A[b]	N/A	Pore and fracture pressure distributions, temperature distribution, trajectory
Tubular sizing	Flow assurance and reservoir calculations to size tubing, DE/CE discussion to size production casing	13[c]	Length and diameter of each tubular string, which casings are long strings, liners and tiebacks, drilling fluid density for each hole section

[a] Completed rows highlighted in gray.
[b] Abandonment pressure and some estimate of reservoir fluid properties are useful when available.
[c] Possibly supplemented by Appendix C for directional wellbores.

Table 2.4 Example table of initial and load case states developed in preliminary calculations

Variable	MD	TVD	Initial	Load Case 1	Δ	Load Case 2	Δ
T_{top}	xx.xx	xx.xx	xx.xx	xx.xx	xx.xx	xx.xx	xx.xx
T_{TOC}	xx.xx	xx.xx	xx.xx	xx.xx	xx.xx	xx.xx	xx.xx
T_{bot}	xx.xx	xx.xx	xx.xx	xx.xx	xx.xx	xx.xx	xx.xx
$\overline{T}$[a]	N/A	N/A	xx.xx	xx.xx	xx.xx	xx.xx	xx.xx
p_{i-top}	xx.xx	xx.xx	xx.xx	xx.xx	xx.xx	xx.xx	xx.xx
p_{i-TOC}	xx.xx	xx.xx	xx.xx	xx.xx	xx.xx	xx.xx	xx.xx
p_{i-bot}	xx.xx	xx.xx	xx.xx	xx.xx	xx.xx	xx.xx	xx.xx
$\overline{p_i}$[a]	N/A	N/A	xx.xx	xx.xx	xx.xx	xx.xx	xx.xx
p_{o-top}	xx.xx	xx.xx	xx.xx	xx.xx	xx.xx	xx.xx	xx.xx
p_{o-TOC}	xx.xx	xx.xx	xx.xx	xx.xx	xx.xx	xx.xx	xx.xx
p_{o-bot}	xx.xx	xx.xx	xx.xx	xx.xx	xx.xx	xx.xx	xx.xx
$\overline{p_o}$[a]	N/A	N/A	xx.xx	xx.xx	xx.xx	xx.xx	xx.xx

[a] Average values are averages above cement top.

2.5. PRELIMINARY CALCULATIONS (SEE SECTIONS 12.5, 12.6, 12.7 AND 12.8 OF CHAPTER 12)

For the tube(s) being designed, obtain or determine/construct the following:

- The load cases to which the tubular will be subjected. Tables 2.6–2.8 can aid in selecting design loads. Once a load case is selected, Table 2.9 summarizes sections of Chapter 12 containing the appropriate equations for constructing a pressure load distribution.
- Construct a table of landmark depths (top of string, cross-over, top of cement, kick-off point, bottom of string) and the internal pressure, external pressure and temperature corresponding to those depths. A sample is Table 2.4:
  - the first column lists the variable names for temperature, internal pressure and external pressure that will be used in the design;

Table 2.5 Design status following preliminary calculations

Task[a]	Calculations	Chapters	Knowns
Initial data collection	N/A[b]	N/A	Pore and fracture pressure distributions, temperature distribution, trajectory
Tubular sizing	Flow assurance and reservoir calculations to size tubing, DE/CE discussion to size production casing	13[c]	Length and diameter of each tubular string, which casings are long strings, liners and tiebacks, drilling fluid density for each hole section
Preliminary calculations	Selection of load cases (including initial condition) and construction of load vs. depth table, graphical check of fidelity of load vs. depth table[d]	12	Detailed information on (pressure, temperature) load values for each load case

[a] Completed rows highlighted in gray.
[b] Abandonment pressure and some estimate of reservoir fluid properties are useful when available.
[c] Possibly supplemented by Appendix C for directional wellbores.
[d] Collection of company-specific design information—approved connections for different strings, design factors (see Table 2.14 for typical industry values), restrictions on metallurgy—are appropriate at this time.

  - the second and third columns record the depths—measured and, if deviated, vertical;
  - the fourth column lists the values of the variables from column 1 in the initial state (i.e., after WOC for casing, after setting packer for tubing);
  - the next columns appear in pairs for each load case—a value of the column 1 variable for the load case and a change column (Δ) to record pressure or temperature change as load case value minus initial value.
- Plot the tabulated values of temperature vs. depth, internal and external pressure vs. depth, and load case pressure differential vs. depth. This will both provide a sense check on the load case data and aid in the selection of a candidate tubular (see next bullet). Typical plots are shown in Figs. 14.2–14.4.
- The dimensions and strengths of the tubulars to be designed (D, t, k_{wall}, f_{ymn}, confining hole input; d, d_{wall}, A_i, A_o, A_s, r_c calculated). Save this step until after the load cases have been tabulated and plotted. Viewing the loads may make selection of a candidate for design easier by allowing a comparison between, for example, differential pressures and the vendor's internal and external pressure ratings.

The narrative of the design procedure continues in Section 2.7 following the preliminary calculations.

Table 2.5 summarizes the status of the design following preliminary calculations.

Table 2.6 Design load summary—surface and intermediate casing[a]

Load	Internal pressure	External pressure	Temperature	Table
Running in hole	RF	RF	G	12.1
Overpull	RF	RF	G	12.2
Initial conditions	RF	RF + SP + CMT	G	12.5
Pressure test	Test pressure + DF	RF	G	12.9
Well control	Fracture pressure at shoe – gas gradient above	One of several[b]	C	12.10
Drill ahead	DF	RF	C	12.11
Lost circulation	Empty to top of DF, then DF	RF	G or C	12.18
Riser margin[c]	SW to mudline, then DF	RF	G or C	12.19

[a] CMT = cement, DF = drilling fluid for next hole section, RF = running fluid, SP = spacer, SW = sea water, G = local geostatic, C = circulating.

[b] See the discussion at the beginning of Section 12.7 of Chapter 12 for external fluid alternatives.

[c] Deepwater wells only.

Table 2.7 Design load summary—production casing[a]

Load	Internal pressure	External pressure	Temperature	Table
Running in hole	RF	RF	G	12.1
Overpull	RF	RF	G	12.2
Initial conditions	RF	RF + SP + CMT	G	12.5
Pressure test	Test pressure + RF	RF	G	12.9
Tubing leak	Shut-in tubing pressure + PF	One of several[b]	G or P	12.12
Riser margin[c]	SW to mudline, then RF	RF	G or C	12.19
Packer leak	Empty to top of PF, then PF	RF	G	12.20
See also Section 12.7.2.3 for possible additional loads associated with other tubulars.				

[a] CMT = cement, PF = packer fluid, RF = running fluid, SP = spacer, SW = sea water, G = local geostatic, C = circulating, P = producing.

[b] See the discussion at the beginning of Section 12.7 of Chapter 12 for external fluid alternatives.

[c] Deepwater wells only.

2.6. DESIGN LOADS (SEE CHAPTER 12)

Design loads depend on the string being designed. Tables 2.6–2.8 summarize the design loads in terms of internal pressure, external pressure and temperature. For more information on a particular design load, see the referenced table in Chapter 12.

When building a design load—internal pressure, external pressure, temperature—Table 2.9 summarizes sections containing the appropriate equations for constructing a pressure load distribution.

Table 2.8 Design load summary—production tubing[a]

Load	Internal pressure	External pressure	Temperature	Table
Running in hole	CF	CF	G	12.3
Overpull	CF	CF	G	12.4
Initial conditions—mechanically-set packer	CF/PF	CF/PF	G	12.6
Initial conditions—hydraulic-set packer	Setting pressure + CF/PF	CF/PF	G	12.7
Initial conditions—hydrostatic-set packer	Setting pressure + CF/PF	Setting pressure + CF/PF	G	12.8
Pressure test	Test pressure + CF	PF	G	12.13
Injection	Injection wellhead pressure + IF	PF	I	12.14
Production	Flowing wellhead pressure + HC	PF	P	12.15
Pump in to kill well	Shut-in tubing pressure + kill margin + IF (start kill), steady state pump pressure + IF (end kill)	PF	I	12.16
Shut-in	Shut-in pressure + HC	PF	G or P	12.17
Annulus pressure test	CF	Test pressure + PF	G	12.21
Production from long term shut-in	Flowing tubing pressure + HC	Shut-in pressure + PF	G	12.22
Safety Valve Leak	Shut-in reservoir pressure at perforations – HC	Annulus pressure + PF (above packer)	G or P	12.23
Evacuation	Empty	PF	G or P	12.24
Consider possible additional loads associated with artificial lift.				

[a] CF = completion fluid, IF = injection fluid, PF = packer fluid, HC = reservoir fluid, G = local geostatic, I = injecting, P = producing.

2.7. DESIGN PROCEDURE

It is assumed that the preliminary data gathering and calculation steps of Section 2.5 are complete. That is, the initial condition and all load cases have been tabulated at landmark depths, along with the change in state between each load case and the initial condition—see Table 2.4.

The following design procedure is recommended, regardless of the tubular in focus:

Table 2.9 Construction of an internal or external pressure load

Fluid	Example[a]	Equation	Number	Comment
Single incompressible fluid	CF, CMT, DF, HC (if oil only), IF, PF, RF, SP, SW	$p_2 - p_1 = \frac{g}{g_c}\rho_{PF}\,(Z_2 - Z_1)$	(12.16)	Intended for hand calculations or simple spreadsheets.
Ideal gas	HC (if gas only), average T known	$p_2 = p_1 \exp\left[\frac{g}{g_c}\frac{1}{\mathcal{R}\overline{T}}\,(Z_2 - Z_1)\right]$	(12.20)	Use in hand calculations or simple spreadsheets. See example problem in section 'Example problem—ideal gas hydrostatic head' of Chapter 12.
Ideal gas	HC (if gas only), linear T distribution	$p_2 = p_1\left(1 + \frac{\gamma_T(Z_2 - Z_1)}{T_1}\right)^{\frac{g}{g_c}\frac{1}{\mathcal{R}\gamma_T}}$	(12.23)	Use in hand calculations or simple spreadsheets. See example problem in section 'Example problem—ideal gas hydrostatic head' of Chapter 12.
Real gas	HC (if gas only), linear T distribution	$p_2 = p_1 \exp\left[\frac{g}{g_c}\frac{1}{Z_c\mathcal{R}\overline{T}}\,(Z_2 - Z_1)\right]$	(12.31)	Use in spreadsheets or design software. See example problem in section 'Example problem—real gas hydrostatic head' of Chapter 12.

[a] CF = completion fluid, CMT = cement, DF = drilling fluid for next hole section, HC = hydrocarbon (reservoir) fluid, IF = injection fluid, PF = packer fluid, RF = running fluid, SP = spacer, SW = sea water.

Table 2.10 Summary of equations for potential length change

ΔL Source[a]	Equation	Number
Temperature	$\Delta L_T = \alpha_T \overline{\Delta T} L$	(11.8)
Ballooning	$\Delta L_B = -\frac{2\nu}{E} \frac{\overline{\Delta p_i} d^2 - \overline{\Delta p_o} D^2}{D^2 - d^2} L$	(11.10)
Shoulder	$\Delta L_S = \frac{[\Delta p_i (d_u^2 - d_l^2) + \Delta p_o (D_l^2 - D_u^2)] L}{E(D_u^2 - d_u^2)}$	(11.12)
Buckling[b]	$\Delta L_{Bu} = -\frac{r_c^2}{4EIw_{eff} \cos\theta} \left(-f_{eff2} + f_{cs}\right) \left(-0.3771 f_{eff2} + 0.3668 f_{cs}\right)$	(11.15)
Buckling[c]	$\Delta L_{Bu} = -\frac{r_c^2 \left(f_{eff2}^2 - f_{eff1}^2\right)}{8EIw_{eff} \cos\theta}$	(11.20)

[a] Each ΔL represents final state minus initial state.
[b] Only applicable if there is buckling and the mode is sinusoidal.
[c] Only applicable if there is buckling and the mode is helical.

1. Preinstallation loads. First check the loads that happen before the initial conditions event. These loads are different from those to follow in that only one end of the tube is fixed. Further, neither of the load cases—"Running in hole" (Section 12.5.1.1 for casing, Section 12.5.2.1 for tubing, both in Chapter 12) or "Overpull" (Section 12.5.1.2 for casing, Section 12.5.2.2 for tubing, both in Chapter 12)—is usually a design determinant. If the available grades and wall thicknesses cannot pass these load cases, or if their variables create issues for the assigned rig, a change of the well design may be in order.
2. For postinstallation loads compute the (potential) length changes due to temperature, ballooning and shoulder forces using pressure and temperature difference from the initial state to the final state. Assume column buckling does not occur. These calculations are aided by pressure and temperature tabulations similar to Table 2.4 and the length change formulas summarized in Table 2.10.
3. Initial conditions. Determine the initial state of the tubular string:
   (a) Using the information from Table 2.4 and the trial string, compute the initial axial force at the bottom of the string. Then compute the axial force along the string to the surface by adding the (hole inclination adjusted) air weight per length of the tubular in each segment between design landmarks. If the landmark is a cross over to a different geometry, calculate the net (inside and outside) shoulder force at the cross over.
   (b) Construct a table similar to Table 2.12 preparing two columns for each load case. For any landmark depths where a discontinuity in axial force can occur, create two rows—one above (+) and one below (–) the landmark.
   (c) Enter the initial axial force distribution in the table.
4. For each load case that follows the initial condition in time:

Table 2.11 Equations to map length change to change in axial force

Location	Equation	Number
Casing above TOC, tubing	$\Delta f_z = -\frac{EA_s \Delta L_{Total}}{L}$	(14.5)
Casing below TOC	$\Delta f_z = -EA_s \alpha_T \Delta T + 2\nu \left(\Delta p_i A_i - \Delta p_o A_o\right)$	(14.10)

$\Delta L_{Total} = \Delta L_T + \Delta L_B + \Delta L_S + \Delta L_{Bu}$.

Table 2.12 Example table of initial and load case axial loads

Location	Initial	Load Case 1		Load Case 2		Load Case 3	
		Increment	Total	Increment	Total	Increment	Total
Top[a]	xx.xx	xx.xx	xx.xx	xx.xx	xx.xx	xx.xx	xx.xx
TOC+[a]	xx.xx	xx.xx	xx.xx	xx.xx	xx.xx	xx.xx	xx.xx
TOC-[b]	xx.xx	xx.xx	xx.xx	xx.xx	xx.xx	xx.xx	xx.xx
Bottom[b]	xx.xx	xx.xx	xx.xx	xx.xx	xx.xx	xx.xx	xx.xx

[a] Use Section 14.2.3.1 of Chapter 14 for load case calculations.
[b] Use Section 14.2.3.2 of Chapter 14 for load case calculations.

(a) Compute the change in axial force corresponding to the total length change from temperature, ballooning and shoulder forces.[2] Table 2.11 summarizes the appropriate equations to use to map potential length change into change in axial force.

(b) Add the change in axial force from the previous step to the initial axial force and enter these values in Table 2.12 as "Increment" and "Total" , respectively.

5. Compute the effective force at any significant depths. For casing, at least check the top of cement; for tubing at least check the packer.

6. If the effective force is less than the critical buckling force, the string has buckled. Repeat steps 4 and 5, now including the length change due to buckling in the incremental axial force calculation. Follow this procedure until an acceptable convergence has been achieved.[3]

7. With the axial force table updated for the possible effects of buckling, compute the safety factors in the string at least at all landmark locations. Table 2.13 summarizes the design equations for limit states used in selecting a tube body. Table 2.14 summarizes typical design factors appearing in the industry for limit states that might

[2] Exception: If the string is production tubing landed in a packer allowing axial motion or the string is an uncemented tieback, skip this step. Instead, calculate the new axial force (in the same manner as the initial axial force was calculated in step 3.a) and enter this value under the "Total" column for each load case. The length changes previously calculated in step 2 are still valuable for determining tubing movement and required seal length in the seal assembly. If buckling is detected in step 6, add the length change due to buckling to the previously calculated total length change.

[3] This trial-and-error procedure can be ignored for many casing strings. The radial clearance between casings is usually small enough to prevent major column buckling. The procedure *cannot* be ignored for almost all tubing strings.

Table 2.13 Design equations for tube body limit states

Design limit state	Equation	Number
Yield[a]	$\hat{f}_{des}(r) = \left(\Sigma_{zz} - \frac{p_i d_{wall}^2 - p_o D^2}{D^2 - d_{wall}^2}\right)^2 + \frac{3}{16r^4}\left(\frac{(p_i - p_o) d_{wall}^2 D^2}{D^2 - d_{wall}^2}\right)^2 - f_{ymn}^2 = 0$	(6.95)
Internal pressure[b]	Included in yield design check	(6.95)
External pressure[c,d]	API collapse procedure, Section 8.2.4 of Chapter 8	(8.10)–(8.23)
Axial yield	Included in yield design check	(6.95)

[a] If $|\mathbf{m}| = 0$, check at $r = \frac{d_{wall}}{2}$; otherwise, replace Σ_{zz} with $\Sigma_a \pm \hat{\Sigma}_b(r) = \Sigma_a \pm \frac{|\mathbf{m}|r}{I}$ and check at $r = \frac{d_{wall}}{2}$, $\Sigma_b = \pm\frac{|\mathbf{m}|d_{wall}}{2I}$ and at $r = \frac{D}{2}$, $\Sigma_b = \pm\frac{|\mathbf{m}|D}{2I}$, using the largest of the latter four results.

[b] The ductile rupture equation can be used in addition to, rather than in replacement of, the design check for yield, a typical example being tube materials for which the margin between f_{ymn} and f_{umn} is small, i.e., high strength steels and solid expandable tubulars.

[c] Yield, as opposed to collapse, due to external pressure, is included in the yield design check.

[d] Should the collapse resistance be increased above the API rating with zero axial stress, ignore the increase.

Table 2.14 Typical design factors for tubular design

Limit State[a]	Tube body	Connection	Comment
Triaxial yield[b]	1.15–1.25[f]	N/A	Difficult to define for a threaded connection.
Internal yield pressure[c,e]	1.00–1.25		Rupture is typically not a design limit state.
Collapse[e]	1.00–1.10		Indicator of inherent conservatism in API collapse equations.
Tension[d]	1.30–1.60		Lower value corresponds to yield-based limit state; higher value corresponds to ultimate-based limit state.
Compression[d]	1.30–1.60	1.00	Lower value corresponds to yield-based limit state; higher value corresponds to ultimate-based limit state.

[a] All limit state design factors may be adjusted upward for tubing by a multiplying factor $k_{corr} \approx 1.10$ to account for corrosion. All limit states except collapse may be adjusted downward for tubing by a multiplying factor $k_{scc} \approx 1.10$ to account for a sour environment.

[b] Includes the limit states for internal yield pressure and yield in tension and compression.

[c] Does not account for bi-dimensional effects.

[d] Does not account for bi-dimensional effects. Recommended for threaded connections, and even then only if a manufacturer's evaluation envelope is not available.

[e] Should be adjusted upward for anticipated wear by a multiplying factor k_{wear}, where k_{wear} is the inverse of the fraction of remaining specified wall thickness under the anticipated wear groove, i.e., for 12% wall loss, $k_{wear} = 1/0.88 = 1.14$.

[f] The lower value usually applies when $k_{wall} = 0.875$; the higher value usually applies when $k_{wall} = 1.000$.

be encountered in a design. Of the limit states, those emphasized in this book are triaxial yield, collapse and a manufacturer's evaluation envelope for threaded connections.

8. Once the above steps yield a satisfactory combination of wall thickness and grade for the tube body, design of the threaded connection is in order. Individual load

Table 2.15 Design status following design procedure

Task[a]	Calculations	Chapters	Knowns
Initial data collection	N/A[b]	N/A	Pore and fracture pressure distributions, temperature distribution, trajectory
Tubular sizing	Flow assurance and reservoir calculations to size tubing, DE/CE discussion to size production casing	13[c]	Length and diameter of each tubular string, which casings are long strings, liners and tiebacks, drilling fluid density for each hole section
Preliminary calculations	Selection of load cases (including initial condition) and construction of load vs. depth table, graphical check of fidelity of load vs. depth table[d]	12	Detailed information on (pressure, temperature) load values for each load case
Design procedure	Compute preinstallation loads	12	Load values for installing tubular
	Compute initial condition, the state to which all post-installation loads are compared	12	Initial condition axial load
	Compute length change, axial load change and final axial load assuming no buckling	11, 14	Initial guess at axial loads for all load cases
	Check for buckling and, if necessary, iterate on axial load calculation	10, 11, 14	Final values of axial load for all load cases
	Use pressure, temperature and axial load for each landmark depth to determine tube resistance and safety factor; restart design procedure if tube is inadequate	6, 8	Tube design, ready for connection selection

[a] Completed rows highlighted in gray.
[b] Abandonment pressure and some estimate of reservoir fluid properties are useful when available.
[c] Possibly supplemented by Appendix C for directional wellbores.
[d] Collection of company-specific design information—approved connections for different strings, design factors (see Table 2.14 for typical industry values), restrictions on metallurgy—are appropriate at this time.

case values of pressures (particularly differential pressure) and temperature, together with final computations of axial force (see Section 9.4 of Chapter 9), are pertinent to connection selection, together with the following:

(a) maximum wellbore curvature;
(b) minimum radial clearance with confining hole;
(c) fluid medium to be sealed—liquid or gas (see Sections 9.5 and 9.6 of Chapter 9);

(d) potential for fatigue (tubulars run above the mudline in a dry tree installation);
(e) potential for loading above tube body yield (thermal wells);
(f) production or injection at high rates (see Section 9.7.1 of Chapter 9).

9. Whenever possible obtain a manufacturer's performance envelope (to be converted to a design envelope with appropriate design factors) for the connection to be used and compare its capacity to the design load cases. If no performance/design envelope is available, create one using the tension and compression, internal pressure and external pressure ratings of the connection and appropriate design factors (see Section 14.2.5 of Chapter 14).

Table 2.15 summarizes the status of the design following the design procedure.

CHAPTER 3

Kinematics

3.1. INTRODUCTION

Under the action of forces and/or force fields, a body can translate, rotate and deform. Translation, a motion in which all points of a body move with a common velocity vector, and rotation, revolution of all points in a body about a single, fixed location, are rigid body motions during which the distance between points is constant. With deformation, on the other hand, the distance between two points in the body is altered, that change being measured by a quantity called strain.

We begin with the definitions of the position and displacement of a point and then consider the possibility that adjacent points may have differing displacements. The resulting displacement gradients in a body can be described by various tensor quantities from deformation gradient to strain. With regard to the latter, several valid definitions exist of which we shall consider three—Lagrangian strain, Eulerian strain and logarithmic strain. Because of its importance in tubular design, work previously expressed in Cartesian (rectangular) coordinates is then reexpressed in cylindrical coordinates.

The developments previewed above are fairly general. A final section considers special cases of the strain tensor for axisymmetric and infinitesimal strain.

3.2. POSITION

Consider the current (spatial) position[1] $\mathbf{x}$ of a point in a deforming body[2] that is a function of its original (material) position $\mathbf{X}$ and time τ

$$\mathbf{x} = \hat{\mathbf{x}}(\mathbf{X}, \tau), \quad x_i = \hat{x}_i(X_I, \tau), \tag{3.1}$$

where the function $\hat{\mathbf{x}}$ and its inverse, $\mathbf{X} = \hat{\mathbf{X}}(\mathbf{x}, \tau)$, are assumed to be single-valued[3] and continuously differentiable[4] in their independent variables.

[1] See Appendix A for a review of tensors and the notation used in this book.

[2] Beginning, as we have, with the discussion of points in a Euclidean coordinate space, we bypass an assumption of kinematics that the ensemble of points $\mathbf{x}$ to which we refer is actually a configuration B of a body $\mathcal{B}$, where $\mathcal{B}$ is a collection of particles. We will not need this level of abstraction in our discussion. The interested reader can consult the chapter on Basic Kinematics in [6] or similar texts.

[3] Two material points $\mathbf{X_1}$ and $\mathbf{X_2}$ are not permitted to occupy the same location as the body deforms; nor is a single point $\mathbf{X_1}$ permitted to split into two points as the body deforms.

[4] Curves, surfaces and regions in the initial state remain curves, surfaces and regions in the deformed state [6].

Elements of Oil and Gas Well Tubular Design
DOI: 10.1016/B978-0-12-811769-9.00003-7

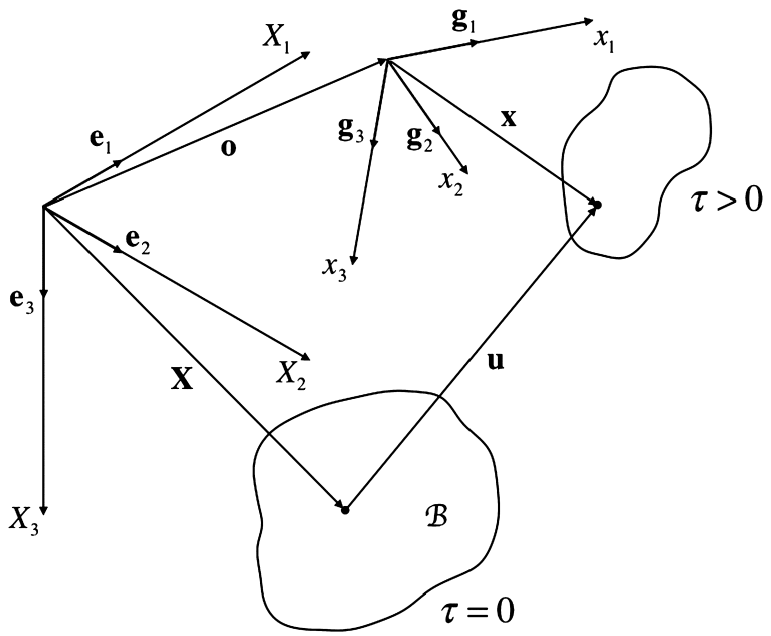

Figure 3.1 ***Illustration of the displacement of a point in the global coordinate system.*** X_1 is North, X_2 is East, X_3 is vertical depth.

Fig. 3.1 illustrates Eq. (3.1) in the global material coordinate system (X_1–X_2–X_3) that will be used almost exclusively in this book.[5] The global material coordinate system appears upside-down to accommodate the alignment of the X_1-axis with North, the X_2-axis with East and the X_3-axis with vertical depth.

Fig. 3.1 also contains another, spatial coordinate system[6] associated with the displaced point, and having axes x_1, x_2 and x_3. The spatial coordinate axes are not necessarily parallel to the material coordinate axes but can, if desired, align or even coincide with the material coordinate axes. The position of the spatial axes depends largely on convenience in the particular problem being addressed.[7] It is sufficient for the present to simply regard the x_1–x_2–x_3 system as another set of axes fixed in space.

The index notation of Eq. (3.1) highlights an important issue regarding the relation between the components of $\mathbf{X}$ and the components of $\mathbf{x}$. The natural decomposition of each of these vectors is in its parent coordinate system—$\mathbf{X}$ in the global material

[5] An expression wherein $\mathbf{X}$ is an independent variable is termed a Lagrangian description.

[6] An expression wherein $\mathbf{x}$ is an independent variable is termed an Eulerian description.

[7] For example, consider the manufacturing process wherein a flat plate is formed along its long axis into the shape of a cylinder and then (electrically) welded to create a tube. It might be convenient to describe the initial, undeformed shape in rectangular coordinates and the formed tube in cylindrical coordinates (see Section 3.6.2).

coordinate system and $\mathbf{x}$ in the spatial coordinate system. For each of these vectors we respectively have (see Eq. (A.1))

$$\mathbf{X} = X_K \mathbf{e}_K, \quad \mathbf{x} = x_k \mathbf{g}_k, \tag{3.2}$$

where the $\mathbf{e}_K$, $K = 1, 2, 3$ are unit base vectors[8] in the global material coordinate system and the $\mathbf{g}_k$, $k = 1, 2, 3$ are unit base vectors in the spatial coordinate system

$$\mathbf{e}_J \cdot \mathbf{e}_K = \delta_{JK}, \quad \mathbf{g}_j \cdot \mathbf{g}_k = \delta_{jk}, \tag{3.3}$$

and we use upper case indices to indicate the global material coordinate system and lower case indices to indicate the spatial coordinate system.

Both δ_{JK} and δ_{jk} in Eq. (3.3) are expressions of the Kronecker delta which has the value 1 if the two indices are the same and 0 otherwise (see Section A.24 of Appendix A).

If, on the other hand, we wish to express $\mathbf{X}$ (or any material vector) in the spatial coordinate system, then we write

$$X_j = X_K \mathbf{e}_K \cdot \mathbf{g}_j = X_K \delta_{Kj}, \quad \delta_{Kj} = \mathbf{e}_K \cdot \mathbf{g}_j. \tag{3.4}$$

Similarly, if we wish to express $\mathbf{x}$ (or any spatial vector) in the global material coordinate system, then we write

$$x_J = x_k \mathbf{g}_k \cdot \mathbf{e}_J = x_k \delta_{kJ}, \quad \delta_{kJ} = \mathbf{g}_k \cdot \mathbf{e}_J. \tag{3.5}$$

The scalars δ_{Kj} and δ_{kJ} are components of shifter tensors [7,8], and should not be confused with the Kronecker delta symbol[9] appearing in Eq. (3.3). Shifters allow one to express the components of a vector in something other than its native coordinate system by (see Eqs. (3.4) and (3.5)) using the dot product to compute the components of the vector's unit base vectors in the alternate coordinate system (see Section A.4 of Appendix A). The components of a shifter tensor will equal the Kronecker delta when the material and spatial reference frames are identical, but in general the two will differ.

3.3. DISPLACEMENT

Returning to Fig. 3.1, the difference between $\mathbf{x}$ and $\mathbf{X}$ is the displacement $\mathbf{u}$ given by

$$\mathbf{u} = \hat{\mathbf{u}}(\mathbf{x}, \tau) = \mathbf{x} - \mathbf{X} + \mathbf{o}, \quad u_i = \hat{u}_i(\mathbf{x}, \tau) = x_i - X_J \delta_{Ji} + o_i, \tag{3.6}$$

[8] A unit base vector is a vector of magnitude one that is collinear with a coordinate axis. If the coordinate line is curved, the unit base vector is collinear with the local tangent to the coordinate line.

[9] The Kronecker delta will have indices that are both of the same case. The indices of the shifter tensor will differ in case.

where we have used Eq. (3.4) to express $\mathbf{X}$ in the spatial coordinate system. The vector $\mathbf{o}$ is the constant offset between the origins of the global material and spatial coordinate systems, $\mathbf{o} = o_m \mathbf{g}_m$.

Alternatively, we can write

$$\mathbf{u} = \hat{\mathbf{U}}(\mathbf{X}, \tau) = \mathbf{x} - \mathbf{X} + \mathbf{o}, \quad U_I = \hat{U}_I(\mathbf{X}, \tau) = x_j \delta_{jI} - X_I + O_I, \tag{3.7}$$

where now we have used Eq. (3.5) to express $\mathbf{x}$ in the global material coordinate system, and the vector $\mathbf{o}$ uses the material coordinates to express the offset between the origins of the global material and spatial coordinate systems, $\mathbf{o} = O_M \mathbf{e}_M$.

In the above expressions, $\mathbf{u} = \hat{u}_i(\mathbf{x}, \tau)\mathbf{g}_i = \hat{U}_I(\mathbf{X}, \tau)\mathbf{e}_I$ and we use shifters to manipulate between components in the global material and spatial coordinate systems.

3.4. DEFORMATION GRADIENT

Now consider an infinitesimal line element within a deforming body. The initial ($\tau = 0$) position of one end of the line element is $\mathbf{X}$ and the initial position of the other end of the element is $\mathbf{X} + d\mathbf{X}$ where, in a rectangular coordinate system,

$$d\mathbf{X} = dX_I d\mathbf{e}_I, \tag{3.8}$$

the $\mathbf{e}_I$, $I = 1, 2, 3$ being unit base vectors along the axes of the global material coordinate system.[10]

Due to deformation, at a later time, $\tau > 0$, the line element becomes $d\mathbf{x}$ (see Fig. 3.2). From Eq. (3.1) we have

$$d\mathbf{x} = \frac{\partial \hat{\mathbf{x}}}{\partial \mathbf{X}} \cdot d\mathbf{X} = \mathbf{F} \cdot d\mathbf{X}, \quad dx_i = \frac{\partial \hat{x}_i}{\partial X_K} dX_K = F_{iK} dX_K, \tag{3.9}$$

where upper case indices refer to the material coordinate system and lower case indices refer to the spatial coordinate system. The tensor $\mathbf{F}$ is the deformation gradient. The determinant of $\mathbf{F}$ must be nonzero and finite.[11]

If Eq. (3.6) is substituted into Eq. (3.9), then

$$d\mathbf{x} = \frac{\partial \left(\mathbf{X} + \hat{\mathbf{U}} - \mathbf{o} \right)}{\partial \mathbf{X}} \cdot d\mathbf{X} = \left(\mathbf{I} + \frac{\partial \hat{\mathbf{U}}}{\partial \mathbf{X}} \right) \cdot d\mathbf{X} = \mathbf{F} \cdot d\mathbf{X},$$

[10] This expression will be somewhat more complicated in Section 3.6.2 when deformation is referenced to a cylindrical coordinate system. The simplicity of Eq. (3.8) follows from the fact that the $\mathbf{e}_I$ are constant.

[11] Consider a simple one-dimensional deformation $dx_1 = k dX_1$, where k is a constant. In this case, $F_{11} = k$, and the determinant of $\mathbf{F}$ is k. If k is zero, then the deformation is collapsing the line element dX_1 to zero length. If k is infinite, then the deformation can take an element dX_1 of zero length and produce a finite length spatial element dx_1. Neither of these extremes is desirable or physically reasonable.

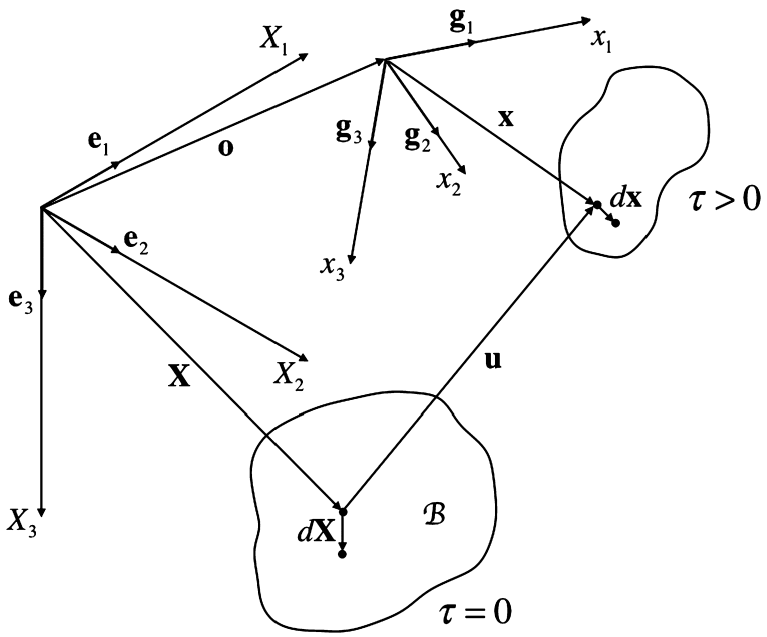

Figure 3.2 ***Illustration of the deformation of a line element in the global coordinate system.***

$$dx_i = \frac{\partial\left(X_J + \hat{U}_J - O_J\right)\delta_{Ji}}{\partial X_K} dX_K = \left(\delta_{JK} + \frac{\partial \hat{U}_J}{\partial X_K}\right)\delta_{Ji} dX_K = F_{iK} dX_K, \tag{3.10}$$

where $\mathbf{I}$ is the identity tensor (unity along its diagonal, zero elsewhere).

From Eqs. (3.9) and (3.10) we get

$$\mathbf{F} = \frac{\partial \hat{\mathbf{x}}}{\partial \mathbf{X}} = \mathbf{I} + \frac{\partial \hat{\mathbf{U}}}{\partial \mathbf{X}}, \quad F_{iK} = \frac{\partial \hat{x}_i}{\partial X_K} = \left(\delta_{JK} + \frac{\partial \hat{U}_J}{\partial X_K}\right)\delta_{Ji}. \tag{3.11}$$

Since the determinant of $\mathbf{F}$ is nonzero, its inverse exists and satisfies

$$\mathbf{F}^{-1} \cdot \mathbf{F} = \mathbf{F} \cdot \mathbf{F}^{-1} = \mathbf{I}, \quad F^{-1}_{Kl} F_{lM} = \delta_{KM} \quad F_{kL} F^{-1}_{Lm} = \delta_{km}. \tag{3.12}$$

Further, since $\frac{\partial X_K}{\partial x_l}\frac{\partial x_l}{\partial X_M} = \delta_{KM}$, we have

$$\frac{\partial \hat{\mathbf{X}}}{\partial \mathbf{x}} \cdot \frac{\partial \hat{\mathbf{x}}}{\partial \mathbf{X}} = \mathbf{I} \Rightarrow \mathbf{F}^{-1} = \frac{\partial \hat{\mathbf{X}}}{\partial \mathbf{x}}, \quad \frac{\partial \hat{X}_K}{\partial x_l}\frac{\partial \hat{x}_l}{\partial X_M} = \delta_{KM} \Rightarrow F^{-1}_{Kl} = \frac{\partial \hat{X}_K}{\partial x_l}. \tag{3.13}$$

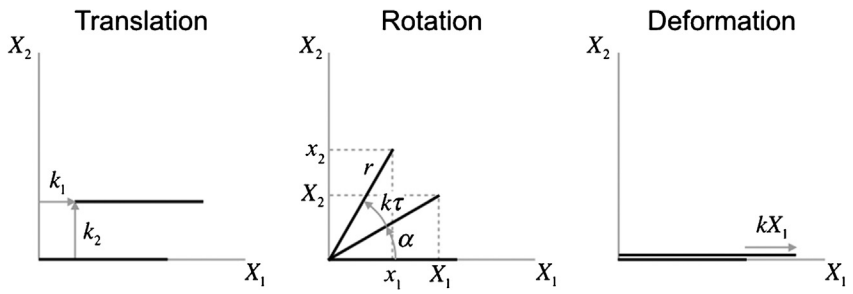

Figure 3.3 ***Examples of translation, rotation and deformation.*** In the deformation example the deformed line element has been offset positively from the X_1-axis to distinguish it from the undeformed line element. The X_3-axis is directed out of the page toward the reader.

If Eq. (3.9) is now multiplied by $\mathbf{F}^{-1}$, then

$$\mathbf{F}^{-1}\cdot d\mathbf{x}=\frac{\partial\hat{\mathbf{X}}}{\partial\mathbf{x}}\cdot d\mathbf{x}=d\mathbf{X},\qquad F_{Ki}^{-1}\,dx_i=\frac{\partial\hat{X}_K}{\partial x_i}dx_i=dX_K, \tag{3.14}$$

and, using Eq. (3.7),

$$\begin{aligned} d\mathbf{X}&=\frac{\partial\left(\mathbf{x}-\hat{\mathbf{u}}+\mathbf{o}\right)}{\partial\mathbf{x}}\cdot d\mathbf{x}=\left(\mathbf{I}-\frac{\partial\hat{\mathbf{u}}}{\partial\mathbf{x}}\right)\cdot d\mathbf{x}=\mathbf{F}^{-1}\cdot d\mathbf{x},\\ dX_I&=\frac{\partial\left[\left(x_i-\hat{u}_i+o_i\right)\delta_{iI}\right]}{\partial x_k}dx_k=\left(\delta_{ik}-\frac{\partial\hat{u}_i}{\partial x_k}\right)\delta_{iI}\,dx_k=F_{Ik}^{-1}\,dx_k. \end{aligned} \tag{3.15}$$

From Eqs. (3.14) and (3.15) we obtain

$$\mathbf{F}^{-1}=\frac{\partial\hat{\mathbf{X}}}{\partial\mathbf{x}}=\mathbf{I}-\frac{\partial\hat{\mathbf{u}}}{\partial\mathbf{x}},\qquad F_{Ik}^{-1}=\frac{\partial\hat{X}_I}{\partial x_k}=\left(\delta_{ik}-\frac{\partial\hat{u}_i}{\partial x_k}\right)\delta_{iI}. \tag{3.16}$$

In the work to follow, $\mathbf{F}$ will be used in developing the Lagrangian and logarithmic strain tensors from the perspective of the undeformed configuration $\mathbf{X}$; $\mathbf{F}^{-1}$ will be used in developing the Eulerian strain tensor from the perspective of the deformed configuration $\mathbf{x}$.

3.4.1 Example problem—the deformation gradient

For selected line elements etched on a body initially lying in the X_1–X_2 plane (see Fig. 3.3), and with the material and spatial coordinate systems coinciding, determine the deformation gradient for the following:

- Translation. The displacement $\hat{U}_1=k_1$, $\hat{U}_2=k_2$, $\hat{U}_3=0$, where k_1 and k_2 are constants, translates all points in the body k_1 units along the X_1-axis and k_2 units along

the X_2-axis, with no change in the original vertical (X_3) position of the points. From Eq. (3.10) we get

$$F_{11} = \frac{\partial\left(X_1 + k_1\right)}{\partial X_1} = 1, \quad F_{22} = \frac{\partial\left(X_2 + k_2\right)}{\partial X_2} = 1, \quad F_{33} = \frac{\partial\left(X_3 + 0\right)}{\partial X_3} = 1, \tag{3.17}$$

and $F_{iK} = 0$ for all other values of i and K. The deformation gradient measures relative changes in position following a motion by deviation from a value of unity.[12] Since all relative positions remain the same in a translation, the only nonzero values of F_{iK} in this instance are all 1.

- Rotation. If a body with etched line element initially lying along an angle α from the X_1-axis is rotated about the X_3-axis and the origin of the line element (assumed to be at $X_1 = 0$) is not allowed to displace, the displaced position of the end of the line element is $x_1 = r\cos\left(\alpha + k\tau\right) = r\left(\cos\alpha\cos k\tau - \sin\alpha\sin k\tau\right) = X_1\cos k\tau - X_2\sin k\tau$, $x_2 = r\sin\left(\alpha + k\tau\right) = r\left(\sin\alpha\cos k\tau + \cos\alpha\sin k\tau\right) = X_2\cos k\tau + X_1\sin k\tau$, where k is a constant. This time using Eq. (3.11) we obtain

$$\begin{aligned} &F_{11} = \frac{\partial x_1}{\partial X_1} = \cos k\tau,\ F_{12} = \frac{\partial x_1}{\partial X_2} = -\sin k\tau, \quad F_{21} = \frac{\partial x_2}{\partial X_1} = \sin k\tau, \\ &F_{22} = \frac{\partial x_2}{\partial X_2} = \cos k\tau, \quad F_{33} = \frac{\partial\left(X_3 + 0\right)}{\partial X_3} = 1, \end{aligned} \tag{3.18}$$

and $F_{iK} = 0$ for all other values of i and K.

- Deformation. Consider the simple extension, $x_1 = kX_1$. From Eq. (3.10) with $\hat{U}_1 = x_1 - X_1 = (k-1)X_1$ we have

$$F_{11} = \frac{\partial\left(X_1 + \left(k-1\right)X_1\right)}{\partial X_1} = k, \quad F_{22} = \frac{\partial\left(X_2 + 0\right)}{\partial X_2} = 1, \quad F_{33} = \frac{\partial\left(X_3 + 0\right)}{\partial X_3} = 1, \tag{3.19}$$

and $F_{iK} = 0$ for all other values of i and K.

3.5. STRAIN

Eqs. (3.9) and (3.10) suggest that the spatial relation between two nearby points in a body can change with motion due to deformation. If $\mathbf{F} \neq \mathbf{I}$, $d\mathbf{x}$ will, with the possible exception of pure rotation, differ in length from $d\mathbf{X}$ (see Eq. (3.10)). This difference can be measured in a variety of ways. Here we will consider three of the more popular definitions—the Lagrangian strain tensor, the Eulerian strain tensor and the logarithmic

[12] Revisiting Eq. (3.9), if $\mathbf{F} = \mathbf{I}$, $d\mathbf{x} = d\mathbf{X}$, implying no change in the original length of $d\mathbf{X}$.

strain tensor. All three definitions use either the Cauchy or Green deformation tensor as an intermediate constituent of strain.

The Lagrangian and Eulerian strains are similar in concept. The former relates deformation to the initial, undeformed configuration whose functional dependence involves $\mathbf{X}$; the latter relates deformation to the deformed configuration whose functional dependence involves $\mathbf{x}$. The Lagrangian strain satisfies one's initial intuition regarding a deformation measure, so its derivation will be given detail while the Eulerian strain development will be abbreviated. For infinitesimal strain that dominates the remainder of the book, the two strains are indistinguishable.

3.5.1 The Cauchy and Green deformation tensors

We wish to further describe the deformation of an infinitesimal line element with time. In its original position, the square of the length of the infinitesimal element $d\mathbf{X}$ in Fig. 3.2 is

$$dS^2 = d\mathbf{X}^T \cdot d\mathbf{X}, \quad dS^2 = dX_I dX_I. \tag{3.20}$$

Similarly, the square of the length of the same infinitesimal element later ($\tau > 0$) is

$$ds^2 = d\mathbf{x}^T \cdot d\mathbf{x}, \quad ds^2 = dx_i dx_i. \tag{3.21}$$

One suitable description of deformation compares the two squared lengths[13] in Eqs. (3.20) and (3.21) by taking the difference

$$ds^2 - dS^2 = d\mathbf{x}^T \cdot d\mathbf{x} - d\mathbf{X}^T \cdot d\mathbf{X}, \quad ds^2 - dS^2 = dx_i dx_i - dX_I dX_I. \tag{3.22}$$

With Eq. (3.9) substituted into Eq. (3.22), we get

$$\begin{aligned} ds^2 - dS^2 &= \left(d\mathbf{X}^T \cdot \mathbf{F}^T\right) \cdot \left(\mathbf{F} \cdot d\mathbf{X}\right) - d\mathbf{X}^T \cdot d\mathbf{X} = d\mathbf{X}^T \cdot \left(\mathbf{F}^T \cdot \mathbf{F} - \mathbf{I}\right) \cdot d\mathbf{X} \\ &= d\mathbf{X}^T \cdot (\mathbf{C} - \mathbf{I}) \cdot d\mathbf{X}, \\ ds^2 - dS^2 &= dX_K^T F_{Ki}^T F_{iL} dX_L - dX_K dX_K = dX_K^T \left(F_{Ki}^T F_{iL} - \delta_{KL}\right) dX_L \\ &= (C_{KL} - \delta_{KL})\, dX_K dX_L, \end{aligned} \tag{3.23}$$

where we have used the associative property of the matrix contraction product (Eq. (A.42)), the relation $(\mathbf{A} \cdot \mathbf{B})^T = \mathbf{B}^T \cdot \mathbf{A}^T$ (see subsection 'Example problem—prove $(\mathbf{A} \cdot \mathbf{B})^T = \mathbf{B}^T \cdot \mathbf{A}^T$' in Section A.4.1.4 of Appendix A) and the fact that dX_K and dX_K^T have the same value.

[13] One could choose to compare lengths, which in this case would introduce square roots, greatly complicating future calculations.

The tensor $\mathbf{C}$ in Eq. (3.23) is the Green deformation tensor. From Eq. (3.11)[14] we have

$$\begin{aligned}
\mathbf{C} = \mathbf{F}^T \cdot \mathbf{F} &= \left(\mathbf{I} + \frac{\partial \hat{\mathbf{U}}}{\partial \mathbf{X}}\right)^T \cdot \left(\mathbf{I} + \frac{\partial \hat{\mathbf{U}}}{\partial \mathbf{X}}\right) = \mathbf{I} + \frac{\partial \hat{\mathbf{U}}}{\partial \mathbf{X}} + \left(\frac{\partial \hat{\mathbf{U}}}{\partial \mathbf{X}}\right)^T + \left(\frac{\partial \hat{\mathbf{U}}}{\partial \mathbf{X}}\right)^T \cdot \frac{\partial \hat{\mathbf{U}}}{\partial \mathbf{X}}, \\
C_{KL} = F_{iK} F_{iL} &= \left(\delta_{JK} + \frac{\partial \hat{U}_J}{\partial X_K}\right) \delta_{Ji} \left(\delta_{ML} + \frac{\partial \hat{U}_M}{\partial X_L}\right) \delta_{Mi} \\
&= \delta_{KL} + \frac{\partial \hat{U}_K}{\partial X_L} + \frac{\partial \hat{U}_L}{\partial X_K} + \frac{\partial \hat{U}_N}{\partial X_K} \frac{\partial \hat{U}_N}{\partial X_L}.
\end{aligned} \tag{3.24}$$

The Cauchy deformation tensor $\breve{\mathbf{C}}$ is the counterpart in the deformed configuration of the Green deformation tensor $\mathbf{C}$. With the aid of Eq. (3.14), an alternative expression of Eq. (3.23) that focuses on the deformed configuration is

$$\begin{aligned}
ds^2 - dS^2 &= d\mathbf{x}^T \cdot d\mathbf{x} - \left(d\mathbf{x}^T \cdot \left(\mathbf{F}^{-1}\right)^T \cdot \mathbf{F}^{-1} \cdot d\mathbf{x}\right) = d\mathbf{x}^T \cdot \left(\mathbf{I} - \left(\mathbf{F}^{-1}\right)^T \cdot \mathbf{F}^{-1}\right) \cdot d\mathbf{x} \\
&= d\mathbf{x}^T \cdot \left(\mathbf{I} - \breve{\mathbf{C}}\right) \cdot d\mathbf{x}, \\
ds^2 - dS^2 &= dx_k dx_k - dx_k^T \left(F^{-1}\right)_{kM}^T F_{Ml}^{-1} dx_l = dx_k^T \left(\delta_{kl} - \left(F^{-1}\right)_{kM}^T F_{Ml}^{-1}\right) dx_l \\
&= \left(\delta_{kl} - \breve{C}_{kl}\right) dx_k dx_l,
\end{aligned} \tag{3.25}$$

or, from Eq. (3.16)[15],

$$\begin{aligned}
\breve{\mathbf{C}} = \left(\mathbf{F}^{-1}\right)^T \cdot \mathbf{F}^{-1} &= \left(\mathbf{I} - \frac{\partial \hat{\mathbf{u}}}{\partial \mathbf{x}}\right)^T \cdot \left(\mathbf{I} - \frac{\partial \hat{\mathbf{u}}}{\partial \mathbf{x}}\right) = \mathbf{I} - \frac{\partial \hat{\mathbf{u}}}{\partial \mathbf{x}} - \left(\frac{\partial \hat{\mathbf{u}}}{\partial \mathbf{x}}\right)^T + \left(\frac{\partial \hat{\mathbf{u}}}{\partial \mathbf{x}}\right)^T \cdot \frac{\partial \hat{\mathbf{u}}}{\partial \mathbf{x}}, \\
\breve{C}_{kl} = F_{Mk}^{-1} F_{Ml}^{-1} &= \left(\delta_{ik} - \frac{\partial \hat{u}_i}{\partial x_k}\right) \delta_{iM} \left(\delta_{jl} - \frac{\partial \hat{u}_j}{\partial x_l}\right) \delta_{jM} = \delta_{kl} - \frac{\partial \hat{u}_k}{\partial x_l} - \frac{\partial \hat{u}_l}{\partial x_k} + \frac{\partial \hat{u}_m}{\partial x_k} \frac{\partial \hat{u}_m}{\partial x_l},
\end{aligned} \tag{3.26}$$

where the displacement is now considered a function of $\mathbf{x}$, i.e., $\mathbf{u} = \hat{\mathbf{u}}(\hat{\mathbf{X}}(\mathbf{x}, \tau), \tau)$.

[14] In arriving at the form of C_{KL} in index notation, a key relation is $\delta_{Ji}\delta_{Mi} = \delta_{JM}$. Recall from Eq. (3.4) that $\delta_{Ji} = \mathbf{e}_J \cdot \mathbf{g}_i$, that is, δ_{Ji} is the dot product between a unit base vector in the global material coordinate system and a unit base vector in the spatial coordinate system. We can therefore write $\delta_{Ji}\delta_{Mi} = (\mathbf{e}_J \cdot \mathbf{g}_i)(\mathbf{e}_M \cdot \mathbf{g}_i)$. For cases when $J = M$, this product is just the sum of the squares of the components of an $\mathbf{e}$ unit vector in the $\mathbf{g}$ (spatial) coordinate system. This sum must be 1 from the definition of a unit vector. If $J \neq M$, the product $(\mathbf{e}_J \cdot \mathbf{g}_i)(\mathbf{e}_M \cdot \mathbf{g}_i)$ is the sum of the components of two dissimilar $\mathbf{e}$ unit base vectors, say $\mathbf{e}_1$ and $\mathbf{e}_2$, in the $\mathbf{g}$ coordinate system. This sum must be 0 since two unit base vectors must be orthogonal. Our conclusion is that the product $\delta_{Ji}\delta_{Mi}$ is 1 when $J = M$ and 0 when $J \neq M$, which is the definition of δ_{JM}. Using this result in Eq. (3.24) will produce the form displayed.

[15] For the transformation of the product $\delta_{iM}\delta_{jM}$ to δ_{ij} see Footnote 14.

3.5.1.1 Example problem—the Green deformation tensor

We continue the problem from Section 3.4.1. For selected line elements etched on a body initially lying in the X_1–X_2 plane, and with the material and spatial coordinate systems coinciding, determine the Green deformation tensor for the following:

- Translation. The displacement $\hat{U}_1 = k_1$, $\hat{U}_2 = k_2$, $\hat{U}_3 = 0$, where k_1 and k_2 are constants, produces a deformation gradient tensor with $F_{11} = F_{22} = F_{33} = 1$ and all other $F_{iK} = 0$. From Eq. (3.24) we have

$$C_{11} = F_{11}^T F_{11} = 1, \quad C_{22} = F_{22}^T F_{22} = 1, \quad C_{33} = F_{33}^T F_{33} = 1, \tag{3.27}$$

  and $C_{KL} = 0$ for all other values of K and L.
- Rotation. For a body with etched line element initially lying along an angle α from the X_1-axis that is rotated about the X_3-axis, with the origin of the line element not allowed to displace, $F_{11} = \cos k\tau$, $F_{12} = -\sin k\tau$, $F_{21} = \sin k\tau$, $F_{22} = \cos k\tau$, $F_{33} = 1$ and all other $F_{iK} = 0$. Again, from Eq. (3.24) we obtain

$$\begin{aligned} &C_{11} = F_{11}^T F_{11} + F_{12}^T F_{21} + F_{13}^T F_{31} = F_{11}F_{11} + F_{21}F_{21} + F_{31}F_{31} = \cos^2 k\tau + \sin^2 k\tau = 1, \\ &C_{12} = C_{21} = 0, C_{22} = 1, \quad C_{33} = F_{33}^T F_{33} = 1, \end{aligned} \tag{3.28}$$

  and $C_{KL} = 0$ for all other values of K and L.
- Deformation. With the simple extension, $x_1 = kX_1$, and Eq. (3.24), $F_{11} = k$, $F_{22} = F_{33} = 1$ and all other $F_{iK} = 0$, and

$$C_{11} = F_{11}^T F_{11} = k^2, \quad C_{22} = F_{22}^T F_{22} = 1, \quad C_{33} = F_{33}^T F_{33} = 1, \tag{3.29}$$

  with $C_{KL} = 0$ for all other values of K and L.

3.5.2 The Lagrangian strain tensor

With Eq. (3.24) substituted into Eq. (3.23),

$$\begin{aligned} ds^2 - dS^2 &= d\mathbf{X}^T \cdot \left[\frac{\partial \hat{\mathbf{U}}}{\partial \mathbf{X}} + \left(\frac{\partial \hat{\mathbf{U}}}{\partial \mathbf{X}} \right)^T + \left(\frac{\partial \hat{\mathbf{U}}}{\partial \mathbf{X}} \right)^T \cdot \frac{\partial \hat{\mathbf{U}}}{\partial \mathbf{X}} \right] \cdot d\mathbf{X} = 2d\mathbf{X}^T \cdot \mathbf{E} \cdot d\mathbf{X}, \\ ds^2 - dS^2 &= dX_K^T \left[\frac{\partial \hat{U}_K}{\partial X_L} + \frac{\partial \hat{U}_L}{\partial X_K} + \frac{\partial \hat{U}_N}{\partial X_K} \frac{\partial \hat{U}_N}{\partial X_L} \right] dX_L = 2dX_K^T E_{KL} dX_L. \end{aligned} \tag{3.30}$$

The tensor $\mathbf{E}$ is the Lagrangian strain tensor, formally defined as

$$\mathbf{E} = \frac{1}{2}(\mathbf{C} - \mathbf{I}) = \frac{1}{2} \left[\frac{\partial \hat{\mathbf{U}}}{\partial \mathbf{X}} + \left(\frac{\partial \hat{\mathbf{U}}}{\partial \mathbf{X}} \right)^T + \left(\frac{\partial \hat{\mathbf{U}}}{\partial \mathbf{X}} \right)^T \cdot \frac{\partial \hat{\mathbf{U}}}{\partial \mathbf{X}} \right],$$

$$E_{KL} = \frac{1}{2}\left(C_{KL} - \delta_{KL}\right) = \frac{1}{2}\left(\frac{\partial \hat{U}_K}{\partial X_L} + \frac{\partial \hat{U}_L}{\partial X_K} + \frac{\partial \hat{U}_N}{\partial X_K}\frac{\partial \hat{U}_N}{\partial X_L}\right). \tag{3.31}$$

Note the following regarding the Lagrangian strain tensor:

- The term $\frac{1}{2}$ appearing in the definition is necessary for $\mathbf{E}$ to properly transform as a tensor;
- The strain contains both linear ($\frac{\partial \hat{\mathbf{U}}}{\partial \mathbf{X}} + \left(\frac{\partial \hat{\mathbf{U}}}{\partial \mathbf{X}}\right)^T$ or $\frac{\partial \hat{U}_K}{\partial X_L} + \frac{\partial \hat{U}_L}{\partial X_K}$) and nonlinear ($\left(\frac{\partial \hat{\mathbf{U}}}{\partial \mathbf{X}}\right)^T \cdot \frac{\partial \hat{\mathbf{U}}}{\partial \mathbf{X}}$ or $\frac{\partial \hat{U}_i}{\partial X_K}\frac{\partial \hat{U}_i}{\partial X_L}$) terms;
- If all the $\frac{\partial \hat{\mathbf{U}}}{\partial \mathbf{X}}$ are of the same order and these quantities are small compared to unity, the nonlinear terms can be neglected;
- The strain is symmetric, that is, $\mathbf{E} = \mathbf{E}^T$ or $E_{KL} = E_{LK}$;
- The deformation datum for the diagonal components (E_{IJ} with $I = J$) of $\mathbf{E}$ is zero, not unity as was the case with $\mathbf{C}$.

3.5.2.1 Example problem—the Lagrangian strain tensor

We continue the problem from Sections 3.4.1 and 3.5.1.1. For selected line elements etched on a body initially lying in the X_1–X_2 plane, and with the material and spatial coordinate systems coinciding, determine the Lagrangian strain tensor for the following:

- Translation. The displacement $\hat{U}_1 = k_1$, $\hat{U}_2 = k_2$, $\hat{U}_3 = 0$, where k_1 and k_2 are constants, produces a Green deformation tensor with $C_{11} = C_{22} = C_{33} = 1$ and all other $C_{KL} = 0$. From Eq. (3.31) we get

$$E_{11} = \frac{1}{2}\left(C_{11} - 1\right) = 0, \quad E_{22} = \frac{1}{2}\left(C_{22} - 1\right) = 0, \quad E_{33} = \frac{1}{2}\left(C_{33} - 1\right) = 0, \tag{3.32}$$

  and $E_{KL} = 0$ for all other values of K and L. This is expected since translation produces no deformation.
- Rotation. For a body with etched line element initially lying along an angle α from the X_1-axis that is rotated about the X_3-axis, with the origin of the line element not allowed to displace, $C_{11} = C_{22} = C_{33} = 1$ and all other $C_{KL} = 0$. As was the case with translation, all E_{KL} vanish, again producing no strain.
- Deformation. For the simple extension, $x_1 = kX_1$, $C_{11} = k^2$, $C_{22} = C_{33} = 1$ and all other $C_{KL} = 0$. From Eq. (3.31) we obtain

$$E_{11} = \frac{1}{2}\left(C_{11} - 1\right) = \frac{1}{2}\left(k^2 - 1\right), \tag{3.33}$$

  and $E_{KL} = 0$ for all other values of K and L. We have stretch of the element along the X_1-axis (i.e., $ds^2 - dS^2 = \left(k^2 - 1\right) dX_1^2$), but no deformation in any other direction.

Table 3.1 Summary comparison of Lagrangian and Eulerian strain tensors[a]

Strain[b]	Coordinates	Deformation[b]	Deformation gradient[b]
Lagrangian (**E**)	Material (**X**)	Green (**C**)	**F**
Eulerian ($\check{\mathbf{E}}$)	Spatial (**x**)	Cauchy ($\check{\mathbf{C}}$)	$\mathbf{F}^{-1}$

[a] The logarithmic strain tensor (Section 3.5.4) is sufficiently different to be considered separately.
[b] Second order tensor.

3.5.3 The Eulerian strain tensor

If Eq. (3.26) is substituted into Eq. (3.25), then

$$ds^2 - dS^2 = d\mathbf{x}^T \cdot \left[\frac{\partial \hat{\mathbf{u}}}{\partial \mathbf{x}} + \left(\frac{\partial \hat{\mathbf{u}}}{\partial \mathbf{x}} \right)^T - \left(\frac{\partial \hat{\mathbf{u}}}{\partial \mathbf{x}} \right)^T \cdot \frac{\partial \hat{\mathbf{u}}}{\partial \mathbf{x}} \right] \cdot d\mathbf{x} = 2 d\mathbf{x}^T \cdot \check{\mathbf{E}} \cdot d\mathbf{x},$$

$$ds^2 - dS^2 = dx_k^T \left[\frac{\partial \hat{u}_k}{\partial x_l} + \frac{\partial \hat{u}_l}{\partial x_k} - \frac{\partial \hat{u}_m}{\partial x_k} \frac{\partial \hat{u}_m}{\partial x_l} \right] dx_l = 2 dx_{k^T} \check{E}_{kl} dx_l. \tag{3.34}$$

The tensor $\check{\mathbf{E}}$ is the Eulerian strain tensor, formally defined as

$$\check{\mathbf{E}} = \frac{1}{2} \left(\mathbf{I} - \check{\mathbf{C}} \right) = \frac{1}{2} \left[\frac{\partial \hat{\mathbf{u}}}{\partial \mathbf{x}} + \left(\frac{\partial \hat{\mathbf{u}}}{\partial \mathbf{x}} \right)^T - \left(\frac{\partial \hat{\mathbf{u}}}{\partial \mathbf{x}} \right)^T \cdot \frac{\partial \hat{\mathbf{u}}}{\partial \mathbf{x}} \right],$$

$$\check{E}_{kl} = \frac{1}{2} \left(\delta_{kl} - \check{C}_{kl} \right) = \frac{1}{2} \left(\frac{\partial \hat{u}_k}{\partial x_l} + \frac{\partial \hat{u}_l}{\partial x_k} - \frac{\partial \hat{u}_m}{\partial x_k} \frac{\partial \hat{u}_m}{\partial x_l} \right). \tag{3.35}$$

Table 3.1 summarizes the distinguishing features of the Lagrangian and Eulerian strain tensors. The Lagrangian strain has as its focus the initial position of an element; the Eulerian strain has as its focus the deformed position of an element.

3.5.4 The Logarithmic strain tensor

Our choosing to measure strain as the difference $ds^2 - dS^2$ led to the definition of the Lagrangian strain tensor. In this section we select an alternative measure of strain involving the stretch ratio $\Lambda_{(\mathbf{N})}$, where

$$\Lambda_{(\mathbf{N})} = \sqrt{\frac{ds^2}{dS^2}} = \sqrt{\frac{d\mathbf{x}^T \cdot d\mathbf{x}}{d\mathbf{X}^T \cdot d\mathbf{X}}}, \quad \Lambda_{(\mathbf{N})} = \sqrt{\frac{dx_k dx_k}{dX_K dX_K}}, \tag{3.36}$$

where the subscript (**N**) indicates that Λ is associated with a direction in the global material coordinate system whose unit vector of direction is **N**. The stretch ratio has the value one if there is no deformation in direction **N**.

By Eq. (3.9),

$$\Lambda_{(\mathbf{N})} = \sqrt{\frac{d\mathbf{X}^T \cdot \mathbf{F}^T \cdot \mathbf{F} \cdot d\mathbf{X}}{d\mathbf{X}^T \cdot d\mathbf{X}}}, \quad \Lambda_{(\mathbf{N})} = \sqrt{\frac{dX_R F_{kR} F_{kS} dX_S}{dX_K dX_K}}, \tag{3.37}$$

or, with the application of Eq. (3.24),

$$\Lambda^2_{(\mathbf{N})} = \frac{d\mathbf{X}^T}{\sqrt{d\mathbf{X}^T \cdot d\mathbf{X}}} \cdot \mathbf{F}^T \cdot \mathbf{F} \cdot \frac{d\mathbf{X}}{\sqrt{d\mathbf{X}^T \cdot d\mathbf{X}}} = \mathbf{N}^T \cdot \mathbf{F}^T \cdot \mathbf{F} \cdot \mathbf{N} = \mathbf{N}^T \cdot \mathbf{C} \cdot \mathbf{N},$$
$$\Lambda^2_{(\mathbf{N})} = \frac{dX_R}{\sqrt{dX_K dX_K}} F_{kR} F_{kS} \frac{dX_S}{\sqrt{dX_L dX_L}} = N_R F_{kR} F_{kS} N_S = N_R C_{RS} N_S, \tag{3.38}$$

where we recognize $\frac{dX_R}{\sqrt{dX_K dX_K}}$ as the component of $\mathbf{N}$ along the X_R-axis.

With the above preliminaries, we define the logarithmic strain as

$$\tilde{\mathbf{E}} = \frac{1}{2} \ln \mathbf{C} = \ln \mathbf{C}^{\frac{1}{2}}. \tag{3.39}$$

The definition of $\tilde{\mathbf{E}}$ is complex, involving the logarithm of a tensor. Using properties of $\ln \mathbf{C}$ detailed by Khan and Huang [9], we can say the following about $\tilde{\mathbf{E}}$:

- $\tilde{\mathbf{E}}$ has the same principal directions (i.e., eigenvectors, see Section A.5.2.3 of Appendix A) as $\mathbf{C}$;
- The principal values (i.e., eigenvalues) of $\tilde{\mathbf{E}}$ are $\frac{1}{2} \ln \lambda_i$, where λ_i are the principal values of $\mathbf{C}$.

Fortunately, all applications of Eq. (3.39) to tubular design in this book are such that, in the local coordinate system, $\mathbf{C}$ is a diagonal tensor, that is, $C_{KL} = 0$ if $K \neq L$. In this special case the characteristic equation for $\mathbf{C}$ (see Section A.5.2.3 of Appendix A) becomes

$$\begin{bmatrix} C_{11} - \lambda & 0 & 0 \\ 0 & C_{22} - \lambda & 0 \\ 0 & 0 & C_{33} - \lambda \end{bmatrix} \begin{bmatrix} v_1 \\ v_2 \\ v_3 \end{bmatrix} = \begin{bmatrix} 0 \\ 0 \\ 0 \end{bmatrix}, \tag{3.40}$$

which has nonzero solution $\mathbf{v}$ if and only if $(C_{11} - \lambda)(C_{22} - \lambda)(C_{33} - \lambda) = 0$. We can write the solutions of this cubic equation by inspection—$\lambda_1 = C_{11}, \lambda_2 = C_{22}, \lambda_3 = C_{33}$. The corresponding logarithmic strain tensor is $\tilde{E}_{11} = \frac{1}{2} \ln C_{11}, \tilde{E}_{22} = \frac{1}{2} \ln C_{22}, \tilde{E}_{33} = \frac{1}{2} \ln C_{33}$, all other $\tilde{E}_{KL} = 0$.

3.5.4.1 Example problem—the Logarithmic strain tensor

We continue the problem from Sections 3.4.1 and 3.5.1.1, only this time choosing logarithmic strain as our strain measure. For selected line elements etched on a body element initially lying in the X_1–X_2 plane, and with the material and spatial coordinate systems coinciding, determine the logarithmic strain tensor for the following:

- Translation. The displacement $\hat{U}_1 = k_1$, $\hat{U}_2 = k_2$, $\hat{U}_3 = 0$, where k_1 and k_2 are constants, produces a Green deformation tensor with $C_{11} = C_{22} = C_{33} = 1$ and all other $C_{KL} = 0$. Inasmuch as C_{11}, C_{22} and C_{33} are the eigenvalues of $\mathbf{C}$, and

from Eq. (3.39),

$$\tilde{E}_{11} = \frac{1}{2}\ln 1 = 0, \quad \tilde{E}_{22} = \frac{1}{2}\ln 1 = 0, \quad \tilde{E}_{33} = \frac{1}{2}\ln 1 = 0, \tag{3.41}$$

and $\tilde{E}_{KL} = 0$ for all other values of K and L. This is expected since translation produces no deformation.

- Rotation. For a body with etched line element initially lying along an angle α from the X_1-axis that is rotated about the X_3-axis, with the origin of the line element not allowed to displace, $C_{11} = C_{22} = C_{33} = 1$ and all other $C_{KL} = 0$. As was the case with translation, all $\tilde{E}_{KL}$ vanish, again producing no strain.
- Deformation. For the simple extension, $x_1 = kX_1$, $C_{11} = k^2$, $C_{22} = C_{33} = 1$ and all other $C_{KL} = 0$. From Eq. (3.39) we have

$$\tilde{E}_{11} = \frac{1}{2}\ln(C_{11}) = \frac{1}{2}\ln k^2 = \ln k, \tag{3.42}$$

and $\tilde{E}_{KL} = 0$ for all other values of K and L. We have stretch of the element along the X_1-axis (i.e., $\Lambda_{(1)} = k$), but no deformation in any other direction.

3.5.5 Relating strain definitions

The strain measures discussed here—Lagrangian, Eulerian and logarithmic—are among a large number of possible strain definition candidates. These three definitions are, however, fairly popular and can be conveniently related.

First, anticipating sections to follow on infinitesimal strain, we note that for the special case of strain only along the X_1-axis of an element initially lying along that axis, the Lagrangian strain is (see Eq. (3.31))

$$E_{11} = \frac{\partial \hat{U}_1}{\partial X_1} + \frac{1}{2}\left(\frac{\partial \hat{U}_1}{\partial X_1}\right)^2, \tag{3.43}$$

and, assuming the global and spatial coordinate systems coincide, the Eulerian strain is (see Eq. (3.35))

$$\breve{E}_{11} = \frac{\partial \hat{u}_1}{\partial x_1} - \frac{1}{2}\left(\frac{\partial \hat{u}_1}{\partial x_1}\right)^2, \tag{3.44}$$

where $\frac{\partial \hat{U}_1}{\partial X_1} = \frac{\partial \hat{u}_1}{\partial x_1}$.

The logarithmic strain is (see Eqs. (3.24) and (3.39))

$$\tilde{E}_{11} = \ln\sqrt{C_{11}} = \frac{1}{2}\ln\left(1 + 2\frac{\partial \hat{U}_1}{\partial X_1} + \left(\frac{\partial \hat{U}_1}{\partial X_1}\right)^2\right) = \ln\sqrt{1 + 2\frac{\partial \hat{U}_1}{\partial X_1} + \left(\frac{\partial \hat{U}_1}{\partial X_1}\right)^2}. \tag{3.45}$$

If the displacements and displacement gradients are small, $\hat{U}_1 \ll 1$ and $\frac{\partial \hat{U}_1}{\partial X_1} \ll 1$, the Lagrangian and Eulerian strains can be respectively approximated by

$$E_{11} \approx \frac{\partial \hat{U}_1}{\partial X_1}, \quad \breve{E}_{11} \approx \frac{\partial \hat{u}_1}{\partial x_1}. \tag{3.46}$$

For the logarithmic strain, and recalling that the series approximation of the natural logarithm is [10]

$$\ln(1+x) = x - \frac{x^2}{2} + \frac{x^3}{3} - \frac{x^4}{4} + \cdots \quad (-1 < x \leq 1), \tag{3.47}$$

we have

$$\tilde{E}_{11} \approx \frac{\partial \hat{U}_1}{\partial X_1}, \tag{3.48}$$

that is, for small displacements and displacement gradients, all three strain measures approach the same value.

From the definition of stretch ratio in Eq. (3.36), aided by use of Eq. (3.7),[16]

$$\Lambda_{(1)} = \frac{dx_1}{dX_1} = \frac{dX_1 + d\hat{U}_1}{dX_1} = 1 + E_{11}|_{inf} = 1 + \tilde{E}_{11}|_{inf}, \tag{3.49}$$

where the $(\ldots)|_{inf}$ signifies "infinitesimal." Further, since for this simple deformation, $\Lambda_{(1)} = \sqrt{C_{11}}$, from Eqs. (3.45) and (3.49) we have

$$\tilde{E}_{11} = \ln\sqrt{C_{11}} = \ln\sqrt{\Lambda_{(1)}^2} = \ln\left(1 + E_{11}|_{inf}\right). \tag{3.50}$$

This relation will be of importance in subsequent problems solving using logarithmic strain.

For large strain the three finite strain definitions diverge. Fig. 3.4 illustrates the behavior of the strain measures for the simple deformation of this section. Also plotted is the displacement gradient itself, $\frac{\partial \hat{U}_1}{\partial X_1}$ $(= \frac{\partial \hat{u}_1}{\partial x_1})$, which from Eqs. (3.46) and (3.48) is also the infinitesimal strain.

3.5.6 Volume and area change with deformation

With deformation, both volume and area changes occur. The ability to quantify these changes is particularly important for finite deformation problems as one must, for example, update the local area during deformation to arrive at an accurate measure of stress (see Section 7.3 of Chapter 7).

[16] The shifter value is unity since the global and spatial coordinate systems are identical.

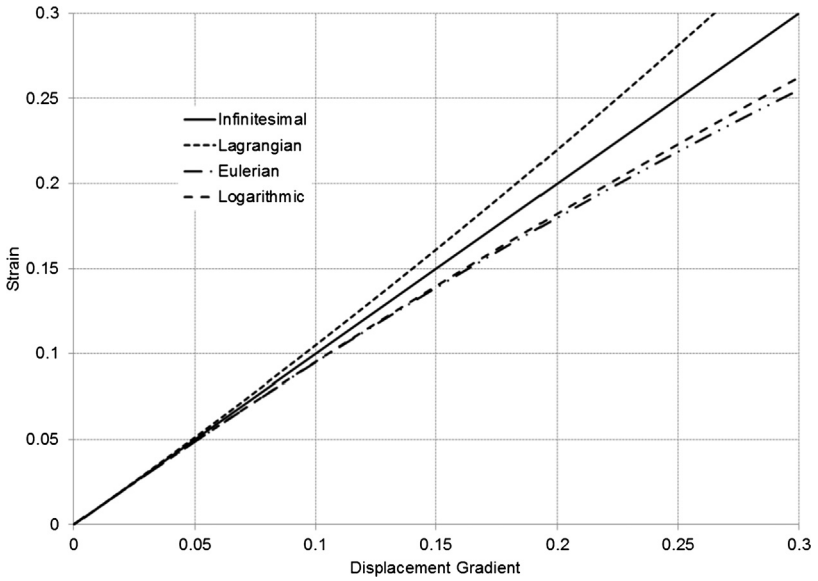

Figure 3.4 ***Comparison of Lagrangian, Eulerian and logarithmic strain measures.*** For small strains, the three measures approach the same value.

3.5.6.1 Volume change

Consider an infinitesimal element (see Fig. 3.5) originally with sides $d\mathbf{P}$, $d\mathbf{Q}$ and $d\mathbf{R}$. The volume of this element is[17]

$$dV = d\mathbf{R} \cdot \left(d\mathbf{P} \times d\mathbf{Q}\right), \quad dV = dR_I \varepsilon_{IJK} dP_J dQ_K. \tag{3.51}$$

From Eq. (3.10), following deformation

$$\begin{aligned} d\mathbf{p} &= \mathbf{F} \cdot d\mathbf{P}, & dp_i &= F_{iJ} dP_J, \\ d\mathbf{q} &= \mathbf{F} \cdot d\mathbf{Q}, & dq_i &= F_{iJ} dQ_J, \\ d\mathbf{r} &= \mathbf{F} \cdot d\mathbf{R}, & dr_i &= F_{iJ} dR_J, \end{aligned} \tag{3.52}$$

the deformed infinitesimal element volume is

$$\begin{aligned} dv &= d\mathbf{r} \cdot \left(d\mathbf{p} \times d\mathbf{q}\right) & dv &= r_i \varepsilon_{ijk} p_j q_k \\ &= \left(\mathbf{F} \cdot d\mathbf{R}\right) \cdot \left[\left(\mathbf{F} \cdot d\mathbf{P}\right) \times \left(\mathbf{F} \cdot d\mathbf{Q}\right)\right], & &= F_{iL} dR_L \varepsilon_{ijk} F_{jM} dP_M F_{kN} dQ_N. \end{aligned} \tag{3.53}$$

[17] The cross product $d\mathbf{P} \times d\mathbf{Q} = |d\mathbf{P}|\,|d\mathbf{Q}| \sin \angle PQ \mathbf{e}_{PQ}$, where $\angle PQ$ is the angle between $d\mathbf{P}$ and $d\mathbf{Q}$ and $\mathbf{e}_{PQ}$ is a unit vector perpendicular to the plane of $d\mathbf{P}$ and $d\mathbf{Q}$—see Section A.3.1.4 of Appendix A. Taking the dot product of $d\mathbf{R}$ with $\mathbf{e}_{PQ}$, which is the height of the parallelepiped, completes the volume calculation.

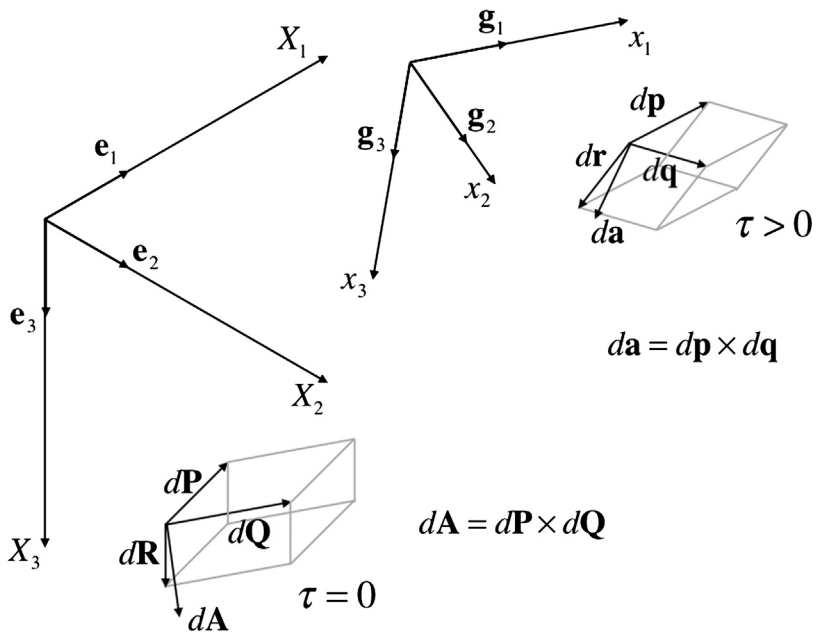

Figure 3.5 ***Volume and area of a deforming infinitesimal element.*** The material volume $dV = d\mathbf{R} \cdot (d\mathbf{P} \times d\mathbf{Q})$ is deformed to the spatial volume $dv = d\mathbf{r} \cdot (d\mathbf{p} \times d\mathbf{q})$. The material area $d\mathbf{A} = d\mathbf{P} \times d\mathbf{Q}$ is deformed to the spatial area $d\mathbf{a} = d\mathbf{p} \times d\mathbf{q}$.

We introduce the Jacobian $\mathcal{J}$, that is, the determinant of the deformation gradient $\mathbf{F}$. From Eq. (A.97) we have

$$\mathcal{J} = \det \mathbf{F} = \frac{1}{6} \varepsilon_{ijk} \varepsilon_{LMN} F_{iL} F_{jM} F_{kN}. \tag{3.54}$$

Further, from the epsilon–delta identity (Eq. (A.26)) we obtain

$$\varepsilon_{ijk} \varepsilon_{ijk} = \delta_{jj} \delta_{kk} - \delta_{jk} \delta_{kj} = 3 \times 3 - 3 = 6. \tag{3.55}$$

Applying Eq. (3.55) to Eq. (3.54), we arrive at the useful relation [11,12]

$$\varepsilon_{LMN} \mathcal{J} = \varepsilon_{LMN} \det \mathbf{F} = \varepsilon_{ijk} F_{iL} F_{jM} F_{kN}. \tag{3.56}$$

If we substitute Eq. (3.56) into Eq. (3.53), then

$$dv = \mathcal{J}\, d\mathbf{R} \cdot \left(d\mathbf{P} \times d\mathbf{Q}\right) = \mathcal{J}\, dV, \quad dv = \mathcal{J} \varepsilon_{LMN} dR_L dP_M dQ_N = \mathcal{J}\, dV, \tag{3.57}$$

where the last substitution in either notation recalls Eq. (3.51).

3.5.6.2 Area change

Consider an infinitesimal area (see Fig. 3.5) originally with sides $d\mathbf{P}$ and $d\mathbf{Q}$. We define an area vector $d\mathbf{A}$ perpendicular to the vectors $d\mathbf{P}$ and $d\mathbf{Q}$ whose area is that of a parallelogram, computed with the cross product (see Section A.3.1.4 of Appendix A)

$$\left|d\mathbf{A}\right| = \left|d\mathbf{P} \times d\mathbf{Q}\right| = \left|d\mathbf{P}\right| \left|d\mathbf{Q}\right| \sin \angle PQ, \qquad dA_I = \varepsilon_{IJK} dP_J dQ_K. \tag{3.58}$$

From Eq. (3.10), following deformation

$$\begin{aligned} d\mathbf{p} &= \mathbf{F} \cdot d\mathbf{P}, & dp_i &= F_{iJ} dP_J, \\ d\mathbf{q} &= \mathbf{F} \cdot d\mathbf{Q}, & dq_i &= F_{iJ} dQ_J, \end{aligned} \tag{3.59}$$

and, using Eq. (A.20), the deformed area is

$$\begin{aligned} d\mathbf{a} &= d\mathbf{p} \times d\mathbf{q} & da_i &= \varepsilon_{ijk} dp_j dq_k \\ &= \left(\mathbf{F} \cdot d\mathbf{P}\right) \times \left(\mathbf{F} \cdot d\mathbf{Q}\right), & &= \varepsilon_{ijk} F_{jM} F_{kN} dP_M dQ_N. \end{aligned} \tag{3.60}$$

Recall Eq. (3.56). Postmultiplying both sides of this relation by F_{Nh}^{-1} [11,12] yields

$$\varepsilon_{LMN} \mathcal{J} F_{Nh}^{-1} = \varepsilon_{ijk} F_{iL} F_{jM} F_{kN} F_{Nh}^{-1} = \varepsilon_{ijk} F_{iL} F_{jM} \delta_{kh} = \varepsilon_{ijh} F_{iL} F_{jM} = \varepsilon_{hij} F_{iL} F_{jM}, \tag{3.61}$$

where we have used the fact that $\mathbf{F} \cdot \mathbf{F} = \mathbf{I}$, $F_{kN} F_{Nh}^{-1} = \delta_{kh}$. If we substitute Eq. (3.61) into Eq. (3.60), then

$$d\mathbf{a} = \mathcal{J} \left(\mathbf{F}^{-1}\right)^T \cdot d\mathbf{A}, \qquad da_i = \mathcal{J} \varepsilon_{OMN} F_{Oi}^{-1} dP_M dQ_N = \mathcal{J} F_{Oi}^{-1} dA_O. \tag{3.62}$$

3.6. LAGRANGIAN STRAIN IN CYLINDRICAL COORDINATES

To this point the kinematic discussion has focused on the X_1–X_2–X_3 coordinate system that is Cartesian or rectangular—the coordinate lines are linear and orthogonal. A second coordinate system playing a major role in tubular studies is the cylindrical coordinate system. The cylindrical coordinate system is termed curvilinear in that the coordinate lines may be curved, although intersections of coordinate lines remain orthogonal.

Fig. 3.6 illustrates an R–Θ–Z cylindrical coordinate system having the same origin as the global X_1–X_2–X_3 coordinate system used previously. The R-coordinate axis lies in the X_1–X_2 plane and is measured along a radius from the origin of the X_1–X_2–X_3 coordinate system. The Θ-coordinate lies in the X_1–X_2 plane and is an angular measurement from the positive X_1-axis toward the positive X_2-axis. The Z-coordinate is collinear with the X_3-axis. The $\mathbf{e}_R$, $\mathbf{e}_\Theta$ and $\mathbf{e}_Z$ unit base vectors are orthogonal and form a right-handed system such that $\mathbf{e}_R \times \mathbf{e}_\Theta = \mathbf{e}_Z$.

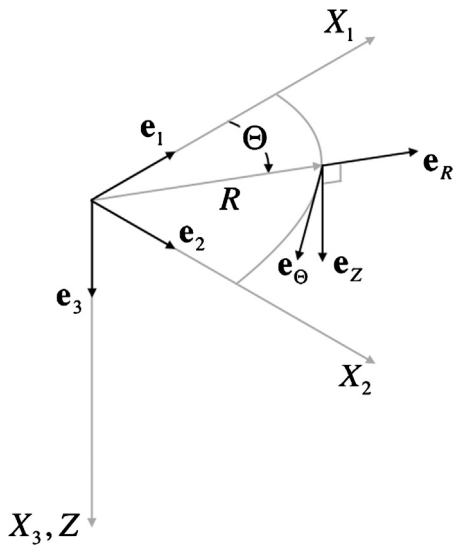

Figure 3.6 ***A cylindrical coordinate system superimposed on the global coordinate system.*** The $\mathbf{e}_\Theta$ base unit vector lies in the X_1–X_2 plane. The $\mathbf{e}_Z$ base unit vector is parallel to the X_3-axis.

A spatial cylindrical coordinate system using coordinates (r–θ–z) and having unit base vectors $\mathbf{g}_r$, $\mathbf{g}_\theta$ and $\mathbf{g}_z$ could similarly be associated with the x_1–x_2–x_3 coordinate system of Fig. 3.2 (see Section 3.7).

The mathematics of tensor analysis is available for general curvilinear systems [13,14], but the use of such is beyond the scope of this text. There exist several alternatives to the elegance of the curvilinear formulations of general tensor analysis. For example, Fung [15] computes[18] the derivatives with respect to X_1, X_2 and X_3 in terms of derivatives with respect to R, Θ and Z, and then applies coordinate transformations to the displacement vector $\mathbf{u}$ and the strain tensor $\mathbf{E}$ to accomplish the transition to cylindrical coordinates. As Fung mentions, this method is straightforward but somewhat tedious. Such computations are further complicated here as we are addressing three dimensions and have not yet ignored any nonlinear terms.

We shall follow an alternative approach that revisits the derivation in rectangular coordinates, this time expressing the position and displacement vectors in cylindrical coordinates. Retracing previous work[19] offers the opportunity to collect insights into the origin of the various terms in the cylindrical coordinate strain formulation.

[18] Fung's exposition [15] is actually for two-dimensional, polar coordinates (no $X_3 = Z$-axis), but the principle can be followed for the three-dimensional case of cylindrical coordinates.

[19] Although we will follow previous work, we will forego explicit derivation of the Green deformation tensor $\mathbf{C}$ as we will not find use for this tensor in subsequent sections.

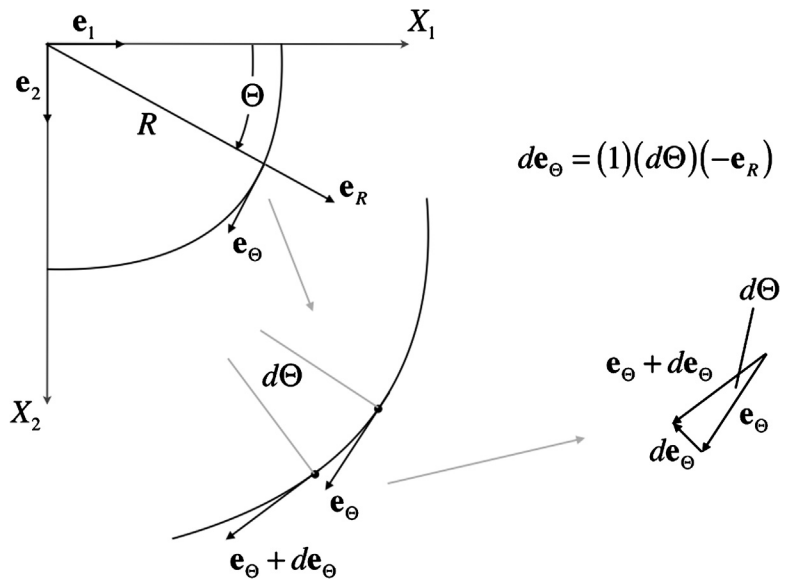

Figure 3.7 ***Illustration of the derivation of*** $d\mathbf{e}_\Theta/d\Theta$**.** The unit vector has a constant magnitude of unity, but its direction changes with Θ. Similar behavior is exhibited by $\mathbf{e}_R$.

As we revisit selected equations, our work will leave the direct notation of expressions untouched; it is the equations in index notation that will require reexpression. These changes will have two sources—the curvilinear nature of the Θ coordinate lines and, as a consequence, the nonconstant character of the $\mathbf{e}_R$ and $\mathbf{e}_\Theta$ unit base vectors. Consider Fig. 3.7 that views the cylindrical system of Fig. 3.6 from a position along the negative Z-axis. The derivatives of $\mathbf{e}_R$ and $\mathbf{e}_\Theta$ with respect to Θ are controlled by the polar angle. There is no change in length of either unit vector, but the azimuth of the vector changes as

$$\frac{d\mathbf{e}_R}{d\Theta} = \mathbf{e}_\Theta, \quad \frac{d\mathbf{e}_\Theta}{d\Theta} = -\mathbf{e}_R, \tag{3.63}$$

implying that for a vector $\mathbf{v} = \hat{\mathbf{V}}(\mathbf{X}, \tau)$ that

$$\begin{aligned} d\mathbf{v} &= \frac{\partial \hat{\mathbf{V}}}{\partial R} dR + \frac{1}{R}\frac{\partial \hat{\mathbf{V}}}{\partial \Theta} R d\Theta + \frac{\partial \hat{\mathbf{V}}}{\partial Z} dZ + \frac{\partial \hat{\mathbf{V}}}{\partial \tau} d\tau \\ &= \left(\frac{\partial \hat{V}_R}{\partial R}\mathbf{e}_R + \frac{\partial \hat{V}_\Theta}{\partial R}\mathbf{e}_\Theta + \frac{\partial \hat{V}_Z}{\partial R}\mathbf{e}_Z \right) dR \\ &\quad + \left(\frac{1}{R}\frac{\partial \hat{V}_R}{\partial \Theta}\mathbf{e}_R + \frac{\hat{V}_R}{R}\frac{\partial \mathbf{e}_R}{\partial \Theta} + \frac{1}{R}\frac{\partial \hat{V}_\Theta}{\partial \Theta}\mathbf{e}_\Theta + \frac{\hat{V}_\Theta}{R}\frac{\partial \mathbf{e}_\Theta}{\partial \Theta} + \frac{1}{R}\frac{\partial \hat{V}_Z}{\partial \Theta}\mathbf{e}_Z \right) R d\Theta \end{aligned}$$

$$+\left(\frac{\partial \hat{V}_R}{\partial Z}\mathbf{e}_R+\frac{\partial \hat{V}_\Theta}{\partial Z}\mathbf{e}_\Theta+\frac{\partial \hat{V}_Z}{\partial Z}\mathbf{e}_Z\right)dZ+\left(\frac{\partial \hat{V}_R}{\partial \tau}\mathbf{e}_R+\frac{\partial \hat{V}_\Theta}{\partial \tau}\mathbf{e}_\Theta+\frac{\partial \hat{V}_Z}{\partial \tau}\mathbf{e}_Z\right)d\tau \tag{3.64}$$

$$\begin{aligned}=&\left[\frac{\partial \hat{V}_R}{\partial R}dR+\left(\frac{1}{R}\frac{\partial \hat{V}_R}{\partial \Theta}-\frac{\hat{V}_\Theta}{R}\right)Rd\Theta+\frac{\partial \hat{V}_R}{\partial Z}dZ+\frac{\partial \hat{V}_R}{\partial \tau}d\tau\right]\mathbf{e}_R\\&+\left[\frac{\partial \hat{V}_\Theta}{\partial R}dR+\left(\frac{\hat{V}_R}{R}+\frac{1}{R}\frac{\partial \hat{V}_\Theta}{\partial \Theta}\right)Rd\Theta+\frac{\partial \hat{V}_\Theta}{\partial Z}dZ+\frac{\partial \hat{V}_\Theta}{\partial \tau}d\tau\right]\mathbf{e}_\Theta\\&+\left[\frac{\partial \hat{V}_Z}{\partial R}dR+\frac{1}{R}\frac{\partial \hat{V}_Z}{\partial \Theta}Rd\Theta+\frac{\partial \hat{V}_Z}{\partial Z}dZ+\frac{\partial \hat{V}_Z}{\partial \tau}d\tau\right]\mathbf{e}_Z,\end{aligned}$$

which contains extra terms in the R and Θ components due to Eq. (3.63). As part of the arrangement of terms, the differential $d\Theta$ in Eq. (3.64) is associated with R, in some cases by multiplying a term by $\frac{R}{R}=1$. This grouping renders all differential quantities' lengths (see Fig. 3.8). Further (see Eq. (3.74)) the grouping makes all the cylindrical components of the Lagrangian strain tensor dimensionless.

In cylindrical coordinates the vectors $\mathbf{X}$ and $\mathbf{x}$ can be written (see Eqs. (3.6) and (3.7) regarding the latter)

$$\mathbf{X}=R\mathbf{e}_R+Z\mathbf{e}_Z, \tag{3.65}$$

$$\mathbf{x}=(R+u_R)\,\mathbf{e}_R+u_\Theta\mathbf{e}_\Theta+(Z+u_Z)\,\mathbf{e}_Z, \tag{3.66}$$

where

$$\begin{aligned}\mathbf{u}=\hat{\mathbf{u}}(r,\theta,z,\tau)&=\hat{u}_r\mathbf{g}_r+\hat{u}_\theta\mathbf{g}_\theta+\hat{u}_z\mathbf{g}_z\\&=\hat{\mathbf{U}}(R,\Theta,Z,\tau)=\hat{U}_R\mathbf{e}_R+\hat{U}_\Theta\mathbf{e}_\Theta+\hat{U}_Z\mathbf{e}_Z,\end{aligned} \tag{3.67}$$

and both $\mathbf{e}_R$ and $\mathbf{e}_\Theta$ are functions of Θ.

In writing Eqs. (3.66) and (3.67), we have simplified all shifters by setting the offset between the material and spatial coordinate systems to zero (i.e., $\mathbf{o}=\mathbf{0}$) and aligning like coordinate axes (i.e., $\mathbf{e}_R=\mathbf{g}_r$, $\mathbf{e}_\Theta=\mathbf{g}_\theta$, $\mathbf{e}_Z=\mathbf{g}_z$). This renders all shifters identical to Kronecker deltas, essentially eliminating these terms from the deformation gradient.

3.6.1 Deformation gradient in cylindrical coordinates

Using Eqs. (3.65) and (3.66) in Eq. (3.11) yields

$$\mathbf{F}=\begin{bmatrix}1+\frac{\partial \hat{U}_R}{\partial R} & \frac{1}{R}\frac{\partial \hat{U}_R}{\partial \Theta}-\frac{\hat{U}_\Theta}{R} & \frac{\partial \hat{U}_R}{\partial Z}\\ \frac{\partial \hat{U}_\Theta}{\partial R} & 1+\frac{\hat{U}_R}{R}+\frac{1}{R}\frac{\partial \hat{U}_\Theta}{\partial \Theta} & \frac{\partial \hat{U}_\Theta}{\partial Z}\\ \frac{\partial \hat{U}_Z}{\partial R} & \frac{1}{R}\frac{\partial \hat{U}_Z}{\partial \Theta} & 1+\frac{\partial \hat{U}_Z}{\partial Z}\end{bmatrix}, \tag{3.68}$$

where now $\mathbf{u}=\hat{\mathbf{U}}(R,\Theta,Z,\tau)$.

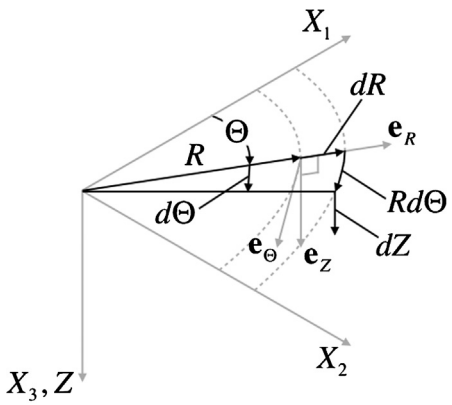

$$d\mathbf{X} = dR\mathbf{e}_R + Rd\Theta\mathbf{e}_\Theta + dZ\mathbf{e}_Z$$

Figure 3.8 ***Illustration of Eq.*** (3.69)**.** The arc length $Rd\Theta$ measures distance along the Θ coordinate. The $\mathbf{e}_\Theta$ base unit vector lies in the X_1–X_2 plane. The $\mathbf{e}_Z$ base unit vector is parallel to the X_3-axis.

3.6.2 Strain in cylindrical coordinates

An increment in $\mathbf{X}$ is

$$d\mathbf{X} = dR\mathbf{e}_R + Rd\Theta\mathbf{e}_\Theta + dZ\mathbf{e}_Z. \tag{3.69}$$

Eq. (3.69) leaves us with what we would expect for a differential element in cylindrical coordinates—a component having the units of length in each of the three coordinate directions. Accounting for $d\mathbf{e}_R/d\Theta$ introduces R to the Θ component of $d\mathbf{X}$ so that the measure of circular arc $Rd\Theta$ appears naturally (see Fig. 3.8).

An increment in $\mathbf{u}$ is found by substituting Eq. (3.67) into Eq. (3.64):

$$\begin{aligned} d\mathbf{u} = &\left[\frac{\partial \hat{U}_R}{\partial R}dR + \left(\frac{1}{R}\frac{\partial \hat{U}_R}{\partial \Theta} - \frac{\hat{U}_\Theta}{R}\right)Rd\Theta + \frac{\partial \hat{U}_R}{\partial Z}dZ + \frac{\partial \hat{U}_R}{\partial \tau}d\tau\right]\mathbf{e}_R \\ &+ \left[\frac{\partial \hat{U}_\Theta}{\partial R}dR + \left(\frac{\hat{U}_R}{R} + \frac{1}{R}\frac{\partial \hat{U}_\Theta}{\partial \Theta}\right)Rd\Theta + \frac{\partial \hat{U}_\Theta}{\partial Z}dZ + \frac{\partial \hat{U}_\Theta}{\partial \tau}d\tau\right]\mathbf{e}_\Theta \\ &+ \left[\frac{\partial \hat{U}_Z}{\partial R}dR + \frac{1}{R}\frac{\partial \hat{U}_Z}{\partial \Theta}Rd\Theta + \frac{\partial \hat{U}_Z}{\partial Z}dZ + \frac{\partial \hat{U}_Z}{\partial \tau}d\tau\right]\mathbf{e}_Z. \end{aligned} \tag{3.70}$$

If we use the fact that $d\mathbf{x} = d\mathbf{X} + d\mathbf{u}$ in Eq. (3.22), then

$$\begin{aligned} ds^2 - dS^2 &= d\mathbf{x}^T \cdot d\mathbf{x} - d\mathbf{X}^T \cdot d\mathbf{X} = \left(d\mathbf{X} + d\mathbf{u}\right)^T \cdot \left(d\mathbf{X} + d\mathbf{u}\right) - d\mathbf{X}^T \cdot d\mathbf{X} \\ &= d\mathbf{X}^T \cdot d\mathbf{X} + 2d\mathbf{X}^T \cdot d\mathbf{u} + d\mathbf{u}^T \cdot d\mathbf{u} - d\mathbf{X}^T \cdot d\mathbf{X} \\ &= 2d\mathbf{X}^T \cdot d\mathbf{u} + d\mathbf{u}^T \cdot d\mathbf{u} = \left(2d\mathbf{X}^T + d\mathbf{u}^T\right) \cdot d\mathbf{u}. \end{aligned} \tag{3.71}$$

Eq. (3.71) makes use of the commutative and distributive properties of the dot product (see Section A.3.1.3 of Appendix A) and the facts that $\left(d\mathbf{X}+d\mathbf{u}\right)^T = d\mathbf{X}^T + d\mathbf{u}^T$ and $d\mathbf{X}^T \cdot d\mathbf{u} = d\mathbf{u}^T \cdot d\mathbf{X}$. With Eqs. (3.69) and (3.70) substituted into Eq. (3.71),[20]

$$\begin{aligned}
ds^2 - dS^2 = &\left\{\left[2dR + \frac{\partial \hat{U}_R}{\partial R}dR + \left(\frac{1}{R}\frac{\partial \hat{U}_R}{\partial \Theta} - \frac{\hat{U}_\Theta}{R}\right)Rd\Theta + \frac{\partial \hat{U}_R}{\partial Z}dZ\right]\mathbf{e}_R\right. \\
&+\left[2Rd\Theta + \frac{\partial \hat{U}_\Theta}{\partial R}dR + \left(\frac{\hat{U}_R}{R} + \frac{1}{R}\frac{\partial \hat{U}_\Theta}{\partial \Theta}\right)Rd\Theta + \frac{\partial \hat{U}_\Theta}{\partial Z}dZ\right]\mathbf{e}_\Theta \\
&\left.+\left[2dZ + \frac{\partial \hat{U}_Z}{\partial R}dR + \frac{1}{R}\frac{\partial \hat{U}_Z}{\partial \Theta}Rd\Theta + \frac{\partial \hat{U}_Z}{\partial Z}dZ\right]\mathbf{e}_Z\right\} \\
&\cdot\left\{\left[\frac{\partial \hat{U}_R}{\partial R}dR + \left(\frac{1}{R}\frac{\partial \hat{U}_R}{\partial \Theta} - \frac{\hat{U}_\Theta}{R}\right)Rd\Theta + \frac{\partial \hat{U}_R}{\partial Z}dZ\right]\mathbf{e}_R\right. \\
&+\left[\frac{\partial \hat{U}_\Theta}{\partial R}dR + \left(\frac{\hat{U}_R}{R} + \frac{1}{R}\frac{\partial \hat{U}_\Theta}{\partial \Theta}\right)Rd\Theta + \frac{\partial \hat{U}_\Theta}{\partial Z}dZ\right]\mathbf{e}_\Theta \\
&\left.+\left[\frac{\partial \hat{U}_Z}{\partial R}dR + \frac{1}{R}\frac{\partial \hat{U}_Z}{\partial \Theta}Rd\Theta + \frac{\partial \hat{U}_Z}{\partial Z}dZ\right]\mathbf{e}_Z\right\}.
\end{aligned} \tag{3.72}$$

Eq. (3.72) can be simplified by carrying out the indicated dot products and collecting terms to

$$\begin{aligned}
ds^2 - dS^2 = &\left[2\frac{\partial \hat{U}_R}{\partial R} + \left(\frac{\partial \hat{U}_R}{\partial R}\right)^2 + \left(\frac{\partial \hat{U}_\Theta}{\partial R}\right)^2 + \left(\frac{\partial \hat{U}_Z}{\partial R}\right)^2\right]dRdR \\
&+\left[2\left(\frac{\hat{U}_R}{R} + \frac{1}{R}\frac{\partial \hat{U}_\Theta}{\partial \Theta}\right) + \left(\frac{1}{R}\frac{\partial \hat{U}_R}{\partial \Theta} - \frac{\hat{U}_\Theta}{R}\right)^2 + \left(\frac{\hat{U}_R}{R} + \frac{1}{R}\frac{\partial \hat{U}_\Theta}{\partial \Theta}\right)^2\right. \\
&\left.+\left(\frac{1}{R}\frac{\partial \hat{U}_Z}{\partial \Theta}\right)^2\right]Rd\Theta Rd\Theta \\
&+\left[2\frac{\partial \hat{U}_Z}{\partial Z} + \left(\frac{\partial \hat{U}_R}{\partial Z}\right)^2 + \left(\frac{\partial \hat{U}_\Theta}{\partial Z}\right)^2 + \left(\frac{\partial \hat{U}_Z}{\partial Z}\right)^2\right]dZdZ \\
&+2\left[\left(\frac{1}{R}\frac{\partial \hat{U}_R}{\partial \Theta} - \frac{\hat{U}_\Theta}{R}\right) + \frac{\partial \hat{U}_R}{\partial R}\left(\frac{1}{R}\frac{\partial \hat{U}_R}{\partial \Theta} - \frac{\hat{U}_\Theta}{R}\right) + \frac{\partial \hat{U}_\Theta}{\partial R}\right. \\
&\left.+\frac{\partial \hat{U}_\Theta}{\partial R}\left(\frac{\hat{U}_R}{R} + \frac{1}{R}\frac{\partial \hat{U}_\Theta}{\partial \Theta}\right) + \frac{\partial \hat{U}_Z}{\partial R}\frac{1}{R}\frac{\partial \hat{U}_Z}{\partial \Theta}\right]RdRd\Theta
\end{aligned} \tag{3.73}$$

[20] In this substitution, $d\tau = 0$ as we wish to examine spatial gradients at a specific time.

$$+2\left[\left(\frac{1}{R}\frac{\partial \hat{U}_R}{\partial \Theta}-\frac{\hat{U}_\Theta}{R}\right)\frac{\partial \hat{U}_R}{\partial Z}+\frac{\partial \hat{U}_\Theta}{\partial Z}+\frac{\partial \hat{U}_\Theta}{\partial Z}\left(\frac{\hat{U}_R}{R}+\frac{1}{R}\frac{\partial \hat{U}_\Theta}{\partial \Theta}\right)\right.$$
$$\left.+\frac{1}{R}\frac{\partial \hat{U}_Z}{\partial \Theta}+\frac{1}{R}\frac{\partial \hat{U}_Z}{\partial \Theta}\frac{\partial \hat{U}_Z}{\partial Z}\right]Rd\Theta dZ$$
$$+2\left[\frac{\partial \hat{U}_Z}{\partial R}+\frac{\partial \hat{U}_R}{\partial Z}+\frac{\partial \hat{U}_R}{\partial Z}\frac{\partial \hat{U}_R}{\partial R}+\frac{\partial \hat{U}_\Theta}{\partial Z}\frac{\partial \hat{U}_\Theta}{\partial R}+\frac{\partial \hat{U}_Z}{\partial Z}\frac{\partial \hat{U}_Z}{\partial R}\right]dZdR.$$

Eq. (3.73) can be rewritten in terms of the components of the strain tensor in cylindrical coordinates as

$$ds^2-dS^2=2E_{RR}dRdR+2E_{\Theta\Theta}Rd\Theta Rd\Theta+2E_{ZZ}dZdZ+2\left(E_{R\Theta}+E_{\Theta R}\right)RdRd\Theta$$
$$+2\left(E_{\Theta Z}+E_{Z\Theta}\right)Rd\Theta dZ+2\left(E_{RZ}+E_{ZR}\right)dZdR, \tag{3.74}$$

where $E_{R\Theta}=E_{\Theta R}$, $E_{\Theta Z}=E_{Z\Theta}$ and $E_{RZ}=E_{ZR}$. When Eqs. (3.73) and (3.74) are compared, the components of strain emerge:

$$E_{RR}=\frac{\partial \hat{U}_R}{\partial R}+\frac{1}{2}\left[\left(\frac{\partial \hat{U}_R}{\partial R}\right)^2+\left(\frac{\partial \hat{U}_\Theta}{\partial R}\right)^2+\left(\frac{\partial \hat{U}_Z}{\partial R}\right)^2\right], \tag{3.75}$$

$$E_{\Theta\Theta}=\frac{\hat{U}_R}{R}+\frac{1}{R}\frac{\partial \hat{U}_\Theta}{\partial \Theta}+\frac{1}{2}\left[\left(\frac{1}{R}\frac{\partial \hat{U}_R}{\partial \Theta}-\frac{\hat{U}_\Theta}{R}\right)^2+\left(\frac{\hat{U}_R}{R}+\frac{1}{R}\frac{\partial \hat{U}_\Theta}{\partial \Theta}\right)^2+\left(\frac{1}{R}\frac{\partial \hat{U}_Z}{\partial \Theta}\right)^2\right], \tag{3.76}$$

$$E_{ZZ}=\frac{\partial \hat{U}_Z}{\partial Z}+\frac{1}{2}\left[\left(\frac{\partial \hat{U}_R}{\partial Z}\right)^2+\left(\frac{\partial \hat{U}_\Theta}{\partial Z}\right)^2+\left(\frac{\partial \hat{U}_Z}{\partial Z}\right)^2\right], \tag{3.77}$$

$$E_{R\Theta}=E_{\Theta R}=\frac{1}{2}\left[\frac{\partial \hat{U}_\Theta}{\partial R}+\left(\frac{1}{R}\frac{\partial \hat{U}_R}{\partial \Theta}-\frac{\hat{U}_\Theta}{R}\right)+\frac{\partial \hat{U}_R}{\partial R}\left(\frac{1}{R}\frac{\partial \hat{U}_R}{\partial \Theta}-\frac{\hat{U}_\Theta}{R}\right)\right.$$
$$\left.+\frac{\partial \hat{U}_\Theta}{\partial R}\left(\frac{\hat{U}_R}{R}+\frac{1}{R}\frac{\partial \hat{U}_\Theta}{\partial \Theta}\right)+\frac{\partial \hat{U}_Z}{\partial R}\frac{1}{R}\frac{\partial \hat{U}_Z}{\partial \Theta}\right], \tag{3.78}$$

$$E_{\Theta Z}=E_{Z\Theta}=\frac{1}{2}\left[\frac{1}{R}\frac{\partial \hat{U}_Z}{\partial \Theta}+\frac{\partial \hat{U}_\Theta}{\partial Z}+\left(\frac{\hat{U}_R}{R}+\frac{1}{R}\frac{\partial \hat{U}_\Theta}{\partial \Theta}\right)\frac{\partial \hat{U}_\Theta}{\partial Z}\right.$$
$$\left.+\left(\frac{1}{R}\frac{\partial \hat{U}_R}{\partial \Theta}-\frac{\hat{U}_\Theta}{R}\right)\frac{\partial \hat{U}_R}{\partial Z}+\frac{1}{R}\frac{\partial \hat{U}_Z}{\partial \Theta}\frac{\partial \hat{U}_Z}{\partial Z}\right], \tag{3.79}$$

$$E_{ZR}=E_{RZ}=\frac{1}{2}\left[\frac{\partial \hat{U}_R}{\partial Z}+\frac{\partial \hat{U}_Z}{\partial R}+\frac{\partial \hat{U}_R}{\partial Z}\frac{\partial \hat{U}_R}{\partial R}+\frac{\partial \hat{U}_\Theta}{\partial Z}\frac{\partial \hat{U}_\Theta}{\partial R}+\frac{\partial \hat{U}_Z}{\partial Z}\frac{\partial \hat{U}_Z}{\partial R}\right]. \tag{3.80}$$

Eqs. (3.75)–(3.80) are the final expressions for the Lagrangian strain tensor expressed in terms of the global material coordinate system and displacement.

3.6.3 Special cases of Lagrangian strain in cylindrical coordinates

The geometry of the structure or the nature of the displacement field may be such as to allow simplification of Eqs. (3.75)–(3.80). The more important of these simplifications to tubular design are detailed in the sections to follow.

3.6.3.1 Infinitesimal deformation

If all displacements and displacement gradients are small enough so that second order terms in these infinitesimals can be neglected (i.e., $\hat{U}_R \ll 1$ and $\frac{\partial \hat{U}_R}{\partial X_R} \ll 1$, etc.), Eqs. (3.75)–(3.80) become[21]

$$E_{RR} = \frac{\partial \hat{U}_R}{\partial R}, \tag{3.81}$$

$$E_{\Theta\Theta} = \frac{\hat{U}_R}{R} + \frac{1}{R}\frac{\partial \hat{U}_\Theta}{\partial \Theta}, \tag{3.82}$$

$$E_{ZZ} = \frac{\partial \hat{U}_Z}{\partial Z}, \tag{3.83}$$

$$E_{R\Theta} = E_{\Theta R} = \frac{1}{2}\left[\frac{\partial \hat{U}_\Theta}{\partial R} + \left(\frac{1}{R}\frac{\partial \hat{U}_R}{\partial \Theta} - \frac{\hat{U}_\Theta}{R}\right)\right], \tag{3.84}$$

$$E_{\Theta Z} = E_{Z\Theta} = \frac{1}{2}\left(\frac{1}{R}\frac{\partial \hat{U}_Z}{\partial \Theta} + \frac{\partial \hat{U}_\Theta}{\partial Z}\right), \tag{3.85}$$

$$E_{ZR} = E_{RZ} = \frac{1}{2}\left(\frac{\partial \hat{U}_R}{\partial Z} + \frac{\partial \hat{U}_Z}{\partial R}\right). \tag{3.86}$$

The volume change for an infinitesimal depends, from Eq. (3.57), on the determinant of the deformation gradient. From Eq. (3.68), we compute

$$\begin{aligned}\mathcal{J} &= \left(1 + \frac{\partial \hat{U}_R}{\partial R}\right)\left[\left(1 + \frac{\hat{U}_R}{R} + \frac{1}{R}\frac{\partial \hat{U}_\Theta}{\partial \Theta}\right)\left(1 + \frac{\partial \hat{U}_Z}{\partial Z}\right) - O(2)\right] - O(2) + O(2) \\ &= 1 + \frac{\partial \hat{U}_R}{\partial R} + \frac{\hat{U}_R}{R} + \frac{1}{R}\frac{\partial \hat{U}_\Theta}{\partial \Theta} + \frac{\partial \hat{U}_Z}{\partial Z} + O(2),\end{aligned} \tag{3.87}$$

[21] Inasmuch as this entire section is devoted to infinitesimal deformation, although the simplifications are applied to the Lagrangian strain tensor, the resulting expressions can be associated with Eulerian and logarithmic strain also, as in the limit of small displacements and displacement gradients, these three strains are indistinguishable (see Section 3.5.5).

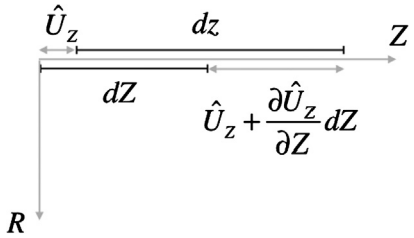

Figure 3.9 ***Physical interpretation of strain component*** E_{ZZ}**.** The Θ-axis is perpendicular to the page, directed away from the reader. For clarity the two states of the infinitesimal element have been slightly offset from the Z-axis.

where $O(2)$ indicates a quantity that is at least second order in infinitesimal quantities. Comparing Eq. (3.87) with Eqs. (3.81)–(3.83) gives

$$\frac{dv}{dV} = \mathcal{J} = 1 + E_{RR} + E_{\Theta\Theta} + E_{ZZ}, \qquad \frac{dv - dV}{dV} = E_{RR} + E_{\Theta\Theta} + E_{ZZ}, \tag{3.88}$$

that is, the change in infinitesimal volume as compared to the original volume is, under the assumption of infinitesimal deformation, the sum of the three normal strain components.[22] This same result for $\mathcal{J}$ can be useful in the formula for area change, Eq. (3.62).

Physical interpretation of infinitesimal strain components

By examining simple deformations of properly aligned infinitesimal line elements, we can attach physical meaning to the components of infinitesimal strain.

Extension Consider an infinitesimal line element originally lying along the Z-axis that undergoes a deformation having only a displacement component along the Z-axis. Then $\hat{U}_R = \hat{U}_\Theta = 0$.

As depicted in Fig. 3.9, initially the element has length dZ. Due to deformation along the Z-axis, the left side of the element displaces a distance $\hat{U}_z$ and the right side of the element displaces a distance $\hat{U}_Z + \left(\partial \hat{U}_Z / \partial Z\right) dZ$, resulting in a length change of $\left(\partial \hat{U}_z / \partial Z\right) dZ$. According to Eqs. (3.74) and (3.83), the length change of the element, as compared to its original length, is

$$ds^2 - dS^2 = \left(ds - dS\right)\left(ds + dS\right) = 2\frac{\partial \hat{U}_Z}{\partial Z} dZ dZ, \tag{3.89}$$

[22] Consideration of the procedure used to arrive at Eq. (3.88) will lead one to conclude that the same is true for volumetric strain in a Cartesian or rectangular coordinate system—under the assumption of infinitesimal deformation, $\frac{dv - dV}{dV} = E_{KK}$.

or

$$ds - dS = \frac{2}{ds + dS} \frac{\partial \hat{U}_Z}{\partial Z} dZ dZ \approx \frac{\partial \hat{U}_Z}{\partial Z} dZ, \tag{3.90}$$

where we have used the fact that for infinitesimal strain, $ds \approx dS = dZ$. That is, for the case of infinitesimal strain, the linear portion of E_{ZZ} is the change in length, as compared to the original length, of a line element originally positioned along the Z-axis and undergoing extension in the Z-direction

$$\frac{ds - dS}{dS} = \frac{dz - dZ}{dZ} \approx \frac{\partial \hat{U}_Z}{\partial Z} = E_{ZZ}. \tag{3.91}$$

The above argument can be used to explain the physical meaning of $E_{RR} = \partial \hat{U}_R / \partial R$ and any of the three $E_{\bar{K}\bar{K}} = \partial \hat{U}_{\bar{K}} / \partial X_{\bar{K}}$ in a rectangular coordinate system, where the bar indicates the indices are not to be summed.

In the Θ coordinate direction for a cylindrical coordinate system, we can also use the same argument as above, provided we recognize (a) the length of the differential element $dS = R d\Theta$ and (b) a displacement in the R direction can also cause a length change in the differential element.

First, consider a deformation where $\hat{U}_R = 0$, that is, the element only stretches along the Θ coordinate line. As depicted in Fig. 3.10, initially the element has length[23] $R d\Theta$. Due to deformation along the Θ coordinate line, the side of the element closest to the X_1-axis displaces[24] a distance $\hat{U}_\Theta$ and the far side of the element displaces a distance $\hat{U}_\Theta + \left(\partial \hat{U}_\Theta / \partial \Theta\right) d\Theta$, resulting in a length change of $\left(\partial \hat{U}_\Theta / \partial \Theta\right) d\Theta$. According to Eq. (3.82) with $\hat{U}_R = 0$, the length change of the element, as compared to its original length, is

$$ds^2 - dS^2 = \left(ds - dS\right)\left(ds + dS\right) = 2 \frac{1}{R} \frac{\partial \hat{U}_\Theta}{\partial \Theta} R d\Theta R d\Theta, \tag{3.92}$$

or

$$ds - dS = \frac{2}{ds + dS} \frac{1}{R} \frac{\partial \hat{U}_\Theta}{\partial \Theta} R d\Theta R d\Theta \approx \frac{1}{R} \frac{\partial \hat{U}_\Theta}{\partial \Theta} R d\Theta, \tag{3.93}$$

where we have used the fact that for infinitesimal strain, $ds \approx dS = R d\Theta$. That is, the linear portion of $E_{\Theta\Theta}$ associated with change along the Θ coordinate line is the change in length, as compared to the original length, of a line element originally positioned

[23] Once more the factor $\frac{R}{R} = 1$ is employed to achieve a length dimension along the Θ coordinate line.

[24] In Fig. 3.10 the displacements are shown having a curvature following the coordinate line. This curvature disappears to whatever degree necessary when the displacements are recognized to be infinitesimal.

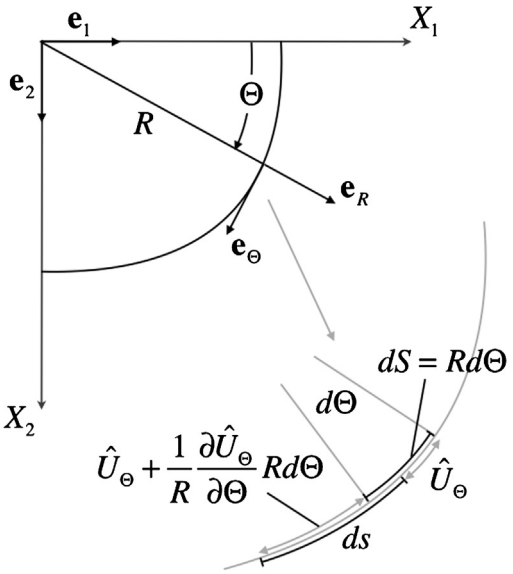

Figure 3.10 ***Physical interpretation of the*** $\frac{1}{R}\frac{\partial \hat{U}_\Theta}{\partial \Theta}$ ***term in strain component*** $E_{\Theta\Theta}$**.** The Z-axis is perpendicular to the page, directed away from the reader. For clarity the two states of the infinitesimal element have been slightly offset from the Θ coordinate line.

along the Θ coordinate line and only undergoing displacement in the Θ-direction

$$\frac{ds - dS}{dS} = \frac{rd\theta - Rd\Theta}{Rd\Theta} \approx \frac{1}{R}\frac{\partial \hat{U}_\Theta}{\partial \Theta} = E_{\Theta\Theta}, \quad \hat{U}_R = 0. \tag{3.94}$$

To examine the $\hat{U}_R/R$ term in the linearized $E_{\Theta\Theta}$ strain component, consider a deformation where $\hat{U}_\Theta = 0$, that is, the element only stretches as it is deformed in the R coordinate direction.[25] As depicted in Fig. 3.11, initially the element has length $Rd\Theta$. Due to deformation along the R coordinate line, the element displaces a distance $\hat{U}_R$, resulting in a length change of $\hat{U}_R d\Theta$. According to Eq. (3.82) with $\hat{U}_\Theta = 0$, the length change of the element, as compared to its original length, is

$$ds^2 - dS^2 = (ds - dS)(ds + dS) = 2\frac{\partial \hat{U}_R}{R} Rd\Theta Rd\Theta, \tag{3.95}$$

or

$$ds - dS = \frac{2}{ds + dS}\frac{\hat{U}_R}{R} Rd\Theta Rd\Theta \approx \frac{\hat{U}_R}{R} Rd\Theta, \tag{3.96}$$

[25] Axisymmetric expansion or contraction of a cylindrical cross section is an example of this type of deformation.

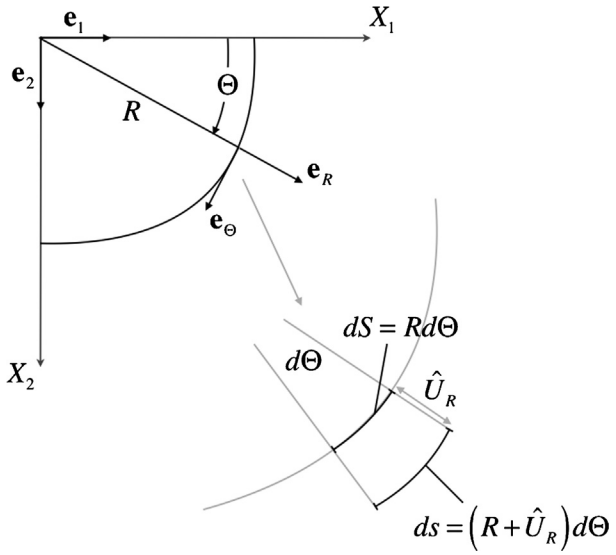

Figure 3.11 ***Physical interpretation of the*** $\frac{\hat{U}_R}{R}$ ***term in strain component*** $E_{\Theta\Theta}$**.** The Z-axis is perpendicular to the page, directed away from the reader.

where we have used the fact that for infinitesimal strain, $ds \approx dS = Rd\Theta$. That is, the linear portion of $E_{\Theta\Theta}$ associated with change along the R coordinate line is the change in length, as compared to the original length, of a line element originally positioned along the Θ coordinate line and only undergoing displacement in the R-direction

$$\frac{ds - dS}{dS} = \frac{rd\theta - Rd\Theta}{Rd\Theta} \approx \frac{\hat{U}_R}{R} = E_{\Theta\Theta}, \quad \hat{U}_\Theta = 0. \tag{3.97}$$

Shear Consider two infinitesimal line elements—one originally lying along the R-axis ($d\mathbf{R} = dR\mathbf{e}_R$) and one originally lying along the Z-axis ($\mathrm{d}\mathbf{Z} = dZ\mathbf{e}_Z$)—that undergo a deformation having no displacement component along the Θ coordinate line. Then $\hat{U}_\Theta = 0$.

As depicted in Fig. 3.12, initially the angle between the two line elements is $\pi/2$ radians or 90°. Due to *radial*[26] deformation along the Z-axis, the left side of element 2 displaces a distance $\hat{U}_R$ and the right side of the element displaces a distance $\hat{U}_R + (\partial \hat{U}_R/\partial Z)dZ$. As Fig. 3.12 illustrates, the differential radial displacement along the element is $(\partial \hat{U}_R/\partial Z)dZ$ and the tangent of the resulting angle with the Z-axis is $\partial \hat{U}_R/\partial Z$. For a small angle, however, the angle (measured in radians) is approximately

[26] As indicated in Fig. 3.12, there also exists a (differential) displacement in the Z direction. This displacement has no effect on the current discussion.

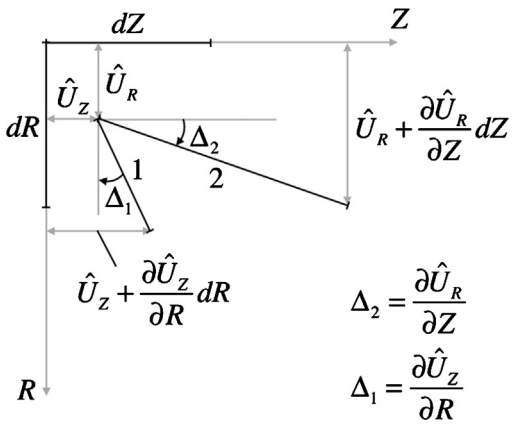

Figure 3.12 ***Physical interpretation of strain component*** $E_{ZR} = E_{RZ}$. The Θ-axis is perpendicular to the page, directed away from the reader.

equal to both its sine and tangent.[27] We may write

$$\Delta_2 = \arctan \frac{\partial \hat{U}_R}{\partial Z} \approx \frac{\partial \hat{U}_R}{\partial Z}. \tag{3.98}$$

By a similar argument along the R-axis, we may conclude

$$\Delta_1 = \arctan \frac{\partial \hat{U}_Z}{\partial R} \approx \frac{\partial \hat{U}_Z}{\partial R}. \tag{3.99}$$

The total decrease in angle between two differential line segments, which were initially perpendicular and aligned with the R and Z-axes, is therefore

$$\Delta_2 + \Delta_1 = \frac{\partial \hat{U}_R}{\partial Z} + \frac{\partial \hat{U}_Z}{\partial R}, \tag{3.100}$$

which, according to Eq. (3.86), is exactly twice the value of the E_{ZR} shear strain.

The above argument can be used to explain the physical meaning of

$$E_{\Theta Z} = (1/2)[(1/R)\partial \hat{U}_Z/\partial \Theta + \partial \hat{U}_\Theta/\partial Z]$$

and any of the three

$$E_{IJ} = (1/2)[\partial \hat{U}_I/\partial X_J + \partial \hat{U}_J/\partial X_I], \quad I \neq J,$$

in a rectangular coordinate system.

[27] The series expansion [10] of the sine function is $\sin\alpha = \alpha - \alpha^3/3! + \alpha^5/5! - \alpha^7/7! + \cdots$, and the series expansion of the tangent function is $\tan\alpha = \alpha + (1/3)\alpha^3 + (2/15)\alpha^5 + (17/315)\alpha^7 + \cdots$. If the higher order terms in both these expressions are ignored, $\alpha \approx \sin\alpha \approx \tan\alpha$.

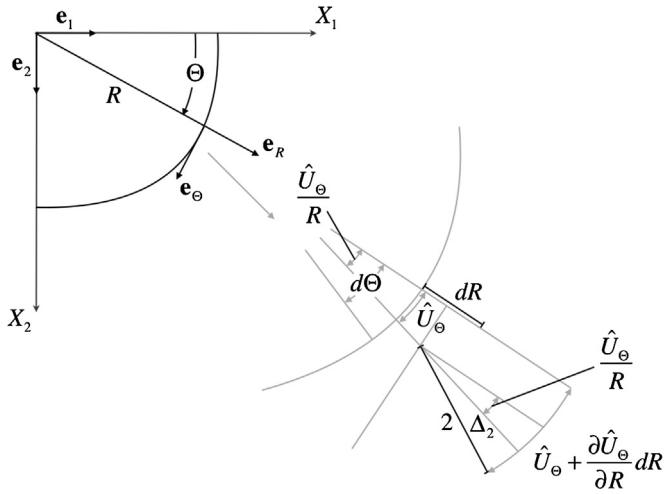

Figure 3.13 ***Physical interpretation of strain component*** $E_{R\Theta} = E_{\Theta R}$**.** Of the two infinitesimal line segments, the line segment in the $\mathbf{e}_\Theta$ direction has been removed for clarity (see Fig. 3.14 for both line segments). The curved Θ-coordinate line requires a correction when measuring angle Δ_2.

Prior to examining $E_{R\Theta}$, we note that the first two terms on the right-hand side of Eq. (3.84) are similar to the work described above in the interpretation of E_{RZ}. It is the origin of the $\hat{U}_\Theta/R$ term that requires further discussion. To this end, consider Fig. 3.13 that omits the line segment along the Θ-coordinate line and concentrates on displacement of the dR differential line element.

Due to circumferential deformation along the R coordinate line, the end of the differential line element closest to the origin displaces a distance $\hat{U}_\Theta$ and the other end of the element displaces a distance $\hat{U}_\Theta + (\partial \hat{U}_\Theta/\partial R)dR$. As Fig. 3.13 illustrates, the differential circumferential displacement along the element is $(\partial \hat{U}_\Theta/\partial R)dR$, and the tangent of the resulting angle with the R-axis is $\partial \hat{U}_\Theta/\partial R$. A correction must be made to this angle, however, since, as indicated in the figure, a portion of the angle is due to $\hat{U}_\Theta$ itself.[28] This corrective angle, to be subtracted from Δ_2, has magnitude $\hat{U}_\Theta/R$. The net angle change from the R-coordinate line is therefore

$$\Delta_2 = \arctan \frac{\partial \hat{U}_\Theta}{\partial R} - \frac{\hat{U}_\Theta}{R} \approx \frac{\partial \hat{U}_\Theta}{\partial R} - \frac{\hat{U}_\Theta}{R}. \tag{3.101}$$

Fig. 3.14 now presents the complete problem. The angle Δ_2 is given by Eq. (3.101). The other angle change is

[28] Consider Fig. 3.13 and a deformation $\hat{U}_\Theta = k$, where k is a constant. Then $\partial \hat{U}_\Theta/\partial R = 0$, and the line segment dR translates in a parallel fashion. The pertinent, intersecting coordinate lines, however, have

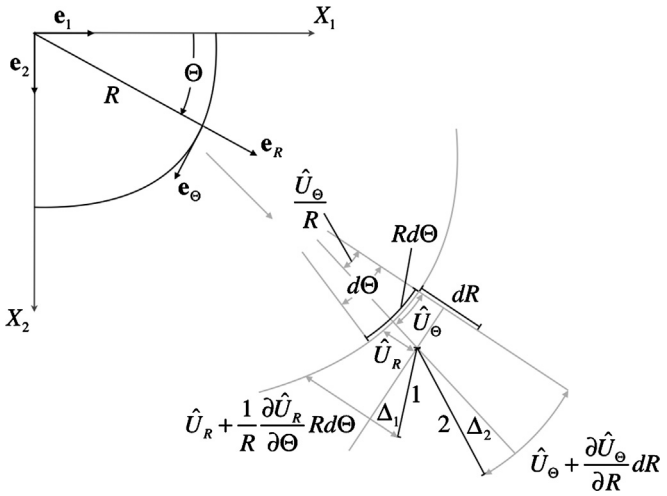

Figure 3.14 ***Physical interpretation of strain component*** $E_{R\Theta} = E_{\Theta R}$**.** Here the complete problem is displayed, with some details from Fig. 3.13 omitted for clarity.

$$\Delta_1 = \arctan \frac{1}{R}\frac{\partial \hat{U}_R}{\partial \Theta} \approx \frac{1}{R}\frac{\partial \hat{U}_R}{\partial \Theta}, \tag{3.102}$$

and the total angle change is therefore

$$\Delta_2 + \Delta_1 = \frac{\partial \hat{U}_\Theta}{\partial R} - \frac{\hat{U}_\Theta}{R} + \frac{1}{R}\frac{\partial \hat{U}_R}{\partial \Theta}, \tag{3.103}$$

which, according to Eq. (3.84), is exactly twice the value of the $E_{R\Theta}$ shear strain.

3.6.3.2 Axisymmetric deformation

If the deformation is axisymmetric, $\partial/\partial\Theta = \hat{U}_\Theta = 0$, and Eqs. (3.75)–(3.80) become

$$E_{RR} = \frac{\partial \hat{U}_R}{\partial R} + \frac{1}{2}\left[\left(\frac{\partial \hat{U}_R}{\partial R}\right)^2 + \left(\frac{\partial \hat{U}_Z}{\partial R}\right)^2\right], \tag{3.104}$$

$$E_{\Theta\Theta} = \frac{\hat{U}_R}{R} + \frac{1}{2}\left(\frac{\hat{U}_R}{R}\right)^2, \tag{3.105}$$

$$E_{ZZ} = \frac{\partial \hat{U}_Z}{\partial Z} + \frac{1}{2}\left[\left(\frac{\partial \hat{U}_R}{\partial Z}\right)^2 + \left(\frac{\partial \hat{U}_Z}{\partial Z}\right)^2\right], \tag{3.106}$$

rotated an amount $\hat{U}_\Theta/R$ without undergoing deformation. Thus, *relative to the orthogonal coordinate lines*, the line segment has undergone a (negative) rotation.

$$E_{R\Theta} = E_{\Theta R} = 0, \tag{3.107}$$

$$E_{\Theta Z} = E_{Z\Theta} = 0, \tag{3.108}$$

$$E_{ZR} = E_{RZ} = \frac{1}{2}\left[\frac{\partial \hat{U}_R}{\partial Z} + \frac{\partial \hat{U}_Z}{\partial R} + \frac{\partial \hat{U}_R}{\partial Z}\frac{\partial \hat{U}_R}{\partial R} + \frac{\partial \hat{U}_Z}{\partial Z}\frac{\partial \hat{U}_Z}{\partial R}\right]. \tag{3.109}$$

3.6.3.3 Axisymmetric, infinitesimal deformation

If the deformation is both axisymmetric and infinitesimal, Eqs. (3.104)–(3.109) (or Eqs. (3.81)–(3.86)) become

$$E_{RR} = \frac{\partial \hat{U}_R}{\partial R}, \tag{3.110}$$

$$E_{\Theta\Theta} = \frac{\hat{U}_R}{R}, \tag{3.111}$$

$$E_{ZZ} = \frac{\partial \hat{U}_Z}{\partial Z}, \tag{3.112}$$

$$E_{R\Theta} = E_{\Theta R} = 0, \tag{3.113}$$

$$E_{\Theta Z} = E_{Z\Theta} = 0, \tag{3.114}$$

$$E_{ZR} = E_{RZ} = \frac{1}{2}\left(\frac{\partial \hat{U}_R}{\partial Z} + \frac{\partial \hat{U}_Z}{\partial R}\right). \tag{3.115}$$

3.6.3.4 Generalized plane strain

Generalized plane strain as defined here[29] and its special case, plane strain, are usually employed if one dimension—in the case of a tubular the Z dimension—is much larger than the other two. For any value of Z the undeformed R–Θ plane defined by that Z value is assumed to remain normal to the Z-axis during deformation and E_{ZZ} is at most constant. This is equivalent to stating that $\hat{U}_z = k_1 Z + k_2$, where k_1 and k_2 are constants, and $\partial \hat{U}_R/\partial Z = \partial \hat{U}_\Theta/\partial Z = 0$. Eqs. (3.75)–(3.80) become

$$E_{RR} = \frac{\partial \hat{U}_R}{\partial R} + \frac{1}{2}\left[\left(\frac{\partial \hat{U}_R}{\partial R}\right)^2 + \left(\frac{\partial \hat{U}_\Theta}{\partial R}\right)^2\right], \tag{3.116}$$

$$E_{\Theta\Theta} = \frac{\hat{U}_R}{R} + \frac{1}{R}\frac{\partial \hat{U}_\Theta}{\partial \Theta} + \frac{1}{2}\left[\left(\frac{1}{R}\frac{\partial \hat{U}_R}{\partial \Theta} - \frac{\hat{U}_\Theta}{R}\right)^2 + \left(\frac{\hat{U}_R}{R} + \frac{1}{R}\frac{\partial \hat{U}_\Theta}{\partial \Theta}\right)^2\right], \tag{3.117}$$

[29] Here we deal with a subset of truly generalized plane strain. In the more general case, the undeformed configuration can be curved, the body to be analyzed being imagined as extruded between two (not necessarily parallel) bounding planes. Applications of generalized plane strain in this book only consider a tube whose bounding planes are parallel and whose extrusion axis is a straight line.

$$E_{ZZ} = \frac{\partial \hat{U}_Z}{\partial Z} + \frac{1}{2}\left(\frac{\partial \hat{U}_Z}{\partial Z}\right)^2 = k_1 + \frac{1}{2}k_1^2, \tag{3.118}$$

$$E_{R\Theta} = E_{\Theta R} = \frac{1}{2}\left[\frac{\partial \hat{U}_\Theta}{\partial R} + \left(\frac{1}{R}\frac{\partial \hat{U}_R}{\partial \Theta} - \frac{\hat{U}_\Theta}{R}\right) + \frac{\partial \hat{U}_R}{\partial R}\left(\frac{1}{R}\frac{\partial \hat{U}_R}{\partial \Theta} - \frac{\hat{U}_\Theta}{R}\right) + \frac{\partial \hat{U}_\Theta}{\partial R}\left(\frac{\hat{U}_R}{R} + \frac{1}{R}\frac{\partial \hat{U}_\Theta}{\partial \Theta}\right)\right], \tag{3.119}$$

$$E_{\Theta Z} = E_{Z\Theta} = 0, \tag{3.120}$$

$$E_{ZR} = E_{RZ} = 0. \tag{3.121}$$

Plane strain, a special case of generalized plane strain, occurs when $k_1 = 0$. In this case, $E_{ZZ} = 0$.

A review of Eqs. (3.116)–(3.121) reveals that at this level of simplification deformation in the R–Θ (cross-sectional) plane is decoupled from deformation normal to a cross-section. The value of k_2 is immaterial to the analysis of cross-sectional deformation.

3.6.3.5 Generalized plane strain, axisymmetric deformation

If to generalized plane strain we add the assumption of axisymmetry, then $\hat{U}_z = k_1 Z + k_2$, where k_1 and k_2 are constants, $\hat{U}_\Theta = 0$, and $\partial \hat{U}_R/\partial Z = \partial \hat{U}_\Theta/\partial Z = \partial/\partial\Theta = 0$, and Eqs. (3.104)–(3.109) (or Eqs. (3.116)–(3.121)) become

$$E_{RR} = \frac{\partial \hat{U}_R}{\partial R} + \frac{1}{2}\left(\frac{\partial \hat{U}_R}{\partial R}\right)^2, \tag{3.122}$$

$$E_{\Theta\Theta} = \frac{\hat{U}_R}{R} + \frac{1}{2}\left(\frac{\hat{U}_R}{R}\right)^2, \tag{3.123}$$

$$E_{ZZ} = k_1 + \frac{1}{2}k_1^2, \tag{3.124}$$

$$E_{R\Theta} = E_{\Theta R} = 0, \tag{3.125}$$

$$E_{\Theta Z} = E_{Z\Theta} = 0, \tag{3.126}$$

$$E_{ZR} = E_{RZ} = 0. \tag{3.127}$$

3.6.3.6 Generalized plane strain, axisymmetric, infinitesimal deformation

Finally, if to generalized plane strain, axisymmetric deformation we wish to add the assumption that all displacements and displacement gradients are small enough to ignore

terms higher than first order, Eqs. (3.122)–(3.127) (or Eqs. (3.110)–(3.115)) become

$$E_{RR} = \frac{\partial \hat{U}_R}{\partial R}, \tag{3.128}$$

$$E_{\Theta\Theta} = \frac{\hat{U}_R}{R}, \tag{3.129}$$

$$E_{ZZ} = k_1, \tag{3.130}$$

$$E_{R\Theta} = E_{\Theta R} = 0, \tag{3.131}$$

$$E_{\Theta Z} = E_{Z\Theta} = 0, \tag{3.132}$$

$$E_{ZR} = E_{RZ} = 0. \tag{3.133}$$

3.7. EULERIAN STRAIN IN CYLINDRICAL COORDINATES

We shall not repeat the above derivation of Lagrangian strain for the Eulerian strain tensor, although we shall summarize the Eulerian results. The two derivations are similar, an important distinction being that in the case of Eulerian strain the deformation is referenced to the deformed configuration, that is, $\mathbf{u} = \hat{\mathbf{u}}(r, \theta, z, \tau)$.

Some useful observations regarding the Eulerian strain can be made by noting the following:

- Recalling the discussion regarding Fig. 3.4, for infinitesimal deformation the Lagrangian and Eulerian strains approach a common value.
- A comparison of Eqs. (3.31) and (3.35) reveals that the two strain measures are nearly identical in form with two exceptions:
  - The Lagrangian strain has $\mathbf{X}$ as its reference, whereas the Eulerian strain has $\mathbf{x}$ as its reference (e.g., in the Eulerian counterpart of Fig. 3.6 r and θ lie in the spatial x_1–x_2 plane and z is parallel to the x_3-axis, the x_1–x_2–x_3 coordinate system having unit base vectors $\mathbf{g}_i$, $i = 1, 2, 3$);
  - The nonlinear terms in the two strain tensors differ by a sign.

The conclusion to be reached from the above is that the discussion in Section 3.6 regarding Lagrangian strain is equally applicable to Eulerian strain, provided one substitutes (r, θ, z) for (R, Θ, Z) and $\hat{\mathbf{u}}$ for $\hat{\mathbf{U}}$. This includes both the forms of the equations (except for the signs of the nonlinear terms) and the physical interpretation of the strain components.

The following subsections summarize the formulas for Eulerian strain for ready reference in the chapters to follow. As the derivations follow closely those for Lagrangian strain, details will be kept to a minimum.

3.7.1 Strain in cylindrical coordinates

An increment in $\mathbf{x}$ is

$$d\mathbf{x} = dr\mathbf{g}_r + rd\theta\mathbf{g}_\theta + dz\mathbf{g}_z. \tag{3.134}$$

Eq. (3.134) leaves us with what we would expect for a differential element in cylindrical coordinates—a component having the units of length in each of the three coordinate directions. Accounting for $d\mathbf{g}_r/d\theta$ introduces r to the θ component of $d\mathbf{x}$ so that the measure of circular arc $rd\theta$ appears naturally.

An increment in $\mathbf{u}$ is found by substituting Eq. (3.67) into Eq. (3.64):

$$\begin{aligned} d\mathbf{u} = &\left[\frac{\partial \hat{u}_r}{\partial r}dr + \left(\frac{1}{r}\frac{\partial \hat{u}_r}{\partial \theta} - \frac{\hat{u}_\theta}{r}\right)rd\theta + \frac{\partial \hat{u}_r}{\partial z}dz + \frac{\partial \hat{u}_r}{\partial \tau}d\tau\right]\mathbf{g}_r \\ &+ \left[\frac{\partial \hat{u}_\theta}{\partial r}dr + \left(\frac{\hat{u}_r}{r} + \frac{1}{r}\frac{\partial \hat{u}_\theta}{\partial \theta}\right)rd\theta + \frac{\partial \hat{u}_\theta}{\partial z}dz + \frac{\partial \hat{u}_\theta}{\partial \tau}d\tau\right]\mathbf{g}_\theta \\ &+ \left[\frac{\partial \hat{u}_z}{\partial r}dr + \frac{1}{r}\frac{\partial \hat{u}_z}{\partial \theta}rd\theta + \frac{\partial \hat{u}_z}{\partial z}dz + \frac{\partial \hat{u}_z}{\partial \tau}d\tau\right]\mathbf{g}_z. \end{aligned} \tag{3.135}$$

If we use the fact that $d\mathbf{X} = d\mathbf{x} - \mathbf{u}$ in Eq. (3.22)

$$\begin{aligned} ds^2 - dS^2 &= d\mathbf{x}^T \cdot d\mathbf{x} - d\mathbf{X}^T \cdot d\mathbf{X} = d\mathbf{x}^T \cdot d\mathbf{x} - \left(d\mathbf{x} - d\mathbf{u}\right)^T \cdot \left(d\mathbf{x} - d\mathbf{u}\right) \\ &= d\mathbf{x}^T \cdot d\mathbf{x} - \left(d\mathbf{x}^T \cdot d\mathbf{x} - 2d\mathbf{x}^T \cdot d\mathbf{u} + d\mathbf{u}^T \cdot d\mathbf{u}\right) \\ &= 2d\mathbf{x}^T \cdot d\mathbf{u} - d\mathbf{u}^T \cdot d\mathbf{u} = \left(2d\mathbf{x}^T - d\mathbf{u}^T\right) \cdot d\mathbf{u}. \end{aligned} \tag{3.136}$$

Eq. (3.136) makes use of the commutative and distributive properties of the dot product (see Section A.3.1.3 of Appendix A) and the facts that $\left(d\mathbf{x} - d\mathbf{u}\right)^T = d\mathbf{x}^T - d\mathbf{u}^T$ and $d\mathbf{x}^T \cdot d\mathbf{u} = d\mathbf{u}^T \cdot d\mathbf{x}$. With Eqs. (3.134) and (3.135) substituted into Eq. (3.136),[30]

$$\begin{aligned} ds^2 - dS^2 = &\left\{\left[2dr - \frac{\partial \hat{u}_r}{\partial r}dr - \left(\frac{1}{r}\frac{\partial \hat{u}_r}{\partial \theta} - \frac{\hat{u}_\theta}{r}\right)rd\theta - \frac{\partial \hat{u}_r}{\partial z}dz\right]\mathbf{g}_r \right. \\ &+ \left[2rd\theta - \frac{\partial \hat{u}_\theta}{\partial r}dr - \left(\frac{\hat{u}_r}{r} + \frac{1}{r}\frac{\partial \hat{u}_\theta}{\partial \theta}\right)rd\theta - \frac{\partial \hat{u}_\theta}{\partial z}dz\right]\mathbf{g}_\theta \\ &\left. + \left[2dz - \frac{\partial \hat{u}_z}{\partial r}dr - \frac{1}{r}\frac{\partial \hat{u}_z}{\partial \theta}rd\theta - \frac{\partial \hat{u}_z}{\partial z}dz\right]\mathbf{g}_z\right\} \\ &\cdot \left\{\left[\frac{\partial \hat{u}_r}{\partial r}dr + \left(\frac{1}{r}\frac{\partial \hat{u}_r}{\partial \theta} - \frac{\hat{u}_\theta}{r}\right)rd\theta + \frac{\partial \hat{u}_r}{\partial z}dz\right]\mathbf{g}_r \right. \\ &+ \left[\frac{\partial \hat{u}_\theta}{\partial r}dr + \left(\frac{\hat{u}_r}{r} + \frac{1}{r}\frac{\partial \hat{u}_\theta}{\partial \theta}\right)rd\theta + \frac{\partial \hat{u}_\theta}{\partial z}dz\right]\mathbf{g}_\theta \\ &\left. + \left[\frac{\partial \hat{u}_z}{\partial r}dr + \frac{1}{r}\frac{\partial \hat{u}_z}{\partial \theta}rd\theta + \frac{\partial \hat{u}_z}{\partial z}dz\right]\mathbf{g}_z\right\}. \end{aligned} \tag{3.137}$$

[30] In this substitution, $d\tau = 0$ as we wish to examine spatial gradients at a specific time.

Eq. (3.137) can be simplified by carrying out the indicated dot products and collecting terms to

$$\begin{aligned} ds^2 - dS^2 = & \left[2\frac{\partial \hat{u}_r}{\partial r} - \left(\frac{\partial \hat{u}_r}{\partial r}\right)^2 - \left(\frac{\partial \hat{u}_\theta}{\partial r}\right)^2 - \left(\frac{\partial \hat{u}_z}{\partial r}\right)^2 \right] dr dr \\ & + \left[2\left(\frac{\hat{u}_r}{r} + \frac{1}{r}\frac{\partial \hat{u}_\theta}{\partial \theta}\right) - \left(\frac{1}{r}\frac{\partial \hat{u}_r}{\partial \theta} - \frac{\hat{u}_\theta}{r}\right)^2 - \left(\frac{\hat{u}_r}{r} + \frac{1}{r}\frac{\partial \hat{u}_\theta}{\partial \theta}\right)^2 \right. \\ & \left. - \left(\frac{1}{r}\frac{\partial \hat{u}_z}{\partial \theta}\right)^2 \right] r d\theta\, r d\theta \\ & + \left[2\frac{\partial \hat{u}_z}{\partial z} - \left(\frac{\partial \hat{u}_r}{\partial z}\right)^2 - \left(\frac{\partial \hat{u}_\theta}{\partial z}\right)^2 - \left(\frac{\partial \hat{u}_z}{\partial z}\right)^2 \right] dz dz \\ & + 2\left[\left(\frac{1}{r}\frac{\partial \hat{u}_r}{\partial \theta} - \frac{\hat{u}_\theta}{r}\right) - \frac{\partial \hat{u}_r}{\partial r}\left(\frac{1}{r}\frac{\partial \hat{u}_r}{\partial \theta} - \frac{\hat{u}_\theta}{r}\right) + \frac{\partial \hat{u}_\theta}{\partial r} \right. \\ & \left. - \frac{\partial \hat{u}_\theta}{\partial r}\left(\frac{\hat{u}_r}{r} + \frac{1}{r}\frac{\partial \hat{u}_\theta}{\partial \theta}\right) - \frac{\partial \hat{u}_z}{\partial r}\frac{1}{r}\frac{\partial \hat{u}_z}{\partial \theta} \right] r dr d\theta \\ & + 2\left[-\left(\frac{1}{r}\frac{\partial \hat{u}_r}{\partial \theta} - \frac{\hat{u}_\theta}{r}\right)\frac{\partial \hat{u}_r}{\partial z} + \frac{\partial \hat{u}_\theta}{\partial z} - \frac{\partial \hat{u}_\theta}{\partial z}\left(\frac{\hat{u}_r}{r} + \frac{1}{r}\frac{\partial \hat{u}_\theta}{\partial \theta}\right) \right. \\ & \left. + \frac{1}{r}\frac{\partial \hat{u}_z}{\partial \theta} - \frac{1}{r}\frac{\partial \hat{u}_z}{\partial \theta}\frac{\partial \hat{u}_z}{\partial z} \right] r d\theta\, dz \\ & + 2\left[\frac{\partial \hat{u}_z}{\partial r} + \frac{\partial \hat{u}_r}{\partial z} - \frac{\partial \hat{u}_r}{\partial z}\frac{\partial \hat{u}_r}{\partial r} - \frac{\partial \hat{u}_\theta}{\partial z}\frac{\partial \hat{u}_\theta}{\partial r} - \frac{\partial \hat{u}_z}{\partial z}\frac{\partial \hat{u}_z}{\partial r} \right] dz dr. \end{aligned} \tag{3.138}$$

Eq. (3.138) can be rewritten in terms of the components of the strain tensor in cylindrical coordinates as

$$\begin{aligned} ds^2 - dS^2 = & 2\breve{E}_{rr} dr dr + 2\breve{E}_{\theta\theta} r d\theta\, r d\theta + 2\breve{E}_{zz} dz dz + 2\left(\breve{E}_{r\theta} + \breve{E}_{\theta r}\right) r dr d\theta \\ & + 2\left(\breve{E}_{\theta z} + \breve{E}_{z\theta}\right) r d\theta\, dz + 2\left(\breve{E}_{rz} + \breve{E}_{zr}\right) dz dr, \end{aligned} \tag{3.139}$$

where $\breve{E}_{r\theta} = \breve{E}_{\theta r}$, $\breve{E}_{\theta z} = \breve{E}_{z\theta}$ and $\breve{E}_{rz} = \breve{E}_{zr}$. When Eqs. (3.138) and (3.139) are compared, the components of strain emerge:

$$\breve{E}_{rr} = \frac{\partial \hat{u}_r}{\partial r} - \frac{1}{2}\left[\left(\frac{\partial \hat{u}_r}{\partial r}\right)^2 + \left(\frac{\partial \hat{u}_\theta}{\partial r}\right)^2 + \left(\frac{\partial \hat{u}_z}{\partial r}\right)^2 \right], \tag{3.140}$$

$$\breve{E}_{\theta\theta} = \frac{\hat{u}_r}{r} + \frac{1}{r}\frac{\partial \hat{u}_\theta}{\partial \theta} - \frac{1}{2}\left[\left(\frac{1}{r}\frac{\partial \hat{u}_r}{\partial \theta} - \frac{\hat{u}_\theta}{r}\right)^2 + \left(\frac{\hat{u}_r}{r} + \frac{1}{r}\frac{\partial \hat{u}_\theta}{\partial \theta}\right)^2 + \left(\frac{1}{r}\frac{\partial \hat{u}_z}{\partial \theta}\right)^2 \right], \tag{3.141}$$

$$\breve{E}_{zz} = \frac{\partial \hat{u}_z}{\partial z} - \frac{1}{2}\left[\left(\frac{\partial \hat{u}_r}{\partial z}\right)^2 + \left(\frac{\partial \hat{u}_\theta}{\partial z}\right)^2 + \left(\frac{\partial \hat{u}_z}{\partial z}\right)^2 \right], \tag{3.142}$$

$$\breve{E}_{r\theta} = \breve{E}_{\theta r} = \frac{1}{2}\left[\frac{\partial \hat{u}_\theta}{\partial r} + \left(\frac{1}{r}\frac{\partial \hat{u}_r}{\partial \theta} - \frac{\hat{u}_\theta}{r}\right) - \frac{\partial \hat{u}_r}{\partial r}\left(\frac{1}{r}\frac{\partial \hat{u}_r}{\partial \theta} - \frac{\hat{u}_\theta}{r}\right) - \frac{\partial \hat{u}_\theta}{\partial r}\left(\frac{\hat{u}_r}{r} + \frac{1}{r}\frac{\partial \hat{u}_\theta}{\partial \theta}\right) - \frac{\partial \hat{u}_z}{\partial r}\frac{1}{r}\frac{\partial \hat{u}_z}{\partial \theta}\right], \tag{3.143}$$

$$\breve{E}_{\theta z} = \breve{E}_{z\theta} = \frac{1}{2}\left[\frac{1}{r}\frac{\partial \hat{u}_z}{\partial \theta} + \frac{\partial \hat{u}_\theta}{\partial z} - \left(\frac{\hat{u}_r}{r} + \frac{1}{r}\frac{\partial \hat{u}_\theta}{\partial \theta}\right)\frac{\partial \hat{u}_\theta}{\partial z} - \left(\frac{1}{r}\frac{\partial \hat{u}_r}{\partial \theta} - \frac{\hat{u}_\theta}{r}\right)\frac{\partial \hat{u}_r}{\partial z} - \frac{1}{r}\frac{\partial \hat{u}_z}{\partial \theta}\frac{\partial \hat{u}_z}{\partial z}\right], \tag{3.144}$$

$$\breve{E}_{zr} = \breve{E}_{rz} = \frac{1}{2}\left[\frac{\partial \hat{u}_r}{\partial z} + \frac{\partial \hat{u}_z}{\partial r} - \left(\frac{\partial \hat{u}_r}{\partial z}\frac{\partial \hat{u}_r}{\partial r} + \frac{\partial \hat{u}_\theta}{\partial z}\frac{\partial \hat{u}_\theta}{\partial r} + \frac{\partial \hat{u}_z}{\partial z}\frac{\partial \hat{u}_z}{\partial r}\right)\right]. \tag{3.145}$$

Eqs. (3.140)–(3.145) are the final expressions for the Eulerian strain tensor expressed in terms of the spatial coordinate system and displacement.

3.7.2 Special cases of Eulerian strain in cylindrical coordinates

The geometry of the structure or the nature of the displacement field may be such as to allow simplification of Eqs. (3.140)–(3.145). The more important of these simplifications to tubular design are detailed in the sections to follow.

3.7.2.1 Infinitesimal deformation

If all displacements and displacement gradients are small enough that second order terms in these infinitesimals can be neglected, Eqs. (3.140)–(3.145) become

$$\breve{E}_{rr} = \frac{\partial \hat{u}_r}{\partial r}, \tag{3.146}$$

$$\breve{E}_{\theta\theta} = \frac{\hat{u}_r}{r} + \frac{1}{r}\frac{\partial \hat{u}_\theta}{\partial \theta}, \tag{3.147}$$

$$\breve{E}_{zz} = \frac{\partial \hat{u}_z}{\partial z}, \tag{3.148}$$

$$\breve{E}_{r\theta} = \breve{E}_{\theta r} = \frac{1}{2}\left[\frac{\partial \hat{u}_\theta}{\partial r} + \left(\frac{1}{r}\frac{\partial \hat{u}_r}{\partial \theta} - \frac{\hat{u}_\theta}{r}\right)\right], \tag{3.149}$$

$$\breve{E}_{\theta z} = \breve{E}_{z\theta} = \frac{1}{2}\left(\frac{1}{r}\frac{\partial \hat{u}_z}{\partial \theta} + \frac{\partial \hat{u}_\theta}{\partial z}\right), \tag{3.150}$$

$$\breve{E}_{zr} = \breve{E}_{rz} = \frac{1}{2}\left(\frac{\partial \hat{u}_r}{\partial z} + \frac{\partial \hat{u}_z}{\partial r}\right). \tag{3.151}$$

The volume change for an infinitesimal is

$$\frac{dv}{dV} = \mathcal{J} = 1 + \breve{E}_{rr} + \breve{E}_{\theta\theta} + \breve{E}_{zz}, \quad \frac{dv - dV}{dV} = \breve{E}_{rr} + \breve{E}_{\theta\theta} + \breve{E}_{zz}. \tag{3.152}$$

3.7.2.2 Axisymmetric deformation

If the deformation is axisymmetric, $\partial/\partial\theta = \hat{u}_\theta = 0$, and Eqs. (3.140)–(3.145) become

$$\breve{E}_{rr} = \frac{\partial \hat{u}_r}{\partial r} - \frac{1}{2}\left[\left(\frac{\partial \hat{u}_r}{\partial r}\right)^2 + \left(\frac{\partial \hat{u}_z}{\partial r}\right)^2\right], \tag{3.153}$$

$$\breve{E}_{\theta\theta} = \frac{\hat{u}_r}{r} - \frac{1}{2}\left(\frac{\hat{u}_r}{r}\right)^2, \tag{3.154}$$

$$\breve{E}_{zz} = \frac{\partial \hat{u}_z}{\partial z} - \frac{1}{2}\left[\left(\frac{\partial \hat{u}_r}{\partial z}\right)^2 + \left(\frac{\partial \hat{u}_z}{\partial z}\right)^2\right], \tag{3.155}$$

$$\breve{E}_{r\theta} = \breve{E}_{\theta r} = 0, \tag{3.156}$$

$$\breve{E}_{\theta z} = \breve{E}_{z\theta} = 0, \tag{3.157}$$

$$\breve{E}_{zr} = \breve{E}_{rz} = \frac{1}{2}\left[\frac{\partial \hat{u}_r}{\partial z} + \frac{\partial \hat{u}_z}{\partial r} - \frac{\partial \hat{u}_r}{\partial z}\frac{\partial \hat{u}_r}{\partial r} - \frac{\partial \hat{u}_z}{\partial z}\frac{\partial \hat{u}_z}{\partial r}\right]. \tag{3.158}$$

3.7.2.3 Axisymmetric, infinitesimal deformation

If the deformation is both axisymmetric and infinitesimal, Eqs. (3.153)–(3.158) (or Eqs. (3.146)–(3.151)) become

$$\breve{E}_{rr} = \frac{\partial \hat{u}_r}{\partial r}, \tag{3.159}$$

$$\breve{E}_{\theta\theta} = \frac{\hat{u}_r}{r}, \tag{3.160}$$

$$\breve{E}_{zz} = \frac{\partial \hat{u}_z}{\partial z}, \tag{3.161}$$

$$\breve{E}_{r\theta} = \breve{E}_{\theta r} = 0, \tag{3.162}$$

$$\breve{E}_{\theta z} = \breve{E}_{z\theta} = 0, \tag{3.163}$$

$$\breve{E}_{zr} = \breve{E}_{rz} = \frac{1}{2}\left(\frac{\partial \hat{u}_r}{\partial z} + \frac{\partial \hat{u}_z}{\partial r}\right). \tag{3.164}$$

3.7.2.4 Generalized plane strain

Generalized plane strain as defined here and its special case, plane strain, are usually employed if one dimension—in the case of a tubular the z dimension—is much larger than the other two. For any value of z the undeformed r–θ plane defined by that z value is assumed to remain normal to the z-axis during deformation and $\breve{E}_{zz}$ is at most constant. This is equivalent to stating that $\hat{u}_z = k_1 z + k_2$, where k_1 and k_2 are constants, and $\partial \hat{u}_r/\partial z = \partial \hat{u}_\theta/\partial z = 0$. Eqs. (3.140)–(3.145) become

$$\breve{E}_{rr} = \frac{\partial \hat{u}_r}{\partial r} - \frac{1}{2}\left[\left(\frac{\partial \hat{u}_r}{\partial r}\right)^2 + \left(\frac{\partial \hat{u}_\theta}{\partial r}\right)^2\right], \tag{3.165}$$

$$\breve{E}_{\theta\theta} = \frac{\hat{u}_r}{r} + \frac{1}{r}\frac{\partial \hat{u}_\theta}{\partial \theta} - \frac{1}{2}\left[\left(\frac{1}{r}\frac{\partial \hat{u}_r}{\partial \theta} - \frac{\hat{u}_\theta}{r}\right)^2 + \left(\frac{\hat{u}_r}{r} + \frac{1}{r}\frac{\partial \hat{u}_\theta}{\partial \theta}\right)^2\right], \tag{3.166}$$

$$\breve{E}_{zz} = \frac{\partial \hat{u}_z}{\partial z} - \frac{1}{2}\left(\frac{\partial \hat{u}_z}{\partial z}\right)^2 = k_1 - \frac{1}{2}k_1^2, \tag{3.167}$$

$$\breve{E}_{r\theta} = \breve{E}_{\theta r} = \frac{1}{2}\left[\frac{\partial \hat{u}_\theta}{\partial r} + \left(\frac{1}{r}\frac{\partial \hat{u}_r}{\partial \theta} - \frac{\hat{u}_\theta}{r}\right) - \frac{\partial \hat{u}_r}{\partial r}\left(\frac{1}{r}\frac{\partial \hat{u}_r}{\partial \theta} - \frac{\hat{u}_\theta}{r}\right) - \frac{\partial \hat{u}_\theta}{\partial r}\left(\frac{\hat{u}_r}{r} + \frac{1}{r}\frac{\partial \hat{u}_\theta}{\partial \theta}\right)\right], \tag{3.168}$$

$$\breve{E}_{\theta z} = \breve{E}_{z\theta} = 0, \tag{3.169}$$

$$\breve{E}_{zr} = \breve{E}_{rz} = 0. \tag{3.170}$$

Plane strain, a special case of generalized plane strain, occurs when $k_1 = 0$. In this case, $\breve{E}_{zz} = 0$.

A review of Eqs. (3.165)–(3.170) reveals that at this level of simplification deformation in the r–θ (cross-sectional) plane is decoupled from deformation normal to a cross-section. The value of k_2 is immaterial to the analysis of cross-sectional deformation.

3.7.2.5 Generalized plane strain, axisymmetric deformation

If to generalized plane strain we add the assumption of axisymmetry, then $\hat{u}_z = k_1 z + k_2$, where k_1 and k_2 are constants, $\hat{u}_\theta = 0$, and $\partial \hat{u}_r/\partial z = \partial \hat{u}_\theta/\partial z = \partial/\partial\theta = 0$, and Eqs. (3.153)–(3.158) (or Eqs. (3.165)–(3.170)) become

$$\breve{E}_{rr} = \frac{\partial \hat{u}_r}{\partial r} - \frac{1}{2}\left(\frac{\partial \hat{u}_r}{\partial r}\right)^2, \tag{3.171}$$

$$\breve{E}_{\theta\theta} = \frac{\hat{u}_r}{r} - \frac{1}{2}\left(\frac{\hat{u}_r}{r}\right)^2, \tag{3.172}$$

$$\breve{E}_{zz} = k_1 - \frac{1}{2}k_1^2, \tag{3.173}$$

$$\breve{E}_{r\theta} = \breve{E}_{\theta r} = 0, \tag{3.174}$$

$$\breve{E}_{\theta z} = \breve{E}_{z\theta} = 0, \tag{3.175}$$

$$\breve{E}_{zr} = \breve{E}_{rz} = 0. \tag{3.176}$$

3.7.2.6 Generalized plane strain, axisymmetric, infinitesimal deformation

Finally, if to generalized plane strain, axisymmetric deformation we wish to add the assumption that all displacements and displacement gradients are small enough to ignore

terms higher than first order, Eqs. (3.171)–(3.176) (or Eqs. (3.159)–(3.164)) become

$$\breve{E}_{rr} = \frac{\partial \hat{u}_r}{\partial r}, \tag{3.177}$$

$$\breve{E}_{\theta\theta} = \frac{\hat{u}_r}{r}, \tag{3.178}$$

$$\breve{E}_{zz} = k_1, \tag{3.179}$$

$$\breve{E}_{r\theta} = \breve{E}_{\theta r} = 0, \tag{3.180}$$

$$\breve{E}_{\theta z} = \breve{E}_{z\theta} = 0, \tag{3.181}$$

$$\breve{E}_{zr} = \breve{E}_{rz} = 0. \tag{3.182}$$

The assumption of generalized plane strain with both axisymmetry and small displacements and displacement gradients will be used to derive the Lamé equations.

3.8. LOGARITHMIC STRAIN IN CYLINDRICAL COORDINATES

In the cylindrical coordinate system of Fig. 3.6, we define the stretch ratios

$$\Lambda_{(\mathbf{R})} = \sqrt{\frac{dr^2}{dR^2}}, \quad \Lambda_{(\mathbf{\Theta})} = \sqrt{\frac{r^2 d\theta^2}{R^2 d\Theta^2}}, \quad \Lambda_{(\mathbf{Z})} = \sqrt{\frac{dz^2}{dZ^2}}, \tag{3.183}$$

where the spatial cylindrical coordinate system (r, θ, z) has the same conceptual relation to the global material cylindrical coordinate system (R, Θ, Z) as the spatial Cartesian coordinate system (x_1, x_2, x_3) have to the global material Cartesian coordinate system (X_1, X_2, X_3) (see Fig. 3.1).

If we restrict our investigations with logarithmic strain to deformations where $\mathbf{C}$ is a diagonal tensor (see Section 3.5.4), then from Eqs. (3.38) and (3.68) we get

$$\Lambda^2_{(\mathbf{R})} = \left(1 + \frac{\partial \hat{U}_R}{\partial R}\right)^2 + \left(\frac{\partial \hat{U}_\Theta}{\partial R}\right)^2 + \left(\frac{\partial \hat{U}_Z}{\partial R}\right)^2, \tag{3.184}$$

$$\Lambda^2_{(\mathbf{\Theta})} = \left(\frac{1}{R}\frac{\partial \hat{U}_R}{\partial \Theta} - \frac{\hat{U}_\Theta}{R}\right)^2 + \left(1 + \frac{\hat{U}_R}{R} + \frac{1}{R}\frac{\partial \hat{U}_\Theta}{\partial \Theta}\right)^2 + \left(\frac{1}{R}\frac{\partial \hat{U}_Z}{\partial \Theta}\right)^2, \tag{3.185}$$

$$\Lambda^2_{(\mathbf{Z})} = \left(\frac{\partial \hat{U}_R}{\partial Z}\right)^2 + \left(\frac{\partial \hat{U}_\Theta}{\partial Z}\right)^2 + \left(1 + \frac{\partial \hat{U}_Z}{\partial Z}\right)^2, \tag{3.186}$$

and from Eq. (3.39), addressing only deformations that are aligned with the coordinate directions,

$$\tilde{\mathbf{E}} = \ln \mathbf{C}^{\frac{1}{2}} = \begin{bmatrix} \ln \Lambda_{(\mathbf{R})} & 0 & 0 \\ 0 & \ln \Lambda_{(\mathbf{\Theta})} & 0 \\ 0 & 0 & \ln \Lambda_{(\mathbf{Z})} \end{bmatrix}. \tag{3.187}$$

3.8.1 Axisymmetric deformation

If the deformation is axisymmetric, $\partial/\partial\Theta = \hat{U}_\Theta = 0$, and Eqs. (3.184)–(3.186) become

$$\Lambda^2_{(\mathbf{R})} = \left(1 + \frac{\partial \hat{U}_R}{\partial R}\right)^2 + \left(\frac{\partial \hat{U}_Z}{\partial R}\right)^2, \tag{3.188}$$

$$\Lambda^2_{(\boldsymbol{\Theta})} = \left(1 + \frac{\hat{U}_R}{R}\right)^2, \tag{3.189}$$

$$\Lambda^2_{(\mathbf{Z})} = \left(\frac{\partial \hat{U}_R}{\partial Z}\right)^2 + \left(1 + \frac{\partial \hat{U}_Z}{\partial Z}\right)^2. \tag{3.190}$$

3.8.2 Generalized plane strain

If for any value of Z the undeformed R–Θ plane defined by that Z value is assumed to remain normal to the Z-axis during deformation and E_{ZZ} is at most constant (see discussion in Section 3.6.3.4), $\hat{U}_z = k_1 Z + k_2$, where k_1 and k_2 are constants, $\partial \hat{U}_R/\partial Z = \partial \hat{U}_\Theta/\partial Z = 0$, and Eqs. (3.184)–(3.186) become

$$\Lambda^2_{(\mathbf{R})} = \left(1 + \frac{\partial \hat{U}_R}{\partial R}\right)^2 + \left(\frac{\partial \hat{U}_\Theta}{\partial R}\right)^2, \tag{3.191}$$

$$\Lambda^2_{(\boldsymbol{\Theta})} = \left(\frac{1}{R}\frac{\partial \hat{U}_R}{\partial \Theta} - \frac{\hat{U}_\Theta}{R}\right)^2 + \left(1 + \frac{\hat{U}_R}{R} + \frac{1}{R}\frac{\partial \hat{U}_\Theta}{\partial \Theta}\right)^2, \tag{3.192}$$

$$\Lambda^2_{(\mathbf{Z})} = (1 + k_1)^2. \tag{3.193}$$

3.8.3 Generalized plane strain, axisymmetric deformation

If to generalized plane strain we add the assumption of axisymmetry, then $\hat{U}_z = k_1 Z + k_2$, where k_1 and k_2 are constants, $\hat{U}_\Theta = 0$, and $\partial \hat{U}_R/\partial Z = \partial \hat{U}_\Theta/\partial Z = \partial/\partial\Theta = 0$, and Eqs. (3.188)–(3.190) (or Eqs. (3.191)–(3.193)) become

$$\Lambda_{(\mathbf{R})} = 1 + \frac{\partial \hat{U}_R}{\partial R}, \tag{3.194}$$

$$\Lambda_{(\boldsymbol{\Theta})} = 1 + \frac{\hat{U}_R}{R}, \tag{3.195}$$

$$\Lambda_{(\mathbf{Z})} = 1 + k_1. \tag{3.196}$$

Eqs. (3.194)–(3.196) will be used in the discussion of ductile rupture in Section 7.3 of Chapter 7.

Table 3.2 Choice of strain measure in this book.

Strain tensor	Major application	Chapter	Section
Lagrangian	Uniaxial stress–strain curve	6	6.2
Eulerian	All infinitesimal deformation problems[a]	Many	
Logarithmic	Ductile rupture	7	7.3

[a] For infinitesimal strain the three strain measures converge.

We shall forego the investigation of logarithmic strain for infinitesimal deformation, as the only use we will make of logarithmic strain is in the presence of finite deformation.

3.9. CHOOSING A STRAIN TENSOR

In this chapter we have discussed three strain tensors—Lagrangian strain, Eulerian strain and logarithmic strain. With the proper constitutive model, any of these strains can be related to a choice of stress tensor (Chapter 4). We have examined these three because they are most pertinent to oil well tubular analyses appearing in the literature.

The Lagrangian strain has been included because it is, at least to this author, the most conceptually straightforward and the one to which most engineers have been exposed. The Eulerian strain is closely related to its Lagrangian counterpart, differing only in the frame to which it is referenced. The logarithmic strain is somewhat unwieldy once one ventures beyond a coordinate system aligned with the axes of principle stress (see Section 3.5.4) but provides the user substantial power when addressing problems involving large strain and behavior beyond yield.

Table 3.2 summarizes the use of these three definitions in this book. The workhorse will be the Eulerian strain primarily as a convenience in handling reference frames. That is, choice of the Eulerian strain will follow our preference for the Cauchy stress that also uses the spatial frame of reference. We will use the other two strain measures, but in limited, special applications to which they are most appropriate. For most of the book we will limit ourselves to infinitesimal strain, so the choice of strain measure will have minimal impact.

CHAPTER 4

Stress

4.1. INTRODUCTION

The previous chapter considered the translation, rotation and deformation of a body without regard to the initiator(s) of the movement. This chapter addresses the action(s) leading to deformation—forces and moments.

A body subjected to contact and field forces deforms. Locally, investigation of the degree to which the body is loaded usually involves a discussion of force intensity. The intensity can either be examined as a surface traction vector of force intensity or, more commonly, by considering the second order stress tensor at the point of interest. The stress tensor contains information regarding force intensity with respect to any orientation of the internal or external surface in focus.

The discussion of kinematics (Chapter 3) initially focused on quantities related to the undeformed or material configuration and its coordinate system. Once basic concepts (the deformation and deformation gradient tensors, the strain tensor) were introduced, alternative measures related to the deformed or spatial configuration and its coordinate system followed. With stress, we shall reverse the process. We first define the Cauchy stress tensor associated with the deformed configuration. This eases the discussion of such important relations as the equation of motion. Having the basic concepts in hand, we then introduce an additional stress tensor—the Piola–Krichhoff stress tensor—related to the undeformed configuration.

4.2. THE CONCEPT OF STRESS

To define terms related to stress, we begin with a fairly general state of loading. Fig. 4.1 illustrates a body of general shape loaded by a variety of external forces which are of two types:

- forces involving contact ($\mathbf{f}_i$, $i = 1, 2, 3, 4$ in Fig. 4.1) between the body shown and its surroundings—for example, the forces of the supports of a casing or tubing rack on a tubular being suspended;
- forces involving a field ($\mathbf{b}_{fi}$, $i = 1$ in Fig. 4.1) between the body and another body where the two bodies are not in contact—for example, the gravitational force of the earth on the tubular suspended on a casing or tubing rack.

If the body is in motion, the vector sum (see Section A.3.1.1 of Appendix A) of all forces equals the body's mass times the acceleration of its center of mass. If the body is moving at constant (or zero) velocity, the vector sum of all forces must be zero.

Elements of Oil and Gas Well Tubular Design
DOI: 10.1016/B978-0-12-811769-9.00004-9

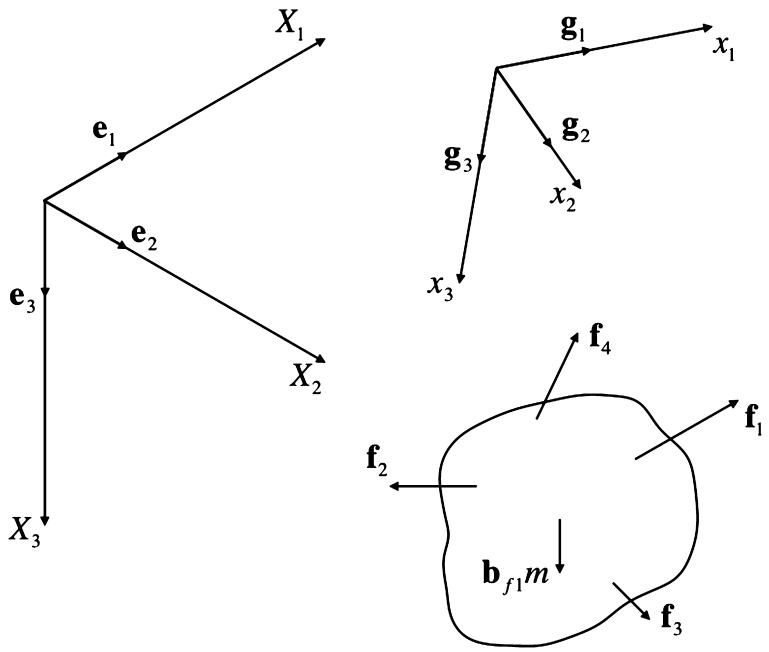

Figure 4.1 ***Contact and body forces.*** The *m* multiplier is used with the body force to indicate this force is expressed per unit mass. Alternately, the body force may be expressed per unit volume.

The contact forces in Fig. 4.1 are idealizations. In reality, each contact force vector shown represents the integration of a force distribution (force per unit area) in the vicinity of the indicated contact force. The area over which the integration occurs is finite, but may be exceedingly small. Body force vectors are usually expressed per unit mass (or, alternately, unit volume).

As mentioned in Section 4.1 in the study of kinematics, it seems reasonable, at least for solids, to reference the deformation quantities to the original, undeformed state from which the quantities proceed. With stress, on the other hand, a more natural reference is the current, deformed state of the body. In Fig. 4.1 therefore the spatial coordinate system assumes immediate importance, and vector and tensor quantities related to stress should be viewed from a spatial perspective. This separation of focus—material coordinates for kinematics, spatial coordinates for stress—seems to invite inconsistencies. We shall demonstrate later, however, that in the case of infinitesimal deformation the distinction between material and spatial coordinates diminishes.

4.2.1 Traction

Fig. 4.2 examines the loading on an internal surface of the body created by imaginarily cutting the body with an intersecting plane. The plane is identified by a unit vector normal to the plane and positive when directed outward. The resultant force acting on

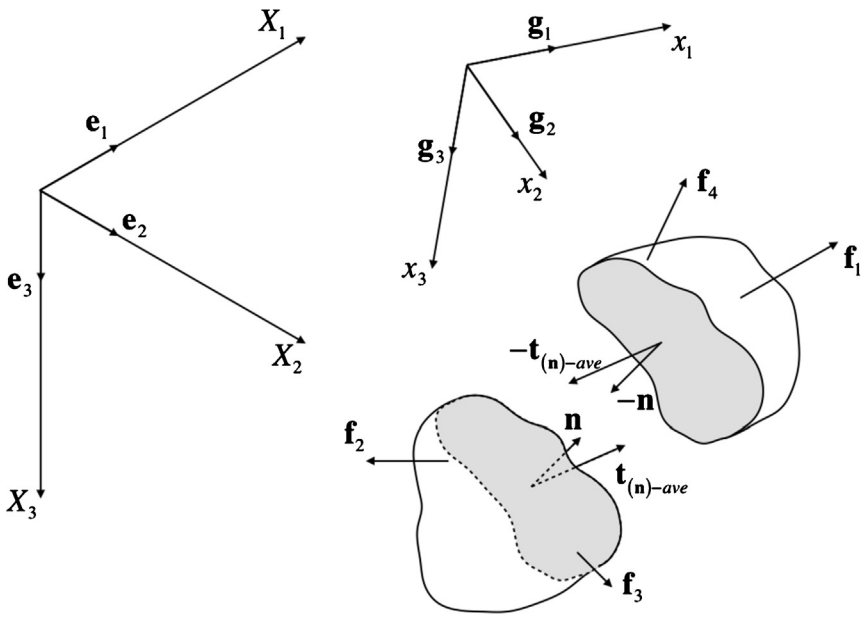

Figure 4.2 ***Average traction.*** The resultant force on the internal surface $\mathbf{f}_{(\mathbf{n})-res}$ is not shown, but has the same location and direction as the average traction vector $\mathbf{t}_{(\mathbf{n})-ave}$. The shaded area is A_S. To simplify the figure, the body force (see Fig. 4.1), although present, is also not shown.

this internal surface (not shown, but at the same location and in the same direction as the vector $\mathbf{t}_{(\mathbf{n})-ave}$) is designated $\mathbf{f}_{(\mathbf{n})-res}$, the subscript $\mathbf{n}$ being used to identify this resultant internal force with a particular cutting plane via the plane's normal. Vector $\mathbf{f}_{(\mathbf{n})-res}$ is the sum (see Section A.3.1.1 of Appendix A) of all force distributions acting on the internal surface created by the intersecting plane.

The portion of the body of which the internal surface is a boundary (the lower left portion in Fig. 4.2) has the following relation to its environment:

- from the perspective of this portion of the body $\mathbf{f}_{(\mathbf{n})-res}$ is an external force;
- the designation of $\mathbf{f}_{(\mathbf{n})-res}$ as an internal force relates to the imaginary nature of the cutting plane used to create the internal surface and examine the resultant force to which that internal surface is subjected;
- this resultant force has an equal and opposite counterpart associated with the remaining portion of the overall body and represented in Fig. 4.2 by the surface with normal $-\mathbf{n}$.

Associated with the resultant contact force $\mathbf{f}_{(\mathbf{n})-res}$ is an average force *intensity* or traction,[1]

[1] The force intensity on a surface is sometimes called the stress vector. Following the example of Malvern [8], the convention adopted here is to use "traction" to designate the vector of force intensity and reserve the term "stress" for the stress tensor.

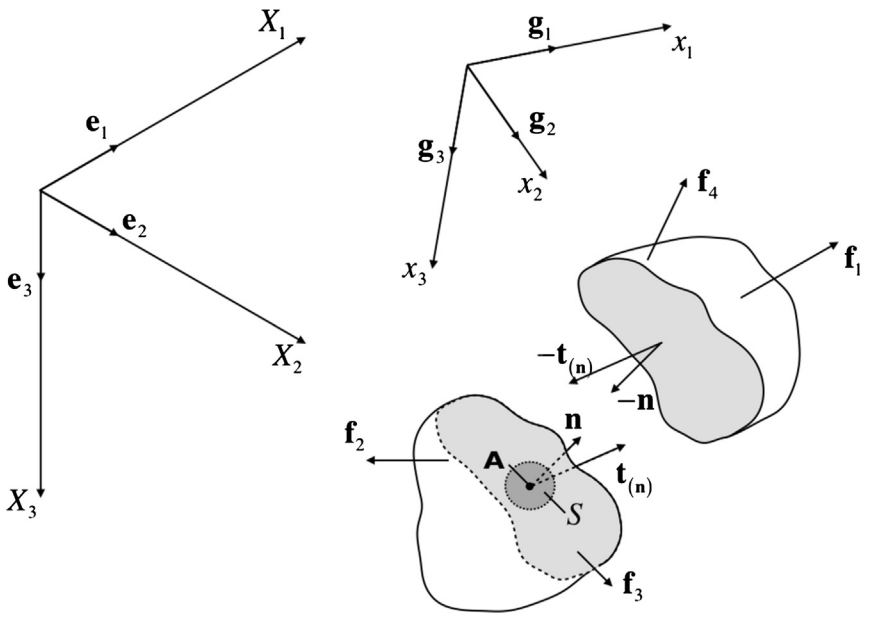

Figure 4.3 ***Local traction.*** The neighborhood of point A is indicated by the dotted circle. The darker shaded area is A_S. To simplify the figure, the body force (see Fig. 4.1), although present, is not shown.

designated by $\mathbf{t}_{(\mathbf{n})-ave}$ and obtained by dividing the resultant force by the area of the internal surface with normal $\mathbf{n}$ (shown shaded in Fig. 4.2)

$$\mathbf{t}_{(\mathbf{n})-ave} = \frac{\mathbf{f}_{(\mathbf{n})-res}}{A_S}, \tag{4.1}$$

where A_S is the area of the shaded surface in Fig. 4.2.

As depicted in Fig. 4.2, the traction $\mathbf{t}_{(\mathbf{n})-ave}$ represents the average intensity of all internal forces acting on the surface associated with the cutting plane with normal $\mathbf{n}$. Of interest in many problems is the local intensity of internal forces acting at a point on the exposed surface. Determination of this local traction is illustrated in Fig. 4.3, where now interest is focused on the immediate neighborhood of the point A. The local traction is defined by the limit

$$\mathbf{t}_{(\mathbf{n})} = \lim_{r_{S-max} \to 0} \frac{\mathbf{f}_{S-res}}{A_S}, \tag{4.2}$$

where $\mathbf{f}_{S-res}$ is the vector sum of all force distributions acting on local area A_S and the limit has the following properties:

- rather than requiring A_S approach zero, we require r_{S-max}, the maximum radius from point A to any point on the boundary of S, to approach zero, thus eliminating the possibility of a limit where S approaches the geometry of a line;

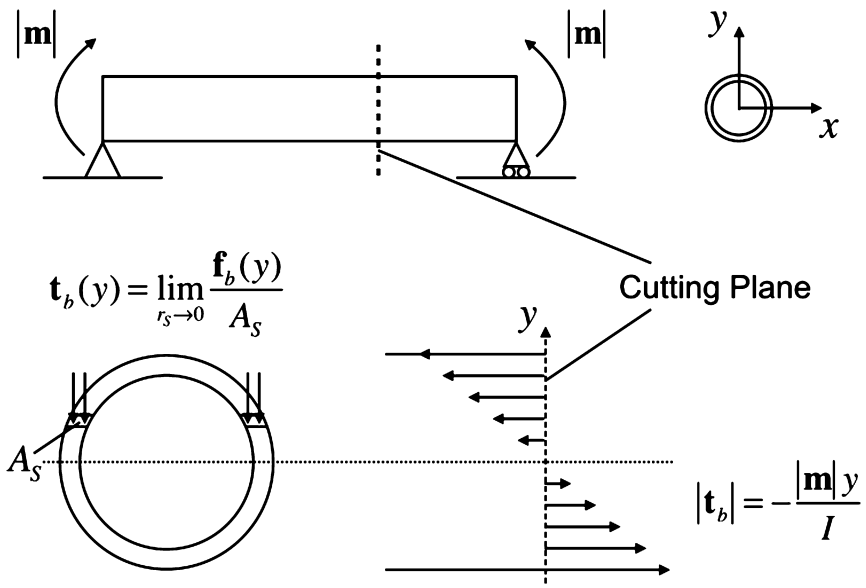

Figure 4.4 ***Traction in pure bending of a tube.*** The lower left-hand diagram indicates the force areal distribution, an example local surface area being A_S. The force distribution vectors in the lower left-hand diagram are shown in perspective relative to the plane of the paper. In actuality these vectors are perpendicular to the view plane and directed into the paper.

- in the limit, as r_{S-max} decreases, the resultant of the force distributions acting on local area A_S will be continually changing.

Although Eq. (4.2) has been introduced in the context of an interior surface created by a cutting plane with normal **n**, the formula is general enough to permit its use in defining the local traction on an external surface having local normal **n**.

4.2.1.1 Example problem—average and local traction

Consider a tubular in a state of pure bending. The tube is loaded by moments on either end, and one end of the tube is free to translate in order to avoid generating an axial force associated with the bending. The loading is depicted in the upper portion of Fig. 4.4.

Within the local x–y coordinate system of the cross-section, the force distribution and the local bending traction distribution are constant along the x direction and vary linearly in the y direction, being compressive in the upper half of the cross-section and tensile in the lower half of the cross-section. If the bending traction is[2] $\mathbf{t}_b(y)$, the corresponding bending force distribution is $\mathbf{f}_b(y)$ with (see Eq. (4.2))

[2] The recommended subscript "n" for traction is not used here since the cutting plane normal is understood to be perpendicular to the tube cross-section.

$$\mathbf{t}_b = \lim_{r_S \to 0} \frac{\mathbf{f}_b}{A_S}, \tag{4.3}$$

where r_S is the maximum lateral dimension of A_S in the plane of the paper.

Although the topic of bending has not yet been discussed, the bending traction distribution in any internal cross-section can be shown to be

$$\mathbf{t}_b(y) = -\frac{|\mathbf{m}|\, y}{I}, \tag{4.4}$$

where $|\mathbf{m}|$ is the magnitude of the bending moment and I is the moment of inertia of the tube cross-section ($I = \frac{\pi}{64}\left(D^4 - d^4\right)$). The average traction on the cross-section is, from Eq. (4.1), determined using the resultant of the force distribution acting on the entire cross-section. From Fig. 4.4, integrating $\mathbf{f}_b$ over the cross-section yields a resultant (axial) force of zero.[3] Eq. (4.1) therefore requires that the average traction on the

[3] Specifically, we take advantage of symmetry about the y-axis in Fig. 4.4 and integrate the force distribution over the cross-sectional area of the tube. Our differential area at each y value is a horizontal strip whose height is dy and width is the difference between the x values corresponding to y at the outer and inner radii of the tube cross-section—see lower left diagram of Fig. 4.4. We also have to account for the fact that for $|y| > d/2$, d no longer participates in the calculation of the width of the differential horizontal strip. Explicitly

$$\int_{A_{Crosssection}} df_b = \int_{-D/2}^{D/2} t_b(y)\, dA(y) = -2\frac{|\mathbf{m}|}{I}\int_{-D/2}^{D/2}\left[\hat{x}(y)\big|_{D/2} - \hat{x}(y)\big|_{d/2}\right] y\, dy$$

$$= -2\frac{|\mathbf{m}|}{I}\left\{\underbrace{\int_{-D/2}^{-d/2}\sqrt{\left(\frac{D}{2}\right)^2 - y^2}\, y\, dy}_{\text{Lower, ``solid'' cross-section}} + \underbrace{\int_{-d/2}^{d/2}\left[\sqrt{\left(\frac{D}{2}\right)^2 - y^2} - \sqrt{\left(\frac{d}{2}\right)^2 - y^2}\right] y\, dy}_{y\text{-range with hole}}\right.$$

$$\left. + \underbrace{\int_{d/2}^{D/2}\sqrt{\left(\frac{D}{2}\right)^2 - y^2}\, y\, dy}_{\text{Upper, ``solid'' cross-section}}\right\},$$

$$= -\frac{2}{3}\frac{|\mathbf{m}|}{I}\left\{-\left[\left(\frac{D}{2}\right)^2 - y^2\right]^{\frac{3}{2}}\Bigg|_{-\frac{D}{2}}^{-\frac{d}{2}} - \left[\left(\frac{D}{2}\right)^2 - y^2\right]^{\frac{3}{2}}\Bigg|_{-\frac{d}{2}}^{\frac{d}{2}} + \left[\left(\frac{d}{2}\right)^2 - y^2\right]^{\frac{3}{2}}\Bigg|_{-\frac{d}{2}}^{\frac{d}{2}}\right.$$

$$\left. - \left[\left(\frac{D}{2}\right)^2 - y^2\right]^{\frac{3}{2}}\Bigg|_{\frac{d}{2}}^{\frac{D}{2}}\right\}$$

$$= -\frac{2}{3}\frac{|\mathbf{m}|}{I}\left\{-\left[\left(\frac{D}{2}\right)^2 - \left(\frac{d}{2}\right)^2\right]^{\frac{3}{2}} + \left[\left(\frac{D}{2}\right)^2 - \left(\frac{d}{2}\right)^2\right]^{\frac{3}{2}}\right\} = 0.$$

cross-section be $\mathbf{t}_{(\mathbf{n})-ave} = \mathbf{0}$. By comparison, the local traction at any distance from the centerline of the tube cross-section is given by Eq. (4.4). In this example, the difference, both qualitatively and quantitatively, between the average and local traction is significant.

4.2.2 Stress and stress components

Consider a special case of Fig. 4.3 when $\mathbf{n} = \mathbf{g}_1$, that is, the cutting plane is parallel to the spatial x_2–x_3 plane, and the normal to the cutting plane is collinear with the unit vector[4] $\mathbf{g}_1$ along the x_1-axis. The resulting traction $\mathbf{t}_{(\mathbf{g}_1)}$ can be written as the sum of its three components along the x_i-axes (see Section A.4 of Appendix A)

$$\begin{aligned}\mathbf{t}_{(\mathbf{g}_1)} &= \left(\mathbf{t}_{(\mathbf{g}_1)} \cdot \mathbf{g}_1\right)\mathbf{g}_1 + \left(\mathbf{t}_{(\mathbf{g}_1)} \cdot \mathbf{g}_2\right)\mathbf{g}_2 + \left(\mathbf{t}_{(\mathbf{g}_1)} \cdot \mathbf{g}_3\right)\mathbf{g}_3 \\ &= \Sigma_{11}\mathbf{g}_1 + \Sigma_{12}\mathbf{g}_2 + \Sigma_{13}\mathbf{g}_3. \end{aligned} \tag{4.5}$$

The components of the traction are called stresses,[5] with the following definitions taken directly from Eq. (4.5):

- Σ_{11} is the Cauchy stress acting on the spatial surface with normal $\mathbf{g}_1$ and in the direction of $\mathbf{g}_1$;
- Σ_{12} is the Cauchy stress acting on the spatial surface with normal $\mathbf{g}_1$ and in the direction of $\mathbf{g}_2$;
- Σ_{13} is the Cauchy stress acting on the spatial surface with normal $\mathbf{g}_1$ and in the direction of $\mathbf{g}_3$.

The Cauchy stress is a second order tensor whose components have units of force per area.

Similar decompositions involving cutting planes with normals collinear with the unit vectors along the x_2- and x_3-axes can be used to introduce stress components Σ_{21}, Σ_{22} and Σ_{23} associated with the plane normal to the x_2-axis and Σ_{31}, Σ_{32} and Σ_{33} associated with the plane normal to the x_3-axis. The general rule of designation is that stress component Σ_{ij} is the component of the local traction acting on a surface whose normal is aligned with the positive x_i-axis, and acting in the direction of the positive x_j-axis. Stress components where the two indices are equal are normal stresses[6]; stress components where the two indices differ are shear stresses.

Fig. 4.5 summarizes the above introduction of the components of stress by showing the positive direction of stress components acting on an infinitesimal element of a body.[7]

[4] Here we recall (see Section 3.2 of Chapter 3) the unit vectors $\mathbf{g}_i$, $i = 1, 2, 3$, which serve the same function for the spatial x_i-axes as the unit vectors $\mathbf{e}_I$ serve for the material X_I-axes.

[5] We introduce the symbol Σ to designate the Cauchy stress. This Σ should not be confused with the identical symbol for summation. The context of the discussion should aid in the distinction.

[6] The designation "normal stress" indicates the stress is normal, or perpendicular, to the surface on which it acts.

[7] Because of the proximity of casing to the wellbore wall, many problems involving both tubular mechanical concepts and rock mechanical concepts become important. Care should be taken in formulating such

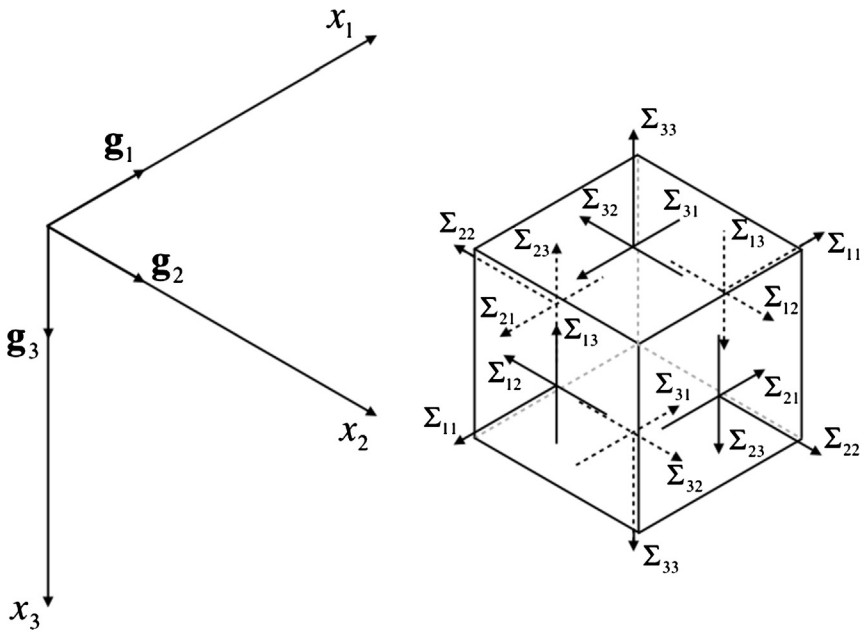

Figure 4.5 ***Components of stress.*** A positive stress component Σ_{ij} acts on the positive *i*-face and in the direction of the positive *j*-axis. All components in the figure are positive as shown. For clarity only the spatial coordinate axes are displayed.

Positive stresses on faces of the element whose normals align with the unit normal vectors for the coordinate axes point in the positive direction of coordinate axes; positive stresses on faces of the element whose normals are the negative of the unit normal vectors for the coordinate axes point in the negative direction of coordinate axes.

For problems involving cylindrical coordinates interpretation of stress components is identical to that described above for rectangular coordinates:

- the cylindrical coordinates r, θ and z replace rectangular coordinates x_1, x_2 and x_3;
- the naming convention for cylindrical coordinates is analogous to that for rectangular coordinates—$\Sigma_{\theta\theta}$ is the normal stress acting on the surface with normal $\mathbf{g}_\theta$ and in the direction of $\mathbf{g}_\theta$; Σ_{rz} is the shear stress acting on the surface with normal $\mathbf{g}_r$ and in the direction of $\mathbf{g}_z$.

The physical components of the stress tensor in cylindrical coordinates can be written in terms of the physical components of the stress tensor in rectangular coordinates and vice versa. A discussion and derivation of these equations is presented in Section A.5.2.1 in Appendix A.

problems as the common practice in rock mechanics is to assume compression, rather than tension, to be positive. The two disciplines do not therefore have positive stress components with the same directional sense.

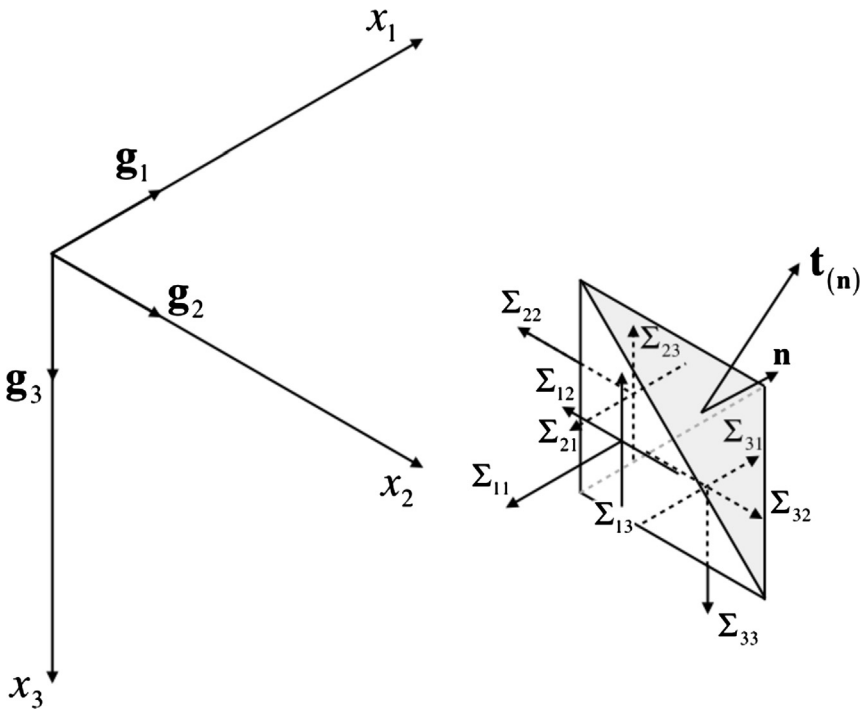

Figure 4.6 ***Determination of the local traction from the stress tensor.*** The shaded surface partially bounding the infinitesimal body is *da*. A body force acting on the infinitesimal volume is not shown in the figure.

4.2.3 Determining traction from stress

Given the components of the stress tensor Σ_{ij}, we may determine the local traction on any surface with normal $\mathbf{n}$. Fig. 4.6 illustrates such a problem.

As it intersects the infinitesimal body (see Fig. 4.5), the cutting plane with normal $\mathbf{n}$ creates a triangle of area da shown shaded in Fig. 4.6. The volume of the irregular tetrahedron is $dv = \frac{1}{3}A_{da}h$, where h is the distance from the surface da to the opposite vertex. The areas of each of the coordinate planes acted on by components of the stress tensor are given by $da_i = (\mathbf{n} \cdot \mathbf{g}_i)da$. Summing forces in each coordinate direction and including any body force acting on the infinitesimal element

$$-\Sigma_{11}\mathbf{n}\cdot\mathbf{g}_1 da - \Sigma_{21}\mathbf{n}\cdot\mathbf{g}_2 da - \Sigma_{31}\mathbf{n}\cdot\mathbf{g}_3 da + \rho\mathbf{b}_f\cdot\mathbf{g}_1 dv + \mathbf{t}_{(\mathbf{n})}\cdot\mathbf{g}_1 da = \frac{\rho}{g_c}\mathbf{a}\cdot\mathbf{g}_1 dv, \quad (4.6)$$

$$-\Sigma_{12}\mathbf{n}\cdot\mathbf{g}_1 da - \Sigma_{22}\mathbf{n}\cdot\mathbf{g}_2 da - \Sigma_{32}\mathbf{n}\cdot\mathbf{g}_3 da + \rho\mathbf{b}_f\cdot\mathbf{g}_2 dv + \mathbf{t}_{(\mathbf{n})}\cdot\mathbf{g}_2 da = \frac{\rho}{g_c}\mathbf{a}\cdot\mathbf{g}_2 dv, \quad (4.7)$$

$$-\Sigma_{13}\mathbf{n}\cdot\mathbf{g}_1 da - \Sigma_{23}\mathbf{n}\cdot\mathbf{g}_2 da - \Sigma_{33}\mathbf{n}\cdot\mathbf{g}_3 da + \rho\mathbf{b}_f\cdot\mathbf{g}_3 dv + \mathbf{t}_{(\mathbf{n})}\cdot\mathbf{g}_3 da = \frac{\rho}{g_c}\mathbf{a}\cdot\mathbf{g}_3 dv, \quad (4.8)$$

where **a** is acceleration and the body force is assumed to be provided per unit mass. Writing Eqs. (4.6)–(4.8) more compactly gives

$$-\Sigma_{jk}\mathbf{n}\cdot\mathbf{g}_j da+\rho\mathbf{b}_f\cdot\mathbf{g}_k dv+\mathbf{t}_{(\mathbf{n})}\cdot\mathbf{g}_k da=\frac{\rho}{g_c}\mathbf{a}\cdot\mathbf{g}_k dv. \tag{4.9}$$

In the limit as the dimensions of the body approach zero, the body force and acceleration terms vanish as their infinitesimal dimensions are one order higher than the other terms, and

$$\left(\mathbf{t}_{(\mathbf{n})}\cdot\mathbf{g}_k-\Sigma_{jk}\mathbf{n}\cdot\mathbf{g}_j\right)da=0, \tag{4.10}$$

which, for a small but nonzero surface area, implies

$$\mathbf{t}_{(\mathbf{n})}=\boldsymbol{\Sigma}^T\cdot\mathbf{n},\quad \left(\mathbf{t}_{(\mathbf{n})}\right)_k=\Sigma_{jk}n_j. \tag{4.11}$$

The kth component of the traction acting on a surface with normal **n** can be determined from the stress tensor $\boldsymbol{\Sigma}$ and **n**.

4.2.4 The equations of motion

Fig. 4.7 illustrates the general stress state on an infinitesimal element whose faces align with the coordinate axes.[8] A continuously varying stress field is examined in the vicinity of a particular point **x**.

Summing forces in the three coordinate directions, the equations of motion are

$$\begin{aligned}&\left[-\Sigma_{11}+\left(\Sigma_{11}+\frac{\partial\Sigma_{11}}{\partial x_1}dx_1\right)\right]dx_2dx_3+\left[-\Sigma_{21}+\left(\Sigma_{21}+\frac{\partial\Sigma_{21}}{\partial x_2}dx_2\right)\right]dx_1dx_3+\\&\left[-\Sigma_{31}+\left(\Sigma_{31}+\frac{\partial\Sigma_{31}}{\partial x_3}dx_3\right)\right]dx_1dx_2+\rho\mathbf{b}_f\cdot\mathbf{g}_1dx_1dx_2dx_3\\&=\frac{\rho}{g_c}\mathbf{a}\cdot\mathbf{g}_1dx_1dx_2dx_3,\end{aligned} \tag{4.12}$$

$$\begin{aligned}&\left[-\Sigma_{12}+\left(\Sigma_{12}+\frac{\partial\Sigma_{12}}{\partial x_1}dx_1\right)\right]dx_2dx_3+\left[-\Sigma_{22}+\left(\Sigma_{22}+\frac{\partial\Sigma_{22}}{\partial x_2}dx_2\right)\right]dx_1dx_3+\\&\left[-\Sigma_{32}+\left(\Sigma_{32}+\frac{\partial\Sigma_{32}}{\partial x_3}dx_3\right)\right]dx_1dx_2+\rho\mathbf{b}_f\cdot\mathbf{g}_2dx_1dx_2dx_3\\&=\frac{\rho}{g_c}\mathbf{a}\cdot\mathbf{g}_2dx_1dx_2dx_3,\end{aligned} \tag{4.13}$$

[8] Fig. 4.5 is a special case of Fig. 4.7 when the stress field in a body is constant.

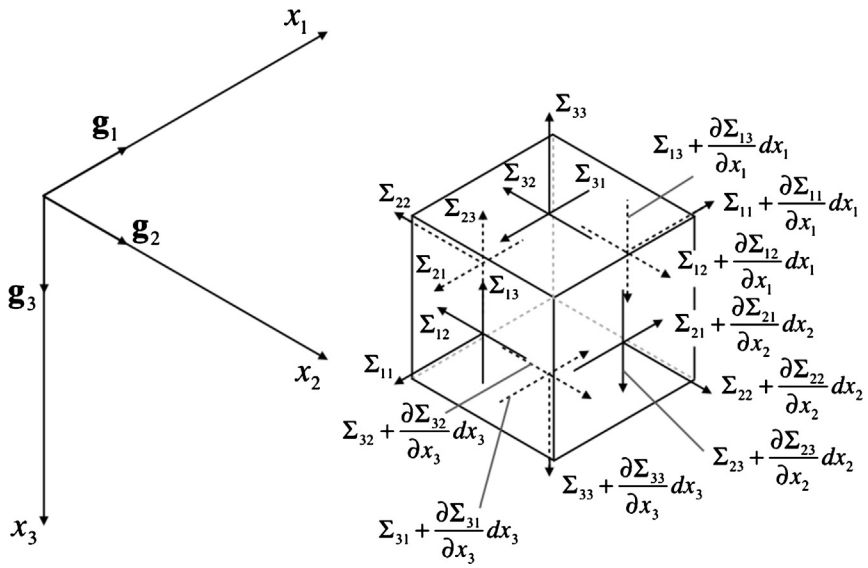

Figure 4.7 ***Forces acting on an infinitesimal element in motion or at rest.*** The body force $\mathbf{b}_f$ is not shown.

$$\left[-\Sigma_{13} + \left(\Sigma_{13} + \frac{\partial \Sigma_{13}}{\partial x_1} dx_1\right)\right] dx_2 dx_3 + \left[-\Sigma_{23} + \left(\Sigma_{23} + \frac{\partial \Sigma_{23}}{\partial x_2} dx_2\right)\right] dx_1 dx_3 +$$
$$\left[-\Sigma_{33} + \left(\Sigma_{33} + \frac{\partial \Sigma_{33}}{\partial x_3} dx_3\right)\right] dx_1 dx_2 + \rho \mathbf{b}_f \cdot \mathbf{g}_3 dx_1 dx_2 dx_3 \tag{4.14}$$
$$= \frac{\rho}{g_c} \mathbf{a} \cdot \mathbf{g}_3 dx_1 dx_2 dx_3,$$

where the body force is assumed to be provided per unit mass. Simplifying Eqs. (4.12)–(4.14) gives

$$\left(\frac{\partial \Sigma_{jk}}{\partial x_j} + \rho \mathbf{b}_f \cdot \mathbf{g}_k - \frac{\rho}{g_c} \mathbf{a} \cdot \mathbf{g}_k\right) dx_1 dx_2 dx_3 = 0, \quad k = 1, 2, 3, \tag{4.15}$$

implying

$$\frac{\partial \Sigma_{jk}}{\partial x_j} + \rho \mathbf{b}_f \cdot \mathbf{g}_k - \frac{\rho}{g_c} \mathbf{a} \cdot \mathbf{g}_k = 0. \tag{4.16}$$

The element must also satisfy the moment of momentum equations. Taking moments about the x_1-axis as an example, Fig. 4.8 shows the stress components that can produce a nonzero moment on the element.

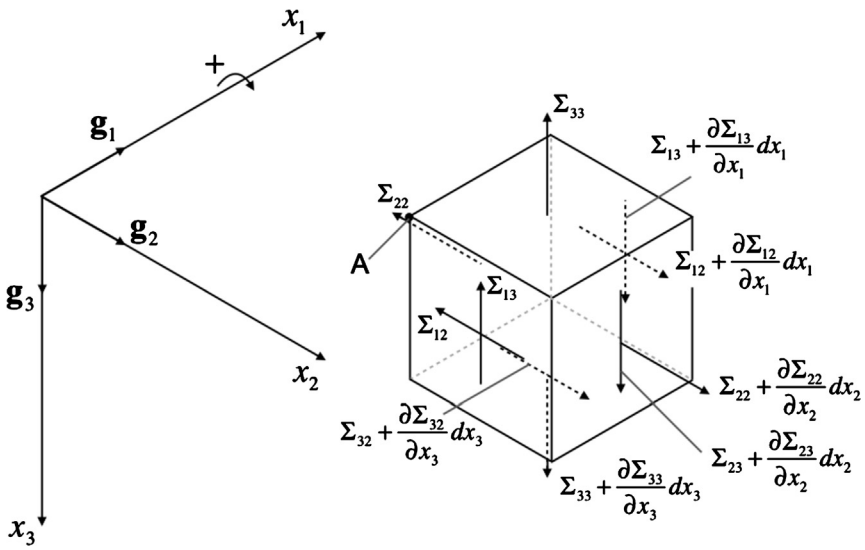

Figure 4.8 ***Moment of momentum in an infinitesimal element.*** Only components contributing to a nonzero moment about the x_1-axis are shown. In addition, although it may contribute to the moment about the x_1-axis (see Eq. (4.17)), the body force $\mathbf{b}_f$ is not shown.

Taking moments about point A in the direction of the x_1-axis, we obtain

$$\begin{aligned}
&\left[\Sigma_{12}-\left(\Sigma_{12}+\frac{\partial\Sigma_{12}}{\partial x_1}dx_1\right)\right]\frac{dx_3}{2}dx_2dx_3-\left[\Sigma_{13}-\left(\Sigma_{13}+\frac{\partial\Sigma_{13}}{\partial x_1}dx_1\right)\right]\frac{dx_2}{2}dx_2dx_3+\\
&\left[\Sigma_{22}-\left(\Sigma_{22}+\frac{\partial\Sigma_{22}}{\partial x_2}dx_2\right)\right]\frac{dx_3}{2}dx_1dx_3+\left[\Sigma_{23}+\frac{\partial\Sigma_{23}}{\partial x_2}dx_2\right]dx_2dx_1dx_3-\\
&\left[\Sigma_{33}-\left(\Sigma_{33}+\frac{\partial\Sigma_{33}}{\partial x_3}dx_3\right)\right]\frac{dx_2}{2}dx_1dx_2-\left[\Sigma_{32}+\frac{\partial\Sigma_{32}}{\partial x_3}dx_3\right]dx_3dx_1dx_2-\\
&\rho\mathbf{b}_f\cdot\mathbf{g}_2\frac{dx_3}{2}dx_1dx_2dx_3+\rho\mathbf{b}_f\cdot\mathbf{g}_3\frac{dx_2}{2}dx_1dx_2dx_3\\
&=\left(-\frac{\rho}{g_c}\mathbf{a}\cdot\mathbf{g}_2\frac{dx_3}{2}+\frac{\rho}{g_c}\mathbf{a}\cdot\mathbf{g}_3\frac{dx_2}{2}\right)dx_1dx_2dx_3,
\end{aligned}\tag{4.17}$$

where the right-hand side is the angular momentum and the body force is assumed to be provided per unit mass. Simplifying and dropping higher order terms gives

$$(\Sigma_{23}-\Sigma_{32})\,dx_1dx_2dx_3=0,\tag{4.18}$$

or

$$\Sigma_{23}=\Sigma_{32}.\tag{4.19}$$

Similar calculations involving moments about the x_2 and x_3-axes lead to the following results:

$$\Sigma_{31} = \Sigma_{13}, \tag{4.20}$$

$$\Sigma_{12} = \Sigma_{21}. \tag{4.21}$$

Eqs. (4.19)–(4.21) imply the Cauchy stress tensor is symmetric, i.e., $\Sigma_{ij} = \Sigma_{ji}$, $i \neq j$.

4.2.5 Principal stresses

In general, the traction $\mathbf{t}_{(\mathbf{n})}$ will not be collinear with the normal $\mathbf{n}$. There will be a normal component of the traction vector $(\mathbf{t}_{(\mathbf{n})})_n$ aligned with $\mathbf{n}$ and a shear component of the traction vector $(\mathbf{t}_{(\mathbf{n})})_s$ lying in the plane with which $\mathbf{n}$ is associated.

An important special case of $\mathbf{n}$ is the normal for which $\mathbf{t}_{(\mathbf{n})}$ is collinear with $\mathbf{n}$, there being no shear component. In this case

$$\mathbf{t}_{(\mathbf{n})} = \lambda \mathbf{n}, \quad (\mathbf{t}_{(\mathbf{n})})_k = \lambda n_k, \tag{4.22}$$

where λ is a scalar. Rearranging Eq. (4.22) gives

$$\mathbf{t}_{(\mathbf{n})} - \lambda \mathbf{n} = \mathbf{0}, \quad (\mathbf{t}_{(\mathbf{n})})_k - \lambda n_k = 0, \tag{4.23}$$

where $\mathbf{0}$ is a vector, all of whose elements are zero, of the same dimension as $\mathbf{t}_{(\mathbf{n})}$ and $\mathbf{n}$.

Using Eq. (4.11) in Eq. (4.23) yields

$$\left(\boldsymbol{\Sigma}^T - \lambda \mathbf{I}\right) \cdot \mathbf{n} = \mathbf{0}, \quad \left(\Sigma_{kj} - \lambda \delta_{jk}\right) n_k = 0, \tag{4.24}$$

where we have used the fact that $\mathbf{In} = \mathbf{n}$, $\mathbf{I}$ being the identity matrix (see Section A.5.1.2 of Appendix A). In expanded form, Eq. (4.24) is

$$\begin{bmatrix} \Sigma_{11} - \lambda & \Sigma_{21} & \Sigma_{31} \\ \Sigma_{12} & \Sigma_{22} - \lambda & \Sigma_{31} \\ \Sigma_{13} & \Sigma_{23} & \Sigma_{33} - \lambda \end{bmatrix} \begin{bmatrix} n_1 \\ n_2 \\ n_3 \end{bmatrix} = \begin{bmatrix} 0 \\ 0 \\ 0 \end{bmatrix}. \tag{4.25}$$

Further, we have the relation

$$\mathbf{n} \cdot \mathbf{n} = 1, \quad n_k n_k = 1, \tag{4.26}$$

since $\mathbf{n}$ is a unit vector.

Eq. (4.25) will have nonzero solutions if and only if the determinant of $\boldsymbol{\Sigma}^T - \lambda \mathbf{I}$ vanishes [16].

4.2.5.1 Example problem—solution for principal stresses

Given the stress tensor[9]

$$\boldsymbol{\Sigma} = \boldsymbol{\Sigma}^T = \begin{bmatrix} -10 & 14 & 23 \\ 14 & -80 & 5 \\ 23 & 5 & 54 \end{bmatrix}, \tag{4.27}$$

find the principal stresses and their respective directions.

From Section A.5.2.3 of Appendix A, we must solve Eq. (A.105), repeated here for reference

$$\lambda^3 - I_1\lambda^2 - I_2\lambda - I_3 = 0, \tag{4.28}$$

where, from Eq. (A.91)

$$I_1 = \Sigma_{jj}^T = -10 - 80 + 54 = -36, \tag{4.29}$$

and from Eq. (A.94)

$$\begin{aligned} I_2 &= \frac{1}{2}\left[\Sigma_{rs}^T\Sigma_{rs}^T - \left(\Sigma_{kk}^T\right)^2\right] \\ &= \left(\Sigma_{12}^T\right)^2 + \left(\Sigma_{23}^T\right)^2 + \left(\Sigma_{31}^T\right)^2 - \Sigma_{11}^T\Sigma_{22}^T - \Sigma_{22}^T\Sigma_{33}^T - \Sigma_{33}^T\Sigma_{11}^T \\ &= (14)^2 + (5)^2 + (23)^2 - (-10)(-80) - (-80)(54) - (54)(-10) \\ &= 4810, \end{aligned} \tag{4.30}$$

and from Eq. (A.97)

$$\begin{aligned} I_3 &= \det \boldsymbol{\Sigma}^{\mathbf{T}} \\ &= -10\left[-80 \times 54 - 5 \times 5\right] - 14\left[14 \times 54 - 5 \times 23\right] + 23\left[14 \times 5 + 80 \times 23\right] \\ &= 78\,406. \end{aligned} \tag{4.31}$$

Eq. (4.28) becomes

$$\lambda^3 + 36\lambda^2 - 4810\lambda - 78\,406 = 0, \tag{4.32}$$

which is of the general form $ax^3 + bx^2 + cx + d = 0$, where $a = 1$, $b = 36$, $c = -4810$ and $d = -78\,406$. To solve this equation (see [10] or any intermediate algebra text), we first use the substitution $x = y - \frac{b}{3a}$ to reexpress the general form as $y^3 + 3py + 2q = 0$. We may now calculate the discriminant $D = -p^3 - q^2$ of the this alternate form of the cubic equation

$$p = \frac{1}{3}\frac{3ac - b^2}{3a^2} = \frac{1}{3}\frac{3 \times 1 \times (-4810) - (36)^2}{3\,(1)^2} = -1747.33, \tag{4.33}$$

[9] The reader uncomfortable with such small stress values can consider the units to be 1 000 s of psi, or ksi.

Table 4.1 Possible solutions of a cubic equation depending on the value of the discriminant D

Condition	Equation roots[a]
$D \geq 0$	Three real roots which are distinct if $D > 0$
$D = 0$	Either a double root (if $p^3 = -q^2 \neq 0$) or a triple zero root (if $p = q = 0$)
$D < 0$	One real root and two complex conjugate roots

[a] Assumes p and q are real.

and

$$\begin{aligned} q &= \frac{1}{2}\left[\frac{2b^3}{27a^3} - \frac{bc}{3a^2} + \frac{d}{a}\right] \\ &= \frac{1}{2}\left[\frac{2\,(36)^3}{27\,(1)^3} - \frac{36\,(-4810)}{3\,(1)^2} + \frac{-78\,406}{1}\right] \\ &= -8615. \end{aligned} \tag{4.34}$$

Finally,

$$D = -p^3 - q^2 = -\,(-1747.33)^3 - (-8615)^2 = 5\,260\,694\,089. \tag{4.35}$$

The solution proceeds according to the value of D, as indicated in Table 4.1. For this example problem, $D > 0$ so the solution for λ has three distinct real roots as illustrated in Fig. 4.9, which displays the functional behavior of Eq. (4.28).

Several methods [10] exist to determine the three roots of Eq. (4.28). The first is simply trial-and-error. A commercial spreadsheet or similar software can be used to straightforwardly solve the equation, particularly if a plot such as Fig. 4.9 is available to help properly seed the initial guess. For this example the three solutions are[10] $\lambda_1 = -82.6986$, $\lambda_2 = -15.2937$, and $\lambda_3 = 61.9923$.

Each root of λ solving Eq. (4.28) may then be substituted into Eq. (4.25) to determine the direction $\mathbf{n}$ corresponding to that principal stress. As an example, for $\lambda_1 = -82.6986$ and the stress tensor given for this example in Eq. (4.27), Eq. (4.25) yields

$$\begin{bmatrix} 72.6986 & 14 & 23 \\ 14 & 2.6986 & 5 \\ 23 & 5 & 136.6986 \end{bmatrix} \begin{bmatrix} n_1 \\ n_2 \\ n_3 \end{bmatrix} = \begin{bmatrix} 0 \\ 0 \\ 0 \end{bmatrix}. \tag{4.36}$$

Multiplying the second row(s) in Eq. (4.36) by 72.6986/14 and subtracting the result from the first row, and multiplying the third row(s) by 72.6986/23 and subtracting the

[10] We carry 4 decimals on the solutions for λ to provide reasonably accurate behavior in the work to follow.

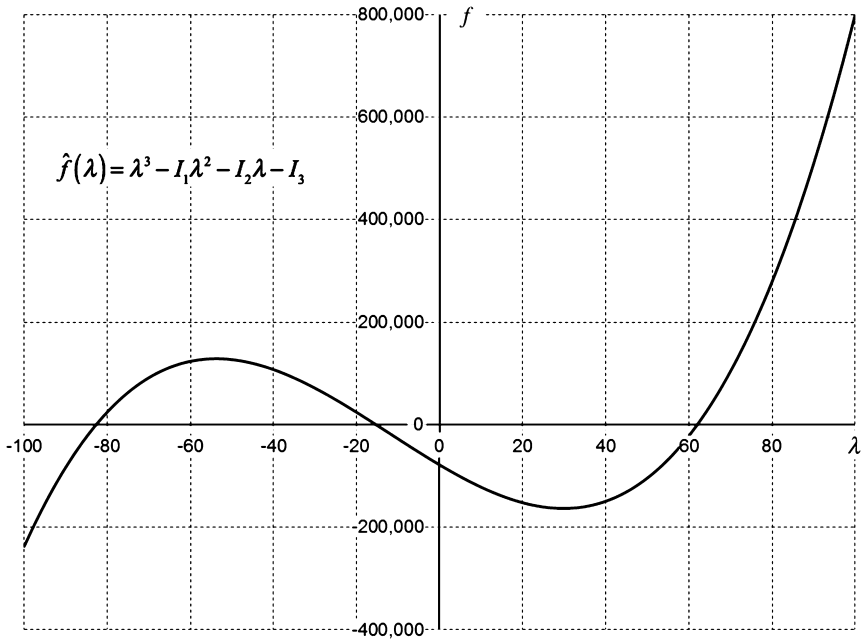

Figure 4.9 ***Behavior of Eq.*** (4.28) ***for example problem.*** Roots of equation are intersections with λ-axis; $I_1 = -36$, $I_2 = 4810$, $I_3 = 78\,406$.

result from the first row produces

$$\begin{bmatrix} 72.6986 & 14 & 23 \\ 0 & -0.01317 & -2.9638 \\ 0 & -1.8040 & -409.0781 \end{bmatrix} \begin{bmatrix} n_1 \\ n_2 \\ n_3 \end{bmatrix} = \begin{bmatrix} 0 \\ 0 \\ 0 \end{bmatrix}. \tag{4.37}$$

Now multiplying the third row(s) in Eq. (4.37) by $-0.01317/-1.8040$ and subtracting the result from the second row gives

$$\begin{bmatrix} 72.6986 & 14 & 23 \\ 0 & -0.01317 & -2.9638 \\ 0 & 0 & 0.02265 \end{bmatrix} \begin{bmatrix} n_1 \\ n_2 \\ n_3 \end{bmatrix} = \begin{bmatrix} 0 \\ 0 \\ 0 \end{bmatrix}. \tag{4.38}$$

The last row in the matrix of coefficients should have all zero elements. The value 0.02265 is solely a consequence of the rounding done in this presentation. This last row disappears because the determinant of the original matrix (see Eq. (4.36)) vanishes from Eq. (4.28) and its associated discussion in Appendix A. As a consequence there are an infinite number of solutions of Eq. (4.36). One such solution can be obtained by setting $n_3 = 1$ and then (see second row of Eq. (4.38)) solving for $n_2 = -225.0418$. These values of n_2 and n_3 can then be used (see first row of Eq. (4.38)) to solve for $n_1 = 43.02125$.

There exists, however, an additional constraint on the components of $\mathbf{n}$; namely, $\mathbf{n}$ is a unit vector. Normalizing the above arbitrary solution by its magnitude gives

$$\mathbf{n}_{(1)} = \begin{bmatrix} 0.1878 \\ -0.9822 \\ 0.004\,365 \end{bmatrix}. \tag{4.39}$$

Similar solution procedures using λ_2 and λ_3 result in the other two eigenvectors (e.g., unit normal vectors in principal stress directions 2 and 3)[11]

$$\mathbf{n}_{(2)} = \begin{bmatrix} -0.930\,32 \\ -0.1764 \\ 0.3215 \end{bmatrix}, \tag{4.40}$$

$$\mathbf{n}_{(3)} = \begin{bmatrix} 0.3150 \\ 0.064\,40 \\ 0.9469 \end{bmatrix}. \tag{4.41}$$

A quick check of the solution is to take the inner products of the principal stress unit normal vectors—they should be mutually perpendicular to each other, i.e., $\mathbf{n}_{(i)} \cdot \mathbf{n}_{(j)} = 0$ for $i \neq j$.

We have now determined both the principal stresses and their directions. If the stress tensor in the spatial coordinate system (x_1–x_2–x_3) given by Eq. (4.27) is expressed in a coordinate system aligned with the unit vectors given by Eqs. (4.39)–(4.41), there will be no shear stresses and

$$\mathbf{\Sigma}^p = \begin{bmatrix} -82.6986 & 0 & 0 \\ 0 & -15.2937 & 0 \\ 0 & 0 & 61.9923 \end{bmatrix}. \tag{4.42}$$

4.2.6 Stress equations in cylindrical coordinates

Fig. 4.10 illustrates the components of the stress tensor in a cylindrical coordinate system, and is the counterpart of Fig. 4.5 for a rectangular coordinate system. For those problems of tubular design dealing with the stresses in the wall of the tube, the cylindrical coordinate system is often the most convenient in which to frame the solution. The important equations derived above are rewritten here in cylindrical coordinates.

[11] Except for the value of the eigenvalue itself, no rounding was used in arriving at the solutions for $\mathbf{n}_{(2)}$ and $\mathbf{n}_{(3)}$.

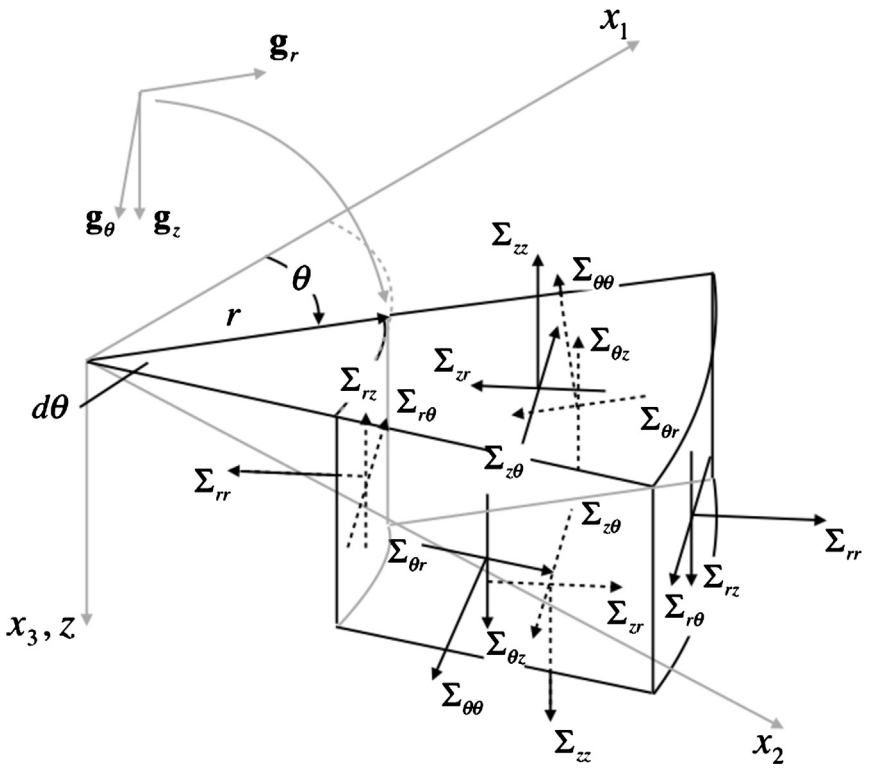

Figure 4.10 ***Components of stress in cylindrical coordinates.*** A positive stress component acts on a positive face and in the direction of a positive axis. All components in the figure are positive as shown.

4.2.6.1 The equations of motion

Conversion of Eq. (4.16) to cylindrical coordinates is a two-step process.[12] First, the physical components of stress and body force in the rectangular global material coordinate system are expressed in terms of their cylindrical counterparts. This process has already been demonstrated in Section A.5.2.1 of Appendix A for a general second order tensor $\mathbf{T}$. The resulting relations, Eqs. (A.85)–(A.90), are repeated here with $\boldsymbol{\Sigma}$

[12] We discussed, but did not use this process in deriving the equations for strain in cylindrical coordinates in Section 3.6 of Chapter 3—see the review of Fung's exposition of strain in polar coordinates [15]. Instead, the approach taken for strain was to start from deformation and rederive the strain expressions in cylindrical coordinates. Here, we will use the coordinate and derivative transformations to convert stress directly from rectangular to cylindrical coordinates. To retrieve the physical insight lost by the transformation process, we will supplement the derivation with an explanation of the physical meaning of the various stress terms in the final expressions for motion. Treating the strain and stress transformations differently will hopefully leave the reader with an appreciation for the difference between the two conversion paths.

substituted for $\mathbf{T}$

$$\Sigma_{11} = \Sigma_{rr}\cos^2\theta - \Sigma_{r\theta}\sin 2\theta + \Sigma_{\theta\theta}\sin^2\theta, \tag{4.43}$$
$$\Sigma_{12} = (\Sigma_{rr} - \Sigma_{\theta\theta})\sin\theta\cos\theta + \Sigma_{r\theta}\cos 2\theta = \Sigma_{21}, \tag{4.44}$$
$$\Sigma_{13} = \Sigma_{rz}\cos\theta - \Sigma_{\theta z}\sin\theta = \Sigma_{31}, \tag{4.45}$$
$$\Sigma_{22} = \Sigma_{rr}\sin^2\theta + \Sigma_{r\theta}\sin 2\theta + \Sigma_{\theta\theta}\cos^2\theta, \tag{4.46}$$
$$\Sigma_{23} = \Sigma_{rz}\sin\theta + \Sigma_{\theta z}\cos\theta = \Sigma_{32}, \tag{4.47}$$
$$\Sigma_{33} = \Sigma_{zz}. \tag{4.48}$$

Similarly, Section A.5.1.1 of Appendix A demonstrates the transformation for a vector. The resulting relation, Eq. (A.66), is repeated here with $\mathbf{g}_k$ substituted for v

$$\mathbf{b}_f\cdot\mathbf{g}_1 = \mathbf{b}_f\cdot\mathbf{g}_r\cos\theta - \mathbf{b}_f\cdot\mathbf{g}_\theta\sin\theta, \quad \mathbf{b}_f\cdot\mathbf{g}_2 = \mathbf{b}_f\cdot\mathbf{g}_r\sin\theta + \mathbf{b}_f\cdot\mathbf{g}_\theta\cos\theta,$$
$$\mathbf{b}_f\cdot\mathbf{g}_3 = \mathbf{b}_f\cdot\mathbf{g}_z. \tag{4.49}$$
$$\mathbf{a}\cdot\mathbf{g}_1 = \mathbf{a}\cdot\mathbf{g}_r\cos\theta - \mathbf{a}\cdot\mathbf{g}_\theta\sin\theta, \quad \mathbf{a}\cdot\mathbf{g}_2 = \mathbf{a}\cdot\mathbf{g}_r\sin\theta + \mathbf{a}\cdot\mathbf{g}_\theta\cos\theta,$$
$$\mathbf{a}\cdot\mathbf{g}_3 = \mathbf{a}\cdot\mathbf{g}_z. \tag{4.50}$$

The second step in the conversion involves expressing the derivatives of x_i in terms of the cylindrical coordinates. We note that

$$x_1 = r\cos\theta, \quad x_2 = r\sin\theta, \quad x_3 = z, \tag{4.51}$$

or

$$r = \sqrt{x_1^2 + x_2^2}, \quad \theta = \tan^{-1}\frac{x_2}{x_1}, \quad z = x_3. \tag{4.52}$$

Using Eqs. (4.51) and (4.52) produces

$$\frac{\partial}{\partial x_1} = \frac{\partial r}{\partial x_1}\frac{\partial}{\partial r} + \frac{\partial\theta}{\partial x_1}\frac{\partial}{\partial\theta} = \cos\theta\frac{\partial}{\partial r} - \frac{\sin\theta}{r}\frac{\partial}{\partial\theta}, \tag{4.53}$$
$$\frac{\partial}{\partial x_2} = \frac{\partial r}{\partial x_2}\frac{\partial}{\partial r} + \frac{\partial\theta}{\partial x_2}\frac{\partial}{\partial\theta} = \sin\theta\frac{\partial}{\partial r} + \frac{\cos\theta}{r}\frac{\partial}{\partial\theta}, \tag{4.54}$$
$$\frac{\partial}{\partial x_3} = \frac{\partial}{\partial z}. \tag{4.55}$$

Substituting the above relations into Eq. (4.16), for $k = 1$ we get

$$\frac{\partial\Sigma_{11}}{\partial x_1} + \frac{\partial\Sigma_{21}}{\partial x_2} + \frac{\partial\Sigma_{31}}{\partial x_3} + \rho\mathbf{b}_f\cdot\mathbf{g}_1 =$$
$$\left(\cos\theta\frac{\partial}{\partial r} - \frac{\sin\theta}{r}\frac{\partial}{\partial\theta}\right)\left(\Sigma_{rr}\cos^2\theta - \Sigma_{r\theta}\sin 2\theta + \Sigma_{\theta\theta}\sin^2\theta\right) +$$
$$\left(\sin\theta\frac{\partial}{\partial r} + \frac{\cos\theta}{r}\frac{\partial}{\partial\theta}\right)\left((\Sigma_{rr} - \Sigma_{\theta\theta})\sin\theta\cos\theta + \Sigma_{r\theta}\cos 2\theta\right) + \tag{4.56}$$

$$\frac{\partial}{\partial z}\left(\Sigma_{rz}\cos\theta-\Sigma_{\theta z}\sin\theta\right)+\rho\left(\mathbf{b}_f\cdot\mathbf{g}_r\cos\theta-\mathbf{b}_f\cdot\mathbf{g}_\theta\sin\theta\right)$$
$$=\frac{\rho}{g_c}\left(\mathbf{a}\cdot\mathbf{g}_r\cos\theta-\mathbf{a}\cdot\mathbf{g}_\theta\sin\theta\right),$$

and, carrying out the indicated differentiations, we obtain

$$\cos\theta\left(\frac{\partial\Sigma_{rr}}{\partial r}+\frac{1}{r}\frac{\partial\Sigma_{r\theta}}{\partial\theta}+\frac{\partial\Sigma_{rz}}{\partial z}+\frac{\Sigma_{rr}-\Sigma_{\theta\theta}}{r}+\rho\mathbf{b}_f\cdot\mathbf{g}_r-\frac{\rho}{g_c}\mathbf{a}\cdot\mathbf{g}_r\right)-$$
$$\sin\theta\left(\frac{\partial\Sigma_{r\theta}}{\partial r}+\frac{1}{r}\frac{\partial\Sigma_{\theta\theta}}{\partial\theta}+\frac{\partial\Sigma_{\theta z}}{\partial z}+\frac{2\Sigma_{r\theta}}{r}+\rho\mathbf{b}_f\cdot\mathbf{g}_\theta-\frac{\rho}{g_c}\mathbf{a}\cdot\mathbf{g}_\theta\right)=0. \tag{4.57}$$

Eq. (4.57) can only be true for all values of θ if the two expressions in parentheses vanish. The first two equations of motion in cylindrical coordinates are therefore

$$\frac{\partial\Sigma_{rr}}{\partial r}+\frac{1}{r}\frac{\partial\Sigma_{r\theta}}{\partial\theta}+\frac{\partial\Sigma_{rz}}{\partial z}+\frac{\Sigma_{rr}-\Sigma_{\theta\theta}}{r}+\rho\mathbf{b}_f\cdot\mathbf{g}_r-\frac{\rho}{g_c}\mathbf{a}\cdot\mathbf{g}_r=0, \tag{4.58}$$
$$\frac{\partial\Sigma_{r\theta}}{\partial r}+\frac{1}{r}\frac{\partial\Sigma_{\theta\theta}}{\partial\theta}+\frac{\partial\Sigma_{\theta z}}{\partial z}+\frac{2\Sigma_{r\theta}}{r}+\rho\mathbf{b}_f\cdot\mathbf{g}_\theta-\frac{\rho}{g_c}\mathbf{a}\cdot\mathbf{g}_\theta=0. \tag{4.59}$$

Returning to Eq. (4.16), for $k=2$ we get

$$\frac{\partial\Sigma_{21}}{\partial x_1}+\frac{\partial\Sigma_{22}}{\partial x_2}+\frac{\partial\Sigma_{32}}{\partial x_3}+\rho\mathbf{b}_f\cdot\mathbf{g}_2=$$
$$\left(\cos\theta\frac{\partial}{\partial r}-\frac{\sin\theta}{r}\frac{\partial}{\partial\theta}\right)\left(\left(\Sigma_{rr}-\Sigma_{\theta\theta}\right)\sin\theta\cos\theta+\Sigma_{r\theta}\cos2\theta\right)+$$
$$\left(\sin\theta\frac{\partial}{\partial r}+\frac{\cos\theta}{r}\frac{\partial}{\partial\theta}\right)\left(\Sigma_{rr}\sin^2\theta+\Sigma_{r\theta}\sin2\theta+\Sigma_{\theta\theta}\cos^2\theta\right)+ \tag{4.60}$$
$$\frac{\partial}{\partial z}\left(\Sigma_{rz}\sin\theta+\Sigma_{\theta z}\cos\theta\right)+\rho\left(\mathbf{b}_f\cdot\mathbf{g}_r\sin\theta+\mathbf{b}_f\cdot\mathbf{g}_\theta\cos\theta\right)$$
$$=\frac{\rho}{g_c}\left(\mathbf{a}\cdot\mathbf{g}_r\sin\theta+\mathbf{a}\cdot\mathbf{g}_\theta\cos\theta\right).$$

Carrying out the indicated operations, and by the same reasoning, Eq. (4.60) also leads to Eqs. (4.58) and (4.59).

Finally, for $k=3$, Eq. (4.16) becomes

$$\frac{\partial\Sigma_{31}}{\partial x_1}+\frac{\partial\Sigma_{32}}{\partial x_2}+\frac{\partial\Sigma_{33}}{\partial x_3}+\rho\mathbf{b}_f\cdot\mathbf{g}_3=\left(\cos\theta\frac{\partial}{\partial r}-\frac{\sin\theta}{r}\frac{\partial}{\partial\theta}\right)\left(\Sigma_{rz}\cos\theta-\Sigma_{\theta z}\sin\theta\right)+$$
$$\left(\sin\theta\frac{\partial}{\partial r}+\frac{\cos\theta}{r}\frac{\partial}{\partial\theta}\right)\left(\Sigma_{rz}\sin\theta+\Sigma_{\theta z}\cos\theta\right)+\frac{\partial\Sigma_{zz}}{\partial z}+\rho\mathbf{b}_f\cdot\mathbf{g}_z=\frac{\rho}{g_c}\mathbf{a}\cdot\mathbf{g}_z. \tag{4.61}$$

Carrying out the indicated differentiations yields

$$\frac{\partial\Sigma_{rz}}{\partial r}+\frac{1}{r}\frac{\partial\Sigma_{\theta z}}{\partial\theta}+\frac{\partial\Sigma_{zz}}{\partial z}+\frac{\Sigma_{rz}}{r}+\rho\mathbf{b}_f\cdot\mathbf{g}_z-\frac{\rho}{g_c}\mathbf{a}\cdot\mathbf{g}_z=0. \tag{4.62}$$

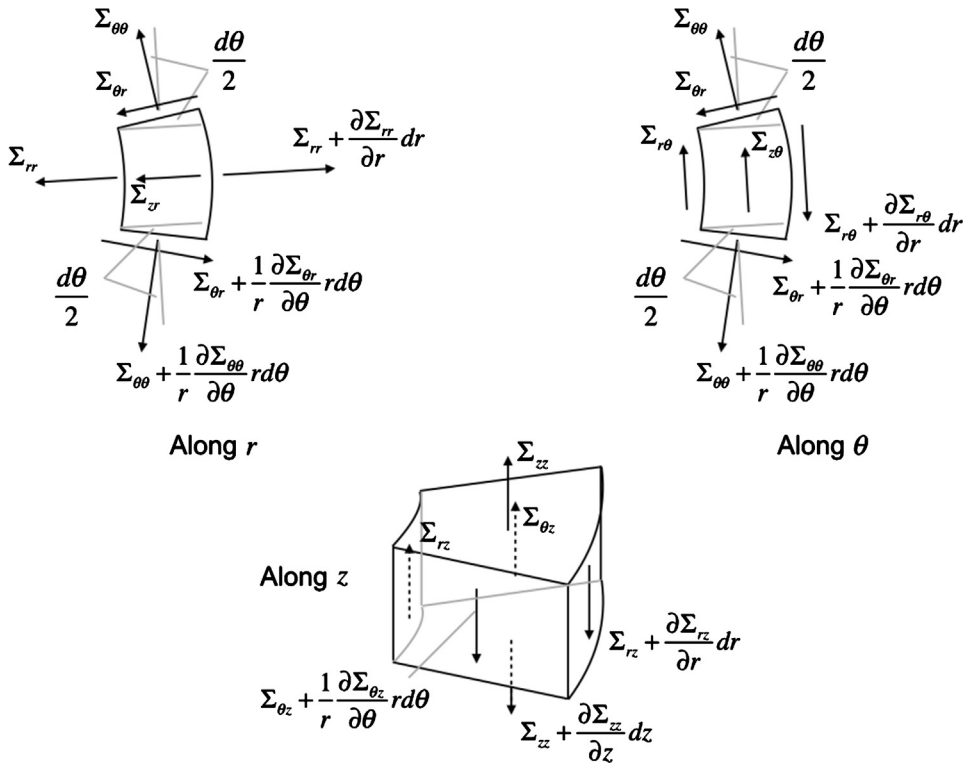

Figure 4.11 ***Forces acting on an infinitesimal element in motion or at rest in cylindrical coordinates.*** The stresses $\Sigma_{zr} + \frac{\partial \Sigma_{zr}}{\partial z} dz$ (along r) and $\Sigma_{z\theta} + \frac{\partial \Sigma_{z\theta}}{\partial z} dz$ (along θ) and the body force $\mathbf{b}_f$ are not shown.

4.2.6.2 Physical interpretation of stress components

Eqs. (4.58), (4.59) and (4.62) are the equations of motion in cylindrical coordinates. Their similarity to Eq. (4.16) (see also the left-hand sides of Eqs. (4.56), (4.60) and (4.61)) is obvious except for the terms $\frac{\Sigma_{rr} - \Sigma_{\theta\theta}}{r}$ (Eq. (4.58)), $\frac{2\Sigma_{r\theta}}{r}$ (Eq. (4.59)) and $\frac{\Sigma_{rz}}{r}$ (Eq. (4.62)). The origin of these terms can be discerned viewing Fig. 4.11.

Consider first motion in the radial direction. Summing forces on the differential element gives

$$
\begin{aligned}
&-\Sigma_{rr} r d\theta\, dz + \left(\Sigma_{rr} + \frac{\partial \Sigma_{rr}}{\partial r} dr\right) \underbrace{(r + dr)}_{\text{origin of extra term}} d\theta\, dz + \\
&\left[-\Sigma_{\theta r} dr dz + \left(\Sigma_{\theta r} + \frac{1}{r}\frac{\partial \Sigma_{\theta r}}{\partial \theta} r d\theta\right) dr dz\right] \cos\frac{d\theta}{2} + \\
&\left[-\Sigma_{zr} + \left(\Sigma_{zr} + \frac{\partial \Sigma_{zr}}{\partial z} dz\right)\right] \frac{r + (r + dr)}{2} d\theta\, dr -
\end{aligned}
\tag{4.63}
$$

$$\underbrace{\left(\Sigma_{\theta\theta}+\Sigma_{\theta\theta}+\frac{1}{r}\frac{\partial\Sigma_{\theta\theta}}{\partial\theta}rd\theta\right)drdz\sin\frac{d\theta}{2}}_{\text{origin of extra term}}+\rho\mathbf{b}_f\cdot\mathbf{g}_r\frac{r+(r+dr)}{2}drd\theta\,dz$$
$$=\frac{\rho}{g_c}\mathbf{a}\cdot\mathbf{g}_r\frac{r+(r+dr)}{2}drd\theta\,dz.$$

If we substitute the small angle approximations $\cos x\approx 1$ and $\sin x\approx x$, and ignore higher order terms, Eq. (4.63) becomes

$$\left(\frac{\partial\Sigma_{rr}}{\partial r}+\frac{1}{r}\frac{\partial\Sigma_{\theta r}}{\partial\theta}+\frac{\partial\Sigma_{zr}}{\partial z}+\frac{\Sigma_{rr}-\Sigma_{\theta\theta}}{r}+\rho\mathbf{b}_f\cdot\mathbf{g}_r-\frac{\rho}{g_c}\mathbf{a}\cdot\mathbf{g}_r\right)rdrd\theta\,dz=0, \tag{4.64}$$

from which Eq. (4.58) follows.

The term $\frac{\Sigma_{rr}-\Sigma_{\theta\theta}}{r}$ in Eq. (4.58) has two sources. The Σ_{rr} contribution is due to the area change with r on either side of the differential element. The $\Sigma_{\theta\theta}$ contribution is associated with a component of $\Sigma_{\theta\theta}$ acting in the radial direction. Both terms are due to the curvilinear nature of cylindrical coordinates. As the radius r increases both of these contributions to the equation of motion decrease.

In the circumferential direction, and again with reference to Fig. 4.11, summing forces perpendicular to both the r and z directions results in the following equation of motion:

$$\begin{aligned}
&-\Sigma_{r\theta}rd\theta\,dz+\left(\Sigma_{r\theta}+\frac{\partial\Sigma_{r\theta}}{\partial r}dr\right)\underbrace{(r+dr)}_{\text{origin of extra term}}d\theta\,dz+\\
&\left[-\Sigma_{\theta\theta}drdz+\left(\Sigma_{\theta\theta}+\frac{1}{r}\frac{\partial\Sigma_{\theta\theta}}{\partial\theta}rd\theta\right)drdz\right]\cos\frac{d\theta}{2}+\\
&\left[-\Sigma_{z\theta}+\left(\Sigma_{z\theta}+\frac{\partial\Sigma_{z\theta}}{\partial z}dz\right)\right]\frac{r+(r+dr)}{2}d\theta\,dr-\\
&\underbrace{\left(\Sigma_{\theta r}+\Sigma_{\theta r}+\frac{1}{r}\frac{\partial\Sigma_{\theta r}}{\partial\theta}rd\theta\right)drdz\sin\frac{d\theta}{2}}_{\text{origin of extra term}}+\rho\mathbf{b}_f\cdot\mathbf{g}_r\frac{r+(r+dr)}{2}drd\theta\,dz\\
&=\frac{\rho}{g_c}\mathbf{a}\cdot\mathbf{g}_r\frac{r+(r+dr)}{2}drd\theta\,dz.
\end{aligned} \tag{4.65}$$

We can simplify Eq. (4.65) as before, leading to the condition

$$\left(\frac{\partial\Sigma_{r\theta}}{\partial r}+\frac{1}{r}\frac{\partial\Sigma_{\theta\theta}}{\partial\theta}+\frac{\partial\Sigma_{z\theta}}{\partial z}+\frac{2\Sigma_{\theta r}}{r}+\rho\mathbf{b}_f\cdot\mathbf{g}_\theta-\frac{\rho}{g_c}\mathbf{a}\cdot\mathbf{g}_\theta\right)rdrd\theta\,dz=0, \tag{4.66}$$

from which Eq. (4.59) follows.

The term $\frac{2\Sigma_{r\theta}}{r} = \frac{2\Sigma_{r\theta}}{r}$ in Eq. (4.59) has two sources. Half the expression is due to the area change with r on either side of the differential element. The other half is associated with a component of $\Sigma_{\theta r}$ acting in the circumferential direction.

Finally, summing forces in the z direction[13] gives

$$\begin{aligned}
&-\Sigma_{rz} r d\theta\, dz + \left(\Sigma_{rz} + \frac{\partial \Sigma_{rz}}{\partial r} dr\right) \underbrace{(r + dr)}_{\text{origin of extra term}} d\theta\, dz - \\
&\Sigma_{\theta z} dr dz + \left(\Sigma_{\theta z} + \frac{1}{r}\frac{\partial \Sigma_{\theta z}}{\partial \theta} r d\theta\right) dr dz + \\
&\left[-\Sigma_{zz} + \left(\Sigma_{zz} + \frac{\partial \Sigma_{zz}}{\partial z} dz\right)\right] \frac{r + (r + dr)}{2} d\theta\, dr + \\
&\rho \mathbf{b}_f \cdot \mathbf{g}_z \frac{r + (r + dr)}{2} dr d\theta\, dz = \frac{\rho}{g_c} \mathbf{a} \cdot \mathbf{g}_z \frac{r + (r + dr)}{2} dr d\theta\, dz.
\end{aligned} \tag{4.67}$$

Simplifying Eq. (4.67) as before produces

$$\left(\frac{\partial \Sigma_{rz}}{\partial r} + \frac{1}{r}\frac{\partial \Sigma_{\theta z}}{\partial \theta} + \frac{\partial \Sigma_{zz}}{\partial z} + \frac{\Sigma_{zr}}{r} + \rho \mathbf{b}_f \cdot \mathbf{g}_z - \frac{\rho}{g_c} \mathbf{a} \cdot \mathbf{g}_z\right) r dr d\theta\, dz = 0, \tag{4.68}$$

from which Eq. (4.62) follows.

Example problem—computing shock load

A casing string is being run in the hole at depth L when the slips are inadvertently set on the rig floor halting constant velocity v downward movement. Ignoring the effect of the surrounding fluid and attenuation associated with threaded connections and hole contact, estimate the shock load seen at the top of the string due to this abrupt cessation of movement.

We ignore fluid effects in order to arrive at a simple solution, recognizing that the interaction between the casing and its fluid environment will probably require a numerical analysis [17–20]. From the equation of motion, Eq. (4.62), and assuming a plane, one-dimensional wave such that $\frac{\partial \Sigma_{rz}}{\partial r} = \frac{\partial \Sigma_{\theta z}}{\partial \theta} = \Sigma_{rz} = 0$, we get

$$\frac{\partial \Sigma_{zz}}{\partial z} + \rho \mathbf{b}_f \cdot \mathbf{g}_z - \frac{\rho}{g_c} \mathbf{a} \cdot \mathbf{g}_z = 0. \tag{4.69}$$

[13] Several of the stresses in the z direction are not shown in Fig. 4.11 but should be obvious from the naming convention introduced in Section 4.2.2 and employed in the figure, and from the first two solutions in this example.

Further, assuming isotropic elastic behavior (Eq. (5.27)) and infinitesimal strain (Eq. (3.148)), Eq. (4.69) becomes

$$\frac{\partial}{\partial z}\left(E\frac{\partial \hat{u}_z}{\partial z}\right)+\rho \mathbf{b}_f\cdot\mathbf{g}_z-\frac{\rho}{g_c}\frac{\partial^2 \hat{u}_z}{\partial \tau^2}=0. \tag{4.70}$$

Finally, taking Young's modulus to be constant along the tubular, Eq. (4.70) becomes

$$E\frac{\partial^2 \hat{u}_z}{\partial z^2}+\rho \mathbf{b}_f\cdot\mathbf{g}_z=\frac{\rho}{g_c}\frac{\partial^2 \hat{u}_z}{\partial \tau^2},\quad 0<z<L,\quad 0<\tau<\infty, \tag{4.71}$$

where $\mathbf{b}_f$ is the (constant) force (per unit mass) of gravity.

The homogeneous form of Eq. (4.71) ($\rho \mathbf{b}_f\cdot\mathbf{g}_z=0$) is the wave equation. We shall solve the homogeneous equation, concentrating on the shock loading of the tube.[14] Our focus therefore is

$$E\frac{\partial^2 \hat{u}_z}{\partial z^2}=\frac{\rho}{g_c}\frac{\partial^2 \hat{u}_z}{\partial \tau^2},\quad 0<z<L,\quad 0<\tau<\infty. \tag{4.72}$$

Eq. (4.72) has the boundary conditions

$$\hat{u}_z(0,\tau)=0,\quad \tau>0, \tag{4.73}$$

$$\frac{\partial \hat{u}_z}{\partial z}(L,\tau)=0,\quad \tau>0. \tag{4.74}$$

Eq. (4.73) states that the string is fixed at the top (by the prematurely set slips). Eq. (4.74) states that the stress ($\hat{\Sigma}_{zz}=E\hat{\hat{E}}_{zz}=E\frac{\partial \hat{u}_z}{\partial z}$ if displacement gradients are assumed infinitesimal—see Section 3.7.2.1 of Chapter 3) at the bottom of the string is zero (the effects of surrounding fluids are being ignored).

Also associated with Eq. (4.72) are initial conditions. We may start the current problem by zeroing the displacement along the string at the instant the slips engage

$$\hat{u}_z(z,0)=\hat{f}_i(z)=0,\quad 0\le z\le L, \tag{4.75}$$

[14] By ignoring the gravity term, we are assuming that during the lowering of the string under constant velocity it has time to stretch under the force of gravity prior to inadvertently setting the slips. To determine the total axial load on the casing, one can superimpose the weight component on the solution from the shock analysis.

Other inhomogeneous solutions to the wave equation are available in the literature and include such additions as fluid/frictional axial drag. A particularly important application of the wave equation in tubular design is the analysis of polished rod and pump dynagraph cards for sucker-rod pumping wells [21,22].

and by assigning all locations along the string the running velocity v, except for the very top of the string whose velocity has been arrested by the slips

$$\frac{\partial \hat{u}_z}{\partial \tau}(z,0) = \hat{g}_i(z) = v\hat{H}(z) = v \times \begin{cases} 0 & \text{for } z = 0, \\ 1 & \text{for } 0 < z \le L, \end{cases} \qquad 0 \le z \le L, \tag{4.76}$$

where $\hat{H}(z)$ is one form of the Heaviside step function[15] that is zero if its argument is nonpositive and unity otherwise.

The solution to Eq. (4.72) can be determined by seeking solutions of the form [23]

$$\hat{u}_z(z,\tau) = \hat{\mathcal{Z}}(z)\hat{\mathcal{T}}(\tau). \tag{4.77}$$

If we substitute Eq. (4.77) into Eq. (4.72), then

$$c_0^2 \frac{\partial^2 \hat{\mathcal{Z}}(z)}{\partial z^2}\hat{\mathcal{T}}(\tau) = \frac{\partial^2 \hat{\mathcal{T}}(\tau)}{\partial \tau^2}\hat{\mathcal{Z}}(z), \quad c_0 = \sqrt{\frac{Eg_c}{\rho}}. \tag{4.78}$$

Eq. (4.78) can be rewritten as

$$\frac{\partial^2 \hat{\mathcal{Z}}(z)}{\partial z^2}\frac{1}{\hat{\mathcal{Z}}(z)} = \frac{\partial^2 \hat{\mathcal{T}}(\tau)}{\partial \tau^2}\frac{1}{c_0^2\hat{\mathcal{T}}(\tau)}. \tag{4.79}$$

The right-hand side of Eq. (4.79) is strictly a function of z; the left-hand side is strictly a function of τ. This is possible only if both sides of the equation are equal to a constant λ and then

$$\frac{\partial^2 \hat{\mathcal{Z}}(z)}{\partial z^2} - \lambda\hat{\mathcal{Z}}(z) = 0, \quad \frac{\partial^2 \hat{\mathcal{T}}(\tau)}{\partial \tau^2} - c_0^2\lambda\hat{\mathcal{T}}(\tau) = 0. \tag{4.80}$$

It can be shown [24] that positive values of λ lead to solutions that are unbounded as $\tau \to \infty$, and a zero value of λ leads to a zero solution for $\hat{u}$ given the current problem's boundary conditions.[16] Therefore only negative values of λ are reasonable. If $\lambda < 0$, the solutions of Eq. (4.80) take the form[17]

$$\hat{\mathcal{Z}}(z) = C\sin(\beta z) + D\cos(\beta z), \quad \hat{\mathcal{T}}(\tau) = A\sin(c_0\beta z) + B\cos(c_0\beta z), \quad \lambda = -\beta^2, \tag{4.81}$$

[15] Differing forms of this function exist depending on the value assigned the function at the zero discontinuity.

[16] Further, solutions for $\lambda \ge 0$ cannot describe a periodic motion [23].

[17] See [25] or any text on ordinary differential equations for solutions to homogeneous equations with constant coefficients.

or, using Eq. (4.77)

$$\hat{u}_z(z,\tau) = \left[C\sin(\beta z) + D\cos(\beta z)\right]\left[A\sin(c_0\beta\tau) + B\cos(c_0\beta\tau)\right], \quad \lambda = -\beta^2. \tag{4.82}$$

Consider first the boundary conditions. From Eq. (4.73) we have

$$\hat{u}_z(0,\tau) = [D]\left[A\sin(c_0\beta\tau) + B\cos(c_0\beta\tau)\right] = 0, \tag{4.83}$$

which, except for the trivial, motionless solution $A = B = 0$, is true for all τ only if $D = 0$. From Eq. (4.74) we obtain

$$\frac{\partial \hat{u}_z(z,\tau)}{\partial z} = C\beta\cos(\beta z)\left[A\sin(c_0\beta\tau) + B\cos(c_0\beta\tau)\right] = 0, \quad z = L, \tag{4.84}$$

which, except for the trivial solutions (either $C = 0$ or $A = B = 0$) implies

$$\cos(\beta L) = 0, \quad \beta = \frac{(2n-1)\pi}{2L}, \quad n = 1, 2, 3, \ldots. \tag{4.85}$$

We conclude from the application of the boundary conditions that $\hat{u}$ is actually a series of solutions[18] depending on the value of n, that is,

$$\begin{aligned}\hat{u}_{zn}(z,\tau) &= \hat{Z}_n(z)\hat{T}_n(\tau)\\ &= \sin(\beta_n z)\left[A_n\sin(\beta_n c_0\tau) + B_n\cos(\beta_n c_0\tau)\right], \quad n = 1, 2, 3, \ldots.\end{aligned} \tag{4.86}$$

Our current solution for $\hat{u}$ is therefore

$$\hat{u}_z(z,\tau) = \sum_{n=1}^{\infty}\sin(\beta_n z)\left[A_n\sin(\beta_n c_0\tau) + B_n\cos(\beta_n c_0\tau)\right]. \tag{4.87}$$

Now we apply the initial conditions. Substituting Eq. (4.87) into Eqs. (4.75) and (4.76) yields

$$\hat{u}_z(z,0) = \sum_{n=1}^{\infty} B_n\sin(\beta_n z) = \hat{f}_i(z) = 0, \tag{4.88}$$

$$\frac{\partial \hat{u}_z}{\partial\tau}(z,0) = \sum_{n=1}^{\infty} A_n\beta_n c_0\sin(\beta_n z) = \hat{g}_i(z) = v\hat{H}(z) = v\times\begin{cases}0 & \text{for } z = 0,\\ 1 & \text{for } 0 < z \le L.\end{cases} \tag{4.89}$$

[18] A_n and B_n are now new constants that, for each n, include $C\beta_n$.

Eqs. (4.88) and (4.89) can be solved for the A_n and B_n by appealing to the condition[19]

$$\int_0^L \sin(\beta_m z)\sin(\beta_n z)\,dz = \begin{cases} 0 & \text{for } m \neq n, \\ L/2 & \text{for } m = n. \end{cases} \tag{4.90}$$

Multiplying each of Eqs. (4.88) and (4.89) through by $\sin(\beta_m z)$ and integrating from 0 to L, from Eq. (4.90) we obtain

$$B_n = \frac{2}{L}\int_0^L \hat{f}_i(z)\sin(\beta_n z)\,dz = 0, \tag{4.91}$$

$$\begin{aligned} A_n &= \frac{2}{\beta_n c_0 L}\int_0^L \hat{g}_i(z)\sin(\beta_n z)\,dz \\ &= \frac{2\nu}{\beta_n c_0 L}\int_0^L \hat{H}(z)\sin(\beta_n z)\,dz \\ &= -\frac{2\nu}{\beta_n^2 c_0 L}\left[\hat{H}(z)\left(\cos(\beta_n z)-1\right)\right]_0^L = \frac{2\nu}{\beta_n^2 c_0 L}, \end{aligned} \tag{4.92}$$

where in the last step we use the integral formula $\int \hat{H}(z)\sin(kz)\,dz = -\frac{\hat{H}(z)[\cos(kz)-1]}{k} +$ constant.

The final expressions for $\hat{u}_z(z,\tau)$ and $\hat{\Sigma}_{zz}(z,\tau)$ are, using Eqs. (4.91) and (4.92) in Eq. (4.87),

$$\hat{u}_z(z,\tau) = \frac{2\nu}{c_0 L}\sum_{n=1}^{\infty}\frac{1}{\beta_n^2}\sin(\beta_n z)\sin(\beta_n c_0 \tau), \quad n = 1, 2, 3\ldots, \tag{4.93}$$

[19] For the cosine function, if we begin with the trigonometric identity $\sin\alpha\sin\beta = \frac{1}{2}\cos(\alpha-\beta) - \frac{1}{2}\cos(\alpha+\beta)$, then

$$\begin{aligned} \hat{I}(m,n) &= \int_0^L \sin\left(\frac{(2m-1)\pi z}{2L}\right)\sin\left(\frac{(2n-1)\pi z}{2L}\right)dz \\ &= \frac{1}{2}\int_0^L \left\{\cos\left[(m-n)\frac{\pi z}{L}\right] - \cos\left[(m+n-1)\frac{\pi z}{L}\right]\right\}dz \\ &= \frac{1}{2}\left\{\frac{L}{(m-n)\pi}\sin\left[(m-n)\frac{\pi z}{L}\right]_0^L - \frac{L}{(m+n-1)\pi}\sin\left[(m+n-1)\frac{\pi z}{L}\right]_0^L\right\} \\ &= \frac{1}{2}\left\{\frac{L}{(m-n)\pi}\sin[(m-n)\pi] - \frac{L}{(m+n-1)\pi}\sin[(m+n-1)\pi]\right\}. \end{aligned}$$

If $m \neq n$, $\hat{I}(m,n) = 0$. If $m = n$, and to avoid dealing with the zero denominator in the first term of the last equation, we return to the second equation in the above series. There, with $m = n$

$$\hat{I}(m,n) = \frac{1}{2}\int_0^L 1 - \cos\left(\frac{(2n-1)\pi z}{L}\right)dz = \frac{1}{2}\left[z - \frac{L}{(2n-1)\pi}\sin\left(\frac{(2n-1)\pi z}{L}\right)\right]_0^L = \frac{L}{2}.$$

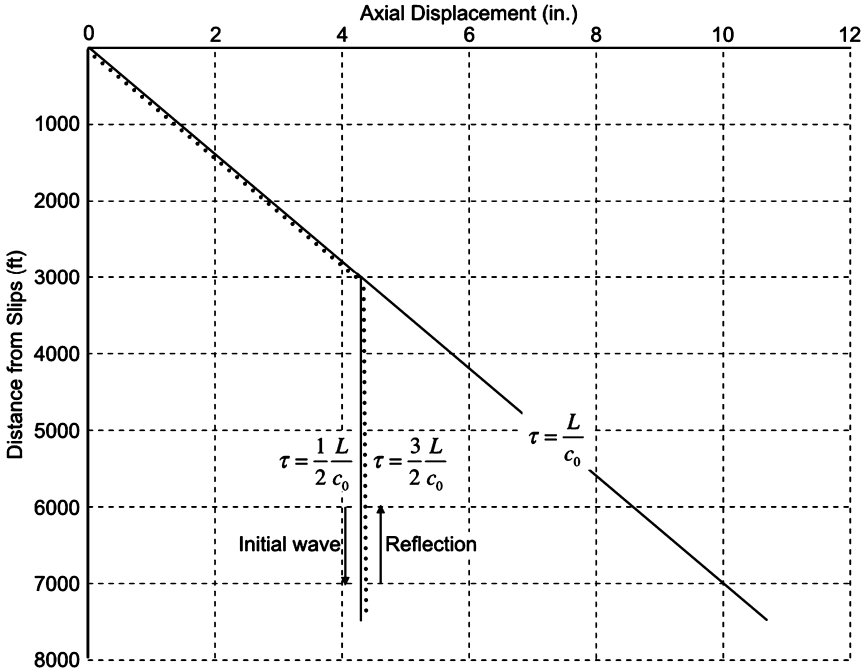

Figure 4.12 ***Displacement with time along tubular undergoing shock load in example problem.*** Initial wave is a solid line; reflected wave is a dotted line.

$$\hat{\Sigma}_{zz} = E\frac{\partial \hat{u}_z(z,\tau)}{\partial z} = \frac{2E\nu}{c_0 L}\sum_{n=1}^{\infty}\frac{1}{\beta_n}\cos(\beta_n z)\sin(\beta_n c_0 \tau), \quad n = 1, 2, 3\ldots. \tag{4.94}$$

In addition, by differentiating $\hat{u}_z(z,\tau)$ with respect to τ, we can recover an expression for the velocity of the tube, namely

$$\frac{\partial \hat{u}_z(z,\tau)}{\partial \tau} = \frac{2\nu}{L}\sum_{n=1}^{\infty}\frac{1}{\beta_n}\sin(\beta_n z)\cos(\beta_n c_0 \tau), \quad n = 1, 2, 3\ldots. \tag{4.95}$$

Figs. 4.12–4.14 demonstrate the behavior of the displacement and stress wave with time if 7500 ft of a steel tubular ($E = 30\,000\,000$ psi, $\rho_s = 0.2836\ \frac{\text{lb}_\text{m}}{\text{in}^3}$, $g_c = 386.088\ \frac{\text{lb}_\text{m}\,\text{in}}{\text{lb}_\text{f}\,\text{s}^2}$, $c_0 = 16\,841\ \frac{\text{ft}}{\text{s}}$) is being lowered at $2\ \frac{\text{ft}}{\text{s}}$ when its uppermost part is arrested by an inadvertent action of the slips.

At $\tau = 0$ when downward movement is arrested at the top of the string, a ramped displacement wave (see Fig. 4.12) forms below the point of fixity. Depending on the running speed and the speed of transmission of the wave, locations in the string that do not yet "know" about the engagement at the top of the string continue to displace—see, for example, the partially ramped solid curve labeled "$\tau = \frac{1}{2}\frac{L}{c_0}$" in Fig. 4.12. Once the

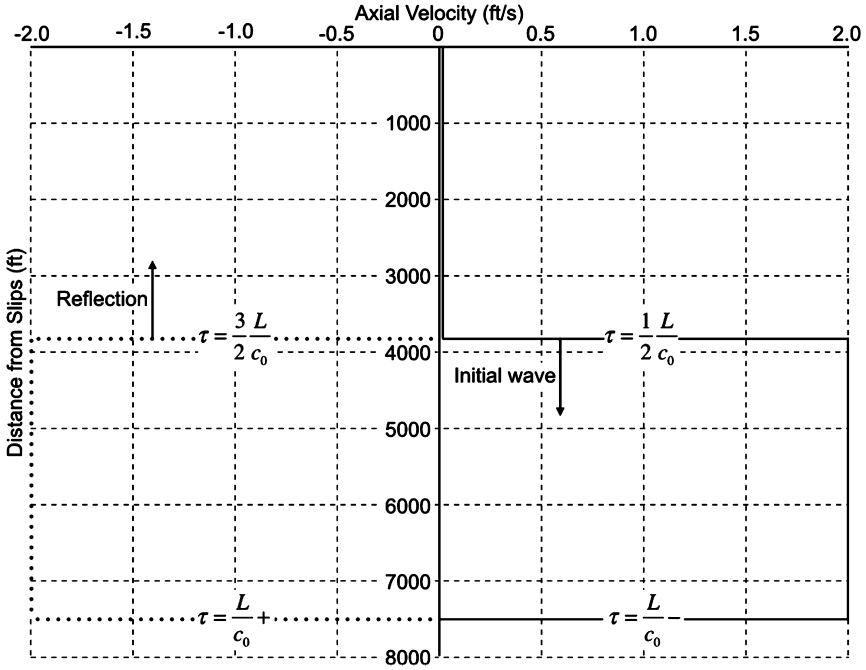

Figure 4.13 ***Velocity with time along tubular undergoing shock load in example problem.*** Initial wave is a solid line; reflected wave is a dotted line. The initial wave is offset slightly from the abscissa for visibility.

wave reaches a given location along the tubular, that location's displacement halts. At $\tau = \frac{L}{c_0}$ (the completely ramped solid curve in the figure) the displacement wave reaches the lowermost end of the tubular, which has now stretched to its maximum extent. Discussion of the reflection of this wave from the end will follow the initial discussions of the velocity and stress waves.

The ramped displacement is related to the step velocity wave (see Fig. 4.13). Moving at the speed c_0, much faster than the running velocity v, portions of the tubular behind the velocity wave abruptly realize zero velocity arresting further displacement. Fig. 4.13 shows two time snapshots by solid curves—the time at which the step velocity curve has traveled one-half of the length of the tubular (labeled "$\tau = \frac{1}{2}\frac{L}{c_0}$") and a time just before the step velocity curve has traversed the entire length of the tubular (labeled "$\tau = \frac{L}{c_0}-$"). At the instant the velocity wave has reached the end of the tubular, the entire tubular length is at zero velocity.

A step tensile stress wave (see Fig. 4.14) traveling at $16\,841\ \frac{\text{ft}}{\text{s}}$ in the tubular begins at $\tau = 0$ with the cessation of movement at the top. As modeled, the wave appears as an expanding square wave. As the stress wave traverses the length of the tubular (cf. the curve labeled "$\tau = \frac{1}{2}\frac{L}{c_0}$"), the stress associated with tension due to the stretching of the

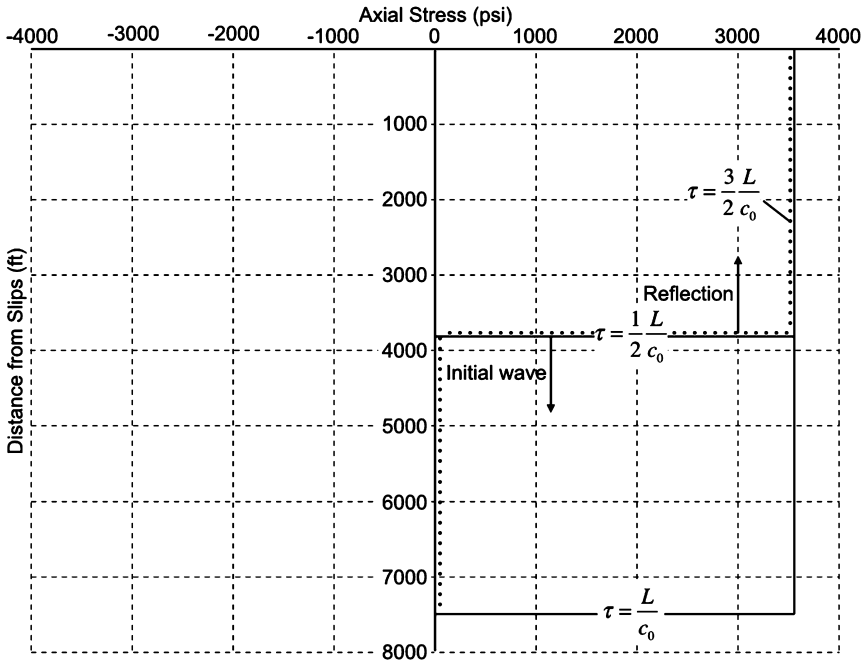

Figure 4.14 ***Stress with time along tubular undergoing shock load in example problem.*** Initial wave is a solid line; reflected wave is a dotted line. The reflected wave is offset slightly from the initial wave and from the abscissa for visibility.

tubular is experienced along the current and all previous axial locations. Just before the stress wave reaches the lower end of the tubular (see the curve labeled "$\tau = \frac{L}{c_0}-$") the entirety of the tubular is subjected to an incremental tensile stress due to the closure of the slips. The magnitude of that stress is, using the strain $\breve{E}_{zz} = \frac{\hat{u}(L, L/c_0)}{L} = \frac{\nu L}{c_0 L} = \frac{\nu}{c_0}$, $\Sigma_{zz} = \frac{E\nu}{c_0} = \frac{30\,000\,000\,\text{psi} \times 2\,\frac{\text{ft}}{\text{s}}}{16\,841\,\frac{\text{ft}}{\text{s}}} = 3563\,\text{psi}$.

The functions $\hat{u}_z(z, \tau)$, $\frac{\partial \hat{u}_z(z,\tau)}{\partial \tau}$ and $\hat{\Sigma}_{zz}$ still supply results for z outside the interval $[0, L]$ although our problem is undefined outside those bounds. One way to view the tubular behavior following the time $\tau = \frac{L}{c_0}$ marking arrival of the displacement, velocity and stress waves at $z = L$ is to consider a new problem in which the boundary conditions, Eqs. (4.73) and (4.74), remain unchanged, but the initial conditions are redefined. In this new problem, the initial conditions at $\tau' = \tau - \frac{L}{c_0} = 0$ are taken from the state of the initial wave problem (Eqs. (4.93) and (4.95)) at $\tau = \frac{L}{c_0}$

$$\hat{u}'_z(z, \tau' = 0) = \hat{f}'_i(z) = \frac{L\nu}{c_0}\frac{z}{L} = \frac{\nu z}{c_0}, \quad 0 \le z \le L, \tag{4.96}$$

and by assigning all locations along the string the running velocity v, except for the very top of the string whose velocity has been arrested by the slips

$$\frac{\partial \hat{u}'_z}{\partial \tau'}(z, \tau' = 0) = \hat{g}'_i(z) = 0, \quad 0 \le z \le L. \tag{4.97}$$

Eq. (4.96) is a snapshot of the tube as it has stretched to its limit, the displacement at any location along the length of the tube being a linear function of that location, with the maximum displacement at $z = L$ being $\frac{vL}{c_0}$. Eq. (4.97) states that at this maximum extension the velocity everywhere along the tube is zero. The tube is about to rebound upward.

Proceeding as before, we substitute the initial conditions in Eqs. (4.96) and (4.97) into Eq. (4.87) (now with τ' rather than τ as the time) to obtain

$$\hat{u}'_z(z, \tau' = 0) = \sum_{n=1}^{\infty} B_n \sin(\beta_n z) = \hat{f}'_i(z) = \frac{Lv}{c_0}\frac{z}{L} = \frac{vz}{c_0}, \tag{4.98}$$

$$\frac{\partial \hat{u}'_z}{\partial \tau'}(z, \tau' = 0) = \sum_{n=1}^{\infty} A_n \beta_n c_0 \sin(\beta_n z) = \hat{g}'_i(z) = 0, \tag{4.99}$$

and integrate as in Eqs. (4.91) and (4.92) to get

$$\begin{aligned} B_n &= \frac{2}{L}\int_0^L \hat{f}'_i(z)\sin(\beta_n z)\,dz \\ &= \frac{2v}{c_0 L}\int_0^L z\sin(\beta_n z)\,dz \\ &= \frac{2v}{c_0 L}\left[\frac{\sin\beta_n z - \beta_n z\cos\beta_n z}{\beta_n^2}\right]_0^L = \frac{2v}{\beta_n^2 c_0 L}(-1)^{n+1}, \end{aligned} \tag{4.100}$$

$$A_n = \frac{2}{L}\int_0^L \hat{g}'_i(z)\sin(\beta_n z)\,dz = 0. \tag{4.101}$$

The displacement $\hat{u}'_z(z, \tau')$ on reflection is therefore

$$\hat{u}_z(z, \tau') = \frac{2v}{c_0 L}\sum_{n=1}^{\infty}\frac{(-1)^{n+1}}{\beta_n^2}\sin(\beta_n z)\cos\left(\beta_n c_0 \tau'\right), \quad n = 1, 2, 3\ldots. \tag{4.102}$$

Noting, however, that $\cos\left(\beta_n c_0 \tau'\right) = \cos\left(\beta_n c_0\left(\tau - \frac{L}{c_0}\right)\right) = (-1)^{n+1}\sin(\beta_n c_0 \tau)$, we may rewrite Eq. (4.102) in terms of τ with a result that is identical to Eq. (4.93). It is sufficient therefore to take the extended time ($\tau > \frac{L}{c_0}$) solutions of Eqs. (4.93)–(4.95) to describe the reflected waves from the bottom of the string back to the surface.

Reflected waves are also presented in Figs. 4.12–4.14. The ramped displacement (Fig. 4.12), at its maximum value at $\tau = \frac{L}{c_0}$, begins to recover its initial, zero displace-

ment. The reflected wave shown half way back to the surface at time $\tau = \frac{3}{2}\frac{L}{c_0}$ will, at $\tau = 2\frac{L}{c_0}$, coincide with the abscissa.

Recovery of the displacement is further illustrated in the display of the step velocity wave (Fig. 4.13). The reflection of the velocity is the negative of the incident wave. At time $\tau = \frac{3}{2}\frac{L}{c_0}$ the location half way down the tubular and all positions below it are traveling at the same velocity. Shallower locations are yet to experience the recovery of displacement and (Fig. 4.12) temporarily retain their stretch from the incident wave.

For $\tau < \frac{L}{c_0}$ the step tension wave successively loads the entire tubular. At $\tau = \frac{L}{c_0}$ the end of the tubular which, due to the boundary condition, can support no stress, sees the stress wave reflect, successively unloading the tubular[20] as the wave returns to the surface.

Shock load for a dropped tubular Another impact problem related to the slip-arrest study presented above is the stress on the lower end of a tubular that has parted as that tubular falls and eventually contacts the bottom of the hole. This problem is identical to that discussed above, except in the case of the falling tubular the velocity of the tube is negative (and, if one investigates the effect of gravity, the sign of the gravity term is reversed). That is, this latter problem is the slip-arrest problem turned upside down and assigned a negative velocity. For the falling tubular the initial/incident stress wave is compressive, and the rebound of the tube creates a reflective tensile wave that, ignoring gravity, unloads the string at time $\tau = 2\frac{L}{c_0}$.

4.2.6.3 Traction from stress

Consider a cylindrical coordinate system whose z-axis aligns with the x_3-axis of the spatial (rectangular) coordinate system.[21] We wish to determine the form Eq. (4.11) takes when transformed from the spatial rectangular coordinate system to the cylindrical coordinate system.

Section A.5.1 in Appendix A, and particularly the example problem shown in Section A.5.1.1, illustrates the transformation of the components of a vector from rectangular coordinates to cylindrical coordinates. Applying Eq. (A.55) to Eq. (4.11) gives

$$\mathbf{L}\cdot\mathbf{t}_{(\mathbf{n})} = \mathbf{L}\cdot\boldsymbol{\Sigma}^T\cdot\mathbf{n}, \quad L_{ik}\left(\mathbf{t}_{(\mathbf{n})}\right)_k = L_{ik}\Sigma_{jk}n_j, \tag{4.103}$$

[20] In discussing a one-dimensional impact wave reaching a free boundary, the point is usually made that the wave, if tensile for example, will reflect as a compression of equal amplitude. In those discussions, however, the incident wave is usually modeled as a pulse of small to infinitesimal length. In the current problem, the tension has persisted behind the wave front on its downward travel, so the effect of the reflected "compressive" wave is to eliminate the residual tension, returning the tubular to its unstressed state.

[21] See Section 4.2.6.2 of this chapter for a discussion of the physical components of stress in cylindrical coordinates.

where (see Section A.5.1.1 in Appendix A)

$$\mathbf{L} = \begin{bmatrix} \cos\Theta & \sin\Theta & 0 \\ -\sin\Theta & \cos\Theta & 0 \\ 0 & 0 & 1 \end{bmatrix}. \tag{4.104}$$

But from Eq. (A.55), $\mathbf{L}\mathbf{t}_{(\mathbf{n})} = \mathbf{t}'_{(\mathbf{n})}$. Further (see Section A.5.1.2), $\mathbf{L}^T\mathbf{L} = \mathbf{I}$. Using these relations in Eq. (4.103) yields

$$\mathbf{t}'_{(\mathbf{n})} = \mathbf{L}\cdot\boldsymbol{\Sigma}^T\cdot\mathbf{L}^T\cdot\mathbf{L}\cdot\mathbf{n}, \quad \left(\mathbf{t}'_{(\mathbf{n})}\right)_i = L_{ik}\Sigma_{jk}L^T_{jr}L_{rm}n_m, \tag{4.105}$$

or, with Eq. (A.78)

$$\mathbf{t}'_{(\mathbf{n})} = \boldsymbol{\Sigma}'^T\cdot\mathbf{n}', \quad \left(\mathbf{t}_{(\mathbf{n})}\right)'_i = \Sigma'_{ri}n'_r. \tag{4.106}$$

That is, the traction-from-stress relation in cylindrical coordinates takes the same form as its counter part in rectangular coordinates.

4.2.7 Special cases of stress

In several important problems in tubular design, due to the geometry of the tube and/or its loading, simplifications can be made to either the rectangular or cylindrical coordinate expressions of the stress tensor.

4.2.7.1 Traction from stress in two dimensions

Consider the special case of Eqs. (4.6)–(4.8) when $\mathbf{n}\cdot\mathbf{g}_3 = \mathbf{t}_{(\mathbf{n})}\cdot\mathbf{g}_3 = \mathbf{b}_f\cdot\mathbf{g}_3 = 0$ (see Fig. 4.15). Recognizing that, as before, the body force and acceleration terms are of higher order, and discarding Eq. (4.8) as offering no additional information on the traction vector,[22] in this special case

$$\left(-\Sigma_{11}\mathbf{n}\cdot\mathbf{g}_1 - \Sigma_{21}\mathbf{n}\cdot\mathbf{g}_2 + \mathbf{t}_{(\mathbf{n})}\cdot\mathbf{g}_1\right)da = 0, \tag{4.107}$$

$$\left(-\Sigma_{12}\mathbf{n}\cdot\mathbf{g}_1 - \Sigma_{22}\mathbf{n}\cdot\mathbf{g}_2 + \mathbf{t}_{(\mathbf{n})}\cdot\mathbf{g}_2\right)da = 0. \tag{4.108}$$

Solving each of these equations in turn yields

$$(\mathbf{t}_{(\mathbf{n})})_1 = \Sigma_{11}\cos\theta + \Sigma_{21}\sin\theta, \tag{4.109}$$

[22] Eq. (4.8) reduces to

$$-\Sigma_{13}\mathbf{n}\cdot\mathbf{e}_1 - \Sigma_{23}\mathbf{n}\cdot\mathbf{e}_2 = -\Sigma_{31}\mathbf{n}\cdot\mathbf{g}_1 - \Sigma_{32}\mathbf{n}\cdot\mathbf{g}_2 = 0,$$

that is, a relation between the out-of-plane shear stresses. One solution, $\Sigma_{13} = \Sigma_{23} = 0$, is similar to, but not identical to, plane stress (see Section 4.2.7.3), the difference being that since $\mathbf{n}\cdot\mathbf{e}_3 = 0$, Σ_{33} is indeterminate, whereas in plane stress Σ_{33} is assumed to vanish. Our primary reason for discarding Eq. (4.8) is that it provides no information regarding the traction $\mathbf{t}_{(\mathbf{n})}$.

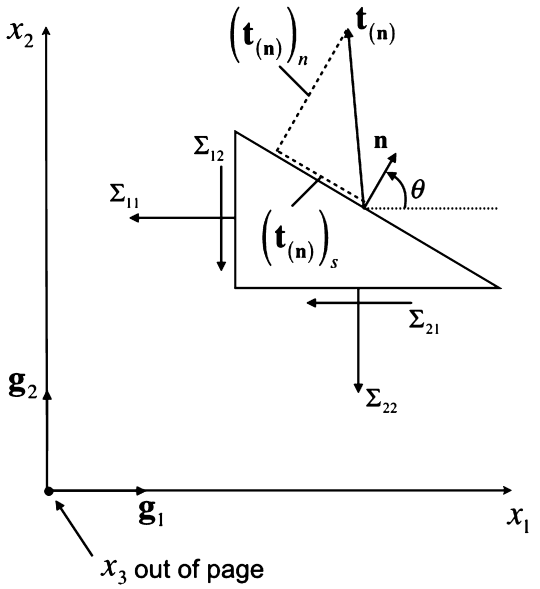

Figure 4.15 ***Determination of the local traction from the stress tensor in a two-dimensional context.*** The shaded surface partially bounding the infinitesimal body in Fig. 4.6 is now perpendicular to the page. A (two-dimensional) body force acting on the infinitesimal surface is not shown in the figure.

$$(\mathbf{t}_{(\mathbf{n})})_2 = \Sigma_{12}\cos\theta + \Sigma_{22}\sin\theta, \tag{4.110}$$

where $\mathbf{n} = (\mathbf{n}\cdot\mathbf{g}_1)\,\mathbf{g}_1 + (\mathbf{n}\cdot\mathbf{g}_2)\,\mathbf{g}_2 = \cos\theta\mathbf{g}_1 + \sin\theta\mathbf{g}_2$.

The component of $\mathbf{t}_{(\mathbf{n})}$ normal to the (two-dimensional) plane of investigation is

$$\begin{aligned}(\mathbf{t}_{(\mathbf{n})})_n &= \mathbf{t}_{(\mathbf{n})}\cdot\mathbf{n}\\ &= \Sigma_{11}\cos^2\theta + \Sigma_{21}\sin\theta\cos\theta + \Sigma_{12}\sin\theta\cos\theta + \Sigma_{22}\sin^2\theta\\ &= \Sigma_{11}\cos^2\theta + \Sigma_{12}\sin 2\theta + \Sigma_{22}\sin^2\theta,\end{aligned} \tag{4.111}$$

where the last step makes use of Eq. (4.21).

The component of $\mathbf{t}_{(\mathbf{n})}$ lying in the plane of the investigation, which we designate the shear component, is

$$\begin{aligned}(\mathbf{t}_{(\mathbf{n})})_s &= \mathbf{t}_{(\mathbf{n})} - (\mathbf{t}_{(\mathbf{n})})_n\mathbf{n}\\ &= (\Sigma_{11}\cos\theta + \Sigma_{12}\sin\theta)\,\mathbf{g}_1 + (\Sigma_{12}\cos\theta + \Sigma_{22}\sin\theta)\,\mathbf{g}_2 -\\ &\quad \left(\Sigma_{11}\cos^2\theta + 2\Sigma_{12}\sin\theta\cos\theta + \Sigma_{22}\sin^2\theta\right)\left(\cos\theta\mathbf{g}_1 + \sin\theta\mathbf{g}_2\right)\\ &= \left[\Sigma_{11}\cos\theta\sin^2\theta + \Sigma_{12}\sin\theta\left(1-2\cos^2\theta\right) - \Sigma_{22}\cos\theta\sin^2\theta\right]\mathbf{g}_1 +\\ &\quad \left[-\Sigma_{11}\cos^2\theta\sin\theta + \Sigma_{12}\cos\theta\left(1-2\sin^2\theta\right) + \Sigma_{22}\cos^2\theta\sin\theta\right]\mathbf{g}_2.\end{aligned} \tag{4.112}$$

The magnitude of the shear component of the traction is, from Eq. (A.8),

$$\begin{aligned}\left|(\mathbf{t}_{(\mathbf{n})})_s\right| &= \left[(\mathbf{t}_{(\mathbf{n})})_s \cdot (\mathbf{t}_{(\mathbf{n})})_s\right]^{\frac{1}{2}} \\ &= \left|(\Sigma_{11} - \Sigma_{22})\cos\theta\sin\theta - \Sigma_{12}\cos 2\theta\right|, \end{aligned} \tag{4.113}$$

a result requiring a moderate amount of algebraic and trigonometric manipulation. The absolute value sign results from taking the square root of the vector's dot product with itself.

4.2.7.2 Mohr's circle in two dimensions

Using the trigonometric identities $\cos 2\theta = 1 - 2\sin^2\theta$ and $\cos 2\theta = 2\cos^2\theta - 1$ in Eqs. (4.111) and (4.113), these equations can be respectively reexpressed as

$$(\mathbf{t}_{(\mathbf{n})})_n - \frac{\Sigma_{11} + \Sigma_{22}}{2} = \frac{\Sigma_{11} - \Sigma_{22}}{2}\cos 2\theta + \Sigma_{12}\sin 2\theta, \tag{4.114}$$

$$\left|(\mathbf{t}_{(\mathbf{n})})_s\right| = \left|\frac{\Sigma_{11} - \Sigma_{22}}{2}\sin 2\theta - \Sigma_{12}\cos 2\theta\right|. \tag{4.115}$$

Squaring both sides of Eqs. (4.114) and (4.115), and then adding, produces

$$\left[(\mathbf{t}_{(\mathbf{n})})_n - \frac{\Sigma_{11} + \Sigma_{22}}{2}\right]^2 + \left[(\mathbf{t}_{(\mathbf{n})})_s\right]^2 = \left(\frac{\Sigma_{11} - \Sigma_{22}}{2}\right)^2 + \Sigma_{12}^2, \tag{4.116}$$

which, in the $(\mathbf{t}_{(\mathbf{n})})_n$–$(\mathbf{t}_{(\mathbf{n})})_s$ space is a circle.

Fig. 4.16 illustrates Eqs. (4.114)–(4.116) graphically. Given a stress state Σ_{11}, Σ_{22}, Σ_{12}, we can plot that state on a graph whose axes are normal and shear traction. The points (Σ_{11}, Σ_{12}) and (Σ_{22}, Σ_{12}) lie on a circle whose center is $\frac{\Sigma_{11}+\Sigma_{22}}{2}$ and whose radius is $\sqrt{\left(\frac{\Sigma_{11}-\Sigma_{22}}{2}\right)^2 + \Sigma_{12}^2}$. The corresponding stresses ($(\mathbf{t}_{(\mathbf{n})})_n$, $(\mathbf{t}_{(\mathbf{n})})_s$) on a plane whose normal $\mathbf{n}$ makes an angle θ with the X_1-axis is found by traversing the circle an arc whose angle is 2θ.

A common convention is to plot the shear stress $(\mathbf{t}_{(\mathbf{n})})_s$ as positive if it produces a clockwise moment on the infinitesimal element of focus [26,15].

If, as is often the case, Σ_{11} and Σ_{22} are principal stresses, say Σ_1^p and Σ_2^p, the corresponding planes whose normals align with the X_1 and X_2-axes have no associated shear stress, and the graph of Mohr's circle takes the simpler form shown in Fig. 4.17, where now the circle has radius $\sqrt{\left(\frac{\Sigma_1^p - \Sigma_2^p}{2}\right)^2}$.

4.2.7.3 Plane stress

The assumption of plane stress usually involves one dimension of the body being significantly smaller than the other two. In rectangular coordinates, assume this dimension

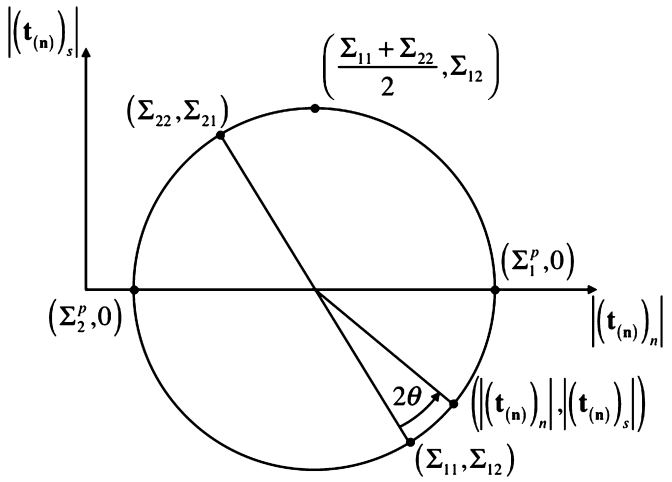

Figure 4.16 ***Mohr's circle in two dimensions.***

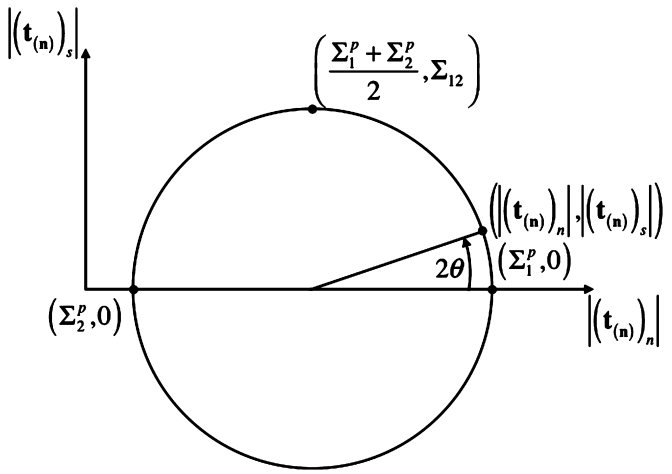

Figure 4.17 ***Mohr's circle in two dimensions for the special case when*** Σ_{11} ***and*** Σ_{22} ***are principal stresses.*** The principal stress values, as indicated in the graphs are Σ_1^p and Σ_2^p, respectively.

is aligned with the x_3-axis. Stresses associated with this axis can be ignored, that is, $\Sigma_{13} = \Sigma_{31} = 0,\ \Sigma_{23} = \Sigma_{32} = 0,\ \Sigma_{33} = 0$. The matrix representation of the stress tensor becomes

$$\boldsymbol{\Sigma} = \begin{bmatrix} \Sigma_{11} & \Sigma_{12} & 0 \\ \Sigma_{21} & \Sigma_{22} & 0 \\ 0 & 0 & 0 \end{bmatrix}. \tag{4.117}$$

4.2.7.4 Axisymmetric stress

If the geometry and loading are symmetric about an axis, for example, the longitudinal axis of the tubular, the assumption of axisymmetry requires $\partial/\partial\theta = 0$, along with $\Sigma_{r\theta} = \Sigma_{\theta r} = 0$, $\Sigma_{\theta z} = \Sigma_{z\theta} = 0$ in a cylindrical coordinate system whose z-axis aligns with the longitudinal axis of the tubular. The matrix representation of the stress tensor becomes

$$\boldsymbol{\Sigma} = \begin{bmatrix} \Sigma_{rr} & 0 & \Sigma_{rz} \\ 0 & \Sigma_{\theta\theta} & 0 \\ \Sigma_{zr} & 0 & \Sigma_{zz} \end{bmatrix}. \tag{4.118}$$

4.3. THE PIOLA–KIRCHHOFF STRESS TENSOR

To this point in the discussion of stress all references have been to the Cauchy stress—a force intensity that is measured in relation to the deformed configuration. At times it is advantageous to use a force intensity measured in relation to the undeformed configuration. For this latter stress—denoted the Piola–Kirchhoff stress—the pertinent coordinate system is the global material coordinate system, either rectangular or cylindrical.

The Cauchy and Piola–Kirchhoff stress tensors can be related inasmuch as both quantities refer to the same force, which allows us to write

$$\mathbf{f} = \mathbf{t}_{(\mathbf{n})}\, da = \mathbf{T}_{(\mathbf{N})}\, dA, \tag{4.119}$$

where da is the magnitude of the differential area with normal $\mathbf{n}$ and dA is the magnitude of the undeformed differential area with normal $\mathbf{N}$ prior to deformation that will become da—see Section 3.5.6.2 of Chapter 3

$$d\mathbf{a} = da\mathbf{n}, \quad d\mathbf{A} = dA\mathbf{N}, \quad da_k = dan_k, \quad dA_K = dAN_K. \tag{4.120}$$

The local traction $\mathbf{T}_{(\mathbf{N})}$ is referenced to the global material coordinate system, i.e., the counterpart of $\mathbf{t}_{(\mathbf{n})}$, and $\mathbf{N}$ is the normal to the local area referenced to the global material coordinate system, i.e., the counterpart of $\mathbf{n}$.

Using Eqs. (4.11) and (4.120) in Eq. (4.119) yields

$$\boldsymbol{\Sigma}^T \cdot \mathbf{n}\, da = \boldsymbol{\Sigma}^T \cdot d\mathbf{a} = \mathbf{T}_{(\mathbf{N})}\, dA. \tag{4.121}$$

It is at this point that we encounter two definitions for the Piola–Kirchhoff stress.

4.3.1 Piola–Kirchhoff stress tensor of the first kind

The natural counterpart of Eq. (4.11) would seem to be a stress defined by the equation

$$\mathbf{T}_{(\mathbf{N})} = \mathbf{S}^T \cdot \mathbf{N}, \quad \left(\mathbf{T}_{(\mathbf{N})}\right)_k = S_{Jk} N_J. \tag{4.122}$$

This Piola–Kirchhoff stress definition provides a fictitious or pseudo-stress that is measured using the current (spatial) force $\mathbf{f}$, but the differential area in the undeformed configuration, and expresses the traction $\mathbf{T}_{(\mathbf{N})}$ in terms of that undeformed area. Using Eq. (4.122) in Eq. (4.121), we obtain

$$\boldsymbol{\Sigma}^T \cdot d\mathbf{a} = \mathbf{S}^T \cdot \mathbf{N} dA = \mathbf{S}^T \cdot d\mathbf{A}. \tag{4.123}$$

Thus the traction $\mathbf{T}_{(\mathbf{N})}$ is the force on the deformed area per unit undeformed area.

The infinitesimal areas $d\mathbf{a}$ and $d\mathbf{A}$ are related (see Section 3.5.6.2 of Chapter 3) by Eq. (3.62). If we substitute this latter expression into Eq. (4.123), then

$$\left[\mathcal{J}\boldsymbol{\Sigma}^T \cdot \left(\mathbf{F}^{-1}\right)^T - \mathbf{S}^T\right] \cdot d\mathbf{A} = 0, \quad \left(\mathcal{J}\Sigma_{jk}F_{Ij}^{-1} - S_{Ik}\right) dA_I = 0. \tag{4.124}$$

Eq. (4.124) also employs the distributive property of the dot product (see Section A.3.1.3 of Appendix A).

As the differential area $d\mathbf{A}$ is nonzero, Eq. (4.124) implies

$$\mathbf{S}^T = \mathcal{J}\boldsymbol{\Sigma}^T \cdot \left(\mathbf{F}^{-1}\right)^T, \quad S_{Ik} = \mathcal{J}\Sigma_{jk}F_{Ij}^{-1} = \mathcal{J}\Sigma_{jk}\frac{\partial X_I}{\partial x_j}. \tag{4.125}$$

Although $\boldsymbol{\Sigma}$ is symmetric, $\mathbf{F}$ is not, implying the Piola–Kirchhoff stress tensor of the first kind is not symmetric. Postmultiplying Eq. (4.125) by $\frac{1}{\mathcal{J}}\mathbf{F}^T$, we arrive at the inverse relation

$$\boldsymbol{\Sigma}^T = \frac{1}{\mathcal{J}}\mathbf{S}^T \cdot \mathbf{F}^T, \quad \Sigma_{jk} = \frac{1}{\mathcal{J}}S_{Ik}F_{jI} = \frac{1}{\mathcal{J}}S_{Ik}\frac{\partial x_j}{\partial X_I}, \tag{4.126}$$

where we have used the fact that (see Section A.44 of Appendix A) $\left(\mathbf{F}^{-1}\right)^T \cdot \mathbf{F}^T = \left(\mathbf{F} \cdot \mathbf{F}^{-1}\right)^T = \mathbf{I}$.

4.3.1.1 Example problem—Piola–Kirchhoff stress tensor of the first kind

Consider a uniaxial tension test (see Section 6.2 of Chapter 6) wherein a circular cylindrical sample is loaded by a force $\mathbf{f}$. The cross-sectional area of the sample is $A(\tau)$, where τ is the time of the test. Use these parameters to differentiate between the Cauchy stress and the Piola–Kirchhoff stress of the first kind.

Assume the x_3-axis of the spatial coordinate system to be collinear with the axis of the test sample. Then at any time during the test the traction is (Eq. (4.2))

$$\mathbf{t}_{(3)}(\tau) = \frac{\mathbf{f}}{A(\tau)}, \tag{4.127}$$

and, from Eq. (4.11), the Cauchy stress is

$$\Sigma_{33} = \left|\mathbf{t}_{(3)}\right| = \frac{|\mathbf{f}|}{A(\tau)}, \quad \text{all other } \Sigma_{ij} = 0. \tag{4.128}$$

The Cauchy stress is sometimes referred to as the true stress.

From Eq. (4.123) with[23] $da = A(\tau)$ and $dA = A(0)$ we may now write the Piola–Kirchhoff stress of the first kind as

$$S_{33} = \frac{|\mathbf{f}|}{A(0)}, \quad \text{all other } S_{Ij} = 0. \tag{4.129}$$

The Piola–Kirchhoff stress of the first kind is sometimes referred to as the engineering stress. It is a fictitious stress quantity in that at no time (except $\tau = 0$) does it represent a true physical measurement of force intensity.

4.3.2 Piola–Kirchhoff stress tensor of the second kind

Although the definition of the Piola–Kirchhoff stress tensor of the first kind is conceptually pleasing, its lack of symmetry is a drawback. As an alternative pseudo-stress definition for the undeformed configuration, consider an alternate, fictitious force $\tilde{\mathbf{f}}$ that draws its correspondence to the true force $\mathbf{f}$ from the relation between the material and spatial incremental position vectors $d\mathbf{X}$ and $d\mathbf{x}$. If we recall from Eq. (3.14) the relation $d\mathbf{X} = \mathbf{F}^{-1} \cdot d\mathbf{x}$, we can in a parallel fashion define this pseudo-force $\tilde{\mathbf{f}}$ in the undeformed configuration that is related to the true force $\mathbf{f}$ in the deformed configuration by

$$\tilde{\mathbf{f}} = \mathbf{F}^{-1} \cdot \mathbf{f}, \quad \tilde{f}_K = F^{-1}_{Kj} f_j. \tag{4.130}$$

The Piola–Kirchhoff stress tensor of the second kind is now defined using Eq. (4.11). In direct analogy to Eq. (4.119) [8], the force definition in Eq. (4.130) implies

$$\tilde{\mathbf{S}}^T \cdot \mathbf{N} dA = \tilde{\mathbf{f}} = \mathbf{F}^{-1} \cdot \mathbf{f} = \mathbf{F}^{-1} \cdot \boldsymbol{\Sigma}^T \cdot \mathbf{n} da, \tag{4.131}$$

or, using Eq. (3.62),

$$\left[\tilde{\mathbf{S}}^T - \mathcal{J}\mathbf{F}^{-1} \cdot \boldsymbol{\Sigma}^T \cdot \left(\mathbf{F}^{-1}\right)^T\right] \cdot d\mathbf{A} = 0, \quad \left(\tilde{S}_{KJ} - \mathcal{J} F^{-1}_{Ji} \Sigma^T_{ij} F^{-1}_{Kj}\right) N_K dA = 0. \tag{4.132}$$

As the differential area $d\mathbf{A}$ is nonzero, Eq. (4.132) implies

$$\tilde{\mathbf{S}}^T = \mathcal{J}\mathbf{F}^{-1} \cdot \boldsymbol{\Sigma}^T \cdot \left(\mathbf{F}^{-1}\right)^T, \quad \tilde{S}_{KJ} = \mathcal{J} F^{-1}_{Ji} \Sigma^T_{ij} F^{-1}_{Kj}. \tag{4.133}$$

Unlike the Piola–Kirchhoff stress tensor of the first kind, the Piola–Kirchhoff stress tensor of the second kind is symmetric.[24] Premultiplying Eq. (4.133) by $\mathbf{F}$ and postmul-

[23] We can, in this instance, equate infinitesimal and finite areas since the local and average tractions are identical.

[24] This is perhaps most easily seen from the index notation expression of Eq. (4.133). Due to the symmetry of the Cauchy stress $\boldsymbol{\Sigma}^T$, exchanging J and K in this expression does not affect the right-hand side of the equation.

tiplying by $\mathbf{F}^T$ gives

$$\boldsymbol{\Sigma}^T = \frac{1}{\mathcal{J}}\mathbf{F}\cdot\tilde{\mathbf{S}}^T\cdot\mathbf{F}^T, \quad \Sigma_{ij}^T = F_{iK}\tilde{S}_{KJ}F_{jJ}. \tag{4.134}$$

4.3.3 Stress relations for infinitesimal deformations

From Eq. (3.15) we obtain

$$\begin{aligned} d\mathbf{X} &= \frac{\partial\left(\mathbf{x}-\hat{\mathbf{u}}\right)}{\partial\mathbf{x}}\cdot d\mathbf{x} = \left(\mathbf{I}-\frac{\partial\hat{\mathbf{u}}}{\partial\mathbf{x}}\right)\cdot d\mathbf{x} = \mathbf{F}^{-1}\cdot d\mathbf{x}, \\ dX_I &= \frac{\partial\left(x_i-\hat{u}_i\right)\delta_{iI}}{\partial x_k}dx_k = \left(\delta_{ik}-\frac{\partial\hat{u}_i}{\partial x_k}\right)\delta_{iI}\,dx_k = F_{Ik}^{-1}\,dx_k. \end{aligned} \tag{4.135}$$

We can substitute Eq. (4.135) into Eq. (4.125) for the Piola–Kirchhoff stress of the first kind

$$\mathbf{S}^T = \mathcal{J}\boldsymbol{\Sigma}^T\cdot\left(\mathbf{I}-\frac{\partial\hat{\mathbf{u}}}{\partial\mathbf{x}}\right)^T, \quad S_{Ik} = \mathcal{J}\Sigma_{jk}\left(\delta_{mj}-\frac{\partial\hat{u}_m}{\partial x_j}\right)\delta_{mI}, \tag{4.136}$$

and into Eq. (4.133) for the Piola–Kirchoff stress of the second kind

$$\begin{aligned} \tilde{\mathbf{S}}^T &= \mathcal{J}\left(\mathbf{I}-\frac{\partial\hat{\mathbf{u}}}{\partial\mathbf{x}}\right)\cdot\boldsymbol{\Sigma}^T\cdot\left(\mathbf{I}-\frac{\partial\hat{\mathbf{u}}}{\partial\mathbf{x}}\right)^T, \\ \tilde{S}_{KJ} &= \mathcal{J}\left(\delta_{mi}-\frac{\partial\hat{u}_m}{\partial x_i}\right)\delta_{mJ}\Sigma_{ij}^T\left(\delta_{nj}-\frac{\partial\hat{u}_n}{\partial x_j}\right)\delta_{nK}. \end{aligned} \tag{4.137}$$

Eqs. (4.136) and (4.137) indicate that when the displacement gradients are small compared to unity (i.e., $\mathbf{I}-\frac{\partial\hat{\mathbf{u}}}{\partial\mathbf{x}}\approx\mathbf{I}$, $\mathcal{J}\approx 1$) the Piola–Kirchhoff stress tensors become indistinguishable from the Cauchy stress tensor (i.e., $S_{Ik}=\Sigma_{jk}\delta_{jI}$, $\tilde{S}_{KJ}=\Sigma_{ij}^T\delta_{iJ}\delta_{jK}$). In future work, unless explicitly needed for a large deformation problem, the Cauchy stress tensor will be the stress measure of choice.

CHAPTER 5

Elastic Behavior

5.1. INTRODUCTION

Chapters 3 and 4, respectively, deal with the deformation and loading of a body or structure. The discussion in both chapters is independent of the material constitution of the body. If we wish to relate deformation and load, however, we must specify the material constitution.

Such a specification will have limits of validity.[1] For example, a structure when loaded below a certain stress level may behave elastically.[2] But as the stress level increases, eventually an elastic model is no longer appropriate. A material description therefore not only relates deformation to load[3] but also provides bounds within which the stated relation is applicable.

In this book we shall consider two constitutive models used in tubular design:

- linear elasticity—stress and strain are related linearly for stress combinations below a certain limit;
- plasticity—an extension (i.e., the behavior is actually elastic-plastic) of linear elasticity for stress combinations beyond the bounds of elastic behavior.

In both of the above behavioral models, temperature dependence will be included.

Linear elasticity will be covered in this chapter. Since the limit of elastic behavior is also a major limit state for most tubular applications, equations derived here will drive most of the design calculations in later chapters. Chapter 6 has two purposes. First, opening sections of the chapter describe yield, the boundary of purely elastic behavior and a primary limit state for tubular design. Later sections of Chapter 6 address post-yield behavior for the purpose of describing the tubular design issues that involve plastic deformation.

5.2. ISOTROPIC ELASTIC BEHAVIOR

We define an elastic material as one whose stress depends only on the deformation gradient (or strain) and temperature at material position $\mathbf{X}$ and time τ. Further, we assume

[1] A classic example of the validity limits of a material constitutive model is water. Depending on the temperature and pressure, one must model different dependencies of water in its incarnations as steam, water and ice.

[2] At this point we use terms such as "elastic" and "stress level" loosely, trusting the reader has an intuitive or qualitative feel for the undefined terms. The need for clarification will be rectified shortly.

[3] In the broader field of continuum mechanics the behavior of other variables, such as entropy and internal energy density, must also be specified [7]. Here, we limit ourselves to thermo-mechanical behavior.

Elements of Oil and Gas Well Tubular Design
DOI: 10.1016/B978-0-12-811769-9.00005-0

the relation between (Cauchy) stress $\mathbf{\Sigma}$ and either (Eulerian) strain $\breve{\mathbf{E}}$ or temperature to be linear and of the form

$$\Sigma_{kl} = \breve{\Sigma}_{klmn}\breve{E}_{mn} - B_{kl}\,(T - T_0)\,, \tag{5.1}$$

where $\breve{\mathbf{\Sigma}}$ is the fourth-order elastic stiffness tensor, $\mathbf{B}$ is the coefficient of linear thermal stress tensor and T is temperature, T_0 being the temperature corresponding to zero strain.

At the outset Eq. (5.1) is imposing inasmuch as $\breve{\mathbf{\Sigma}}$ has $3^4 = 81$ components. The number of independent components of $\breve{\mathbf{\Sigma}}$ can be reduced, however, by the following considerations:

- $\mathbf{\Sigma}$ is symmetric (see Eqs. (4.19)–(4.21)) implying $\breve{\Sigma}_{klmn} = \breve{\Sigma}_{lkmn}$ and $B_{kl} = B_{lk}$. Since only six of the Σ_{kl} are independent, this reduces the number of independent terms in $\breve{\Sigma}_{klmn}$ to $6 \times 3 \times 3$, or 54, and the number of independent terms in B_{kl} to 6.
- $\breve{\mathbf{E}}$ is symmetric (see Eq. (3.35) and the bullets to follow) implying $\breve{\Sigma}_{klmn} = \breve{\Sigma}_{klnm}$. Since only six of the $\breve{E}_{kl}$ are independent, this reduces the number of independent terms in $\breve{\Sigma}_{klmn}$ to 6×6, or 36.
- Since $\mathbf{\Sigma}$ could be represented as the strain derivative of a potential, $\breve{\Sigma} = \frac{1}{2}\breve{\Sigma}_{klmn}\breve{E}_{kl}\breve{E}_{mn} = \frac{1}{2}\breve{\Sigma}_{klmn}\breve{E}_{mn}\breve{E}_{kl}$, and since $\Sigma_{kl} = \frac{\partial \breve{\Sigma}}{\partial \breve{E}_{kl}} = \frac{\partial \breve{\Sigma}}{\partial \breve{E}_{mn}}$, $\breve{\Sigma}_{klmn} = \breve{\Sigma}_{mnkl}$. This further reduces the number of independent terms in $\breve{\Sigma}_{klmn}$ to 21 [7].

The final forms of $\mathbf{B}_T$ and $\breve{\mathbf{\Sigma}}$ are

$$\mathbf{B}_T = \begin{bmatrix} B_{11} & B_{12} & B_{13} \\ & B_{22} & B_{23} \\ symm & & B_{33} \end{bmatrix}, \tag{5.2}$$

$$\breve{\mathbf{\Sigma}} = \begin{bmatrix} \breve{\Sigma}_{1111} & \breve{\Sigma}_{1122} & \breve{\Sigma}_{1133} & \breve{\Sigma}_{1123} & \breve{\Sigma}_{1113} & \breve{\Sigma}_{1112} \\ & \breve{\Sigma}_{2222} & \breve{\Sigma}_{2233} & \breve{\Sigma}_{2223} & \breve{\Sigma}_{2213} & \breve{\Sigma}_{2212} \\ & & \breve{\Sigma}_{3333} & \breve{\Sigma}_{3323} & \breve{\Sigma}_{3313} & \breve{\Sigma}_{3312} \\ & symm & & \breve{\Sigma}_{2323} & \breve{\Sigma}_{2313} & \breve{\Sigma}_{2312} \\ & & & & \breve{\Sigma}_{1313} & \breve{\Sigma}_{1312} \\ & & & & & \breve{\Sigma}_{1212} \end{bmatrix}. \tag{5.3}$$

The above equations only depend on the symmetries of the preceding bulleted list and are therefore completely general with regard to material symmetry.

Various special cases of Eqs. (5.2) and (5.3) can be exploited depending on the material under consideration. For example, a common symmetry used by rock mechanists is symmetry with respect to a plane (i.e., planar isotropy), where the elastic properties of a material are invariant within a plane, but differ perpendicular to the plane. This isotropy can be used to model certain depositional consequences on rock stiffness.

In tubular design, any directional variation in elastic properties is usually ignored and the material is considered to be isotropic. In this case, it can be demonstrated [7] that $\mathbf{B}$ and $\check{\mathbf{\Sigma}}$ reduce to the forms

$$\mathbf{B}_T = \begin{bmatrix} \beta_T & 0 & 0 \\ & \beta_T & 0 \\ symm & 0 & \beta_T \end{bmatrix}, \tag{5.4}$$

$$\check{\mathbf{\Sigma}} = \begin{bmatrix} \lambda_E + 2\mu_E & \lambda_E & \lambda_E & 0 & 0 & 0 \\ & \lambda_E + 2\mu_E & \lambda_E & 0 & 0 & 0 \\ & & \lambda_E + 2\mu_E & 0 & 0 & 0 \\ & symm & & \mu_E & 0 & 0 \\ & & & & \mu_E & 0 \\ & & & & & \mu_E \end{bmatrix}, \tag{5.5}$$

where β_T is the (isotropic) coefficient of linear thermal stress and λ_E and μ_E are known as the Lamé constants. Returning to Eq. (5.1), we may now, using Eqs. (5.4) and (5.5), write explicitly for an isotropic elastic material the following expressions:

$$\Sigma_{11} = (\lambda_E + 2\mu_E)\,\check{E}_{11} + \lambda_E\left(\check{E}_{22} + \check{E}_{33}\right) - \beta_T\,(T - T_0)\,, \tag{5.6}$$

$$\Sigma_{22} = (\lambda_E + 2\mu_E)\,\check{E}_{22} + \lambda_E\left(\check{E}_{33} + \check{E}_{11}\right) - \beta_T\,(T - T_0)\,, \tag{5.7}$$

$$\Sigma_{33} = (\lambda_E + 2\mu_E)\,\check{E}_{33} + \lambda_E\left(\check{E}_{11} + \check{E}_{22}\right) - \beta_T\,(T - T_0)\,, \tag{5.8}$$

$$\begin{aligned} \Sigma_{12} &= \check{\Sigma}_{12kl}\check{E}_{kl} = \check{\Sigma}_{1212}\check{E}_{12} + \check{\Sigma}_{1221}\check{E}_{21} = \left(\check{\Sigma}_{1212} + \check{\Sigma}_{1221}\right)\check{E}_{12} \\ &= 2\check{\Sigma}_{1212}\check{E}_{12} = 2\mu_E\check{E}_{12}, \end{aligned} \tag{5.9}$$

$$\Sigma_{23} = 2\mu_E\check{E}_{23}, \tag{5.10}$$

$$\Sigma_{31} = 2\mu_E\check{E}_{31}, \tag{5.11}$$

with the equations for Σ_{21}, Σ_{32} and Σ_{13} understood by symmetry from Eqs. (5.9)–(5.11), respectively. The substitution $\check{\Sigma}_{1212} = \check{\Sigma}_{1221}$ in Eq. (5.9) follows from the symmetry of the strain tensor.

5.2.1 Alternate elastic constants

As legitimate as Eqs. (5.6)–(5.11) may be, other elastic constants have assumed greater relevance to many engineers. As a first step in considering alternate elastic constants, we solve Eqs. (5.6)–(5.8) simultaneously. The solution for $\check{E}_{11}$ is

$$\check{E}_{11} = \frac{2\,(\lambda_E + \mu_E)\,\Sigma_{11} - \lambda_E\,(\Sigma_{22} + \Sigma_{33}) + 2\mu_E\beta_T\,(T - T_0)}{2\left[(\lambda_E + 2\mu_E)\,(\lambda_E + \mu_E) - \lambda_E^2\right]}. \tag{5.12}$$

In the case of isothermal, uniaxial loading with Σ_{11} being the only nonzero stress, Eq. (5.12) can be solved for Σ_{11} as

$$\Sigma_{11} = \frac{\mu_E (3\lambda_E + 2\mu_E)}{(\lambda_E + \mu_E)} \breve{E}_{11}. \tag{5.13}$$

To simplify Eq. (5.13), we may write

$$\Sigma_{11} = E\breve{E}_{11}, \tag{5.14}$$

where E is Young's modulus.[4] Comparing this expression with Eq. (5.13) gives

$$E = \frac{\mu_E (3\lambda_E + 2\mu_E)}{(\lambda_E + \mu_E)}. \tag{5.15}$$

Although Σ_{11} is the only nonzero stress, strain along the x_1-axis will be accompanied by a smaller strain of opposite sign along the x_2 and x_3-axes. The measure of these lateral strains is termed Poisson's ratio, the ratio being, for example, $-\breve{E}_{22}/\breve{E}_{11}$. Writing the solution for $\breve{E}_{22}$ (see Eq. (5.12)) as

$$\breve{E}_{22} = \frac{2(\lambda_E + \mu_E)\Sigma_{22} - \lambda_E(\Sigma_{11} + \Sigma_{33}) + 2\mu_E\beta_T(T - T_0)}{2\left[(\lambda_E + 2\mu_E)(\lambda_E + \mu_E) - \lambda_E^2\right]}, \tag{5.16}$$

and then once more requiring $T - T_0 = \Sigma_{22} = \Sigma_{33} = 0$, gives

$$\breve{E}_{22} = \frac{-\lambda_E \Sigma_{11}}{2\mu_E(3\lambda_E + 2\mu_E)}, \tag{5.17}$$

and Poisson's ratio becomes

$$\nu = -\frac{\breve{E}_{22}}{\breve{E}_{11}} = \frac{\lambda_E}{2(\lambda_E + \mu_E)}. \tag{5.18}$$

As a final comment, we note that μ_E is sometimes replaced by the symbol G. Both these terms are denoted the shear modulus (see Eqs. (5.9)–(5.11)). Table 5.1 presents a summary of the relations between the various moduli.

5.2.2 Stress–strain relations using E and ν

From Table 5.1, $\lambda_E + 2\mu_E = \frac{E(1-\nu)}{(1+\nu)(1-2\nu)}$. Using this result in Eqs. (5.6)–(5.8) yields

$$\Sigma_{11} = \frac{E}{(1+\nu)(1-2\nu)}\left[(1-\nu)\breve{E}_{11} + \nu\left(\breve{E}_{22} + \breve{E}_{33}\right)\right] - \beta_T(T - T_0), \tag{5.19}$$

[4] Imagine a uniaxial stress–strain experiment (see Section 6.2 of Chapter 6). Conveniently, the single variable E appears naturally as the slope of a plot of specimen stress as a function of specimen strain.

Table 5.1 Summary of elastic constants and their relations for an isotropic material

Symbol[a]	$f(E,\nu)$	$f(\lambda_E,\mu_E)$
E	E	$\dfrac{\mu_E(3\lambda_E+2\mu_E)}{(\lambda_E+\mu_E)}$
G	$\dfrac{E}{2(1+\nu)}$	μ_E
ν	ν	$\dfrac{\lambda_E}{2(\lambda_E+\mu_E)}$
λ_E	$\dfrac{E\nu}{(1+\nu)(1-2\nu)}$	λ_E
μ_E	$\dfrac{E}{2(1+\nu)}$	μ_E

[a] G and μ_E are identical.

$$\Sigma_{22}=\frac{E}{(1+\nu)(1-2\nu)}\left[(1-\nu)\breve{E}_{22}+\nu\left(\breve{E}_{33}+\breve{E}_{11}\right)\right]-\beta_T(T-T_0), \tag{5.20}$$

$$\Sigma_{33}=\frac{E}{(1+\nu)(1-2\nu)}\left[(1-\nu)\breve{E}_{33}+\nu\left(\breve{E}_{11}+\breve{E}_{22}\right)\right]-\beta_T(T-T_0), \tag{5.21}$$

and substituting G for μ_E produces

$$\Sigma_{12}=2G\breve{E}_{12}, \tag{5.22}$$

$$\Sigma_{23}=2G\breve{E}_{23}, \tag{5.23}$$

$$\Sigma_{31}=2G\breve{E}_{31}. \tag{5.24}$$

It is these forms of the mechanical constitutive equations for an isotropic elastic solid that we will use most frequently in all discussion to follow. Solving Eqs. (5.19)–(5.21) for the strains gives

$$\breve{E}_{11}=\frac{1}{E}\left[\Sigma_{11}-\nu(\Sigma_{22}+\Sigma_{33})\right]+\alpha_T(T-T_0), \tag{5.25}$$

$$\breve{E}_{22}=\frac{1}{E}\left[\Sigma_{22}-\nu(\Sigma_{33}+\Sigma_{11})\right]+\alpha_T(T-T_0), \tag{5.26}$$

$$\breve{E}_{33}=\frac{1}{E}\left[\Sigma_{33}-\nu(\Sigma_{11}+\Sigma_{22})\right]+\alpha_T(T-T_0). \tag{5.27}$$

$$\breve{E}_{12}=\frac{1}{2G}\Sigma_{12}, \tag{5.28}$$

$$\breve{E}_{23}=\frac{1}{2G}\Sigma_{23}, \tag{5.29}$$

$$\breve{E}_{31}=\frac{1}{2G}\Sigma_{31}. \tag{5.30}$$

$$\alpha_T=\frac{1-2\nu}{E}\beta_T, \tag{5.31}$$

where α_T is the linear coefficient of thermal expansion. Eqs. (5.19)–(5.31) apply to cylindrical coordinates with the index substitutions $1 = R$, $2 = \Theta$ and $3 = Z$.

5.2.3 Finite strain

Aside from the material presented in the preceding sections, we will pass on further development of elastic deformation for finite strain. On the few occasions when we address finite deformation in this book, the inelastic strains are large enough that the elastic strain contribution to total strain can be ignored.

5.2.4 Infinitesimal strain

Elastic, infinitesimal strain is applicable to a host of analyses for tubulars at stress states below yield. Recall from Section 3.5.5 of Chapter 3 that the three strain definitions discussed—Lagrangian, Eulerian and logarithmic—converge. Purely for consistency, we shall retain the Eulerian notation.

5.2.4.1 Straight, vertical tube in generalized plane strain

A central result for future work is the stress state in a tubular cross-section when the tube is placed in a service environment. Central to that result is the case of a vertical tube, to which additional results for bending, buckling and temperature change can be superimposed.

Consider an initially straight tube loaded by circumferentially uniform internal and external pressure and axial load which has no bending component (see Fig. 5.1). Each cross-sectional plane of the tube is such that it remains plane with deformation. Displacements and their gradients are assumed to be infinitesimal. The vertical configuration of the tube means the body force is aligned with the positive z axis. We assume constant or zero velocity and no temperature change.

Equilibrium equation for tube cross-section

The problem is axisymmetric, which from Section 4.2.7.4 of Chapter 4 implies $\frac{\partial}{\partial\theta} = 0$, along with $\Sigma_{r\theta} = \Sigma_{\theta r} = 0$, $\Sigma_{\theta z} = \Sigma_{z\theta} = 0$ in a cylindrical coordinate system whose z-axis aligns with the longitudinal axis of the tubular. From Eqs. (4.58) and (4.62) we get

$$\frac{\partial \Sigma_{rr}}{\partial r} + \frac{\partial \Sigma_{rz}}{\partial z} + \frac{\Sigma_{rr} - \Sigma_{\theta\theta}}{r} = 0, \tag{5.32}$$

$$\frac{\partial \Sigma_{rz}}{\partial r} + \frac{\partial \Sigma_{zz}}{\partial z} + \frac{\Sigma_{rz}}{r} + \rho \frac{g}{g_c} \mathbf{b}_f \cdot \mathbf{g}_z = 0. \tag{5.33}$$

In Eq. (5.32) we have also dropped the body force term. For an axisymmetric problem this term must disappear since otherwise $\mathbf{b}_f \cdot \mathbf{g}_r$ renders equilibrium a function of θ through the θ dependence of $\mathbf{g}_r$ (recall Eq. (3.63)).

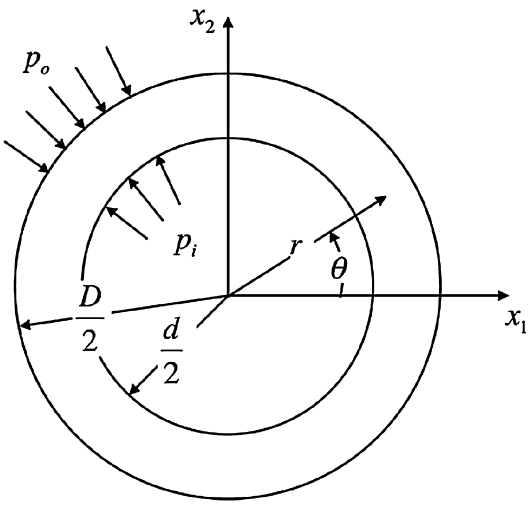

Figure 5.1 ***Problem variables for analysis of a tube in plane strain.***

For the subset of generalized plane strain (and its subset plane strain) used in this book (see Section 3.7.2.4 of Chapter 3) Eq. (3.170) states that $\breve{E}_{zr} = 0$, which from the cylindrical coordinates equivalent of Eq. (5.24) implies $\Sigma_{zr} = \Sigma_{rz} = 0$. This fact further simplifies the equilibrium equations (5.32) and (5.33) to

$$\frac{\partial \Sigma_{rr}}{\partial r} + \frac{\Sigma_{rr} - \Sigma_{\theta\theta}}{r} = 0, \tag{5.34}$$

$$\frac{\partial \Sigma_{zz}}{\partial z} + \rho \frac{g}{g_c} \mathbf{b}_f \cdot \mathbf{g}_z = 0. \tag{5.35}$$

Eq. (5.34) addresses equilibrium in the r–θ plane, that is, the tube cross-section. Eq. (5.35) addresses equilibrium along the length of the tube. In the discussion that follows we shall primarily be interested in the former relation. For future reference, substitution of the stress–strain relations for an isotropic, elastic material (Eqs. (5.19)–(5.21)) into Eq. (5.34) yields

$$(1-\nu)\frac{\partial \breve{E}_{rr}}{\partial r} + \nu\left(\frac{\partial \breve{E}_{\theta\theta}}{\partial r} + \frac{\partial \breve{E}_{zz}}{\partial r}\right) + \frac{1-2\nu}{r}\left[\breve{E}_{rr} - \breve{E}_{\theta\theta}\right] = 0, \tag{5.36}$$

Strain–displacement relations for tube cross-section

For generalized plane strain, axisymmetric, infinitesimal deformation the strain–displacement relations are given in Section 3.7.2.6 of Chapter 3. With the substitution

of Eqs. (3.177)–(3.179) into Eq. (5.36),

$$\frac{\partial^2 \hat{u}_r}{\partial r^2} + \frac{1}{r}\frac{\partial \hat{u}_r}{\partial r} - \frac{\hat{u}_r}{r^2} = 0. \tag{5.37}$$

This equation has a solution of the form[5] $\hat{u}_r = kr^m$, where k and m are constants. Upon substitution of this form into Eq. (5.37),

$$km\,(m-1)\,r^{m-2} + \frac{1}{r}kmr^{m-1} - \frac{kr^m}{r^2} = kr^{m-2}\left[m^2 - 1\right] = 0, \tag{5.38}$$

which has the solutions $m = \pm 1$. We may therefore write

$$\hat{u}_r = k_1 r + k_2 \frac{1}{r}, \tag{5.39}$$

along with

$$\hat{\breve{E}}_{rr} = \frac{\partial \hat{u}_r}{\partial r} = k_1 - k_2 \frac{1}{r^2}, \tag{5.40}$$

$$\hat{\breve{E}}_{\theta\theta} = \frac{\hat{u}_r}{r} = k_1 + k_2 \frac{1}{r^2}. \tag{5.41}$$

To determine the constants k_1 and k_2 we use the boundary conditions

$$\Sigma_{rr} = -p_i \quad \text{at } r = \frac{d}{2}, \tag{5.42}$$

$$\Sigma_{rr} = -p_o \quad \text{at } r = \frac{D}{2}. \tag{5.43}$$

Substituting these expressions into the cylindrical coordinates equivalent of Eq. (5.19) gives

$$\begin{aligned} -p_i &= \frac{E}{(1+\nu)\,(1-2\nu)}\left\{(1-\nu)\,\breve{E}_{rr}\Big|_{r=\frac{d}{2}} + \nu\left[\breve{E}_{\theta\theta}\Big|_{r=\frac{d}{2}} + \breve{E}_{zz}\right]\right\} \\ &= \frac{E}{(1+\nu)\,(1-2\nu)}\left\{(1-\nu)\left(k_1 - k_2\frac{4}{d^2}\right) + \nu\left[\left(k_1 + k_2\frac{4}{d^2}\right) + \breve{E}_{zz}\right]\right\} \\ &= \frac{E}{(1+\nu)\,(1-2\nu)}\left[k_1 - (1-2\nu)\,k_2\frac{4}{d^2} + \nu\breve{E}_{zz}\right], \end{aligned} \tag{5.44}$$

[5] See [25] or any text on ordinary differential equations for solutions to homogeneous second order linear equations.

$$
\begin{aligned}
-p_o &= \frac{E}{(1+\nu)(1-2\nu)}\left\{(1-\nu)\,\breve{E}_{rr}\Big|_{r=\frac{D}{2}} + \nu\left[\breve{E}_{\theta\theta}\Big|_{r=\frac{D}{2}} + \breve{E}_{zz}\right]\right\} \\
&= \frac{E}{(1+\nu)(1-2\nu)}\left\{[1-\nu)\left(k_1 - k_2\frac{4}{D^2}\right) + \nu\left[\left(k_1 + k_2\frac{4}{D^2}\right) + \breve{E}_{zz}\right]\right\} \\
&= \frac{E}{(1+\nu)(1-2\nu)}\left[k_1 - (1-2\nu)\,k_2\frac{4}{D^2} + \nu\breve{E}_{zz}\right].
\end{aligned}
\tag{5.45}
$$

When Eqs. (5.44) and (5.45) are solved simultaneously for k_1 and k_2,

$$
k_1 = \frac{(1+\nu)(1-2\nu)}{E}\frac{p_i d^2 - p_o D^2}{D^2 - d^2} - \nu\breve{E}_{zz}, \tag{5.46}
$$

$$
k_2 = \frac{1+\nu}{4E}\frac{d^2 D^2}{D^2 - d^2}\left(p_i - p_o\right). \tag{5.47}
$$

By successive back-substitutions we now find, for the radial displacement from Eq. (5.39),

$$
\hat{u}_r = \frac{1+\nu}{E\left(D^2 - d^2\right)}\left[(1-2\nu)\left(p_i d^2 - p_o D^2\right)r + \frac{d^2 D^2}{4r}\left(p_i - p_o\right)\right] - \nu\breve{E}_{zz}r, \tag{5.48}
$$

for the strains from Eqs. (5.40) and (5.41),

$$
\hat{\breve{E}}_{rr} = \frac{1+\nu}{E\left(D^2 - d^2\right)}\left[(1-2\nu)\left(p_i d^2 - p_o D^2\right) - \frac{d^2 D^2}{4r^2}\left(p_i - p_o\right)\right] - \nu\breve{E}_{zz}, \tag{5.49}
$$

$$
\hat{\breve{E}}_{\theta\theta} = \frac{1+\nu}{E\left(D^2 - d^2\right)}\left[(1-2\nu)\left(p_i d^2 - p_o D^2\right) + \frac{d^2 D^2}{4r^2}\left(p_i - p_o\right)\right] - \nu\breve{E}_{zz}, \tag{5.50}
$$

and for the stresses from the cylindrical coordinate equivalents of Eqs. (5.19)–(5.21),

$$
\Sigma_{rr} = \frac{1}{D^2 - d^2}\left[\left(p_i d^2 - p_o D^2\right) - \frac{d^2 D^2}{4r^2}\left(p_i - p_o\right)\right], \tag{5.51}
$$

$$
\Sigma_{\theta\theta} = \frac{1}{D^2 - d^2}\left[\left(p_i d^2 - p_o D^2\right) + \frac{d^2 D^2}{4r^2}\left(p_i - p_o\right)\right], \tag{5.52}
$$

$$
\Sigma_{zz} = E\breve{E}_{zz} + \frac{2\nu\left(p_i d^2 - p_o D^2\right)}{D^2 - d^2}, \tag{5.53}
$$

where for plane strain, $\breve{E}_{zz} = 0$. Eqs. (5.51) and (5.52) are called the Lamé equations.

At the extremes of r,

$$
\Sigma_{rr} = -p_i, \quad r = \frac{d}{2}, \tag{5.54}
$$

$$
\Sigma_{\theta\theta} = \frac{p_i\left(D^2 + d^2\right) - 2p_o D^2}{D^2 - d^2}, \quad r = \frac{d}{2}, \tag{5.55}
$$

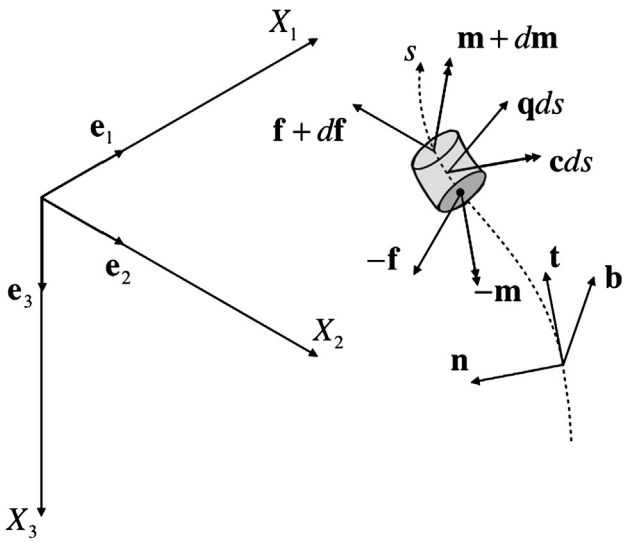

Figure 5.2 ***Forces and moments acting on an infinitesimal length of a tube or beam in space.*** The centerline of the beam is indicated by the trajectory whose coordinate is *s*. The double arrowhead on the moment signifies a moment obeying the right-hand rule with the thumb of the hand pointing in the direction of the arrowheads. The dot on the rearward face of the element is the point about which moments are evaluated. The global material coordinate system is displayed to indicate $\mathbf{e}_3$ as the direction of gravity.

$$\Sigma_{rr} = -p_o, \quad r = \frac{D}{2}, \tag{5.56}$$

$$\Sigma_{\theta\theta} = \frac{2p_i d^2 - p_o\left(D^2 + d^2\right)}{D^2 - d^2}, \quad r = \frac{D}{2}. \tag{5.57}$$

5.2.4.2 Tube as a beam

We first consider a three-dimensional tube (beam with a hollow, circular cylindrical cross-section) subjected to distributed forces per length and moments per length whose source identities are unknown. Once the governing equations are derived, the contributors to these distributed forces will be identified and discussed.

Equations of motion

Consider an infinitesimal length of a tube subjected to end force **f**, a distributed force per length **q**, an end moment **m** and a distributed moment per length **c**, as depicted in Fig. 5.2. The equation of motion is

$$\left(\mathbf{f} + d\mathbf{f}\right) - \mathbf{f} + \mathbf{q}ds = \frac{\rho}{g_c}\mathbf{a}A_s ds, \tag{5.58}$$

or

$$\frac{d\mathbf{f}}{ds} + \mathbf{q} = \frac{\rho}{g_c}\mathbf{a}A_s, \qquad \frac{df_i}{ds} + q_i = \frac{\rho_s}{g_c}a_i A_s. \tag{5.59}$$

The force **f** may be decomposed into three components—the **t** component, directed along the tangent to the tube centerline, is the axial force (tension positive), and the normal and binormal components, directed along **n** and **b**, respectively, are shear forces, the **n** component being directed toward the instantaneous center of curvature of the tube centerline.[6] The distributed load **q** has a variety of sources to be explained in the sections to follow, perhaps the most familiar being the effect of gravity on the tube mass.

Similarly for moment of momentum about the center of the rearward cross-section (see dot in Fig. 5.2),

$$(\mathbf{m} + d\mathbf{m}) - \mathbf{m} + \mathbf{t}ds \times (\mathbf{f} + d\mathbf{f}) + \frac{1}{2}\mathbf{t}ds \times \mathbf{q}ds + \mathbf{c}ds = \frac{1}{2}\mathbf{t}ds \times \frac{\rho_s}{g_c}\mathbf{a}A_s ds, \tag{5.60}$$

or, eliminating higher order terms,

$$\frac{d\mathbf{m}}{ds} + \mathbf{t} \times \mathbf{f} + \mathbf{c} = 0, \qquad \frac{dm_i}{ds} + \varepsilon_{ijk}t_j f_k + c_i = 0. \tag{5.61}$$

The moment **m** may be decomposed into three components—the **t** component, directed along the tangent to the tube centerline, is the torsion, and the normal and binormal components, directed along **n** and **b**, respectively, are bending moments, the **n** component causing bending around the instantaneous center of curvature of the tube centerline. The distributed moment **c** has a variety of sources to be explained in the sections to follow, perhaps the most familiar being the torsional resistance caused by friction between the tube and its radial confinement.

Components of **q**

Depending on the problem, the distributed force per length **q** is the vector sum of one or more components[7]:

Fluid and pressure $\mathbf{q}_f$ [27,28] Fig. 5.3 depicts only the forces from Fig. 5.2. An element of length[8] δs is viewed along the binormal vector as the lower (from the reader's perspective) end of the element lies instantaneously in the **t**–**n** plane. The element is referenced to a spatial coordinate system.

[6] For details on the unit vectors **t**, **n** and **b** see Appendix B.

[7] The references cited with each component are representative of applications of that component in a tubular problem and are not intended to be all-inclusive.

[8] The incremental length is characterized by δs rather than ds to signify that it may not be infinitesimal.

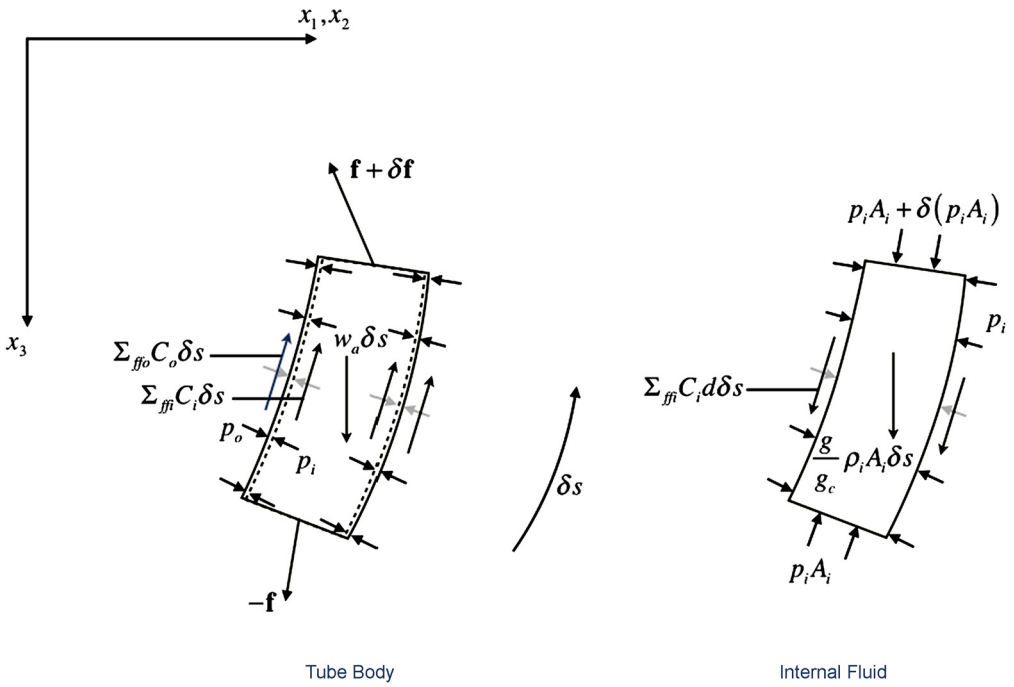

Figure 5.3 ***Forces due to fluid presence and flow on a length of a tube.*** All forces associated with wall contact, as well as all moments, have been omitted from the figure for the sake of clarity. The global material coordinate system containing the unit vector $\mathbf{e}_3$ along the positive $X_3 = Z$ axis is not shown (see Fig. 5.2). The symbol δ is used, rather than d, to signal changes are not necessarily infinitesimal. The figure is drawn in the plane normal to the binormal vector **b** (see Fig. 5.2 for coordinate system) at the element's lower end.

First consider the right-hand portion of Fig. 5.3 detailing the tractions to which the control volume[9] consisting of the bounding surface of the fluid internal to the tube is exposed. According to the balance of momentum equation the net force $\mathbf{f}_f$ on the control volume must equal the net change in momentum of the fluid in the control volume.

To address the momentum balance requires a short excursion into fluid balance equations. Following this excursion we will return to the specific issue of Fig. 5.3 so that the force on the internal fluid can be properly combined with the fluid's momentum and with the equation of motion for the tubular.

The equation for rate of change of a quantity b per unit mass being conveyed by a fluid which is instantaneously enclosed by a (control) surface fixed relative to an

[9] A control volume is a volume in space through which a fluid flows. A control surface is a closed envelope that defines the boundary of the control volume.

inertial[10] frame of reference is given by [31,32]

$$\int_V \rho \frac{Db}{D\tau} dV = \int_S b\rho \mathbf{v} \cdot \check{\mathbf{n}} dS + \int_V \frac{\partial (b\rho)}{\partial \tau} dV,$$
$$\int_V \rho \frac{Db}{D\tau} dV = \int_S b\rho v_k \check{n}_k dS + \int_V \frac{\partial (b\rho)}{\partial \tau} dV, \tag{5.62}$$

where S is the (control) surface surrounding the (control) volume V and τ is time. From the right-hand side of Eq. (5.62) we discern the following two contributors to the rate of change of b:

- portions of the mass containing b are being conveyed through the bounding surface of the control volume by the velocity field $\mathbf{v}$, with both entry and exit of the control volume possible;
- portions of the mass containing b that are instantaneously inside the control volume are experiencing a change in b due to the time derivative of b at their location.

As we anticipate our eventual return to Fig. 5.2, the unit normal vectors $\mathbf{n}$ and $\check{\mathbf{n}}$ must be distinguished. The former is the local normal to the trajectory of the tube centerline (see Fig. 5.2). The latter is the normal to a surface, in this case the outward normal to the control surface through which the fluid is flowing.

The operator $\frac{D}{D\tau}$ is a means of taking a material derivative in a spatial context. If we wish to trace a physical property b of a single fluid particle, associating the history of that particle with its undeformed configuration seems natural. In the material (undeformed) description the identity of the particle, represented by its initial position $\mathbf{X}$, does not change so that a time derivative of the property is simply $\frac{db(\mathbf{X},\tau)}{d\tau}$. Unfortunately, with fluid flow tracing all particles in such a manner is cumbersome—the spatial description is a better choice. How then, might one follow an individual particle using a spatial description? The solution is to recognize that the spatial position is $\mathbf{x}((\mathbf{X},\tau),\tau)$ such that the total time derivative of property b can be written as

$$\frac{Db(\mathbf{x},\tau)}{D\tau} = \frac{\partial b}{\partial \mathbf{x}} \cdot \frac{\partial \mathbf{x}(\mathbf{X},\tau)}{\partial \tau} + \frac{\partial b}{\partial \tau} = \frac{\partial b}{\partial \mathbf{x}} \cdot \mathbf{v}(\mathbf{X},\tau) + \frac{\partial b}{\partial \tau},$$
$$\frac{Db(\mathbf{x},\tau)}{D\tau} = \frac{\partial b}{\partial x_k} \frac{\partial x_k(X_K,\tau)}{\partial \tau} + \frac{\partial b}{\partial \tau} = \frac{\partial b}{\partial x_k} v_k(X_K,\tau) + \frac{\partial b}{\partial \tau}, \tag{5.63}$$

where $\mathbf{v} = \frac{\partial \mathbf{x}(\mathbf{X},\tau)}{\partial \tau}$ is velocity. The operator $\frac{D}{D\tau}$ is called the material derivative and may only be used with spatial variables.

[10] If the control surface is not inertial, additional considerations must be made. Problems involving flow induced instability can fall into this category of investigation. Such problems also require additional actions such as external fluid drag on the moving tubular [29,30].

Applying Gauss's theorem for a vector[11] to the surface integral in Eq. (5.62) gives

$$\int_V \rho \frac{Db}{d\tau} dV = \int_V \left[\nabla \cdot (b\rho \mathbf{v}) + \frac{\partial (b\rho)}{\partial \tau} \right] dV,$$
$$\int_V \rho \frac{Db}{d\tau} dV = \int_V \left[\frac{\partial}{\partial x_k} (b\rho v_k) + \frac{\partial (b\rho)}{\partial \tau} \right] dV. \tag{5.64}$$

Among the many useful applications of Eq. (5.64) two are of importance to the present discussion—conservation of mass and conservation of momentum.

To derive the equation for conservation of mass, we set $b = 1$ in Eq. (5.64) with the result

$$\int_V \left[\nabla \cdot (\rho \mathbf{v}) + \frac{\partial \rho}{\partial \tau} \right] dV = 0, \quad \int_V \left[\frac{\partial}{\partial x_k} (\rho v_k) + \frac{\partial \rho}{\partial \tau} \right] dV = 0, \tag{5.65}$$

or, if V is constant, in differential form

$$\nabla \cdot (\rho \mathbf{v}) + \frac{\partial \rho}{\partial \tau} = 0, \quad \frac{\partial}{\partial x_k} (\rho v_k) + \frac{\partial \rho}{\partial \tau} = 0. \tag{5.66}$$

As mentioned previously, the momentum conservation equation follows from the fact that the total rate of change of momentum ($\rho \mathbf{v}$) of the fluid associated with a (control) volume must equal $\mathbf{f}_f$, the vector resultant of all tractions and body forces exerted on the fluid by its surroundings. Here b in Eq. (5.64) is being replaced by a vector, but the substitution is acceptable if we view the vector as being defined by its three scalar components. With the substitution of $\mathbf{v}$ for b,

$$\mathbf{f}_f = \frac{1}{g_c} \int_V \rho \frac{D\mathbf{v}}{d\tau} dV = \frac{1}{g_c} \int_V \left[\nabla \cdot (\rho \mathbf{v}\mathbf{v}) + \frac{\partial (\rho \mathbf{v})}{\partial \tau} \right] dV, \tag{5.67}$$

where $\mathbf{v}\mathbf{v}$ is the tensor product of the velocity vector with itself—see Section A.4.1.3 of Appendix A.

We may most easily evaluate the term $\nabla \cdot (\rho \mathbf{v}\mathbf{v})$ in Eq. (5.67) using index notation. With the coordinate system of Fig. 5.3,

$$[\nabla \cdot (\rho \mathbf{v}\mathbf{v})]_k = \frac{\partial}{\partial x_j} (\rho v_j v_k), \tag{5.68}$$

[11] Gauss's theorem, or the divergence theorem, states that for any scalar a, $\int_S a \check{\mathbf{n}} dS = \int_V \nabla a dV$, where $\nabla = \frac{\partial}{\partial x_1}\mathbf{g}_1 + \frac{\partial}{\partial x_2}\mathbf{g}_2 + \frac{\partial}{\partial x_3}\mathbf{g}_3$, and $\check{\mathbf{n}}$ is the unit outward normal to the surface S enclosing volume V [15]. The expression of the theorem for a vector $\mathbf{v}$ is $\int_S \mathbf{v} \cdot \check{\mathbf{n}} dS = \int_V \nabla \cdot \mathbf{v} dV$ ($\int_S v_k \check{n}_k dS = \int_V \frac{\partial v_k}{\partial x_k} dV$). The Gauss theorem for a second order tensor $\mathbf{T}$ is $\int_S \mathbf{T} \cdot \check{\mathbf{n}} dS = \int_V \nabla \cdot \mathbf{T} dV$ ($\int_S T_{ij} \check{n}_j dS = \int_V \frac{\partial T_{ij}}{\partial x_j} dV$).

or $\nabla \cdot (\rho \mathbf{vv})$ is a vector whose components are[12]

$$\nabla \cdot (\rho \mathbf{vv}) = \begin{bmatrix} \frac{\partial}{\partial x_1}(\rho v_1 v_1) + \frac{\partial}{\partial x_2}(\rho v_2 v_1) + \frac{\partial}{\partial x_3}(\rho v_3 v_1) \\ \frac{\partial}{\partial x_1}(\rho v_1 v_2) + \frac{\partial}{\partial x_2}(\rho v_2 v_2) + \frac{\partial}{\partial x_3}(\rho v_3 v_2) \\ \frac{\partial}{\partial x_1}(\rho v_1 v_3) + \frac{\partial}{\partial x_2}(\rho v_2 v_3) + \frac{\partial}{\partial x_3}(\rho v_3 v_3) \end{bmatrix}. \tag{5.69}$$

This ends the excursion into fluid conservation relations.

If we now return to the fluid diagram in the right-hand portion of Fig. 5.3, the resultant force on the fluid $\mathbf{f}_f$ has the components

$$\begin{aligned} \mathbf{f}_f &= \int_S \mathbf{t}_{(\check{\mathbf{n}})} dS + \int_V \frac{g}{g_c} \rho \mathbf{e}_3 dV \\ &= \int_S \left\{ \left(\mathbf{t}_{(\check{\mathbf{n}})} \cdot \check{\mathbf{n}} \right) \check{\mathbf{n}} + \left[\mathbf{t}_{(\check{\mathbf{n}})} - \left(\mathbf{t}_{(\check{\mathbf{n}})} \cdot \check{\mathbf{n}} \right) \check{\mathbf{n}} \right] \right\} dS + \int_V \frac{g}{g_c} \rho \mathbf{e}_3 dV, \end{aligned}$$

[12] At this point in fluid mechanics texts one often sees the simplification of Eqs. (5.67)–(5.69) by application of the conservation of mass, Eq. (5.66). From Eq. (5.68) for the kth component of the vector $\nabla \cdot (\rho \mathbf{vv})$,

$$\nabla \cdot (\rho \mathbf{vv}) = \rho (\mathbf{v} \cdot \nabla) \mathbf{v} + \mathbf{v} [\nabla \cdot (\rho \mathbf{v})], \quad \frac{\partial}{\partial x_j}(\rho v_j v_k) = \rho v_j \frac{\partial v_k}{\partial x_j} + v_k \frac{\partial}{\partial x_j}(\rho v_j).$$

Using this expression in the right-hand side of Eq. (5.67) gives

$$\int_V \rho \frac{D\mathbf{v}}{d\tau} dV = \int_V \left\{ \rho (\mathbf{v} \cdot \nabla) \mathbf{v} + \mathbf{v} \underbrace{\left[[\nabla \cdot (\rho \mathbf{v})] + \frac{\partial \rho}{\partial \tau} \right]}_{\text{Conservation of mass}} + \rho \frac{\partial \mathbf{v}}{\partial \tau} \right\} dV,$$

where the contents of Eq. (5.66), the conservation of mass relation, vanishes, leaving

$$\int_V \rho \frac{D\mathbf{v}}{d\tau} dV = \int_V \left[\rho (\mathbf{v} \cdot \nabla) \mathbf{v} + \rho \frac{\partial \mathbf{v}}{\partial \tau} \right] dV, \quad \int_V \rho \frac{Dv_k}{d\tau} dV = \int_V \left[\rho v_j \frac{\partial v_k}{x_j} + \rho \frac{\partial v_k}{\partial \tau} \right] dV,$$

where the components of vector $(\mathbf{v} \cdot \nabla) \mathbf{v}$ are

$$(\mathbf{v} \cdot \nabla) \mathbf{v} = \begin{bmatrix} v_1 \frac{\partial v_1}{\partial x_1} + v_2 \frac{\partial v_1}{\partial x_2} + v_3 \frac{\partial v_1}{\partial x_3} \\ v_1 \frac{\partial v_2}{\partial x_1} + v_2 \frac{\partial v_2}{\partial x_2} + v_3 \frac{\partial v_2}{\partial x_3} \\ v_1 \frac{\partial v_3}{\partial x_1} + v_2 \frac{\partial v_3}{\partial x_2} + v_3 \frac{\partial v_3}{\partial x_3} \end{bmatrix}.$$

Using this simplification in Eq. (5.67), we can write the momentum conservation equation as

$$\mathbf{f}_f = \frac{1}{g_c} \int_V \left[\rho (\mathbf{v} \cdot \nabla) \mathbf{v} + \rho \frac{\partial \mathbf{v}}{\partial \tau} \right] dV, \quad \left(\mathbf{f}_f \right)_k = \frac{1}{g_c} \int_V \left[\rho v_j \frac{\partial v_k}{x_j} + \rho \frac{\partial v_k}{\partial \tau} \right] dV.$$

As tempting as this expression is, we will forego substitution of the continuity equation into the momentum conservation equation for the simple reason that, for tubular problems, maintaining Eq. (5.67) in its present form results in a more useful form, particularly with regard to expressions involving the effective force Σ_{eff}.

$$\begin{aligned}\left(\mathbf{f}_f\right)_k &= \int_S \left(\mathbf{t}_{(\check{\mathbf{n}})}\right)_k dS + \int_V \frac{g}{g_c}\rho\left(\mathbf{e}_3\cdot\mathbf{g}_k\right)dV \\ &= \int_S \left\{\left(\left(\mathbf{t}_{(\check{\mathbf{n}})}\right)_j \check{n}_j\right)\check{n}_k + \left[\left(\mathbf{t}_{(\check{\mathbf{n}})}\right)_k - \left(\left(\mathbf{t}_{(\check{\mathbf{n}})}\right)_j \check{n}_j\right)\check{n}_k\right]\right\} dS + \int_V \frac{g}{g_c}\rho\left(\mathbf{e}_3\cdot\mathbf{g}_k\right)dV,\end{aligned} \tag{5.70}$$

where we require $\mathbf{e}_3$ in the global material coordinate system, but not necessarily $\mathbf{g}_3$ in the spatial coordinate system, to align with the gravitational body force.

In the last, expanded integrand in Eq. (5.70), the normal component is pressure on the surface of the fluid control volume, and the remaining term is shear stress along the surface of the fluid control volume:

$$\begin{aligned}\left(\mathbf{t}_{(\check{\mathbf{n}})}\cdot\check{\mathbf{n}}\right)\check{\mathbf{n}} &= -p\check{\mathbf{n}}, \quad \mathbf{t}_{(\check{\mathbf{n}})} - \left(\mathbf{t}_{(\check{\mathbf{n}})}\cdot\check{\mathbf{n}}\right)\check{\mathbf{n}} = \Sigma_s\mathbf{s}, \\ \left(\left(\mathbf{t}_{(\check{\mathbf{n}})}\right)_j\check{n}_j\right)\check{n}_k &= -p\check{n}_k, \quad \left(\mathbf{t}_{(\check{\mathbf{n}})}\right)_k - \left(\left(\mathbf{t}_{(\check{\mathbf{n}})}\right)_j\check{n}_j\right)\check{n}_k = \Sigma_s s_k,\end{aligned} \tag{5.71}$$

where p is the local pressure, Σ_s is a shear stress in the direction of $\mathbf{s}$, and $\mathbf{s}$ is a unit vector on the surface S and normal to $\check{\mathbf{n}}$. With Eq. (5.71) substituted into Eq. (5.70), and the result substituted into Eq. (5.67),

$$\begin{aligned}\int_S\left[-p\check{\mathbf{n}} + \Sigma_s\mathbf{s}\right]dS + \int_V\frac{g}{g_c}\rho\mathbf{e}_3 dV &= \frac{1}{g_c}\int_V\left[\nabla\cdot(\rho\mathbf{v}\mathbf{v}) + \frac{\partial(\rho\mathbf{v})}{\partial\tau}\right]dV, \\ \int_S\left[-p\check{n}_k + \Sigma_s s_k\right]dS + \int_V\frac{g}{g_c}\rho\left(\mathbf{e}_3\cdot\mathbf{g}_k\right)dV &= \frac{1}{g_c}\int_V\left[\frac{\partial}{\partial x_j}\left(\rho v_j v_k\right) + \frac{\partial(\rho v_k)}{\partial\tau}\right]dV.\end{aligned} \tag{5.72}$$

If we apply Gauss's theorem (see Footnote 11) to the surface integral in Eq. (5.72), then

$$\begin{aligned}\int_V\left\{\nabla\cdot\left[-p\check{\mathbf{n}} + \Sigma_s\mathbf{s}\right] + \frac{g}{g_c}\rho\mathbf{e}_3 - \frac{1}{g_c}\nabla\cdot(\rho\mathbf{v}\mathbf{v}) - \frac{1}{g_c}\frac{\partial(\rho\mathbf{v})}{\partial\tau}\right\}dV &= 0, \\ \int_V\left\{\frac{\partial}{\partial x_k}\left[-p\check{n}_k + \Sigma_s s_k\right] + \frac{g}{g_c}\rho\left(\mathbf{e}_3\cdot\mathbf{g}_k\right) - \frac{1}{g_c}\frac{\partial}{\partial x_j}\left(\rho v_j v_k\right) - \frac{1}{g_c}\frac{\partial(\rho v_k)}{\partial\tau}\right\}dV &= 0.\end{aligned} \tag{5.73}$$

Finallly, if V is constant in Eq. (5.67), we have the differential form of the conservation of momentum equation, namely

$$\begin{aligned}\bar{\mathbf{f}}_f - \frac{1}{g_c}\nabla\cdot(\rho\mathbf{v}\mathbf{v}) - \frac{1}{g_c}\frac{\partial(\rho\mathbf{v})}{\partial\tau} &= 0, \quad \bar{\mathbf{f}}_f = \frac{\mathbf{f}}{V} \\ \left(\bar{\mathbf{f}}_f\right)_k - \frac{1}{g_c}\frac{\partial}{\partial x_j}\left(\rho v_j v_k\right) - \frac{1}{g_c}\frac{\partial(\rho v_k)}{\partial\tau} &= 0, \quad \left(\bar{\mathbf{f}}_f\right)_k = \frac{f_k}{V}.\end{aligned} \tag{5.74}$$

For steady-state flow the last term of Eq. (5.74) vanishes.

Any of Eqs. (5.72)–(5.74) can be used both inside and outside the tube. We will use Eq. (5.72) because it preserves the physical origins of the various contributions to force and momentum change.

For internal flow, $\Sigma_s = \Sigma_{ffi}$ in Fig. 5.3, $p = p_i$, $\rho = \rho_i$, and $V = V_i$, the internal volume of the tube for the distance δs. Further, we align the spatial axes such that $\mathbf{g}_1 = \mathbf{t}$, where $\mathbf{t}$ both aligns with the centerline of the tubular and is in the direction of flow, $\mathbf{g}_2 = \mathbf{n}$ and $\mathbf{g}_3 = \mathbf{b}$, $\mathbf{t}$, $\mathbf{n}$ and $\mathbf{b}$ being a vector triad (at the bottom of the tube element) associated with the Frenet–Serret formulas in Appendix B. In Eq. (5.72) it is reasonable to set $\mathbf{s} = \mathbf{g}_1$ with the implication that $\Sigma_{ffi}\mathbf{t} = -\Sigma_s\mathbf{s}$ since it opposes flow. We further refine the fluid velocity $\mathbf{v}$ to be equal in magnitude to $\frac{Q}{A_i}$, where Q is the fluid volumetric flow rate, and to be collinear with $\mathbf{t}$. Finally, we subdivide the control volume into the following three segments:

- the surface S_i, where $\delta S_i = C_i \delta s$, $C_i = \pi d$ being the circumference of the tube based on its inside diameter;
- the surface A_i at the base (lower end) of the element in Fig. 5.3—the outward normal to this surface is $\breve{\mathbf{n}} = -\mathbf{t}$;
- the surface $A_i + \delta A_i$ at the upper end of the element—the outward normal to this surface is $\breve{\mathbf{n}} = \mathbf{t} + \delta\mathbf{t}$.

Since the flow is in the $\mathbf{t} = \mathbf{g}_1$ direction, from Eq. (5.69)[13] we can write for each position along s

$$\begin{aligned}\nabla \cdot (\rho_i \mathbf{v}\mathbf{v}) &= \left(\frac{\partial}{\partial s}\mathbf{t}\right) \cdot \left(\rho_i \frac{Q}{A_i}\mathbf{t}\frac{Q}{A_i}\mathbf{t}\right) = \frac{\partial\left[\rho_i\left(\frac{Q}{A_i}\right)^2\mathbf{t}\right]}{\partial s} \\ &= \frac{\partial\left[\rho_i\left(\frac{Q}{A_i}\right)^2\right]}{\partial s}\mathbf{t} + \left[\rho_i\left(\frac{Q}{A_i}\right)^2\right]\kappa\mathbf{n},\end{aligned} \tag{5.75}$$

where κ is the local curvature of the centerline of the tubular.

With the above specifics and Eq. (5.75), Eq. (5.72) becomes

[13] There is a subtle difference between our current, explicit formulation and Eq. (5.69). The right-hand side of Eq. (5.69) is written for a spatial coordinate system whose unit base vectors are stationary (or, possibly, translating at constant velocity). In our current application, we are using the **t**–**n**–**b** triad that follows coordinate s and therefore may have rotating base unit vectors. For our problem, $\mathbf{v} = v\mathbf{t}$, so that Eq. (5.69) becomes

$$\nabla \cdot (\rho \mathbf{v}\mathbf{v}) = \left(\frac{d}{ds}\mathbf{t}\right) \cdot (\rho v\mathbf{t} v\mathbf{t}) = \frac{d}{ds}\left(\rho v^2\mathbf{t}\right) = \frac{d\left(\rho v^2\right)}{ds}\mathbf{t} + \rho v^2\kappa\mathbf{n},$$

$$[\nabla \cdot (\rho \mathbf{v}\mathbf{v})]_k = \left(\frac{d}{ds}t_j\right)\left(\rho v t_j v t_k\right) = \frac{d\left(\rho v^2\right)}{ds}t_k + \rho v^2\kappa n_k$$

where $\mathbf{t} \cdot \mathbf{t} = 1$ and the last step uses Eq. (B.3), $d\mathbf{t} = \kappa\mathbf{n}ds$, $dt_i = \kappa n_i ds$. As indicated in the final, expanded form of Eq. (5.75), when expanded the dyad term $\mathbf{v}\mathbf{v}$ exposes two components—one associated with the change of $\rho_i\mathbf{v}\mathbf{v}$ as one follows the flow path along its tangent $\mathbf{t}$ and one associated with the change of direction of the flow path that is in the direction of $\mathbf{n}$, the path derivative of $\mathbf{t}$.

$$\begin{aligned}
&\int_{S_i}\left[-p_i\breve{\mathbf{n}}-\Sigma_{ffi}\mathbf{t}\right]dS+\mathbf{t}\int_{A_i}p_i dS-(\mathbf{t}+\delta\mathbf{t})\int_{A_i+\delta A_i}\left(p_i+\delta p_i\right)dS\\
&\qquad+\frac{g}{g_c}\int_{V_i}\rho_i\mathbf{e}_3 dV=\frac{1}{g_c}\int_{V_i}\left\{\frac{\partial\left[\rho_i\left(\frac{Q}{A_i}\right)^2\mathbf{t}\right]}{\partial s}+\frac{\partial\left(\rho_i\frac{Q}{A_i}\right)}{\partial\tau}\mathbf{t}\right\}dV,\\
&\int_{S_i}\left[-p_i\breve{n}_k-\Sigma_{ffi}t_k\right]dS+t_k\int_{A_i}p_i dS-\left(t_k+dt_k\right)\int_{A_i+\delta A_i}\left(p_i+dp_i\right)dS\\
&\qquad+\frac{g}{g_c}\int_{V_i}\rho_i\left(\mathbf{e}_3\cdot\mathbf{g}_k\right)dV=\frac{1}{g_c}\int_{V_i}\left\{\frac{\partial\left[\rho_i\left(\frac{Q}{A_i}\right)^2 t_k\right]}{\partial s}+\frac{\partial\left(\rho_i\frac{Q}{A_i}\right)}{\partial\tau}t_k\right\}dV.
\end{aligned}\tag{5.76}$$

We can further simplify Eq. (5.76) by assuming the pressure p_i is constant over a cross-section,[14,15] allowing us to move occurrences of p_i outside the surface integrals involving A_i and $A_i+\delta A_i$[16]:

$$\begin{aligned}
&\int_{S_i}\left[-p_i\breve{\mathbf{n}}-\Sigma_{ffi}\mathbf{t}\right]dS+\mathbf{t}p_iA_i-(\mathbf{t}+\delta\mathbf{t})\left(p_i+\delta p_i\right)\left(A_i+\delta A_i\right)\\
&\qquad+\frac{g}{g_c}\int_{V_i}\rho_i\mathbf{e}_3 dV=\frac{1}{g_c}\int_{V_i}\left\{\frac{\partial\left[\rho_i\left(\frac{Q}{A_i}\right)^2\mathbf{t}\right]}{\partial s}+\frac{\partial\left(\rho_i\frac{Q}{A_i}\right)}{\partial\tau}\mathbf{t}\right\}dV,\\
&\int_{S_i}\left[-p_i\breve{n}_k-\Sigma_{ffi}t_k\right]dS+t_kp_iA_i-\left(t_k+\delta t_k\right)\left(p_i+\delta p_i\right)\left(A_i+\delta A_i\right)\\
&\qquad+\frac{g}{g_c}\int_{V_i}\rho_i\left(\mathbf{e}_3\cdot\mathbf{g}_k\right)dV=\frac{1}{g_c}\int_{V_i}\left\{\frac{\partial\left[\rho_i\left(\frac{Q}{A_i}\right)^2 t_k\right]}{\partial s}+\frac{\partial\left(\rho_i\frac{Q}{A_i}\right)}{\partial\tau}t_k\right\}dV.
\end{aligned}\tag{5.77}$$

[14] This assumption loses fidelity with the inclination of the wellbore, reaching its worst state for a horizontal wellbore. Even if the wellbore is horizontal, however, the difference in pressure between the high and low sides of the tubular cross section is small.

[15] An alternative is to use the average pressure at a cross section, but this would require two distinct pressure terms in Eq. (5.76)—one for the pressure acting on surface S_i and one for the integrals on surfaces A_i and $A_i+\delta A_i$.

[16] In particular, for the second and third integrals on the left-hand side of Eq. (5.76) we have

$$\begin{aligned}
\mathbf{t}\int_{A_i}p_i dS-(\mathbf{t}+\delta\mathbf{t})\int_{A_i+\delta A_i}\left(p_i+\delta p_i\right)dS&=\mathbf{t}p_iA_i-(\mathbf{t}+\delta\mathbf{t})\left(p_i+\delta p_i\right)\left(A_i+\delta A_i\right),\\
t_k\int_{A_i}p_i dS-\left(t_k+\delta t_k\right)\int_{A_i+\delta A_i}\left(p_i+\delta p_i\right)dS&=t_kp_iA_i-\left(t_k+\delta t_k\right)\left(p_i+\delta p_i\right)\left(A_i+\delta A_i\right).
\end{aligned}$$

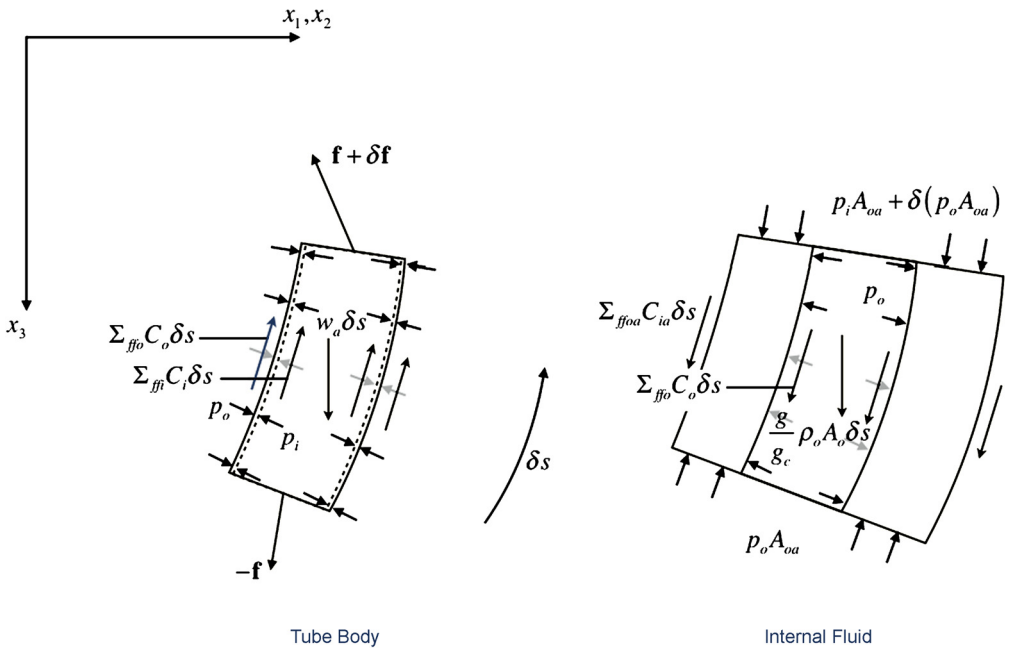

Figure 5.4 ***Forces due to fluid presence and flow in the annulus of a length of a tube.*** All forces associated with wall contact, as well as all moments, have been omitted from the figure for the sake of clarity. The global material coordinate system containing the unit vector $\mathbf{e}_3$ along the positive $X_3 = Z$ axis is not shown (see Fig. 5.2). The symbol δ is used, rather than d, to signal changes are not necessarily infinitesimal. The figure is drawn in the plane normal to the binormal vector at the element's lower end.

The treatment of external fluids is similar to that of internal fluids. Fig. 5.4 repeats the left-hand diagram of Fig. 5.3, with the right-hand diagram illustrating a control volume for the tube annulus. The control volume consists of a length δs along the annulus between the exterior of the tube and the interior of its confining hole.

With Eq. (5.72) applied to external flow $\Sigma_s = \Sigma_{ffo}$ in Fig. 5.4, $p = p_o$, $\rho = \rho_o$, and $V = V_o$, the annular volume of the tube for the distance δs. Using the same **t**–**n**–**b** coordinate system as was used with the internal fluid analysis, we now imagine an annular flow such that the fluid velocity **v** is equal in magnitude to $\frac{Q_a}{A_{oa}}$, where Q_a is annular volumetric flow rate, and is collinear with **t**. The cross-sectional area of the annulus is denoted A_{oa}. Finally, we subdivide the control volume into the following four segments:

- the surface S_o, where $\delta S_o = C_o \delta s$, $C_o = \pi D$ being the circumference of the tube based on its outside diameter;
- the surface S_{ia} that is the surface of the outer boundary of the annulus exposed to external fluid flow;
- the surface A_{oa} at the base (lower end) of the element in Fig. 5.4—the outward normal to this surface is $\breve{\mathbf{n}} = -\mathbf{t}$;

- the surface $A_{oa}+\delta A_{oa}$ at the upper end of the element—the outward normal to this surface is $\breve{\mathbf{n}}=\mathbf{t}+d\mathbf{t}$.

In a manner similar to that of Eq. (5.75) we can write for each position along s as

$$\begin{aligned}\nabla\cdot(\rho_o\mathbf{vv}) &= \left(\frac{\partial}{\partial s}\mathbf{t}\right)\cdot\left(\rho_o\frac{Q_a}{A_{oa}}\mathbf{t}\frac{Q_a}{A_{oa}}\mathbf{t}\right)\\ &= \frac{\partial\left[\rho_o\left(\frac{Q_a}{A_{oa}}\right)^2\mathbf{t}\right]}{\partial s}=\frac{\partial\left[\rho_o\left(\frac{Q_a}{A_{oa}}\right)^2\right]}{\partial s}\mathbf{t}+\left[\rho_o\left(\frac{Q_a}{A_{oa}}\right)^2\right]\kappa\mathbf{n},\end{aligned}\tag{5.78}$$

and Eq. (5.72) becomes

$$\begin{aligned}&\int_{S_o}\left[-p_o\breve{\mathbf{n}}-\Sigma_{ffo}\mathbf{t}\right]dS+\mathbf{t}\int_{A_{oa}}p_o dS-(\mathbf{t}+d\mathbf{t})\int_{A_{oa}+\delta A_{oa}}(p_o+dp_o)\,dS\\ &\quad+\int_{S_{ia}}\left[-p_o\breve{\mathbf{n}}-\Sigma_{ffoa}\mathbf{t}\right]dS+\frac{g}{g_c}\int_{V_o}\rho_o\mathbf{e}_3 dV\\ &\quad=\frac{1}{g_c}\int_{V_o}\left\{\frac{\partial\left[\rho_o\left(\frac{Q_a}{A_{oa}}\right)^2\mathbf{t}\right]}{\partial s}+\frac{\partial\left(\rho_o\frac{Q_a}{A_{oa}}\right)}{\partial\tau}\mathbf{t}\right\}dV,\\ &\int_{S_o}\left[-p_o\breve{n}_k-\Sigma_{ffo}t_k\right]dS+t_k\int_{A_{oa}}p_o dS-(t_k+dt_k)\int_{A_{oa}+\delta A_{oa}}(p_o+dp_o)\,dS\\ &\quad+\int_{S_{ia}}\left[-p_o\breve{n}_k-\Sigma_{ffoa}t_k\right]dS+\frac{g}{g_c}\int_{V_o}\rho_o\left(\mathbf{e}_3\cdot\mathbf{g}_k\right)dV\\ &\quad=\frac{1}{g_c}\int_{V_o}\left\{\frac{\partial\left[\rho_o\left(\frac{Q_a}{A_{oa}}\right)^2 t_k\right]}{\partial s}+\frac{\partial\left(\rho_o\frac{Q_a}{A_{oa}}\right)}{\partial\tau}t_k\right\}dV.\end{aligned}\tag{5.79}$$

Simplification of Eq. (5.79) proceeds in a manner identical to that used with Eq. (5.76). Under the assumptions of constant cross-sectional p_o and flow velocity collinear with $\mathbf{t}$,

$$\begin{aligned}&\int_{S_o}\left[-p_o\breve{\mathbf{n}}-\Sigma_{ffo}\mathbf{t}\right]dS+\mathbf{t}p_o A_{oa}-(\mathbf{t}+\delta\mathbf{t})\left(p_o+\delta p_o\right)\left(A_{oa}+\delta A_{oa}\right)\\ &\quad+\int_{S_{ia}}\left[-p_o\breve{\mathbf{n}}-\Sigma_{ffoa}\mathbf{t}\right]dS+\frac{g}{g_c}\int_{V_o}\rho_o\mathbf{e}_3 dV\\ &\quad=\frac{1}{g_c}\int_{V_o}\left\{\frac{\partial\left[\rho_o\left(\frac{Q_a}{A_{oa}}\right)^2\mathbf{t}\right]}{\partial s}+\frac{\partial\left(\rho_o\frac{Q_a}{A_{oa}}\right)}{\partial\tau}\mathbf{t}\right\}dV,\end{aligned}$$

$$\begin{aligned}
&\int_{S_o}\left[-p_o\breve{n}_k-\Sigma_{ffo}t_k\right]dS+t_kp_oA_{oa}-\left(t_k+\delta t_k\right)\left(p_o+\delta p_o\right)\left(A_{oa}+\delta A_{oa}\right) \\
&\quad+\int_{S_{ia}}\left[-p_o\breve{n}_k-\Sigma_{ffoa}t_k\right]dS+\frac{g}{g_c}\int_{V_o}\rho_o\left(\mathbf{e}_3\cdot\mathbf{g}_k\right)dV \\
&\quad=\frac{1}{g_c}\int_{V_o}\left\{\frac{\partial\left[\rho_o\left(\frac{Q_a}{A_{oa}}\right)^2\mathbf{t}\right]}{\partial s}+\frac{\partial\left(\rho_o\frac{Q_a}{A_{oa}}\right)}{\partial\tau}t_k\right\}dV.
\end{aligned}\tag{5.80}$$

We now have expressions of momentum balance for the fluid inside the tubular (Eq. (5.77), Fig. 5.3) and in the tubular's annulus (Eq. (5.80), Fig. 5.4). Next consider the left-hand portion of either Fig. 5.3 or Fig. 5.4 and the tractions to which the length of the tube conveying fluid is exposed. Adopting the nomenclature used earlier in the fluid momentum balances and summing forces gives

$$\begin{aligned}
&\delta\mathbf{f}+\frac{g}{g_c}\int_{V_s}\rho_s\mathbf{e}_3dV+\int_{S_i}\left[-p_i\breve{\mathbf{n}}+\Sigma_{ffi}\mathbf{t}\right]dS+\int_{S_o}\left[-p_o\breve{\mathbf{n}}+\Sigma_{ffo}\mathbf{t}\right]dS \\
&\quad=\int_{V_s}\frac{\rho_s}{g_c}\mathbf{a}dV, \\
&\delta f_k+\frac{g}{g_c}\int_{V_s}\rho_s\left(\mathbf{e}_3\cdot\mathbf{g}_k\right)dV+\int_{S_i}\left[-p_i\breve{n}_k+\Sigma_{ffi}t_k\right]dS+\int_{S_o}\left[-p_o\breve{n}_k+\Sigma_{ffo}t_k\right]dS \\
&\quad=\int_{V_s}\frac{\rho_s}{g_c}a_kdV,
\end{aligned}\tag{5.81}$$

where ρ_s is the mass density of steel and V_s is the volume of steel along length δs. At this point the cross-sectional area of the tubular may not be constant, so $dV_s=A_s(s)ds$.

In Eq. (5.81) the two surface integrals over S_i and S_o are matched by identical, but oppositely directed integrals in Eqs. (5.77) and (5.80). Eliminating these terms, we may combine[17] Eqs. (5.77), (5.80) and (5.81) to obtain

$$\delta\mathbf{f}+\frac{g}{g_c}\int_{V_s}\rho_s\mathbf{e}_3dV+\mathbf{t}p_iA_i-\left(\mathbf{t}+\delta\mathbf{t}\right)\left(p_i+\delta p_i\right)\left(A_i+\delta A_i\right)+\frac{g}{g_c}\int_{V_i}\rho_i\mathbf{e}_3dV$$

[17] The integrals $\int_{S_i}\left[-p_i\breve{\mathbf{n}}+\Sigma_{ffi}\mathbf{t}\right]dS$ and $\int_{S_o}\left[-p_o\breve{\mathbf{n}}+\Sigma_{ffo}\mathbf{t}\right]dS$ assume the same role as internal forces in a free body diagram. When two portions of a structure originally cut to view internal forces are rejoined, the internal forces on either side of the cut cancel each other. In the present case we recognize two facts:

- at any point on the surface S_i the normal $\breve{\mathbf{n}}$ on the tube is in the opposite direction of its counterpart at the same location on S_i for the fluid, and similarly for the surface S_o;
- the wall shear stress Σ_{ffi} on the tube is in the opposite direction of its counterpart on S_i for the fluid, and similarly for the surface S_o,

which, when applied to the integrals, render each fluid integral the negative of its tube counterpart.

$$
\begin{aligned}
&-\frac{1}{g_c}\int_{V_i}\left\{\frac{\partial\left[\rho_i\left(\frac{Q}{A_i}\right)^2\mathbf{t}\right]}{\partial s}+\frac{\partial\left(\rho_i\frac{Q}{A_i}\right)}{\partial\tau}\mathbf{t}\right\}dV+\mathbf{t}p_oA_{oa}\\
&-(\mathbf{t}+\delta\mathbf{t})\left(p_o+\delta p_o\right)\left(A_{oa}+\delta A_{oa}\right)+\frac{g}{g_c}\int_{V_o}\rho_o\mathbf{e}_3dV+\int_{S_{ia}}\left[-p_o\breve{\mathbf{n}}-\Sigma_{ffoa}\mathbf{t}\right]dS\\
&-\frac{1}{g_c}\int_{V_o}\left\{\frac{\partial\left[\rho_o\left(\frac{Q_a}{A_{oa}}\right)^2\mathbf{t}\right]}{\partial s}+\frac{\partial\left(\rho_o\frac{Q_a}{A_{oa}}\right)}{\partial\tau}\mathbf{t}\right\}dV=\int_{V_s}\frac{\rho_s}{g_c}\mathbf{a}dV,
\end{aligned}
\tag{5.82}
$$

$$
\begin{aligned}
&\delta f_k+\frac{g}{g_c}\int_{V_s}\rho_s\mathcal{G}_kdV+t_kp_iA_i-(t_k+\delta t_k)\left(p_i+\delta p_i\right)\left(A_i+\delta A_i\right)+\frac{g}{g_c}\int_{V_i}\rho_i\mathcal{G}_kdV\\
&-\frac{1}{g_c}\int_{V_i}\left\{\frac{\partial\left[\rho_i\left(\frac{Q}{A_i}\right)^2t_k\right]}{\partial s}+\frac{\partial\left(\rho_i\frac{Q}{A_i}\right)}{\partial\tau}t_k\right\}dV+t_kp_oA_{oa}-(t_k+\delta t_k)\\
&\times\left(p_o+\delta p_o\right)\left(A_{oa}+\delta A_{oa}\right)+\frac{g}{g_c}\int_{V_o}\rho_o\mathcal{G}_kdV+\int_{S_{ia}}\left[-p_o\breve{n}_k-\Sigma_{ffoa}t_k\right]dS\\
&-\frac{1}{g_c}\int_{V_o}\left\{\frac{\partial\left[\rho_o\left(\frac{Q_a}{A_{oa}}\right)^2t_k\right]}{\partial s}+\frac{\partial\left(\rho_o\frac{Q_a}{A_{oa}}\right)}{\partial\tau}t_k\right\}dV=\int_{V_s}\frac{\rho_s}{g_c}a_kdV,
\end{aligned}
$$

where for the index notation we have introduced the shorthand $\mathcal{G}_k=\left(\mathbf{e}_3\cdot\mathbf{g}_k\right)$.

Eq. (5.82) is formidable, but may be simplified with the following:

- As pointed out by Mitchell [27], both coiled tubing and aluminum drill pipe may come with tapered wall thickness. As our primary interest is casing and tubing, we assume a constant cross section for both the tubular and its confining hole,[18] that is, $\delta A_i=\delta A_o=\delta A_{ia}=\delta A_{oa}=0$. Further an integral over a flow stream volume—either inside the tube or in its annulus—is now associated with the path length, i.e., $\int_{V_i}\{\ldots\}\,dV=A_i\int_{\delta s}\{\ldots\}\,dl$ and[19] $\int_{V_o}\{\ldots\}\,dV=A_{oa}\int_{\delta s}\{\ldots\}\,dl$. For $\delta A_i=0$ we can write

$$
\mathbf{t}p_iA_i-(\mathbf{t}+\delta\mathbf{t})\left(p_i+\delta p_i\right)\left(A_i+\delta A_i\right)=-\left(\mathbf{t}\delta p_i+\delta\mathbf{t}p_i\right)A_i-\delta\mathbf{t}\delta p_iA_i,
\tag{5.83}
$$

[18] When addressing problems where either the tubular or its confining hole is a string consisting of a series of piecewise constant diameters, we work the problem for a series of control volumes, each member of the series having a tubular and confining hole of constant diameter.

[19] In the case of the annulus, moving A_{oa} outside the integral implies $A_{ia}-A_o$ is constant, that is, the tubular and its confining hole follow paths that are "parallel", although the two are not necessarily concentric. The two cross-section centers trace paths such that A_o and A_{ia} are in the same plane. For straight well bores, this offset would be measured as eccentricity.

and for $\delta A_o = \delta A_{ia} = \delta A_{oa} = 0$,

$$\mathbf{t} p_o A_{oa} - (\mathbf{t} + \delta\mathbf{t})\left(p_o + \delta p_o\right)\left(A_{oa} + \delta A_{oa}\right) = -\left(\mathbf{t}\delta p_o + \delta\mathbf{t} p_o\right) A_{oa} - \delta\mathbf{t}\delta p_o A_{oa}. \tag{5.84}$$

- We may remove the term $\int_{S_{ia}} \left[-p_o \breve{\mathbf{n}} - \Sigma_{ffoa}\mathbf{t}\right] dS$ that relates to the outer boundary of the annulus by the following adjustment. In Fig. 5.4, and as was also the case in Fig. 5.3, the lateral boundaries of the control volume are at the interface between the fluid and its confining tubular(s). This gives rise to the terms such as $\int_{S_{ia}} \left[-p_o \breve{\mathbf{n}} - \Sigma_{ffoa}\mathbf{t}\right] dS$, which have a counterpart associated with the tubular, both terms disappearing when we reassemble the fluid and tubular into a single control volume. For the term in focus, and since it has no direct effect on the inner tubular's tractions, we may proceed as follows:
  - introduce the assumption that the confining hole is rigid;
  - extend the outer boundary of the annulus control volume in Fig. 5.4 so that it encompasses the interface between the fluid and the confining hole (i.e., penetrates the material of the confining hole just slightly), thus eliminating $\int_{S_{ia}} \left[-p_o \breve{\mathbf{n}} - \Sigma_{ffoa}\mathbf{t}\right] dS$ as it is canceled by its counterpart on the former control volume boundary.
- A large number of problems are amenable to the case of steady flow for which $\frac{\partial}{\partial \tau} = 0$. If the flow is steady, we also have from continuity Eq. (5.66) $\nabla \cdot (\rho \mathbf{v}) = 0$, or for the flow channels internal and external to the tube, respectively,

$$\left(\frac{d}{ds}\mathbf{t}\right) \cdot \left(\rho_i \frac{Q}{A_i}\mathbf{t}\right) = \frac{d\left(\rho_i \frac{Q}{A_i}\right)}{ds} = 0 \quad \text{over } A_i, \tag{5.85}$$

$$\left(\frac{d}{ds}\mathbf{t}\right) \cdot \left(\rho_o \frac{Q_a}{A_{oa}}\mathbf{t}\right) = \frac{d\left(\rho_o \frac{Q_a}{A_{oa}}\right)}{ds} = 0 \quad \text{over } A_{oa} = A_{ia} - A_o. \tag{5.86}$$

With the above assumptions, Eq. (5.82) takes the form

$$\begin{aligned}
&\delta\mathbf{f} + \frac{g}{g_c}\mathbf{e}_3 \left[\rho_s A_s \delta s + A_i \int_{\delta s} \rho_i dl - A_o \int_{\delta s} \rho_o dl\right] \\
&\quad - \left[\delta\left(p_i\mathbf{t}\right) + \frac{1}{g_c}\int_{\delta s} \frac{d\left[\rho_i \left(\frac{Q}{A_i}\right)^2 \mathbf{t}\right]}{ds} dl\right] A_i + \left[\delta\left(p_o\mathbf{t}\right) + \frac{1}{g_c}\int_{\delta s} \frac{d\left[\rho_o \left(\frac{Q_a}{A_{oa}}\right)^2 \mathbf{t}\right]}{ds} dl\right] A_o \\
&\quad - \left\{\delta\left(p_o\mathbf{t}\right) + \frac{1}{g_c}\int_{\delta s} \frac{d\left[\rho_o \left(\frac{Q_a}{A_{oa}}\right)^2 \mathbf{t}\right]}{ds} dl\right\} A_{ia} + \frac{g}{g_c}\mathbf{e}_3 A_{ia} \int_{\delta s} \rho_o dl - \delta\mathbf{t}\delta p_i A_i - \delta\mathbf{t}\delta p_o A_{oa} \\
&\quad = \mathbf{0},
\end{aligned}$$

$$\delta f_k + \frac{g}{g_c}\left[\rho_s A_s \int_{\delta s} \mathcal{G}_k dl + A_i \int_{\delta s} \rho_i \mathcal{G}_k dl - A_o \int_{\delta s} \rho_o \mathcal{G}_k dl\right] \tag{5.87}$$
$$- \left[\delta\left(p_i t_k\right) + \frac{1}{g_c}\int_{\delta s} \frac{d\left[\rho_i \left(\frac{Q}{A_i}\right)^2 t_k\right]}{ds} dl\right] A_i + \left[\delta\left(p_o t_k\right) + \frac{1}{g_c}\int_{\delta s} \frac{d\left[\rho_o \left(\frac{Q_a}{A_{oa}}\right)^2 t_k\right]}{ds} dl\right] A_o$$
$$- \left\{\delta\left(p_o t_k\right) + \frac{1}{g_c}\int_{\delta s} \frac{d\left[\rho_o \left(\frac{Q_a}{A_{oa}}\right)^2 t_k\right]}{ds} dl\right\} A_{ia}$$
$$+ \frac{g}{g_c} A_{oa} \int_{\delta s} \rho_o \mathcal{G}_k dl - \delta t_k \delta p_i A_i - \delta t_k \delta p_o A_{oa} = 0.$$

Eq. (5.87) applies when δs is finite. If we now allow δs to tend toward the infinitesimal, then the quantities in the integrals become local values and, after a slight rearrangement of terms, we obtain

$$\underbrace{\frac{d\mathbf{f}}{ds} - \frac{d}{ds}\left\{\left[p_i + \frac{\rho_i}{g_c}\left(\frac{Q}{A_i}\right)^2\right]\mathbf{t}\right\} A_i + \frac{d}{ds}\left\{\left[p_o + \frac{\rho_o}{g_c}\left(\frac{Q_a}{A_{oa}}\right)^2\right]\mathbf{t}\right\} A_o}_{s \text{ derivative of effective force}}$$
$$+ \underbrace{\left(w_a + \gamma_i A_i - \gamma_o A_o\right)}_{\text{Effective weight}} \mathbf{e}_3$$
$$\underbrace{- \frac{d}{ds}\left\{\left[p_o + \frac{\rho_o}{g_c}\left(\frac{Q_a}{A_{oa}}\right)^2\right]\mathbf{t}\right\} A_{ia} + \gamma_o A_{ia}\mathbf{e}_3}_{\text{Contribution of confining hole}} = \mathbf{0},$$

$$\frac{df_k}{ds} - \frac{d}{ds}\left\{\left[p_i + \frac{\rho_i}{g_c}\left(\frac{Q}{A_i}\right)^2\right] t_k\right\} A_i + \frac{d}{ds}\left\{\left[p_o + \frac{\rho_o}{g_c}\left(\frac{Q_a}{A_{oa}}\right)^2\right] t_k\right\} A_o \tag{5.88}$$
$$+ \left[w_a + \left(\gamma_i A_i - \gamma_o A_o\right)\right]\mathcal{G}_k$$
$$- \frac{d}{ds}\left\{\left[p_o + \frac{\rho_o}{g_c}\left(\frac{Q_a}{A_{oa}}\right)^2\right] t_k\right\} A_{ia} + \gamma_o A_{ia}\mathcal{G}_k = 0.$$

Eq. (5.88) deserves examination:

- Consider the relation

$$f_{eff}\mathbf{t} = \left\{\left(\mathbf{f}\cdot\mathbf{t}\right) - \left[p_i + \frac{\rho_i}{g_c}\left(\frac{Q}{A_i}\right)^2\right] A_i + \left[p_o + \frac{\rho_o}{g_c}\left(\frac{Q_a}{A_{oa}}\right)^2\right] A_o\right\}\mathbf{t},$$
$$f_{eff}\, t_k = \left\{f_t - \left[p_i + \frac{\rho_i}{g_c}\left(\frac{Q}{A_i}\right)^2\right] A_i + \left[p_o + \frac{\rho_o}{g_c}\left(\frac{Q_a}{A_{oa}}\right)^2\right] A_o\right\} t_k. \tag{5.89}$$

This is a generalization[20] of the effective force[21] discussed extensively in Chapter 10 and defined in Eq. (10.1) for the case of no fluid flow. If we differentiate Eq. (5.89) as required by Eq. (5.88), then

$$\begin{aligned}\frac{d\left(f_{eff}\mathbf{t}\right)}{ds} &= \left\{\frac{df_t}{ds} - \frac{d}{ds}\left[p_i + \frac{\rho_i}{g_c}\left(\frac{Q}{A_i}\right)^2\right]A_i + \frac{d}{ds}\left[p_o + \frac{\rho_o}{g_c}\left(\frac{Q_a}{A_{oa}}\right)^2\right]A_o\right\}\mathbf{t} \\ &\quad + \underbrace{\left\{f_t - \left[p_i + \frac{\rho_i}{g_c}\left(\frac{Q}{A_i}\right)^2\right]A_i + \left[p_o + \frac{\rho_o}{g_c}\left(\frac{Q_a}{A_{oa}}\right)^2\right]A_o\right\}}_{f_{eff}}\kappa\mathbf{n}, \\ \frac{d\left(f_{eff}t_k\right)}{ds} &= \left\{\frac{df_t}{ds} - \frac{d}{ds}\left[p_i + \frac{\rho_i}{g_c}\left(\frac{Q}{A_i}\right)^2\right]A_i + \frac{d}{ds}\left[p_o + \frac{\rho_o}{g_c}\left(\frac{Q_a}{A_{oa}}\right)^2\right]A_o\right\}\mathbf{t} \\ &\quad + \left\{f_t - \left[p_i + \frac{\rho_i}{g_c}\left(\frac{Q}{A_i}\right)^2\right]A_i + \left[p_o + \frac{\rho_o}{g_c}\left(\frac{Q_a}{A_{oa}}\right)^2\right]A_o\right\}\kappa\mathbf{n}.\end{aligned} \tag{5.90}$$

Section 10.2.1 of Chapter 10, and especially Fig. 10.4, offers a visual, qualitative explanation of the influence of the pressure terms in the expression for effective force in buckling and bending environments. Eq. (5.90) complements that discussion with a mathematical explanation for the effect of internal and external pressure. Differentiation of the effective force introduces an **n** component which acts laterally on the tubular either promoting bending (internal pressure and flow[22]) by diminishing the effect of f_t or opposing bending (annulus pressure and flow) by incrementing f_t in the direction of more tension.

- The effective weight term is the same discussed in Chapter 10 and defined in Eq. (10.2).
- Although our primary interest is in the first two terms—these terms involve direct fluid contact with the inner tube—we must solve the entire momentum balance to properly account for flow in the annulus. As noted by Mitchell [27], this can be difficult for eccentric annuli. We can take some comfort in Mitchell's conclusion that often the annular flow effects can be ignored because they are small. As we continue, we will assume that this difficult calculation has been accomplished.

[20] It is not a complete generalization. We are assuming A_i and A_o are constant and steady fluid flow.

[21] As a further generalization of the effective force, one could also consider the **n** and **b** components of **f**. At some point, however, the connection with the classic meaning of effective force begins to fade.

[22] Experientially, the internal flow term, coupled with the curvature κ, acts as city water pressure does to rotate the curved nozzles on a lawn sprinkler.

- In their current forms, p_i and p_o are total pressures. In some instances it will be useful to distinguish between the components of the total pressure [33]:

$$dp_i + \frac{1}{g_c} d\left[\rho_i \left(\frac{Q}{A_i}\right)^2\right] - \frac{g}{g_c}\rho_i \left(\mathbf{e}_3 \cdot \mathbf{t}\right) ds + \Sigma_{ffi} C_i ds = 0,$$
$$dp_o + \frac{1}{g_c} d\left[\rho_o \left(\frac{Q_a}{A_{oa}}\right)^2\right] - \frac{g}{g_c}\rho_o \left(\mathbf{e}_3 \cdot \mathbf{t}\right) ds + \left(\Sigma_{ffo} C_o + \Sigma_{ffoa} C_{ia}\right) ds = 0, \tag{5.91}$$

where the signs of the pressure terms conform to the assumed directions of flow in Figs. 5.3 and 5.4.

We are now in a position to record the character of $\mathbf{q}_f$ from Eqs. (5.88) and (5.90) as

$$\begin{aligned}\mathbf{q}_f &= -\frac{d}{ds}\left\{\left[p_i + \frac{\rho_i}{g_c}\left(\frac{Q}{A_i}\right)^2\right]\mathbf{t}\right\} A_i + \frac{d}{ds}\left\{\left[p_o + \frac{\rho_o}{g_c}\left(\frac{Q_a}{A_{oa}}\right)^2\right]\mathbf{t}\right\} A_o \\ &\quad + \left(w_a + \gamma_i A_i - \gamma_o A_o\right)\mathbf{e}_3, \\ \left(\mathbf{q}_f\right)_k &= -\frac{d}{ds}\left\{\left[p_i + \frac{\rho_i}{g_c}\left(\frac{Q}{A_i}\right)^2\right] t_k\right\} A_i + \frac{d}{ds}\left\{\left[p_o + \frac{\rho_o}{g_c}\left(\frac{Q_a}{A_{oa}}\right)^2\right] t_k\right\} A_o \\ &\quad + \left[w_a + \left(\gamma_i A_i - \gamma_o A_o\right)\right]\left(\mathbf{e}_3 \cdot \mathbf{g}_k\right).\end{aligned} \tag{5.92}$$

Contact traction with confining hole $\mathbf{q}_c$ [34–39] Each infinitesimal length of this distributed load lies in the **b**–**n** plane normal to the tangent of the tube centerline. Further, $\mathbf{q}_c$ is normal to the surface of the tube at the point of contact and is therefore directed radially inward:

$$\mathbf{q}_c \cdot \mathbf{t} = 0, \quad \mathbf{q}_c = -\left|\mathbf{q}_c\right| \mathbf{g}_r, \quad q_{ci} t_i = 0, \quad \left(\mathbf{q}_c\right)_i = -\left|\mathbf{q}_c\right| \left(\mathbf{g}_r \cdot \mathbf{g}_i\right), \tag{5.93}$$

where $\mathbf{g}_r$ is a unit vector from the center of the tube (see Fig. 5.5) and $\mathbf{g}_i$ is either **n** or **b**.

Frictional traction from confining hole $\mathbf{q}_{fr}$ [34–37,40,38,39] Associated with the contact traction is a distributed friction force which is opposite in direction to the relative actual or impending velocity between the tube and its confining hole. Using a Coulomb friction model, the resisting traction from the confining hole wall is

$$\mathbf{q}_{fr} = \begin{cases} -\mathbf{q}_s & \text{if } \left|\mathbf{q}_s\right| \le \mu_s \left|\mathbf{q}_c\right|, \\ -\mu_k \left|\mathbf{q}_c\right| \frac{\mathbf{v}}{|\mathbf{v}|} & \text{if } \left|\mathbf{q}_s\right| > \mu_s \left|\mathbf{q}_c\right|, \end{cases} \tag{5.94}$$

where μ_s is the static coefficient of friction, μ_k is the kinetic coefficient of friction, $\mathbf{q}_s$ is the shear traction between the tube and its confining hole. The behavior of μ is illus-

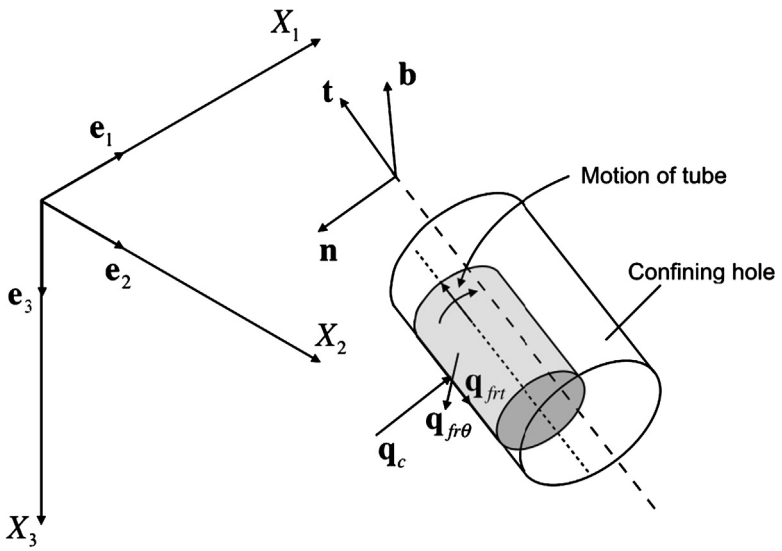

Figure 5.5 ***Distributed contact forces on an infinitesimal length of a tube.*** The dashed line representing the centerline of the beam is collinear with **t**. As indicated the tube is simultaneously moving in the direction of positive **t** and rotating about its centerline in a positive sense according to the right-hand rule. Distributed contact traction $\mathbf{q}_c$ is in the **b**–**n** plane normal to **t**. Distributed contact friction $\mathbf{q}_{fr\theta}$ due to rotation is in this same plane. Distributed contact friction $\mathbf{q}_{frt}$ due to axial movement is parallel to **t**.

trated in Fig. 5.6 for forces acting on a block [41]. Up to the point that the imposed force f_s exceeds a value $\mu_s f_c$, the friction force f_{fr} is equal to f_s in magnitude and opposite to $\mathbf{f}_s$ in direction. Once static friction is "broken", f_{fr} takes the constant value $\mu_k f_c$ and is opposite to $\mathbf{v}$ in direction, where $\mathbf{v}$ is the relative velocity between the surfaces in contact.

Decomposing the frictional traction into axial and circumferential components gives

$$\mathbf{q}_{fr} = \underbrace{(\mathbf{q}_{fr} \cdot \mathbf{t})\,\mathbf{t}}_{\text{Axial}} + \underbrace{(\mathbf{q}_{fr} \cdot \mathbf{g}_\theta)\,\mathbf{g}_\theta}_{\text{Circumferential}},$$
$$(\mathbf{q}_{fr})_k = \left[(\mathbf{q}_{fr})_i\, t_i\right] t_k, \quad (\mathbf{q}_{fr})_k = \left[(\mathbf{q}_{fr})_i\, (\mathbf{g}_\theta)_i\right] (\mathbf{g}_\theta)_k, \tag{5.95}$$

where $\mathbf{g}_\theta$ is a unit vector in the same local (to the tube) cylindrical coordinate system as $\mathbf{g}_r$ and the subscripts i and k refer to the spatial coordinate system upon which the **t**-**n**-**b** system is based. The axial component of $\mathbf{q}_{fr}$ can be positive or negative depending on the direction of axial movement relative to the local unit vector **t**.

Kinematics

The strains are infinitesimal. Further, in accordance with conventional beam theory, we assume that cross-sections remain plane during deformation, regardless of whether the

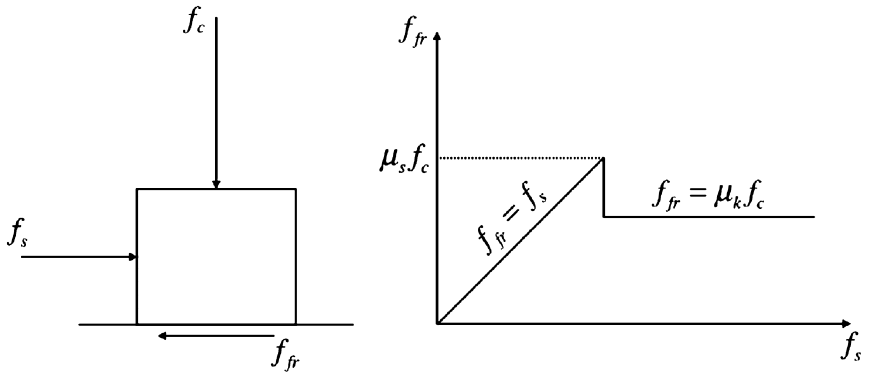

Figure 5.6 ***Illustration of the Coulomb friction model.*** In the simple diagram of a block on a surface, forces rather than distributed tractions are depicted. The coefficients of friction μ_s and μ_k are assumed to be independent of the surface area of contact and the relative velocity between the surfaces.

deformation is elastic or inelastic. Consider an isothermal tube (beam) that is originally straight (as it sets on the rack at the rig site) but deforms due to the action of external forces and moments (as it undergoes service loads, Fig. 5.2).

To describe the deformation, we employ a coordinate system such as depicted in Fig. 5.2 where the following relations hold (see Appendix B):

- **t** is directed along the instantaneous centerline of the tube;
- **n** is normal to **t** (i.e., lies in the plane of the deformed cross-section) and points toward the instantaneous center of curvature of the centerline of the tube;
- $\mathbf{b} = \mathbf{t} \times \mathbf{n}$.

This is the same coordinate system employed previously, redefined here solely for clarity. Fig. 5.7 depicts the deformation of the tube from its initial state. If the displacements and displacement gradients are infinitesimal, then the axial strain (see subsection 'Extension' in Section 3.6.3.1 of Chapter 3) along fiber $\overline{be}$ is

$$\breve{E}_{tt} = \frac{1}{\kappa}\frac{d\theta}{dS} - 1, \quad \overline{be}. \tag{5.96}$$

For fibers along $\overline{ad}$ and $\overline{cf}$,

$$\begin{aligned} \breve{E}_{tt} &= \frac{\frac{d\theta}{\kappa} + |\gamma|\, d\theta}{dS} - 1 \approx \breve{E}_{tt0} + |\gamma|\,\kappa, \quad \overline{cf}, \\ \breve{E}_{tt} &= \frac{\frac{d\theta}{\kappa} - |\gamma|\, d\theta}{dS} - 1 \approx \breve{E}_{tt0} - |\gamma|\,\kappa, \quad \overline{ad}, \end{aligned} \tag{5.97}$$

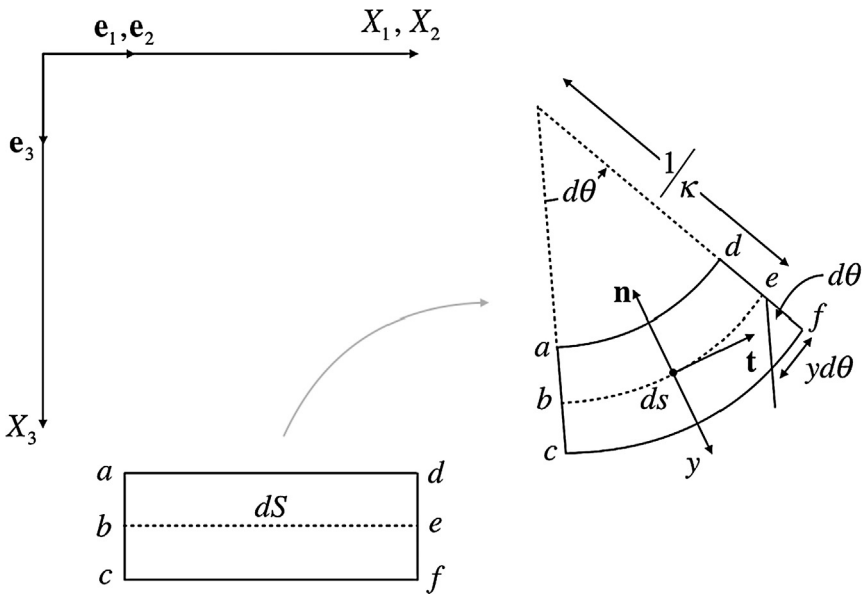

Figure 5.7 ***Axial strain in a tube acting as a beam.*** The differential element *dS* is deformed to *ds*, with the **t** and **n** axes forming the instantaneous plane of curvature in which *ds* lies. The deformation is greatly exaggerated in the figure. The **b** unit vector points out of the paper.

where the added subscript "0" is applied to the middle surface[23] of the tube and the $\approx$ sign refers to $ds \approx dS$ for infinitesimal strain. Either above or below the beam middle surface the strain is a linear function of γ, and since the slope is κ both above and below the middle surface, the cross-section remains plane. The γ-axis is directed opposite to **n** so that fibers that stretch have a positive strain. Generally, we write

$$\hat{\check{E}}_{tt}(\gamma) = \check{E}_{tt0} + \gamma\kappa. \tag{5.98}$$

As the beam bends its cross-section will also deform. On the tension side ($\gamma > 0$), the cross-section will become thinner and shorter; on the compression side ($\gamma > 0$), the cross-section will become wider and longer. We shall ignore this distortion associated with Poisson's ratio, which is equivalent to stating $\check{E}_{bb} = \check{E}_{nn} = 0$. From Eqs. (5.25)–(5.27),

$$\check{E}_{nn} = 0, \tag{5.99}$$

$$\check{E}_{bb} = 0, \tag{5.100}$$

[23] The middle surface of the tube passes through the centroid of the tube cross-section and has **n** as its instantaneous normal.

$$\hat{\check{E}}_{tt}(\gamma) = \frac{1}{E}\Sigma_{tt}(\gamma) = \check{E}_{tt0} + \gamma\kappa, \quad \hat{\Sigma}_{tt}(\gamma) = E\left(\check{E}_{tt0} + \gamma\kappa\right) = \Sigma_a + \hat{\Sigma}_b(\gamma), \tag{5.101}$$

where Σ_a captures the portion of axial stress not associated with bending and Σ_b is the portion of axial stress due to bending. Both the elastic axial stress and strain are linear in distance from the middle surface.

The section axial force and section moment along the **b**-axis on the tube are, respectively,

$$f_t = \mathbf{f}\cdot\mathbf{t} = \int_{A_s}\hat{\Sigma}_{tt}(\gamma)dA = E\int_{A_s}\left[\check{E}_{tt0} + \gamma\kappa\right]dA = E\left(\check{E}_{tt0}A_s + \kappa\int_{A_s}\gamma dA\right), \tag{5.102}$$

$$m_b = \mathbf{m}\cdot\mathbf{b} = \int_{A_s}\hat{\Sigma}_{tt}(\gamma)\gamma dA = E\int_{A_s}\left[\left(\check{E}_{tt0} + \gamma\kappa\right)\gamma\right]dA = E\left(\check{E}_{tt0}\int_{A_S}\gamma dA + \kappa\int_{A_s}\gamma^2 dA\right). \tag{5.103}$$

For a hollow circular cross-section such as a tube,

$$\int_{A_s}\gamma dA = \int_{\frac{d}{2}}^{\frac{D}{2}}\int_0^{2\pi}(r\sin\theta)\,rd\theta\,dr = \int_{\frac{d}{2}}^{\frac{D}{2}}\left[-\cos\theta\right]_0^{2\pi}r^2dr = 0, \tag{5.104}$$

$$\begin{aligned} I &= \int_{A_s}\gamma^2 dA = \int_{\frac{d}{2}}^{\frac{D}{2}}\int_0^{2\pi}(r\sin\theta)^2\,rd\theta\,dr \\ &= \int_{\frac{d}{2}}^{\frac{D}{2}}\left[\frac{1}{2}(\theta - \sin\theta\cos\theta)\right]_0^{2\pi}r^3dr = \pi\left[\frac{r^4}{4}\right]_{\frac{d}{2}}^{\frac{D}{2}} = \frac{\pi}{64}\left(D^4 - d^4\right), \end{aligned} \tag{5.105}$$

so that Eqs. (5.102) and (5.103), respectively, become

$$f_t = E\check{E}_{tt0}A_s, \tag{5.106}$$

$$m_b = E\kappa I = E\kappa\frac{\pi}{64}\left(D^4 - d^4\right). \tag{5.107}$$

The product EI in Eq. (5.107) is the bending stiffness.

We also introduce shear force components f_n and f_b in the **n** and **b** directions, respectively, and the torsion m_t, although for casing and tubing our use for the latter will be minimal. Returning to Eqs. (5.59) and (5.61), with

$$\mathbf{f} = f_t\mathbf{t} + f_n\mathbf{n} + f_b\mathbf{b}, \tag{5.108}$$

and

$$\mathbf{m} = m_t\mathbf{t} + m_b\mathbf{b}, \tag{5.109}$$

and recalling Eqs. (B.3), (B.11) and (B.9), respectively, for the derivatives of **t**, **n** and **b**, we can write

$$\left(\frac{df_t}{ds} - \kappa f_n\right)\mathbf{t} + \left(\frac{df_n}{ds} + \kappa f_t - \tau f_b\right)\mathbf{n} + \left(\frac{df_b}{ds} + \tau f_n\right)\mathbf{b} + \mathbf{q} = \frac{\rho}{g_c}\mathbf{a}A_s, \tag{5.110}$$

$$\left(\frac{dm_t}{ds}\right)\mathbf{t} + \left(\kappa m_t - \tau m_b - f_b\right)\mathbf{n} + \left(\frac{dm_b}{ds} + f_n\right)\mathbf{b} + \mathbf{c} = 0. \tag{5.111}$$

The equations for the individual components of the force **f** and moment **m** are therefore

$$\frac{df_t}{ds} - \kappa f_n + q_t = \frac{\rho}{g_c}a_t A_s, \tag{5.112}$$

$$\frac{df_n}{ds} + \kappa f_t - \tau f_b + q_n = \frac{\rho}{g_c}a_n A_s, \tag{5.113}$$

$$\frac{df_b}{ds} + \tau f_n + q_b = \frac{\rho}{g_c}a_b A_s, \tag{5.114}$$

$$\frac{dm_t}{ds} + c_t = 0, \tag{5.115}$$

$$\kappa m_t - \tau m_b - f_b + c_n = 0, \quad \kappa m_t - \tau EI\kappa - f_b + c_n = 0, \tag{5.116}$$

$$\frac{dm_b}{ds} + f_n + c_b = 0, \quad EI\frac{d\kappa}{ds} + f_n + c_b = 0, \tag{5.117}$$

where in Eqs. (5.116) and (5.117) we have included the results from Eq. (5.107). For equilibrium, the components of **a** on the right-hand side of Eqs. (5.112)–(5.114) vanish.

Example problem—contact force Consider a tubular at equilibrium ($\mathbf{a} = \mathbf{0}$). Tubular designs often assume that the only nonzero component of **f** is f_t (i.e., $f_n = f_b = 0$). Under this assumption, derive an equation for the contact traction distribution q_c.

From Eqs. (5.113) and (5.114) we have

$$\kappa f_t + q_n = 0, \quad q_b = 0. \tag{5.118}$$

The components q_n and q_b have two constituents—one due to contact (our unknown) and one due to $\mathbf{q}_f$. We write

$$q_n = \mathbf{n}\cdot\left(\mathbf{q}_c + \mathbf{q}_f\right), \quad q_b = \mathbf{b}\cdot\left(\mathbf{q}_c + \mathbf{q}_f\right). \tag{5.119}$$

From Eq. (5.92) under a condition of no flow,

$$\mathbf{n}\cdot\mathbf{q}_f = -\left(p_i A_i - p_o A_o\right)\kappa + w_{eff}\left(\mathbf{e}_3\cdot\mathbf{n}\right), \quad \mathbf{b}\cdot\mathbf{q}_f = w_{eff}\left(\mathbf{e}_3\cdot\mathbf{b}\right), \tag{5.120}$$

where $w_a + (\gamma_i A_i - \gamma_o A_o)$ (see Eq. (10.2)). From Eq. (5.93),

$$\mathbf{n}\cdot\mathbf{q}_c = -\left|\mathbf{q}_c\right|\cos\eta, \quad \mathbf{b}\cdot\mathbf{q}_c = -\left|\mathbf{q}_c\right|\sin\eta, \tag{5.121}$$

where η is the angle between $\mathbf{g}_r$ and the instantaneous $\mathbf{n}$ unit vector (see Eq. (5.93)).

From Eq. (B.4), and assuming the centerline of the tubular conforms to the centerline of the wellbore, the curvature κ in Eq. (5.118) is

$$\kappa = \left| \frac{d\hat{\mathbf{t}}}{ds} \right|, \tag{5.122}$$

where from Eq. (B.16) we get

$$\mathbf{t} = \hat{\mathbf{t}}(s) = \sin\theta\cos\phi\,\mathbf{e}_1 + \sin\theta\sin\phi\,\mathbf{e}_2 + \cos\theta\,\mathbf{e}_3, \tag{5.123}$$

where θ is the inclination of the wellbore from vertical ($\mathbf{e}_3 \cdot \mathbf{t} = \cos\theta$) and ϕ is the azimuth ($\mathbf{e}_1 \cdot \mathbf{t} = \sin\theta\cos\phi$). The derivative of $\mathbf{t}$ with respect to the wellbore centerline coordinate s is

$$\begin{aligned} \frac{d\hat{\mathbf{t}}}{ds} = &\left(-\sin\theta\sin\phi\frac{d\phi}{ds} + \cos\theta\cos\phi\frac{d\theta}{ds} \right)\mathbf{e}_1 + \left(\sin\theta\cos\phi\frac{d\phi}{ds} + \cos\theta\sin\phi\frac{d\theta}{ds} \right)\mathbf{e}_2 \\ &- \sin\theta\frac{d\theta}{ds}\mathbf{e}_3, \end{aligned} \tag{5.124}$$

in the global material coordinate system (see Fig. 3.1). Using Eq. (5.123) to evaluate Eq. (5.122) produces

$$\begin{aligned} \kappa &= \sqrt{\frac{d\hat{\mathbf{t}}}{ds} \cdot \frac{d\hat{\mathbf{t}}}{ds}} \\ &= \left[\left(-\sin\theta\sin\phi\frac{d\phi}{ds} + \cos\theta\cos\phi\frac{d\theta}{ds} \right)^2 + \left(\sin\theta\cos\phi\frac{d\phi}{ds} + \cos\theta\sin\phi\frac{d\theta}{ds} \right)^2 \right. \\ &\quad \left. + \left(-\sin\theta\frac{d\theta}{ds} \right)^2 \right]^{\frac{1}{2}} \\ &= \sqrt{\left(\sin\theta\frac{d\phi}{ds} \right)^2 + \left(\frac{d\theta}{ds} \right)^2}. \end{aligned} \tag{5.125}$$

Combining Eqs. (5.118)–(5.121), the $\mathbf{n}$ component of $\mathbf{q}_c$ is

$$\kappa f_t - |\mathbf{q}_c|\cos\eta - \left(p_i A_i - p_o A_o\right)\kappa + w_{eff}\left(\mathbf{e}_3 \cdot \mathbf{n}\right) = 0, \tag{5.126}$$

or

$$\begin{aligned} |\mathbf{q}_c|\cos\eta &= \kappa f_t - \left(p_i A_i - p_o A_o\right)\kappa + w_{eff}\left(\mathbf{e}_3 \cdot \mathbf{n}\right) \\ &= f_{eff}\kappa + w_{eff}\left(\mathbf{e}_3 \cdot \mathbf{n}\right), \end{aligned} \tag{5.127}$$

where κ is given by Eq. (5.125). Similarly, for the $\mathbf{b}$ component of $\mathbf{q}_c$ we have

$$|\mathbf{q}_c| \sin\eta = w_{\mathit{eff}} \left(\mathbf{e}_3 \cdot \mathbf{b}\right). \tag{5.128}$$

Squaring and summing Eqs. (5.127) and (5.128) yields

$$|\mathbf{q}_c|^2 = f_{\mathit{eff}}^2 \kappa^2 + 2 f_{\mathit{eff}}\, \kappa\, w_{\mathit{eff}} \left(\mathbf{e}_3 \cdot \mathbf{n}\right) + w_{\mathit{eff}}^2 \left(\mathbf{e}_3 \cdot \mathbf{n}\right)^2 + w_{\mathit{eff}}^2 \left(\mathbf{e}_3 \cdot \mathbf{b}\right)^2. \tag{5.129}$$

Guided by the insight of Mitchell and Samuel [37], we can write

$$\mathbf{e}_3 \cdot \mathbf{t} = \cos\theta, \qquad \frac{d}{ds}\left(\mathbf{e}_3 \cdot \mathbf{t}\right) = \mathbf{e}_3 \cdot \frac{d\mathbf{t}}{ds} = \kappa\, \mathbf{e}_3 \cdot \mathbf{n} = -\sin\theta \frac{d\theta}{ds}, \tag{5.130}$$

where we make use of Eq. (B.3) and of the fact that $\frac{d\mathbf{e}_3}{ds} = \mathbf{0}$. Since $\mathbf{e}_3$ is a unit vector, we may also write

$$1 - \left(\mathbf{e}_3 \cdot \mathbf{t}\right)^2 = \left(\mathbf{e}_3 \cdot \mathbf{n}\right)^2 + \left(\mathbf{e}_3 \cdot \mathbf{b}\right)^2 = \sin^2\theta. \tag{5.131}$$

If we substitute Eqs. (5.125), (5.130) and (5.131) into Eq. (5.129), then

$$\begin{aligned} |\mathbf{q}_c|^2 &= f_{\mathit{eff}}^2 \kappa^2 - 2 f_{\mathit{eff}} w_{\mathit{eff}} \sin\theta \frac{d\theta}{ds} + w_{\mathit{eff}}^2 \sin^2\theta \\ &= \left(f_{\mathit{eff}} \sin\theta \frac{d\phi}{ds}\right)^2 + \left(f_{\mathit{eff}} \frac{d\theta}{ds} - w_{\mathit{eff}} \sin\theta\right)^2, \end{aligned} \tag{5.132}$$

or

$$|\mathbf{q}_c| = \sqrt{\left(f_{\mathit{eff}} \sin\theta \frac{d\phi}{ds}\right)^2 + \left(f_{\mathit{eff}} \frac{d\theta}{ds} - w_{\mathit{eff}} \sin\theta\right)^2}. \tag{5.133}$$

This same expression was derived by Sheppard et al. [42].

CHAPTER 6

Yield and Inelastic Behavior

6.1. INTRODUCTION

Elastic behavior as described in Chapter 5 is limited to a material-dependent range of stress (or strain[1]). Beyond that range, the material yields, and its behavior is then governed by the theory of plasticity.

Plastic behavior complicates analysis and, in addition to altered behavior, also signifies that the material is undergoing increasing damage to its crystalline structure. For this reason, yield, marking the onset of plastic behavior, is usually taken as one of the two major mechanical limit states for the tube body,[2] the other being collapse (Chapter 8). Notable exceptions to the designation of yield as a limit state include the expansion process of solid expandable tubulars, investigation of actual rupture of the tube body and the plastic collapse mode for external pressure loading.

A complete description of plastic behavior involves three phenomena—yield, a flow rule and a hardening law. Yield marks the departure from elastic behavior and is defined by a surface in a space having components of stress as its coordinate axes. Once yield occurs and plastic deformation begins, the flow rule determines the increment or rate of deformation experienced. This deformation can both displace and distort the original yield surface, the alteration of the yield surface being addressed by the hardening law.

In the sections to follow, each of the above aspects of plasticity is discussed in more detail for the case of multiple active stresses. As a phenomenological bearing, however, we begin the discussion with a one-dimensional load state.

A word on terminology is in order. Throughout the majority of this book the preferred stress is the Cauchy stress, $\boldsymbol{\Sigma}$, which is defined relative to the deformed state of the body in focus. As described in Section 4.3.1.1 of Chapter 4, however, the conventional stress definition for a uniaxial tension test is the Piola–Kirchhoff stress of the first kind, $\mathbf{S}$—the so-called engineering stress. We will maintain this distinction in the present chapter as follows. When discussing conventional uniaxial stress–strain curves at the onset, $\mathbf{S}$ will be used. Later, when the discussion turns to multidimensional topics and the general theory, $\boldsymbol{\Sigma}$ will be the stress definition of choice.

[1] The elastic limit and possible inelastic behavior are usually referred to a multidimensional stress space. There are instances, however, when it is more convenient to refer elastic-plastic behavior to strain space. For the theoretical background of strain space plasticity see [43]; for an example application see [44]. The treatment of elastic limit and possible inelastic behavior here will only address stress space plasticity.

[2] Yield of the critical cross-section of a connection is also a limit state. Long before the connection yields at its critical cross-section, however, one can expect minor yielding at the roots of some threads.

Elements of Oil and Gas Well Tubular Design
DOI: 10.1016/B978-0-12-811769-9.00006-2

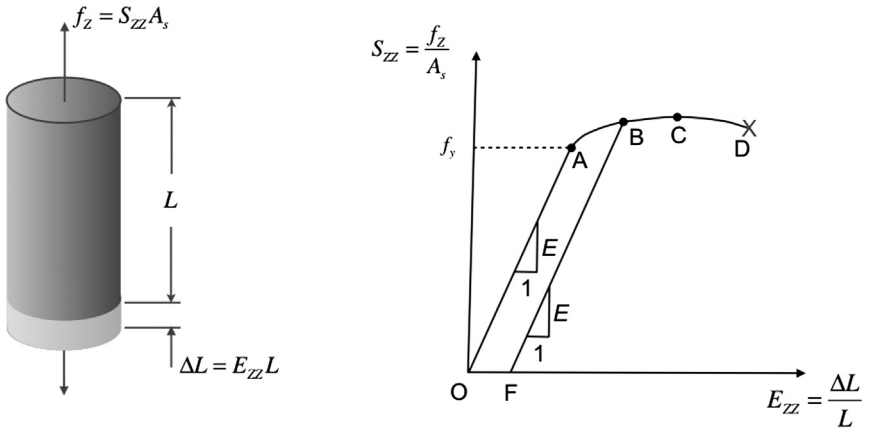

Figure 6.1 ***Typical uniaxial stress–strain curve.***

6.2. THE UNIAXIAL STRESS–STRAIN CURVE

Fig. 6.1 illustrates typical one-dimensional behavior of a crystalline solid such as steel in a uniaxial tension test. A circular cylindrical specimen is subjected to tension along its axis, while simultaneously measuring the elongation of the specimen from its original length. The axes of the graph are axial strain (see subsection 'Extension' in Section 3.6.3.1 of Chapter 3) and axial stress.[3,4]

Starting at the origin (point O), application of tension to the specimen in the region $0 \leq S_{ZZ} \leq f_y$ elicits elastic response characterized by the following two behaviors:

- Linear. The relation between axial stress and axial strain is a straight line. The equation for this line is

$$S_{ZZ} = E\,E_{ZZ}, \tag{6.1}$$

  where E, the slope of the stress–strain line, is Young's modulus.
- Recoverable. If the axial stress is increased, resulting in a corresponding strain determined by line OA, upon removal of the axial stress, all of the axial strain is recovered, and the stress–strain state returns to the origin.

The above response is characterized as elastic as discussed in Chapter 5.

[3] Strictly speaking, the external load is a traction. Due to (a) the fact that in this uniaxial experiment the traction and the axial stress are intimately related and (b) the long history of using stress in naming the curve in Fig. 6.1, we will leave well enough alone and call the axial component of load intensity "stress".

[4] One could choose elongation and force as the coordinate axes in Fig. 6.1. Doing so renders the figure dependent on the geometry of the specimen. By using relative elongation (strain) and force intensity (stress) the geometry of the sample is accounted for, and the response curve only depends on the specimen material.

6.2.1 Yield on a uniaxial stress–strain curve

Once the stress–strain path passes point A ($S_{ZZ} > f_y$), both of the above elastic characteristics are lost, and the response of the material becomes elastic-plastic, characterized by the following two changes to purely elastic behavior:

- Nonlinear. As depicted in Fig. 6.1, the portion of the stress–strain curve between points A and D no longer has constant slope; the stress–strain relation is no longer linear. The instantaneous or local slope of the stress–strain curve between points A and D is the tangent modulus

$$E_t = \frac{dS_{ZZ}}{dE_{ZZ}}. \tag{6.2}$$

  Some developments in plasticity theory also employ the secant modulus which is the ratio of total stress to total strain

$$E_s = \frac{S_{ZZ}}{E_{ZZ}}, \tag{6.3}$$

  where $E_t \leq E_s \leq E$, the equal signs applying in the elastic region of the stress–strain curve.
- Irrecoverable. As illustrated in Fig. 6.1, imagine that loading of a specimen proceeds from the origin to point A and then continues to point B. If the specimen is unloaded from this stress level, it will not retrace the path BAO but rather will follow a path BF that is parallel to path OA. When all axial load has been removed from the specimen, it will have accrued a permanent change in length characterized by the residual axial strain OF, commonly designated plastic strain.

The importance of point A and its corresponding value f_y on the S_{ZZ}-axis is clear. Point A serves as a boundary between elastic and elastic-plastic behavior, a boundary between two approaches to modeling the constitution of the specimen material. The value of f_y, termed the yield stress,[5] thus becomes a key parameter in defining the yield limit state. In this regard, consider the left-hand diagram in Fig. 6.2.

[5] From a metallurgical point of view, a number of important boundaries lie in the vicinity of point A [45,14]:

- the elastic limit—the greatest stress the material can experience without suffering permanent strain when the load is removed;
- the proportional limit—usually slightly less than the elastic limit, this is the maximum stress for which Eq. (6.1) is valid;
- the yield stress—usually *defined* to be slightly greater than the elastic limit, the two are tantamount;
- the upper yield point—usually slightly higher than the yield stress, this is a stress realized by some materials with a flat postyield stress–strain curve. Immediately following the strain corresponding to the upper yield point, the stress–strain curve drops to a plateau, with stress remaining constant for an appreciable range of strain.

In tubular design, and therefore in this book, all the above points are assumed to be collocated and designated the yield stress.

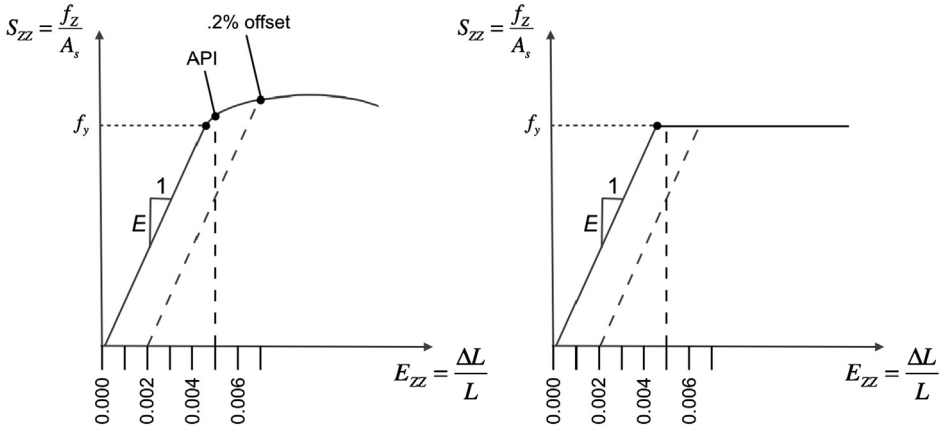

Figure 6.2 ***Definition of yield from a uniaxial stress–strain curve.***

Popular in academia and a number of industries is the so-called "0.2% offset" definition of yield. Yield is defined as the intersection of the stress–strain curve with a straight line constructed by starting at a strain[6] of 0.002, or 0.2%, and having a slope equal to Young's modulus. An example construction to determine the 0.2% offset yield is indicated in the left-hand diagram. The fact that the intersection occurs above f_y is a consequence of its definition. The apparent large discrepancy between the 0.2% offset yield and f_y is due to the low value assigned to E in the drawing—the 0.2% offset yield is usually a good approximation of the onset of plasticity.

In contrast to the 0.2% offset method, the API uses an alternate definition of yield, found by the intersection of the stress–strain curve with a vertical line usually drawn at a strain of 0.005. For higher yield strength materials, in fact, any material having a value of $f_y \geq 150,000$ psi, yield will be predicted when the material is still elastic. For this reason, for higher yield materials the abscissa intersection may be raised above 0.005.

Table 6.1 lists the current API material grades for casing and tubing. The grade naming convention consists of a letter followed by the API minimum yield stress in 1000 s of psi. The letters themselves were assigned historically and have no significance other than to aid in grade name differentiation.[7]

Returning to the discussion of Fig. 6.2, there is no reason why the two offered definitions of yield should be equal, or why either of them should equal f_y. Fortunately, as indicated by the right-hand diagram in the figure, most API tubular products have

[6] All strain definitions used in this book are dimensionless, having "units" of in/in or mm/mm. Strain can also be expressed without units or multiplied by 100 and expressed as a percent.

[7] Such is not the case for letters appearing in proprietary (non-API) grade offerings. Acronyms used in proprietary grade designations are explained by the manufacturer in a published catalog or on a commercial website.

Table 6.1 API material grades [46]. All yield and ultimate stress values are in alternate units of psi/MPa

Grade	Yield strain, %	Min yield stress	Max yield stress	Min ultimate stress[a]
H40	0.5	40 000/276	80 000/552	60 000/414
J55	0.5	55 000/379	80 000/552	75 000/517
K55	0.5	55 000/379	80 000/552	95 000/655
N80[b]	0.5	80 000/552	110 000/758	100 000/689
R95	0.5	95 000/655	110 000/758	105 000/724
M65	0.5	65 000/448	85 000/586	85 000/586
L80[c]	0.5	80 000/552	95 000/655	95 000/655
C90[d]	0.5	90 000/621	105 000/724	100 000/689
T95[e]	0.5	95 000/655	110 000/758	105 000/724
C110	0.67	110 000/758	120 000/828	115 000/793
P110	0.6	110 000/758	140 000/965	125 000/862
Q125[f]	0.65	125 000/862	150 000/1034	135 000/931

[a] API terminology is tensile strength.
[b] Applicable to both Type 1 and Type Q.
[c] Applicable to Type 1, Type 9Cr and Type 13Cr.
[d] Applicable to Type 1, regardless of wall thickness.
[e] Applicable to Type 1, regardless of wall thickness.
[f] Applicable to Type 1, regardless of wall thickness.

a relatively flat postyield stress–strain curve, which renders the three values equal. This behavior, however, is not evidenced by all API grades—in particular, the lower strength materials and the high-chrome products.

6.2.1.1 Effect of temperature

Yield stress is inversely proportional to temperature, the relation being reasonably approximated by a straight line. Temperature dependency varies with chemistry. Although the majority of low-alloy API tubular grades have behavior that may be fit with a single curve, the chrome products and any proprietary high-alloy steels can vary noticeably in their sensitivity to temperature increase. Two guidelines are as follows:

- Whenever possible, consult the source of the tubulars to be purchased to see if temperature-dependent yield stress data is available.
- If absolutely no external data is available, and especially for low-carbon API grades (all grades in Table 6.1 except L80 Type 9Cr and L80 Type 13Cr), modeling a ten percent decrease in yield stress at 300 °F (149 °C) is a reasonable approximation

$$\hat{f}_y(T) = f_y(70)\left(1 - 0.1\frac{T-70}{300-70}\right) = f_y(70)\,(1.0304 - 0.000\,435 \times T)\,, \quad T \geq 70, \tag{6.4}$$

where T is in units of °F. If the temperature is less than 70 °F, make no adjustment for temperature. The corresponding formula for the Celsius scale is

$$\hat{f}_\gamma(T) = f_\gamma(21.1) \times \begin{cases} 1.0165 - 0.000\,783 \times T & \text{if } T \geq 21.1, \\ 1.0 & \text{otherwise.} \end{cases} \tag{6.5}$$

The resulting yield stress should be used in all pertinent calculations—design for yield, collapse, joint strength, etc.

6.2.2 Postyield behavior on a uniaxial stress–strain curve

Phenomenologically, postyield behavior has already been noted in the bulleted comments accompanying Fig. 6.1 in Section 6.2.1. In detail, and with reference to the points in Fig. 6.1, the behavior is as follows:

- Initially the yield stress of the material corresponds to point A.
- If the material is loaded beyond point A, the yield stress changes so as to always contain the stress. For example, if the material is loaded beyond yield in tension to point B, the yield stress increases and at the end of loading is now the stress corresponding to point B. In a single dimension the phenomenon is readily discernible as the yield condition is a point on the S_{ZZ}-axis. When two or more stresses are active, the response of the yield condition to plastic deformation becomes increasingly complex, since the yield condition is now represented by a surface in multidimensional stress space (see Section 6.3). Combinations of expansion or contraction, translation and local distortion of the yield surface at the point of penetration in stress space are common.
- If the material is unloaded from point B the material response is elastic, following the curve BF. A perfect metal crystal is much stronger than a macroscopic specimen, the weakness of the latter being attributed to imperfections in the atomic structure. An example of such a weakness is a dislocation, a region where one or more atoms are out of position with respect to the material's crystal structure. Movement of dislocations, usually under the action of a macroscopic shear load, results in displacement but little alteration of the main lattice structure [47]. Movement is also aided by the presence of slip planes—planes along which atomic packing is most dense—in the structure. Displacement of multiple dislocations can be arrested by other microscopic imperfections, such as grain boundaries.[8] This combination of (a) substantial structural integrity of the lattice and (b) relatively major (and irreversible) movement along planes of weakness leads to a curve such as ABF. The AB

[8] The accumulation of dislocations, as opposed to continued, unimpeded flow, means an increasing load will be required to continue deformation. This work-hardening results in a nonzero slope to the stress–strain curve beyond yield. Compare the left-hand (work-hardening) and right-hand (no work-hardening) diagrams in Fig. 6.2.

segment reflects the large, plastic movement associated with mobile dislocations and planes of atomic close-packing; the BF segment indicates elastic-only recovery of interatomic distance when the distorting load is removed.

- When the load is totally removed from a yielded specimen, an irrecoverable strain will exist—in the current example the irrecoverable, or plastic strain is OF.
- If the sample remains in the test fixture and is reloaded in tension, the response path begins at point F and follows line FB until a point near B is reached. The sample then yields at its new yield stress corresponding approximately to point B, and under continued loading follows the path BC. Deformation under increasing load along any portion of the segment ABC is an indication of work-hardening.
- According to the stress–strain curve in Fig. 6.1, the maximum axial stress the sample can withstand corresponds to point C, but the sample does not break until, as indicated by the "x", point D. This is an anomaly of a typical stress–strain curve and is not real:
  - The "decreasing" axial stress is a sign of material instability as the sample undergoes significant plastic deformation and necking[9] prior to its ultimate fracture.
  - The curve shown in Fig. 6.1 is a so-called "engineering" stress–strain curve (see Section 4.3.1.1 of Chapter 4). In constructing such a curve, the geometry of the sample—its cross-sectional area and length—is only measured at the beginning of the test. Each text fixture axial force value that is converted into axial stress uses the original cross-sectional area to compute force intensity (stress). Were each axial force value instead divided by its corresponding current cross-sectional area, and similarly for the division by length to compute strain, the resulting "true" stress–strain curve would be monotonically increasing to failure at the ultimate stress.

6.2.2.1 The Bauschinger effect

Fig. 6.3 displays both tension and compression uniaxial stress–strain response for an isotropic crystalline solid such as steel. Consider the following three load paths:

1. Path 1 (slightly offset from the stress–strain curve so as to be discernible) is the tension path discussed in reference to Fig. 6.1. With increasing load the sample experiences, in succession, elastic behavior, yield and postyield elastic-plastic behavior.

[9] The postyield effective Poisson's ratio of a sample in a uniaxial tension test begins at yield with a value of approximately 0.3 (steel) and increases with increasing plastic deformation, limited to a theoretical maximum value of 0.5. With increasing Poisson's ratio, the change in cross-sectional area of the sample with an increment of axial strain also increases. For ductile samples the decrease in cross-sectional area at the point of fracture can be substantial. This near-failure cross-sectional behavior is referred to as "necking.".

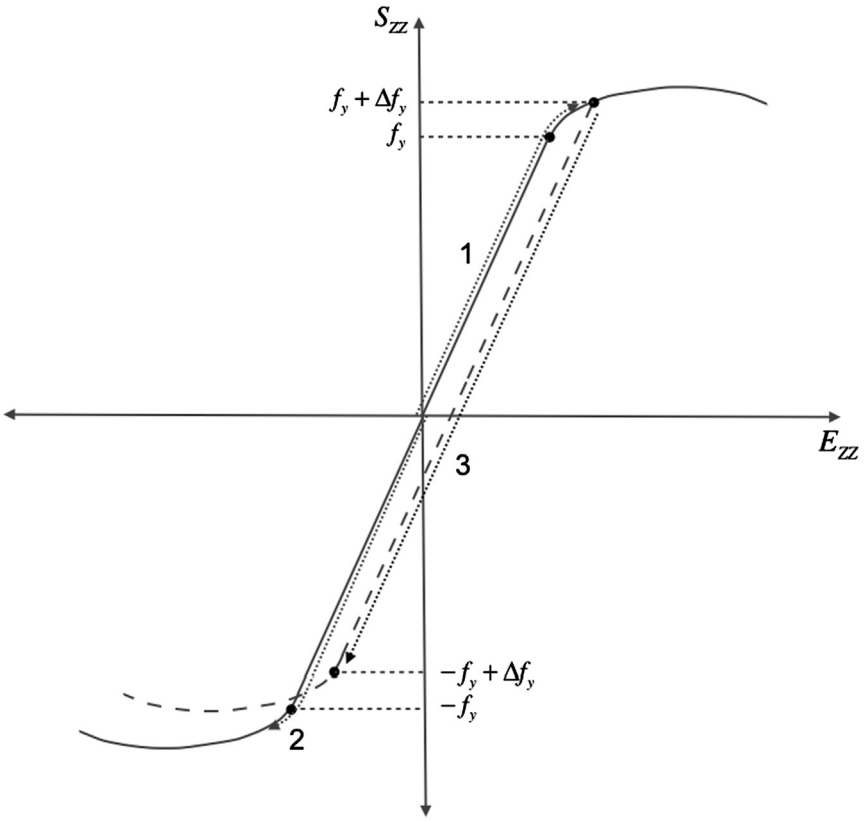

Figure 6.3 ***The Bauschinger effect.***

2. Path 2, performed on a new specimen, exposes the sample to the same behaviors, only in compression. Provided the samples are identical and the material is isotropic, the sample will yield in compression at the same absolute value under which its companion yielded in tension.
3. Path 3, once again using a new specimen, is initially identical to Path 1—the sample is loaded in tension beyond yield. From the initial discussion on postyield behavior in this section, we recognize that the initial yield stress f_y is supplanted with plastic loading, such that the new yield stress is $f_y + \Delta f_y$. Now the sample is unloaded and again, according to preceding discussion, elastically unloads along a path parallel to the original elastic path. Once all the load is removed, we do not, however, remove the specimen from the test fixture. Rather, we begin to load the specimen in compression. We observe that now the yield stress in compression is no longer $-f_y$, but has decreased (in an absolute value sense) to a value of $-f_y + \Delta f_y$, where Δf_y is the amount by which yield was exceeded during the initial application of tension.

This phenomenon, the decrease in yield in one direction when unloading a specimen from postyield behavior in the opposite direction, is termed the Bauschinger effect.

6.2.2.2 Cyclic loading

Some completions, most notably those associated with the recovery of viscous oil, involve processes that cyclically load wellbore tubulars beyond yield. Both CSS (cyclic steam stimulation) and SAGD (steam-assisted gravity drainage) involve high temperature 570–640 °F (300–340 °C) thermal cycles that simultaneously induce thermal stress and reduce yield stress (Section 6.2.1.1). This load increase/resistance decrease can yield axially constrained tubulars on both the steam injection (compression) and soak into production (reduction in compression to tension) cycles [48], aided by a coincident reduction in yield stress on reverse loading due to the Bauschinger effect (Section 6.2.2.1).

6.2.3 Modeling a uniaxial stress–strain curve

When stress–strain data is unavailable, or to pursue solutions as far as possible, it is sometimes useful to substitute a mathematical model for experimental uniaxial material behavior. Two such models have gained acceptance in tubular design.

6.2.3.1 Needleman's model

Needleman's model [49] offers the following relation between uniaxial stress and strain:

$$\frac{S_{ZZ}}{f_y} = \begin{cases} \frac{E_{ZZ}}{\varepsilon_y} & \text{for } E_{ZZ} \le \varepsilon_y, \\ \left[n\frac{E_{ZZ}}{\varepsilon_y} + 1 - n\right]^{\frac{1}{n}} & \text{for } E_{ZZ} > \varepsilon_y, \end{cases} \tag{6.6}$$

where ε_y is the strain corresponding to f_y, that is, $\varepsilon_y = f_y/E$, and the variable n determines the shape of the stress–strain curve beyond initial yield. The tangent modulus and secant modulus are, respectively,

$$E_t = \frac{dS_{ZZ}}{dE_{ZZ}} = E \times \begin{cases} 1 & \text{for } E_{ZZ} \le \varepsilon_y, \\ \left(\frac{f_y}{S_{ZZ}}\right)^{n-1} & \text{for } E_{ZZ} > \varepsilon_y, \end{cases} \tag{6.7}$$

$$E_s = \frac{S_{ZZ}}{E_{ZZ}} = E \times \begin{cases} 1 & \text{for } E_{ZZ} \le \varepsilon_y, \\ \frac{\frac{S_{ZZ}}{f_y}}{\frac{1}{n}\left[\left(\frac{S_{ZZ}}{f_y}\right)^n - 1\right] + 1} & \text{for } E_{ZZ} > \varepsilon_y. \end{cases} \tag{6.8}$$

A plot of Eq. (6.6) illustrating its sensitivity to n is provided in Fig. 6.4.

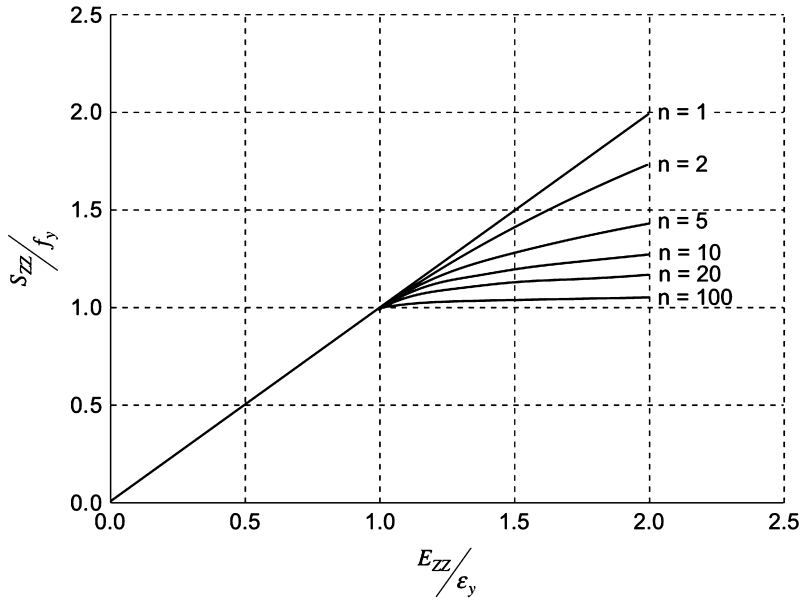

Figure 6.4 ***Needleman's model for a uniaxial stress–strain curve [49].*** The yield values ε_y and f_y are related by $f_y = E\varepsilon_y$.

6.2.3.2 Ludwik's model

Ludwik's model [50] offers the following relation between uniaxial stress and strain[10]:

$$\Sigma_{zz} = C\tilde{E}_{ZZ}^{n_{NR}}, \quad C = \left(\frac{e}{n_{NR}}\right)^{n_{NR}} f_u, \tag{6.9}$$

where $\mathbf{\Sigma}$ is the Cauchy stress—force intensity related to current area—$\tilde{\mathbf{E}}$ is the logarithmic strain, f_u is the ultimate (Cauchy) stress, n_{NR} determines the shape of the stress–strain curve, and e is the base of the natural logarithm. Ludwik's model is not linear in the low stress region, but we will only use this model for describing ductile rupture and therefore will apply the model to material behavior at large inelastic strain.[11]

[10] Regarding the notation used in this section, the fact that Ludwik's model is normally used with large deformation problems fosters a small issue in notation consistency. The Cauchy stress is normally expressed relative to a spatial coordinate system and the logarithmic strain is normally expressed relative to the material coordinate system. For this one-dimensional stress state we simply assume the two coordinate systems align, which allows us to maintain lower case indices for the stress and upper case indices for the strain.

[11] In practice, the strain $\tilde{E}_{ZZ}$ in Ludwik's model is not the total strain but the inelastic part of the total strain (cf. Section 7.3.2 in Chapter 7). Since the elastic strain prior to yield is small, this is a reasonable use of the model.

Table 6.2 Ludwik's n_{NR} for API grades [51]

Grade	n_{NR}	Grade	n_{NR}
H40	0.14	L80 Chrome	0.10
J55	0.12	C90	0.10
K55	0.12	R95	0.09
M65	0.12	T95	0.09
N80	0.10	P110	0.08
L80 Type 1	0.10	Q125	0.07

For future reference, the local slope E_L of the Ludwik stress–strain curve is

$$E_L = \frac{d\Sigma_{zz}}{d\tilde{E}_{ZZ}} = n_{NR} C \tilde{E}_{ZZ}^{n_{NR}-1} = e^{n_{NR}} f_u \left(\frac{\tilde{E}_{ZZ}}{n_{NR}} \right)^{n_{NR}-1} = e f_u \left(\frac{\Sigma_{zz}}{f_u} \right)^{\frac{n_{NR}-1}{n_{NR}}}. \tag{6.10}$$

A convenient relation associated with Eq. (6.10) specifies that if $\Sigma_{zz} = kE_L$, then

$$k n_{NR} C \tilde{E}_{ZZ}^{n_{NR}-1} = C \tilde{E}_{ZZ}^{n_{NR}} \Rightarrow \tilde{E}_{ZZ} = k n_{NR}, \quad \Sigma_{zz} = (ek)^{n_{NR}} f_u \quad \text{if } \Sigma_{zz} = kE_L. \tag{6.11}$$

The API [51] provides both recommended values of n_{NR} for API grades (see Table 6.2) and an equation to determine n_{NR} for nonstandard materials

$$n_{NR} = 0.1693 - \left\{ \begin{array}{ll} 0.000\,118\,\frac{1}{\text{MPa}} & \text{for SI units} \\ 0.000\,000\,812\,\frac{1}{\text{psi}} & \text{for USC units} \end{array} \right\} \times f_y. \tag{6.12}$$

A plot of Eq. (6.9) for selected values of n_{NR} is provided in Fig. 6.5. In applications the strain labeled "Logarithmic strain" in the figure is often the plastic part of the total logarithmic strain. This will result in a poor fit of Ludwik's model for small strain—Eq. (6.9) assigns zero strain to zero stress whereas at zero plastic strain the stress should be the initial yield stress. With increasing strain—the primary application of this model is for ultimate strength limit states—the fit of Ludwik's model to experimental plastic strain can be excellent.

6.3. YIELD IN MULTIPLE DIMENSIONS

On the uniaxial stress–strain curve yield is represented by a point, e.g., point A in Fig. 6.1. If the stress state is two-dimensional the yield criterion will be represented by a closed line, the line serving as a boundary between elastic behavior (its interior) and plastic behavior (its exterior). In the three-dimensional case yield is represented by a (possibly open) surface.

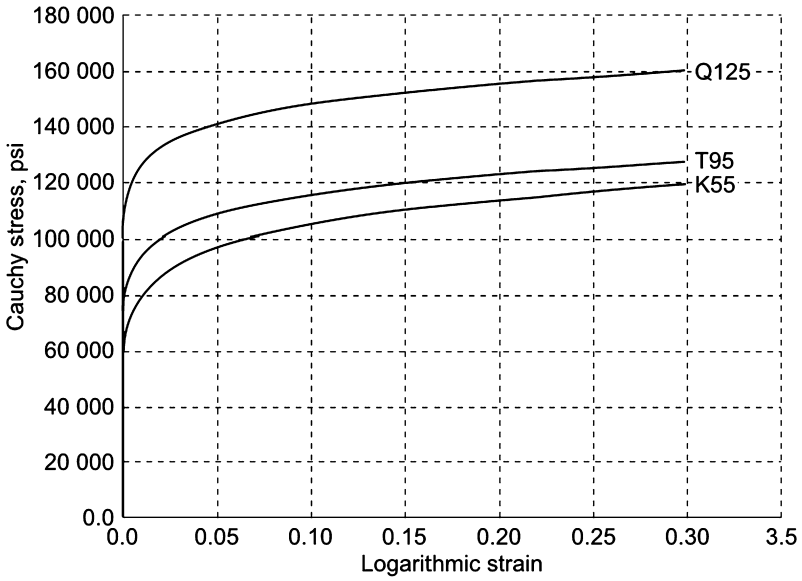

Figure 6.5 ***Ludwik's model for a uniaxial stress–strain curve [50].*** In application the abscissa is actually plastic logarithmic strain.

6.3.1 Isotropic yield and the von Mises yield criterion [52]

Consider the behavior of a homogeneous, isotropic crystalline metal as plotted in principal stress space. The orthogonal principal stress axes are arranged such that $\Sigma_1^p \geq \Sigma_2^p \geq \Sigma_3^p$ form a right-handed coordinate system.

An important experimental observation for crystalline solids is that, at least within the limits of investigation of this discussion, yield is independent of the mean or hydrostatic component of the stress tensor, where the mean stress is defined as

$$\Sigma_m = \frac{1}{3}\mathrm{tr}\left(\boldsymbol{\Sigma}\right), \quad \Sigma_m = \frac{1}{3}\Sigma_{ii}, \tag{6.13}$$

which for a stress tensor aligned with the principal stress axes, becomes

$$\Sigma_m = \frac{1}{3}\mathrm{tr}\left(\boldsymbol{\Sigma}^p\right), \quad \Sigma_m = \frac{1}{3}\left(\Sigma_1^p + \Sigma_2^p + \Sigma_3^p\right). \tag{6.14}$$

For a hydrostatic stress state[12] where $\Sigma_1^p = \Sigma_2^p = \Sigma_3^p$, a unit vector in principal stress space will have the components

[12] Here we use the term "hydrostatic" to denote a stress state in which the three principal stresses are equal and, from Eq. (6.13), equal to the mean stress. This definition can be applied to solids as well as liquids, although in the case of liquids it does conform to the state one normally describes when speaking of hydrostatic pressure.

$$\mathbf{g}_{hyd} = \frac{\Sigma_1^p \mathbf{g}_1^p + \Sigma_2^p \mathbf{g}_2^p + \Sigma_3^p \mathbf{g}_3^p}{\sqrt{\Sigma_1^{p2} + \Sigma_2^{p2} + \Sigma_3^{p2}}} = \frac{1}{\sqrt{3}} \left(\mathbf{g}_1^p + \mathbf{g}_2^p + \mathbf{g}_3^p \right), \quad \Sigma_1^p = \Sigma_2^p = \Sigma_3^p, \tag{6.15}$$

where $\mathbf{g}_i^p$ is a unit base vector in the Σ^p coordinate system. From Eq. (6.15) the unit vector $\mathbf{g}_{hyd}$ will possess equal angles with each of the coordinate axes. That is, its direction cosines are $\mathbf{g}_{hyd} \cdot \mathbf{g}_i = 1/\sqrt{3}$, $i = 1, 2, 3$. Additional conclusions to be reached regarding the position of a stress state relative to the hydrostatic stress include the following:

- As long as the current stress state lies on the hydrostatic axis, the material has no tendency to yield;
- Departure of a stress state from the hydrostatic axis, which initiates an increasing tendency to yield, is accompanied by the introduction of shear, that is, a state where at least one of $\Sigma_1^p \neq \Sigma_2^p$, $\Sigma_2^p \neq \Sigma_3^p$ or $\Sigma_3^p \neq \Sigma_1^p$ is true;
- Yield will occur when departure from the hydrostatic axis reaches a critical value, this critical value representing a radius in principal stress from an axis collinear with the hydrostatic stress unit vector;
- For an isotropic material, the critical value of departure from the hydrostatic axis should be the same regardless of the direction of this departure in stress space;
- This critical departure will be in a plane whose normal is the hydrostatic stress unit vector.

Mathematically, the implications of the bulleted list above are as follows:

- The equation of the plane normal to the hydrostatic stress unit vector follows from the fact that the dot product of any vector in that plane with $\mathbf{g}_{hyd}$ must vanish, or, from Eq. (6.15)

$$(\mathbf{v}_\pi)_1 \, \Sigma_1^p + (\mathbf{v}_\pi)_2 \, \Sigma_2^p + (\mathbf{v}_\pi)_3 \, \Sigma_3^p = 0, \quad \Sigma_1^p = \Sigma_2^p = \Sigma_3^p, \tag{6.16}$$

  where $(\mathbf{v}_\pi)_1 = \mathbf{v}_\pi \cdot \mathbf{g}_i$, $i = 1, 2, 3$. This plane is designated the "π-plane" in mechanics literature and is depicted in Fig. 6.6.
- Viewed in the π-plane, the criterion for yield of an isotropic material suggests a circle, since (a) yield depends on departure from the hydrostatic stress axis, and (b) departure to yield in any direction should be the same. Consider a π_1–π_2–π_3 coordinate system (see Fig. 6.7) where the π_1-axis lies in the Σ_2^p–Σ_3^p plane, the π_2-axis lies in the plane formed by the hydrostatic stress unit vector (Eq. (6.15)) and the Σ_1^p-axis, and π_3-axis aligns with the hydrostatic stress unit vector. The transformation matrix from the Σ^p coordinate system to the π coordinate system is, due to Eq. (A.56),

$$\mathbf{L} = \begin{bmatrix} \mathbf{g}_1^\pi \cdot \mathbf{g}_1^p & \mathbf{g}_1^\pi \cdot \mathbf{g}_2^p & \mathbf{g}_1^\pi \cdot \mathbf{g}_3^p \\ \mathbf{g}_2^\pi \cdot \mathbf{g}_1^p & \mathbf{g}_2^\pi \cdot \mathbf{g}_2^p & \mathbf{g}_2^\pi \cdot \mathbf{g}_3^p \\ \mathbf{g}_3^\pi \cdot \mathbf{g}_1^p & \mathbf{g}_3^\pi \cdot \mathbf{g}_2^p & \mathbf{g}_3^\pi \cdot \mathbf{g}_3^p \end{bmatrix} = \begin{bmatrix} 0 & -\frac{1}{\sqrt{2}} & \frac{1}{\sqrt{2}} \\ \sqrt{\frac{2}{3}} & -\frac{1}{\sqrt{6}} & -\frac{1}{\sqrt{6}} \\ \frac{1}{\sqrt{3}} & \frac{1}{\sqrt{3}} & \frac{1}{\sqrt{3}} \end{bmatrix}, \tag{6.17}$$

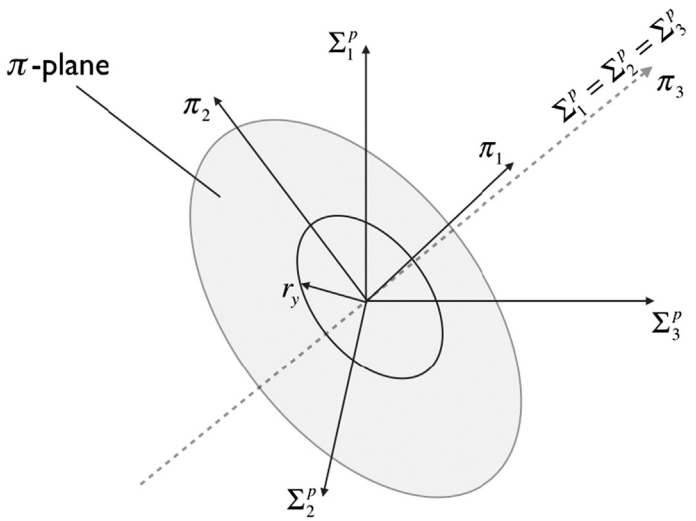

Figure 6.6 ***The π-plane, shown in relation to the principal stress axes.*** The π_1 and π_2-axes lie in the π-plane. The π_3-axis is normal to the π-plane, aligned with the hydrostatic stress unit vector $\mathbf{g}_{hyd}$ of Eq. (6.15). The angle between the π_2-axis and the Σ_1^p-axis is $\frac{\pi}{2} - \cos^{-1}\frac{1}{\sqrt{3}}$. The projection of the π_3-axis onto the Σ_2^p–Σ_3^p plane makes an angle of $\frac{\pi}{4}$ with both the Σ_2^p and Σ_3^p-axes. The projection of the π_2-axis onto the Σ_2^p–Σ_3^p plane makes an angle of $\frac{3\pi}{4}$ with both the Σ_2^p and Σ_3^p-axes.

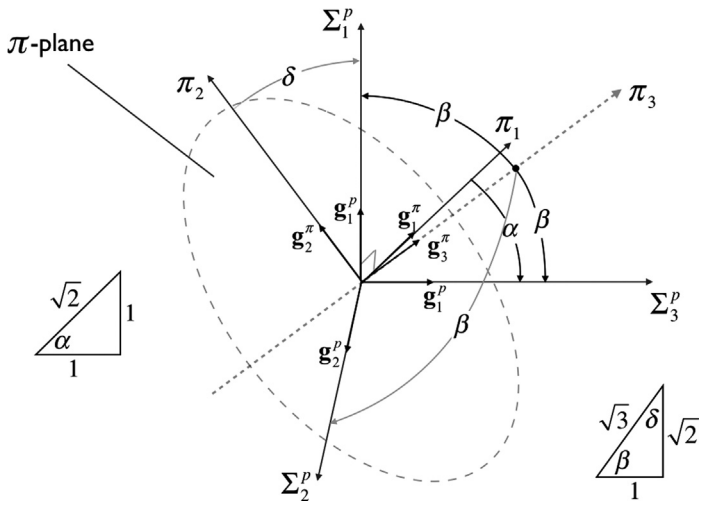

Figure 6.7 ***Illustration of angles used to determine direction cosines between the π coordinate system and the Σ^p coordinate system.***

where $\mathbf{g}_i^{\pi}$ is a unit base vector in the π coordinate system. A circle in the π-plane is

$$\pi_1^2 + \pi_2^2 - r_y^2 = 0, \tag{6.18}$$

where r_y is the radius of the circle representing incipient yield. Using Eq. (6.17) to express the π_i in terms of the Σ_I^p we get

$$\pi_1 = -\frac{1}{\sqrt{2}}\Sigma_2^p + \frac{1}{\sqrt{2}}\Sigma_3^p, \tag{6.19}$$

$$\pi_2 = \sqrt{\frac{2}{3}}\Sigma_1^p - \frac{1}{\sqrt{6}}\Sigma_2^p - \frac{1}{\sqrt{6}}\Sigma_3^p, \tag{6.20}$$

$$\pi_3 = \frac{1}{\sqrt{3}}\Sigma_1^p + \frac{1}{\sqrt{3}}\Sigma_2^p + \frac{1}{\sqrt{3}}\Sigma_3^p. \tag{6.21}$$

Substituting Eqs. (6.19) and (6.20) into Eq. (6.18), the equation of the yield surface in principal stress space is

$$\hat{f} = \frac{2}{3}\left(\Sigma_1^{p2} + \Sigma_2^{p2} + \Sigma_3^{p2} - \Sigma_1^p\Sigma_2^p - \Sigma_2^p\Sigma_3^p - \Sigma_3^p\Sigma_1^p\right) - r_y^2 = 0. \tag{6.22}$$

The radius r_y can be evaluated by considering a uniaxial tension test along the direction of Σ_1^p. At yield, only $\Sigma_1^p = f_y$ is nonzero, and Eq. (6.22) reduces to $\frac{2}{3}f_y^2 = r_y^2$, or $r_y = \sqrt{\frac{2}{3}}f_y$. Using this value in Eq. (6.22), the final form of the yield surface in principal stress space is

$$\hat{f} = \Sigma_1^{p2} + \Sigma_2^{p2} + \Sigma_3^{p2} - \Sigma_1^p\Sigma_2^p - \Sigma_2^p\Sigma_3^p - \Sigma_3^p\Sigma_1^p - f_y^2 = 0. \tag{6.23}$$

The surface defined by Eq. (6.23) is illustrated in Fig. 6.8. The surface is a right circular cylinder extending indefinitely in both directions from the origin of principal stress space. The axis of the cylinder makes equal angles with the three principal stress axes and the radius of the cylinder is $\sqrt{\frac{2}{3}}f_y$.

- Do not confuse the right circular cylinder in Fig. 6.8 with a physical tubular. A separate von Mises yield surface as depicted in Fig. 6.8 exists for every point along the length and through the wall of a physical tube.
- For most tubular problems, the principal stresses can be identified with the normal stresses in a cylindrical coordinate system whose Z-axis aligns with the axis of the tube.[13] Mapping of Σ_{rr}, $\Sigma_{\theta\theta}$ and Σ_{zz} to Σ_1^p, Σ_2^p and Σ_3^p could be complicated by the fact that principal stresses are usually ranked from highest to lowest in value. That potential problem does not exist, however, since Eq. (6.23) is symmetric with respect to the three principal stresses. Each of the cylindrical coordinate normal

[13] An exception would be drilling with casing if the drilling involves application of torque to the casing itself. This introduces a torsional shear stress in addition to Σ_{rr}, $\Sigma_{\theta\theta}$ and Σ_{zz}.

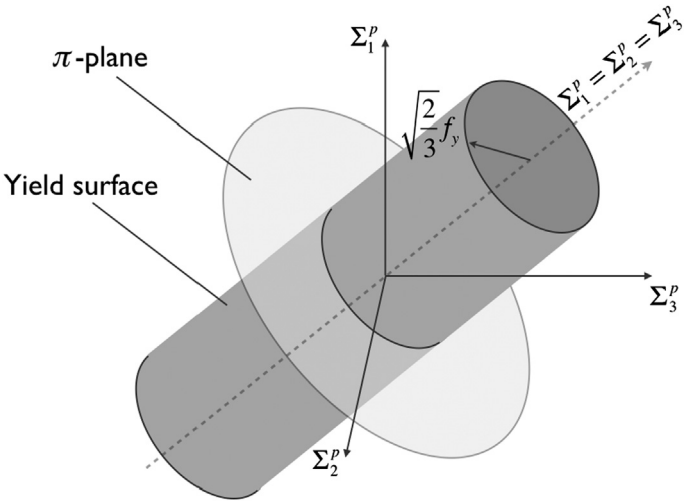

Figure 6.8 ***The surface corresponding to the von Mises yield criterion, shown in relation to the principal stress axes.*** The broken line representing the axis of the right circular cylindrical surface makes equal angles with the three principal stress axes. The cylinder is open and extends infinitely in both axial directions.

stresses can be mapped to whichever principal stress desired without affecting the condition for yield.

Although several investigators formulated the yield criterion[14] discussed above, Eq. (6.23) is almost universally designated the von Mises yield criterion. Comparing the criterion to its one-dimensional form governing a uniaxial tension test, one finds the following correspondences:

- In one dimension, provided the nonzero stress is less than the yield stress, the material behaves elastically. In three dimensional principal stress space, provided the combined, triaxial stress state lies within the circular cylindrical yield surface, the material behaves elastically.
- In one dimension, when the nonzero stress equals the yield stress, yield is incipient. Yield is incipient in the full principal stress space if the stress path in that space touches any portion of the cylindrical yield surface.
- In one dimension, if loading is attempted beyond the initial value of the yield stress, the yield stress will increase so that it is not exceeded. This alteration of the, for example, tensile value of the yield stress can also affect the compressive yield stress. The effect will depend on how inelastic loading is modeled. In three dimensions,

[14] In particular, Heinrich Hencky [53] arrived independently at the same yield criterion, and the criterion is often referred to as the Hencky–von Mises yield criterion. In this book we use von Mises' name alone primarily to conform to the criterion's common designation in the petroleum industry.

if loading is attempted such that the initial yield surface is penetrated, and again according to the inelastic loading model, the yield surface may translate, expand and locally deform to prevent the stress state from reaching its exterior.

6.3.2 Alternative derivation of the von Mises yield criterion

This section presents an alternative, less phenomenological approach to the von Mises yield criterion, the purpose being to introduce new variables and concepts that will be useful in later discussions. We begin by defining a new stress, the deviatoric stress, which is the stress minus a diagonal tensor whose components are all equal to the mean stress (see Eq. (6.13))

$$\boldsymbol{\Sigma}' = \boldsymbol{\Sigma} - \Sigma_m \mathbf{I}, \quad \Sigma'_{ij} = \Sigma_{ij} - \Sigma_m \delta_{ij}. \tag{6.24}$$

The deviatoric stress tensor has invariants defined as those for the stress tensor that we will distinguish with the letter J. From Eqs. (A.91), (A.94) and (A.97), respectively, we obtain

$$J_1 = \Sigma'_{jj} = \left(\Sigma_{jj} - 3\Sigma_m\right) = 0, \tag{6.25}$$

$$J_2 = \frac{1}{2}\left[\Sigma'_{rs}\Sigma'_{rs} - \left(\Sigma'_{kk}\right)^2\right] = \frac{1}{2}\Sigma'_{rs}\Sigma'_{rs}, \tag{6.26}$$

$$J_3 = \det \boldsymbol{\Sigma}', \quad J_3 = \frac{1}{6}\varepsilon_{ijk}\varepsilon_{pqr}\Sigma'_{ip}\Sigma'_{jq}\Sigma'_{kr}. \tag{6.27}$$

An alternative statement of the von Mises yield criterion is

$$J_2 - k^2 = 0, \tag{6.28}$$

where k is discussed below. With Eq. (6.24) we may write J_2 in terms of stress as

$$\begin{aligned} J_2 &= \frac{1}{2}\left(\Sigma_{rs} - \delta_{rs}\Sigma_m\right)\left(\Sigma_{rs} - \delta_{rs}\Sigma_m\right) \\ &= \frac{1}{2}\left(\Sigma_{rs}\Sigma_{rs} - 2\delta_{rs}\Sigma_m\Sigma_{rs} + 3\Sigma_m^2\right) \\ &= \frac{1}{2}\left(\Sigma_{rs}\Sigma_{rs} - 3\Sigma_m^2\right), \end{aligned} \tag{6.29}$$

where we have used Eq. (6.13) and the fact that $\delta_{kk} = 3$.

The following observations are in order:

- If $\boldsymbol{\Sigma}$ is a principal stress tensor, then $\Sigma_{rs} = 0$ if $r \neq s$. We may therefore explicitly write Eq. (6.26) as

$$\begin{aligned} J_2 &= \frac{1}{2}\left[\Sigma_{11}^2 + \Sigma_{22}^2 + \Sigma_{33}^2 - \frac{1}{3}\left(\Sigma_{11} + \Sigma_{22} + \Sigma_{33}\right)^2\right] \\ &= \frac{1}{3}\left(\Sigma_{11}^2 + \Sigma_{22}^2 + \Sigma_{33}^2 - \Sigma_{11}\Sigma_{22} - \Sigma_{22}\Sigma_{33} - \Sigma_{33}\Sigma_{11}\right). \end{aligned} \tag{6.30}$$

Using a uniaxial test ($J_2 = \frac{1}{3}\Sigma_{11}^2 = \frac{1}{3}f_y^2$) to determine $k = \frac{1}{\sqrt{3}}\Sigma_{11}$ in Eq. (6.28), we get

$$J_2 - \frac{1}{3}f_y^2 = 0, \tag{6.31}$$

which is tantamount to Eq. (6.23).

- If $\boldsymbol{\Sigma}$ is not a principal stress tensor but a general, symmetric tensor of stress components, then Eq. (6.28) provides a compact means of expressing yield. Explicitly, with Eq. (6.29) we may write Eq. (6.28) as

$$\begin{aligned} J_2 - k^2 &= \frac{1}{2}\left[\Sigma_{rs}\Sigma_{rs} - \frac{1}{3}\Sigma_{ii}^2\right] - k^2 \\ &= \frac{1}{2}\left[\Sigma_{11}^2 + \Sigma_{22}^2 + \Sigma_{33}^2 + 2\Sigma_{12}^2 + 2\Sigma_{23}^2 + 2\Sigma_{31}^2 - \frac{1}{3}(\Sigma_{11} + \Sigma_{22} + \Sigma_{33})^2\right] - k^2 \\ &= \frac{1}{3}\left[\left(\Sigma_{11}^2 + \Sigma_{22}^2 + \Sigma_{33}^2 - \Sigma_{11}\Sigma_{22} - \Sigma_{22}\Sigma_{33} - \Sigma_{33}\Sigma_{11}\right)\right. \\ &\quad \left. + 3\left(\Sigma_{12}^2 + \Sigma_{23}^2 + \Sigma_{31}^2\right)\right] - k^2. \end{aligned} \tag{6.32}$$

The variable k, as determined from a uniaxial test is $\frac{1}{\sqrt{3}}f_y$, so that finally,

$$\Sigma_{11}^2 + \Sigma_{22}^2 + \Sigma_{33}^2 - \Sigma_{11}\Sigma_{22} - \Sigma_{22}\Sigma_{33} - \Sigma_{33}\Sigma_{11} + 3\left(\Sigma_{12}^2 + \Sigma_{23}^2 + \Sigma_{31}^2\right) - f_y^2 = 0. \tag{6.33}$$

- Eq. (6.33) is often rewritten as

$$\Sigma_e^2 - f_y^2 = 0, \tag{6.34}$$

where

$$\Sigma_e = \sqrt{\Sigma_{11}^2 + \Sigma_{22}^2 + \Sigma_{33}^2 - \Sigma_{11}\Sigma_{22} - \Sigma_{22}\Sigma_{33} - \Sigma_{33}\Sigma_{11} + 3\left(\Sigma_{12}^2 + \Sigma_{23}^2 + \Sigma_{31}^2\right)}, \tag{6.35}$$

is called the von Mises equivalent stress, or VME stress. Comparing Eqs. (6.35) and (6.32) yields

$$\Sigma_e = \sqrt{3J_2}. \tag{6.36}$$

The von Mises equivalent stress is a powerful simplification of yield:

- Using Σ_e, and with regard to the yield limit state, one is able to characterize the entire local stress state by a single quantity.
- Since for $\Sigma_{11} \neq 0$, all other $\Sigma_{ij} = 0$, we have $\Sigma_e = \Sigma_{11}$, the von Mises equivalent stress can be used as a bridge between uniaxial and multidimensional stress concepts. Recall the bulleted discussion at the end of Section 6.3.1. The correspondence between one and multiple dimensions of stress is treated identically using Σ_e.

6.3.3 Isotropic yield and the Tresca yield criterion [54]

An alternative to the von Mises yield criterion is that proposed by Tresca [54]. Yield is defined as the load state at which the maximum shear stress in the material equals the shear stress at yield from a uniaxial stress–strain curve, namely

$$\Sigma_{smax} - k = 0, \tag{6.37}$$

where Σ_{smax} is the maximum shear stress.

Aligning a set of working coordinates with the principal stresses, we may write the stress tensor in these coordinates as

$$\boldsymbol{\Sigma}^p = \begin{bmatrix} \Sigma_1^p & 0 & 0 \\ 0 & \Sigma_2^p & 0 \\ 0 & 0 & \Sigma_3^p \end{bmatrix}, \tag{6.38}$$

where $\Sigma_1^p \geq \Sigma_2^p \geq \Sigma_3^p$. Let us now search for the plane on which the maximum shear stress occurs. If the normal to that plane is $\mathbf{n}$, then the traction normal to that plane is given by Eq. (4.11) and is

$$\mathbf{t}_{(\mathbf{n})} = \begin{bmatrix} \Sigma_1^p & 0 & 0 \\ 0 & \Sigma_2^p & 0 \\ 0 & 0 & \Sigma_3^p \end{bmatrix} \begin{bmatrix} \mathbf{n} \cdot \mathbf{g}_1^p \\ \mathbf{n} \cdot \mathbf{g}_2^p \\ \mathbf{n} \cdot \mathbf{g}_3^p \end{bmatrix} = \begin{bmatrix} \Sigma_1^p \mathbf{n} \cdot \mathbf{g}_1^p \\ \Sigma_2^p \mathbf{n} \cdot \mathbf{g}_2^p \\ \Sigma_3^p \mathbf{n} \cdot \mathbf{g}_3^p \end{bmatrix}. \tag{6.39}$$

The $\mathbf{n} \cdot \mathbf{g}_k^p$ are direction cosines of $\mathbf{n}$ with the x_k^p axes, that is, the coordinate system that aligns with the directions of the principal stresses. To shorten the notation, let $\beta_k = \mathbf{n} \cdot \mathbf{g}_k^p$. The magnitude of the normal component of the traction is

$$\begin{aligned} \left| \left(\mathbf{t}_{(\mathbf{n})} \right)_n \right| = \mathbf{t}_{(\mathbf{n})} \cdot \mathbf{n} &= \begin{bmatrix} \Sigma_1^p \beta_1 & \Sigma_2^p \beta_2 & \Sigma_3^p \beta_3 \end{bmatrix} \begin{bmatrix} \beta_1 \\ \beta_2 \\ \beta_3 \end{bmatrix} \\ &= \Sigma_1^p \beta_1^2 + \Sigma_2^p \beta_2^2 + \Sigma_3^p \beta_3^2. \end{aligned} \tag{6.40}$$

The magnitude of the shear component of the traction is, from Eqs. (6.39) and (6.40) and Pythagorus' theorem (see Fig. 6.9),

$$\left| \left(\mathbf{t}_{(\mathbf{n})} \right)_s \right|^2 = \left(\Sigma_1^p \right)^2 \beta_1^2 + \left(\Sigma_2^p \right)^2 \beta_2^2 + \left(\Sigma_3^p \right)^2 \beta_3^2 - \left(\Sigma_1^p \beta_1^2 + \Sigma_2^p \beta_2^2 + \Sigma_3^p \beta_3^2 \right)^2. \tag{6.41}$$

For the unit vector $\mathbf{n}$ we can write

$$\mathbf{n} \cdot \mathbf{n} = \beta_1^2 + \beta_2^2 + \beta_3^2 = 1. \tag{6.42}$$

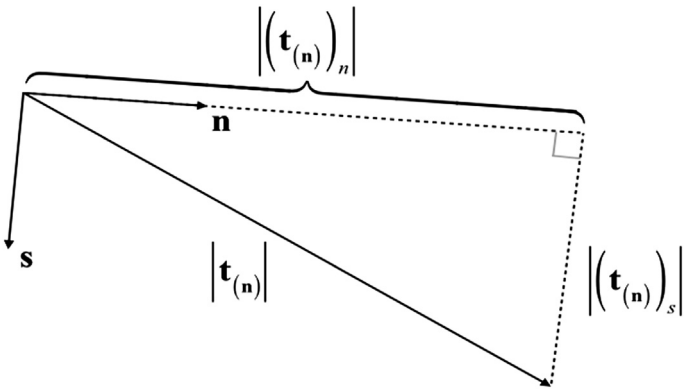

Figure 6.9 ***Determination of the shear component of*** $\mathbf{t_n}$**.** The unit vector **s** lies in the plane of investigation whose normal is **n**.

Using Eq. (6.42) in Eq. (6.41) to eliminate β_1, we obtain (cf. P.A. Kelly, 'Mechanics Lecture Notes: An Introduction to Solid Mechanics', http://homepages.engineering.auckland.ac.nz/~pkel015/SolidMechanicsBooks/index.html)

$$\begin{aligned}\left|\left(\mathbf{t}_{(\mathbf{n})}\right)_s\right|^2 &= \left(\Sigma_1^p\right)^2\left(1-\beta_2^2-\beta_3^2\right)+\left(\Sigma_2^p\right)^2\beta_2^2+\left(\Sigma_3^p\right)^2\beta_3^2\\ &\quad-\left[\Sigma_1^p\left(1-\beta_2^2-\beta_3^2\right)+\Sigma_2^p\beta_2^2+\Sigma_3^p\beta_3^2\right]^2\\ &=\left(\Sigma_1^p\right)^2+\left[\left(\Sigma_2^p\right)^2-\left(\Sigma_1^p\right)^2\right]\beta_2^2+\left[\left(\Sigma_3^p\right)^2-\left(\Sigma_1^p\right)^2\right]\beta_3^2\\ &\quad-\left[\Sigma_1^p+\left(\Sigma_2^p-\Sigma_1^p\right)\beta_2^2+\left(\Sigma_3^p-\Sigma_1^p\right)\beta_3^2\right]^2.\end{aligned}\tag{6.43}$$

The extrema of the shear component of the traction occur when the differential of $\left|\left(\mathbf{t}_{(\mathbf{n})}\right)_s\right|^2$ with respect to β_2 and β_3 vanishes:

$$\begin{aligned}d\left|\left(\mathbf{t}_{(\mathbf{n})}\right)_s\right|^2 &= 2\beta_2\left[\left(\Sigma_2^p\right)^2-\left(\Sigma_1^p\right)^2\right]d\beta_2+2\beta_3\left[\left(\Sigma_3^p\right)^2-\left(\Sigma_1^p\right)^2\right]d\beta_3-2\left[\Sigma_1^p+\left(\Sigma_2^p-\Sigma_1^p\right)\beta_2^2\right.\\ &\quad\left.+\left(\Sigma_3^p-\Sigma_1^p\right)\beta_3^2\right]\left[2\beta_2\left(\Sigma_2^p-\Sigma_1^p\right)d\beta_2+2\beta_3\left(\Sigma_3^p-\Sigma_1^p\right)d\beta_3\right]\\ &=2\beta_2\left(\Sigma_2^p-\Sigma_1^p\right)\left\{\Sigma_2^p-\Sigma_1^p-2\left[\left(\Sigma_2^p-\Sigma_1^p\right)\beta_2^2+\left(\Sigma_3^p-\Sigma_1^p\right)\beta_3^2\right]\right\}d\beta_2\\ &\quad+2\beta_3\left(\Sigma_3^p-\Sigma_1^p\right)\left\{\Sigma_3^p-\Sigma_1^p-2\left[\left(\Sigma_2^p-\Sigma_1^p\right)\beta_2^2+\left(\Sigma_3^p-\Sigma_1^p\right)\beta_3^2\right]\right\}d\beta_3=0.\end{aligned}\tag{6.44}$$

One solution to Eq. (6.44) is $\beta_2=\beta_3=0$, $\beta_1=\pm1$. This solution has the normal **n** to a plane of stationary shear stress aligning with a principal stress axis, for which case the shear stress is zero—the extremum is a minimum. A second solution to Eq. (6.44) is to arbitrarily set $\beta_3=0$ and solve for a nonzero value of β_2 that causes the coefficient of $d\beta_2$ in Eq. (6.44) to vanish. For this case

$$\beta_2\left(\Sigma_2^p-\Sigma_1^p\right)\left\{\Sigma_2^p-\Sigma_1^p-2\left(\Sigma_2^p-\Sigma_1^p\right)\beta_2^2\right\}d\beta_2=0,\quad \beta_2=\pm\sqrt{\frac{1}{2}},\tag{6.45}$$

which, using Eq. (6.42), leads us to conclude that $\beta_1 = \pm\sqrt{\frac{1}{2}}$ also. That is, the normal to the plane of extreme shear stress makes an angle of 45° with the 1 and 2 principle axes. The value of this shear stress is, from Eq. (6.41),

$$\left|\left(\mathbf{t}_{(\mathbf{n})}\right)_s\right|^2 = \frac{1}{2}\left[\left(\Sigma_1^p\right)^2 + \left(\Sigma_2^p\right)^2\right] - \frac{1}{4}\left(\Sigma_1^p + \Sigma_2^p\right)^2 = \frac{1}{4}\left(\Sigma_1^p - \Sigma_2^p\right)^2, \tag{6.46}$$

or

$$\left|\left(\mathbf{t}_{(\mathbf{n})}\right)_s\right| = \pm\frac{1}{2}\left(\Sigma_1^p - \Sigma_2^p\right), \quad \beta_1 = \beta_2 = \pm\sqrt{\frac{1}{2}},\ \beta_3 = 0. \tag{6.47}$$

If we repeat the above work starting with Eq. (6.44) and setting $\beta_2 = 0$, the symmetry of Eq. (6.44) indicates that our solution will be

$$\left|\left(\mathbf{t}_{(\mathbf{n})}\right)_s\right| = \pm\frac{1}{2}\left(\Sigma_1^p - \Sigma_3^p\right), \quad \beta_1 = \beta_3 = \pm\sqrt{\frac{1}{2}},\ \beta_2 = 0. \tag{6.48}$$

Further, the form of Eq. (6.41) suggests that if we were to now search for other extrema of the shear stress magnitude by successively eliminating β_2 and β_3 using Eq. (6.42) in Eq. (6.41), the results would be index permutations of Eqs. (6.47) and (6.48). We conclude that in principal stress space the maximum shear stress is

$$\Sigma_{smax} = \frac{1}{2}\max\left\{\left|\Sigma_1^p - \Sigma_2^p\right|, \left|\Sigma_2^p - \Sigma_3^p\right|, \left|\Sigma_3^p - \Sigma_1^p\right|\right\}, \tag{6.49}$$

and it occurs on a plane whose normal makes an angle of 45° with the two principal stress axes having the same subscripts as those of the maximum shear stress.

Consider now a uniaxial tension test. If we align the Σ_1^p-axis with the specimen, $\Sigma_2^p = \Sigma_3^p = 0$. When the specimen yields, $\Sigma_1^p = f_y$, and from Eq. (6.49) the maximum shear stress at yield is $\Sigma_{smax} = \frac{f_y}{2}$. Our final form of the Tresca yield criterion is therefore

$$f_y = \max\left\{\left|\Sigma_1^p - \Sigma_2^p\right|, \left|\Sigma_2^p - \Sigma_3^p\right|, \left|\Sigma_3^p - \Sigma_1^p\right|\right\}. \tag{6.50}$$

The Tresca yield surface can also be plotted in the π-plane (recall Fig. 6.6). Solving Eqs. (6.19)–(6.21) for the principal stresses in terms of the π coordinate system produces

$$\Sigma_1^p = \sqrt{\frac{2}{3}}\pi_2 + \frac{1}{\sqrt{3}}\pi_3, \tag{6.51}$$

$$\Sigma_2^p = -\frac{1}{\sqrt{2}}\pi_1 - \frac{1}{\sqrt{6}}\pi_2 + \frac{1}{\sqrt{3}}\pi_3, \tag{6.52}$$

$$\Sigma_3^p = \frac{1}{\sqrt{2}}\pi_1 - \frac{1}{\sqrt{6}}\pi_2 + \frac{1}{\sqrt{3}}\pi_3. \tag{6.53}$$

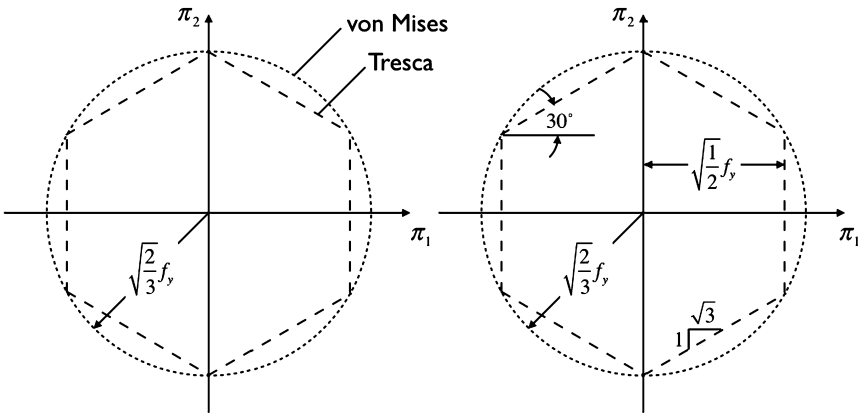

Figure 6.10 ***The surface corresponding to the Tresca yield criterion plotted in the π-plane.*** The cross-section of the yield surface is a hexagon that is circumscribed by the cross-section of the von Mises yield criterion.

Substituting Eqs. (6.51)–(6.53) into the constituents of Eq. (6.50) gives

$$\Sigma_1^p - \Sigma_2^p = \sqrt{\frac{3}{2}}\left(\frac{1}{\sqrt{3}}\pi_1 + \pi_2\right) = \pm f_y, \tag{6.54}$$

$$\Sigma_2^p - \Sigma_3^p = -\sqrt{2}\pi_1 = \pm f_y, \tag{6.55}$$

$$\Sigma_3^p - \Sigma_1^p = \sqrt{\frac{3}{2}}\left(\frac{1}{\sqrt{3}}\pi_1 - \pi_2\right) = \pm f_y. \tag{6.56}$$

Eq. (6.55) supplies two vertical lines, and Eqs. (6.54) and (6.56) provide four straight lines with positive and negative slopes and y intercepts

$$\pm\pi_2 = -\frac{1}{\sqrt{3}}\pi_1 \pm \sqrt{\frac{2}{3}}f_y, \tag{6.57}$$

where we note the value $\frac{1}{\sqrt{3}}$ is the tangent of 30°. Neither of the equations defining the Tresca yield surface depend on π_3 which means that, like the von Mises yield surface, the cross-section of the Tresca yield surface extends infinitely along the hydrostatic stress axis on either side of the π-plane.

A plot of Eqs. (6.55) and (6.57) is shown in Fig. 6.10 in comparison to the von Mises yield surface. Both yield surfaces are cylinders whose axes are normal to the π-plane. The circular cross-section of the von Mises yield surface circumscribes[15] the hexagonal

[15] At $\pi_1 = \pm f_y$ (see Eq. (6.55)), Eq. (6.57) becomes $\pi_2 = \pm\frac{1}{\sqrt{6}}f_y$, and therefore $\pi_1^2 + \pi_2^2 = \frac{2}{3}f_y^2$. That is, the circumscribing circle (von Mises) touches the Tresca yield surface at the vertices/intersections of the faces of the Tresca yield surface.

cross-section of the Tresca yield surface. As indicated in the right-hand diagram of Fig. 6.10, the four sloped faces of the Tresca hexagon can be traced to Eq. (6.57); the two vertical faces can be traced to Eq. (6.55).

The Tresca yield criterion is simpler in concept than that of von Mises, and a body of evidence indicates yield occurring between the two surfaces giving the Tresca surface a slight advantage in conservatism. The primary disadvantage of the Tresca surface is that in a general stress state its mathematical statement and implementation is more difficult, particularly at the vertices which assume importance in load paths that exceed yield (e.g., defining the normal to the yield surface at a vertex).

6.3.4 First yield of a tube in the absence of bending

It is important for our study to consider explicit forms of Eq. (6.33) specific to tubulars. Section 5.2.4.1 of Chapter 5 introduces Eqs. (5.51)–(5.53) governing stress in a deforming tube subject to neither bending nor torsion.[16] These equations are valid up to the point of incipient yield and may therefore be substituted in Eq. (6.35) to arrive at a criterion for yield in terms of axial stress and internal and external pressure. Performing this substitution ($\Sigma_{11} = \Sigma_{zz}$, $\Sigma_{22} = \Sigma_{\theta\theta}$, $\Sigma_{33} = \Sigma_{rr}$, all other $\Sigma_{ij} = 0$), the resulting expression can be written as

$$\hat{\Sigma}_e^2(r) = \left(\Sigma_{zz} - \frac{p_i d^2 - p_o D^2}{D^2 - d^2}\right)^2 + \frac{3}{16r^4}\left(\frac{(p_i - p_o)\, d^2 D^2}{D^2 - d^2}\right)^2. \tag{6.58}$$

Differentiating the left-hand side of this equation with respect to the tube radial coordinate r gives

$$\frac{d\hat{\Sigma}_e^2(r)}{dr} = -\frac{3}{4}\frac{1}{r^5}\left(\frac{(p_i - p_o)\, d^2 D^2}{D^2 - d^2}\right)^2 \leq 0. \tag{6.59}$$

If $p_i = p_o$, $\frac{d\hat{\Sigma}_e^2(r)}{dr}$ vanishes for all r, implying a constant value of $\hat{\Sigma}_e(r)$ through the cross-section. If $p_i \neq p_o$, $\frac{d\hat{\Sigma}_e^2(r)}{dr}$ is negative for all r, implying that the maximum value of $\hat{\Sigma}_e(r)$ is at the inner diameter of the tube. In the absence of bending, we reach the conclusion that, regardless of internal and external pressure and axial load, $\hat{\Sigma}_e(r)$ is always greatest, and therefore yield always has its first occurrence at the tube's inner diameter.

[16] Later (Section 6.3.5) we shall include bending by superimposing the results of Section 5.2.4.2 of Chapter 5. API Technical Report 5C3 [51] also includes the torsional stress $\Sigma_{\theta z}$ in its formulation of the von Mises yield criterion (see again Section 5.2.4.2 of Chapter 5). This shear stress was included to accommodate the torsion associated with the process of drilling with casing. As this aspect of tubular design will not be discussed in this book, the term $\Sigma_{\theta z}$ has been dropped from consideration.

Substituting this result into Eq. (6.34) by setting $r = \frac{d}{2}$ in Eq. (6.58) gives

$$\hat{f} = \left(\Sigma_{zz} - \frac{p_i d^2 - p_o D^2}{D^2 - d^2}\right)^2 + \left(\sqrt{3}\frac{(p_i - p_o)\, D^2}{D^2 - d^2}\right)^2 - f_y^2 = 0. \tag{6.60}$$

Three forms of Eq. (6.60) are commonly used in tubular design:

6.3.4.1 First yield expressed with Σ_{eff}

Chapter 10 introduces the concept of effective force (see Eq. (10.1)), an important concept when analyzing bending and buckling. For the present, it is sufficient to note that if Eq. (10.1) is divided by the cross-sectional area $(A_o - A_i)$, one arrives at the first parenthetical term in Eq. (6.60), namely

$$\Sigma_{eff} = \frac{f_z - (p_i A_i - p_o A_o)}{A_o - A_i} = \Sigma_{zz} - \frac{p_i d^2 - p_o D^2}{D^2 - d^2}. \tag{6.61}$$

Further, noting that

$$\frac{D^2}{D^2 - d^2} = \frac{\left(\frac{D}{t}\right)^2}{4\left(\frac{D}{t} - 1\right)}, \tag{6.62}$$

we can reexpress Eq. (6.60) as

$$\hat{f} = \Sigma_{eff}^2 + \left(\sqrt{3}\frac{\left(\frac{D}{t}\right)^2}{4\left(\frac{D}{t} - 1\right)}(p_i - p_o)\right)^2 - f_y^2 = 0. \tag{6.63}$$

As indicated in Fig. 6.11, Eq. (6.63) is a circle, centered at the origin and having radius f_y. The space in which the surface is plotted has abscissa Σ_{eff} and ordinate $\frac{\sqrt{3}\left(\frac{D}{t}\right)^2}{4\left(\frac{D}{t}-1\right)}(p_i - p_o)$.

The circle in Fig. 6.11 is actually very close to the circular cross-section of the yield surface represented by Eq. (6.23), the only difference between the two circles being a factor of $\sqrt{\frac{2}{3}}$, with the radius of the cylinder represented by Eq. (6.23) being the smaller. The yield surface radial metric of the circle represented by Eq. (6.63) is stretched relative to its more general counterpart.

On the surface, the two circles differ significantly in their coordinate axes. If we notice from Eqs. (5.51) and (5.52), however, that at $r = d/2$

$$\Sigma_{rr} + \Sigma_{\theta\theta} = 2\frac{p_i d^2 - p_o D^2}{D^2 - d^2}, \tag{6.64}$$

$$\Sigma_{rr} - \Sigma_{\theta\theta} = -2\frac{(p_i - p_o)\, D^2}{D^2 - d^2}, \quad r = \frac{d}{2}, \tag{6.65}$$

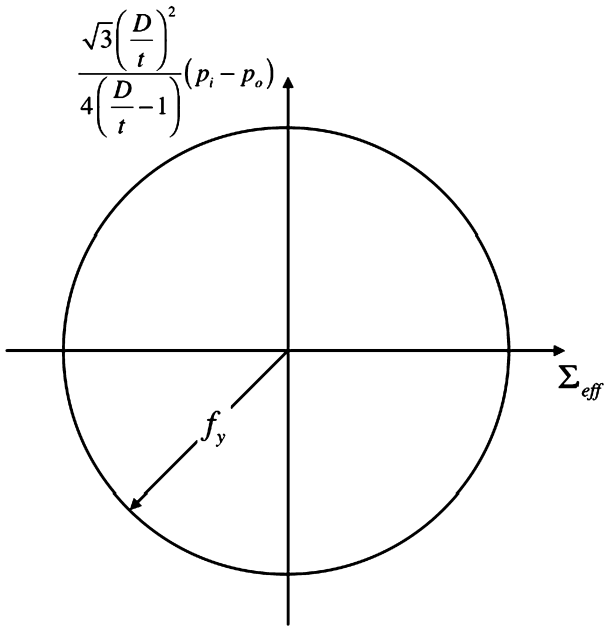

Figure 6.11 ***The surface corresponding to the von Mises yield criterion expressed in terms of effective stress.***

with the help of Eqs. (6.61) and (6.62) we may rewrite Eq. (6.63) as

$$\hat{f} = \left(\Sigma_{zz} - \frac{\Sigma_{rr} + \Sigma_{\theta\theta}}{2}\right)^2 + \left(-\frac{\sqrt{3}\,(\Sigma_{rr} - \Sigma_{\theta\theta})}{2}\right)^2 - f_y^2 = 0. \tag{6.66}$$

Now let $\Sigma_{zz} = \Sigma_{11} = \Sigma_1^p$, $\Sigma_{\theta\theta} = \Sigma_{22} = \Sigma_2^p$ and $\Sigma_{rr} = \Sigma_{33} = \Sigma_3^p$. Using Eqs. (6.19) and (6.20), we can rewrite Eq. (6.66) as

$$\hat{f} = \pi_2^2 + (-\pi_1)^2 - \left(\sqrt{\frac{2}{3}} f_y\right)^2 = 0. \tag{6.67}$$

Comparing Eqs. (6.67) and (6.63) indicates the abscissae and ordinates of the two coordinate systems are aligned, with the respective circle radii differing by a factor of $\sqrt{\frac{2}{3}}$. Fig. 6.12 illustrates the relation between Eqs. (6.63) and (6.67), particularly at their intersection with the π-plane. Both circles predict yield at the same state of stress—the two circles differ in that their generating coordinate axes have different scales.

Because the circle of Fig. 6.11 is coplanar and concentric with the cross-section of the general expression of the von Mises yield criterion, no information is lost using Fig. 6.11's presentation. This allows us to maintain a fully three-dimensional treatment in a two-dimensional presentation.

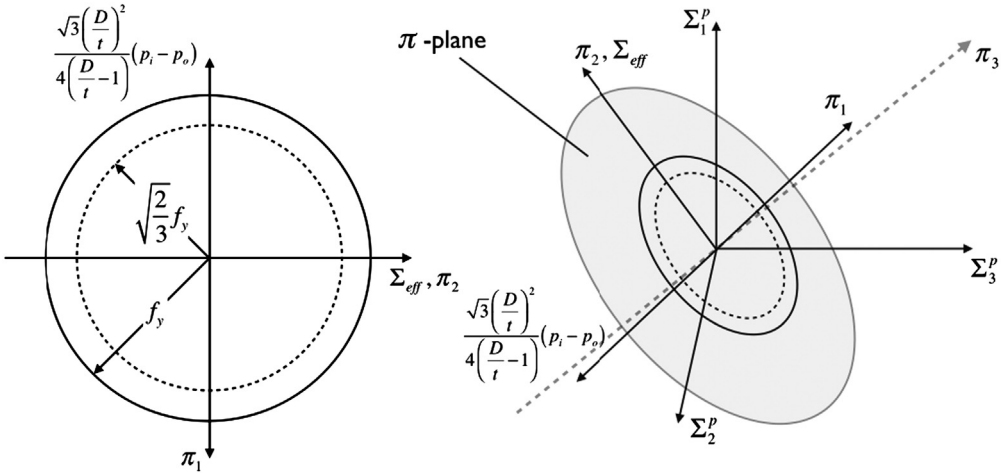

Figure 6.12 ***The surface corresponding to the von Mises yield criterion expressed in terms of effective stress and its relation to the intersection of the von Mises yield criterion with the π-plane.***

6.3.4.2 First yield expressed with $\Sigma_{zz} + p_i$

As an alternative to expressing the von Mises yield surface in terms of effective stress, algebraic manipulation of Eq. (6.60) can be rearranged to the form

$$\hat{f} = \left(\Sigma_{zz} + p_i\right)^2 + \left(\frac{\left(\frac{D}{t}\right)^2}{2\left(\frac{D}{t}-1\right)}\left(p_i - p_o\right)\right)^2 - \left(\frac{\left(\frac{D}{t}\right)^2}{2\left(\frac{D}{t}-1\right)}\left(p_i - p_o\right)\right)\left(\Sigma_{zz} + p_i\right) - f_y^2 = 0. \tag{6.68}$$

As indicated in Fig. 6.13, Eq. (6.68) is an ellipse, centered at the origin. The major axis of the ellipse makes an angle of $\pi/4$ with the abscissa. The space in which the surface is plotted has abscissa $\Sigma_{zz} + p_i$ and ordinate $\frac{\left(\frac{D}{t}\right)^2}{2\left(\frac{D}{t}-1\right)}\left(p_i - p_o\right)$.

Although it is less easy to see, the ellipse of Fig. 6.13 also contains complete information regarding three-dimensional yield in a two-dimensional display.

6.3.4.3 First yield expressed with Σ_{zz}

The third presentation of yield[17] is particularly useful in a testing environment, and as such has found home in both the API recommended practice for testing casing and tubing connections [56] and the API specification for packers and bridge plugs [55]. In both these test environments, simultaneous application of internal and external pressure

[17] Some implementations of this presentation use axial force f_z rather than axial stress as the abscissa [55,56]. This simply extends the horizontal axis by a factor equal to the cross-sectional area of the tube.

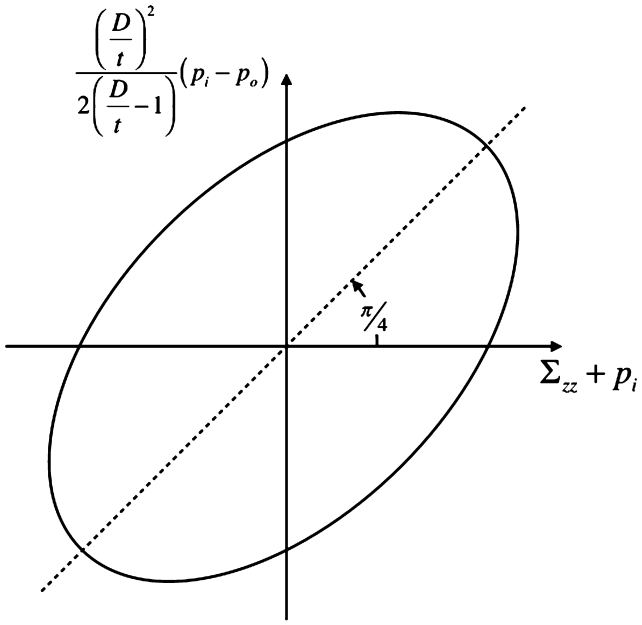

Figure 6.13 ***The surface corresponding to the von Mises yield criterion expressed in terms of*** $\Sigma_{zz} + p_i$.

is rare. Therefore, two half-ellipses are used to handle the separate conditions of internal pressure only and external pressure only testing.

Consider first the case of testing with internal pressure. Setting $p_o = 0$ in Eq. (6.60) produces

$$\hat{f} = \frac{d^4 + 3D^4}{\left(D^2 - d^2\right)^2} p_i^2 + \left(-2\Sigma_{zz} \frac{d^2}{D^2 - d^2}\right) p_i + \Sigma_{zz}^2 - f_y^2 = 0. \tag{6.69}$$

Solving this quadratic equation for p_i yields

$$p_i = \frac{-k_B \pm \sqrt{k_B^2 - 4k_A k_C}}{2k_A}, \tag{6.70}$$

where

$$k_A = k_{pi}^2 + k_{pi} + 1, \tag{6.71}$$

$$k_B = \left(1 - k_{pi}\right) \Sigma_{zz}, \tag{6.72}$$

$$k_C = \Sigma_{zz}^2 - f_y^2, \tag{6.73}$$

$$k_{pi} = \frac{D^2 + d^2}{D^2 - d^2}. \tag{6.74}$$

Similarly, for the case of testing with external pressure, setting $p_i = 0$ in Eq. (6.60) gives

$$\hat{f} = \left(\frac{2D^2}{D^2 - d^2}\right)^2 p_o^2 + \left(2\Sigma_{zz}\frac{D^2}{D^2 - d^2}\right)p_o + \Sigma_{zz}^2 - f_y^2 = 0. \tag{6.75}$$

Solving this quadratic equation for p_o yields

$$p_o = \frac{-k_B \pm \sqrt{k_B^2 - 4k_A k_C}}{2k_A}, \tag{6.76}$$

where now

$$k_A = k_{po}^2, \tag{6.77}$$

$$k_B = k_{po}\Sigma_{zz}, \tag{6.78}$$

$$k_C = \Sigma_{zz}^2 - f_y^2, \tag{6.79}$$

with

$$k_{po} = \frac{2D^2}{D^2 - d^2}. \tag{6.80}$$

For $\Sigma_{zz} = f_y$, Eqs. (6.69) and (6.75) admit the solutions $p_i = 0$ and $p_o = 0$, respectively, implying that the two half-ellipses will maintain continuity as they approach the Σ_{zz}-axis, but their slopes will rarely be equal, since the parameters in Eqs. (6.70) and (6.76) differ in definition and magnitude. This is illustrated in Fig. 6.14 where a typical composite ellipse is shown.

Further, as the two half-ellipses involve a simplification to the governing equation, the presentation of Fig. 6.14 is not fully three-dimensional as was the case with the first two alternatives. Consider, for example, an open-ended tubing string lowered in a fluid environment in a vertical wellbore. The von Mises yield criterion posits independence of yield on a hydrostatic stress state. Thus one should be able to lower the tubing indefinitely without yielding its lowermost end. And such is the case for the ellipses in Figs. 6.11 and 6.13.[18] For Fig. 6.14, however, the increasing compressive stress at the bottom of the tubing as it is lowered will eventually "yield" the tubing, counter to theory. The consequences of this will be discussed in Section 9.8.2 of Chapter 9.

[18] At any depth, the axial force at the lower end of the tubing is $f_z = -p(A_o - A_i)$. For Fig. 6.11, $\Sigma_e = \left[f_z - p(A_i - A_o)\right]/(A_o - A_i) = 0$. For Fig. 6.13, $\Sigma_{zz} + p_i = -p + p = 0$. In both cases, the ordinate value, $p_i - p_o$, is zero. As the tubing is lowered into the wellbore, its coordinates in Figs. 6.11 and 6.13 remain at the origin.

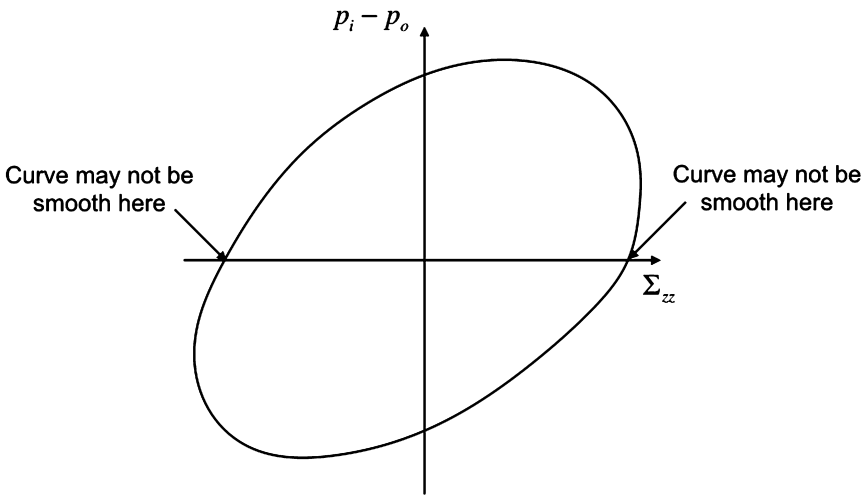

Figure 6.14 ***The surface corresponding to the von Mises yield criterion expressed in terms of*** Σ_{zz}**.** The indicated locations are the connections of an upper ellipse, governed by Eq. (6.70) and applicable to internal pressure-dominant loads, and a lower ellipse, governed by Eq. (6.76) and applicable to external pressure-dominant loads.

6.3.4.4 A simple expression of first yield

The three preceding subsections have manipulated Eq. (6.60) to arrive at various expressions of yield at the inner radius of a tube in the absence of bending. These relations are used extensively in detailed calculations of material yield, both in spreadsheets and in tubular-specific software design tools. As productive as these tools are, however, they represent a degree of complexity that may be just beyond the bounds of quick reasoning. For example, given a state of pressures and axial force, it is not always clear in Eqs. (6.63), (6.68) and (6.69)/(6.75) whether a change in that state—doubling the internal pressure, for example—places one closer or further from yield. As a remedy, the current section targets a simple expression of the von Mises yield surface that captures the essence, if not the accuracy, of the previous expressions. It will be this simpler yield criterion to which we will appeal in future work when we desire an explanation of tubular behavior but do not wish to smother the answer with calculation exactness.

As a first step we replace the Lamé equations, Eqs. (5.51) and (5.52), with the following expressions of hoop and radial stress:

$$\Sigma_{\theta\theta} = \frac{\bar{D}}{2t}\left(p_i - p_o\right), \tag{6.81}$$

$$\Sigma_{rr} = 0, \tag{6.82}$$

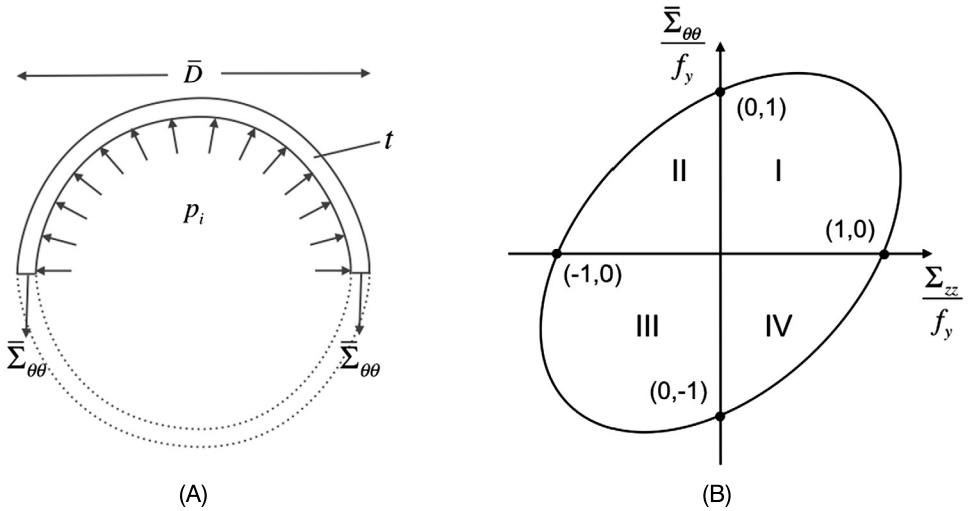

Figure 6.15 ***The surface corresponding to the von Mises yield criterion expressed with approximate stresses.*** Diagram (A) justifies ignoring the radial stress; Diagram (B) presents the resulting ellipse.

where $\bar{D} = \frac{D+d}{2}$ is the mean diameter of the tube. These relations have been shown to be zeroth-order correct in $\frac{t}{\bar{D}}$ [57] in an expression for virtual work of a tube loaded by axial force and internal and external pressure. For further comfort, particularly with the fact that the radial stress is to be ignored, consider the left-hand diagram in Fig. 6.15.

For simplicity, the tube cross-section is loaded with internal pressure only. Further, the tube cross-section is cut to investigate the internal stresses, in particular the average[19] hoop stress $\bar{\Sigma}_{\theta\theta}$. Summing forces in the vertical direction with up designated as positive and assuming the tube to extend 1 unit of length into the paper gives

$$-2\bar{\Sigma}_{\theta\theta}t(1) + \int_0^{\pi} p_i \sin\theta \frac{\bar{D}}{2} d\theta(1) = -2\bar{\Sigma}_{\theta\theta}t(1) + p_i\frac{\bar{D}}{2}\underbrace{\int_0^{\pi} \sin\theta\, d\theta}_{=2}(1), \quad \bar{\Sigma}_{\theta\theta} = \frac{p_i\bar{D}}{2t}. \tag{6.83}$$

The average $\frac{\bar{D}}{t}$ for casing is roughly 20; the average $\frac{\bar{D}}{t}$ for tubing is roughly 10. The maximum absolute value of Σ_{rr} in the cross-section is p_i at the inner diameter. Therefore, for typical oil well tubulars the average value of $\Sigma_{\theta\theta}$ is 5–10 times the maximum value of Σ_{rr}. Ignoring Σ_{rr} per Eq. (6.82) is a reasonable measure.

[19] We could just as easily used the outside diameter or inside diameter in this calculation. The tube is assumed to be thin ($\Sigma_{\theta\theta}$ is constant through the thickness) so $\bar{D} \approx D \approx d$.

If we substitute Eqs. (6.81) and (6.82) into Eq. (6.33) (e.g., $\Sigma_{11} = \Sigma_{rr}$, $\Sigma_{22} = \Sigma_{\theta\theta}$, $\Sigma_{33} = \Sigma_{zz}$, all other $\Sigma_{ij} = 0$), then

$$\Sigma_{\theta\theta}^2 + \Sigma_{zz}^2 - \Sigma_{\theta\theta}\Sigma_{zz} - f_y^2 = \left(\frac{(p_i - p_o)\bar{D}}{2t}\right)^2 + \Sigma_{zz}^2 - \frac{(p_i - p_o)\bar{D}}{2t}\Sigma_{zz} - f_y^2 = 0. \quad (6.84)$$

This is the equation of an ellipse whose major axis makes an angle of $\frac{\pi}{4}$ with the abscissa. The ellipse is shown in the right-hand diagram in Fig. 6.15. From Eq. (6.84) and Eq. (6.35) we get

$$\Sigma_e = \sqrt{\Sigma_{\theta\theta}^2 + \Sigma_{zz}^2 - \Sigma_{\theta\theta}\Sigma_{zz}} = \sqrt{\left(\frac{(p_i - p_o)\bar{D}}{2t}\right)^2 + \Sigma_{zz}^2 - \frac{(p_i - p_o)\bar{D}}{2t}\Sigma_{zz}}, \quad (6.85)$$

which has the following implications:

- The upper half of the ellipse, quadrants I and II where $p_i - p_o > 0$, addresses loads tending toward internal pressure resistance or burst (Chapter 7).
- The lower half of the ellipse, quadrants III and IV where $p_i - p_o < 0$, addresses loads tending toward external pressure resistance or collapse (Chapter 8).
- The right half of the ellipse, quadrants I and IV where $\Sigma_{zz} > 0$, addresses axial tension loads.
- The left half of the ellipse, quadrants II and III where $\Sigma_{zz} < 0$, addresses axial compression loads.
- Combinations are appropriate. For example, quadrant II may be used to address the effect of compression on internal pressure resistance.
- Usually, the object of design will be to render Σ_e as small as possible, that is, to distance the state of combined stress from the yield surface.

With the above bulleted orientation, Eq. (6.85) can yield immediate insights. Consider a tube loaded by a pressure that is internally dominant, that is, $p_i - p_o > 0$. Viewing Eq. (6.85) in its rightmost form, the first term $\left(\frac{(p_i - p_o)\bar{D}}{2t}\right)^2$ and the second term Σ_{zz}^2 are squared and therefore always positive. The first portion of the third term $\frac{(p_i - p_o)\bar{D}}{2t}$ is, for the current example, positive, so that the stress state will be most damaging (i.e., high value of Σ_e) when $\Sigma_{zz} < 0$. Stated in words, "compression lowers resistance to internal pressure."[20]

A corresponding conclusion can be reached from Eq. (6.85) for quadrant IV regarding the effect of tension on collapse, i.e., "tension lowers resistance to external pressure." Both of these insights would be more difficult to discern if one appealed to the expression of equivalent stress involving the full Lamé equations for pressure dependence. We

[20] A similar conclusion can be reached by appealing to quadrant II of Fig. 6.15. As one moves along the abscissa in a negative direction, there is less ordinate value available before one intersects the yield surface.

shall have occasion in future chapters to call on this section and Eqs. (6.84) and (6.85) for aid in understanding the implications of multidimensional stress environments.

Example problem—using Σ_e to determine yield

A tube ($D = 7.000$ in., $t = 0.408$ in.) of T95 material is loaded with:

- 5000 psi internal pressure, 1000 psi external pressure, such that the hoop stress at the inner radius of the tube is, from Eq. (5.52), 31 438 psi.
- 500 000 lb_f axial compression.

The cross-sectional area of the tube is 8.449 in^2.

What are the values of the axial, radial and hoop stress? Has the tube yielded?

The radial stress at the inner radius is, by inspection or by Eq. (5.51), $\Sigma_{rr} = -5000$ psi. The hoop stress is given in the problem statement as $\Sigma_{\theta\theta} = 31\,438$ psi. The axial stress is compressive, and is $\Sigma_{zz} = -500\,000\,\text{lb}_\text{f}/8.449\,\text{in}^2 = -59\,176$ psi.

From Eq. (6.35), the von Mises equivalent stress is

$$\begin{aligned}\Sigma_e &= \left[\Sigma_{rr}^2 + \Sigma_{\theta\theta}^2 + \Sigma_{zz}^2 - \Sigma_{rr}\Sigma_{\theta\theta} - \Sigma_{\theta\theta}\Sigma_{zz} - \Sigma_{zz}\Sigma_{rr}\right]^{\frac{1}{2}} \\ &= \left[(-5000)^2 + (31\,438)^2 + (-59\,176)^2 - (-5000)(31\,438)\right. \\ &\qquad \left. -(31\,438)(-59\,176) - (-59\,176)(-5000)\right]^{\frac{1}{2}} \\ &= 78\,973\,\text{psi}.\end{aligned} \tag{6.86}$$

The von Mises equivalent stress is less than the yield stress (95 000 psi), so the tube has not yielded.

In reviewing this answer note the following:

- The radial stress at the inner radius of the tube is determined solely by the traction on the tube's inner surface and knows nothing of the 1000 psi external pressure.
- It would be difficult, other than performing a complete recalculation, to determine the effect with regard to yield of increasing the internal pressure to 6000 psi.

Example problem—using the simplified Σ_e to determine yield

Repeat the example problem of section 'Example problem—using Σ_e to determine yield' using the simple yield model of Section 6.3.4.4.

From Eq. (6.82), the radial stress is $\Sigma_{rr} = 0$ psi. The hoop stress is calculated from Eq. (6.81) as

$$\Sigma_{\theta\theta} = \frac{\bar{D}}{2t}\left(p_i - p_o\right) = \frac{7.000\,\text{in.} - 0.408\,\text{in.}}{2 \times 0.408\,\text{in.}}\left(5000\,\text{psi} - 1000\,\text{psi}\right) = 32\,314\,\text{psi}. \tag{6.87}$$

The axial stress remains $\Sigma_{zz} = -59\,176$ psi.

The simplified von Mises equivalent stress is

$$\begin{aligned}\Sigma_e &= \left[\Sigma_{\theta\theta}^2 + \Sigma_{zz}^2 - \Sigma_{\theta\theta}\Sigma_{zz}\right]^{\frac{1}{2}} \\ &= \left[(32\,314)^2 + (-59\,176)^2 - (32\,314)(-59\,176)\right]^{\frac{1}{2}} \\ &= 80\,363\,\text{psi}.\end{aligned} \tag{6.88}$$

The von Mises equivalent stress is less than the yield stress (95 000 psi), so the tube has not yielded.

In reviewing this answer note the following:

- The hoop stress, being a single, thin cylinder quantity, is determined by the full differential pressure on the tube cross-section.
- The error in $\Sigma_{\theta\theta}$ compared to the Lamé value is $\frac{32\,314-31\,438}{31\,438} \times 100$, or less than 3%.
- The error in Σ_e compared to Section 6.85 is $\frac{80\,363-78\,973}{78\,973} \times 100$, or less than 2%. The simplified yield envelope, although not as accurate as its companions in Sections 6.3.4.1–6.3.4.3, is not wildly inaccurate.
- It is fairly easy to see from Eqs. (6.87) and (6.88) that increasing the internal pressure to 6000 psi (a) increases the $\Sigma_{\theta\theta}$, which (b) increases Σ_e, which (c) nudges the multidimensional stress state closer to yield.

6.3.5 First yield of a tube in the presence of bending

In the presence of bending, and if we ignore shear stresses due to bending, Eq. (6.58) can be rendered applicable by adding the axial stress due to bending to Σ_{zz} (see Eqs. (5.101) and (5.107)), i.e.,

$$\Sigma_{zz} = \hat{\Sigma}_{zz}(r) = \Sigma_a \pm \hat{\Sigma}_b(r) = \Sigma_a \pm \frac{|\mathbf{m}|\, r}{I}, \tag{6.89}$$

where Σ_a is that portion of Σ_{zz} not due to bending, Σ_b is that portion of Σ_{zz} due to bending, $\mathbf{m}$ is the bending moment and I is the moment of inertia. Eq. (6.89), when substituted into Eq. (6.58), yields

$$\hat{\Sigma}_e^2(r) = \left(\Sigma_a \pm \frac{|\mathbf{m}|\, r}{I} - \frac{p_i d^2 - p_o D^2}{D^2 - d^2}\right)^2 + \frac{3}{16 r^4}\left(\frac{\left(p_i - p_o\right) d^2 D^2}{D^2 - d^2}\right)^2. \tag{6.90}$$

Differentiating the left-hand side of this equation with respect to r, the first term (see Eq. (6.59)) is no longer constant across the cross-section [58]:

$$\frac{d\hat{\Sigma}_e^2(r)}{dr} = \pm 2\frac{|\mathbf{m}|}{I}\left(\Sigma_a \pm \frac{|\mathbf{m}|\, r}{I} - \frac{p_i d^2 - p_o D^2}{D^2 - d^2}\right) - \frac{3}{4}\frac{1}{r^5}\left(\frac{\left(p_i - p_o\right) d^2 D^2}{D^2 - d^2}\right)^2. \tag{6.91}$$

In the absence of bending (see discussion surrounding Eq. (6.59)), the above derivative is always nonpositive, implying $\hat{\Sigma}_e^2(r)$ is always greatest on the inner diameter. Now,

depending on the values of $|\mathbf{m}|$ and I, $\frac{d\hat{\Sigma}_e^2(r)}{dr}$ can possibly vanish. To determine the character of a possible extremum, we take the second derivative

$$\frac{d^2\hat{\Sigma}_e^2(r)}{dr^2} = 2\left(\frac{|\mathbf{m}|}{I}\right)^2 + \frac{15}{4}\frac{1}{r^6}\left(\frac{(p_i - p_o)\,d^2D^2}{D^2 - d^2}\right)^2 \geq 0. \tag{6.92}$$

The following possibilities exist for Eqs. (6.91) and (6.92):

- If $p_i = p_o$, Eq. (6.91) becomes

$$\frac{d\hat{\Sigma}_e^2(r)}{dr} = \pm 2\frac{|\mathbf{m}|}{I}\left(\Sigma_a \pm \frac{|\mathbf{m}|\,r}{I}\right)^2. \tag{6.93}$$

  For $|\mathbf{m}| \neq 0$, $\frac{d\hat{\Sigma}_e^2(r)}{dr}$ vanishes at $r = \mp\frac{\Sigma_a I}{|\mathbf{m}|}$ and in Eq. (6.92) $\frac{d^2\hat{\Sigma}_e^2(r)}{dr^2}$ is positive at the radial location at which $\frac{d\hat{\Sigma}_e^2(r)}{dr}$ vanishes implying a local minimum at that radius.
- If $p_i \neq p_o$, we can solve Eq. (6.91) for the value of r at which $\frac{d\hat{\Sigma}_e^2(r)}{dr}$ vanishes. Eq. (6.92), however, dictates that $\frac{d\hat{\Sigma}_e^2(r)}{dr}$ be positive at the point at which $\frac{d\hat{\Sigma}_e^2(r)}{dr}$ vanishes, again implying a local minimum at that radius.

There is therefore no point in the cross-section for which $\frac{d\hat{\Sigma}_e^2(r)}{dr}$ is negative. That is, there is no $d/2 < r < D/2$ for which $\hat{\Sigma}_e(r)$ is a local maximum. The maximum value must occur at either $r = d/2$ or $r = D/2$. The conclusion to be reached from this investigation is that, in the presence of bending, one must check four locations for the maximum value of $\hat{\Sigma}_e(r)$:

- $r = d/2$, $\Sigma_b = \frac{|\mathbf{m}|r}{I} > 0$;
- $r = D/2$, $\Sigma_b > 0$;
- $r = d/2$, $\Sigma_b < 0$;
- $r = D/2$, $\Sigma_b < 0$.

The location at which the greatest value of $\hat{\Sigma}_e(r)$ occurs is the location in the tube cross-section closest to yield.

Reviewing Sections 6.3.4 and the present, Eq. (6.90)—using either Σ_{zz} or $\Sigma_a \pm \hat{\Sigma}_b(r) = \Sigma_a \pm \frac{|\mathbf{m}|r}{I}$ as the term(s) addressing axial stress—is the primary limit state for triaxial yield used in the remainder of this book.

6.3.6 Design equation for yield in multiple dimensions

Limit state Eq. (6.60) can be rendered a design equation by the following substitutions [51]:

- Replace the yield stress f_y with the specified minimum yield stress f_{ymn}.
- Replace the specified wall thickness t by a wall thickness that includes the effect of manufacturing process. Within the industry tubular standards [46], the manufacturing process is permitted to produce a product whose wall thickness is $k_{wall}t$, where

k_{wall} has a default that can be altered by an agreement of the user and manufacturer.[21] The wall thickness does not appear in Eq. (6.60), but the inside diameter d, which depends on t, does.[22] We introduce a new variable d_{wall} where

$$d_{wall} = D - 2k_{wall}t. \tag{6.94}$$

With these two substitutions, Eq. (6.34) with Eq. (6.58) becomes[23]

$$\hat{f}_{des}(r) = \left(\Sigma_{zz} - \frac{p_i d_{wall}^2 - p_o D^2}{D^2 - d_{wall}^2}\right)^2 + \frac{3}{16r^4}\left(\frac{(p_i - p_o)\, d_{wall}^2 D^2}{D^2 - d_{wall}^2}\right)^2 - f_{ymn}^2 = 0. \tag{6.95}$$

In the absence of bending, $r = \frac{d_{wall}}{2}$. In cases involving bending, Eq. (6.95) is still applicable if we replace Σ_{zz} with $\Sigma_a \pm \hat{\Sigma}_b(r) = \Sigma_a \pm \frac{|\mathbf{m}|r}{I}$ [51] and evaluate $\hat{f}_{des}$ at $r = \frac{d_{wall}}{2}$ and $r = \frac{D}{2}$ per the bulleted procedure at the end of Section 6.3.5. A positive value of $\hat{f}_{des}$ indicates yield.

6.3.6.1 *Example problem—Σ_e and the design equation*

Relate Eq. (6.95) to Σ_e.

Consider the definition of Σ_e given in Eq. (6.35). In the absence of shear ($\Sigma_{12}^2 = \Sigma_{23}^2 = \Sigma_{31}^2 = 0$) and bending,

$$\begin{aligned}\Sigma_e &= \sqrt{\Sigma_{11}^2 + \Sigma_{22}^2 + \Sigma_{33}^2 - \Sigma_{11}\Sigma_{22} - \Sigma_{22}\Sigma_{33} - \Sigma_{33}\Sigma_{11}} \\ &= \frac{1}{\sqrt{2}}\sqrt{(\Sigma_{11} - \Sigma_{22})^2 + (\Sigma_{22} - \Sigma_{33})^2 + (\Sigma_{33} - \Sigma_{11})^2}.\end{aligned} \tag{6.96}$$

Further, recall from Eqs. (5.51) and (5.52) that the Lamé equations can be written as

$$\Sigma_{rr} = A - \frac{B}{4r^2}, \tag{6.97}$$

$$\Sigma_{\theta\theta} = A + \frac{B}{4r^2}, \tag{6.98}$$

where

$$A = \frac{p_i d^2 - p_o D^2}{D^2 - d^2}, \quad B = \frac{(p_i - p_o)\, d^2 D^2}{D^2 - d^2}. \tag{6.99}$$

[21] For example, if the wall tolerance is – 10%, $k_{wall} = 0.90$.

[22] In the API standards D and t are the independent dimensions and d is derived from the formula $d = D - 2t$.

[23] In the substitution $d \to d_{wall}$ leading to Eq. (6.95) only the stresses most affected by wall thinning—Σ_{rr} and $\Sigma_{\theta\theta}$—are affected. These two terms suffer directly from even a local loss of wall thickness. Axial stress is less affected by local wall thinning since it depends on the area of the entire cross-section. For more detail on the effect of wall thinning on axial stress see Section 15.3.2 of Chapter 15.

In cylindrical coordinates we can set $\Sigma_{11} = \Sigma_{rr}$, $\Sigma_{22} = \Sigma_{\theta\theta}$ and $\Sigma_{33} = \Sigma_{zz}$ which, with the inclusion of Eqs. (6.97)–(6.99), yields

$$\begin{aligned}\Sigma_e &= \frac{1}{\sqrt{2}}\sqrt{\left(2\frac{B}{4r^2}\right)^2 + \left(A + \frac{B}{4r^2} - \Sigma_{zz}\right)^2 + \left(\Sigma_{zz} - A + \frac{B}{4r^2}\right)^2} \\ &= \frac{1}{\sqrt{2}}\sqrt{6\left(\frac{B}{4r^2}\right)^2 + 2\left(\Sigma_{zz} - A\right)^2} \\ &= \sqrt{\left(\Sigma_{zz} - \frac{p_i d^2 - p_o D^2}{D^2 - d^2}\right)^2 + \frac{3}{16r^4}\left(\frac{\left(p_i - p_o\right) d^2 D^2}{D^2 - d^2}\right)^2}.\end{aligned} \tag{6.100}$$

With the substitution $d = d_{wall}$, we recover the first two terms on the right-hand side of Eq. (6.95), leading to the final form

$$\hat{f}_{des}(r) = \Sigma_e^2 - f_{ymn}^2 = 0, \quad d = d_{wall},\ r = \frac{d_{wall}}{2}, \tag{6.101}$$

which we could have anticipated from Eq. (6.34). This form of the design equation for triaxial yield will be useful in the discussion of radial safety factors for triaxial yield in Section 12.9.2.1 of Chapter 12.

6.4. POSTYIELD BEHAVIOR

Consider a stress state—uniaxial or multidimensional—that has reached incipient yield from an unloaded initial state. Then the stress state at the point of focus satisfies the equation

$$\hat{f}(\boldsymbol{\Sigma}) = 0, \quad \hat{f}(\Sigma_{ij}) = 0. \tag{6.102}$$

An example of such a relation would be Eq. (6.31) (or Eq. (6.34)) for the von Mises yield surface.

For many applications where yield represents a design limit state, we need go no further. Our design goal is to maintain the multidimensional stress state within the confines of Eq. (6.102), and any violation is considered unacceptable. There do exist instances, however, when exceeding the yield criterion does not constitute a failed design. Specific examples in tubular design are ductile rupture, the installation of expandable tubulars and accessories such as patches and liner hangers, and the design of thermal wells. It is those applications to which this discussion of postyield behavior is addressed.

As a first step, a definition of inelastic or plastic loading is in order. For a point in the tubular in a state of incipient yield there exist three possible states corresponding to the next increment of stress(es). These states view Eq. (6.102) as a surface in stress space, and use the gradient of $\hat{f}$ as a determinate of direction. For generality, we assume some inelastic deformation has already taken place such that now

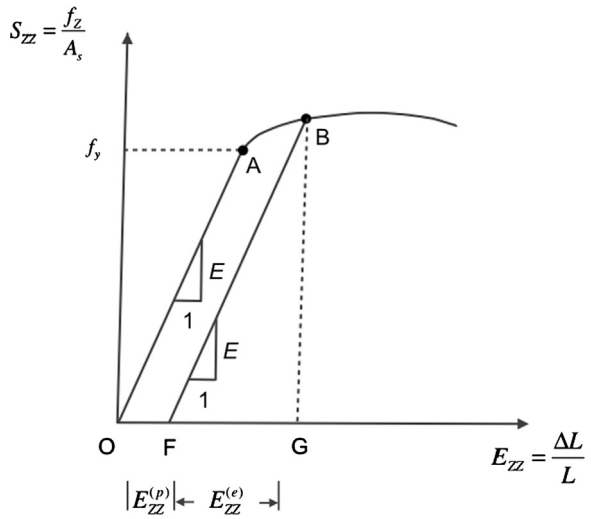

Figure 6.16 ***Uniaxial stress–strain curve illustrating the decomposition of total strain into elastic and plastic components.***

$$\hat{f}(\boldsymbol{\Sigma}, \breve{\mathbf{E}}^{(p)}, \kappa_w) = 0, \quad \hat{f}(\Sigma_{ij}, \breve{E}_{ij}^{(p)}, \kappa_w) = 0. \tag{6.103}$$

Two new entities are introduced in Eq. (6.103):

- Inelastic or plastic strain. A common assumption in postyield behavior (plastic behavior) is that the total strain, which to now we have simply denoted strain, is the sum of an elastic part and a plastic part, namely

$$\breve{\mathbf{E}} = \breve{\mathbf{E}}^{(e)} + \breve{\mathbf{E}}^{(p)}, \quad \breve{E}_{ij} = \breve{E}_{ij}^{(e)} + \breve{E}_{ij}^{(p)}, \tag{6.104}$$

  where here we allow the Eulerian strain[24] to be typical of any strain measure. Fig. 6.16 is an illustration of Eq. (6.104) for a uniaxial stress state. If there is no postyield loading, there is no increase in $\breve{\mathbf{E}}^{(p)}$.

  A relation useful in future discussions follows from the experimental work of Bridgman and states that the plastic portion of volume change is zero.[25] For infinitesimal strain, from Eq. (3.88)[26] we obtain

$$\frac{dv - dV}{dv} \approx \frac{dv - dV}{dV} = \breve{E}_{kk} = \breve{E}_{kk}^{(e)}, \quad \breve{E}_{kk}^{(p)} = 0. \tag{6.105}$$

[24] Expression of the total strain as the sum of elastic and plastic strains is mathematically legitimate for infinitesimal strain and for logarithmic strain.

[25] This result is valid even at high hydrostatic pressure. See [9] for discussion and references.

[26] The derivation of Eq. (3.88) was performed in cylindrical coordinates, but following a brief review of Section 3.7.2.1 in Chapter 3 one can gather that the same conclusion will be reached in Cartesian coordinates.

One immediate consequence of Eq. (6.105) is that, at least for small strains, $\breve{\mathbf{E}}^{(p)}$ and its deviatoric counterpart, $\breve{E}_{ij}^{(p)\prime} = \breve{E}_{ij}^{(p)} - \frac{1}{3}\delta_{ij}\breve{E}_{mm}^{(p)}$, are equal.

- Work-hardening parameter. The parameter κ_w depends on the plastic deformation history of the material and will assume its functionality depending on how one models work hardening.

Returning to the subject of loading, with the stress state residing on the yield surface (see Eq. (6.103)), subsequent behavior is determined by

$$\dot{\hat{f}} = \frac{\partial \hat{f}}{\partial \boldsymbol{\Sigma}} : \dot{\boldsymbol{\Sigma}} + \frac{\partial \hat{f}}{\partial \breve{\mathbf{E}}^{(p)}} : \dot{\breve{\mathbf{E}}}^{(p)} + \frac{\partial \hat{f}}{\partial \kappa_w}\dot{\kappa_w}, \quad \dot{\hat{f}} = \frac{\partial \hat{f}}{\partial \Sigma_{ij}}\dot{\Sigma}_{ij} + \frac{\partial \hat{f}}{\partial \breve{E}_{ij}^{(p)}}\dot{\breve{E}}_{ij}^{(p)} + \frac{\partial \hat{f}}{\partial \kappa_w}\dot{\kappa}_w, \tag{6.106}$$

where the superimposed dot denotes the time rate of the marked quantity. There exist three possible outcomes for $\dot{\hat{f}}$:

- Unloading. Unloading from an inelastic state,[27] which means returning to elastic behavior, implies no increment in plastic strain ($\dot{\breve{\mathbf{E}}}^{(p)} = 0$) and since there is no further inelastic deformation, $\dot{\kappa}_w = 0$, or

$$\hat{f} = 0, \quad \dot{\hat{f}} = \frac{\partial \hat{f}}{\partial \boldsymbol{\Sigma}} : \dot{\boldsymbol{\Sigma}} < 0, \quad \dot{\hat{f}} = \frac{\partial \hat{f}}{\partial \Sigma_{ij}}\dot{\Sigma}_{ij} < 0. \tag{6.107}$$

- Neutral loading. During neutral loading there is no further accumulation of either plastic strain or the work-hardening parameter, but the stress state remains on the yield surface

$$\hat{f} = 0, \quad \dot{\hat{f}} = \frac{\partial \hat{f}}{\partial \boldsymbol{\Sigma}} : \dot{\boldsymbol{\Sigma}} = 0, \quad \dot{\hat{f}} = \frac{\partial \hat{f}}{\partial \Sigma_{ij}}\dot{\Sigma}_{ij} = 0. \tag{6.108}$$

- Loading. During inelastic loading[28] there will occur increments in both $\breve{\mathbf{E}}^{(p)}$ and κ_w. We wish, however, to consider (as we did with unloading and neutral loading) the effect of the stress increment only on the current yield surface. We therefore define inelastic loading as

$$\hat{f} = 0, \quad \dot{\hat{f}} = \frac{\partial \hat{f}}{\partial \boldsymbol{\Sigma}} : \dot{\boldsymbol{\Sigma}} > 0, \quad \dot{\hat{f}} = \frac{\partial \hat{f}}{\partial \Sigma_{ij}}\dot{\Sigma}_{ij} > 0. \tag{6.109}$$

Provided the yield surface is formulated conveniently, the above definitions will lead to a surface in stress space for which the stress increment vector is pointing to the interior (unloading), to the exterior (loading) or along the surface (neutral loading).

[27] For example, from point B to point F in Fig. 6.16 for uniaxial loading.
[28] For example, from point A to point B in Fig. 6.16 for uniaxial loading.

6.4.1 Work hardening

A stress state cannot penetrate the yield surface. Rather, as briefly described in Section 6.2.2, the yield surface will translate and/or deform such that a new yield surface is continually generated in response to continued inelastic loading. This alteration of the yield surface involves plastic work.

Consider once more a state of stress that is coincident with the yield surface, i.e., a state of incipient plasticity. Following the work of Drucker [59], we imagine a small additional increment of stress $d\mathbf{\Sigma}$ and corresponding strain $d\breve{\mathbf{E}}$. If $\breve{\mathbf{E}}^{(e)}$ is the elastic strain recovered upon the removal of $d\mathbf{\Sigma}$, then a work-hardening material is characterized by the two relations [14], namely

$$d\mathbf{\Sigma} : d\breve{\mathbf{E}} > 0, \quad d\Sigma_{ij} d\breve{E}_{ij} > 0 \quad \text{during loading,} \tag{6.110}$$

$$d\mathbf{\Sigma} : \left(d\breve{\mathbf{E}} - d\breve{\mathbf{E}}^{(e)}\right) \geq 0, \quad d\Sigma_{ij}\left(d\breve{E}_{ij} - d\breve{E}_{ij}^{(e)}\right) \geq 0 \quad \text{over a cycle.} \tag{6.111}$$

Eq. (6.110) states that positive work must be done during the application of $d\mathbf{\Sigma}$. Eq. (6.111) states that during the application/removal cycle for additional stress $d\mathbf{\Sigma}$ the work done must be nonnegative. Using Eq. (6.104) we may also write Eq. (6.111) as

$$d\mathbf{\Sigma} : d\breve{\mathbf{E}}^{(p)} \geq 0, \quad d\Sigma_{ij} d\breve{E}_{ij}^{(p)} \geq 0 \quad \text{over a cycle.} \tag{6.112}$$

6.4.2 Flow rule

Drucker's work outlined in Section 6.4.1 has profound consequences for yield and postyield behavior. Fung [14], following the explanation of Naghdi [60], lists and proves the following:

- The yield surface and all subsequent loading[29] (yield) surfaces must be convex.
- The increment of plastic strain corresponding to loading must be directed:
  - normal to the loading surface at smooth points;
  - between adjacent normals if the loading surface has a corner.[30]
- The rate of change of plastic strain must be a linear function of the rate of change of the stress.

In this discussion we will use, but not prove, the above three important results.

[29] Because of its close relation to the determination of postyield behavior the yield surface is sometimes called the loading surface (recall our use of the yield surface in determining loading in Eqs. (6.107)–(6.109)). When, as assumed here, the loading surface and yield surface are identical, the flow rule is termed "associated." When they differ, the flow rule is termed "nonassociated."

[30] An example of a yield surface with corners is the Tresca yield surface.

With the second of the above observations, we may now write the increment of plastic strain that occurs during loading as

$$\dot{\overset{\cdot}{\mathbf{E}}}^{(p)} = \Lambda \frac{\partial \hat{f}}{\partial \boldsymbol{\Sigma}}, \quad \dot{\overset{\cdot}{E}}_{ij}^{(p)} = \Lambda \frac{\partial \hat{f}}{\partial \Sigma_{ij}}, \tag{6.113}$$

where Λ is a scalar function.

6.4.3 Hardening law

A final step in the construction of a model for postyield behavior is the declaration of a hardening law, that is, how does the loading/yield surface respond to plastic loading. Here we shall only consider the two simplest models—isotropic hardening and kinematic hardening.

An important parameter in defining hardening laws is the plastic strain. Its presence in such laws usually occurs in the context of work. We may write the rate of (internal) work per unit volume during deformation as

$$\dot{W} = \boldsymbol{\Sigma} : \dot{\overset{\cdot}{\mathbf{E}}} = \boldsymbol{\Sigma} : \left(\dot{\overset{\cdot}{\mathbf{E}}}^{(e)} + \dot{\overset{\cdot}{\mathbf{E}}}^{(p)} \right), \quad \dot{W} = \Sigma_{ij} \dot{\overset{\cdot}{E}}_{ij} = \Sigma_{ij} \left(\dot{\overset{\cdot}{E}}_{ij}^{(e)} + \dot{\overset{\cdot}{E}}_{ij}^{(p)} \right), \tag{6.114}$$

or

$$\dot{W} = \dot{W}^{(e)} + \dot{W}^{(p)}, \tag{6.115}$$

where

$$\dot{W}^{(e)} = \boldsymbol{\Sigma} : \dot{\overset{\cdot}{\mathbf{E}}}^{(e)}, \quad \dot{W}^{(p)} = \boldsymbol{\Sigma} : \dot{\overset{\cdot}{\mathbf{E}}}^{(p)}, \quad \dot{W}^{(e)} = \Sigma_{ij} \dot{\overset{\cdot}{E}}_{ij}^{(e)}, \quad \dot{W}^{(p)} = \Sigma_{ij} \dot{\overset{\cdot}{E}}_{ij}^{(p)}. \tag{6.116}$$

For future reference, we note that in instances where Eq. (6.105) is applicable the plastic work definition can use either the stress or its deviatoric counterpart since

$$\begin{aligned} \dot{W}^{(p)} &= \boldsymbol{\Sigma} : \dot{\overset{\cdot}{\mathbf{E}}}^{(p)} = \left(\boldsymbol{\Sigma}' + \frac{1}{3} \mathbf{I} \operatorname{tr}\{\boldsymbol{\Sigma}\} \right) : \dot{\overset{\cdot}{\mathbf{E}}}^{(p)} = \boldsymbol{\Sigma}' : \dot{\overset{\cdot}{\mathbf{E}}}^{(p)}, \\ \dot{W}^{(p)} &= \Sigma_{ij} \dot{\overset{\cdot}{E}}_{ij}^{(p)} = \left(\Sigma'_{ij} + \frac{1}{3} \delta_{ij} \Sigma_{mm} \right) \dot{\overset{\cdot}{E}}_{ij}^{(p)} = \Sigma'_{ij} \dot{\overset{\cdot}{E}}_{ij}^{(p)}, \end{aligned} \tag{6.117}$$

since $\delta_{ij} \dot{\overset{\cdot}{E}}_{ij}^{(p)} = \dot{\overset{\cdot}{E}}_{jj}^{(p)} = 0$.

We have already noted the convenience of the von Mises equivalent stress Σ_e in providing a bridge between the uniaxial stress in a mechanical test and the multidimensional stress state in design (see Section 6.3.2). Similarly, in parallel to Eq. (6.36) for stress, we can write for the plastic strain rate [9]

$$\dot{\breve{E}}_e^{(p)} = \sqrt{\frac{2}{3} \dot{\overset{\cdot}{E}}_{ij}^{(p)} \dot{\overset{\cdot}{E}}_{ij}^{(p)}}, \tag{6.118}$$

where $\breve{E}_e^{(p)}$ is the equivalent plastic strain.

Imagine a multidimensional deviatoric stress space[31] in which each axis is a measure of one of the Σ'_{ij}. The deviatoric stress $\boldsymbol{\Sigma}'$ can therefore be visualized as a vector in that space, as can the plastic strain rate $\dot{\mathbf{E}}^{(p)}$. The quantity $\boldsymbol{\Sigma}' : \dot{\mathbf{E}}^{(p)}$ ($\Sigma'_{ij}\dot{E}^{(p)}_{ij}$) becomes an inner product[32] in this multidimensional space. An alternative way of writing the inner product of two vectors $\boldsymbol{\Sigma}'$ and $\dot{\mathbf{E}}^{(p)}$ is $\left|\boldsymbol{\Sigma}'\right|\left|\dot{\mathbf{E}}^{(p)}\right|\cos\psi$, where ψ is an "angle" in this multidimensional space and, using Eqs. (6.26) and (6.36) we get

$$\left|\boldsymbol{\Sigma}'\right| = \sqrt{\Sigma'_{ij}\Sigma'_{ij}} = \sqrt{2J_2} = \sqrt{\frac{2}{3}}\Sigma_e, \tag{6.119}$$

and, using Eq. (6.118),

$$\left|\dot{\mathbf{E}}^{(p)}\right| = \sqrt{\dot{E}^{(p)}_{ij}\dot{E}^{(p)}_{ij}} = \sqrt{\frac{3}{2}}\dot{E}^{(p)}_e. \tag{6.120}$$

For instances where the deviatoric stress and the plastic strain rate are collinear,[33] $\cos\psi = 1$, and we may use Eqs. (6.119) and (6.120) to write the rate of plastic work as

$$\dot{W}^{(p)} = \boldsymbol{\Sigma} : \dot{\mathbf{E}}^{(p)} = \boldsymbol{\Sigma}' : \dot{\mathbf{E}}^{(p)} = \Sigma_e\dot{E}^{(p)}_e, \quad \dot{W}^{(p)} = \Sigma_{ij}\dot{E}^{(p)}_{ij} = \Sigma'_{ij}\dot{E}^{(p)}_{ij} = \Sigma_e\dot{E}^{(p)}_e. \tag{6.121}$$

Eq. (6.121) provides a convenient link between calculated plastic work in multidimensional stress space and the experimental results of a uniaxial stress–strain curve.

6.4.3.1 Isotropic hardening

Isotropic hardening assumes neither translation nor distortion of the yield surface in stress space. Rather, the yield surface proportionately expands to accommodate the latest loading increment of stress. Consider, for example, the von Mises yield criterion whose surface may be written by Eq. (6.28), where k^2 performs the function of the work-hardening parameter κ_w. In Section 6.3.2 we used a uniaxial tension test to set the initial value of k^2 to $\frac{1}{3}f_y^2$. Under the isotropic hardening assumption, loading beyond the initial yield state will simply increase the value of f_y, which aligns with uniaxial behavior as discussed in Section 6.2.2. Subsequent to the loading, the material acts as if its yield stress has been increased.

[31] We will soon, for convenience, express the rate of plastic work in terms of deviatoric stress instead of stress (see Eq. (6.117)).

[32] The quantity $\boldsymbol{\Sigma}' : \dot{\mathbf{E}}^{(p)}$ is an "inner product" as it is a generalization of the dot product for a space with dimensions greater than three—see Footnote 2 in Section A.3.1.3 of Appendix A. The dimensions of this space are $3 \times 3 = 9$, where we assume no benefit for the symmetry of the deviatoric stress and plastic strain rate tensors.

[33] An important example is the von Mises yield criterion—see Section 6.4.3.1, especially Eq. (6.124).

Example problem—isotropic hardening with von Mises yield criterion

Consider a material whose yield is adequately defined by isotropic hardening of the von Mises yield surface. Expressing the yield criterion as

$$\hat{f} = J_2 - \frac{1}{3} f_\gamma^2 = 0, \quad f_\gamma = \hat{f}_\gamma(\dot{W}^{(p)}), \tag{6.122}$$

where $\dot{W}^{(p)}$ is given by Eq. (6.116), we perform the preliminary calculation

$$\begin{aligned} \frac{\partial \hat{f}}{\partial \Sigma_{ij}} &= \frac{\partial \hat{f}}{\partial J_2}\frac{\partial J_2}{\partial \Sigma_{ij}} = \frac{1}{2}\frac{\partial \left(\Sigma'_{rs}\Sigma'_{rs}\right)}{\partial \Sigma_{ij}} = \frac{1}{2}\frac{\partial \left(\Sigma_{rs} - \frac{1}{3}\delta_{rs}\Sigma_{pp}\right)\left(\Sigma_{rs} - \frac{1}{3}\delta_{rs}\Sigma_{qq}\right)}{\partial \Sigma_{ij}} \\ &= \left(\delta_{ri}\delta_{sj} - \frac{1}{3}\delta_{rs}\delta_{pi}\delta_{pj}\right)\left(\Sigma_{rs} - \frac{1}{3}\delta_{rs}\Sigma_{qq}\right) = \Sigma_{ij} - \frac{1}{3}\delta_{ij}\Sigma_{qq} = \Sigma'_{ij}. \end{aligned} \tag{6.123}$$

Using this result in Eq. (6.113) gives

$$\dot{\mathbf{E}}^{(p)} = \Lambda \boldsymbol{\Sigma}', \quad \dot{E}_{ij}^{(p)} = \Lambda \Sigma'_{ij}. \tag{6.124}$$

The rate of plastic work $\dot{W}^{(p)}$ for a von Mises material is therefore

$$\dot{W}^{(p)} = \boldsymbol{\Sigma} : \dot{\mathbf{E}}^{(p)} = \boldsymbol{\Sigma}' : \dot{\mathbf{E}}^{(p)} = \Lambda \boldsymbol{\Sigma}' : \boldsymbol{\Sigma}', \quad \dot{W}^{(p)} = \Sigma_{ij}\dot{E}_{ij}^{(p)} = \Sigma'_{ij}\dot{E}_{ij}^{(p)} = \Lambda \Sigma'_{ij}\Sigma'_{ij}. \tag{6.125}$$

Recalling Eq. (6.121), we can write

$$\dot{W}^{(p)} = \Sigma_e \dot{E}_e^{(p)}, \tag{6.126}$$

which has the important consequence that the evolution of plastic work can be determined from a uniaxial stress–strain curve. From Eqs. (6.125) and (6.126),

$$\dot{W}^{(p)} = \Lambda \Sigma'_{ij}\Sigma'_{ij} = \Sigma_e \dot{E}_e^{(p)}, \quad \Lambda = \frac{3\dot{E}_e^{(p)}}{2\Sigma_e}, \tag{6.127}$$

where we have used Eqs. (6.26) and (6.36) to recognize that $\Sigma'_{ij}\Sigma'_{ij} = 2J_2 = \frac{2}{3}\Sigma_e^2$. If we substitute Eq. (6.127) into Eq. (6.124), then

$$\dot{\mathbf{E}}^{(p)} = \frac{3\dot{E}_e^{(p)}}{2\Sigma_e}\boldsymbol{\Sigma}', \quad \dot{E}_{ij}^{(p)} = \frac{3\dot{E}_e^{(p)}}{2\Sigma_e}\Sigma'_{ij}. \tag{6.128}$$

Eq. (6.128) allows us to compute the individual increments of plastic strain given a uniaxial stress strain curve (to capture Σ_e and $\dot{E}_e^{(p)}$) and the current value of each Σ'_{ij}. For a specific, extended example of the application to isotropic hardening of the equations derived in this more general example, see Section 7.3 of Chapter 7, which summarizes the derivation of the API limit state and design equations for ductile rupture.

6.4.3.2 Kinematic hardening

Kinematic hardening assumes neither expansion/contraction nor distortion of the yield surface in stress space. Rather, the yield surface translates to accommodate the latest loading increment of stress. Consider, for example, the von Mises yield criterion whose surface may be written by Equation (6.28). In one of the more popular kinematic hardening models, Ziegler's modification to Prager's hardening, the yield surface is written as

$$\hat{J}_2(\boldsymbol{\Sigma} - \mathbf{A}) - \frac{1}{3} f_y^2 = 0, \quad \hat{J}_2(\Sigma_{ij} - A_{ij}) - \frac{1}{3} f_y^2 = 0, \tag{6.129}$$

where the initial yield stress f_y remains unchanged and the translation of the centroid of the initial yield surface $\mathbf{A}$ evolves according to the relation

$$\dot{\mathbf{A}} = \dot{M}(\boldsymbol{\Sigma} - \mathbf{A}). \tag{6.130}$$

In the kinematic hardening model the yield stress changes due to translation of the yield surface. Recalling Section 6.2.2.1, the uniaxial behavior that produces the Bauschinger effect can be modeled with kinematic hardening. In one-dimensional stress space the extent of the yield surface is the (algebraic) difference between yield in tension and yield in compression. With, for example, tensile loading beyond initial yield, the tensile yield value increases with the side effect that, in order to maintain the extent of the yield surface constant, yield in compression is reduced.

Example problem—kinematic hardening with von Mises yield criterion

When manufacturing tubing of some high alloy steels, the work hardening accompanying forming of the tube can result in a product that has a tensile axial yield stress that is higher than its compressive axial yield stress. Consider the two-dimensional representations of the three-dimensional von Mises yield surface that have as their abscissa either the effective stress (Section 6.3.4.1, Fig. 6.11) or the sum of the axial stress and internal pressure (Section 6.3.4.2, Fig. 6.13). We wish to determine how these yield surfaces should be altered to model anisotropic yield in the axial direction only. We assume the tensile yield stress is 110 000 psi and the compressive yield stress is 90 000 psi.

One heuristic method of altering the yield surfaces is fairly accurate and involves some variation of the following technique:

- Begin with a yield surface for an isotropic material with $f_y = 110\,000$ psi.
- Locate a new point on the abscissa to represent the compressive yield stress $f_y = 90\,000$ psi.
- For the entire compressive side of the yield envelope, proportionately alter each ordinate value by the formula

$$y_{new}(x_{new}) = y_{old}(x_{new} \times \frac{f_{y-old}}{f_{y-new}}). \tag{6.131}$$

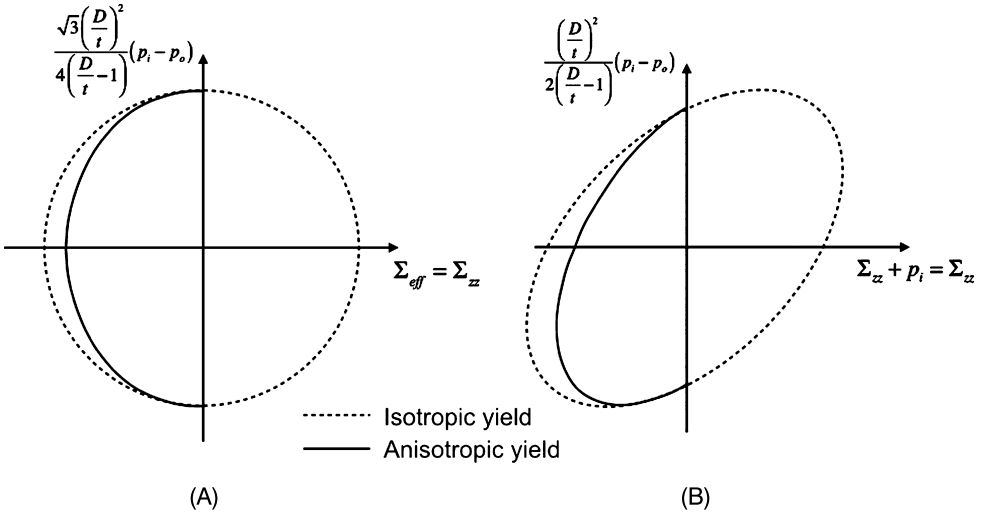

Figure 6.17 ***Alteration of von Mises yield surface to accommodate axial anisotropic yield using a heuristic method.*** Positive abscissa values of the yield surface are unaltered. During manufacture the pressures vanish so both abscissas become Σ_{zz}. (A) Effective stress; (B) Axial stress $+p_i$.

For example, the new γ value for a compressive stress that is one-half of compressive yield in the current problem would be

$$\gamma_{new}(-45\,000\,\text{psi}) = \gamma_{old}(-45\,000\,\text{psi} \times \frac{110\,000\,\text{psi}}{90\,000\,\text{psi}}) = \gamma_{old}(-55\,000\,\text{psi}), \qquad (6.132)$$

that is, γ_{new} half way to compressive yield on the altered yield surface equals γ_{old} half way to compressive yield on the original yield surface. We have essentially pushed the isotropic compressive yield value to the anisotropic yield value, allowing the yield surface to shift proportionately for all negative values on the abscissa. This method is illustrated in Fig. 6.17 for the two yield expressions from Sections 6.3.4.1 and 6.3.4.2.

Let us, as an alternative to the heuristic model, seek a yield surface which results from the application of kinematic hardening. We could repeat the calculation for plastic strain as we did in the isotropic hardening example of Section 6.4.3.1. Our primary concern, however, is the translation of the yield surface, so we will limit our consideration to that aspect of the plastic deformation.

Initially, $\mathbf{A} = \mathbf{0}$ in Eq. (6.130). Further, since during manufacturing there is no internal or external pressure, the abscissa of both of the presentations considered here is Σ_{zz}. This means that in both presentations the drawing process takes place along the abscissa and the only nonzero component of translation is $\dot{A}_{zz} = \dot{M}(\Sigma_{zz} - A_{zz})$. That is, even it we do not evaluate $\dot{M}$, we know that in each case the translation will

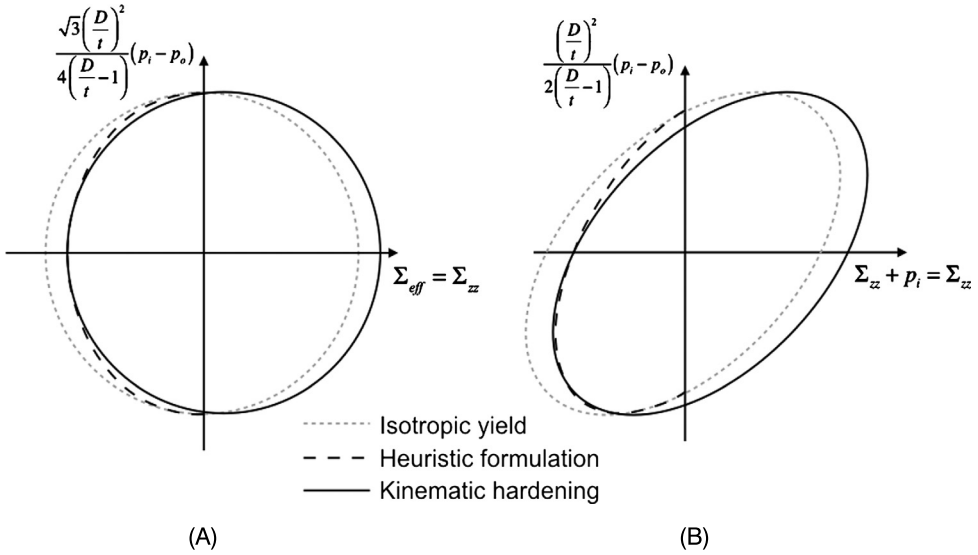

Figure 6.18 ***Alteration of von Mises yield surface to accommodate axial anisotropic yield using kinematic hardening.*** During manufacture the pressures vanish so both abscissas become Σ_{ZZ}. (A) Effective stress; (B) Axial stress $+p_i$.

occur along the Σ_{zz}-axis. Further, we know that (a) the shape and size of the yield surface do not change and (b) the difference between the yield in tension and compression is $110\,000\,\text{psi} - (-90\,000\,\text{psi}) = 200\,000\,\text{psi}$. Assuming we started the drawing process with an isotropic tube, this implies the initial yield stress—both in tension and compression—was 100 000 psi. The drawing process has translated the sample 10 000 psi along the positive Σ_{zz}-axis.

Fig. 6.18 compares the results of kinematic hardening with the heuristic model just presented. In the effective stress formulation of the initial yield surface shown on the left-hand diagram in the figure, the difference is small. The right-hand diagram indicates a greater difference, particularly in the vicinity of the ordinate boundary between quadrants 1 and 2 of the graph. Both diagrams illustrate the size-preserving translation the yield surface undergoes under kinematic hardening beyond initial yield.

CHAPTER 7

Internal Pressure Resistance

7.1. INTRODUCTION

In almost all design calculations for tubulars, a specific limit state for internal pressure resistance is superfluous. Rather, Chapter 6 defines a yield criterion that is applicable to first yield of a tubular in a general load state involving internal pressure, external pressure and axial traction, even when the axial load has a bending component (see Sections 6.3.4 (without bending) and 6.3.5 (with bending)). This more general criterion will be the starting point for developments presented below.

There do exist, however, instances where knowledge of the resistance vis-à-vis yield due strictly to internal pressure (or internal pressure differential) is useful. As a simple example, a tabulation of internal pressure resistance in a rating table allows one to quickly consider or discard candidate tubes for a known maximum surface pressure. Because of this, our discussion will begin with special cases of the yield criterion developed in Chapter 6 for loads dominated by internal pressure.

The use of yield as a limit state for internal pressure resistance is almost universal within the petroleum industry. Investigation of actual rupture of a tube can be important, however, both in failure analysis and in determining the closeness to rupture of a particular design. These considerations will lead us to also consider ductile rupture as treated by industry standards documents.

Finally, minimal coverage will also be given to two limit states that address the issue of fracture toughness, an internal pressure failure mode that may be realized with the propagation of a preexisting crack or environmental cracking. Though not covered here, fracture is addressed in outline form in API TR 5C3 [51,61].

7.2. LIMIT STATE EQUATIONS BASED ON YIELD

Recall Eqs. (6.34) and (6.58) that lead to the limit state equation

$$\hat{f}(r) = \left(\Sigma_{zz} - \frac{p_i d^2 - p_o D^2}{D^2 - d^2}\right)^2 + \frac{3}{16r^4}\left(\frac{(p_i - p_o)\, d^2 D^2}{D^2 - d^2}\right)^2 - f_y^2 = 0. \tag{7.1}$$

In the absence of bending, it was shown that the worst condition is always at $r = \frac{d}{2}$, leading to the simpler expression (Eq. (6.60))

$$\hat{f} = \left(\Sigma_{zz} - \frac{p_i d^2 - p_o D^2}{D^2 - d^2}\right)^2 + \left(\sqrt{3}\frac{(p_i - p_o)\, D^2}{D^2 - d^2}\right)^2 - f_y^2 = 0. \tag{7.2}$$

DOI: 10.1016/B978-0-12-811769-9.00007-4

Further, based on Eq. (6.58), the design equation for multidimensional yield is Eq. (6.95), namely

$$\hat{f}_{des}(r) = \left(\Sigma_{zz} - \frac{p_i d_{wall}^2 - p_o D^2}{D^2 - d_{wall}^2} \right)^2 + \frac{3}{16 r^4} \left(\frac{\left(p_i - p_o\right) d_{wall}^2 D^2}{D^2 - d_{wall}^2} \right)^2 - f_{ymn}^2 = 0. \tag{7.3}$$

Consider the following special cases of Eqs. (7.2)–(7.3).

7.2.1 Internal pressure resistance—capped end, $p_o = 0$

Care must be taken in this derivation. If a single value such as t is used for wall thickness, the capped end condition is equivalent to a condition of zero effective stress.[1] In the present case, however, we are dealing with two values of wall thickness. The manufactured wall thickness, $k_{wall}t$, is the thickness used with both the radial stress Σ_{rr} and the hoop stress $\Sigma_{\theta\theta}$ in arriving at Eq. (7.3). The axial stress Σ_{zz}, however, uses the specified wall thickness[2] t, i.e., $f_Z = \frac{\pi}{4}\left(D^2 - d^2\right)\Sigma_{zz}$, even for the design equation.

For the limit state equation, no differentiation exists between wall thickness, so we may note that Σ_{eff}, the first term in Eq. (7.1), vanishes. The solution for p_i is straightforward, i.e.,

$$p_i = f_y \frac{D^2 - d^2}{d^2 D^2} \frac{4}{\sqrt{3}} r^2. \tag{7.4}$$

The design equation cannot be treated as a special case of the above limit state equation. Rather, we must return to Eq. (7.3) and write[3]

$$\hat{f}(r) = \left(\frac{p_i d^2}{D^2 - d^2} - \frac{p_i d_{wall}^2}{D^2 - d_{wall}^2} \right)^2 + \frac{3}{16 r^4} \left(\frac{p_i d_{wall}^2 D^2}{D^2 - d_{wall}^2} \right)^2 - f_{ymn}^2 = 0. \tag{7.5}$$

We can solve Eq. (7.5) for p_i, leading to the design equation

$$p_i = f_{ymn} \frac{\left(D^2 - d^2\right)\left(D^2 - d_{wall}^2\right)}{D^2 \sqrt{\left(d^2 - d_{wall}^2\right)^2 + \frac{3 d_{wall}^4}{16 r^4}\left(D^2 - d^2\right)^2}}, \tag{7.6}$$

[1] The effective stress Σ_{eff} (see Chapter 10) is defined in Eq. (6.61). In a capped-end load environment the axial force is $f_Z = p_i A_i$ so that from Eq. (6.61) with $p_o = 0$, $\Sigma_{eff} = 0$.

[2] The differentiation of wall thicknesses can be traced to a desire to arrive at a deterministically reasonable worst case stress state at the circumferential location of yield. The radial and hoop stresses, Σ_{rr} and $\Sigma_{\theta\theta}$, respectively, are significantly impacted by a circumferentially local wall thinning. A locally thin wall, on the other hand, has less impact on the axial stress as it is a function of the circumferential average of wall thickness, not a local value.

[3] In the first term of Eq. (7.5) note in the first parenthetical expression the use of d in the first term and d_{wall} in the second term. Eq. (6.66) indicates that the first term is related to Σ_{zz} and the second term is related to Σ_{rr} and $\Sigma_{\theta\theta}$.

or, at $r = \frac{d_{wall}}{2}$,

$$p_i = f_{ymn} \frac{\left(D^2 - d^2\right)\left(D^2 - d_{wall}^2\right)}{D^2 \sqrt{\left(d^2 - d_{wall}^2\right)^2 + 3\left(D^2 - d^2\right)^2}}, \qquad r = \frac{d_{wall}}{2}. \tag{7.7}$$

7.2.2 Internal pressure resistance—$\Sigma_{zz} = p_o = 0$

If both axial traction and external pressure are zero, one has an equation useful for presentation in a table as a relative measure of internal pressure resistance between candidate tubes. Solving for p_i in Eqs. (7.1)–(7.3), we arrive at the limit state

$$p_i = f_y \frac{D^2 - d^2}{d^2} \frac{1}{\sqrt{\frac{3D^4}{16r^4} + 1}}, \tag{7.8}$$

and the design equation

$$p_i = f_{ymn} \frac{D^2 - d_{wall}^2}{d_{wall}^2} \frac{1}{\sqrt{\frac{3D^4}{16r^4} + 1}}, \tag{7.9}$$

or, at $r = \frac{d_{wall}}{2}$,

$$p_i = f_{ymn} \frac{D^2 - d_{wall}^2}{\sqrt{3D^4 + d_{wall}^4}}, \qquad r = \frac{d_{wall}}{2}. \tag{7.10}$$

An interesting special case of Eq. (7.10) occurs for large $\frac{D}{t}$ ratios. With the substitution $d_{wall} = D - 2k_{wall}t$, Eq. (7.10) becomes

$$p_i = f_{ymn} \frac{4\frac{k_{wall}t}{D}\left[1 - \left(\frac{k_{wall}t}{D}\right)\right]}{2\sqrt{1 - 2\frac{k_{wall}t}{D} + 6\left(\frac{k_{wall}t}{D}\right)^2 - 8\left(\frac{k_{wall}t}{D}\right)^3 + 4\left(\frac{k_{wall}t}{D}\right)^4}}. \tag{7.11}$$

As $\frac{D}{t}$ becomes large, we may drop all the $\frac{k_{wall}t}{D}$ terms that are to be compared to 1 with the result

$$p_i \approx 2\frac{k_{wall}t f_{ymn}}{D}. \tag{7.12}$$

Eq. (7.12) is identical to the API historical, one-dimensional yield pressure design equation,[4] sometimes associated with the acronym MIYP—minimum internal yield pressure.

[4] Although identical in form, Eq. (7.12) and the API historical, one dimensional yield pressure design equation have different pedigrees. The latter traces its origin to the Barlow equation, an expression derived by equating the force due to internal pressure (using a free-body diagram that constitutes half of

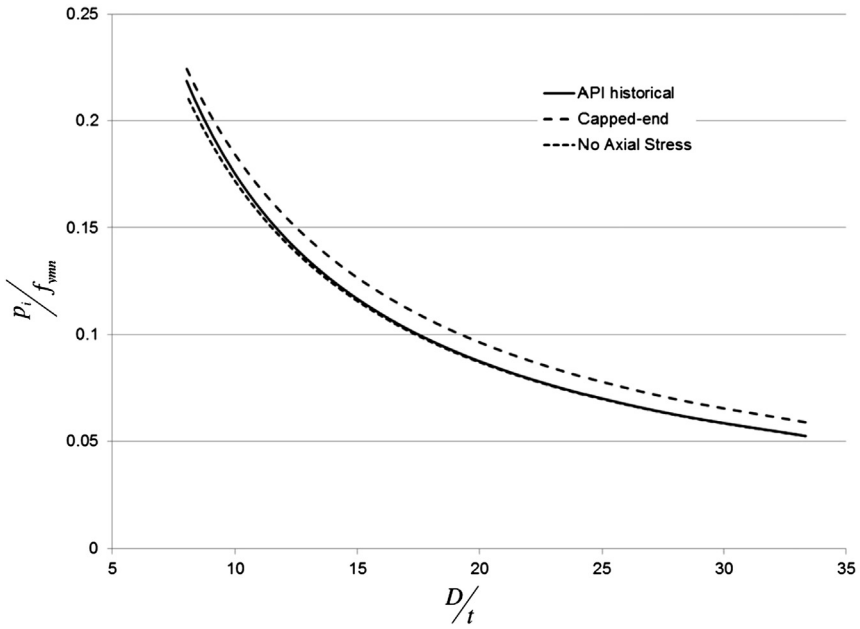

Figure 7.1 ***Comparison of expressions for minimum internal yield pressure.*** For all models $k_{wall} = 0.875$.

Fig. 7.1 compares the three design formulas mentioned above for minimum internal yield pressure—capped-end, $f_z = 0$, and the historical API (Barlow) equation. The comparison has been nondimensionalized by dividing each equation by f_{ymn} so that the right-hand side of each formula is strictly a function of tube geometry. The internal pressure at yield for the API historical formula is always greater than that derived from the Lamé equations (Eqs. (7.7) and (7.10)), implying the Lamé equations are slightly more conservative. The capped-end model has an associated tension which lowers the von Mises equivalent stress and therefore increases the internal pressure at yield.

7.3. LIMIT STATE EQUATION BASED ON RUPTURE

The API equation for ductile rupture [51] of casing and tubing has its origin in work by Klever [62] extending earlier work by Klever and Stewart [63].

Let the geometry of the tube be defined by its undeformed mean radius $\bar{R} = \frac{D-t}{2}$ and wall thickness t. As we will examine the tube undergoing large deformation prior

a tube cross section) with the resisting *average* hoop stress in the tube wall. The version of the formula used by the API also assumes that the tube outside diameter can be substituted for its inside diameter, an acceptable approximation if the tube is thin.

to rupture, we describe force intensity with the Cauchy stress (see Chapter 4) and the deformation with the logarithmic strain (see Section 3.5.4 of Chapter 3).

7.3.1 Preliminary definitions

The deformation is assumed to be generalized plane strain, axisymmetric so that Eqs. (3.194)–(3.196) will be used to determine the strain. Specifically, for this analysis Eq. (3.68) reduces to

$$\mathbf{F} = \begin{bmatrix} 1+\frac{\partial \hat{U}_R}{\partial R} & 0 & 0 \\ 0 & 1+\frac{\hat{U}_R}{R} & 0 \\ 0 & 0 & 1+k_1 \end{bmatrix} = \begin{bmatrix} \Lambda_{(\mathbf{R})} & 0 & 0 \\ 0 & \Lambda_{(\mathbf{\Theta})} & 0 \\ 0 & 0 & \Lambda_{(\mathbf{Z})} \end{bmatrix}, \tag{7.13}$$

with

$$\mathbf{F}^{-1} = \begin{bmatrix} \left(1+\frac{\partial \hat{U}_R}{\partial R}\right)^{-1} & 0 & 0 \\ 0 & \left(1+\frac{\hat{U}_R}{R}\right)^{-1} & 0 \\ 0 & 0 & \left(1+k_1\right)^{-1} \end{bmatrix} = \begin{bmatrix} \Lambda_{(\mathbf{R})}^{-1} & 0 & 0 \\ 0 & \Lambda_{(\mathbf{\Theta})}^{-1} & 0 \\ 0 & 0 & \Lambda_{(\mathbf{Z})}^{-1} \end{bmatrix}, \tag{7.14}$$

and

$$\mathcal{J} = \left(1+\frac{\partial \hat{U}_R}{\partial R}\right)\left(1+\frac{\hat{U}_R}{R}\right)(1+k_1) = F_{rR}F_{\theta\Theta}F_{zZ} = \Lambda_{(\mathbf{R})}\Lambda_{(\mathbf{\Theta})}\Lambda_{(\mathbf{Z})}, \tag{7.15}$$

such that

$$\mathcal{J}\left(F_{Rr}^{-1}\right)^T = \frac{F_{rR}F_{\theta\Theta}F_{zZ}}{F_{rR}} = F_{\theta\Theta}F_{zZ} = \Lambda_{(\mathbf{\Theta})}\Lambda_{(\mathbf{Z})}, \tag{7.16}$$

$$\mathcal{J}\left(F_{\Theta\theta}^{-1}\right)^T = \frac{F_{rR}F_{\theta\Theta}F_{zZ}}{F_{\theta\Theta}} = F_{zZ}F_{rR} = \Lambda_{(\mathbf{Z})}\Lambda_{(\mathbf{R})}, \tag{7.17}$$

$$\mathcal{J}\left(F_{Zz}^{-1}\right)^T = \frac{F_{rR}F_{\theta\Theta}F_{zZ}}{F_{zZ}} = F_{rR}F_{\theta\Theta} = \Lambda_{(\mathbf{R})}\Lambda_{(\mathbf{\Theta})}. \tag{7.18}$$

We may now compute spatial areas in terms of material areas and the deformation. With the substitution of Eqs. (7.16)–(7.18) into Eq. (3.62),

$$da_r = F_{\theta\Theta}F_{zZ}dA_R = \Lambda_{(\mathbf{\Theta})}\Lambda_{(\mathbf{Z})}dA_R = e^{\tilde{E}_{\Theta\Theta}+\tilde{E}_{ZZ}}dA_R, \tag{7.19}$$

$$da_\theta = F_{zZ}F_{rR}dA_\Theta = \Lambda_{(\mathbf{Z})}\Lambda_{(\mathbf{R})}dA_\Theta = e^{\tilde{E}_{ZZ}+\tilde{E}_{RR}}dA_\Theta, \tag{7.20}$$

$$da_z = F_{rR}F_{\theta\Theta}dA_Z = \Lambda_{(\mathbf{R})}\Lambda_{(\mathbf{\Theta})}dA_Z = e^{\tilde{E}_{RR}+\tilde{E}_{\Theta\Theta}}dA_Z, \tag{7.21}$$

where the last substitution in each of Eqs. (7.19)–(7.21) employs Eq. (3.187). These relations will be useful in updating the Cauchy stress by expressing the current areas in terms of the original tube dimensions.

The tractions used in [62] are first order in $\frac{t}{\bar{R}}$, where $\bar{R}$ is the mean radius of the tube. Originally derived in the context of collapse (see [57]), which does not necessarily require finite deformation theory, the relations are suitable if we account for the change in area with deformation. Using Eq. (7.21), the axial stress is[5]

$$\Sigma_{zz} = \frac{f_z}{a_z} = \frac{f_z}{e^{\tilde{E}_{RR}+\tilde{E}_{\Theta\Theta}} A_Z} = \frac{f_z}{2\pi \bar{R} t} e^{-\left(\tilde{E}_{RR}+\tilde{E}_{\Theta\Theta}\right)}, \tag{7.22}$$

and the effective stress[6] is

$$\Sigma_{\mathit{eff}} = \frac{f_{\mathit{eff}}}{a_z} = \frac{f_{\mathit{eff}}}{2\pi \bar{R} t} e^{-\left(\tilde{E}_{RR}+\tilde{E}_{\Theta\Theta}\right)}, \tag{7.23}$$

where

$$\Sigma_{\mathit{eff}} = \Sigma_{zz} - \frac{1}{2}\left(\Sigma_{\theta\theta} + \Sigma_{rr}\right). \tag{7.24}$$

Due to its convenience in this analysis, Σ_{eff} will be preferred to Σ_{zz} in the remainder of this discussion.

The differential pressure is related to hoop and radial stress by

$$\Sigma_{\theta\theta} - \Sigma_{rr} = \left(p_i - p_o\right) \frac{\bar{R}}{t} e^{\tilde{E}_{\Theta\Theta}-\tilde{E}_{RR}}, \tag{7.25}$$

where the last factor accounts for finite changes in $\bar{R}$ and t, respectively.

The radial stress is

$$\Sigma_{rr} = -\frac{1}{2}\left(p_i + p_o\right), \tag{7.26}$$

which is the average of its two extreme values at the inner and outer surfaces of the tube, respectively.

[5] Regarding the notation used in the ductile rupture discussion, the fact that this is a large deformation problem fosters a small issue in notation consistency. The Cauchy stress is normally expressed relative to a spatial coordinate system and the logarithmic strain is normally expressed relative to the material coordinate system. We could legitimately select either coordinate system and express all quantities in either upper or lower case. We choose, however, the alternative of assuming the two coordinate systems align, which allows us to maintain lower case indices for the stress and upper case indices for the strain. Fortunately, for this problem the assumed stress state is simple enough that there should be no confusion—the indices "rr" for the stress and "RR" for the strain are in alignment, as are the upper and lower case indices for the other two directions.

[6] The effective stress was introduced in Section 6.3.4.1 of Chapter 6 and will be given detailed treatment in Chapter 10.

7.3.2 Constitutive relations

The total strain is assumed to be the sum of elastic and plastic contributions (see Section 6.4 of Chapter 6). The elastic stress–strain relations are identical to Eqs. (5.25)–(5.27) with the index substitutions $1 = r$, $2 = \theta$ and $3 = z$. Even though these relations were derived for Lagrangian strain, the fact that the elastic deformation will only involve infinitesimal strain permits the substitution of logarithmic strain (see Section 3.5.5 of Chapter 3). Similarly, for infinitesimal deformations the various stress definitions used in this book are indistinguishable (see Section 4.3.3 of Chapter 4).

Uniaxial postyield stress–strain behavior is approximated with Ludwik's model (see Section 6.2.3.2 of Chapter 6). If we take Ludwik's model as representative of the stress–plastic strain relation, then the tangent modulus—the local slope of the uniaxial stress–total strain relation—is

$$E_t = \frac{d\Sigma_{zz}}{d\tilde{E}_{ZZ}}, \quad \frac{1}{E_t} = \frac{d\left(\tilde{E}^{(e)}_{ZZ} + \tilde{E}^{(p)}_{ZZ}\right)}{d\Sigma_{zz}} = \frac{1}{E} + \frac{1}{E_L}, \tag{7.27}$$

where E_L is given by Eq. (6.10).

For future convenience we reexpress the von Mises yield criterion (see Eq. (6.34)) in terms of Σ_{eff} and $\Sigma_{\theta\theta} - \Sigma_{rr}$. From Eq. (6.35) with $\Sigma_{11} = \Sigma_{rr}$, $\Sigma_{22} = \Sigma_{\theta\theta}$ and $\Sigma_{33} = \Sigma_{zz}$ we obtain

$$\begin{aligned}\Sigma_e^2 - f_y^2 &= \Sigma_{rr}^2 + \Sigma_{\theta\theta}^2 + \Sigma_{zz}^2 - \Sigma_{rr}\Sigma_{\theta\theta} - \Sigma_{\theta\theta}\Sigma_{zz} - \Sigma_{zz}\Sigma_{rr} - f_y^2 \\ &= (\Sigma_{zz} - \Sigma_{rr})^2 - (\Sigma_{zz} - \Sigma_{rr})(\Sigma_{\theta\theta} - \Sigma_{rr}) + (\Sigma_{\theta\theta} - \Sigma_{rr})^2 - f_y^2 \\ &= \Sigma_{\mathit{eff}}^2 + \frac{3}{4}(\Sigma_{\theta\theta} - \Sigma_{rr})^2 - f_y^2 = 0.\end{aligned} \tag{7.28}$$

Further, due to Eq. (6.121), the rate of plastic work can be written as

$$\dot{W}^{(p)} = \Sigma_{rr}\dot{\tilde{E}}^{(p)}_{RR} + \Sigma_{\theta\theta}\dot{\tilde{E}}^{(p)}_{\Theta\Theta} + \Sigma_{zz}\dot{\tilde{E}}^{(p)}_{ZZ} = \Sigma_e\dot{\tilde{E}}^{(p)}_e, \tag{7.29}$$

where Σ_e and $\tilde{E}^{(p)}_e$ assume the roles of Σ_{zz} and $\tilde{E}_{ZZ}$, respectively, in Eqs. (6.9)–(6.11), as well as in Eq. (7.27) in the current discussion.

Our problem at this point is identical to the isotropic hardening example problem in Section 6.4.3.1 of Chapter 6. If we recognize (see Eq. (6.24)) that the deviatoric stresses can be written as

$$\Sigma'_{rr} = \frac{1}{3}[2\Sigma_{rr} - (\Sigma_{\theta\theta} + \Sigma_{zz})], \tag{7.30}$$

$$\Sigma'_{\theta\theta} = \frac{1}{3}[2\Sigma_{\theta\theta} - (\Sigma_{zz} + \Sigma_{rr})], \tag{7.31}$$

$$\Sigma'_{zz} = \frac{1}{3}[2\Sigma_{zz} - (\Sigma_{rr} + \Sigma_{\theta\theta})] = \frac{2}{3}\Sigma_{\mathit{eff}}, \tag{7.32}$$

then, using Eq. (6.128),

$$\dot{\tilde{E}}^{(p)}_{RR} = \frac{\dot{\tilde{E}}^{(p)}_e}{\Sigma_e}\left[\Sigma_{rr} - \frac{1}{2}\left(\Sigma_{\theta\theta} + \Sigma_{zz}\right)\right], \tag{7.33}$$

$$\dot{\tilde{E}}^{(p)}_{\Theta\Theta} = \frac{\dot{\tilde{E}}^{(p)}_e}{\Sigma_e}\left[\Sigma_{\theta\theta} - \frac{1}{2}\left(\Sigma_{zz} + \Sigma_{rr}\right)\right], \tag{7.34}$$

$$\dot{\tilde{E}}^{(p)}_{ZZ} = \frac{\dot{\tilde{E}}^{(p)}_e}{\Sigma_e}\Sigma_{\mathit{eff}}, \tag{7.35}$$

and

$$\dot{\tilde{E}}^{(p)}_{\Theta\Theta} - \dot{\tilde{E}}^{(p)}_{RR} = \frac{3\dot{\tilde{E}}^{(p)}_e}{2\Sigma_e}\left(\Sigma_{\theta\theta} - \Sigma_{rr}\right), \tag{7.36}$$

$$\dot{\tilde{E}}^{(p)}_{\Theta\Theta} + \dot{\tilde{E}}^{(p)}_{RR} = -\frac{\dot{E}^{(p)}_e}{\Sigma_e}\Sigma_{\mathit{eff}}. \tag{7.37}$$

7.3.3 Rupture with multidimensional loading

Klever's publication [62] which serves as the source for the API ductile rupture calculation derives several limit states:

- necking—commonly associated with the localization of deformation at and beyond the maximum load in a uniaxial tension test, but possible in multidimensional loading (i.e., including pressure) where the axial traction is dominant;
- rupture—the loss of internal pressure integrity in a multidimensional loading where the pressure load is dominant;
- wrinkling—a term referring to the effect of plastic buckling of the tube as a column when the loads render the effective stress negative;
- collapse—the loss of external pressure integrity, which is not addressed in detail in [62].

Here we shall only address the prediction of ductile rupture.[7]

In rate form, Eq. (7.25) becomes

$$\begin{aligned}\dot{\Sigma}_{\theta\theta} - \dot{\Sigma}_{rr} &= \frac{\bar{R}}{t}\left[\left(\dot{p}_i - \dot{p}_o\right)e^{\tilde{E}_{\Theta\Theta}-\tilde{E}_{RR}} + \left(p_i - p_o\right)\left(\dot{\tilde{E}}_{\Theta\Theta} - \dot{\tilde{E}}_{RR}\right)e^{\tilde{E}_{\Theta\Theta}-\tilde{E}_{RR}}\right] \\ &= \frac{\Sigma_{\theta\theta} - \Sigma_{rr}}{p_i - p_o}\left(\dot{p}_i - \dot{p}_o\right) + \left(\Sigma_{\theta\theta} - \Sigma_{rr}\right)\left(\dot{\tilde{E}}_{\Theta\Theta} - \dot{\tilde{E}}_{RR}\right),\end{aligned} \tag{7.38}$$

[7] An annex to API TR 5C3 [51] offers two crack-propagation failure modes in overview form. API tubulars are, however, typically ductile, even in the presence of a small crack, except when the material is exposed to an unfriendly—usually hydrogen sulfide—environment.

or

$$\dot{p}_i - \dot{p}_o = (p_i - p_o)\left[\frac{\dot{\Sigma}_{\theta\theta} - \dot{\Sigma}_{rr}}{\Sigma_{\theta\theta} - \Sigma_{rr}} - \left(\dot{\tilde{E}}_{\Theta\Theta} - \dot{\tilde{E}}_{RR}\right)\right]. \tag{7.39}$$

Eq. (7.39) will vanish when $p_i - p_o$ reaches an extremum (i.e., $\dot{p}_i - \dot{p}_o = 0$), leading to the condition

$$\frac{\dot{\Sigma}_{\theta\theta} - \dot{\Sigma}_{rr}}{\Sigma_{\theta\theta} - \Sigma_{rr}} = \left(\dot{\tilde{E}}_{\Theta\Theta} - \dot{\tilde{E}}_{RR}\right). \tag{7.40}$$

Consider a stress path in which, from an unloaded state, Σ_{eff} and $\Sigma_{\theta\theta} - \Sigma_{rr}$ are incremented proportionately, that is, at a fixed ratio k_{DR} to each other.[8] Then, for example, $\Sigma_{\mathit{eff}} = k_{DR}(\Sigma_{\theta\theta} - \Sigma_{rr})$ and $\dot{\Sigma}_{\mathit{eff}} = k_{DR}\left(\dot{\Sigma}_{\theta\theta} - \dot{\Sigma}_{rr}\right)$, so that $\frac{\dot{\Sigma}_{\mathit{eff}}}{\Sigma_{\mathit{eff}}} = \frac{\dot{\Sigma}_{\theta\theta} - \dot{\Sigma}_{rr}}{\Sigma_{\theta\theta} - \Sigma_{rr}}$, and from Eq. (7.28) we have

$$\begin{aligned}\Sigma_e \dot{\Sigma}_e &= \Sigma_{\mathit{eff}} \dot{\Sigma}_{\mathit{eff}} + \frac{3}{4}(\Sigma_{\theta\theta} - \Sigma_{rr})\left(\dot{\Sigma}_{\theta\theta} - \dot{\Sigma}_{rr}\right) \\ &= \left(k_{DR}^2 + \frac{3}{4}\right)(\Sigma_{\theta\theta} - \Sigma_{rr})\left(\dot{\Sigma}_{\theta\theta} - \dot{\Sigma}_{rr}\right),\end{aligned} \tag{7.41}$$

or

$$\begin{aligned}\frac{\dot{\Sigma}_e}{\Sigma_e} &= \frac{\left(k_{DR}^2 + \frac{3}{4}\right)(\Sigma_{\theta\theta} - \Sigma_{rr})\left(\dot{\Sigma}_{\theta\theta} - \dot{\Sigma}_{rr}\right)}{\Sigma_e^2} = \frac{\left(k_{DR}^2 + \frac{3}{4}\right)(\Sigma_{\theta\theta} - \Sigma_{rr})\left(\dot{\Sigma}_{\theta\theta} - \dot{\Sigma}_{rr}\right)}{\left(k_{DR}^2 + \frac{3}{4}\right)(\Sigma_{\theta\theta} - \Sigma_{rr})^2} \\ &= \frac{\dot{\Sigma}_{\theta\theta} - \dot{\Sigma}_{rr}}{\Sigma_{\theta\theta} - \Sigma_{rr}}.\end{aligned} \tag{7.42}$$

From Eq. (7.42) and Eq. (7.27), and ignoring the elastic part of the total strain as being relatively small in a loading to rupture,

$$\frac{\dot{\Sigma}_{\theta\theta} - \dot{\Sigma}_{rr}}{\Sigma_{\theta\theta} - \Sigma_{rr}} = \frac{\dot{\Sigma}_e}{\Sigma_e} = \frac{E_L \dot{E}_e^{(p)}}{\Sigma_e}, \tag{7.43}$$

which, along with Eq. (7.36), can be substituted into Eq. (7.40) with the result being

$$\Sigma_e = \frac{2\Sigma_e}{3(\Sigma_{\theta\theta} - \Sigma_{rr})} E_L = \frac{2\sqrt{k_{DR}^2 + \frac{3}{4}}}{3} E_L. \tag{7.44}$$

Let $(\ldots)_{rup}$ be the value of quantity $(\ldots)$ at the extremum condition defined by Eq. (7.40), and let us retain k_{DR} as the factor of proportional loading. Then from

[8] The variable k_{DR} is identical to $\tan\phi$ in [62].

Eqs. (7.44) and (6.11),[9]

$$\left(E_e^{(p)}\right)_{rup} = \frac{2\sqrt{k_{DR}^2 + \frac{3}{4}}}{3} n_{NR}, \tag{7.45}$$

and from Eq. (6.9),

$$(\Sigma_e)_{rup} = \left(e \frac{2\sqrt{k_{DR}^2 + \frac{3}{4}}}{3} \right)^{n_{NR}} f_u. \tag{7.46}$$

If we continue to ignore elastic strains, Eqs. (7.36) and (7.37) become[10]

$$\left(E_{\Theta\Theta}^{(p)}\right)_{rup} - \left(E_{RR}^{(p)}\right)_{rup} = n_{NR}, \tag{7.47}$$

$$\left(E_{\Theta\Theta}^{(p)}\right)_{rup} + \left(E_{RR}^{(p)}\right)_{rup} = -\frac{2}{3} n_{NR} k_{DR}. \tag{7.48}$$

Finally, using Eq. (7.36) (once more in its integrated rather than rate form) with Eqs. (7.45)–(7.47) produces

$$(\Sigma_{\theta\theta})_{rup} - (\Sigma_{rr})_{rup} = e^{n_{NR}} f_u \frac{2}{3^{\frac{1+n_{NR}}{2}}} \left(\frac{3}{3 + 4k_{DR}^2} \right)^{\frac{1-n_{NR}}{2}}, \tag{7.49}$$

and from Eqs. (7.23) and (7.48),

$$\left(\Sigma_{\bar{eff}}\right)_{rup} = k_{DR} \left[(\Sigma_{\theta\theta})_{rup} - (\Sigma_{rr})_{rup} \right] = \frac{\left(f_{\bar{eff}}\right)_{rup}}{2\pi \bar{R} t} e^{\frac{2}{3} n_{NR} k_{DR}}, \tag{7.50}$$

or

$$\left(f_{\bar{eff}}\right)_{rup} = 2\pi \bar{R} t e^{-\frac{2}{3} n_{NR} k_{DR}} \left(\Sigma_{\bar{eff}}\right)_{rup}. \tag{7.51}$$

The rupture differential pressure itself follows from Eq. (7.25) with Eqs. (7.47) and (7.49) as

$$\left(p_i - p_o\right)_{rup} = \frac{t}{\bar{R}} e^{-n_{NR}} \left[(\Sigma_{\theta\theta})_{rup} - (\Sigma_{rr})_{rup} \right] = \frac{t}{\bar{R}} f_u \frac{2}{3^{\frac{1+n_{NR}}{2}}} \left(\frac{3}{3 + 4k_{DR}^2} \right)^{\frac{1-n_{NR}}{2}}. \tag{7.52}$$

[9] Eqs. (7.45) and (7.46) use the mappings $\tilde{E}_{zz} \to E_e^{(p)}$ and $\Sigma_{zz} \to \Sigma_e$. See Section 6.2.3.2 of Chapter 6.

[10] Eqs. (7.36) and (7.37) are differential, or rate equations. For proportional loading, however, $\frac{\Sigma_e}{\Sigma_{\theta\theta} - \Sigma_{rr}} = \sqrt{k_{DR}^2 + \frac{3}{4}}$ and $\frac{\Sigma_e}{\Sigma_{\bar{eff}}} = \sqrt{1 + \frac{3}{4k_{DR}^2}}$, so that both equations can be integrated, with the results taking the same forms as the rate equations, only with the superimposed rate symbols removed.

For later use, an important special case of Eq. (7.25) is the capped-end rupture test when $k_{DR} = 0$, namely

$$\left(p_i - p_o\right)_{rup} = \frac{t}{\bar{R}} f_u \frac{2}{3^{\frac{1+n_{NR}}{2}}}, \quad k_{DR} = 0. \tag{7.53}$$

The work from Eq. (7.28) through Eq. (7.48) assumes yield to be defined by the von Mises yield criterion. Klever chooses to also repeat the calculations using the Tresca yield criterion[11] (see Section 6.3.3 of Chapter 6). Summarizing the results of this second derivation for the most pertinent facet of the Tresca yield surface, we have

$$\left(E^{(p)}_{\Theta\Theta}\right)_{rup} - \left(E^{(p)}_{RR}\right)_{rup} = n_{NR} \quad \text{Tresca yield criterion,} \tag{7.54}$$

$$\left(E^{(p)}_{\Theta\Theta}\right)_{rup} + \left(E^{(p)}_{RR}\right)_{rup} = 0 \quad \text{Tresca yield criterion,} \tag{7.55}$$

$$\left(\Sigma_{\theta\theta}\right)_{rup} - \left(\Sigma_{rr}\right)_{rup} = e^{n_{NR}} f_u \left(\frac{1}{2}\right)^{n_{NR}} \quad \text{Tresca yield criterion,} \tag{7.56}$$

$$\left(f_{eff}\right)_{rup} = 2\pi \bar{R} t \left(\Sigma_{eff}\right)_{rup} \quad \text{Tresca yield criterion,} \tag{7.57}$$

$$\left(p_i - p_o\right)_{rup} = \frac{t}{\bar{R}} e^{-n_{NR}} \left[\left(\Sigma_{\theta\theta}\right)_{rup} - \left(\Sigma_{rr}\right)_{rup}\right] = \frac{t}{\bar{R}} f_u \left(\frac{1}{2}\right)^{n_{NR}} \quad \text{Tresca yield criterion,} \tag{7.58}$$

which is also the rupture pressure according to the Tresca yield criterion for the capped-end test.

The ductile rupture limit state is only valid in a certain region of f_{eff}–$\left(p_i - p_o\right)$ space. In particular, on the high tension side when f_{eff} is the dominant load the tube will fail axially due to necking, somewhat as if the tube and its pressure environment were a sample in a large uniaxial tension experiment.[12] We will consider this limit immediately

[11] Depending on the source, experimental data on multidimensional yield often locates the yield point between the von Mises and Tresca surfaces. In particular, Klever [62] cites the work of Steward et al. [64] and Klever and Stewart [63] as finding the average of the von Mises and Tresca rupture pressures to be an unbiased predictor of experiment. Positing the yield surface as the average of the two is a reasonable gesture.

[12] Why is there a differentiation between rupture and necking in this investigation when no such differentiation exists for initial yield—with, for example, the von Mises yield criterion—where everywhere on the yield surface loss of elastic behavior is not distinguished as being dominated by pressure or axial force? The difference can be traced to the criteria used to determine rupture and necking. For rupture, recall that the condition for the limit state (see Eq. (7.40)) follows from a search for an extremum of the load $p_i - p_o$. When (effective) tension is the dominant load we are led to search for a maximum value of f_z. By Eq. (7.22), this occurs at

$$\dot{f}_z = 2\pi \bar{R} t \left[\dot{\Sigma}_{zz} e^{\left(\tilde{E}_{RR} + \tilde{E}_{\Theta\Theta}\right)} + \Sigma_{zz}\left(\dot{\tilde{E}}_{RR} + \dot{\tilde{E}}_{\Theta\Theta}\right) e^{\left(\tilde{E}_{RR} + \tilde{E}_{\Theta\Theta}\right)}\right] = f_z \left[\frac{\dot{\Sigma}_{zz}}{\Sigma_{zz}} + \left(\dot{\tilde{E}}_{RR} + \dot{\tilde{E}}_{\Theta\Theta}\right)\right] = 0.$$

The solution by Klever [62] follows a path similar to that we have detailed for rupture.

below when discussing the design equation for ductile rupture. Both ductile rupture and necking are limit states recognized by API TR 5C3 [51].

7.3.3.1 The design equation

The work above can be converted from a limit state calculation to a design calculation by the following substitutions [51]:

- Replace the ultimate stress f_u with the specified minimum ultimate stress f_{umn}.
- Assume that any crack-like imperfection existing in the tube wall is coincident with the minimum wall thickness of the tube. In the absence of a crack, the minimum wall thickness is $k_{wall}t$, where k_{wall} is the manufacturing allowance (see Section 6.3.6 of Chapter 6). If, as is assumed in the API ductile rupture property rating, a crack-like imperfection appears at the location of manufactured wall thickness $k_{wall}t$, the design wall thickness for ductile rupture is further diminished by two additional parameters:
  - an inspection threshold a_N that corresponds to the maximum depth of a crack-like imperfection that could go undetected by the tube inspection system;
  - a so-called "burst strength factor" k_a—suggested values are 1.0 for quenched and temperated tubes with a martensitic grain structure or grades with minimum 13% chromium and 2.0 for as-rolled and normalized tubes—which offers a measure (which may optionally be determined experimentally) of the ductility of the tube material.

  With the above factors, the design wall thickness of the tube is

$$t_{DR} = k_{wall}t - k_a a_N. \tag{7.59}$$

  As was the case with the triaxial yield design equation, t_{DR} is only used with the radial and hoop stress calculations, not with calculations involving the axial stress.
- The API ductile rupture calculation uses a non-dimensional stress space where effective force is factored by an effective force scaling factor (f_{uts})[13] and pressure differential is factored by a scaling factor based on pressure differential (p_{uts}). The axial force scaling factor is defined with specified dimensions

$$f_{uts} = 2\pi \bar{R} t f_{umn} = \pi\,(D - t)\,t f_{umn}. \tag{7.60}$$

  The differential pressure scaling factor is defined with t_{DR} as

$$p_{uts} = f_{umn}\frac{t_{DR}}{\bar{R}} = 2 f_{umn}\frac{t_{DR}}{D - t_{DR}}. \tag{7.61}$$

[13] The API [51] symbol is F_{uts}. We lower its case and use f_{uts} in order to honor this book's symbol convention while attempting to cause minimum disruption to the API calculation format.

- For calculations in an industry standard, the generation and deployment of the rupture envelope ($\frac{f_{eff}}{f_{uts}}$ vs. $\frac{p_i - p_o}{p_{uts}}$) developed in the previous sections is somewhat cumbersome. As a friendlier alternative Klever [62] simplifies the envelope with a less complicated approximation that is constrained to fit through four important points on the true envelope:
  - pure tension ($f_{eff} = f_z > 0$, $p_i - p_o = 0$, $k_{DR} = +\infty$);
  - pure compression ($f_{eff} = f_z < 0$, $p_i - p_o = 0$, $k_{DR} = -\infty$);
  - capped-end rupture ($f_{eff} = 0$, $p_i - p_o > 0$, $k_{DR} = 0$);
  - the intersection of the rupture and necking limit states ($f_{eff} > 0$, $p_i - p_o > 0$, $k_{DR} = \frac{3}{2}$).

  The resulting envelope is given by the equation

$$\left(\frac{4^{1-n_{NR}} - 1}{3^{1-n_{NR}}}\right)\left(\frac{f_{eff}}{k_{BR} f_{uts}}\right)^2 + \left(\frac{3^{1+n_{NR}}}{4}\right)\left(\frac{p_i - p_o}{k_{BR} p_{uts}}\right)^2 = 1, \tag{7.62}$$

  where the API currently sets the bias factor k_{BR} for necking and rupture to unity. If we solve Eq. (7.62) for $p_i - p_o$, then

$$\underbrace{p_i - p_o}_{p_M} = \underbrace{\frac{2}{\sqrt{3}^{1+n_{NR}}} k_{BR} p_{uts}}_{k_{BR} p_{refM}} \sqrt{1 - \underbrace{\left(\frac{4^{1-n_{NR}} - 1}{3^{1-n_{NR}}}\right)}_{k_R}\left(\frac{f_{eff}}{k_{BR} f_{uts}}\right)^2}, \tag{7.63}$$

  where the underbraces indicate variable names in the API TR 5C3 [51] presentation.
- Replace the capped-end rupture pressures—both von Mises and Tresca—with expressions using t_{DR}. The von Mises capped-end rupture pressure (Eq. (7.53)) becomes

$$p_{refM} = 2\frac{t_{DR}}{D - t_{DR}} f_{umn} \frac{2}{3^{\frac{1+n_{NR}}{2}}} = \frac{2}{3^{\frac{1+n_{NR}}{2}}} p_{uts}. \tag{7.64}$$

  Note the appearance of p_{refM} in Eq. (7.63) for the rupture envelope. The Tresca capped-end differential rupture pressure (Eq. (7.58)) becomes

$$p_{refT} = 2\frac{t_{DR}}{D - t_{DR}} f_{umn} \left(\frac{1}{2}\right)^{n_{NR}} = \left(\frac{1}{2}\right)^{n_{NR}} p_{uts}, \tag{7.65}$$

  where in both instances we have replaced the pressure differential $p_i - p_o$ with an internal-only pressure. The effective tension can now be written as a design variable

$$f_{eff} = f_z + p_o \pi t (D - t) - p_M \frac{t(D - t)}{t_{DR}(D - t_{DR})}\left[\frac{\pi}{4}(D - 2t_{DR})^2\right], \tag{7.66}$$

where f_z is given by Eq. (7.22) *without* the correction for large displacement,

$$f_z = \pi\,(D - t)\,t\Sigma_{zz}, \tag{7.67}$$

and p_M is defined in Eq. (7.63). The formula for f_{eff} takes care not to discount the wall thickness twice—the area for p_o is based on specified wall thickness.

7.3.4 Example problem—computing rupture pressure

Compute the ductile rupture pressure of a tube of 9.625 in., 53.5 $\frac{\text{lb}_\text{m}}{\text{ft}}$ P110 casing (0.545 in. wall thickness) exposed to 200 000 lb_f compression and 1000 psi external pressure. The tube material is quenched and tempered and the inspection threshold is 5%. Assume a wall thickness tolerance factor of $k_{wall} = 0.875$.

The API/ISO method for determining the ultimate resistance of a tube to an internal fluid pressure differential is outlined in API TR 5C3 [51] and its equivalent ISO TR 10400 [65]. Given the specified outside diameter D, specified wall thickness t, specified minimum ultimate stress f_{umn} and corresponding characteristic value for the Ludwik's model n_{NR}, applied axial traction Σ_{zz} and external pressure p_o, the ductile rupture resistance of a tube is calculated by the following procedure.

7.3.4.1 Perform preliminary calculations

Preliminary calculations include determination of the following:

- Ludwik's parameter (n_{NR}). The parameter n_{NR} is listed for API grades in Table 6.2 [51]. For grades in which the parameter is not tabulated, Eq. (6.12) is recommended. For the current example, from Table 6.2, $n_{NR} = 0.08$.
- Design wall thickness (t_{DR}). From Eq. (7.59)

$$t_{DR} = 0.875 \times 0.545\,\text{in.} - 1.0 \times (0.05 \times 0.545\,\text{in.}) = 0.450\,\text{in.} \tag{7.68}$$

- Scaling parameters (f_{uts}, p_{uts}). From Eqs. (7.60) and (7.61), respectively, we get

$$f_{uts} = \pi\,(9.625\,\text{in.} - 0.545\,\text{in.})\,0.545\,\text{in.} \times 125\,000\,\text{psi} = 1\,943\,311\,\text{lb}_\text{f}. \tag{7.69}$$

The differential pressure scaling factor is defined with t_{DR} as

$$p_{uts} = 2 \times 125\,000\,\text{psi}\frac{0.450\,\text{in.}}{9.625\,\text{in.} - 0.450\,\text{in.}} = 12\,251\,\text{psi}. \tag{7.70}$$

7.3.4.2 Compute von Mises and Tresca capped-end rupture pressures

From design Eqs. (7.64) and (7.65) we have

$$p_{refM} = \frac{2}{3^{\frac{1+0.08}{2}}}12\,251\,\text{psi} = 13\,538\,\text{psi}, \tag{7.71}$$

$$p_{refT} = \left(\frac{1}{2}\right)^{0.08} 12\,251\,\text{psi} = 11\,590\,\text{psi}. \tag{7.72}$$

7.3.4.3 Compute the von Mises rupture pressure

With the above knowns, the von Mises rupture pressure with (effective) axial force can now be computed by solving Eqs. (7.66) and (7.63) simultaneously to construct a quadratic equation in p_M. Let the temporary variables A, B and C be defined, respectively, as

$$A = \left(\frac{f_{uts}}{p_{refM}}\right)^2 + k_R k_M^2, \tag{7.73}$$

$$B = -2k_R k_M \left[f_z + p_o \pi t (D - t)\right], \tag{7.74}$$

$$C = k_R \left(f_z + p_o \pi t (D - t)\right)^2 - \left(k_{BR} f_{uts}\right)^2, \tag{7.75}$$

where k_R is defined in Eq. (7.63) and k_M is shorthand for the terms multiplying p_M in Eq. (7.66), namely

$$k_M = \frac{t(D-t)}{t_{DR}(D - t_{DR})}\left[\frac{\pi}{4}(D - 2t_{DR})^2\right]. \tag{7.76}$$

Then

$$p_M = \frac{-B + \sqrt{B^2 - 4AC}}{2A}. \tag{7.77}$$

If we carry out the indicated operations, then

$$A = \left(\frac{1\,943\,311\,\text{lb}_\text{f}}{13\,538\,\text{psi}}\right)^2 + \left(\frac{4^{1-0.08} - 1}{3^{1-0.08}}\right)(71.730\,\text{in}^2)^2 = 25\,437.1\,\text{in}^4, \tag{7.78}$$

$$B = -2\left(\frac{4^{1-0.08} - 1}{3^{1-0.08}}\right)(71.730\,\text{in}^2)\left[-200\,000\,\text{lb}_\text{f} + 1000\,\text{psi} \times \pi \times 0.545\,\text{in.} \times (9.625\,\text{in.} - 0.545\,\text{in.})\right] = 2.484\,880\,1 \times 10^7\,\text{lb}_\text{f}\text{in}^2, \tag{7.79}$$

$$C = \left(\frac{4^{1-0.08} - 1}{3^{1-0.08}}\right)\left[-200\,000\,\text{lb}_\text{f} + 1000\,\text{psi} \times \pi \times 0.545\,\text{in.} \times (9.625\,\text{in.} - 0.545\,\text{in.})\right]^2 - (1 \times 1\,943\,311\,\text{lb}_\text{f})^2 = -3.744\,51 \times 10^{12}\,\text{lb}_\text{f}^2, \tag{7.80}$$

where k_R is defined in Eq. (7.63) and from Eq. (7.66) we have

$$k_M = \frac{0.545\,\text{in.}\,(9.625\,\text{in.} - 0.545\,\text{in.})}{0.450\,\text{in.}\,(9.625\,\text{in.} - 0.450\,\text{in.})}\left[\frac{\pi}{4}(9.625\,\text{in.} - 2 \times 0.450\,\text{in.})^2\right] = 71.730\,\text{in}^2, \tag{7.81}$$

thus

$$p_M = \left\{-2.484\,880\,1 \times 10^7\,\mathrm{lb_f in^2} + \sqrt{\left(2.484\,880\,1 \times 10^7\,\mathrm{lb_f in^2}\right)^2 - 4 \times 25\,437.1\,\mathrm{in^4} \times -3.744\,51 \times 10^{12}\,\mathrm{lb_f^2}}\right\} / \left\{2 \times 25\,437.1\,\mathrm{in^4}\right\} = 11\,654\,\mathrm{psi}. \tag{7.82}$$

The effective force can now be determined from Eq. (7.66) as

$$f_{eff} = -200\,000\,\mathrm{lb_f} + 1000\,\mathrm{psi} \times \pi \times 0.545\,\mathrm{in.} \times (9.625\,\mathrm{in.} - 0.545\,\mathrm{in.}) - 11\,654\,\mathrm{psi}\frac{0.545\,\mathrm{in.}\,(9.625\,\mathrm{in.} - 0.545\,\mathrm{in.})}{0.450\,\mathrm{in.}\,(9.625\,\mathrm{in.} - 0.450\,\mathrm{in.})}\left[\frac{\pi}{4}(9.625\,\mathrm{in.} - 2 \times 0.450\,\mathrm{in.})^2\right] = -1.020\,419 \times 10^6\,\mathrm{lb_f}. \tag{7.83}$$

A check is necessary to ensure the ductile rupture limit state applies to the current stress path. Assuming that to be the case, the final design rupture pressure is the minimum of (a) the average of the rupture pressures predicted by the von Mises and Tresca criteria and (b) the rupture pressure computed using the von Mises yield criterion.

Rupture is the applicable limit state when

$$\left(\frac{\sqrt{3}}{2}\right)^{1-n_{NR}} \geq \frac{f_{eff}}{f_{uts}}. \tag{7.84}$$

In the current problem, $\frac{f_{eff}}{f_{uts}} = \frac{-1.020\,419 \times 10^6\,\mathrm{lb_f}}{1\,943\,311\,\mathrm{lb_f}} = -0.525 \leq 0.876 = \left(\frac{\sqrt{3}}{2}\right)^{1-0.08}$, so the rupture limit state is applicable.

The final answer for the rupture pressure is

$$p_{dr} = p_o + \min\left\{\frac{p_M + p_{refT}}{2}, p_M\right\} = 1000\,\mathrm{psi} + \min\left\{\frac{11\,654\,\mathrm{psi} + 11\,590\,\mathrm{psi}}{2}, 11\,654\,\mathrm{psi}\right\} = 12\,622\,\mathrm{psi}. \tag{7.85}$$

7.3.5 Comments on the API ductile rupture equation

As a design implementation review of this section, the following comments are in order:

- The limit state (not design) equations presented in this discussion have proved extremely accurate in reproducing experimental results. API TR 5C3 [51] summarizes results of 106 capped-end rupture tests with an actual-to-predicted (Eq. (7.53)) ratio of 1.004 and coefficient of variation of 4.7%.
- Within the limits of their stated assumptions, Eqs. (7.13)–(7.37) are quite general and could be used in an analysis of plastic loading and unloading under a variety of stress paths under the assumption of isotropic hardening.

- The strategy of assuming a fixed (i.e., constant k_{DR}) relation between Σ_{eff} and $\Sigma_{\theta\theta} - \Sigma_{rr}$ for the general solution means that the modeled stress path to rupture may not correspond to that actually experienced by the tubular in service. The assumption of isotropic hardening, however, means that radial expansion of the initial and subsequent yield surfaces is adhering to behavior that should be close to that strategized.
- Given the ductility of current tubular materials one might expect a significant increase in internal pressure resistance when choosing rupture rather than yield as a limit state. This is not always the case, as the design equation assumption of coincidence between the manufactured minimum tube wall thickness $k_{wall}t$ and the undetected crack-like imperfection represented by a_N can counter much of the gain associated with the ratio of f_{umn} to f_{ymn}.
- Klever [62] offers two applications for the ductile rupture limit state in design, both of which are applicable to tube materials for which the margin between f_{ymn} and f_{umn} is small—high strength steels and solid expandable tubulars. Even in these instances, his suggestion, with which this author agrees, is that the rupture check be in addition to, rather than in replacement of, the design check for yield. As an addition, the ductile rupture equation has proved useful in postfailure analysis to determine when actual loss of internal pressure should have been expected.

7.4. EFFECT OF WEAR ON INTERNAL PRESSURE RESISTANCE

Both theoretical and experimental evidence points to the importance of wall thickness in resistance to internal pressure dominated loads. Both the API minimum internal yield pressure (see Eq. (7.12)) and capped-end ductile rupture (see Eqs. (7.64) and (7.65)) design equations indicate a direct proportionality between (remaining) wall thickness and internal limit pressure.

Tool joint wear[14] directly impacts casing wall thickness. Further, the wear groove is usually of sufficient circumferential extent to reduce the mitigating effect of surrounding wall. For this reason, the impact of tool joint wear on casing internal pressure resistance is judged linear [66]—a 13% loss of wall thickness implies a 13% loss of resistance to internal pressure.

[14] Both logic and experience suggest wear associated with logging wirelines should also impact tubular internal pressure resistance. Unfortunately, this author is not aware of a body of experimental work that would further justify this concern. Qualitative arguments both help and hurt. For example, with the smaller groove associated with wireline wear one would anticipate structural support from surrounding wall. On the other hand, the diameter of a wireline groove suggests a larger effect of stress intensity.

CHAPTER 8

External Pressure Resistance

8.1. INTRODUCTION

Internal pressure resistance (Chapter 7) is governed by the response of the material and geometry of the cross-section—primarily embodied in the circumferential or hoop stress—to imposed internal pressure differential. At least up to the vicinity of rupture the response of the cross-section is stable. Collapse, on the other hand, is largely governed by considerations of cross-sectional instability. The cross-section deforms under increasing external pressure differential with the character of the deformation reflecting initial imperfections. At a critical pressure the response of the cross-section reaches a maximum, and the cross-section buckles. Postbuckled deformation proceeds with decreasing external differential pressure.

8.2. COLLAPSE RESISTANCE TO UNIFORM LOADING

Collapse failures can be divided into two categories—those due to uniform loading by a fluid (differential) pressure and those due to nonuniform loading, usually by an adjacent, mobile formation. Response of the cross-section to these differing loads is sufficiently unique that the two cases will be considered separately. The initial discussion concentrates on uniform pressure loading.

8.2.1 The analogy between collapse and buckling of a column

The internal/external pressure resistance of a tube cross-section has a direct analog in the tension/compression response of a specimen in a load frame used to capture stress–strain response. Fig. 6.1 illustrates the response of a steel solid bar specimen when loaded in tension. The only active stress is the axial stress, and the resulting stress–strain curve captures the behavior, including yield and ultimate stresses, of the parent material.

An additional concern arises if one attempts to load the solid bar specimen in compression. As illustrated in Fig. 6.3, when loaded in compression an isotropic sample will duplicate, with appropriate sign changes, the stress–strain response of the tension curve. In the case of compression, however, an additional failure mode exists that is not depicted in Fig. 6.3. If the solid bar specimen is sufficiently slender, an imperfection in the experimental setup—an inaccurately machined sample, offset between the clamp ends of the test fixture—can cause the specimen to buckle as a column (see Fig. 8.1), thus interrupting the intended purpose of the test and rendering the sample useless.

Buckling of a column can occur in one of two modes—elastic buckling or plastic buckling. Imagine a strain gauge placed on each specimen in Fig. 8.1 to record strain

Elements of Oil and Gas Well Tubular Design
DOI: 10.1016/B978-0-12-811769-9.00008-6

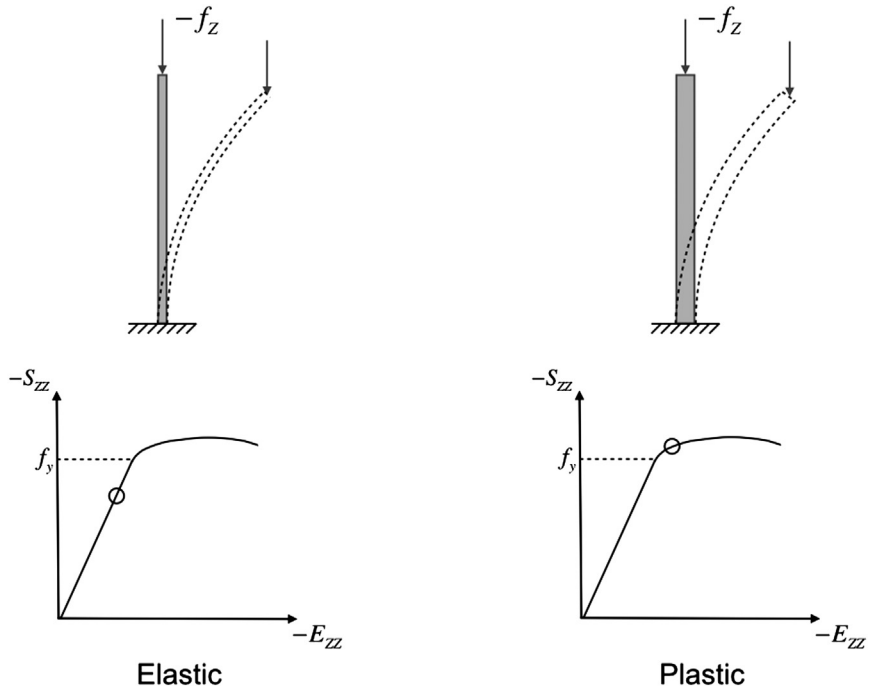

Figure 8.1 ***An analogy to collapse—the buckling of a column under compression.*** The buckling mode can be designated "elastic" or "plastic" depending on the value of S_{ZZ} relative to the yield stress at the onset of buckling.

before, at the moment of, and following buckling. As the column is loaded in compression, its axial stress will increase in a negative sense. For a column that is thin relative to its length, the resistance to buckling can be so small that *at the moment of buckling* the stress in the column is less than the compressive yield stress.[1] In such instances the buckling is termed "elastic." As the thickness of the cross-section is increased, eventually the column's stiffness will be such that, at the moment of buckling, the axial stress in the column exceeds the compressive yield stress of the column material. In this case the buckling is termed[2] "plastic."

Finally, and in anticipation of the discussion of collapse resistance, imagine a column whose cross-section is massive relative to its length (in the extreme, think of a column with the dimensions of a tree stump). In this case, the compressive loading necessary to

[1] To be sure, once the column buckles and begins to deflect, bending stresses associated with the deflection will add to the axial stress causing the column to yield. For the purpose of classifying the buckling, however, we are only interested in the stress state at the instant buckling initiates.

[2] Alternate terminology includes descriptors such as "inelastic" and "elasto-plastic." The adjective "plastic" is used here to complete the analogy with industry terminology for cross-sectional collapse.

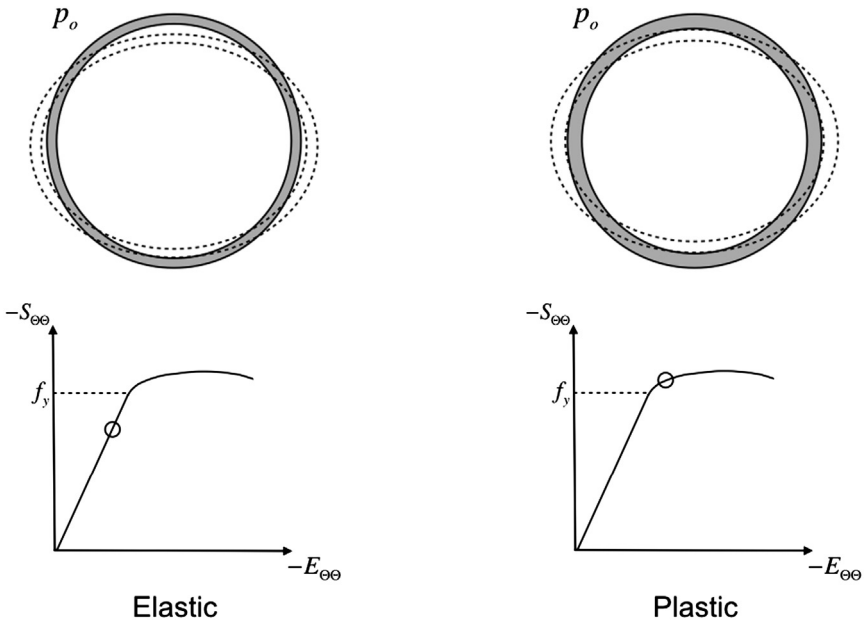

Figure 8.2 ***Collapse modes for a cross-section.*** The collapse mode can be designated "elastic" or "plastic" depending on the value of $S_{\Theta\Theta}$ relative to the yield stress at the onset of collapse.

buckle the "column" may be so huge that substantial postyield damage precedes lateral deflection of the column rendering it unusable as a structure prior to loss of stability.

To complete the present analogy, now consider the response of a tube cross-section to external pressure differential as depicted in Fig. 8.2. Note the mapping:

- the load of concern changes from axial force f_Z to external pressure p_o;
- the stress of concern changes from S_{ZZ} to[3,4] $S_{\Theta\Theta}$;
- as the load (compressive force for column, external pressure for tube) is increased the stress of significance approaches, and may exceed, the yield stress of the parent material;
- provided the material is isotropic, the stress–strain curve itself does not change.

First consider a tubular cross-section whose wall thickness is small compared to its diameter—in the extreme, a soft drink can. As the external pressure load on the tube is increased, the hoop stress increases in a negative sense until the tube cross-section reaches

[3] With axial loading of the column the prebuckled stress state is uniform over the cross-section. With external pressure loading of the cross-section the prebuckled stress state is not uniform through the wall thickness, but for the purposes of this analogy, considering an average circumferential/hoop stress is adequate.

[4] In this discussion we ignore the possible presence of axial force. Collapse in the presence of combined loading will be discussed in Section 8.2.3.1.

Table 8.1 Examples of elastic collapse resistance

20.000 in., 94.0 $\frac{\text{lb}_\text{m}}{\text{ft}}$		13.375 in., 68.0 $\frac{\text{lb}_\text{m}}{\text{ft}}$	
Grade	**Collapse resistance**[a] (psi)	**Grade**	**Collapse resistance**[a] (psi)
H40	520	H40	1660
J/K55	520	J/K55	1950
L/N80	520	L/N80	2260
T95	520	T95	2330
P110	520	P110	2330
Q125	520	Q125	2330

[a] API minimum collapse rating [51], though not all entries are API diameter, mass per length combinations.

a state of instability (see dashed curve in Fig. 8.2), and buckling of the cross-section initiates. If, at this moment, the representative hoop stress in the cross-section is less than the compressive hoop yield stress,[5] the collapse is termed "elastic."

If a tube collapses elastically, that is, no portion of the cross-section has yielded, then the only two relevant material parameters are Young's modulus E and Poisson's ratio ν. The yield stress of the material does not enter the calculation for elastic collapse, and therefore the collapse resistance is independent of yield stress.

Two examples of elastic collapse resistance behavior are presented in Table 8.1. In the first example, 20.000 in., 94.0 $\frac{\text{lb}_\text{m}}{\text{ft}}$ casing, the diameter-to-thickness (D/t) ratio is so high that, regardless of grade, the collapse resistance is 520 psi. No benefit in external pressure resistance is afforded by the purchase of a higher grade tubular. In the second example, 13.375 in., 68.0 $\frac{\text{lb}_\text{m}}{\text{ft}}$ casing, lower grades have sufficiently low yield stress that yield in the hoop direction will occur prior to the onset of collapse. As the grade/yield stress is increased, eventually a grade is reached where collapse initiates prior to yield. Again, the purchase of a higher grade offers no benefit to the tube's collapse resistance for the higher grades.

As the thickness of the cross-section is increased, eventually the tube's cross-sectional stiffness will be such that, at the moment of buckling, the hoop stress in the column exceeds the compressive hoop yield stress of the column material. In this case the collapse is termed "plastic."

At the lower end of tubular D/t ratios exist tubulars—thicker-walled casing, many tubing sizes—for which a third collapse resistance mode, "yield" collapse, has been adopted by the API. In parallel to the tree stump in column buckling, these tubulars are sufficiently thick, compared to their diameters, that the term "plastic collapse" does not seem appropriate to the industry.[6] Here we will adhere to the industry practice,

[5] Usually, for low carbon steels the tensile and compressive axial yield stresses, as well as the tensile and compressive hoop yield stresses, are all considered to be equal.

[6] In reality many of these tubes simply possess cross-sections that perform on the high end of plastic collapse.

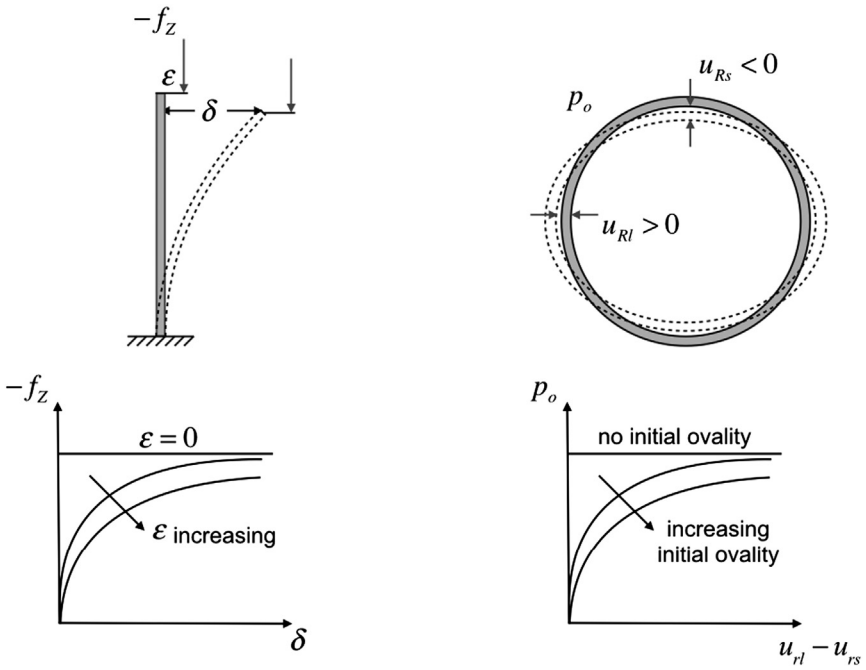

Figure 8.3 ***Bifurcation and buckling.*** In the right-hand diagram $u_{rl} - u_{rs}$ is the difference between the displacement of the tube along the long and short axes of the postbuckled shape.

recognizing that the limit state equation for yield collapse does not describe a stability failure but does fall in a natural progression of behavior with decreasing D/t ratio.

8.2.2 Perfect and imperfect cross sections

In collapse studies, as in most stability studies, two approaches are employed—those that consider instability as a bifurcation (division into two branches) from a perfect state and those that consider instability as an amplification (and eventual overload) of an initial imperfection.[7] We describe these now, as both are used in current collapse resistance investigations, and both can be related to the analogy to column buckling discussed in the previous section.

Fig. 8.3 illustrates two examples of the buckling of perfect and imperfect structures. A column loaded in compression by $-f_Z$ is considered in the left-hand diagram. If the column is without imperfection and is loaded symmetric to its cross-section ($\varepsilon = 0$), there will be no deflection of the column ($\delta = 0$) until a critical value of $-f_Z$ is reached. At that point, two equilibrium paths are possible. One path has the column continuing

[7] The snap-through failure to be discussed is an example of a load path that does not bifurcate [67].

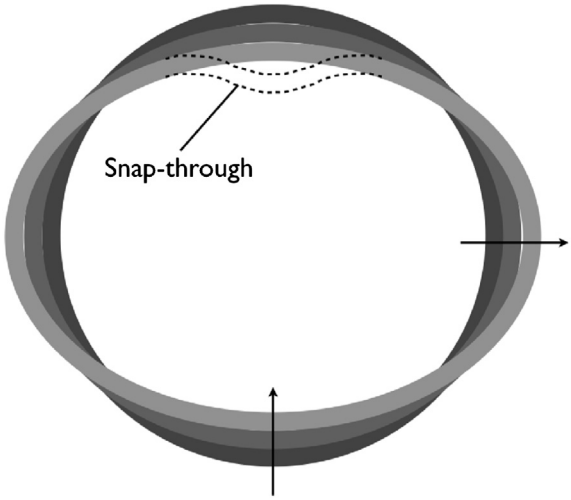

Figure 8.4 ***Progressive ovalization leading to collapse.*** Snap-through buckling of the upper arch can lead to the familiar crescent failure mode.

to resist increasing compression without deflection—the plot of $-f_Z$ vs. δ is a straight vertical line that coincides with the ordinate. The second path, labeled in the figure "$\varepsilon = 0$", allows δ to suddenly increase unchecked as indicated by the horizontal branch of the bifurcated equilibrium path.

Fig. 8.3 also indicates the behavior of an imperfect column or, in this case, a column with an imperfect load. As indicated in the plots of $-f_Z$ vs. δ, if $\varepsilon \neq 0$ the column will begin to deflect immediately (i.e., no bifurcation), the deflection increasing with increasing load. Depending on the value of ε the behavior of the imperfect column will either approach the behavior of a perfect column (as ε decreases) or exhibit significant deviation (as ε increases).

Similarly for a tube, if the tube cross-section is initially without imperfection, increasing external pressure will cause the tube to axisymmetrically decrease in radial dimension until a critical external pressure is reached. At that point, the equilibrium path for the tube will bifurcate. One path has the tube continuing to decrease in radius axisymmetrically—the plot of p_o vs. $u_{rl} - u_{rs}$ is a straight vertical line that coincides with the ordinate. The second path, labeled in the figure "no initial ovality", is characterized by the tube cross-section suddenly assuming a noncircular shape as indicated by the horizontal branch of the bifurcated equilibrium path.[8]

If the initial cross-sectional shape of the tubular is not perfectly circular, for example, if there is a slight as-manufactured ovality, then bifurcation is no longer the failure path. Consider the tube geometry in Fig. 8.4, which has a simple ovality imperfection in

[8] For most well tubulars the alternate, noncircular shape is an oval.

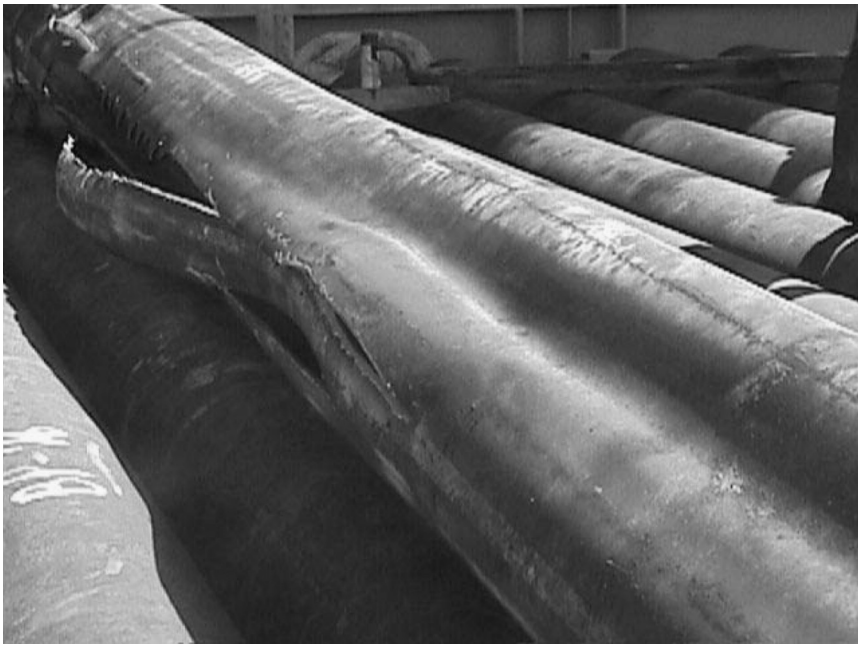

Figure 8.5 ***Recovered*** 16.000 in**.** ***collapse sample from Pompano platform, Gulf of Mexico [69].*** Damage in upper left of figure occurred while recovering sample. Copyright 2004, Society of Petroleum Engineers Inc. Reproduced with permission of SPE. Further reproduction prohibited without permission.

its as-manufactured state.[9] With increasing external pressure differential the ovality is magnified (greatly exaggerated in both Figs. 8.3 and 8.4) until a load is reached where the tube cross-section undergoes a form of snap-through buckling.[10]

In a laboratory environment the tube will normally not collapse completely, as a seal between the sample and the test fixture will fail, thus relieving the collapse pressure differential. In an oil well such is not the case, as evidenced by the 16.000 in. casing in Fig. 8.5 whose ovalization continued until it reached and stalled the rotating drill string inside. Collapse failures have been known to even propagate across threaded connections with the resulting failure of a number of joints prior to arrest of the failure [68]. The recovered tubular often experiences complete closure of its cross-section.

[9] With modern tubular mills the ovality imperfection can be small—on the order of fractions of a percent of the tube diameter.

[10] Depending on the D/t ratio and material properties of the tube, usually only one "arch" of the ovalized cross-section will buckle—the half of the cross-section which is weaker due to some additional imperfection such as, but not limited to, nonuniform wall thickness.

8.2.2.1 Modeling collapse

The two extremes of collapse—elastic collapse and yield collapse—have been modeled with closed form solutions. Assuming the tube to be constructed of an isotropic material and of infinite length:

- Elastic collapse
  - Bifurcation buckling. The tube is assumed to be of perfect cross-section with constant diameter D and wall thickness t, and loaded by a uniform external pressure. The solutions for buckling/collapse pressure p_c usually assume a thin tube ($\frac{t}{D} \ll 1$). Timoshenko and Gere [70] derive the solution

$$\bar{p}_c = \frac{2E}{1-\nu^2}\left(\frac{t}{\bar{D}}\right)^3, \tag{8.1}$$

which, with the substitutions $\bar{D} = D - t$ for the mean diameter $\bar{D}$ and $\bar{p}_c = \left(1 + \frac{t}{D}\right) p_{oc}$ for the collapse pressure $\bar{p}_c$ acting on $\bar{D}$, becomes

$$p_{oc} = \frac{2E}{1-\nu^2}\frac{1}{\left(\frac{D}{t} - \frac{t}{D}\right)\left(\frac{D}{t} - 1\right)^2}, \tag{8.2}$$

which is tantamount to the API average elastic collapse equation [71,51]

$$p_{oc} = \frac{2E}{1-\nu^2}\frac{1}{\frac{D}{t}\left(\frac{D}{t} - 1\right)^2}, \tag{8.3}$$

under the assumption $\frac{t}{D} \ll 1$.

- Yield collapse
  - Bifurcation buckling. The tube is assumed to be of perfect cross-section with constant diameter D and wall thickness t, and loaded by a uniform external pressure. Recall from the discussion in Section 8.2.1 that yield collapse is not an actual collapse mode. Rather, most investigators obtain a yield collapse formula by simply following the cross-section to its maximum external pressure capacity without searching for an alternate equilibrium configuration.

    The API average yield collapse equation [51] may be derived from Eq. (6.60) by setting $\Sigma_{zz} = p_i = 0$ and solving for the external pressure necessary to cause first yield at the tube inside diameter

$$p_{oc} = 2f_y\frac{\frac{D}{t} - 1}{\left(\frac{D}{t}\right)^2}. \tag{8.4}$$

By contrast, Klever and Tamano [57] derive an expression for through-wall yield of a tube loaded with external pressure

$$p_{oc} = 2f_y \frac{\frac{\bar{D}}{t} - \frac{1}{2}}{\left(\frac{\bar{D}}{t}\right)^2}, \tag{8.5}$$

which, with the substitution $\bar{D} = D - t$ for the mean diameter $\bar{D}$, becomes

$$p_{oc} = 2f_y \frac{\frac{D}{t} - \frac{3}{2}}{\left(\frac{D}{t} - 1\right)^2}. \tag{8.6}$$

Comparing the yield collapse expressions, the through-wall yield equation is greater than the first yield equation by factors of 1.17, 1.08 and 1.05 for D/t ratios of 10, 20 and 30, respectively.

Plastic collapse prediction is the more difficult of the three modes to predict in that the collapse will occur when the cross-section has yielded. This means that the stiffness of the tube cross-section is continually changing with incremental additions of external pressure. Once more assuming a tube constructed of an isotropic material and having infinite length, typical solutions include the following:

- Bifurcation buckling. This problem has been worked by Huang and Pattillo [72] for a thin tube and includes the effect of axial traction. For $\Sigma_{zz} = p_i = 0$, the solution is

$$\bar{p}_c = 2E\left(\frac{t}{\bar{D}}\right)^3 \frac{\frac{E}{E_t} - 3}{\frac{E}{E_t}\left(\frac{E}{E_t} - 3\right) - \left[\frac{E}{E_t} - (1 - 2\nu)\right]^2}, \tag{8.7}$$

which, with the substitutions $\bar{D} = D - t$ for the mean diameter $\bar{D}$ and $\bar{p}_c = \left(1 + \frac{t}{D}\right) p_{oc}$ for the collapse pressure $\bar{p}_c$ acting on $\bar{D}$, becomes

$$p_{oc} = \frac{2E}{\frac{D}{t}\left(\frac{D}{t} - 1\right)^2} \frac{\frac{E}{E_t} - 3}{\frac{E}{E_t}\left(\frac{E}{E_t} - 3\right) - \left[\frac{E}{E_t} - (1 - 2\nu)\right]^2}, \tag{8.8}$$

where E_t is the tangent modulus to a uniaxial stress–strain curve that is connected to the isotropic work-hardening plastic deformation of the tube through the von Mises equivalent stress (see Section 6.4.3.1 of Chapter 6).

The difficulty with this solution is evident. The tangent modulus E_t is only known if the external pressure is known, but in turn the critical value of the external pressure depends on E_t. The solution is one of trail-and-error.

- Snap-through buckling. The snap-through buckling approach to tubular collapse is the strategy of choice for numerical solutions [69,73]. Typically, a two-dimensional

problem is posed where the cross-section is assigned an ovality manufacturing imperfection[11] ω, where

$$\omega = 2\frac{D_{max} - D_{min}}{D_{max} + D_{min}}, \tag{8.9}$$

where D_{max} and D_{min} are modeled as occurring along perpendicular axes of the cross-section. Typical manufacturer ovalities of oil field tubulars are on the order of fractions of a percent of $\frac{D_{max}+D_{min}}{2}$.

One shortcoming of two-dimensional modeling is that it usually yields collapse predictions that are lower than experiment. Possible explanations for this behavior include the following:

- The chosen cross-section is assumed to be representative of the entire sample and does not include the rotation of ovality possibly associated with passage through rollers during manufacture—such rotation would lead to support between neighboring cross-sections;
- The tube is, by nature of the two-dimensional formulation, infinite in length and therefore insulated from the effects of end conditions in a laboratory test frame;
- The ovality measured on the test sample may not conform to the ovality defined in Eq. (8.9), particularly with regard to the perpendicularity of the D_{max} and D_{min} axes, thus rendering the numerical model nonrepresentative of the sample (i.e., weaker) to which it is being compared [74].

An outstanding example of numerical modeling of snap-through buckling is the work of Toscano et al. [75] who use detailed maps of diameter and wall thickness of samples to build three-dimensional finite element models, and then collapse test the samples to verify the software predictions. Without bending, baseline comparisons of predicted to measured collapse pressure (3 samples) are 1.02 (using the measured data with no axial residual stress); in the one test where bending preceded application of external pressure the ratio is 0.964.

8.2.3 API collapse modes

The collapse modes discussed above—elastic, plastic, yield—apply to both the limit state equation (describing anticipated behavior for a particular sample geometry and material) and the design equation (describing a reasonable minimum behavior using minimally favorable geometry and material).

[11] Other candidate imperfections include eccentricity (offset of the inner diameter circle of the cross-section from the center of the outer diameter circle), wall thickness, residual stress and the external traction.

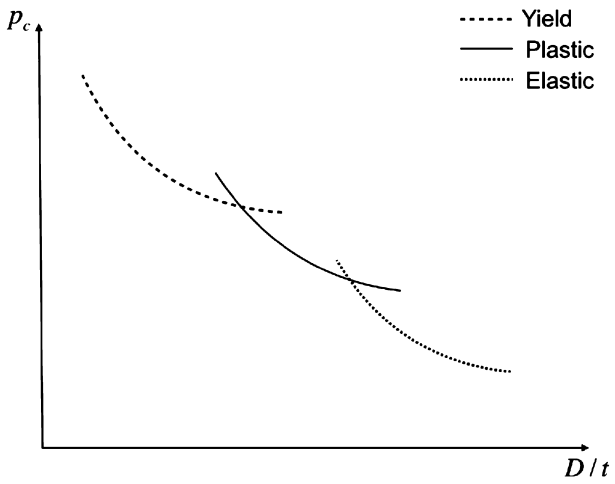

Figure 8.6 ***API average collapse resistance modes.***

8.2.3.1 API average collapse resistance

A summary of API *average* collapse resistance is presented in Fig. 8.6. For the three collapse modes discussed above (see Section 8.2.1) the following origins can be traced (see [51] for details):

- As discussed in Section 8.2.2.1, the average elastic collapse formula, Eq. (8.3) [71], closely resembles a formula presented by Timoshenko and Gere [70]—the collapse resistance is proportional to $1/(D/t)^3$;
- From Section 8.2.2.1, even simple theoretical expressions for plastic collapse require trial-and-error solution. As an alternative, the average plastic collapse formula is empirical [71]—the collapse resistance is proportional to $1/(D/t)$;
- The average yield collapse formula, Eq. (8.4), is proportional to $1/(D/t)^2$.

All three equations have the form $\frac{1}{x^n}$ as illustrated in Fig. 8.6. Given D, t and f_y for a tube, one must calculate all three collapse mode pressures, with the actual collapse pressure being the smallest of the three numbers. For constant yield stress, and beginning with thin-walled (high D/t ratio) tubulars, the applicable collapse resistance mode is elastic, then plastic for thicker tubulars, and finally yield collapse for the thickest tubes.

External pressure resistance in the yield and plastic collapse modes—the former involves incipient yield, the latter involves postyield behavior—is affected by axial traction, with tension lowering collapse resistance and compression increasing collapse resistance. Elastic collapse is unaffected by axial traction.[12]

[12] Recall from the discussion of Section 8.2.1 that, aside from geometry (D/t), elastic collapse is a function only of Young's modulus and Poisson's ration, neither of which is a function of axial traction.

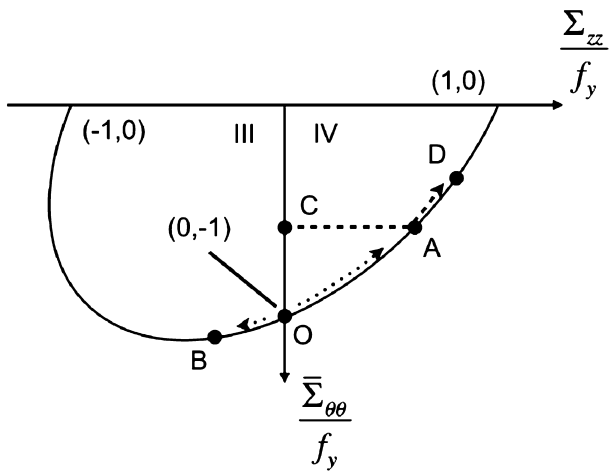

Figure 8.7 ***Simplified illustration of collapse with axial paths.***

Consider Fig. 8.7, which is the lower half of the simple VME ellipse introduced in Section 6.3.4.4 of Chapter 6, that is, the portion of the yield surface that addresses external pressure (i.e., negative hoop stress) and axial traction. Roughly speaking, plastic collapse in the absence of Σ_{zz} is represented by the hoop stress corresponding to the point $(0,-1)$.[13] As Σ_{zz} is added to a sample its ability to support hoop stress before yielding decreases, as does its collapse resistance. This effect is represented by the path OA in the figure. If, instead, Σ_{zz} is negative, the sample can support additional hoop stress at yield; its collapse resistance increases. This effect[14] is represented by the path OB in the figure.[15]

Now consider a combination of cross-sectional geometry and material strength that results in elastic collapse. The hoop stress in such a tube could, in the absence of Σ_{zz}, be represented by point C in the figure at its instant of collapse. As Σ_{zz} is increased, the tube's geometry and material properties do not change, and neither does its collapse

[13] This is not strictly true, even in the case of vanishing Σ_{zz}. Except in the extreme case at the boundary between elastic and plastic collapse, the average hoop stress in the cross-section will, given any amount of work-hardening, be somewhat above yield. This implies a certain amount of plastic flow and expansion/translation/distortion of the yield surface local to the point at which the yield surface is penetrated. For the purpose of illustrating the concept of adjustment of collapse for axial stress, however, assuming negligible alteration of the yield surface is tolerable.

[14] Although the increase in collapse resistance in an axial compression environment is substantiated by experimental evidence, common industry design practice is to ignore this benefit. If the wellbore contains any deviation, associated wall friction between the tubular and its confining hole render an exact knowledge of the axial compression value difficult.

[15] These same observations are deduced from the governing equation for the simple VME ellipse, Eq. (6.85), in Section 6.3.4.4 of Chapter 6.

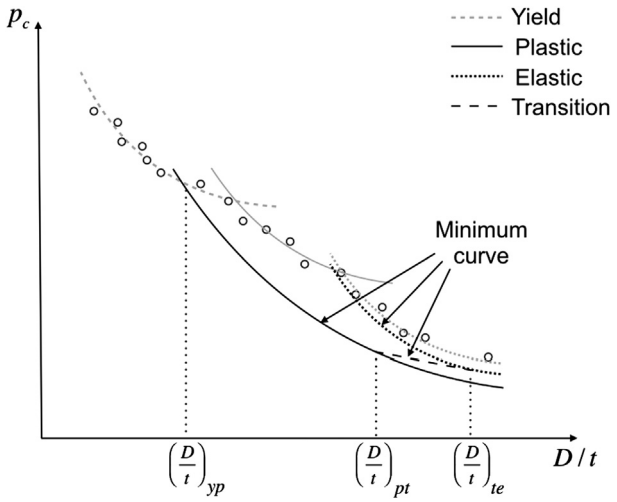

Figure 8.8 ***API minimum collapse resistance modes.*** Gray curves are average collapse curves from Fig. 8.6; black curves are minimum collapse curves. Open circles represent collapse test data used to arrive at the API design equations. A total of 2488 tests were used in the statistical regression analysis employed to arrive at the plastic collapse limit state and design equations.

pressure, as suggested by path CA. If, however, Σ_{zz} is increased to a value that does not permit realization of the hoop stress corresponding to collapse without yielding the tube, the limit of elastic collapse has been reached (point A in the figure). Any further increase in Σ_{zz} will change the collapse mode from elastic to plastic and begin to reduce the tube's ability to support hoop stress at yield (path AD in the figure). The collapse resistance is decreasing with increasing Σ_{zz}.

Recall that the simple VME ellipse used in the above discussion is approximate. The actual API adjustment of collapse for axial traction uses an abscissa that includes an internal pressure term and an ordinate that is differential (collapse) pressure (see Eq. (8.10) in Section 8.2.4 and the associated example calculation). The collapse behavior with axial load described above, however, is still applicable provided the axial stress value is supplemented by p_i.

8.2.3.2 API minimum collapse resistance

In addition to the three limit state equations described above, the API has also provided design equations for industry use [51]. The background of these collapse design equations is summarized in Fig. 8.8. This figure is an extension of Fig. 8.6 and includes the average collapse resistance curves. To reduce the average collapse resistance values to design minimum collapse values the following adjustments were applied [51]:

- No adjustment is applied for the API yield collapse mode. The formulas for average and minimum yield collapse resistance are identical;

- For all values of D/t the API minimum elastic collapse resistance is 75% of the API average elastic collapse resistance;
- The API minimum plastic collapse resistance was derived from the average plastic collapse resistance by a statistical calculation based on a 0.95 confidence level that 0.995 of the sample population meets or exceeds the minimum collapse resistance value.

When the above adjustments to the API average collapse resistance formulas were implemented, the elastic and plastic collapse curves no longer intersected. To rectify this anomaly, a new minimum collapse mode—transition collapse—was introduced. The transition collapse curve is constructed such that it "intersects the D/t value where the average plastic collapse pressure equation gives a collapse pressure of zero and is tangent to the minimum elastic collapse pressure… This equation is used to determine minimum collapse pressures between its tangency to the elastic collapse pressure curve and its intersection with the plastic collapse pressure curve" [51].

8.2.4 Calculating resistance to uniform external pressure

The API/ISO method for determining the resistance of a tube to an external fluid pressure differential is documented in API TR 5C3 [51] and its counterpart ISO TR 10400 [65]. Given the specified outside diameter D, specified wall thickness t, specified minimum yield stress f_{ymn}, applied axial traction Σ_{zz} and internal pressure p_i, the differential collapse pressure $p_c - p_i$ of a tube is calculated by the following procedure.

8.2.4.1 Adjust yield stress for the presence of axial stress and internal pressure

As a first step in the calculation, the specified yield stress f_{ymn} is adjusted for the presence of axial traction and internal pressure. Earlier versions of the API calculation procedure listed a similar adjustment as last in the calculation procedure.[16] This inconsistency emphasizes the fact that the relation between axial traction and external pressure resistance is physically intimate. In fact, more involved collapse models [72] perform the calculation considering the effects of axial traction and external pressure simultaneously. Here, however, the calculation flow favors the user who has no access to complex models.

The formula for adjusting yield stress for axial traction and internal pressure is[17]

$$f_{ycom} = \left(\sqrt{1 - 0.75 \left(\frac{\Sigma_{zz} + p_i}{f_{ymn}} \right)^2} - 0.5 \frac{\Sigma_{zz} + p_i}{f_{ymn}} \right) f_{ymn}, \quad \Sigma_{zz} + p_i \geq 0. \tag{8.10}$$

[16] In the earlier editions the adjustment was applied to the collapse resistance rather than the yield stress.
[17] The experimental program and analysis used to arrive at Eq. (8.10) is discussed in [76].

Regarding the combined loading equivalent grade resulting from the adjustment for the presence of axial traction and internal pressure, the following observations are in order:

- Once the combined loading equivalent grade is calculated the resulting modified yield stress f_{ycom} is treated as the yield stress in all subsequent calculations. The original, unadjusted yield stress is no longer pertinent to the procedure.
- The adjustment to yield stress can, according to the sign of $\Sigma_{zz} + p_i$, either increase or decrease the yield stress for the purpose of the remainder of the collapse calculation. API TR 5C3 [51] only applies the correction to cases where $\Sigma_{zz} + p_i \geq 0$.
- Focusing on the square root term, the maximum compressive value of $\Sigma_{zz} + p_i$ that avoids an imaginary root(s) is $\Sigma_{zz} + p_i \geq -\sqrt{4/3} f_{ymn} = -1.155 f_{ymn}$. That is, it is possible within the context of the von Mises yield criterion upon which Eq. (8.10) is based to undergo a compressive load greater than f_{ymn} without suffering collapse (although the collapse resistance might be reduced). This feature of the correction embodied in Eq. 8.10 is frequently ignored, and both the tension and compression limits of the axial tension adjustment are set to f_{ymn}.
- The form of the axial stress adjustment is not totally *ad hoc*. Rearranging Eq. (8.10) yields

$$\left(\frac{f_{ycom}}{f_{ymn}}\right)^2 + \frac{\Sigma_{zz} + p_i}{f_{ymn}} \frac{f_{ycom}}{f_{ymn}} + \left(\frac{\Sigma_{zz} + p_i}{f_{ymn}}\right)^2 = 1, \tag{8.11}$$

  which is identical in form to the ellipse presented in Fig. 6.13 (associated with Eq. (6.68))[18] with X-axis $\frac{\Sigma_{zz}+p_i}{f_{ymn}}$ and Y-axis $\frac{f_{ycom}}{f_{ymn}}$. The ordinate in Fig. 6.13 is, from Eq. (5.55), $\Sigma_{\theta\theta} + p_i$ at the inner radius of the tube. Fig. 6.13 is roughly a yield surface in a space defined by $\Sigma_{zz} + p_i$ and $\Sigma_{\theta\theta} + p_i$. Therefore, with the understanding that p_i, though significant, is the minor variable in a collapse discussion, a rough interpretation of Eq. (8.10) and the variable f_{ycom} is that, for a given $\Sigma_{zz} + p_i$, Eq. (8.10) is providing a new yield stress that is equal to the hoop stress to cause yield in the presence of $\Sigma_{zz} + p_i$.[19]
- Eq. (8.10) is applicable to collapse modes that involve inelastic deformation. It should not be used to adjust elastic collapse for the presence of axial stress.

8.2.4.2 Calculate empirical values

The yield and elastic collapse mode formulas were derived from theoretical considerations. The plastic collapse mode formula, on the other hand, is empirical and as such

[18] Note the sign difference between the unsquared terms in Eqs. (8.11) and (6.68). The former's focus is $p_o - p_i$; the latter's focus is $p_i - p_o$.

[19] This is essentially the same argument that has been made in Section 8.2.3.1 of this chapter and Section 6.3.4.4 of Chapter 6 using the simple VME ellipse.

depends on factors which have been curve fit to collapse data to provide formula behavior that best predicts the original collapse values. Five factors are to be determined—A_c, B_c, C_c, F_c and G_c:

$$A_c = 2.8762 + 1.0679 \times 10^{-6} f_{ycom} + 2.1301 \times 10^{-11} f_{ycom}^2 - 5.3132 \times 10^{-17} f_{ycom}^3, \quad (8.12)$$

$$B_c = 0.026\,233 + 5.0609 \times 10^{-7} f_{ycom}, \quad (8.13)$$

$$C_c = -465.93 + 0.030\,867 f_{ycom} - 1.0483 \times 10^{-8} f_{ycom}^2 + 3.6989 \times 10^{-14} f_{ycom}^3, \quad (8.14)$$

$$F_c = \frac{4.695 \times 10^7 \left(\frac{3B_c/A_c}{2+B_c/A_c}\right)^3}{f_{ycom}\left[\frac{3B_c/A_c}{2+B_c/A_c} - B_c/A_c\right]\left[1 - \frac{3B_c/A_c}{2+B_c/A_c}\right]^2}, \quad (8.15)$$

$$G_c = \frac{F_c B_c}{A_c}. \quad (8.16)$$

8.2.4.3 Determine D/t values at boundaries between collapse modes

Usually in collapse calculations, the governing mode of collapse is determined by computing the collapse resistance of all modes, and then taking the smallest value as the governing mode. The API procedure is slightly different but accomplishes the same purpose. In the API procedure formulas are provided for the D/t boundaries at which precedence switches from one collapse mode to another. The process is twofold:

1. Calculate the D/t boundaries between the four API collapse modes.
2. Use the D/t of the tube being investigated, as it compares to the D/t boundaries, to determine the governing collapse mode.

The formulas for the D/t boundaries between the API collapse modes are as follows:

- Boundary between yield and plastic collapse modes $(D/t)_{yp}$ is

$$\left(\frac{D}{t}\right)_{yp} = \frac{\sqrt{(A_c - 2)^2 + 8\left(B_c + C_c/f_{ycom}\right)} + (A_c - 2)}{2\left(B_c + C_c/f_{ycom}\right)}. \quad (8.17)$$

- Boundary between plastic and transition collapse modes $(D/t)_{pt}$ is

$$\left(\frac{D}{t}\right)_{pt} = \frac{f_{ycom}(A_c - F_c)}{C_c + f_{ycom}(B_c - G_c)}. \quad (8.18)$$

- Boundary between transition and elastic collapse modes $(D/t)_{te}$ is

$$\left(\frac{D}{t}\right)_{te} = \frac{2 + B_c/A_c}{3B_c/A_c}. \quad (8.19)$$

8.2.4.4 Select appropriate collapse mode

Once the above boundaries are determined, the appropriate collapse mode for the target D/t can be determined. For example, if the target D/t value falls between $\left(\frac{D}{t}\right)_{pt}$ and $\left(\frac{D}{t}\right)_{te}$, the appropriate collapse mode is the transition collapse mode. Should a target D/t value fall exactly on the boundary between two collapse modes, either mode can be used in the final collapse resistance calculation.

8.2.4.5 Compute collapse resistance

The formulas governing the four API collapse modes are as follows:

- Yield collapse mode, $D/t \le (D/t)_{yp}$,

$$\Delta p_c = p_{oc} - p_i = 2 f_{ycom} \frac{(D/t) - 1}{(D/t)^2}. \tag{8.20}$$

- Plastic collapse mode, $(D/t)_{yp} \le D/t \le (D/t)_{pt}$,

$$\Delta p_c = p_{oc} - p_i = f_{ycom} \left[\frac{A_c}{D/t} - B_c \right] - C_c. \tag{8.21}$$

- Transition collapse mode, $(D/t)_{pt} \le D/t \le (D/t)_{te}$,

$$\Delta p_c = p_{oc} - p_i = f_{ycom} \left[\frac{F_c}{D/t} - G_c \right]. \tag{8.22}$$

- Elastic collapse mode, $(D/t)_{te} \le D/t$,

$$\Delta p_c = p_{oc} - p_i = \frac{46.95 \times 10^6}{(D/t)\left[(D/t) - 1\right]^2}, \tag{8.23}$$

where Δp_c is the differential pressure corresponding to collapse and p_{oc} is the external pressure corresponding to collapse. The quantity Δp_c is independent of the internal pressure p_i; the quantity p_{oc} is not.

Only one of Eqs. (8.20)–(8.23) should be employed, depending on the governing collapse mode.

8.2.4.6 Example problem—uniform external pressure

At a certain depth in a well a tube of 9.625 in., 53.5 $\frac{\text{lb}_\text{m}}{\text{ft}}$ P110 casing (0.545 in. wall thickness) is subjected to an axial tension of 20 000 psi. The local internal pressure is 1000 psi. Compute the collapse resistance of the tube.

The solution follows the procedure outline above.

Adjust yield stress for the presence of axial tension and internal pressure

From Eq. (8.10) we have

$$f_{ycom} = \left(\sqrt{1 - 0.75 \left(\frac{20\,000\,\text{psi} + 1000\,\text{psi}}{110\,000\,\text{psi}} \right)^2} - 0.5 \frac{20\,000\,\text{psi} + 1000\,\text{psi}}{110\,000\,\text{psi}} \right) 110\,000\,\text{psi}$$
$$= 97\,986\,\text{psi}. \tag{8.24}$$

Calculate empirical values

The empirical values given in Eqs. (8.12)–(8.16) are

$$A_c = 2.8762 + 1.0679 \times 10^{-6} (97\,986) + 2.1301 \times 10^{-11} (97\,986)^2 - 5.3132 \times 10^{-17} (97\,986)^3 \tag{8.25}$$
$$= 3.135,$$
$$B_c = 0.026\,233 + 5.0609 \times 10^{-7} (97\,986) = 0.0758, \tag{8.26}$$
$$C_c = -465.93 + 0.030\,867 (97\,986) - 1.0483 \times 10^{-8} (97\,986)^2 + 3.6989 \times 10^{-14} (97\,986)^3$$
$$= 2493, \tag{8.27}$$
$$F_c = \frac{4.695 \times 10^7 \left(\frac{3(0.0758)/(3.135)}{2+0.0758/3.135} \right)^3}{97\,986 \left[\frac{3(0.0758)/(3.135)}{2+0.0758/3.135} - 0.0758/3.135 \right] \left[1 - \frac{3(0.0758)/(3.135)}{2+0.0758/3.135} \right]^2}$$
$$= 2.036, \tag{8.28}$$
$$G_c = \frac{(2.036)(0.0758)}{3.135} = 0.0492. \tag{8.29}$$

Determine D/t values at boundaries between collapse modes

The D/t boundaries between collapse modes are given by Eqs. (8.17)–(8.19),

- Boundary between yield and plastic collapse modes $(D/t)_{yp}$ is

$$\left(\frac{D}{t} \right)_{yp} = \frac{\sqrt{(3.135 - 2)^2 + 8\,(0.0758 + 2493/97\,986)} + (3.135 - 2)}{2\,(0.0758 + 2493/97\,986)}$$
$$= 12.76. \tag{8.30}$$

- Boundary between plastic and transition collapse modes $(D/t)_{pt}$ is

$$\left(\frac{D}{t} \right)_{pt} = \frac{(97\,986)\,(3.135 - 2.036)}{2493 + (97\,986)\,(0.0758 - 0.0492)} = 21.13. \tag{8.31}$$

- Boundary between transition and elastic collapse modes $(D/t)_{te}$ is

$$\left(\frac{D}{t}\right)_{te} = \frac{2 + 0.0758/3.135}{3(0.0758)/3.135} = 27.90. \tag{8.32}$$

Select appropriate collapse mode

The target value of D/t is $9.625/0.545 = 17.66$, which means the tube collapses in the plastic collapse mode.

Compute collapse resistance in the presence of internal pressure

Using Eq. (8.21), we have

$$\Delta p_c = p_{oc} - p_i = (97\,986)\left[\frac{3.135}{17.66} - 0.0758\right] - 2493 = 7474\,\text{psi}, \quad p_{oc} = 8474\,\text{psi}. \tag{8.33}$$

8.2.5 Effect of length-to-diameter ratio on collapse resistance

The API collapse calculation is intended to model a long tube such as an entire joint of casing or tubing. Instances do exist, however, when one's interest lies in the external pressure resistance of a tube whose length-to-diameter (L/D) ratio is small:

- Collapse testing. Given the expense and logistics associated with collapse testing a full tubular joint, the question arises as to what length of tubular one must test to realize essentially the same result as a long tube.
- Collapse design of polished bore receptacles (PBRs). In a casing tieback or tubing design/installation involving a seal stem and polished bore receptacle, it is not always appropriate to maintain the two parts with complete overlap—some length of exposed PBR may or should be exposed. From a negative viewpoint, this exposes a part which can have lower external pressure resistance than the casing or production tubing. From a positive viewpoint, both intuition and experiment lead one to believe that the short exposure length of the PBR affords it collapse support from the pieces to which it is attached or with which it has sliding contact.

The effect of length on collapse resistance has been calculated numerically in a study by Huang and Pattillo [77,78] based on Sanders' nonlinear shell equations [79] with inelastic behavior addressed using the von Mises equivalent stress and mapping from a uniaxial tension test (see Section 6.3.2 of Chapter 6). Typical results are displayed in Figs. 8.9 and 8.10.

Fig. 8.9 illustrates the effect of work-hardening of the tube material by using Needleman's model (see Section 6.2.3.1 of Chapter 6) to define uniaxial stress–strain curve shape beyond yield. The results are plotted on a log–log scale, where the abscissa is the ratio of sample length to its mean radius/diameter. The ordinate is dimensionless collapse pressure.

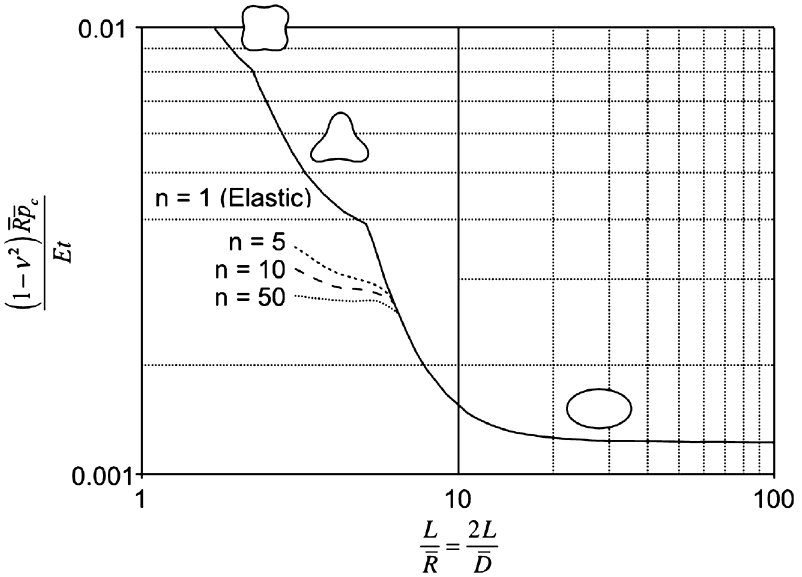

Figure 8.9 ***Effect of stress–strain curve on inelastic collapse,*** $f_y = 80\,000$ psi, $\frac{\bar{D}}{t} = 30$ **[78].** The numerical values identifying individual curves are associated with the work-hardening parameter in Needleman's model. Copyright 2007, Society of Petroleum Engineers Inc. Reproduced with permission of SPE. Further reproduction prohibited without permission.

The solid line in Fig. 8.9 is the solution for elastic buckling [70]. As illustrated by the deformed cross-sections, an elastic tube will collapse with one of an infinite number of cross-sectional mode shapes—the modes illustrated in the figure are, from right to left, modes 2, 3 and 4, respectively—depending on the L/D ratio of the tube, with short samples exhibiting the higher mode shapes.[20] Also included in the figure are the analysis results for a tube with material of yield stress 80 000 psi. As the material work-hardening coefficient from Needleman's model increases (work-hardening decreases), the deviation of the tube from elastic behavior increases.

Fig. 8.10 offers further insight into the effect of length on collapse resistance by comparing samples with the same Needleman work-hardening parameter but differing yield stresses. Once more, the greater the deviation from elastic behavior, in this instance with decreasing yield stress, the lower the collapse resistance. For the lowest yield stress, the cross-section yields even with long samples.

Of importance to the current discussion is the ratio of $L/\bar{D}$ at which length no longer has an effect on a sample's collapse resistance. For the particular case of the relatively thin tube used to generate Figs. 8.9 and 8.10, this occurs somewhere between a value of $L/\bar{R}$ of 20 and 30, or an $L/\bar{D}$ of 10 to 15. The minimum L/D ratio for

[20] Oil field tubulars have a yield stress and D/t ratio that almost always results in a mode 2 cross-section at collapse.

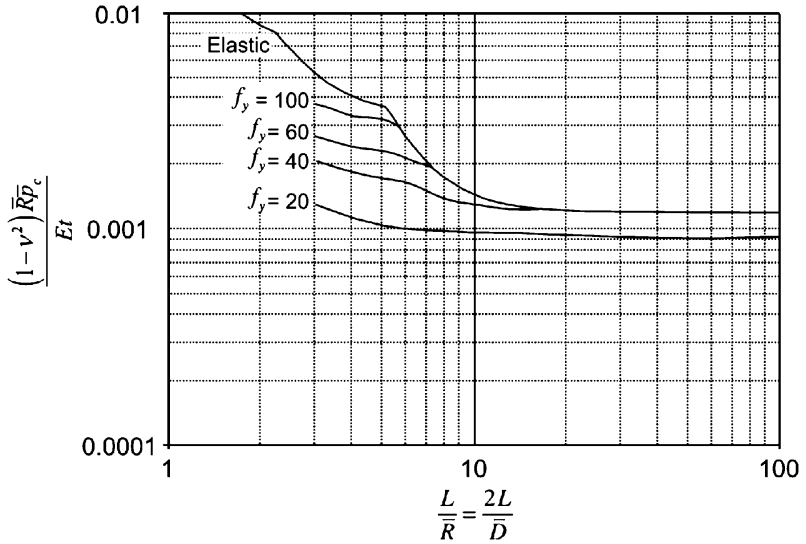

Figure 8.10 ***Effect of yield stress on inelastic collapse,*** $n = 5$, $\frac{\bar{D}}{t} = 30$ ***[78].*** Copyright 2007, Society of Petroleum Engineers Inc. Reproduced with permission of SPE. Further reproduction prohibited without permission.

collapse testing suggested by API TR 5C3 [51] is eight for sizes 9.625 in. and smaller, seven for larger sizes.[21]

For PBR design, a tool such as that described here can be used to analyze the impact of exposed, unaided length on the collapse integrity of a PBR cross-section. Inasmuch as the limit state modeled by the analysis is bifurcation buckling of a perfect cross-section, application of the model to a machined PBR is appropriate.

The model used to generate Figs. 8.9 and 8.10 has been demonstrated to reproduce the results of $L/\bar{D}$ collapse experiments fairly well, usually over-predicting sample collapse strength [78]. The comparisons, however, were made to tubes of API casing. Similar comparisons with machined products, such as a PBR, would be expected to improve.

8.3. NONUNIFORM EXTERNAL PRESSURE

If the source of the external casing load is formation contact rather than fluid pressure, the load will more likely be nonuniform. Instances of nonuniform external casing load associated with formation movement include the following:

- Mobile salts [80–82];

[21] The $\bar{D}/t$ ratio of the samples in Fig. 8.9 is more typical of larger sized tubulars implying the API may be nonconservative in its test recommendation. From a logistical viewpoint, however, it would be difficult to handle samples long enough to accommodate the conclusion reached from Fig. 8.9.

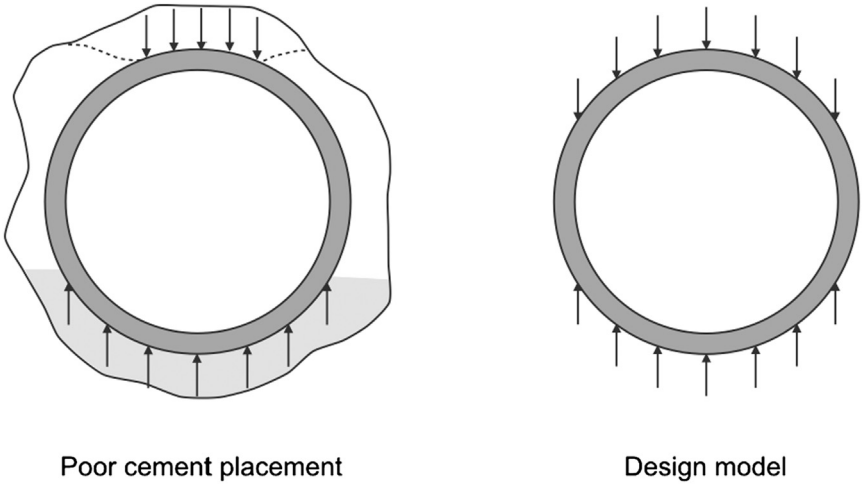

Figure 8.11 ***Converting nonuniform loading in service into a design model.***

- Reservoir compaction due to depletion, sometimes accompanied by surface/mudline subsidence [83–89];
- Tectonic stresses [90,91];
- Thermal processes [92].

Perhaps the most severe form of nonuniform loading—point loading where the casing or tubing cross-section is loaded by opposing line loads rather than opposing distributed loads—occurs when one tubular is loaded externally by another, collapsing tubular. This often causes a cascade of collapse failures that may not be arrested until the production tubing is damaged. Typical of this extreme nonuniform load are APB failures, where solid evidence exists of the damage done by one collapsing tube on its neighbor (cf. [68,69,93]).

An example of nonuniform loading from salt is illustrated in Fig. 8.11. It is often difficult to maintain a gauge hole while drilling a mobile salt, with the result that proper conditioning of the hole and cement placement are also complicated. Once the cement has solidified, a location of (a) possible washout and (b) incomplete circumferential cement coverage invites creep of salt and eventual contact with the adjacent casing. On one side of the cross-section the salt is advancing in its preferred displacement direction; on the other side of the cross-section the partial cement sheath reacts to the imposed load (left-hand diagram of Fig. 8.11). The resulting external load on the casing can be approximated by the stress distribution shown[22] in the right-hand diagram of

[22] The figure can be used to describe more sources than loading from a mobile formation such as salt. A similar load distribution can be imagined, for example, for the cross-section of casing in a horizontal wellbore penetrating a compacting reservoir.

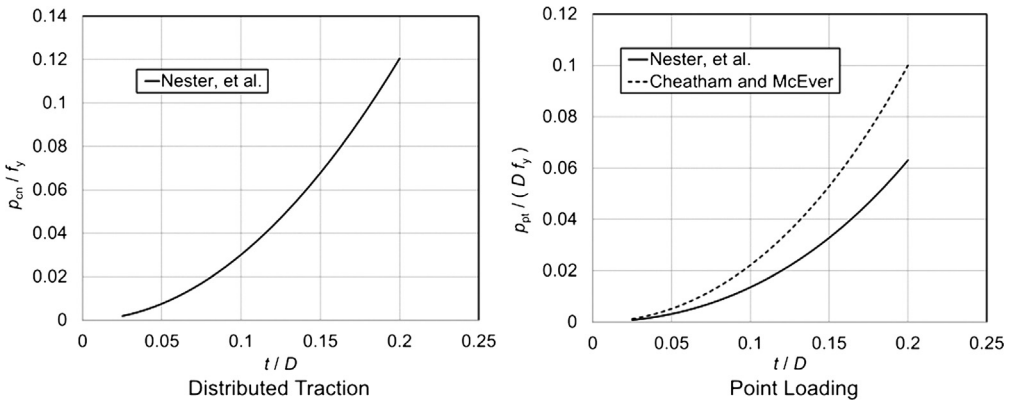

Figure 8.12 ***Selection of proposed models for nonuniform traction.*** In all cases the tube is assumed to be of infinite length.

Fig. 8.11. Problems of this nature have been addressed both analytically [94,80] and numerically [83].

8.3.1 The role of wall thickness

A number of models have been proposed to characterize the resistance of a casing cross-section to nonuniform loading. Fig. 8.12 illustrates the behavior of several of these models on a common plot of traction at limit load as a function of t/D ratio. The left-hand diagram in the figure addresses forms of distributed load; the right-hand diagram in the figure addresses forms of point loading. Displayed are the following[23]:

- Nester, Jenkins and Simon [94] offer two different solutions:
  - Opposing unidirectional tractions, each applied to one-half of the outer surface of the tubular and of uniform magnitude (see the right-hand diagram in Fig. 8.11). The equation for first yield of a thick-walled tube using the Tresca yield criterion is

$$\frac{p_{cn}}{f_y} = 3.01\left(\frac{t}{D}\right)^2. \tag{8.34}$$

  - Opposing line loads. The equation for first yield of a thick-walled tube using the Tresca yield criterion is

$$\frac{p_{pt}}{Df_y} = 1.13\left(\frac{t}{D}\right)^2 \frac{1}{\left(1-\frac{t}{D}\right)\left(0.96-0.32\frac{t}{D}\right)}. \tag{8.35}$$

[23] In some cases the author also applies a uniform pressure to either internal or external surfaces of the cross-section. These uniform tractions are assumed in Fig. 8.12 to be of zero magnitude.

In more general forms of both of the above equations, Nester et al. investigate the effect of internal pressure, concluding that its effect on nonuniform load resistance is minor (on the order of 10% for small D/t ratios and declining for larger D/t ratios).

- Cheatham and McEver [80] use curved beam theory to compute the line load necessary to form a plastic hinge (entire cross-section yielded) of a cross-section with no work-hardening with the result

$$\frac{p_{pt}}{Df_y} = 2\left(\frac{t}{D}\right)^2 \frac{1}{1-\frac{t}{D}}. \tag{8.36}$$

In all cases in Eqs. (8.34)–(8.36) the load is proportional to $\left(\frac{t}{D}\right)^2$. This is perhaps the most important principle to apply in designing for nonuniform formation loading—the most efficient mitigation is to increase the t/D ratio of the cross-section. Doubling the yield stress doubles the cross-section's resistance to nonuniform loading; doubling the t/D ratio, usually by doubling the wall thickness, quadruples the cross-section's resistance.

8.3.2 Concentric casing

A proven construction to mitigate the effects of nonuniform cross-sectional loading is the so-called concentric casing configuration [95]. Positive results in field installations can be duplicated analytically [83]. The term "concentric casing" refers to a configuration where one casing is run and cemented inside another casing for the purpose of presenting an effectively greater wall thickness to the nonuniform lateral traction. The cement is particularly important in providing the communication between the inner and outer casings to effect the increase in wall thickness.

Most concentric installations involve creating the inner tubular by either extending a liner lap up to the zone of concern or, if that proves impractical, running a scab liner. Either solution may affect the well design if the mobile formation will contact production casing. Running the second string may then, for example, limit the depth to which gas lift mandrels may be run or may hamper the access necessary for intelligent completion components.

Important aspects of concentric casing design include the following:

- It is not crucial that the two tubulars be of exotically high yield stress. Of primary concern is that the outer casing be able to withstand any potential nonuniform traction prior to the installation of the inner casing. Depending on the particular formation and the size of the borehole, the time following the installation of the outer casing until first contact may be a week or more. If the formation creep is rapid, a thick-walled casing alternative may be more appropriate than concentric strings.
- Although optimum, it is not necessary that the two tubulars be concentric. Numerical simulation [96] indicates a minor (less than 10%) loss of integrity for a 75%

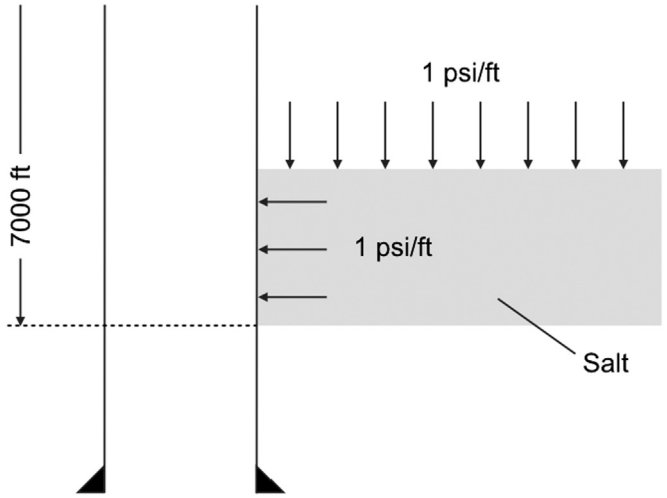

Figure 8.13 ***Example of design for mobile salt.***

eccentric cross-section. Even eccentric cross-sections provide an increase in the effective cross-sectional wall thickness.

- Although the strength of the cross-section increases with the unconfined compressive strength of the cement, the sensitivity is not what one might expect. Again, numerical simulation [96] indicates that an order of magnitude increase in cement compressive strength increases the resistance of the cross-section to nonuniform load by approximately 30%. It is this author's recommendation that there be more design focus on placement and thickening of the cement than on its strength. The crucial issue is that the cement be present to promote communication of the two tubular members.

8.3.3 Example problem—design of casing for formation mobility

Consider Fig. 8.13 that presents a typical problem of mobile salt design. A commonly applied method of designing for mobile salt employs the following reasoning:

- A fairly accurate estimate of the overburden (vertical) stress gradient is 1 $\frac{\text{psi}}{\text{ft}}$.
- Given time, the creep behavior of a mobile salt will cause it to act essentially as a fluid such that the horizontal traction it imposes on adjacent casing will have the same magnitude as the vertical stress to which the salt is subjected. Given this assumption and the estimate of the previous bullet, the expected traction from salt on the casing would be 1 $\frac{\text{psi}}{\text{ft}}$. As a numerical example, if the depth of the salt being designed against is 7000 ft, the assumed horizontal traction on the casing is 7000 psi.
- To design casing opposite the salt, one searches a table of casing performance properties for a mass/grade combination whose collapse resistance is 7000 psi.

The above reasoning contains an inconsistency that will (a) typically lead to casing designed opposite the salt having higher wall thickness, but (b) result in an underdesigned cross-section that, though substantial, will not be substantial enough. The problem lies in the last bulleted item. All published tables of casing and tubing collapse resistance with which this author is familiar are tables of resistance to *uniform* external pressure, not a nonuniform traction. As an example, a failure analysis of salt-damaged casing in the Gulf of Suez [97] illustrates casing deformation when the computed collapse safety factor according to the bulleted design method above is 4.8. The last step in the bulleted design method above is not a recommended practice for nonuniform collapse design.

Given the unsatisfactory nature of using uniform collapse ratings to design for nonuniform traction, the following guidelines for design are offered:

- Conversations between drilling and completions are in order, focusing on the radial clearance available to design against the nonuniform traction. Once a radial clearance is confirmed, and honoring adequate annular space for such issues as cement placement, the maximum radial dimensions should be devoted to applying wall thickness—either with a single, thick-walled tubular or with concentric tubulars—to combat the external load.
- Eqs. (8.34)–(8.36) are, at a minimum, useful for ranking competing tubular candidates according to their ability to resist nonuniform loading.
- If it is possible to cement outside the tubular(s) being designed, in all instances but one[24] this should be pursued. Cement outside the (outer) casing will tend to spread the formation traction, thus lowering its severity.
- If a thick-walled casing is required, the following operational issues should be considered [96]:
  - Such a nonstandard tubular may be difficult to obtain. Further, the associated threaded connection may require qualification. A long lead time for delivery should not be surprising.
  - In wellbores with long horizontal extensions it may be difficult to run the tubular the entire length of the extension. Torque-drag modeling is recommended.
  - The bending stiffness of the thick-walled tubular may complicate its installation through large doglegs.
  - The weight of the thick-walled tubular may exceed the load bearing capacity of the drilling rig. This problem occurs infrequently as many thick-walled tubular strings for mobile formation mitigation are run as liners.
- In many instances it will be necessary to model the casing/formation interaction numerically. Numerical modeling can handle complex geometric issues that are

[24] If there is a possibility that the nonuniform loading is due to formation shear rather than simply mobility—for example, loading by seismic events—a more appropriate response is to delay contact between the formation and well tubulars.

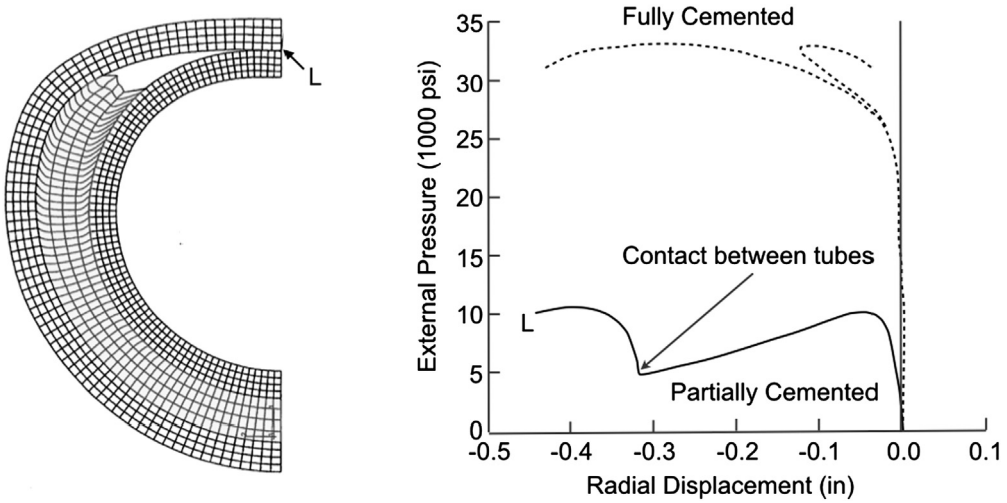

Figure 8.14 ***Examination of the effect of cement channeling on the integrity of a concentric casing configuration [96].*** The left-had diagram is a displaced plot of the concentric configuration after the outer tube ($7.000\,\text{in.}$, $29.0\,\frac{\text{lb}_\text{m}}{\text{ft}}$, N80) has snapped-through and displaced sufficiently to contact the inner tubular ($5.000\,\text{in.}$, $18.0\,\frac{\text{lb}_\text{m}}{\text{ft}}$, Q125). All tubes have 0.1% ovality; the unconfined compressive strength of the cement is $1000\,\text{psi}$. Copyright 1995, Society of Petroleum Engineers Inc. Reproduced with permission of SPE. Further reproduction prohibited without permission.

difficult to approach analytically. As an example, consider Fig. 8.14 which illustrates modeling performed after the early failure of a concentric production casing string due to formation compaction in a long extension of a horizontal well. Following the failure, the designers began to question the potential of achieving complete cement circumferential coverage in a long horizontal section. The figure illustrates the response of a partially (75% coverage with channeling on high side of hole) cemented concentric configuration to uniform external traction (response to a compaction load would be worse).

The finite element mesh used in the analysis is presented in the left-hand diagram, with the cement elements shaded. Due to symmetry, only half the cross-section need be considered. As is common in finite element studies of this nature, the outer casing is seeded with a small ovality (major axes of ellipse are horizontal and vertical) to promote the collapse process (see discussion in Section 8.2.2).

The right-hand diagram in Fig. 8.14 plots radial displacement of the innermost node on the outer casing (point L) in response to the application of external pressure. With increasing external load, the outer tube eventually (radial displacement $\approx 0.3\,\text{in.}$) undergoes snap-through buckling with a rapid increase in radial displacement. This first maximum for the outer tubular occurs at a load approximately 20%

higher than the collapse load of the outer casing alone demonstrating the beneficial effect of the cement and inner casing on even this poorly cemented cross-section. As indicated in Fig. 8.14, the collapsing outer tubular contacts the inner tubular and its radial displacement is temporarily arrested.[25] With the reapplication of external pressure, however, a second maximum is reached only slightly above the first maximum. Beyond this traction both tubes and the enclosed cement are collapsing together. The following comparisons can be made:

- Also shown in Fig. 8.14 is the response of a fully cemented concentric configuration to uniform external pressure. The loss in integrity due to the channeled cement at the top of the horizontal wellbore is apparent.
- Not shown in the figure is the predicted collapse resistance of the 5.000 in. inner string alone, which is on the order of 17 000 psi. The point loading of the 5.000 in. inner tube by the 7.000 in. outer tube is so severe that one would have been better off without the concentric configuration.

With the results of the analysis summarized in Fig. 8.14, the operator abandoned the use of concentric casing for long horizontals, replacing the configuration with a single, thick-walled tube. The problem of well integrity was solved but at the expense of living with shorter horizontals due to torque-drag limitations associated with installing the replacement casing.

8.4. EFFECT OF WEAR ON EXTERNAL PRESSURE RESISTANCE

In the case of internal pressure resistance (see Section 7.4 of Chapter 7), the structural nature of the limit state intuitively ties resistance with wall thickness. As collapse is a stability phenomenon with the cross-section reacting to structural imperfections, the link between limit state and localized wall thickness loss is less obvious, but the direct proportionality between tool joint wear and resistance is the same—a 13% loss of wall thickness implies a 13% loss of resistance to external pressure.

Experimental evidence for the above statement is available from two separate studies. Fig. 8.15 [99] summarizes full scale collapse tests on 9.625 in., 53.5 $\frac{\text{lb}_\text{m}}{\text{ft}}$ L80 casing with 0%, 25% and 50% wear, where in the latter two cases wear grooves simulating tool joint wear were machined along the full length of each sample. The linear relation between percent wall loss and collapse resistance is apparent. Earlier, similar results were obtained by Kuriyama et al. [100] with 5.500 in., 17.0 $\frac{\text{lb}_\text{m}}{\text{ft}}$ N80 samples.

[25] The drop in pressure with increasing radial deformation of the outer casing is due to the software solution employed. This analysis was performed using the ABAQUS general purpose finite element software (Dassault Systèmes Simulia Corp., 1301 Atwood Ave, Suite 101W, Johnston, Rhode Island, USA 02919, https://www.3ds.com). For problems involving solutions beyond a maximum load (such as snap-through buckling) one analysis option in ABAQUS employs a modification of the Riks algorithm [98] which can follow an instability through the buckling load.

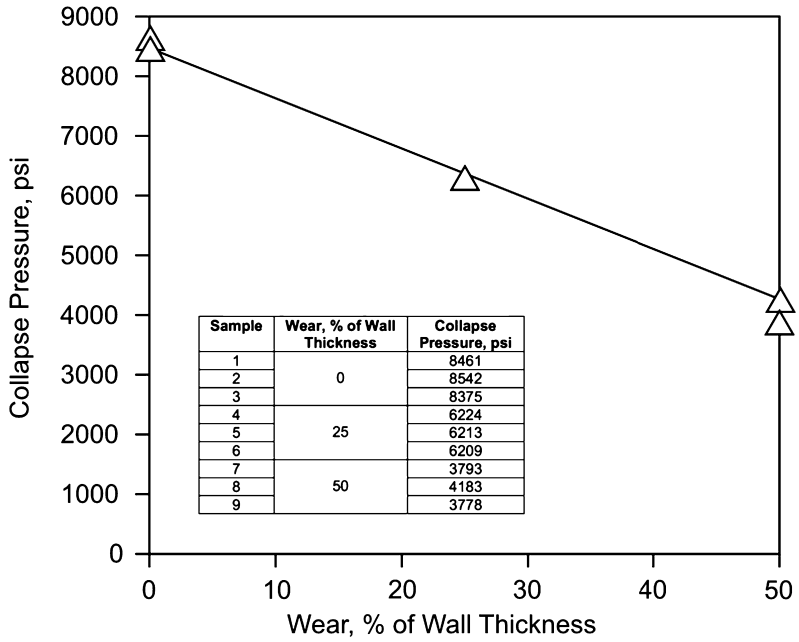

Sample	Wear, % of Wall Thickness	Collapse Pressure, psi
1	0	8461
2		8542
3		8375
4	25	6224
5		6213
6		6209
7	50	3793
8		4183
9		3778

Figure 8.15 ***Effect of groove-type tool joint wear on casing collapse resistance [99].*** Casing is $9.625\,\text{in.}$, $53.5\,\frac{\text{lb}_\text{m}}{\text{ft}}$ L80. Inset table tabulates experimental results. Copyright 2004, Society of Petroleum Engineers Inc. Reproduced with permission of SPE. Further reproduction prohibited without permission.

Using the minimum wall thickness under the wear groove as the t parameter in the API calculation procedure (Section 8.2.4) is not recommended for the case of groove-type wear. Such a procedure might be appropriate for uniform wear due to, for example, milling or severe corrosion, but in the case of tool joint wear yields overly conservative results.

CHAPTER 9

Connections

9.1. INTRODUCTION

The most complex component of a tubular joint is the threaded connection[1] used to attached adjacent tubes [102]. The intricacies of the thread profile and sealing method usually render any detailed investigation a candidate for numerical analysis [103–108]. Even with modern finite element techniques, the response of a connection to qualification testing in a laboratory is not always as anticipated.

The perfect or ideal [101] connection arguably does not exist. Such a connection would have the same cross-sectional dimensional limitations as the tube body, while being equivalent to the tube body in both axial force and pressure integrity, a condition that might be achieved by welding two tubes together, with the exception of possible post-weld metallurgical issues at the juncture. As will become clear below, the connection selection process usually involves a compromise between competing issues, including cost.

In the sections to follow, the individual aspects of connection behavior are addressed separately. Beginning with axial strength integrity, we investigate the behavior of the threaded region under load. Various failure mechanisms characteristic of API and non-API or proprietary thread designs are considered, along with a companion review of the development of thread profiles.

Structural considerations are followed by the all-important performance aspect of leak integrity. The so-called thread lubricant seal used by most of the API family of connections is discussed, along with more sophisticated alternatives such as seal rings and metal-to-metal seals. A clear distinction is established between the latter and a torque shoulder.

A closing discussion of performance deals with additional aspects of connection design such as internal flow profile and assembly. The chapter ends with a discussion of connection qualification as performed in the industry-standard test protocol(s).

[1] In this chapter we deal almost exclusively with connections where at least the pin member is machined directly onto the tube body. For large diameter tubes, weld-on connections are often used. Such connections, although suitable for the tubulars to which they are attached, are outside the scope of this discussion. One author [101] distinguishes these products as "connectors for pipe, not pipe connections" so as to isolate them from the type of connections to which we limit ourselves here.

Elements of Oil and Gas Well Tubular Design
DOI: 10.1016/B978-0-12-811769-9.00009-8

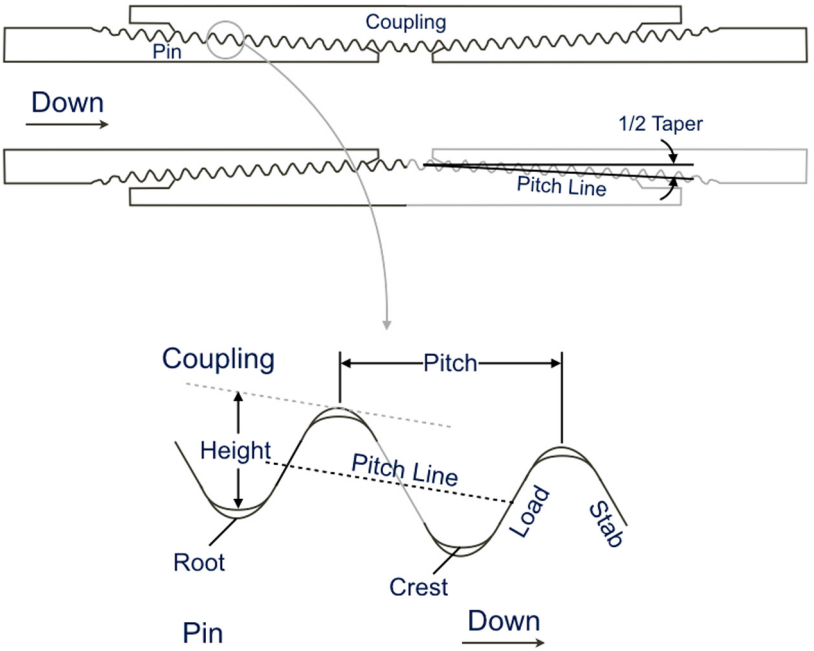

Figure 9.1 ***Drawing of an API long thread and coupling casing connection illustrating key thread elements.*** The root shown is for a pin thread; the crest shown is for a coupling/box thread. The taper is exaggerated. A torque shoulder and metal-to-metal seal are not shown in the figure—see Fig. 9.3 for these features.

9.2. ELEMENTS OF THREAD DESIGN

To facilitate the discussion to follow, Fig. 9.1 presents an API long thread connections consisting of a pin—the portion of the thread machined on the tube body—and coupling—the portion of the connection into which the pin is screwed. If the coupling is separate from the pipe body, a connection is termed "threaded and coupled" (T&C)—see Sections 9.3.1 and 9.3.2. If the coupling is formed as part of the tube body, a connection is termed integral—see Sections 9.3.3, 9.3.4 and 9.3.6—and the "coupling" is termed the "box."

The threaded region as shown in the expanded portion of Fig. 9.1 consists of a number of defined and toleranced [109] elements:

- The crest of a single pin thread is the point, arc or surface on the thread form having the greatest radial value; the root of a single pin thread is the point, arc or surface having the least radial value. The crest of a single coupling/box thread is the point, arc or surface on the thread form having the least radial value; the root of a single coupling/box thread is the point, arc or surface having the greatest radial value.

- Pitch is the axial distance from the crest of one thread to its neighbor. Common units are length (i.e., the thread pitch is 0.125 in.) or number of threads per a specified length (i.e., 8 threads per inch (TPI)).
- Lead is the axial distance the thread travels in one complete rotation of the pin relative to the coupling/box. Usually lead and pitch are equal, but thread designs do exist where two separate spirals traverse the thread form. In this case the lead is twice the pitch.
- Pitch diameter is the local diameter of the pitch line, a cone concentric with the thread axis where the width of the thread groove (metal removed during machining) and the thread body (metal remaining after machining) are equal.
- Taper is the rate of increase of pitch diameter with axial position and is usually measured as either inches (increase in pitch line diameter) per foot (of axial distance) or inches per inch.
- The load flank of a thread is that flank most highly loaded when the connection is in tension. The stab flank of a thread is that flank which will normally make first contact on assembly when the pin is inserted in the coupling or box.
- Height is the radial distance, taking due account of the taper (see Fig. 9.1), between the root and crest of a thread.

9.3. TYPES OF THREADED CONNECTIONS

Depending on the application, threaded connections possess specific features. In most instances, the transparency of an ideal connection is compromised in either strength or geometry [101,110].

9.3.1 API casing connections and NUE tubing

In contrast to the proprietary threaded and coupled (T&C) connection of Section 9.3.2, the API entries for casing[2]—short round thread,[3] long round thread[4] and buttress[5] casing, and NUE[6] tubing—have neither a metal-to-metal seal[7] nor a torque shoulder.

[2] Traditionally API has recognized a close relation between size and function, with the crossover occurring at 4.500 in. Sizes greater than or equal to 4.500 in. are termed casing; sizes less than or equal to 4.500 in. are termed tubing. Particularly for connections, this distinction was strong enough to prompt one connection manufacturer to offer separate casing and tubing connections for 4.500 in. diameter tubes. With the advent of high volume wells wherein the production tubing may be 7.000 in. or larger this distinction has diminished. Remnants of the casing–tubing terminology do still exist, however, a prime example being the API segregation of threaded connections.

[3] Commonly denoted STC signifying "short thread and coupling."

[4] Commonly denoted LTC signifying "long thread and coupling."

[5] Commonly denoted BTC signifying "buttress thread and coupling."

[6] NUE signifies "nonupset end."

[7] The flank-to-flank thread contact in the threaded region is usually not designated a metal-to-metal seal.

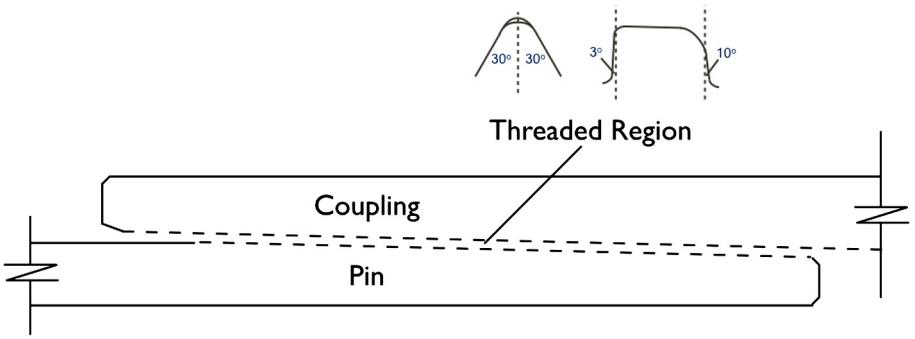

Figure 9.2 ***Drawing of generic threaded and coupled (T&C) API casing connection.*** The threaded region is indicated with phantom dashed lines, with typical thread forms illustrated in profile.

There still exist, however, a number of low pressure applications suitable for API connections. The majority of casing and tubing connections run worldwide are API. API Specification 5B [109] details the tapers, thread forms and dimensions of the API offerings. API Technical Report 5C3 [51] contains the formulas used to calculate axial joint strength.

Fig. 9.2 illustrates a generic sample of such a connection. Variations on the connection shown in the figure include the following:

- The thread lubricant seal[8] may be supplemented by a resilient seal ring installed in a groove machined in the coupling.
- At least one vendor offers a variation on the API T&C round thread design with an insert placed between the two pin ends.[9] This insert can serve as a torque shoulder to prevent excess turns when assembling the connection.
- The buttress threaded version of the API T&C connection can, in some cases, be ordered with the next higher grade coupling attached, which in some cases increases the joint strength of the product.[10] Care should be exercised when using this option, particularly if the intended well environment contains hydrogen sulfide.
- A special-clearance version of the buttress connection is manufactured by machining the outside diameter of the coupling.

[8] See Section 9.5.1.1 for a discussion of the suitability of classifying thread lubricant as a seal.

[9] The area between the two pin ends on an API round thread connection is termed the "J" area, as this is the letter assigned to this axial region in API Specification 5B [109].

[10] The addition of increasing wall thicknesses to API tube bodies historically led to API connections for greater tube wall thicknesses being strength-limited by the geometry of the coupling. Higher grade coupling availability was introduced as an alternative to designing new coupling geometries for these products.

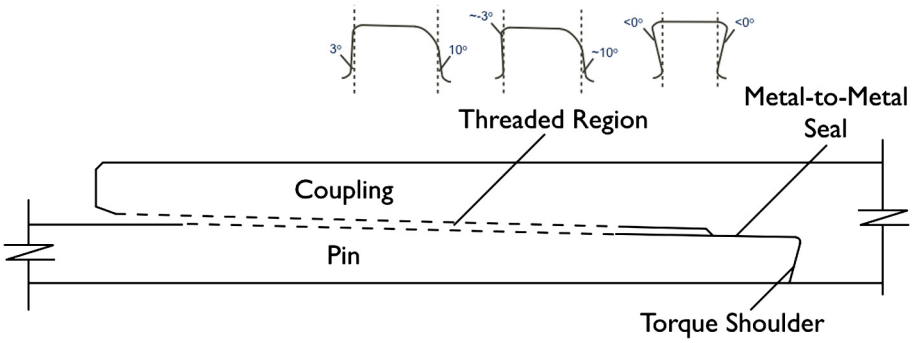

Figure 9.3 ***Drawing of generic threaded and coupled (T&C) casing and/or tubing connection.*** The threaded region is indicated with phantom dashed lines, with typical thread forms illustrated in profile. Not all offerings have the torque shoulder.

9.3.2 Threaded and coupled (T&C) connections

Threaded and coupled connections usually meet or surpass the axial tension, internal pressure and external pressure performance properties of the tube body. In some instances, even the tube's axial compression performance can be matched. To reliably provide pressure integrity, the connection typically employs a metal-to-metal seal and/or a resilient seal ring. The thread form usually has a negative load flank and, in some instances, a negative stab flank. A torque shoulder is employed to limit assembly stresses.

Fig. 9.3 illustrates a generic sample of such a connection. Variations on the connection shown in the figure include the following:

- Some proprietary versions of this connection also have an external metal-to-metal seal.
- The metal-to-metal seal may be supplemented by a resilient seal ring installed in a groove machined in the coupling.
- More than one vendor offers a T&C connection with no metal-to-metal seal, but with shoulders on both pin members which contact on assembly, forming a torque shoulder which could be conceived to act as a metal-to-metal seal. Rating a torque shoulder as a metal-to-metal seal is not recommended by this author.
- A special-clearance version of this connection is manufactured by machining the outside diameter of the coupling.

9.3.3 Nonflush integral clearance connections

Nonflush integral[11] connections are machined on tubes which have been cold formed—expansion of the box, swaging of the pin—followed by stress relief via heat treatment.

[11] The term "integral" indicates the coupling has been integrated into the tube body. One advantage of this strategy is the removal of half the pin-to-coupling matings, theoretically reducing the possibility of a connection leak.

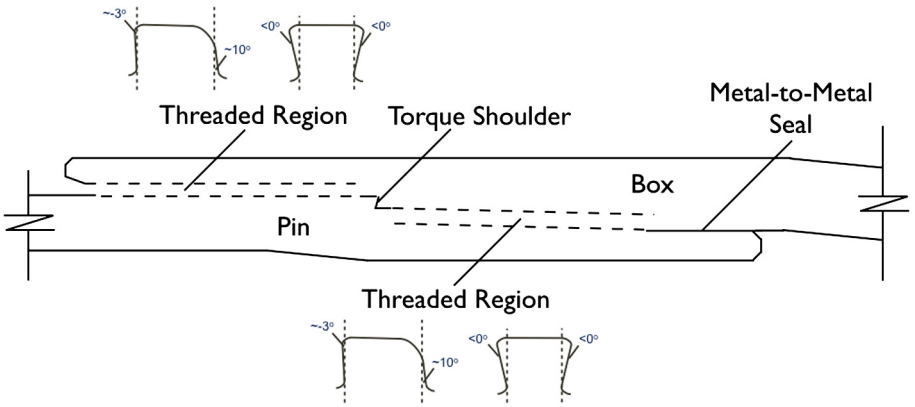

Figure 9.4 ***Drawing of generic integral casing connection.*** The threaded region is indicated with phantom dashed lines, with typical thread forms illustrated in profile. Not all offerings have the intermediate torque shoulder.

These connections usually meet or surpass the internal pressure and external pressure performance properties of the tube body. The axial tension joint efficiency of this family falls in the range of 70–75%. The compression joint efficiency of this family is normally low, on the order of 30–50% of the tube body, often due to the small torque shoulder area.[12] To reliably provide pressure integrity, the connection typically employs a metal-to-metal seal. The thread form usually has a negative load flank and, in some instances, a negative stab flank. The torque shoulder serves to limit assembly stresses.

Fig. 9.4 illustrates a generic sample of such a connection. Variations on the connection shown in the figure include the following:

- Some proprietary versions of this connection also have an external metal-to-metal seal.
- Versions of this connection type, particularly when aimed at application as a drilling liner, may be obtained without the metal-to-metal seal.

9.3.4 Flush integral clearance connections

Flush integral[13] connections usually meet or surpass the internal pressure and, perhaps, external pressure performance properties of the tube body. The axial tension joint efficiency of this family falls in the range of 60–65%. The compression joint efficiency of this family is low, on the order of 30–50% of the tube body, often due to the small

[12] Non-flush integral clearance connections that do not have the intermediate torque shoulder, but do have a negative stab flank thread form, may have a compression joint efficiency that exceeds the tensile efficiency.

[13] The term "flush" indicates the connection—both pin and box—has been machined directly into the tube body. The pin end may be cold formed.

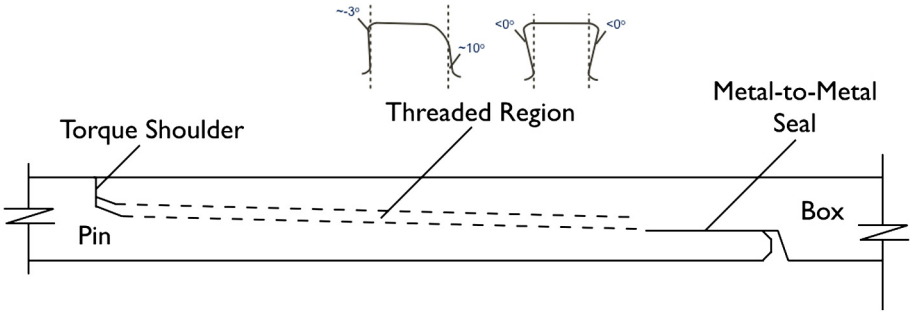

Figure 9.5 ***Drawing of generic flush casing connection.*** The threaded region is indicated with phantom dashed lines, with typical thread forms illustrated in profile. Not all offerings have the torque shoulder.

torque shoulder area.[14] To reliably provide pressure integrity, the connection typically employs a metal-to-metal seal. The thread form usually has a negative load flank and, in some instances, a negative stab flank. The torque shoulder serves to limit assembly stresses.

Fig. 9.5 illustrates a generic sample of such a connection. Variations on the connection shown in the figure include the following:

- Some proprietary versions of this connection also have an external metal-to-metal seal.
- Versions of this connection type, particularly when aimed at application as a drilling liner, may be obtained without the metal-to-metal seal.

9.3.5 API upset tubing connections

The pin ends of the API EUE[15] tubing connection are hot upset. API EUE is threaded and coupled, and provides a connection with round thread having a tension joint efficiency of 100%. The upset limits the number of thread recuts.

Fig. 9.6 illustrates a generic sample of such a connection. Variations on the connection shown in the figure include the following:

- The thread lubricant seal[16] may be supplemented by a resilient seal ring installed in a groove machined in the coupling.
- At least one vendor offers a variation on the API T&C round thread design with an insert placed between the two pin ends. This insert can serve as a torque shoulder to prevent excess turns when assembling the connection.

[14] Flush integral clearance connections that do not have the intermediate torque shoulder, but do have a negative stab flank thread form, may have a compression joint efficiency that exceeds the tensile efficiency.

[15] EUE signifies "external upset end."

[16] See Section 9.5.1.1 for a discussion of the suitability of classifying thread lubricant as a seal.

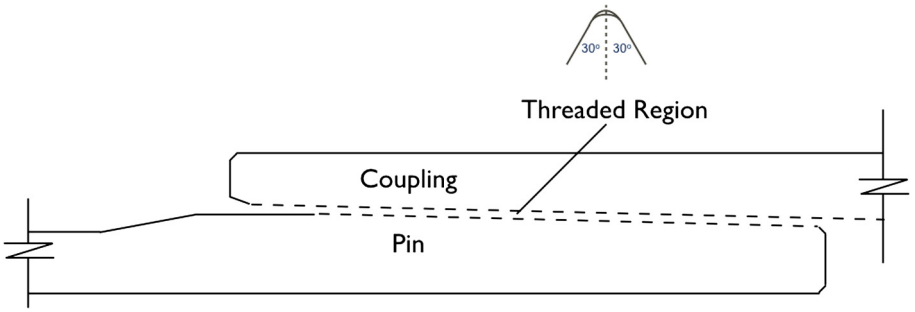

Figure 9.6 ***Drawing of generic API upset tubing connection.*** The threaded region is indicated with phantom dashed lines, with typical thread forms illustrated in profile.

- A special-clearance version of the EUE connection is manufactured by machining the outside diameter of the coupling.

9.3.6 Two-step tubing and work string connections

The two-step integral connection design possesses a threaded region that is not tapered, but rather has constant pitch diameter. Both the pin and box of the connection are upset. Assembly torque is counteracted at the metal-to-metal seal and the torque shoulder, the latter carrying the preponderance. In addition to its use as a tubing connection, this connection family has gained wide use on work strings.

Fig. 9.7 illustrates a generic sample of such a connection. Variations on the connection shown in the figure include the following:

- Particularly if the tubing is coated, the small gap between the end of the pin and the box can be filled with a seal ring.

9.4. AXIAL RESISTANCE

At the outset of the discussion of axial resistance a few definitions are in order. First, the joint strength R_{jt} of a connection is its capacity to withstand axial load and is usually (an important exception being the API family of connections) expressed by the formula

$$R_{jt} = f_x A_{cr}, \tag{9.1}$$

where f_x is the stress level representing the limit state and A_{cr} is the critical cross-sectional area corresponding to the location at which R_{jt} is being measured. The limit state is reached when the stress at the critical cross-sectional area reaches the critical value f_x.

The critical stress level is either the yield stress f_y or the ultimate stress f_u of the connection material. A proprietary connection manufacturer's internet and hardcopy content may report R_{jt} based on one or both of these stress values. Either value is

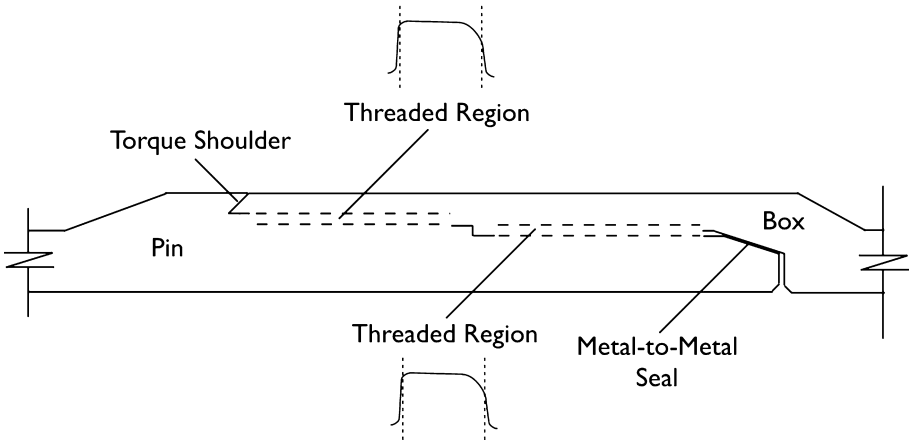

Figure 9.7 ***Drawing of generic two-step tubing and work string connection.*** The threaded region is indicated with phantom dashed lines, with typical thread forms illustrated in profile.

legitimate, provided it is clearly stated. If the ultimate stress is used, its entry may be labeled the "parting load" of the connection.

It is important that the value of f_x used match one's joint strength design factor basis. Most operators base their joint strength design factor on connection yield. If that is the case, then the value of f_x used should be f_y. Use of f_u in this instance will result in a nonconservative design, as the connection is being rated (for yield) with a higher value than appropriate. This warning is particularly important when dealing with API connections. API casing threaded connections have an axial resistance based on ultimate stress, whereas most proprietary connections have an axial resistance based on yield stress. Both API and proprietary tubing connections have an axial resistance usually based on yield stress.

The value of A_{cr}, the cross-sectional area at the location of yield ($f_x = f_y$) or parting ($f_x = f_u$), is determined by the manufacturer as a result of design calculations and experiment. In a well designed connection, failure in pure tension in the laboratory should consistently occur at the axial location corresponding to A_{cr}.

Continuing with introductory definitions, joint efficiency E_{jt} is the ratio of the joint strength to the strength of the tube body R_{ta}, expressed in percent as

$$E_{jt} = \frac{R_{jt}}{R_{ta}} \times 100\% = \frac{f_x A_{cr}}{f_x A_s} \times 100\% = \frac{A_{cr}}{A_s} \times 100\%, \tag{9.2}$$

where A_s is the cross-sectional area of the tube body.

Again, f_x can take the value f_y or f_u in Eq. (9.2), provided it takes the same value in both the numerator and denominator. Thus, for connections whose joint strength can

be written in the form of Eq. (9.1), the calculation of tension joint efficiency reduces to a calculation of areas.

Notable exceptions to the above calculations are the API threaded connections [51]:

- API round thread and buttress threaded connections have fracture strength equations that resemble Eq. (9.1), but A_{cr} is the minimum of a critical section area in the coupling and a critical section area in the pin.
- API round thread also has an additional failure mode normally called jumpout, but termed pullout in the API literature. Again, the limit state equation takes the form of Eq. (9.1), but in this case with a slightly different meaning.

9.4.1 Example problem—joint efficiency

A nonflush integral clearance connection for 7 in., 32 $\frac{\text{lb}_\text{m}}{\text{ft}}$ (0.453 in. wall) T95 casing has a manufacturer-reported critical cross-sectional area of 6.470 in^2. Compute the connection's joint strength and joint efficiency in tension, assuming the manufacturer rates his product on yield strength.

The yield strength of API grade T95 is 95 000 psi. From Eq. (9.1), the joint strength of the connection in tension is

$$R_{jt} = 95\,000\,\text{psi} \times 6.470\,\text{in}^2 = 614\,650\,\text{lb}_\text{f}. \tag{9.3}$$

The cross-sectional area of the tube body is

$$A_s = (\pi/4) \times \left[7.000^2 - (7.000 - 2 \times 0.453)^2\right] = 9.317\,\text{in}^2. \tag{9.4}$$

The joint efficiency of the connection is, from Eq. (9.2),

$$E_{jt} = \frac{6.470\,\text{in}^2}{9.317\,\text{in}^2} \times 100\% = 69.4\%. \tag{9.5}$$

9.4.2 Example problem—yield-based API casing joint strength

API calculates tubing connection joint strength[17] based on minimum yield stress f_{ymn} [51]. API calculates casing connection joint strength[18] based on minimum ultimate stress f_{umn} [51]. Many operators, however, base their design factor for both tubing and casing joint strength in tension assuming the connection rating is based on yield. Provide a reasonable procedure for expressing API casing joint strengths in terms of minimum yield stress.

[17] API tubing connections are NUE (nonupset end), EUE (external upset end) and IJ (integral joint).

[18] The API casing connections considered here are STC and LTC (round thread), BTC (buttress) and XC (extreme-line).

All of the API formulas for casing joint strength [51] are either directly proportional to f_{umn} (i.e., $R_{jt} = f_{umn} \times fcn(\text{Connection geometry})$)[19] or almost so (i.e., $R_{jt} = f_{umn} \times \text{fcn(Connection geometry)} + f_{ymn} \times \text{fcn(Connection geometry)}$).[20] Regardless, a reasonable approximation for yield-based API joint strength can be obtained by multiplying the API published rating [51] by the ratio of f_{ymn} to f_{umn}, that is,

$$R_{jt-yield} = R_{jt-API}\frac{f_{ymn}}{f_{umn}}. \tag{9.6}$$

For example, the f_{umn}-based API joint strength of 9.625 in., 40.0 $\frac{\text{lb}_\text{m}}{\text{ft}}$ K55 ($f_{ymn} = 55\,000$ psi, $f_{umn} = 95\,000$ psi, see Table 6.1) LTC casing is 561 000 lb_f. To compute an f_{ymn}-based yield strength using the approximate method presented in Eq. (9.6),

$$R_{jt-yield} = 561\,000\,\text{lb}_\text{f}\frac{55\,000\,\text{psi}}{95\,000\,\text{psi}} = 324\,800\,\text{lb}_\text{f}. \tag{9.7}$$

The reduction taken by K55 connections is large due to the difference between the minimum yield and ultimate stresses for this grade.

9.4.3 Tension resistance

Of obvious concern in the selection of a threaded connection is its performance under tension and compression, fully appreciating the possibility of bending. First, consider axial load in the absence of bending. Fig. 9.8 depicts a connection in a vertical wellbore under tension. Moving vertically upward from the bottom of the connection, examination of its geometry relative to the load suggests that, although at the base of the pin all of the axial load is carried by the pin, by the time one reaches the longitudinal center of the coupling all of the axial load will be supported by the central coupling cross sections. The load transfer from pin to coupling occurs in the threaded region. This transfer is complex, especially in the presence of other loads such as pressure and bending, but can sufficiently be described for the purposes of this discussion as linear. That is, once one has traversed upwards two-thirds of the way through the threaded region (and recognizing the approximate nature of the linear model), the pin will have shed two-thirds of the axial load which has been transferred to the coupling.[21]

The critical section area for the pin in a geometry like, or similar to, that of Fig. 9.8 is usually at the base of the pin, as it is here that the pin is most highly loaded. This is

[19] Applicable to the formulas for round thread coupling and pipe thread fracture strength, buttress coupling thread strength and extreme-line joint strength.

[20] Applicable to the formulas for round thread jumpout and buttress pipe thread strength.

[21] Why is the critical section area of the pin not located at the end of the pin where, due to the taper, its cross-section is smallest? Because by the time the end of the pin is reached all of the axial load will have been transferred to the coupling.

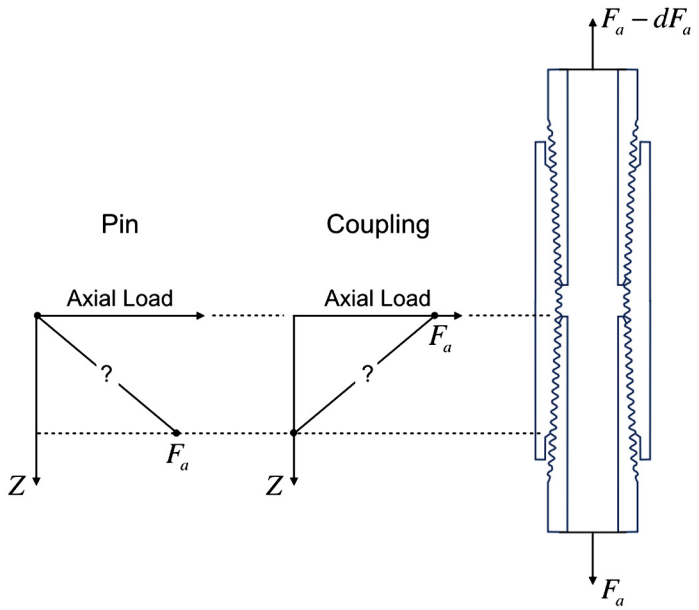

Figure 9.8 ***Axial load transfer in a threaded connection.*** Although the API round thread is depicted, the principle is similar for all casing and tubing connections. The question marks indicate that the load transfer, although assumed linear in the discussion of this figure, is often complex.

particularly true of the API round thread depicted in the figure. As a round thread pin is cut, the majority of the threaded region has a taper of 0.0625 $\frac{\text{in}}{\text{in}}$ on the diameter [109]. As the cutting tool reaches the base of the pin, however, this taper abruptly increases as the tool is extracted from the threading operation. This region of so-called incomplete threads cannot be used in the load transfer as these threads are not engaged with the coupling. As indicated in the figure, at the start of load transfer the cross-sectional area of the pin is less than that of the tube body. Since both the first thread involved in the load transfer and the tube body are exposed to the same axial force, the stress in the pin must be higher than that of the tube body. In a pure tension environment the pin threaded region will be more likely to fail than the tube body—the tension joint efficiency of the API round thread is therefore less than 100 percent.

One solution to this shortcoming in the API round thread is to machine the pin thread on an upset (see Section 9.3.5), with the diameter of the pin at the starting point of load transfer at least equal to that of the tube body. This design increases the tension joint efficiency of the API round thread connection to 100%, but not without complications:

- The upsetting process itself adds cost to the connection manufacture;
- Once upset, the tube end must be heat treated to reduce residual stresses introduced by the upsetting process;

- The number of recuts before the tube must be reupset is limited.

Nevertheless, upsetting is a recognized solution to the penalty in tension joint efficiency associated with the API round thread design.

The API buttress thread, along with a number of proprietary threads, does not have the manufacturing taper change described above for API round thread. The machining tool is simply constrained to the same taper until there is no more tube body to machine.[22] One might expect 100% tension joint efficiency from this process, and such is almost, but not quite achieved. The offset in axial force due to the mean radii in the pin and coupling induces a moment which separates the first few imperfect threads at the base of the connection, rendering the buttress connection slightly more stressed than the tube body.

9.4.3.1 Excursion: jumpout

In addition to the dominant over-stressed limit state described by Eq. (9.1), API round thread can succumb to a second failure mode termed jumpout.[23] The origin of jumpout is displayed in Figs. 9.9 and 9.10. Following the discussion of Clinedinst [111], the left-hand diagram in Fig. 9.9 focuses on one of the threads of a round thread connection. Following assembly the load and stab flanks of the thread are exposed to approximately equal contact tractions.[24] As indicated in the right-had diagram of the figure, when the connection is lowered into the well and subjected to tension under service, the contact traction on the stab flank will be transferred to the load flank. Eventually, an external axial force can be reached that results in the load flanks of the thread supporting all the tension.

Fig. 9.10 continues the discussion by further detailing the load flank of a single thread once all the axial tension has been transferred to that flank of the thread profile. Assume for simplicity that contact between the pin and coupling load flanks is frictionless.[25] Then the contact traction vector will be perpendicular to the surface of the thread flank. We may therefore decompose the vector into components along the axis and radius of the tube on which the round thread has been cut. The axial component of the traction is that portion of the contact supporting the axial load. The radial component, on the other hand, is acting so as to separate the pin from the coupling. With increasing axial load, eventually the pin will yield and, due to the inelastic counterpart to Poisson's ratio, begin to radially shrink away from the coupling. Once this radial displacement has

[22] As a consequence of this machining process one creates so-called black-crested threads—i.e., those threads for which there is insufficient tube material left to achieve full design thread height, thus leaving evidence of the tube outside diameter on the crest of the thread.

[23] An alternate name also used by the API is pullout.

[24] The loading will not be precisely equal because of the thread taper.

[25] The discussion will be altered slightly, but not conceptually changed, if one includes friction.

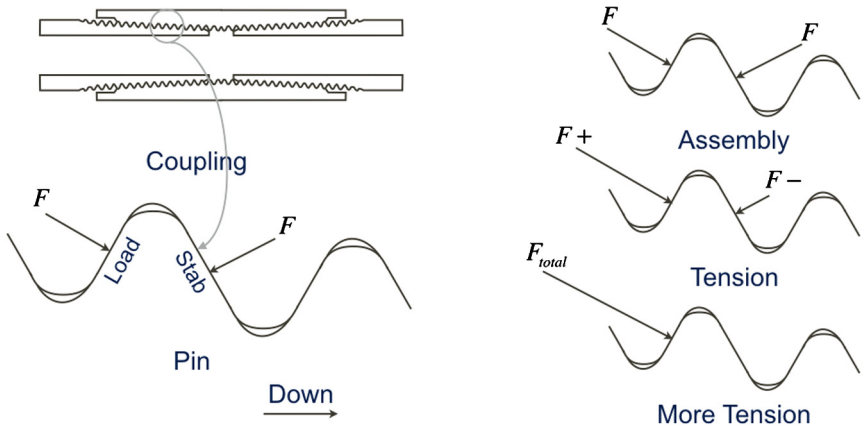

Figure 9.9 ***The origin of jumpout.*** Increasing tension transfers more of the thread flank contact traction to the load flank.

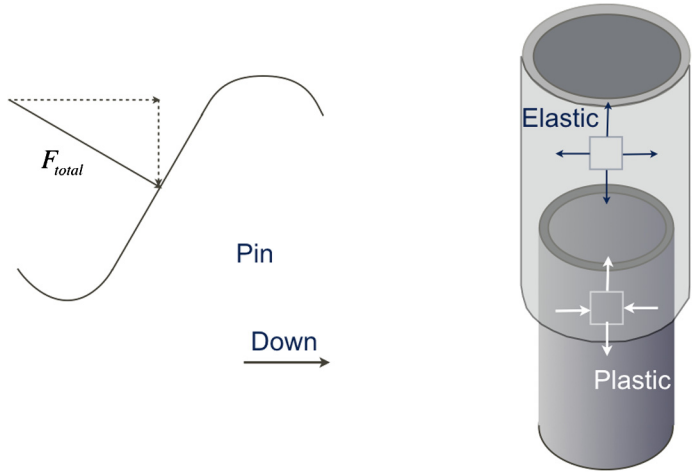

Figure 9.10 ***The mechanism of jumpout.*** The respective stress states promote earlier yield in the pin than the coupling.

reached a value equal to the thread height, the pin will separate from the coupling in the phenomenon of jumpout.

Given the amount of deformation preceding jumpout, the threads themselves are relatively undamaged. The notable feature of a jumpout failure is the gross radial displacement the pin experiences as it undergoes massive inelastic deformation in the radial (actually circumferential) direction.

9.4.3.2 Example problem—pin-first yielding

Fig. 9.10 depicts the stress states in the pin (plastic) and coupling (elastic) during jumpout, which provides an explanation for why the pin member undergoes the preponderance of deformation during this failure mode.

Due to assembly and the taper of the thread profile, the pin member of an API round thread connection will, as indicated by the traction arrows on the small pin element in Fig. 9.10, be in hoop compression. Correspondingly, the coupling will be in hoop tension. Due to the tensile axial load, both the pin and coupling will, as also indicated in the figure, be exposed to axial tension. The radial stress will be enough smaller than either axial or hoop stress that we can consider it zero in this discussion.

Recalling the discussion of yield in Section 6.3.1 of Chapter 6, closeness to yield for a crystalline metal increases with shear. Comparing the stress states in Fig. 9.10, both the axial and hoop stress in the coupling are positive when the connection is loaded in tension, whereas the axial and hoop stresses in the pin have opposite signs. The tendency to yield will be greater in the pin than the coupling, leading to the pin's dominant role in jumpout.

9.4.3.3 Alternate thread profiles

Compare the left-hand diagram in Fig. 9.10 with the upper-left diagram in Fig. 9.11. Both the load and stab flanks in an API round thread have an angle with the tube radius of 30°, this angle being the source of the radial component of the contact traction vector. Reducing this component's influence will reduce the possibility of thread jumpout. In this regard, notice (Fig. 9.10) that as the angle of the load flank is decreased, the magnitude of the radial component of the contact traction vector also decreases. Comparing the API round thread profile with that of, for example, API buttress (see lower-left diagram in Fig. 9.11) that has a load flank angle of 3°, the latter should and does render the buttress thread less susceptible to jumpout.

Experimental data collected during the establishment of the API formulas for joint strength [111], however, indicate that for larger diameter-to-thickness ratios even API buttress can fail in tension due to jumpout. In fact, failure of a number of clearance casing connections possessing load flanks similar to buttress led to a joint industry project to verify connection performance experimentally [112]. Subsequent to these experiences, the introduction of the hook thread (see upper-right diagram in Fig. 9.11) virtually eliminated jumpout in oil well tubulars. The hook thread has a negative load flank angle which reverses the behavior of the radial component of the contact traction vector. With a hook thread, the radial component actually serves to increase the intimacy of contact within the threaded region.

If there is a disadvantage to the hook thread, it lies in its ability to withstand compressive loads—the stab flank of a hook thread is has a positive flank angle. For this reason, most designs incorporating a hook thread profile also include an opposing contact angle

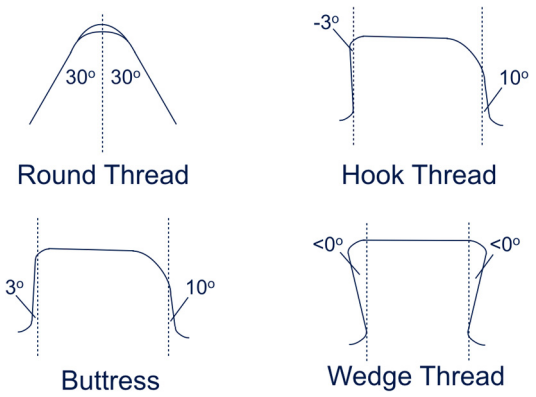

Figure 9.11 ***Alternate thread profiles.*** Flank angels on hook and wedge thread are typical and may vary with an individual manufacturer.

at the torque shoulder to withstand compression (see Fig. 9.3). An alternative to assigning compression resistance to the torque shoulder is the dovetail or wedge thread design, which accommodates negative flank angles on both the load and stab flanks. This design is particularly amenable to bending applications and has been used in the design of a high torque tool joint [113]. The potential of both the hook and dovetail/wedge thread forms to eliminate jumpout as a failure mode comes at the cost of increased machining and inspection complexity.

9.4.4 Compression resistance

The axial compression resistance of a threaded connection is not always related to its structural capacity when loaded with a negative axial force. In fact, the structural resistance of a connection to compression may exceed its structural resistance to tension. The often lower compression joint efficiency of a threaded connection can usually be traced to a separate limit state, for example, yielding of an internal (torque) shoulder that in itself is bad, but may also affect the pin-to-coupling relative positioning of a metal-to-metal seal.

9.5. INTERNAL PRESSURE RESISTANCE

Most proprietary threaded connections are rated equal to the tube body in internal pressure resistance. Many API connections are also rated at least as strong as the tube body when exposed to internal pressure. There do exist, however, API connections wherein the structural internal pressure resistance of the connection is less than that of

the tube body.[26] For the API buttress connection it is possible to order a "next higher grade" coupling to once more render the tube body the weaker component of the joint [46,51].

A corollary to a tubular's usefulness as a conduit for fluids is its ability to contain those fluids, separating internal and (possible) external flow streams. This not only requires the threaded connection to maintain structural integrity (i.e., burst resistance) but also includes an expectation of leak resistance. Leak resistance presents a peculiar design issue in that the probability of its occurrence is difficult to predict. Leak resistance depends not only on the design of the connection but also on the assembly procedure at the rig site.

9.5.1 Sealing mechanisms

In the current market environment there exist three mechanisms by which leak resistance is pursued—thread lubricant, seal rings and metal-to-metal seals. Each of these alternatives, which are sometimes incorporated in a single design, will be considered in the sections to follow.

9.5.1.1 Thread lubricant

Fig. 9.12 pictures a portion of an API round thread connection, focusing on the 0.003 in. gap [109] between the root of a pin/coupling thread and the crest on the mating coupling/pin thread. Also shown for orientation is the centerline of the tube on which the thread is cut.

The label 1 in Fig. 9.12 indicates that if one were to follow a pin thread root path around the connection circumference, a spiral path exists connecting the pin roots. Similarly, following the pin crests along the connection's machined spiral reveals a second path connecting the pin crests. These two paths, as they stand, represent two potential leak paths for internal fluids.[27]

The standard means of closing the leak paths illustrated in Fig. 9.12 is thread compound. Using a petroleum soap-constituted grease base, a thread compound carries solids—originally soft metals such as lead, zinc, copper and graphite [114], but now more commonly polytetrafluoroethylene (PTFE) and proprietary blends—intended to both mitigate galling and, somewhere in the spiral potential leak path, block fluid move-

[26] This phenomenon is usually a consequence of history. The API connection, when originally introduced met or exceeded the internal pressure resistance of the tube body. With time, however, additional, increasing wall thicknesses introduced into the API inventory favored the resistance of the tube body, as the coupling dimensions did not change. See also Footnote 10.

[27] Recalling the discussion of Section 9.4.3.1, another possible leak path exists in the API round thread connection. Under sufficient tension, the stab flanks of the round thread can separate providing a third avenue for fluid escape [102]. This path will also close when the tension is removed. Unfortunately, this potential leak path is load-induced and cannot be remedied with thread lubricant.

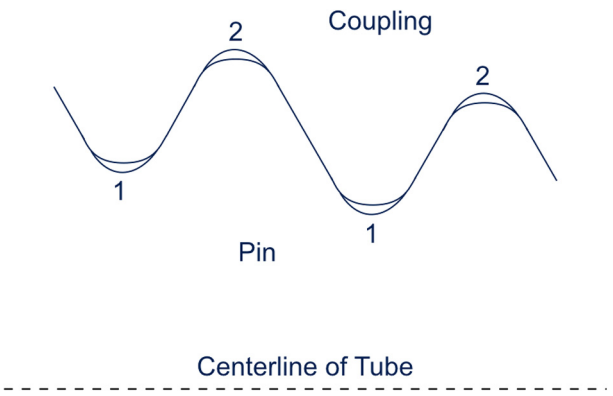

Figure 9.12 ***Dual potential leak paths in an API round thread connection.***

ment. The following comments are in order regarding an interstitial thread lubricant seal:

- If used in production tubing, the hydrocarbon based grease can be leached by chemical reaction with the reservoir fluids;
- Above approximately 275–300 °F (135–150 °C) a *standard* grease base can boil off;
- In the time interval of a relatively short field pressure test, it is not possible to verify that an effective seal in the thread root–crest gaps has been achieved.[28]

The above list suggests alternate sealing methods may be in order if one desires to contain gas for long periods of time. Two common alternate seal strategies are considered in the sections to follow—seal rings and metal-to-metal seals.

9.5.1.2 Seal ring

Among several topics aimed at improving API connection leak resistance reliability, API Supplemental Requirement (SR) 13 to Specification 5CT [46] offers the user an additional sealing mechanism in the form of a PTFE ring (with 25% fiberglass filler) inserted in a groove cut in the coupling member of a connection (see Fig. 9.13).[29]

[28] Consider a 7.000 in. round thread casing connection. The (axial) length of effective threads $L_2 = 3.715$ in., multiplied by the number of threads per inch is $3.715 \times 8 = 29.72$ circumferences [109]. Taking the average pitch diameter to occur at $L_2/2$, this diameter is the pitch diameter $E_1 = 6.903\,37$ in., measured at the hand-tight plane $L_1 = 2.921$ in. from the end of the pin, moved to $L_2/2$. Using the round thread taper of $0.0625\ \frac{\text{in}}{\text{in}}$, the average pitch diameter is $6.903\,37 - (2.921 - 3.615/2) \times 0.0625 = 6.232\,49$ in. Thus the (approximate) total leak path length of 29.72 circumferences of a 7.000 in. API round thread is $\pi \times 6.232\,49 \times 29.72 = 582$ in., or 48.5 foot. Actual detection of a thread lubricant leak can take a long time-24 hours has been observed in the laboratory with a buttress connection whose leak path cross-sectional area can be larger than that of the round thread [115].

[29] Seal rings are also offered as additions to proprietary thread designs.

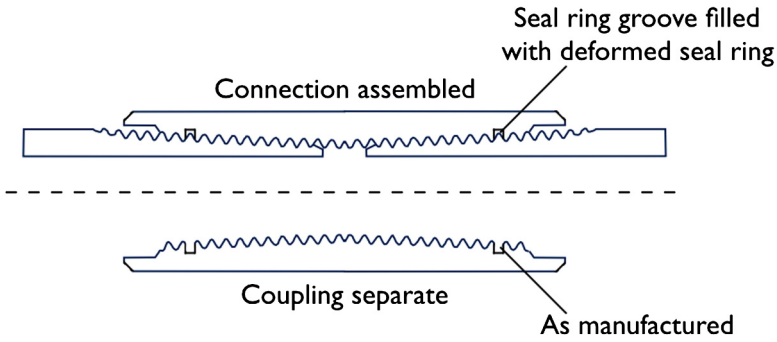

Figure 9.13 ***Seal ring groove shown as machined (lower diagram) and following assembly (upper diagram).*** One or both ends of the coupling may be attached to the pin(s) at the rig site. Prior to assembly a PTFE seal ring is inserted in each groove. Figure is not to scale.

A specific area of concern in designing or implementing a seal ring connection is temperature. The coefficient of thermal expansion of PTFE is approximately ten times that of steel[30]—confinement to a ring groove can therefore cause PTFE to induce internal stresses in a threaded connection. Notwithstanding this behavior, seal rings have been used with success in extreme downhole environments [117].

9.5.1.3 Metal-to-metal seal

The most popular of seals used in high pressure oil well tubular applications are interference-activated metal-to-metal seals. The coupling/box and pin seal surfaces are usually machined at a angle of 5–30° with the axis of the tube, being forced together due to geometry interference as the connection is assembled. Higher angles raise concern for maintenance of design contact pressure under tension; lower angles can increase the possibility of galling, especially during repeated assembly. Additional independent variables considered in the design of a metal-to-metal seal include the following:

- Contact stress distribution [118,119]. Both the maximum value of contact stress and the character of the axial distribution of contact stress influence the ability of the seal to prevent pressure/fluid escape or entry and accommodate leak channels of short length.
- Surface roughness and coatings [118,119]. The inherent roughness of the machined surface of the seal can be altered by surface treatments such as zinc or manganese phosphate coating[31] (usually applied to the coupling).

[30] The coefficient of thermal expansion of unfilled PTFE is approximately $7 \times 10^{-5}\ \frac{1}{°F}$, whereas the coefficient of thermal expansion of steel is approximately $7 \times 10^{-6}\ \frac{1}{°F}$. The former can be slightly reduced by adding filler, with Hilbert and Bergström [116] quoting a reduction of approximately 12% while noting that the coefficient of thermal expansion of PTFE varies significantly with temperature.

[31] In addition to sealability, the coating is also applied to reduce galling potential.

- Thread compound [118,119]. Although thread compound is primarily intended to reduce friction and galling in the threaded region, evidence does exist that thread compound on the seal surface can improve leak resistance, particularly if the size of the solid particles in the thread compound is close to the amplitude of surface roughness of the seal [120].
- Assembly. The act of assembling the connection will cause the pin and box/coupling seal surfaces to interact at high interference-induced contact stresses. Local inelastic deformation of machined peaks on the seal surface has been demonstrated to reduce the contact pressure required to achieve a specified sealability [120,119]. Proper axial alignment of the mating coupling/box and pin seal surfaces is crucial and is usually controlled by the presence of a torque shoulder (cf. Figs. 9.3, 9.4, 9.5 and 9.7).
- Seal geometry [119]. Seal geometry (macroscopic shape, contact length, diameter, interference) affects the contact stress profile—the distribution of contact stress per axial length of seal surface—opposing release of internal fluids.

Fig. 9.14 depicts the behavior of a typical metal-to-metal seal used on a threaded connection. The horizontal axis is internal pressure, that is, the pressure of the fluid to be contained. The vertical axis is some measure of the contact stress profile at the metal-to-metal seal. Depending on the character of the contacting surfaces, the contact pressure distribution will vary—the ordinate in Fig. 9.14 is intended to represent a peak or effective contact stress. The 45° line in the graph is the leak criterion—leak is assumed to occur if the internal pressure exceeds the contact pressure.

When the connection is assembled on the rig floor, the interference between the diameters of the pin and coupling seal surfaces means the two surfaces must be "forced together" as the pin advances into the coupling—a visible change in the slope of the torque-turn graph generated by the power tongs should be noticeable. Once fully assembled, the seal is at point A in the figure.

Assume that once in service, the pressure associated with the contained fluid begins to increase. The horizontal, dashed line originating at point A indicates that internal pressure increase. Notice, however, that the sealing capacity of the metal-to-metal seal is not horizontal. The same increase in internal pressure promoting a leak is also acting on the inside surface of the pin—particularly in the vicinity of the metal-to-metal seal—increasing the contact pressure between the pin and coupling seal surfaces. This is known as self-energization and is a characteristic of many metal-to-metal seals.

The dashed line in the plot attempts to accurately display that the mapping of internal pressure into increased contact pressure is not one-to-one—the slope of the line AB is less than 45°. As the action of the internal pressure must be transmitted through the metal thickness under the pin seal surface, some pressure is necessary to deform the pin at the seal location. The degree of energization lost will depend on, among other factors, the thickness of the pin beneath its seal surface. With each increment of internal pressure, however, a portion of the leaking pressure increment is also transferred to resist

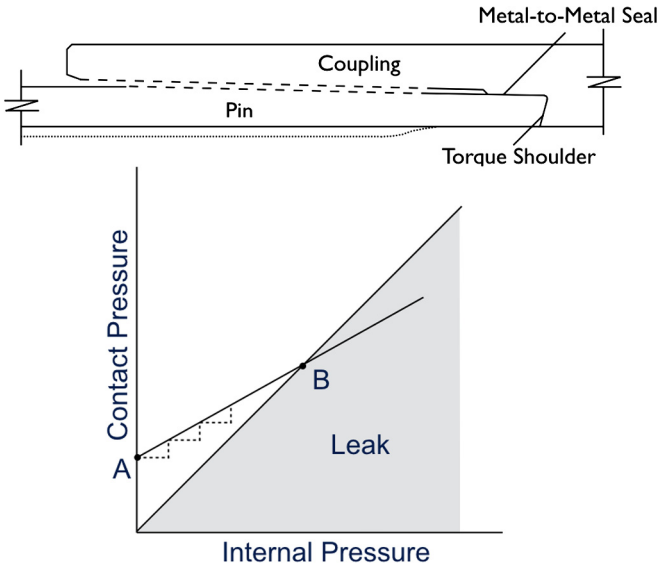

Figure 9.14 ***Behavior of a metal-to-metal seal.*** The location of point A can be controlled by initial seal interference. The slope of the line AB can be controlled by the thickness of the pin at the seal location.

the leak pressure. Eventually, a point is reached (point B in the figure) where the seal contact pressure is less than the internal pressure, and a leak ensues.

Also included in the upper portion of the figure is a diagram of a threaded and coupled connection possessing a metal-to-metal seal. At this point, notice the dotted line indicating a second pin/tube body having greater wall thickness than that used in the previous discussion. Further, assume that through analysis and testing the designer has, with the previous wall thickness, arrived at a pin seal design considered optimum. It may be that the best course of action—from the viewpoint of leak resistance alone—is to machine the pin as indicated by the dotted lines, that is, to use the tube wall thickness near the base of the pin and the optimum seal thickness near the end of the pin. If so, and as we shall see shortly, the design may now be exposed to turbulence under high internal fluid flow rates. Such tradeoffs as this permeate the design of a threaded connection metal-to-metal seal. Less metal under the pin seal surface may promote self-energization, but altering the internal profile of the connection may lead to other issues unrelated to leak integrity.

Similarly, another means of increasing leak resistance would be to raise the value of point A, the initial interference contact pressure. Unfortunately, this solution also may complicate other aspects of the connection design, such as galling during assembly and/or exposing the pin end to a (primarily hoop) stress too close to yield. Threaded connection design is a complex process involving compromise between a number of competing design objectives.

9.6. EXTERNAL PRESSURE RESISTANCE

External pressure resistance is not addressed as frequently in connection design as resistance to internal pressure. There do exist, however, a number of load cases (cf. Section 12.8 of Chapter 12 and Section 15.2 of Chapter 15) in which resistance to external pressure is desirable. The importance of such load cases to the overall string design may suggest the need for a connection possessing an external (usually metal-to-metal) seal.

9.7. ADDITIONAL DESIGN CONSIDERATIONS

Other attributes of casing and tubing connections worthy of consideration in design include the following.

9.7.1 Flush internal profile

For low flow rate wells the actual velocity profile of the internal fluid may be of minor concern. As production rate increases, however, even minor changes in internal profile can induce turbulence in the vicinity of the connection. Such turbulence can promote corrosion or, in the presence of produced solids, erosion to the interior, near-connection region. For production tubing in wells whose production is primarily gas, a reasonable flow rate at which the internal profile should cause concern is 100 mmscfd.

9.7.2 Torsional resistance

The existence of a torque shoulder enhances the structural resistance of a threaded connection in several ways:

- Limiting axial displacement during assembly. Inasmuch as most threaded connections possess a positive thread taper,[32] assembly of the connection induces a positive hoop stress in the box/coupling and a negative hoop stress in the pin. Aside from reducing the box/coupling's resistance to a hydrogen sulfide environment, unchecked axial engagement during assembly can increase the risk of galling. Further, thread profiles possessing gaps on the load and stab thread flanks (as opposed to the thread roots and crests) undergo a Poisson's ratio induced relative axial movement during assembly. This coupling-to-pin relative movement, common to API buttress, casts further doubt on the leak integrity available in the threaded region. Both of these concerns—high induced stresses and interstitial movement during assembly—are either limited or eliminated by the presence of a torque shoulder.
- Pipe rotation. The ability to rotate the tubular string (during cementing, for example) can positively affect the installation and survivability of a tubular. Further, work

[32] Recall thread taper measures the change in thread pitch diameter as one axially traverses the threaded region of the connection.

strings and smaller diameter casing strings have been employed in rotary drilling operations with success.

Both the hook thread in concert with a torque shoulder and especially the wedge thread with its self-contained thread profile torque resistance are suitable in minimizing the adverse effects accompanying torsion.

Notwithstanding its importance in the structural integrity of the connection, with regard to leak integrity a torque shoulder should not be considered a metal-to-metal seal for the following reasons:

- The machined tribological characteristics of a torque shoulder are usually different than those of a metal-to-metal seal;
- Rig-site operations, such as stabbing the pin into the coupling/box during assembly, pose a risk of (leak resistance, not structural) damage to the torque shoulder, whereas a metal-to-metal seal with its more radially-oriented surface normal is less susceptible.

9.8. QUALIFICATION AND TESTING

The industry is currently served by two documents to aid in standardizing the testing threaded connections—"API Recommended Practice on Procedures for Testing Casing and Tubing Connections" [56] and "ISO/PAS 12835:2013, Qualification of Casing Connections for Thermal Wells" [121]. The former serves the majority of tubular connection applications. The latter is particularly applicable to casing used in thermal recovery methods such as Cyclic Steam Stimulation (CSS) and Steam Assisted Gravity Drainage (SAGD) where the connection's service environment may involve loads beyond yield.

9.8.1 Brief summary of API 5C5 testing

Qualification of a threaded connection at the highest application level can be both time consuming and expensive. The knowledge gained, on the other hand, from testing a connection's structural and leak resistance to one's specific operating environment can reduce project economic risk.

In a qualification exercise that follows API 5C5 the following activities are noteworthy:

- The connection sample(s) and performance properties, including a connection evaluation envelope[33] (CEE), are supplied by the manufacturer. The CEE then defines

[33] The test connection evaluation envelope is a closed two-dimensional region when plotted in a space where the abscissa is axial tension (+) and compression (−), and the ordinate is internal (+) or external (−) pressure. A typical connection evaluation envelope will consist of several segments, with possible abrupt corners but is almost always convex.

the extent of a test load envelope[34] (TLE). The manufacturer is under no obligation to participate in the conversion of a CEE into a design envelope that the user may employ in his design calculations.

- The number and dimensional combinations of the test sample(s) depends on the connection application level (CAL) to which the connection design will be qualified. There currently exist four CALs, with CAL IV being the most severe.
- Tests to which the connection sample(s) are subjected include the following, depending on the CAL. In all tests the (pressure, axial force) load points are referenced to the von Mises yield surface of the associated tube body. The underlying plot is identical to that presented in Section 6.3.4.3 of Chapter 6. Brief summaries of the test series are as follows:
  - Series A—the connection sample is tested to various combinations of axial force and internal or external pressure in all four quadrants of the axial force vs. pressure plot.
  - Series B—the connection sample is tested to various combinations of axial force, internal pressure and bending in the upper two quadrants (i.e., no external pressure) of the axial force vs. pressure plot.
  - Series C—the connection sample is tested to various combinations of axial force and internal pressure with thermal cycles in the first quadrant (i.e., no axial compression or external pressure) of the axial force vs. pressure plot.

  The Series A and B tests may be performed at room or elevated temperature. Further, depending on the CAL, the tests may be performed with either liquid or gas as the pressure fluid.

9.8.2 Envelope presentations for connection design

Of importance to the designer is the means by which a qualification test and its resulting performance envelope are compared to operational loads to which the connection will be subjected.

Fig. 9.15, an application of Fig. 6.14, has been adopted[35] in two API documents as the preferred method of presenting the axial force/pressure performance envelope for threaded connections [56] and some tubing accessories [55]. One can, however, also use the other two three-dimensional alternatives presented in Section 6.3.4 of Chapter 6

[34] The test load envelope is derived from a manufacturer-supplied connection evaluation envelope (CEE) and defines the extents to which the connection will actually be tested. The test load envelope is constructed from the CEE by a calculation that scales the CEE values—along both the axial load and pressure axes—by 80–100%, depending on the character of the sample and the conditions of the test. "If the CEE is less than the pipe body reference envelope, it needs to be disclosed by the manufacturer . . . whether the CEE limitation is based on material yield strength or some other factor." [56].

[35] Exception: Fig. 9.15 uses axial stress for the abscissa, whereas the referenced API documents use axial force.

Table 9.1 Evaluation envelope for a generic connection. The sample connection has a yield stress of 110 000 psi. The principles illustrated apply equally well to accessories. All values are in psi

Point	Axial stress	Pressure[a]	Point	Axial stress	Pressure[a]
A	110 000	0	E	−110 000	−10 000
B	110 000	12 228	F	0	−10 000
C	0	12 228	G	51 897	−10 000
D	−110 000	0	H	110 000	0

[a] A positive value incites internal pressure; a negative value indicates external pressure.

Table 9.2 Load points shown in Figs. 9.15–9.17. All values are in psi

Load point	Internal pressure	External pressure
Surface qualification test		
Initial conditions	0	0
Positive test	10 000	0
Negative test	0	10 000
Bottom of string		
Initial conditions	15 000	15 000
Positive test	25 000	15 000
Negative test	5000	15 000

to gain additional insight into connection and accessory behavior, particularly when (a) selecting test points in a qualification exercise and (b) translating a manufacturer's performance envelope from laboratory to downhole conditions. In fact, the latter two presentation alternatives provide more physically acceptable load displays than Fig. 9.15 when downhole conditions are of concern.

It is important to state that calculations of stress and yield state are not at issue in this section. Rather, the discussion centers on presentation, that is, proper representation of the relative positions of the loads with respect to the performance ellipse to which they are being compared. Consider, for example, the crude performance envelope—representing no particular tubular connection—whose defining points are summarized in Table 9.1.

Now review Figs. 9.15–9.17. Each figure is a duplicate of its counterpart in Figs. 6.14, 6.13 and 6.11, respectively, with two additions. First, the connection evaluation envelope values of Table 9.1 have been added to each figure. Secondly, three sample load points—initial conditions, positive pressure test, negative pressure test—have also been added to the figures. The load points are summarized in Table 9.2 with the symbol × denoting a surface qualification experiment and the symbol ∘ denoting an anticipated downhole load condition, where the downhole position is the bottom of the tubular string.

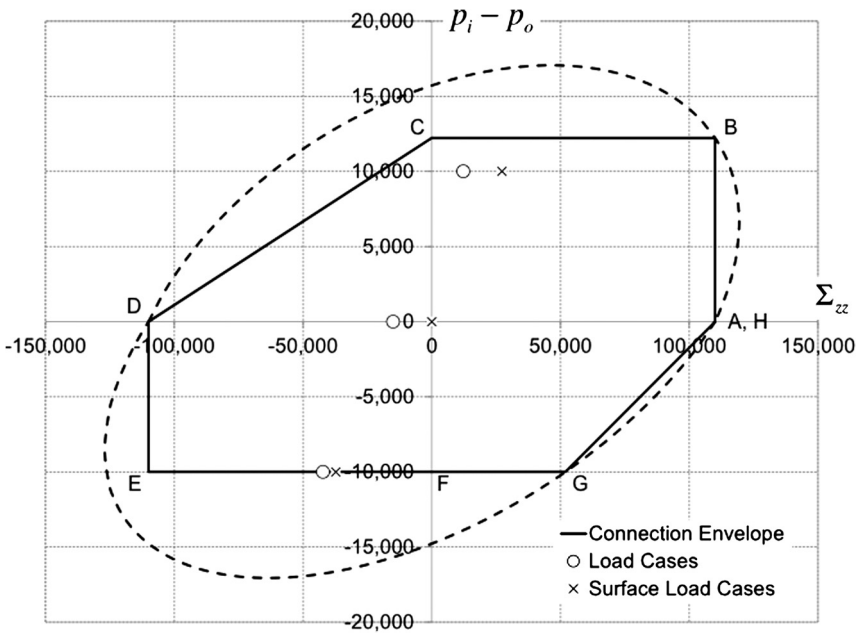

Figure 9.15 ***Connection evaluation envelope plotted with the von Mises yield criterion expressed in terms of*** S_{ZZ}**.** The tube body ellipse is shown as a dashed curve and follows Fig. 6.14. Vertices of the envelope labeled A–H correspond to the points in Table 9.1.

Fig. 9.15, with the exception of using axial stress rather than axial force for the abscissa, is the API RP 5C5 [56] space in which connection evaluation tests are designed and performed.[36]

There are no issues with the evaluation envelope as prepared for a laboratory environment. The "initial condition" for a laboratory experiment is one of no loading and therefore plots at the origin of Fig. 9.15. The problem arises when comparing the laboratory test points to the sample downhole load points. Although the differential pressures—initial conditions = 0 psi, positive test = 10 000 psi, negative test = −10 000 psi—are correct, the use of axial force as the abscissa displaces the load points to the left. For example, the initial conditions are no longer at the origin of the coordinate axes. The performance ellipse and the downhole conditions to which it is being compared are not reflecting the same load state.

Fig. 9.15 is accurately reflecting the variables it was asked to plot—there is nothing wrong with the underlying calculations. Likewise, the evaluation envelope accurately depicts the loads to which the connection was or will be tested. The issue is that the two presentations involve loads that differ by 15 000 psi hydrostatic pressure. Inasmuch

[36] These axes are also employed in the API Spec 11D1 [55] presentation of an accessory envelope. Some embodiments of this presentation may rotate the figure 90° counterclockwise.

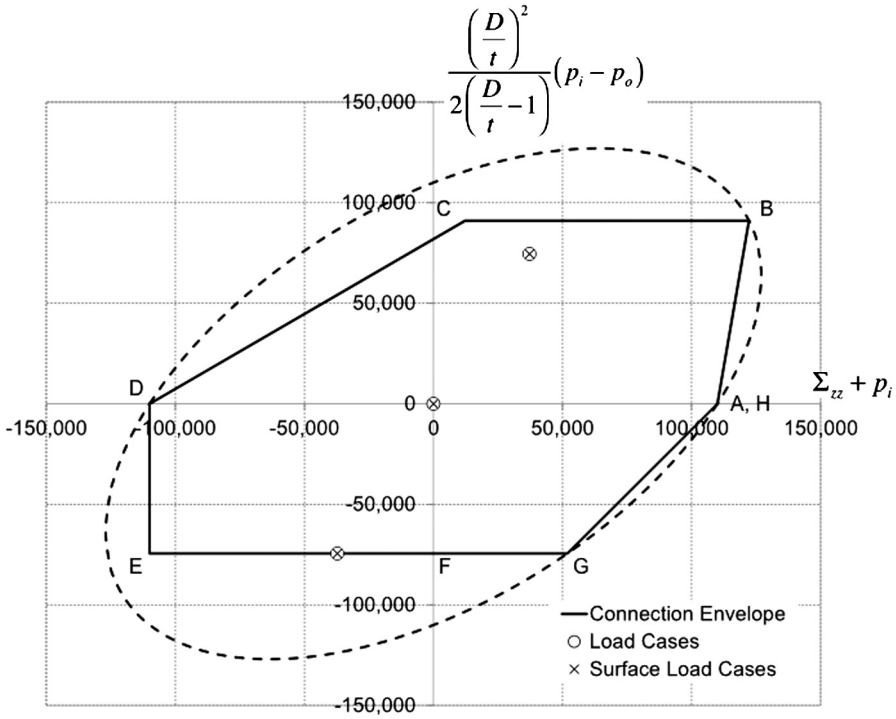

Figure 9.16 ***Connection evaluation envelope plotted with the von Mises yield criterion expressed in terms of*** $S_{ZZ} + p_i$**.** The tube body ellipse is shown as a dashed curve and follows Fig. 6.13. Vertices of the envelope labeled A–H correspond to the points in Table 9.1.

as (a) the emphasis of the plot is material yield and (b) material yield is independent of hydrostatic pressure, the two load states should be compatible. The fact that they are not can, as discussed in Section 6.3.4.3 of Chapter 6, be traced to the fact that the axes of Figs. 6.14 and 9.15 do not admit a complete picture of three-dimensional yield.

In contrast to Fig. 9.15, Figs. 9.16 and 9.17 accurately portray the relation between the laboratory test of the connection in a surface experiment and the loads to which the connector will be subjected in the downhole environment. The initial condition for the downhole environment is not offset from the surface initial condition, indicating both are benign points with respect to material yield.

Given D, t and f_y, the condition of a tubular at surface conditions (initial $p = 0$ everywhere) and downhole conditions at the string bottom (initial p is the hydrostatic pressure of the surrounding fluid column) will, from the perspective of yield, be the same. This statement relies on the assumption that yield of a crystalline metal is independent of the mean stress, which in this case is the local hydrostatic pressure. Provided a tube at the two locations—surface and downhole—is subjected to the same increments of pressure (above or below hydrostatic) the equivalence vis-á-vis yield will remain.

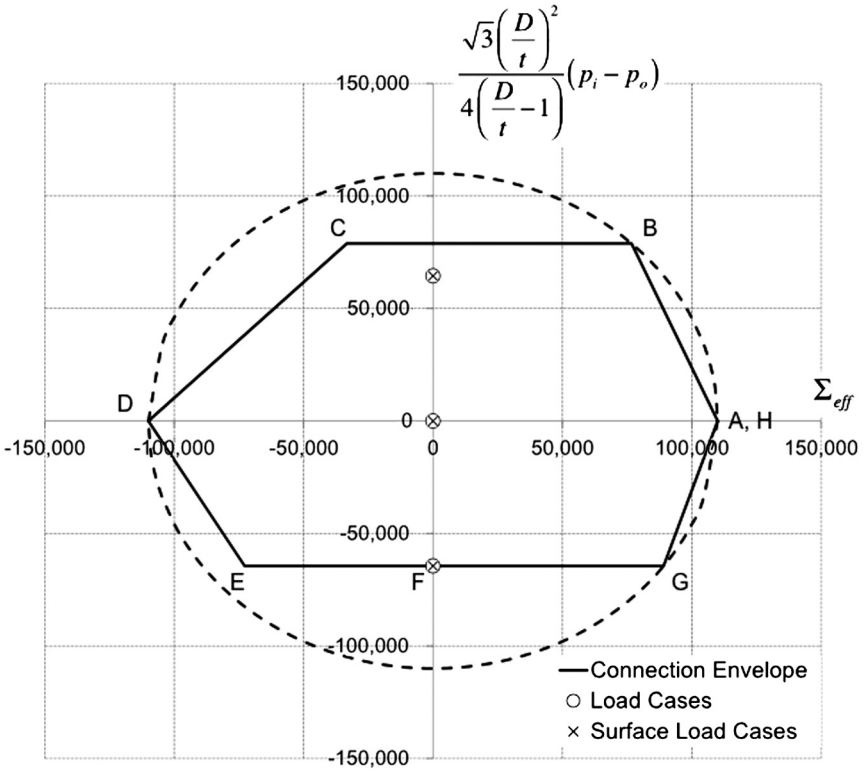

Figure 9.17 ***Connection evaluation envelope plotted with the von Mises yield criterion expressed in terms of effective stress.*** The tube body ellipse is shown as a dashed curve and follows Fig. 6.11. Vertices of the envelope labeled A–H correspond to the points in Table 9.1.

Two final, qualifying comments are in order:

- For a connector the equivalence in stress state (i.e., hydrostatic) to that of the tube body is close, but not exact. Stresses associated with assembly in the threaded region, particularly if the thread profile is tapered, will distort the stress state applicable to a simple tube. The presentations of Figs. 9.16 and 9.17 are still preferred. Fig. 9.15 implies that if one ran the tubular string deep enough, the bottom connection would structurally yield in a hydrostatic state of stress.
- The advantage of Figs. 9.16 and 9.17 over Fig. 9.15 is directly related to the formers' ability to accurately capture material yield. As is the case with many casing and tubing proprietary connections, should any portion of the part's performance envelope be governed by a limit state other than material yield, further adjustment of the load vs. envelope presentation may be necessary to allow simultaneous display of both laboratory and downhole conditions. This latter issue does not usually exist in the case of accessories. The vast majority of assemblies and subassemblies of an accessory are designed based on their resemblance to a thick-walled tube.

CHAPTER 9

Connections

9.1. INTRODUCTION

The most complex component of a tubular joint is the threaded connection[1] used to attached adjacent tubes [102]. The intricacies of the thread profile and sealing method usually render any detailed investigation a candidate for numerical analysis [103–108]. Even with modern finite element techniques, the response of a connection to qualification testing in a laboratory is not always as anticipated.

The perfect or ideal [101] connection arguably does not exist. Such a connection would have the same cross-sectional dimensional limitations as the tube body, while being equivalent to the tube body in both axial force and pressure integrity, a condition that might be achieved by welding two tubes together, with the exception of possible post-weld metallurgical issues at the juncture. As will become clear below, the connection selection process usually involves a compromise between competing issues, including cost.

In the sections to follow, the individual aspects of connection behavior are addressed separately. Beginning with axial strength integrity, we investigate the behavior of the threaded region under load. Various failure mechanisms characteristic of API and non-API or proprietary thread designs are considered, along with a companion review of the development of thread profiles.

Structural considerations are followed by the all-important performance aspect of leak integrity. The so-called thread lubricant seal used by most of the API family of connections is discussed, along with more sophisticated alternatives such as seal rings and metal-to-metal seals. A clear distinction is established between the latter and a torque shoulder.

A closing discussion of performance deals with additional aspects of connection design such as internal flow profile and assembly. The chapter ends with a discussion of connection qualification as performed in the industry-standard test protocol(s).

[1] In this chapter we deal almost exclusively with connections where at least the pin member is machined directly onto the tube body. For large diameter tubes, weld-on connections are often used. Such connections, although suitable for the tubulars to which they are attached, are outside the scope of this discussion. One author [101] distinguishes these products as "connectors for pipe, not pipe connections" so as to isolate them from the type of connections to which we limit ourselves here.

Elements of Oil and Gas Well Tubular Design
DOI: 10.1016/B978-0-12-811769-9.00009-8

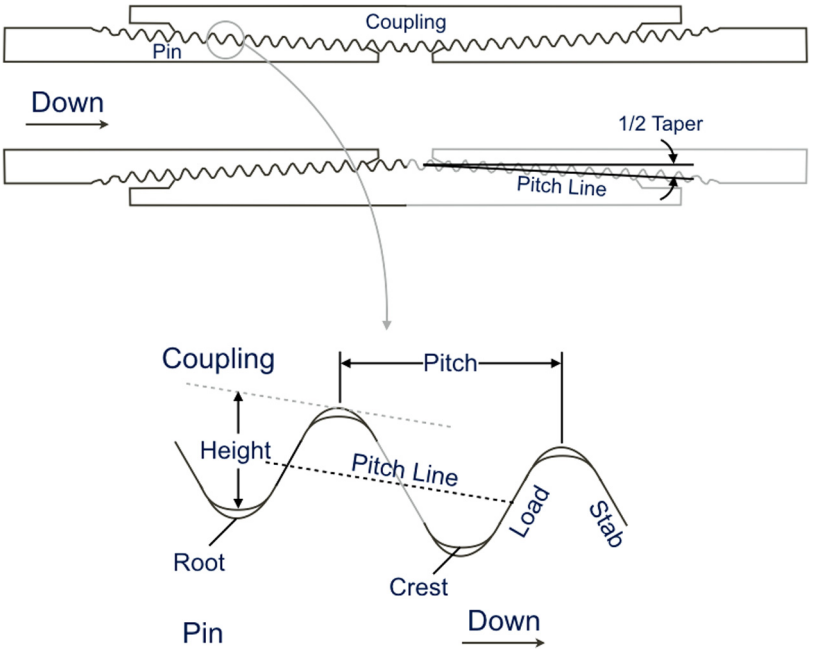

Figure 9.1 ***Drawing of an API long thread and coupling casing connection illustrating key thread elements.*** The root shown is for a pin thread; the crest shown is for a coupling/box thread. The taper is exaggerated. A torque shoulder and metal-to-metal seal are not shown in the figure—see Fig. 9.3 for these features.

9.2. ELEMENTS OF THREAD DESIGN

To facilitate the discussion to follow, Fig. 9.1 presents an API long thread connections consisting of a pin—the portion of the thread machined on the tube body—and coupling—the portion of the connection into which the pin is screwed. If the coupling is separate from the pipe body, a connection is termed "threaded and coupled" (T&C)—see Sections 9.3.1 and 9.3.2. If the coupling is formed as part of the tube body, a connection is termed integral—see Sections 9.3.3, 9.3.4 and 9.3.6—and the "coupling" is termed the "box."

The threaded region as shown in the expanded portion of Fig. 9.1 consists of a number of defined and toleranced [109] elements:

- The crest of a single pin thread is the point, arc or surface on the thread form having the greatest radial value; the root of a single pin thread is the point, arc or surface having the least radial value. The crest of a single coupling/box thread is the point, arc or surface on the thread form having the least radial value; the root of a single coupling/box thread is the point, arc or surface having the greatest radial value.

- Pitch is the axial distance from the crest of one thread to its neighbor. Common units are length (i.e., the thread pitch is 0.125 in.) or number of threads per a specified length (i.e., 8 threads per inch (TPI)).
- Lead is the axial distance the thread travels in one complete rotation of the pin relative to the coupling/box. Usually lead and pitch are equal, but thread designs do exist where two separate spirals traverse the thread form. In this case the lead is twice the pitch.
- Pitch diameter is the local diameter of the pitch line, a cone concentric with the thread axis where the width of the thread groove (metal removed during machining) and the thread body (metal remaining after machining) are equal.
- Taper is the rate of increase of pitch diameter with axial position and is usually measured as either inches (increase in pitch line diameter) per foot (of axial distance) or inches per inch.
- The load flank of a thread is that flank most highly loaded when the connection is in tension. The stab flank of a thread is that flank which will normally make first contact on assembly when the pin is inserted in the coupling or box.
- Height is the radial distance, taking due account of the taper (see Fig. 9.1), between the root and crest of a thread.

9.3. TYPES OF THREADED CONNECTIONS

Depending on the application, threaded connections possess specific features. In most instances, the transparency of an ideal connection is compromised in either strength or geometry [101,110].

9.3.1 API casing connections and NUE tubing

In contrast to the proprietary threaded and coupled (T&C) connection of Section 9.3.2, the API entries for casing[2]—short round thread,[3] long round thread[4] and buttress[5] casing, and NUE[6] tubing—have neither a metal-to-metal seal[7] nor a torque shoulder.

[2] Traditionally API has recognized a close relation between size and function, with the crossover occurring at 4.500 in. Sizes greater than or equal to 4.500 in. are termed casing; sizes less than or equal to 4.500 in. are termed tubing. Particularly for connections, this distinction was strong enough to prompt one connection manufacturer to offer separate casing and tubing connections for 4.500 in. diameter tubes. With the advent of high volume wells wherein the production tubing may be 7.000 in. or larger this distinction has diminished. Remnants of the casing–tubing terminology do still exist, however, a prime example being the API segregation of threaded connections.

[3] Commonly denoted STC signifying "short thread and coupling."

[4] Commonly denoted LTC signifying "long thread and coupling."

[5] Commonly denoted BTC signifying "buttress thread and coupling."

[6] NUE signifies "nonupset end."

[7] The flank-to-flank thread contact in the threaded region is usually not designated a metal-to-metal seal.

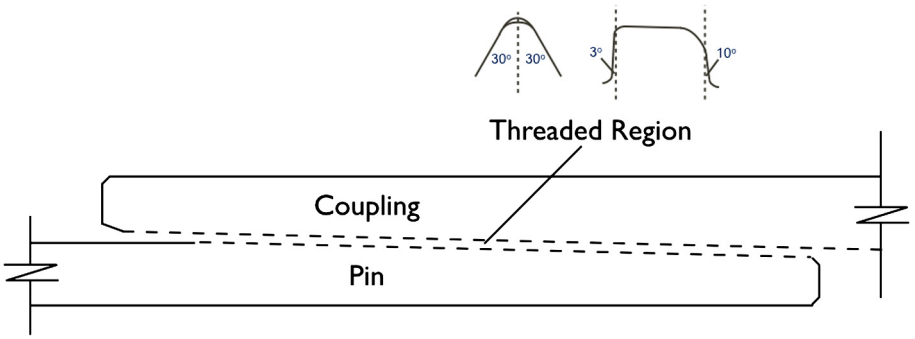

Figure 9.2 ***Drawing of generic threaded and coupled (T&C) API casing connection.*** The threaded region is indicated with phantom dashed lines, with typical thread forms illustrated in profile.

There still exist, however, a number of low pressure applications suitable for API connections. The majority of casing and tubing connections run worldwide are API. API Specification 5B [109] details the tapers, thread forms and dimensions of the API offerings. API Technical Report 5C3 [51] contains the formulas used to calculate axial joint strength.

Fig. 9.2 illustrates a generic sample of such a connection. Variations on the connection shown in the figure include the following:

- The thread lubricant seal[8] may be supplemented by a resilient seal ring installed in a groove machined in the coupling.
- At least one vendor offers a variation on the API T&C round thread design with an insert placed between the two pin ends.[9] This insert can serve as a torque shoulder to prevent excess turns when assembling the connection.
- The buttress threaded version of the API T&C connection can, in some cases, be ordered with the next higher grade coupling attached, which in some cases increases the joint strength of the product.[10] Care should be exercised when using this option, particularly if the intended well environment contains hydrogen sulfide.
- A special-clearance version of the buttress connection is manufactured by machining the outside diameter of the coupling.

[8] See Section 9.5.1.1 for a discussion of the suitability of classifying thread lubricant as a seal.

[9] The area between the two pin ends on an API round thread connection is termed the "J" area, as this is the letter assigned to this axial region in API Specification 5B [109].

[10] The addition of increasing wall thicknesses to API tube bodies historically led to API connections for greater tube wall thicknesses being strength-limited by the geometry of the coupling. Higher grade coupling availability was introduced as an alternative to designing new coupling geometries for these products.

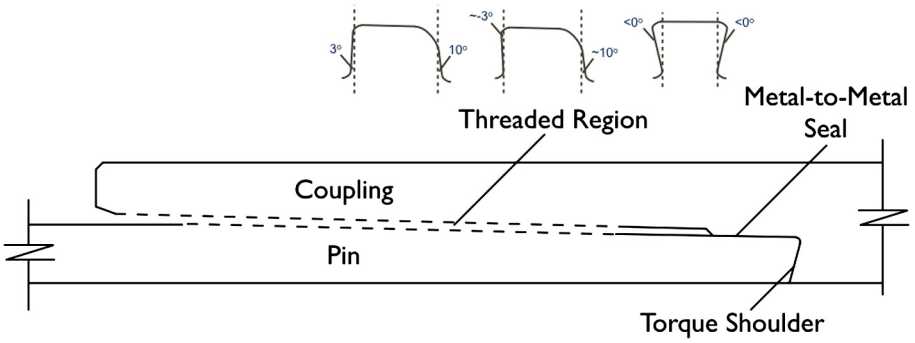

Figure 9.3 ***Drawing of generic threaded and coupled (T&C) casing and/or tubing connection.*** The threaded region is indicated with phantom dashed lines, with typical thread forms illustrated in profile. Not all offerings have the torque shoulder.

9.3.2 Threaded and coupled (T&C) connections

Threaded and coupled connections usually meet or surpass the axial tension, internal pressure and external pressure performance properties of the tube body. In some instances, even the tube's axial compression performance can be matched. To reliably provide pressure integrity, the connection typically employs a metal-to-metal seal and/or a resilient seal ring. The thread form usually has a negative load flank and, in some instances, a negative stab flank. A torque shoulder is employed to limit assembly stresses.

Fig. 9.3 illustrates a generic sample of such a connection. Variations on the connection shown in the figure include the following:

- Some proprietary versions of this connection also have an external metal-to-metal seal.
- The metal-to-metal seal may be supplemented by a resilient seal ring installed in a groove machined in the coupling.
- More than one vendor offers a T&C connection with no metal-to-metal seal, but with shoulders on both pin members which contact on assembly, forming a torque shoulder which could be conceived to act as a metal-to-metal seal. Rating a torque shoulder as a metal-to-metal seal is not recommended by this author.
- A special-clearance version of this connection is manufactured by machining the outside diameter of the coupling.

9.3.3 Nonflush integral clearance connections

Nonflush integral[11] connections are machined on tubes which have been cold formed—expansion of the box, swaging of the pin—followed by stress relief via heat treatment.

[11] The term "integral" indicates the coupling has been integrated into the tube body. One advantage of this strategy is the removal of half the pin-to-coupling matings, theoretically reducing the possibility of a connection leak.

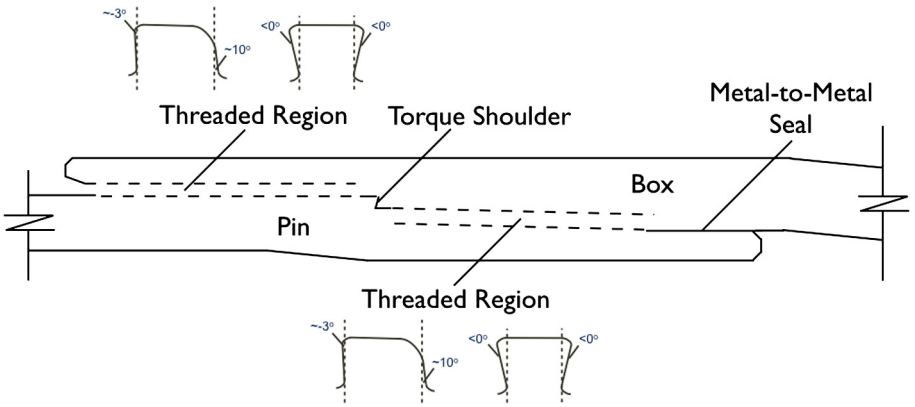

Figure 9.4 ***Drawing of generic integral casing connection.*** The threaded region is indicated with phantom dashed lines, with typical thread forms illustrated in profile. Not all offerings have the intermediate torque shoulder.

These connections usually meet or surpass the internal pressure and external pressure performance properties of the tube body. The axial tension joint efficiency of this family falls in the range of 70–75%. The compression joint efficiency of this family is normally low, on the order of 30–50% of the tube body, often due to the small torque shoulder area.[12] To reliably provide pressure integrity, the connection typically employs a metal-to-metal seal. The thread form usually has a negative load flank and, in some instances, a negative stab flank. The torque shoulder serves to limit assembly stresses.

Fig. 9.4 illustrates a generic sample of such a connection. Variations on the connection shown in the figure include the following:

- Some proprietary versions of this connection also have an external metal-to-metal seal.
- Versions of this connection type, particularly when aimed at application as a drilling liner, may be obtained without the metal-to-metal seal.

9.3.4 Flush integral clearance connections

Flush integral[13] connections usually meet or surpass the internal pressure and, perhaps, external pressure performance properties of the tube body. The axial tension joint efficiency of this family falls in the range of 60–65%. The compression joint efficiency of this family is low, on the order of 30–50% of the tube body, often due to the small

[12] Non-flush integral clearance connections that do not have the intermediate torque shoulder, but do have a negative stab flank thread form, may have a compression joint efficiency that exceeds the tensile efficiency.

[13] The term "flush" indicates the connection—both pin and box—has been machined directly into the tube body. The pin end may be cold formed.

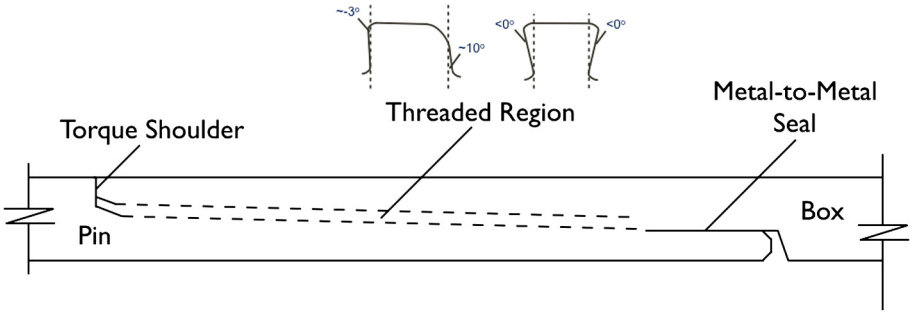

Figure 9.5 ***Drawing of generic flush casing connection.*** The threaded region is indicated with phantom dashed lines, with typical thread forms illustrated in profile. Not all offerings have the torque shoulder.

torque shoulder area.[14] To reliably provide pressure integrity, the connection typically employs a metal-to-metal seal. The thread form usually has a negative load flank and, in some instances, a negative stab flank. The torque shoulder serves to limit assembly stresses.

Fig. 9.5 illustrates a generic sample of such a connection. Variations on the connection shown in the figure include the following:

- Some proprietary versions of this connection also have an external metal-to-metal seal.
- Versions of this connection type, particularly when aimed at application as a drilling liner, may be obtained without the metal-to-metal seal.

9.3.5 API upset tubing connections

The pin ends of the API EUE[15] tubing connection are hot upset. API EUE is threaded and coupled, and provides a connection with round thread having a tension joint efficiency of 100%. The upset limits the number of thread recuts.

Fig. 9.6 illustrates a generic sample of such a connection. Variations on the connection shown in the figure include the following:

- The thread lubricant seal[16] may be supplemented by a resilient seal ring installed in a groove machined in the coupling.
- At least one vendor offers a variation on the API T&C round thread design with an insert placed between the two pin ends. This insert can serve as a torque shoulder to prevent excess turns when assembling the connection.

[14] Flush integral clearance connections that do not have the intermediate torque shoulder, but do have a negative stab flank thread form, may have a compression joint efficiency that exceeds the tensile efficiency.

[15] EUE signifies "external upset end."

[16] See Section 9.5.1.1 for a discussion of the suitability of classifying thread lubricant as a seal.

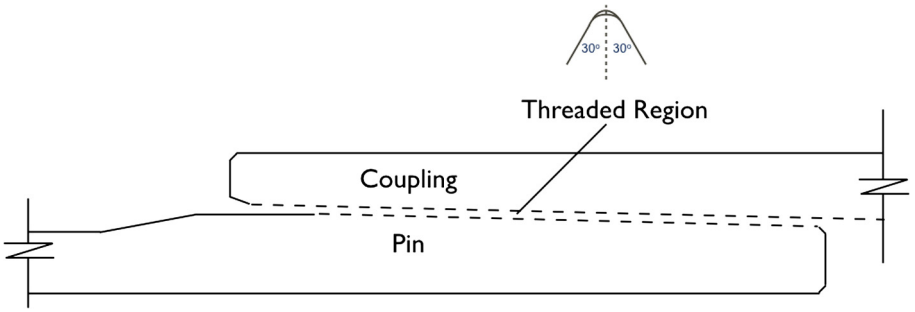

Figure 9.6 ***Drawing of generic API upset tubing connection.*** The threaded region is indicated with phantom dashed lines, with typical thread forms illustrated in profile.

- A special-clearance version of the EUE connection is manufactured by machining the outside diameter of the coupling.

9.3.6 Two-step tubing and work string connections

The two-step integral connection design possesses a threaded region that is not tapered, but rather has constant pitch diameter. Both the pin and box of the connection are upset. Assembly torque is counteracted at the metal-to-metal seal and the torque shoulder, the latter carrying the preponderance. In addition to its use as a tubing connection, this connection family has gained wide use on work strings.

Fig. 9.7 illustrates a generic sample of such a connection. Variations on the connection shown in the figure include the following:

- Particularly if the tubing is coated, the small gap between the end of the pin and the box can be filled with a seal ring.

9.4. AXIAL RESISTANCE

At the outset of the discussion of axial resistance a few definitions are in order. First, the joint strength R_{jt} of a connection is its capacity to withstand axial load and is usually (an important exception being the API family of connections) expressed by the formula

$$R_{jt} = f_x A_{cr}, \tag{9.1}$$

where f_x is the stress level representing the limit state and A_{cr} is the critical cross-sectional area corresponding to the location at which R_{jt} is being measured. The limit state is reached when the stress at the critical cross-sectional area reaches the critical value f_x.

The critical stress level is either the yield stress f_y or the ultimate stress f_u of the connection material. A proprietary connection manufacturer's internet and hardcopy content may report R_{jt} based on one or both of these stress values. Either value is

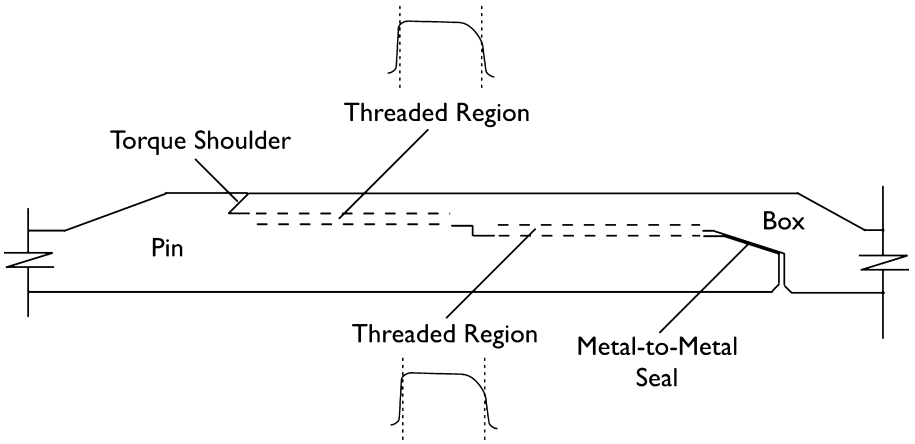

Figure 9.7 ***Drawing of generic two-step tubing and work string connection.*** The threaded region is indicated with phantom dashed lines, with typical thread forms illustrated in profile.

legitimate, provided it is clearly stated. If the ultimate stress is used, its entry may be labeled the "parting load" of the connection.

It is important that the value of f_x used match one's joint strength design factor basis. Most operators base their joint strength design factor on connection yield. If that is the case, then the value of f_x used should be f_y. Use of f_u in this instance will result in a nonconservative design, as the connection is being rated (for yield) with a higher value than appropriate. This warning is particularly important when dealing with API connections. API casing threaded connections have an axial resistance based on ultimate stress, whereas most proprietary connections have an axial resistance based on yield stress. Both API and proprietary tubing connections have an axial resistance usually based on yield stress.

The value of A_{cr}, the cross-sectional area at the location of yield ($f_x = f_y$) or parting ($f_x = f_u$), is determined by the manufacturer as a result of design calculations and experiment. In a well designed connection, failure in pure tension in the laboratory should consistently occur at the axial location corresponding to A_{cr}.

Continuing with introductory definitions, joint efficiency E_{jt} is the ratio of the joint strength to the strength of the tube body R_{ta}, expressed in percent as

$$E_{jt} = \frac{R_{jt}}{R_{ta}} \times 100\% = \frac{f_x A_{cr}}{f_x A_s} \times 100\% = \frac{A_{cr}}{A_s} \times 100\%, \tag{9.2}$$

where A_s is the cross-sectional area of the tube body.

Again, f_x can take the value f_y or f_u in Eq. (9.2), provided it takes the same value in both the numerator and denominator. Thus, for connections whose joint strength can

be written in the form of Eq. (9.1), the calculation of tension joint efficiency reduces to a calculation of areas.

Notable exceptions to the above calculations are the API threaded connections [51]:

- API round thread and buttress threaded connections have fracture strength equations that resemble Eq. (9.1), but A_{cr} is the minimum of a critical section area in the coupling and a critical section area in the pin.
- API round thread also has an additional failure mode normally called jumpout, but termed pullout in the API literature. Again, the limit state equation takes the form of Eq. (9.1), but in this case with a slightly different meaning.

9.4.1 Example problem—joint efficiency

A nonflush integral clearance connection for 7 in., 32 $\frac{\text{lb}_\text{m}}{\text{ft}}$ (0.453 in. wall) T95 casing has a manufacturer-reported critical cross-sectional area of 6.470 in^2. Compute the connection's joint strength and joint efficiency in tension, assuming the manufacturer rates his product on yield strength.

The yield strength of API grade T95 is 95 000 psi. From Eq. (9.1), the joint strength of the connection in tension is

$$R_{jt} = 95\,000\,\text{psi} \times 6.470\,\text{in}^2 = 614\,650\,\text{lb}_\text{f}. \tag{9.3}$$

The cross-sectional area of the tube body is

$$A_s = (\pi/4) \times \left[7.000^2 - (7.000 - 2 \times 0.453)^2\right] = 9.317\,\text{in}^2. \tag{9.4}$$

The joint efficiency of the connection is, from Eq. (9.2),

$$E_{jt} = \frac{6.470\,\text{in}^2}{9.317\,\text{in}^2} \times 100\% = 69.4\%. \tag{9.5}$$

9.4.2 Example problem—yield-based API casing joint strength

API calculates tubing connection joint strength[17] based on minimum yield stress f_{ymn} [51]. API calculates casing connection joint strength[18] based on minimum ultimate stress f_{umn} [51]. Many operators, however, base their design factor for both tubing and casing joint strength in tension assuming the connection rating is based on yield. Provide a reasonable procedure for expressing API casing joint strengths in terms of minimum yield stress.

[17] API tubing connections are NUE (nonupset end), EUE (external upset end) and IJ (integral joint).

[18] The API casing connections considered here are STC and LTC (round thread), BTC (buttress) and XC (extreme-line).

All of the API formulas for casing joint strength [51] are either directly proportional to f_{umn} (i.e., $R_{jt} = f_{umn} \times fcn(\text{Connection geometry})$)[19] or almost so (i.e., $R_{jt} = f_{umn} \times \text{fcn(Connection geometry)} + f_{ymn} \times \text{fcn(Connection geometry)}$).[20] Regardless, a reasonable approximation for yield-based API joint strength can be obtained by multiplying the API published rating [51] by the ratio of f_{ymn} to f_{umn}, that is,

$$R_{jt-yield} = R_{jt-API}\frac{f_{ymn}}{f_{umn}}. \tag{9.6}$$

For example, the f_{umn}-based API joint strength of 9.625 in., 40.0 $\frac{\text{lb}_\text{m}}{\text{ft}}$ K55 ($f_{ymn} = 55\,000$ psi, $f_{umn} = 95\,000$ psi, see Table 6.1) LTC casing is 561 000 lb_f. To compute an f_{ymn}-based yield strength using the approximate method presented in Eq. (9.6),

$$R_{jt-yield} = 561\,000\,\text{lb}_\text{f}\frac{55\,000\,\text{psi}}{95\,000\,\text{psi}} = 324\,800\,\text{lb}_\text{f}. \tag{9.7}$$

The reduction taken by K55 connections is large due to the difference between the minimum yield and ultimate stresses for this grade.

9.4.3 Tension resistance

Of obvious concern in the selection of a threaded connection is its performance under tension and compression, fully appreciating the possibility of bending. First, consider axial load in the absence of bending. Fig. 9.8 depicts a connection in a vertical wellbore under tension. Moving vertically upward from the bottom of the connection, examination of its geometry relative to the load suggests that, although at the base of the pin all of the axial load is carried by the pin, by the time one reaches the longitudinal center of the coupling all of the axial load will be supported by the central coupling cross sections. The load transfer from pin to coupling occurs in the threaded region. This transfer is complex, especially in the presence of other loads such as pressure and bending, but can sufficiently be described for the purposes of this discussion as linear. That is, once one has traversed upwards two-thirds of the way through the threaded region (and recognizing the approximate nature of the linear model), the pin will have shed two-thirds of the axial load which has been transferred to the coupling.[21]

The critical section area for the pin in a geometry like, or similar to, that of Fig. 9.8 is usually at the base of the pin, as it is here that the pin is most highly loaded. This is

[19] Applicable to the formulas for round thread coupling and pipe thread fracture strength, buttress coupling thread strength and extreme-line joint strength.

[20] Applicable to the formulas for round thread jumpout and buttress pipe thread strength.

[21] Why is the critical section area of the pin not located at the end of the pin where, due to the taper, its cross-section is smallest? Because by the time the end of the pin is reached all of the axial load will have been transferred to the coupling.

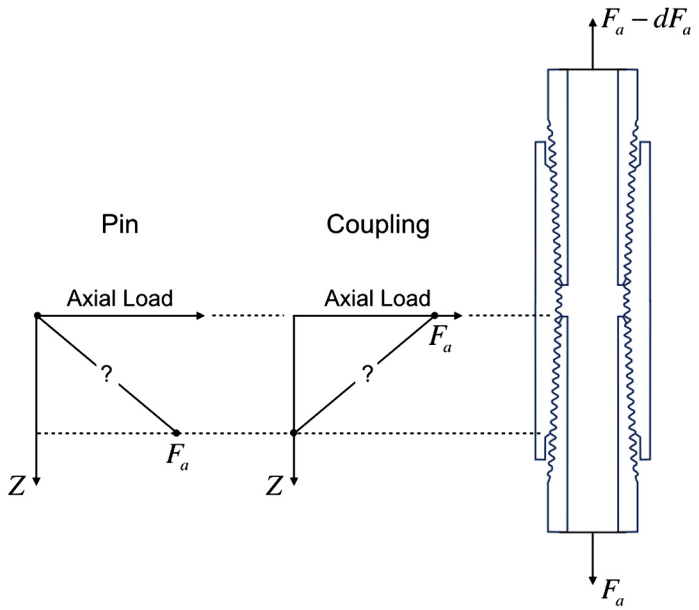

Figure 9.8 ***Axial load transfer in a threaded connection.*** Although the API round thread is depicted, the principle is similar for all casing and tubing connections. The question marks indicate that the load transfer, although assumed linear in the discussion of this figure, is often complex.

particularly true of the API round thread depicted in the figure. As a round thread pin is cut, the majority of the threaded region has a taper of 0.0625 $\frac{\text{in}}{\text{in}}$ on the diameter [109]. As the cutting tool reaches the base of the pin, however, this taper abruptly increases as the tool is extracted from the threading operation. This region of so-called incomplete threads cannot be used in the load transfer as these threads are not engaged with the coupling. As indicated in the figure, at the start of load transfer the cross-sectional area of the pin is less than that of the tube body. Since both the first thread involved in the load transfer and the tube body are exposed to the same axial force, the stress in the pin must be higher than that of the tube body. In a pure tension environment the pin threaded region will be more likely to fail than the tube body—the tension joint efficiency of the API round thread is therefore less than 100 percent.

One solution to this shortcoming in the API round thread is to machine the pin thread on an upset (see Section 9.3.5), with the diameter of the pin at the starting point of load transfer at least equal to that of the tube body. This design increases the tension joint efficiency of the API round thread connection to 100%, but not without complications:

- The upsetting process itself adds cost to the connection manufacture;
- Once upset, the tube end must be heat treated to reduce residual stresses introduced by the upsetting process;

- The number of recuts before the tube must be reupset is limited.

Nevertheless, upsetting is a recognized solution to the penalty in tension joint efficiency associated with the API round thread design.

The API buttress thread, along with a number of proprietary threads, does not have the manufacturing taper change described above for API round thread. The machining tool is simply constrained to the same taper until there is no more tube body to machine.[22] One might expect 100% tension joint efficiency from this process, and such is almost, but not quite achieved. The offset in axial force due to the mean radii in the pin and coupling induces a moment which separates the first few imperfect threads at the base of the connection, rendering the buttress connection slightly more stressed than the tube body.

9.4.3.1 Excursion: jumpout

In addition to the dominant over-stressed limit state described by Eq. (9.1), API round thread can succumb to a second failure mode termed jumpout.[23] The origin of jumpout is displayed in Figs. 9.9 and 9.10. Following the discussion of Clinedinst [111], the left-hand diagram in Fig. 9.9 focuses on one of the threads of a round thread connection. Following assembly the load and stab flanks of the thread are exposed to approximately equal contact tractions.[24] As indicated in the right-had diagram of the figure, when the connection is lowered into the well and subjected to tension under service, the contact traction on the stab flank will be transferred to the load flank. Eventually, an external axial force can be reached that results in the load flanks of the thread supporting all the tension.

Fig. 9.10 continues the discussion by further detailing the load flank of a single thread once all the axial tension has been transferred to that flank of the thread profile. Assume for simplicity that contact between the pin and coupling load flanks is frictionless.[25] Then the contact traction vector will be perpendicular to the surface of the thread flank. We may therefore decompose the vector into components along the axis and radius of the tube on which the round thread has been cut. The axial component of the traction is that portion of the contact supporting the axial load. The radial component, on the other hand, is acting so as to separate the pin from the coupling. With increasing axial load, eventually the pin will yield and, due to the inelastic counterpart to Poisson's ratio, begin to radially shrink away from the coupling. Once this radial displacement has

[22] As a consequence of this machining process one creates so-called black-crested threads—i.e., those threads for which there is insufficient tube material left to achieve full design thread height, thus leaving evidence of the tube outside diameter on the crest of the thread.

[23] An alternate name also used by the API is pullout.

[24] The loading will not be precisely equal because of the thread taper.

[25] The discussion will be altered slightly, but not conceptually changed, if one includes friction.

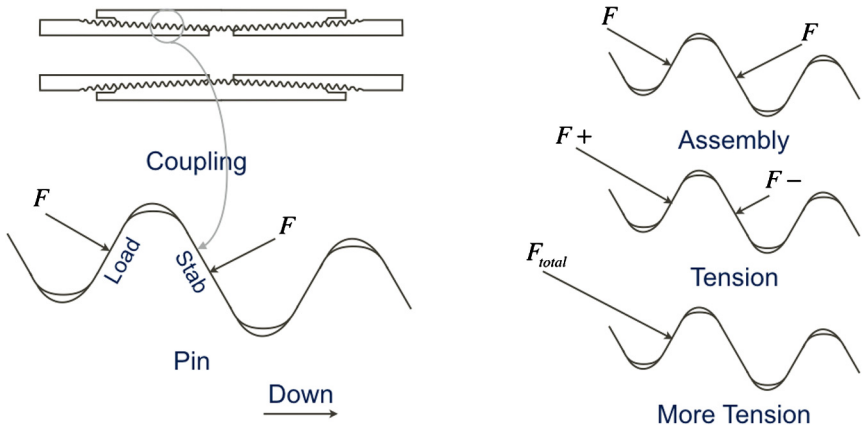

Figure 9.9 ***The origin of jumpout.*** Increasing tension transfers more of the thread flank contact traction to the load flank.

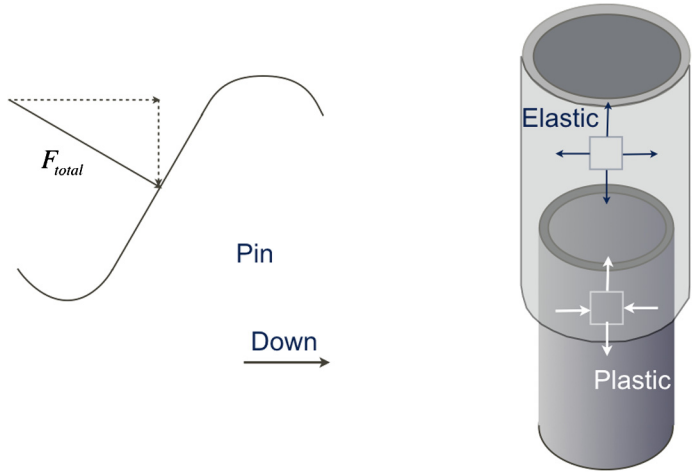

Figure 9.10 ***The mechanism of jumpout.*** The respective stress states promote earlier yield in the pin than the coupling.

reached a value equal to the thread height, the pin will separate from the coupling in the phenomenon of jumpout.

Given the amount of deformation preceding jumpout, the threads themselves are relatively undamaged. The notable feature of a jumpout failure is the gross radial displacement the pin experiences as it undergoes massive inelastic deformation in the radial (actually circumferential) direction.

9.4.3.2 Example problem—pin-first yielding

Fig. 9.10 depicts the stress states in the pin (plastic) and coupling (elastic) during jumpout, which provides an explanation for why the pin member undergoes the preponderance of deformation during this failure mode.

Due to assembly and the taper of the thread profile, the pin member of an API round thread connection will, as indicated by the traction arrows on the small pin element in Fig. 9.10, be in hoop compression. Correspondingly, the coupling will be in hoop tension. Due to the tensile axial load, both the pin and coupling will, as also indicated in the figure, be exposed to axial tension. The radial stress will be enough smaller than either axial or hoop stress that we can consider it zero in this discussion.

Recalling the discussion of yield in Section 6.3.1 of Chapter 6, closeness to yield for a crystalline metal increases with shear. Comparing the stress states in Fig. 9.10, both the axial and hoop stress in the coupling are positive when the connection is loaded in tension, whereas the axial and hoop stresses in the pin have opposite signs. The tendency to yield will be greater in the pin than the coupling, leading to the pin's dominant role in jumpout.

9.4.3.3 Alternate thread profiles

Compare the left-hand diagram in Fig. 9.10 with the upper-left diagram in Fig. 9.11. Both the load and stab flanks in an API round thread have an angle with the tube radius of 30°, this angle being the source of the radial component of the contact traction vector. Reducing this component's influence will reduce the possibility of thread jumpout. In this regard, notice (Fig. 9.10) that as the angle of the load flank is decreased, the magnitude of the radial component of the contact traction vector also decreases. Comparing the API round thread profile with that of, for example, API buttress (see lower-left diagram in Fig. 9.11) that has a load flank angle of 3°, the latter should and does render the buttress thread less susceptible to jumpout.

Experimental data collected during the establishment of the API formulas for joint strength [111], however, indicate that for larger diameter-to-thickness ratios even API buttress can fail in tension due to jumpout. In fact, failure of a number of clearance casing connections possessing load flanks similar to buttress led to a joint industry project to verify connection performance experimentally [112]. Subsequent to these experiences, the introduction of the hook thread (see upper-right diagram in Fig. 9.11) virtually eliminated jumpout in oil well tubulars. The hook thread has a negative load flank angle which reverses the behavior of the radial component of the contact traction vector. With a hook thread, the radial component actually serves to increase the intimacy of contact within the threaded region.

If there is a disadvantage to the hook thread, it lies in its ability to withstand compressive loads—the stab flank of a hook thread is has a positive flank angle. For this reason, most designs incorporating a hook thread profile also include an opposing contact angle

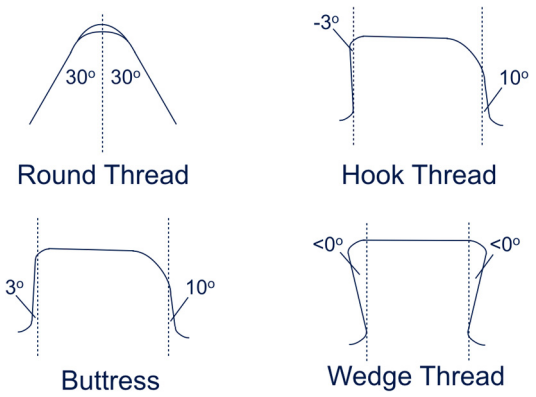

Figure 9.11 ***Alternate thread profiles.*** Flank angels on hook and wedge thread are typical and may vary with an individual manufacturer.

at the torque shoulder to withstand compression (see Fig. 9.3). An alternative to assigning compression resistance to the torque shoulder is the dovetail or wedge thread design, which accommodates negative flank angles on both the load and stab flanks. This design is particularly amenable to bending applications and has been used in the design of a high torque tool joint [113]. The potential of both the hook and dovetail/wedge thread forms to eliminate jumpout as a failure mode comes at the cost of increased machining and inspection complexity.

9.4.4 Compression resistance

The axial compression resistance of a threaded connection is not always related to its structural capacity when loaded with a negative axial force. In fact, the structural resistance of a connection to compression may exceed its structural resistance to tension. The often lower compression joint efficiency of a threaded connection can usually be traced to a separate limit state, for example, yielding of an internal (torque) shoulder that in itself is bad, but may also affect the pin-to-coupling relative positioning of a metal-to-metal seal.

9.5. INTERNAL PRESSURE RESISTANCE

Most proprietary threaded connections are rated equal to the tube body in internal pressure resistance. Many API connections are also rated at least as strong as the tube body when exposed to internal pressure. There do exist, however, API connections wherein the structural internal pressure resistance of the connection is less than that of

the tube body.[26] For the API buttress connection it is possible to order a "next higher grade" coupling to once more render the tube body the weaker component of the joint [46,51].

A corollary to a tubular's usefulness as a conduit for fluids is its ability to contain those fluids, separating internal and (possible) external flow streams. This not only requires the threaded connection to maintain structural integrity (i.e., burst resistance) but also includes an expectation of leak resistance. Leak resistance presents a peculiar design issue in that the probability of its occurrence is difficult to predict. Leak resistance depends not only on the design of the connection but also on the assembly procedure at the rig site.

9.5.1 Sealing mechanisms

In the current market environment there exist three mechanisms by which leak resistance is pursued—thread lubricant, seal rings and metal-to-metal seals. Each of these alternatives, which are sometimes incorporated in a single design, will be considered in the sections to follow.

9.5.1.1 Thread lubricant

Fig. 9.12 pictures a portion of an API round thread connection, focusing on the 0.003 in. gap [109] between the root of a pin/coupling thread and the crest on the mating coupling/pin thread. Also shown for orientation is the centerline of the tube on which the thread is cut.

The label 1 in Fig. 9.12 indicates that if one were to follow a pin thread root path around the connection circumference, a spiral path exists connecting the pin roots. Similarly, following the pin crests along the connection's machined spiral reveals a second path connecting the pin crests. These two paths, as they stand, represent two potential leak paths for internal fluids.[27]

The standard means of closing the leak paths illustrated in Fig. 9.12 is thread compound. Using a petroleum soap-constituted grease base, a thread compound carries solids—originally soft metals such as lead, zinc, copper and graphite [114], but now more commonly polytetrafluoroethylene (PTFE) and proprietary blends—intended to both mitigate galling and, somewhere in the spiral potential leak path, block fluid move-

[26] This phenomenon is usually a consequence of history. The API connection, when originally introduced met or exceeded the internal pressure resistance of the tube body. With time, however, additional, increasing wall thicknesses introduced into the API inventory favored the resistance of the tube body, as the coupling dimensions did not change. See also Footnote 10.

[27] Recalling the discussion of Section 9.4.3.1, another possible leak path exists in the API round thread connection. Under sufficient tension, the stab flanks of the round thread can separate providing a third avenue for fluid escape [102]. This path will also close when the tension is removed. Unfortunately, this potential leak path is load-induced and cannot be remedied with thread lubricant.

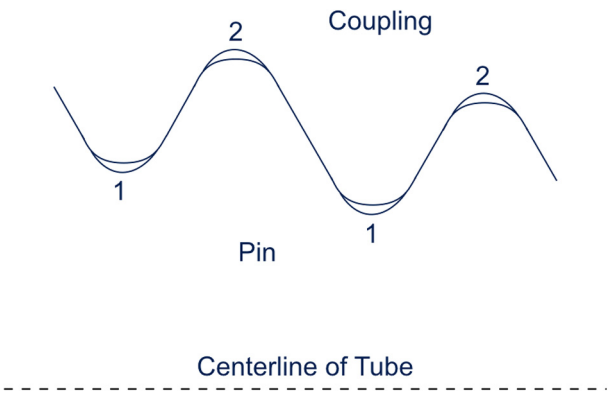

Figure 9.12 ***Dual potential leak paths in an API round thread connection.***

ment. The following comments are in order regarding an interstitial thread lubricant seal:

- If used in production tubing, the hydrocarbon based grease can be leached by chemical reaction with the reservoir fluids;
- Above approximately 275–300 °F (135–150 °C) a *standard* grease base can boil off;
- In the time interval of a relatively short field pressure test, it is not possible to verify that an effective seal in the thread root–crest gaps has been achieved.[28]

The above list suggests alternate sealing methods may be in order if one desires to contain gas for long periods of time. Two common alternate seal strategies are considered in the sections to follow—seal rings and metal-to-metal seals.

9.5.1.2 Seal ring

Among several topics aimed at improving API connection leak resistance reliability, API Supplemental Requirement (SR) 13 to Specification 5CT [46] offers the user an additional sealing mechanism in the form of a PTFE ring (with 25% fiberglass filler) inserted in a groove cut in the coupling member of a connection (see Fig. 9.13).[29]

[28] Consider a 7.000 in. round thread casing connection. The (axial) length of effective threads $L_2 = 3.715$ in., multiplied by the number of threads per inch is $3.715 \times 8 = 29.72$ circumferences [109]. Taking the average pitch diameter to occur at $L_2/2$, this diameter is the pitch diameter $E_1 = 6.903\,37$ in., measured at the hand-tight plane $L_1 = 2.921$ in. from the end of the pin, moved to $L_2/2$. Using the round thread taper of $0.0625\ \frac{\text{in}}{\text{in}}$, the average pitch diameter is $6.903\,37 - (2.921 - 3.615/2) \times 0.0625 = 6.232\,49$ in. Thus the (approximate) total leak path length of 29.72 circumferences of a 7.000 in. API round thread is $\pi \times 6.232\,49 \times 29.72 = 582$ in., or 48.5 foot. Actual detection of a thread lubricant leak can take a long time-24 hours has been observed in the laboratory with a buttress connection whose leak path cross-sectional area can be larger than that of the round thread [115].

[29] Seal rings are also offered as additions to proprietary thread designs.

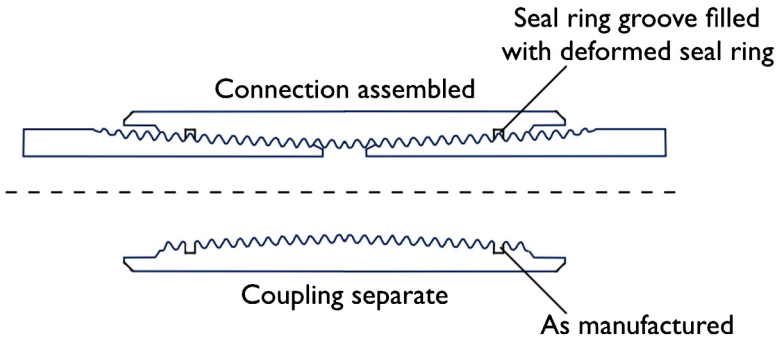

Figure 9.13 ***Seal ring groove shown as machined (lower diagram) and following assembly (upper diagram).*** One or both ends of the coupling may be attached to the pin(s) at the rig site. Prior to assembly a PTFE seal ring is inserted in each groove. Figure is not to scale.

A specific area of concern in designing or implementing a seal ring connection is temperature. The coefficient of thermal expansion of PTFE is approximately ten times that of steel[30]—confinement to a ring groove can therefore cause PTFE to induce internal stresses in a threaded connection. Notwithstanding this behavior, seal rings have been used with success in extreme downhole environments [117].

9.5.1.3 Metal-to-metal seal

The most popular of seals used in high pressure oil well tubular applications are interference-activated metal-to-metal seals. The coupling/box and pin seal surfaces are usually machined at a angle of 5–30° with the axis of the tube, being forced together due to geometry interference as the connection is assembled. Higher angles raise concern for maintenance of design contact pressure under tension; lower angles can increase the possibility of galling, especially during repeated assembly. Additional independent variables considered in the design of a metal-to-metal seal include the following:

- Contact stress distribution [118,119]. Both the maximum value of contact stress and the character of the axial distribution of contact stress influence the ability of the seal to prevent pressure/fluid escape or entry and accommodate leak channels of short length.
- Surface roughness and coatings [118,119]. The inherent roughness of the machined surface of the seal can be altered by surface treatments such as zinc or manganese phosphate coating[31] (usually applied to the coupling).

[30] The coefficient of thermal expansion of unfilled PTFE is approximately $7 \times 10^{-5}\ \frac{1}{°F}$, whereas the coefficient of thermal expansion of steel is approximately $7 \times 10^{-6}\ \frac{1}{°F}$. The former can be slightly reduced by adding filler, with Hilbert and Bergström [116] quoting a reduction of approximately 12% while noting that the coefficient of thermal expansion of PTFE varies significantly with temperature.

[31] In addition to sealability, the coating is also applied to reduce galling potential.

- Thread compound [118,119]. Although thread compound is primarily intended to reduce friction and galling in the threaded region, evidence does exist that thread compound on the seal surface can improve leak resistance, particularly if the size of the solid particles in the thread compound is close to the amplitude of surface roughness of the seal [120].
- Assembly. The act of assembling the connection will cause the pin and box/coupling seal surfaces to interact at high interference-induced contact stresses. Local inelastic deformation of machined peaks on the seal surface has been demonstrated to reduce the contact pressure required to achieve a specified sealability [120,119]. Proper axial alignment of the mating coupling/box and pin seal surfaces is crucial and is usually controlled by the presence of a torque shoulder (cf. Figs. 9.3, 9.4, 9.5 and 9.7).
- Seal geometry [119]. Seal geometry (macroscopic shape, contact length, diameter, interference) affects the contact stress profile—the distribution of contact stress per axial length of seal surface—opposing release of internal fluids.

Fig. 9.14 depicts the behavior of a typical metal-to-metal seal used on a threaded connection. The horizontal axis is internal pressure, that is, the pressure of the fluid to be contained. The vertical axis is some measure of the contact stress profile at the metal-to-metal seal. Depending on the character of the contacting surfaces, the contact pressure distribution will vary—the ordinate in Fig. 9.14 is intended to represent a peak or effective contact stress. The 45° line in the graph is the leak criterion—leak is assumed to occur if the internal pressure exceeds the contact pressure.

When the connection is assembled on the rig floor, the interference between the diameters of the pin and coupling seal surfaces means the two surfaces must be "forced together" as the pin advances into the coupling—a visible change in the slope of the torque-turn graph generated by the power tongs should be noticeable. Once fully assembled, the seal is at point A in the figure.

Assume that once in service, the pressure associated with the contained fluid begins to increase. The horizontal, dashed line originating at point A indicates that internal pressure increase. Notice, however, that the sealing capacity of the metal-to-metal seal is not horizontal. The same increase in internal pressure promoting a leak is also acting on the inside surface of the pin—particularly in the vicinity of the metal-to-metal seal—increasing the contact pressure between the pin and coupling seal surfaces. This is known as self-energization and is a characteristic of many metal-to-metal seals.

The dashed line in the plot attempts to accurately display that the mapping of internal pressure into increased contact pressure is not one-to-one—the slope of the line AB is less than 45°. As the action of the internal pressure must be transmitted through the metal thickness under the pin seal surface, some pressure is necessary to deform the pin at the seal location. The degree of energization lost will depend on, among other factors, the thickness of the pin beneath its seal surface. With each increment of internal pressure, however, a portion of the leaking pressure increment is also transferred to resist

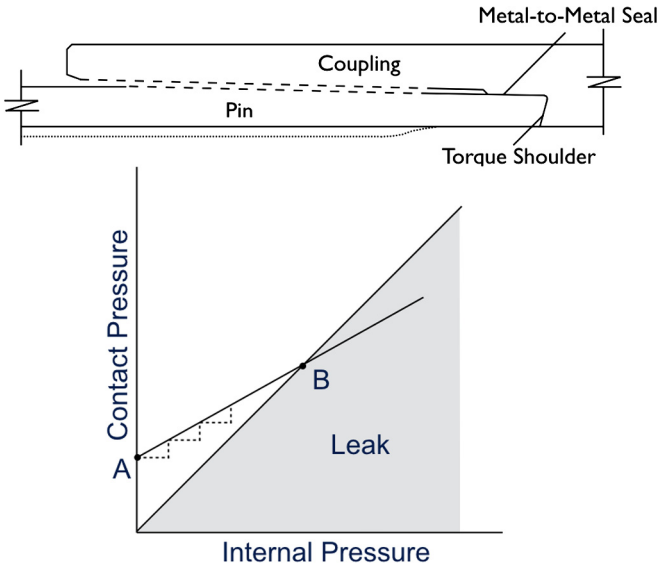

Figure 9.14 ***Behavior of a metal-to-metal seal.*** The location of point A can be controlled by initial seal interference. The slope of the line AB can be controlled by the thickness of the pin at the seal location.

the leak pressure. Eventually, a point is reached (point B in the figure) where the seal contact pressure is less than the internal pressure, and a leak ensues.

Also included in the upper portion of the figure is a diagram of a threaded and coupled connection possessing a metal-to-metal seal. At this point, notice the dotted line indicating a second pin/tube body having greater wall thickness than that used in the previous discussion. Further, assume that through analysis and testing the designer has, with the previous wall thickness, arrived at a pin seal design considered optimum. It may be that the best course of action—from the viewpoint of leak resistance alone—is to machine the pin as indicated by the dotted lines, that is, to use the tube wall thickness near the base of the pin and the optimum seal thickness near the end of the pin. If so, and as we shall see shortly, the design may now be exposed to turbulence under high internal fluid flow rates. Such tradeoffs as this permeate the design of a threaded connection metal-to-metal seal. Less metal under the pin seal surface may promote self-energization, but altering the internal profile of the connection may lead to other issues unrelated to leak integrity.

Similarly, another means of increasing leak resistance would be to raise the value of point A, the initial interference contact pressure. Unfortunately, this solution also may complicate other aspects of the connection design, such as galling during assembly and/or exposing the pin end to a (primarily hoop) stress too close to yield. Threaded connection design is a complex process involving compromise between a number of competing design objectives.

9.6. EXTERNAL PRESSURE RESISTANCE

External pressure resistance is not addressed as frequently in connection design as resistance to internal pressure. There do exist, however, a number of load cases (cf. Section 12.8 of Chapter 12 and Section 15.2 of Chapter 15) in which resistance to external pressure is desirable. The importance of such load cases to the overall string design may suggest the need for a connection possessing an external (usually metal-to-metal) seal.

9.7. ADDITIONAL DESIGN CONSIDERATIONS

Other attributes of casing and tubing connections worthy of consideration in design include the following.

9.7.1 Flush internal profile

For low flow rate wells the actual velocity profile of the internal fluid may be of minor concern. As production rate increases, however, even minor changes in internal profile can induce turbulence in the vicinity of the connection. Such turbulence can promote corrosion or, in the presence of produced solids, erosion to the interior, near-connection region. For production tubing in wells whose production is primarily gas, a reasonable flow rate at which the internal profile should cause concern is 100 mmscfd.

9.7.2 Torsional resistance

The existence of a torque shoulder enhances the structural resistance of a threaded connection in several ways:

- Limiting axial displacement during assembly. Inasmuch as most threaded connections possess a positive thread taper,[32] assembly of the connection induces a positive hoop stress in the box/coupling and a negative hoop stress in the pin. Aside from reducing the box/coupling's resistance to a hydrogen sulfide environment, unchecked axial engagement during assembly can increase the risk of galling. Further, thread profiles possessing gaps on the load and stab thread flanks (as opposed to the thread roots and crests) undergo a Poisson's ratio induced relative axial movement during assembly. This coupling-to-pin relative movement, common to API buttress, casts further doubt on the leak integrity available in the threaded region. Both of these concerns—high induced stresses and interstitial movement during assembly—are either limited or eliminated by the presence of a torque shoulder.
- Pipe rotation. The ability to rotate the tubular string (during cementing, for example) can positively affect the installation and survivability of a tubular. Further, work

[32] Recall thread taper measures the change in thread pitch diameter as one axially traverses the threaded region of the connection.

strings and smaller diameter casing strings have been employed in rotary drilling operations with success.

Both the hook thread in concert with a torque shoulder and especially the wedge thread with its self-contained thread profile torque resistance are suitable in minimizing the adverse effects accompanying torsion.

Notwithstanding its importance in the structural integrity of the connection, with regard to leak integrity a torque shoulder should not be considered a metal-to-metal seal for the following reasons:

- The machined tribological characteristics of a torque shoulder are usually different than those of a metal-to-metal seal;
- Rig-site operations, such as stabbing the pin into the coupling/box during assembly, pose a risk of (leak resistance, not structural) damage to the torque shoulder, whereas a metal-to-metal seal with its more radially-oriented surface normal is less susceptible.

9.8. QUALIFICATION AND TESTING

The industry is currently served by two documents to aid in standardizing the testing threaded connections—"API Recommended Practice on Procedures for Testing Casing and Tubing Connections" [56] and "ISO/PAS 12835:2013, Qualification of Casing Connections for Thermal Wells" [121]. The former serves the majority of tubular connection applications. The latter is particularly applicable to casing used in thermal recovery methods such as Cyclic Steam Stimulation (CSS) and Steam Assisted Gravity Drainage (SAGD) where the connection's service environment may involve loads beyond yield.

9.8.1 Brief summary of API 5C5 testing

Qualification of a threaded connection at the highest application level can be both time consuming and expensive. The knowledge gained, on the other hand, from testing a connection's structural and leak resistance to one's specific operating environment can reduce project economic risk.

In a qualification exercise that follows API 5C5 the following activities are noteworthy:

- The connection sample(s) and performance properties, including a connection evaluation envelope[33] (CEE), are supplied by the manufacturer. The CEE then defines

[33] The test connection evaluation envelope is a closed two-dimensional region when plotted in a space where the abscissa is axial tension (+) and compression (−), and the ordinate is internal (+) or external (−) pressure. A typical connection evaluation envelope will consist of several segments, with possible abrupt corners but is almost always convex.

the extent of a test load envelope[34] (TLE). The manufacturer is under no obligation to participate in the conversion of a CEE into a design envelope that the user may employ in his design calculations.

- The number and dimensional combinations of the test sample(s) depends on the connection application level (CAL) to which the connection design will be qualified. There currently exist four CALs, with CAL IV being the most severe.
- Tests to which the connection sample(s) are subjected include the following, depending on the CAL. In all tests the (pressure, axial force) load points are referenced to the von Mises yield surface of the associated tube body. The underlying plot is identical to that presented in Section 6.3.4.3 of Chapter 6. Brief summaries of the test series are as follows:
  - Series A—the connection sample is tested to various combinations of axial force and internal or external pressure in all four quadrants of the axial force vs. pressure plot.
  - Series B—the connection sample is tested to various combinations of axial force, internal pressure and bending in the upper two quadrants (i.e., no external pressure) of the axial force vs. pressure plot.
  - Series C—the connection sample is tested to various combinations of axial force and internal pressure with thermal cycles in the first quadrant (i.e., no axial compression or external pressure) of the axial force vs. pressure plot.

  The Series A and B tests may be performed at room or elevated temperature. Further, depending on the CAL, the tests may be performed with either liquid or gas as the pressure fluid.

9.8.2 Envelope presentations for connection design

Of importance to the designer is the means by which a qualification test and its resulting performance envelope are compared to operational loads to which the connection will be subjected.

Fig. 9.15, an application of Fig. 6.14, has been adopted[35] in two API documents as the preferred method of presenting the axial force/pressure performance envelope for threaded connections [56] and some tubing accessories [55]. One can, however, also use the other two three-dimensional alternatives presented in Section 6.3.4 of Chapter 6

[34] The test load envelope is derived from a manufacturer-supplied connection evaluation envelope (CEE) and defines the extents to which the connection will actually be tested. The test load envelope is constructed from the CEE by a calculation that scales the CEE values—along both the axial load and pressure axes—by 80–100%, depending on the character of the sample and the conditions of the test. "If the CEE is less than the pipe body reference envelope, it needs to be disclosed by the manufacturer . . . whether the CEE limitation is based on material yield strength or some other factor." [56].

[35] Exception: Fig. 9.15 uses axial stress for the abscissa, whereas the referenced API documents use axial force.

Table 9.1 Evaluation envelope for a generic connection. The sample connection has a yield stress of 110 000 psi. The principles illustrated apply equally well to accessories. All values are in psi

Point	Axial stress	Pressure[a]	Point	Axial stress	Pressure[a]
A	110 000	0	E	−110 000	−10 000
B	110 000	12 228	F	0	−10 000
C	0	12 228	G	51 897	−10 000
D	−110 000	0	H	110 000	0

[a] A positive value incites internal pressure; a negative value indicates external pressure.

Table 9.2 Load points shown in Figs. 9.15–9.17. All values are in psi

Load point	Internal pressure	External pressure
Surface qualification test		
Initial conditions	0	0
Positive test	10 000	0
Negative test	0	10 000
Bottom of string		
Initial conditions	15 000	15 000
Positive test	25 000	15 000
Negative test	5000	15 000

to gain additional insight into connection and accessory behavior, particularly when (a) selecting test points in a qualification exercise and (b) translating a manufacturer's performance envelope from laboratory to downhole conditions. In fact, the latter two presentation alternatives provide more physically acceptable load displays than Fig. 9.15 when downhole conditions are of concern.

It is important to state that calculations of stress and yield state are not at issue in this section. Rather, the discussion centers on presentation, that is, proper representation of the relative positions of the loads with respect to the performance ellipse to which they are being compared. Consider, for example, the crude performance envelope—representing no particular tubular connection—whose defining points are summarized in Table 9.1.

Now review Figs. 9.15–9.17. Each figure is a duplicate of its counterpart in Figs. 6.14, 6.13 and 6.11, respectively, with two additions. First, the connection evaluation envelope values of Table 9.1 have been added to each figure. Secondly, three sample load points—initial conditions, positive pressure test, negative pressure test—have also been added to the figures. The load points are summarized in Table 9.2 with the symbol × denoting a surface qualification experiment and the symbol ∘ denoting an anticipated downhole load condition, where the downhole position is the bottom of the tubular string.

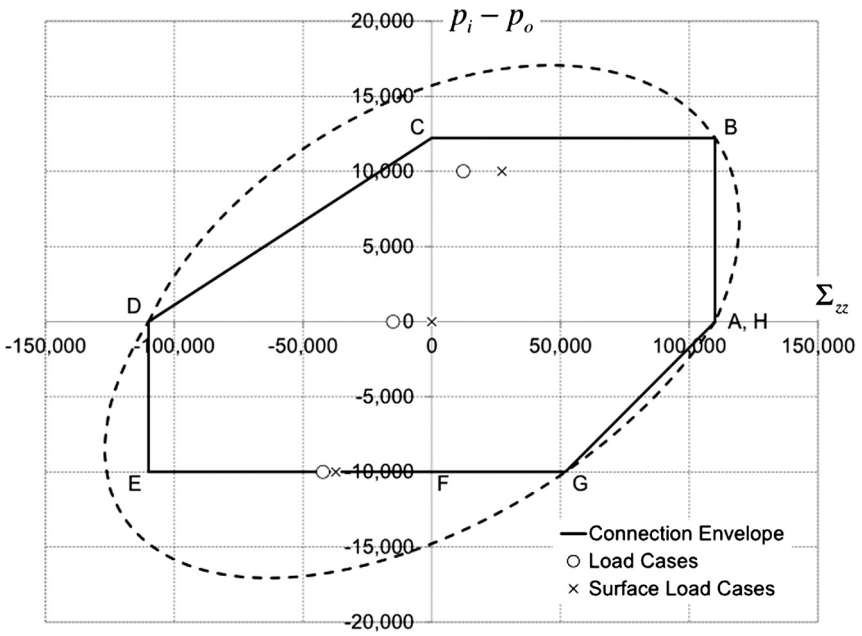

Figure 9.15 ***Connection evaluation envelope plotted with the von Mises yield criterion expressed in terms of*** S_{ZZ}**.** The tube body ellipse is shown as a dashed curve and follows Fig. 6.14. Vertices of the envelope labeled A–H correspond to the points in Table 9.1.

Fig. 9.15, with the exception of using axial stress rather than axial force for the abscissa, is the API RP 5C5 [56] space in which connection evaluation tests are designed and performed.[36]

There are no issues with the evaluation envelope as prepared for a laboratory environment. The "initial condition" for a laboratory experiment is one of no loading and therefore plots at the origin of Fig. 9.15. The problem arises when comparing the laboratory test points to the sample downhole load points. Although the differential pressures—initial conditions = 0 psi, positive test = 10 000 psi, negative test = −10 000 psi—are correct, the use of axial force as the abscissa displaces the load points to the left. For example, the initial conditions are no longer at the origin of the coordinate axes. The performance ellipse and the downhole conditions to which it is being compared are not reflecting the same load state.

Fig. 9.15 is accurately reflecting the variables it was asked to plot—there is nothing wrong with the underlying calculations. Likewise, the evaluation envelope accurately depicts the loads to which the connection was or will be tested. The issue is that the two presentations involve loads that differ by 15 000 psi hydrostatic pressure. Inasmuch

[36] These axes are also employed in the API Spec 11D1 [55] presentation of an accessory envelope. Some embodiments of this presentation may rotate the figure 90° counterclockwise.

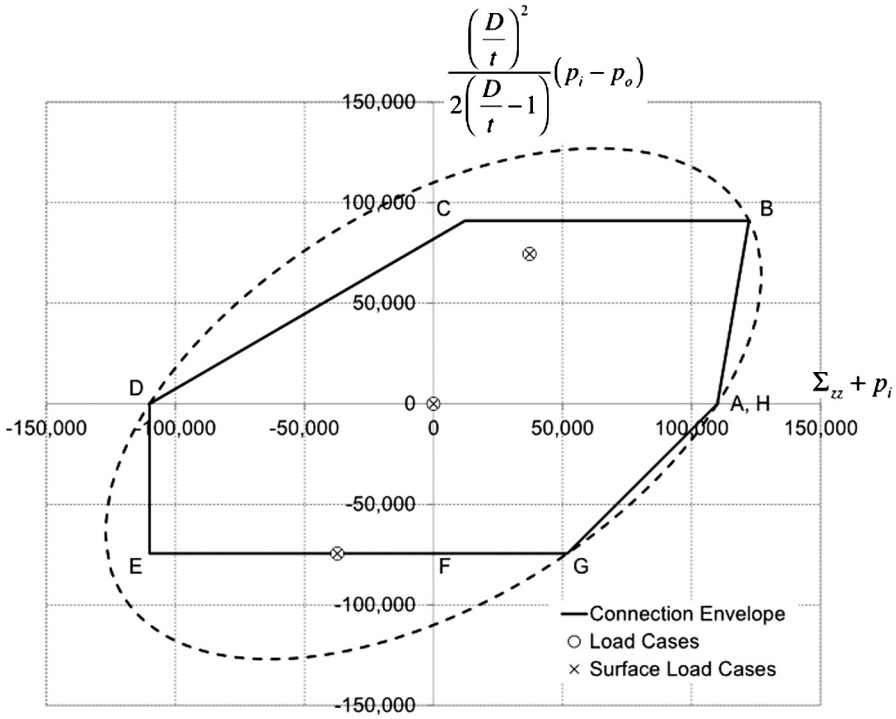

Figure 9.16 ***Connection evaluation envelope plotted with the von Mises yield criterion expressed in terms of*** $S_{ZZ} + p_i$**.** The tube body ellipse is shown as a dashed curve and follows Fig. 6.13. Vertices of the envelope labeled A–H correspond to the points in Table 9.1.

as (a) the emphasis of the plot is material yield and (b) material yield is independent of hydrostatic pressure, the two load states should be compatible. The fact that they are not can, as discussed in Section 6.3.4.3 of Chapter 6, be traced to the fact that the axes of Figs. 6.14 and 9.15 do not admit a complete picture of three-dimensional yield.

In contrast to Fig. 9.15, Figs. 9.16 and 9.17 accurately portray the relation between the laboratory test of the connection in a surface experiment and the loads to which the connector will be subjected in the downhole environment. The initial condition for the downhole environment is not offset from the surface initial condition, indicating both are benign points with respect to material yield.

Given D, t and f_y, the condition of a tubular at surface conditions (initial $p = 0$ everywhere) and downhole conditions at the string bottom (initial p is the hydrostatic pressure of the surrounding fluid column) will, from the perspective of yield, be the same. This statement relies on the assumption that yield of a crystalline metal is independent of the mean stress, which in this case is the local hydrostatic pressure. Provided a tube at the two locations—surface and downhole—is subjected to the same increments of pressure (above or below hydrostatic) the equivalence vis-á-vis yield will remain.

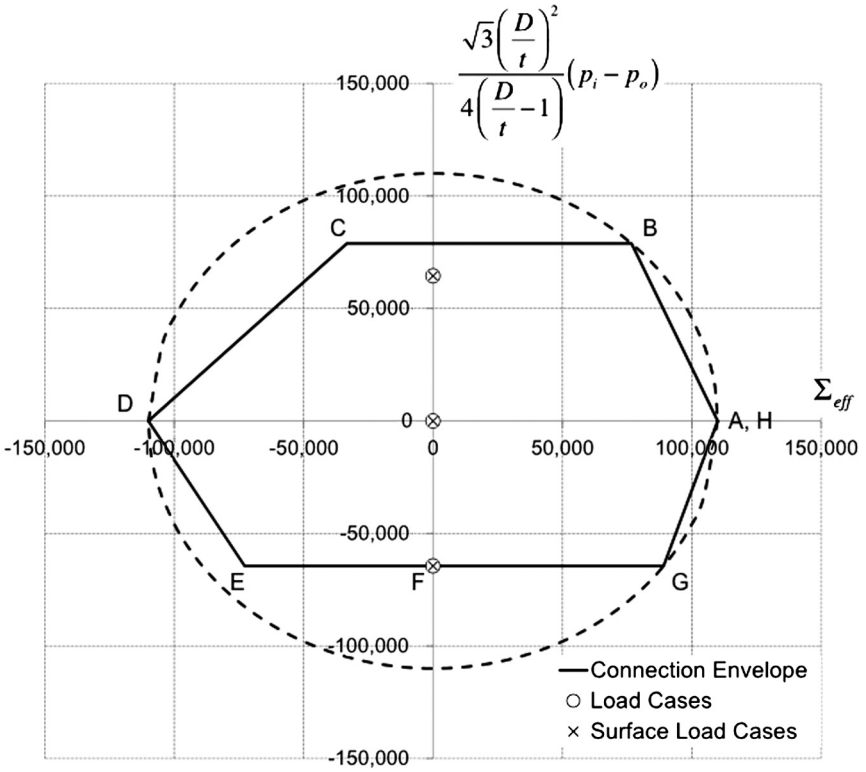

Figure 9.17 ***Connection evaluation envelope plotted with the von Mises yield criterion expressed in terms of effective stress.*** The tube body ellipse is shown as a dashed curve and follows Fig. 6.11. Vertices of the envelope labeled A–H correspond to the points in Table 9.1.

Two final, qualifying comments are in order:

- For a connector the equivalence in stress state (i.e., hydrostatic) to that of the tube body is close, but not exact. Stresses associated with assembly in the threaded region, particularly if the thread profile is tapered, will distort the stress state applicable to a simple tube. The presentations of Figs. 9.16 and 9.17 are still preferred. Fig. 9.15 implies that if one ran the tubular string deep enough, the bottom connection would structurally yield in a hydrostatic state of stress.
- The advantage of Figs. 9.16 and 9.17 over Fig. 9.15 is directly related to the formers' ability to accurately capture material yield. As is the case with many casing and tubing proprietary connections, should any portion of the part's performance envelope be governed by a limit state other than material yield, further adjustment of the load vs. envelope presentation may be necessary to allow simultaneous display of both laboratory and downhole conditions. This latter issue does not usually exist in the case of accessories. The vast majority of assemblies and subassemblies of an accessory are designed based on their resemblance to a thick-walled tube.

CHAPTER 11

Length Change and Axial Force

11.1. INTRODUCTION

Axial load resistance, in a manner similar to internal pressure resistance, is an integral part of the triaxial yield calculation and therefore does not necessitate a separate treatment. Axial load itself, however, is another matter. The axial load, once calculated, can produce significant side effects.

A recurring calculation in tubular design involves the determination of the effect of environmental change—internal pressure, external pressure, temperature—on the loads to which the tubular is subjected. These changes can affect the axial traction, and through the axial stress, affect closeness to yield (Chapter 6), resistance to internal pressure (Chapter 7), collapse resistance (Chapter 8) and the (bending) stresses associated with column stability (Chapter 10). The problem is one of interaction. The pressure and temperature changes that alter the axial stress thereby alter the resistance of the tubular to the initiating changes. In the worst case of multiple fluids and a tapered tubular string, solution of this problem can be one of trial-and-error, particularly if column buckling is involved. Here, we will leave those calculations to software and focus on understanding the pertinent mechanics with simpler examples.

11.2. LENGTH CHANGE VERSUS AXIAL FORCE

Consider a weightless tube suspended vertically with its lower end free to elongate or shorten. For reasons we shall discuss momentarily, a change in the tube's environment—for example, its temperature is increased—will induce a length change but no axial force. Now consider that same tube whose lower end is constrained from axial movement. If the same environmental change is applied to the tube, its length will not change, but an axial force will be induced.

This behavior is embedded in equations we have already visited. Consider, for example, the relation between stress and strain for an elastic body presented in Eq. (5.25), reproduced here in its one-dimensional form as

$$\breve{E}_{11} = \frac{1}{E}\Sigma_{11} + \alpha_T (T - T_0)\,. \tag{11.1}$$

In the first instance we discussed, a free body diagram will show that $\Sigma_{11} = 0$. If we increase the temperature, then Eq. (11.1) becomes

$$\breve{E}_{11} = \alpha_T (T - T_0)\,, \tag{11.2}$$

Elements of Oil and Gas Well Tubular Design
DOI: 10.1016/B978-0-12-811769-9.00011-6

so that an increase in temperature causes the tube to elongate, i.e., $\breve{E}_{11} > 0$.

Now consider the second instance sighted when both ends of the tube are constrained. In this case, $\breve{E}_{11} = 0$ and Eq. (11.1) becomes

$$0 = \frac{1}{E}\Sigma_{11} + \alpha_T (T - T_0), \quad \Sigma_{11} = -\alpha_T E (T - T_0), \tag{11.3}$$

and an increase in temperature causes the tube to go into compression, i.e., $\Sigma_{11} < 0$, with no change in length.

One final point is important to future discussion. Comparing Eqs. (11.2) and (11.3), when the tube is constrained, the stress produced in the constrained instance has the same value as it would if we had performed the following two steps:

1. Remove the constraint at the lower end of the tube and allow the tube to elongate (with a strain given by Eq. (11.2)), and then
2. Force the tube back to its position of no strain by applying a (compressive) stress equal to the value given in Eq. (11.3).

That is, when a number of environmental changes are acting to alter the axial stress state in a constrained tubular, we may compute the stress generated by first computing the potential length change from all environmental sources and then computing the axial traction necessary to push the tube back to a position of zero length change.

11.3. SOURCES OF LENGTH CHANGE

In computing length change, we will typically be integrating the effect of a local change environment over the length of the tubular

$$\Delta L = \int_{L_1}^{L_2} \breve{E}_{tt}(s)\, ds, \tag{11.4}$$

where $\breve{E}_{tt}$ is the normal strain along the axis of the tube. The interval L_1 to L_2 is an interval in the well bounded by at least one constraint. If the other end is free, as is the case of tubing in a polished bore receptacle, this is the sole calculation. If both ends are constrained, as with tubing integral to or latched to a packer or with cemented casing, determination of the length change is followed by a second calculation to determine the axial force.

Focusing on length change only for the moment, if the strain is a linear function of environmental parameter p, that is, $\breve{E}_{tt}(s) = a + bp(s)$, where a and b are constants, then

$$\Delta L = \int_L \breve{E}_{tt}(s)\, ds = \int_L \left[a + bp(s)\right] ds = aL + b\int_L p(s)\, ds, \tag{11.5}$$

where $L = L_2 - L_1$. Since we can define the average value of a parameter that depends on s as

$$\bar{p} = \frac{1}{L}\int_L p(s)ds, \tag{11.6}$$

using Eq. (11.6) in Eq. (11.5) gives

$$\Delta L = aL + b\bar{p}L = \left[a + b\bar{p}\right]L. \tag{11.7}$$

An important limitation to the application of Eq. (11.7) involves that fact that s traces measured depth, not vertical depth. Quantities such as temperature and pressure are often defined by their dependence on vertical depth. To use Eq. (11.7) in a deviated wellbore therefore requires recasting temperature/pressure as a function of measured depth.

Of the various sources of length change/axial force change pertinent to tubular design the following are prevalent.

11.3.1 Temperature

From Eq. (5.25), $\breve{E}_{11} = \alpha_T(T - T_0) = \alpha_T \Delta T$. Assuming α_T is constant, we may use Eq. (11.7) with $a = 0$, $b = \alpha_T$ and $p(s) = \Delta T(s)$ so that

$$\Delta L_T = \alpha_T \overline{\Delta T} L. \tag{11.8}$$

To summarize Eq. (11.8):[1]

- an increase in the average temperature of an unrestrained tubular induces a length increase, or, if the tubular is restrained at both ends, a compressive axial force;
- a decrease in the average temperature of an unrestrained tubular induces a length decrease, or, if the tubular is restrained at both ends, a tensile axial force.

Eq. (11.8) only addresses the first half of each of the summary bullets. The constrained conclusion was obtained from the discussion of Section 11.2.

11.3.2 Ballooning

In tubular design the term "ballooning" is associated with the effect of Poisson's ratio when loading a tube laterally with internal and external pressure. If we wish to examine

[1] A question may arise regarding the $\overline{\Delta T}$ term in Eq. (11.8)—does it represent change in average temperature or average change in temperature? From Eq. (11.6), the change in average temperature can be written as

$$\overline{\Delta T} = \frac{1}{L}\left[\int_L T(s)ds - \int_L T_0(s)ds\right] = \frac{1}{L}\int_L \left[T(s) - T_0(s)\right]ds,$$

where the first set of integrals is the change in average T's and the solitary integral to the far right is the average change in T. That is, the two expressions refer to the same quantity.

the unrestrained length change associated solely with changes in internal and external pressure, setting $\Sigma_{zz} = 0$ in Eq. (5.53) yields

$$\breve{E}_{tt} = -\frac{2\nu}{E}\frac{\Delta p_i d^2 - \Delta p_o D^2}{D^2 - d^2}, \tag{11.9}$$

and $\breve{E}_{tt}$ is linear in $p(s) = \Delta p_i(s)$ with $a = 0$ and $b = -\frac{2\nu}{E}\frac{d^2}{D^2-d^2}$ and also in $p(s) = \Delta p_o(s)$ with $a = 0$ and $b = \frac{2\nu}{E}\frac{D^2}{D^2-d^2}$. Using Eq. (11.7), we can write

$$\Delta L_B = -\frac{2\nu}{E}\frac{\overline{\Delta p_i} d^2 - \overline{\Delta p_o} D^2}{D^2 - d^2} L. \tag{11.10}$$

To summarize Eq. (11.10):

- an increase in the average internal pressure of an unrestrained tubular induces a length decrease, or, if the tubular is restrained at both ends, a tensile axial force;
- a decrease in the average internal pressure of an unrestrained tubular induces a length increase, or, if the tubular is restrained at both ends, a compressive axial force;
- an increase in the average external pressure of an unrestrained tubular induces a length increase, or, if the tubular is restrained at both ends, a compressive axial force;
- a decrease in the average external pressure of an unrestrained tubular induces a length decrease, or, if the tubular is restrained at both ends, a tensile axial force.

11.3.3 Shoulder

The term "shoulder" in this context refers to an area exposed due to a change in either internal or external diameter, or both. Typical examples of shoulders are cross-overs and the exposed cross-sectional area at the bottom of the tubular.[2] Unlike the previous two length changes, the length change due to a change in the (pressure) force on a shoulder does not depend on change in average pressure but on change in local pressure at the shoulder.

The governing equation for this length change shall prove useful not only here but also later in this discussion. From Eq. (5.25) we have

$$\breve{E}_{tt} = \frac{\Delta L}{L} = \frac{1}{E}\frac{\Delta f_t}{A}, \quad \Delta L_S = \frac{\Delta f_t L}{EA}, \tag{11.11}$$

where Δf_t is the change in axial load at the shoulder, and the A is a generic term for the cross-sectional area. Examples of the forms Eq. (11.11) can take include the following:

[2] Shoulders such as the axially exposed area of the coupling on a threaded connection are usually ignored, since (a) the two axially exposed end areas on the top and bottom of the coupling are identical and (b) the short length of the coupling means the two areas are exposed to essentially the same pressure change.

- Consider a cross-over from a tube having diameters D_u and d_u to a tube having diameters D_l and d_l, where the subscripts "u" and "l" stand for "upper" and "lower", respectively. Writing the exposed area so that positive pressure changes Δp_i and Δp_o result in an elongation of the tubulars above the cross-over

$$\Delta L_S = \frac{\left[\Delta p_i \left(d_u^2 - d_l^2\right) + \Delta p_o \left(D_l^2 - D_u^2\right)\right] L}{E\left(D_u^2 - d_u^2\right)}. \tag{11.12}$$

- A special case of Eq. (11.12) occurs at the bottom of the string where, assuming a close-ended string, $D_l = d_l = 0$, and

$$\Delta L_S = \frac{\left[\Delta p_i d^2 - \Delta p_o D^2\right] L}{E\left(D^2 - d^2\right)}, \tag{11.13}$$

or, if the tube is open-ended, $p_i = p_o = p$, and

$$\Delta L_S = \frac{\Delta p\left[d^2 - D^2\right] L}{E\left(D^2 - d^2\right)} = -\frac{\Delta p L}{E}. \tag{11.14}$$

11.3.4 Buckling

When computing length change due to sources other than buckling, we assume a stable tubular and integrate the tangential strain along its length. In the case of buckling, the mechanism is similar, but the length change we pursue is actually the shortening of the axis of the tube relative to its prebuckled state, that is, the axis about which it buckles. Since the buckling displacement is lateral to this prebuckled axis, our goal is to uncover the change in "axial" distance between the two ends of the tubular, which is not the actual tangential strain in the buckled tube.

The problem is further complicated by the fact that there exist two successive configurations in the postbuckled state of a tubular—sinusoidal buckling and helical buckling. Not only do all of these configurations admit a different calculation of buckling length change, but a buckled tubular may also have a portion of its length buckled sinusoidally and a portion buckled helically. Section 10.2.3 of Chapter 10 defines the boundaries between these two configurations.

11.3.4.1 Length change when sinusoidally buckled

For portions of the string where $f_{ch} < f_{eff} < f_{cs}$ the tubular is sinusoidally buckled. In a detailed study of sinusoidal buckling Mitchell [131,137,125] provides an answer for the length change due to sinusoidal buckling by curve fitting numerical results. The recommended formula is

$$\Delta L_{Bu} = -\frac{r_c^2}{4EIw_{eff}\cos\theta}\left(-f_{eff2} + f_{cs}\right)\left(-0.3771 f_{eff2} + 0.3668 f_{cs}\right), \tag{11.15}$$

where f_{eff2} is the effective force at the more established end of the sinusoid (the end furthest from the neutral point), and f_{cs} is the effective force at the point of initiation of sinusoidal buckling. The (algebraic) minimum value f_{eff2} can assume is f_{ch}, at which point the length change calculation should follow Section 11.3.4.2 addressing helical buckling.

11.3.4.2 Length change when helically buckled

For portions of the string where $f_{eff} < f_{ch}$ the tubular is helically buckled, and we may eliminate the helical pitch p_h from Eqs. (10.83) and (10.86) [58] as

$$\frac{\Delta L_{Bu}(s_h)}{L} = \frac{r_c^2 f_{eff}}{4EI}. \tag{11.16}$$

For the general case when f_{eff} is a function of length along the helix,

$$\Delta L_{Bu} = \frac{r_c^2}{4EI}\int_{L_1}^{L_2} f_{eff}(s_h)\, ds_h, \tag{11.17}$$

where s_h is length along the buckled helical path measured from either the neutral point (vertical well) or from the transition from a sinusoidal to a helical configuration. In most instances, s_h and the wellbore measured depth coordinate as sufficiently close that we may consider them interchangeable.

For the global material coordinate system $dZ = \mathbf{t}\cdot\mathbf{e}_3 ds_h$, so that from Eq. (10.4) we have

$$f_{eff}(s_h) = f_{eff0} - \int_0^{s_h} w_{eff}\cos\theta\, ds_h. \tag{11.18}$$

If the hole section is straight and single fluids exist inside and outside a tubular of constant cross-section, then

$$f_{eff}(s_h) = f_{eff0} - w_{eff}\cos\theta\, s_h, \tag{11.19}$$

and we can, using the change of variables $ds_h = -\frac{df_{eff}}{w_{eff}\cos\theta}$, rewrite Eq. (11.17) as

$$\Delta L_{Bu} = -\frac{r_c^2}{4EIw_{eff}\cos\theta}\int_{f_{eff1}}^{f_{eff2}} f_{eff}\, df_{eff} = -\frac{r_c^2\left(f_{eff2}^2 - f_{eff1}^2\right)}{8EIw_{eff}\cos\theta}. \tag{11.20}$$

Eq. (11.20) is applicable to helical buckling in straight sections of hole with constant tubular dimensions (and material) and with single fluids inside and outside. As an approximation, a more complex environment can be addressed by segmenting the wellbore into sections where Eq. (11.20) is applicable.

11.3.5 Self-weight

This length change is rarely used as it requires a change in the disposition of the tubular string relative to the direction of the gravity field. As the most common choice for the initial condition in a design problem is with the tubular already installed in the wellbore, there will be no change is its disposition to gravity. A notable exception to this rule is a stretch calculation (see Section 11.4) when the tubular begins the calculation lying horizontally on the rack and ends the calculation suspended in the wellbore.

From Eq. (5.112) we get

$$\frac{df_t}{ds} - \kappa f_n + q_t = \frac{d}{ds}\int_{A_s} \Sigma_{tt} dA - \kappa f_n + w_a (\mathbf{t}\cdot\mathbf{e}_3) = \frac{d}{ds}\int_{A_s} \Sigma_{tt} dA - \kappa f_n + w_a \cos\theta = 0, \quad (11.21)$$

where we have set the weight per length of the tubular as the only contributor[3] to the distributed axial force $\mathbf{q} = w_a \mathbf{e}_3$, and θ is the inclination of the wellbore tangent $\mathbf{t}$ from downward vertical,[4] i.e., $\cos\theta\, ds = dZ$. If we ignore the threaded connection, we can write $w_a = \frac{g}{g_c}\rho A_s$, but here we choose to retain w_a to accommodate a specified mass per length value.

If we use Eq. (5.101) in the first term in Eq. (11.21), then

$$\begin{aligned}
\frac{d}{ds}\left(\int_{A_s} \Sigma_{tt} dA\right) &= E\frac{d}{ds}\left(\int_{A_s}\left[\breve{E}_{tt0}(s) + \gamma\kappa\right] dA\right) \\
&= E\frac{d}{ds}\left(\breve{E}_{tt0}(s) A_s + \kappa \underbrace{\int_{A_s} \gamma dA}_{=0,\ \text{see Eq. (5.104)}}\right) \\
&= EA_s \frac{d\breve{E}_{tt0}(s)}{ds}.
\end{aligned} \quad (11.22)$$

With Eq. (11.22), Eq. (11.21) becomes

$$EA_s d\breve{E}_{tt0}(s) - \kappa f_n ds + w_a \cos\theta\, ds = 0, \quad (11.23)$$

or

$$\breve{E}_{tt0}(s) = \frac{1}{EA_s}\left[\int_s \kappa f_n ds - w_a \int_s \cos\theta\, ds\right]. \quad (11.24)$$

[3] Ignoring axial friction as we have implies either (a) all friction is nonaxial, as is the case when rotating off bottom, or (b) the tube/wall contact is assumed frictionless.

[4] Sign convention is important and a bit confusing. If we are traveling along ds from the bottom or deeper end of the tubular string to its top such that ds is directed in the general direction of decreasing $X_3 = Z$, then $\cos\theta = \frac{dZ}{ds} \le 0$. If, on the other hand, we choose to travel from the top of the tubular to its bottom, then $\cos\theta = \frac{dZ}{ds} \ge 0$ as expected.

Table 11.1 Stretch example—initial and final states

Variable	Initial	Final[a]	Change (Δ)
T_{top}	70	70	0
T_{bot}	70	$70 + 1.1 \times \frac{10.000}{100} = 180$	110
$\bar{T}$	70	$\frac{70+180}{2} = 125$	55
p_{top}	0	0	0
p_{bot}	0	$0.052 \times 10 \times 10\,000 = 5200$	5200
$\bar{p}$	0	$\frac{0+5200}{2} = 2600$	2600

[a] $0.052\ \frac{\text{psi}}{\text{ft ppg}}$ is a convenient conversion factor.

In writing Eq. (11.24) with $\breve{E}_{tt0}(0) = 0$, we have implicitly assumed that the integration begins at the bottom of the string. Integrating Eq. (11.24) and recognizing that (if ds is directed "upward") $\cos\theta \leq 0$ yields

$$\Delta L_W = \int_L \breve{E}_{tt0}(s)ds = \frac{1}{EA_s}\int_L \left\{\int_s \kappa f_n ds - w_a \Delta Z(s)\right\} ds, \tag{11.25}$$

where ΔZ is the change in vertical distance corresponding to s. As a simple example, if the wellbore is straight ($\kappa = 0$) and vertical ($\cos\theta = -1$) then $\Delta Z(s) = -s$ and Eq. (11.25) reduces to

$$\Delta L_W = \frac{w_a}{EA_s}\int_L s\, ds = \frac{w_a L^2}{2EA_s}, \quad \text{vertical wellbore.} \tag{11.26}$$

11.4. EXAMPLE PROBLEM—STRETCH

A 5.500 in., 20 $\frac{\text{lb}_\text{m}}{\text{ft}}$ (0.361 in. wall thickness) tubing string is run in a straight, vertical wellbore to 10 000 ft—see Fig. 11.1. The tubing is run in a 10 ppg completion fluid. The surface temperature is 70 °F and the temperature gradient is 1.1 $\frac{\text{°F}}{100\ \text{ft}}$. Compute the length change of the tubing from its horizontal position on the surface rack to its vertical position in the wellbore.

The initial state of the tubing is its surface configuration—horizontal at 70 °F and exposed to zero pressure. The final state of the tubing is hanging under its own weight in the downhole pressure and temperature environment.

11.4.1 Preliminary calculations

A number of preliminary calculations are in order. In particular, the initial and final states can be summarized as in Table 11.1. The common units chosen for this problem are lb_f, in. and °F. All entries in the table are expressed in these common units to ease substitution in the length change formulas.

For steel $\gamma_s = 0.2836\ \frac{\text{lb}_\text{m}}{\text{in}^3}$, $\alpha_T = 6.9 \times 10^{-6}\ \frac{1}{\text{°F}}$, $E = 30 \times 10^6$ psi and $\nu = 0.3$.

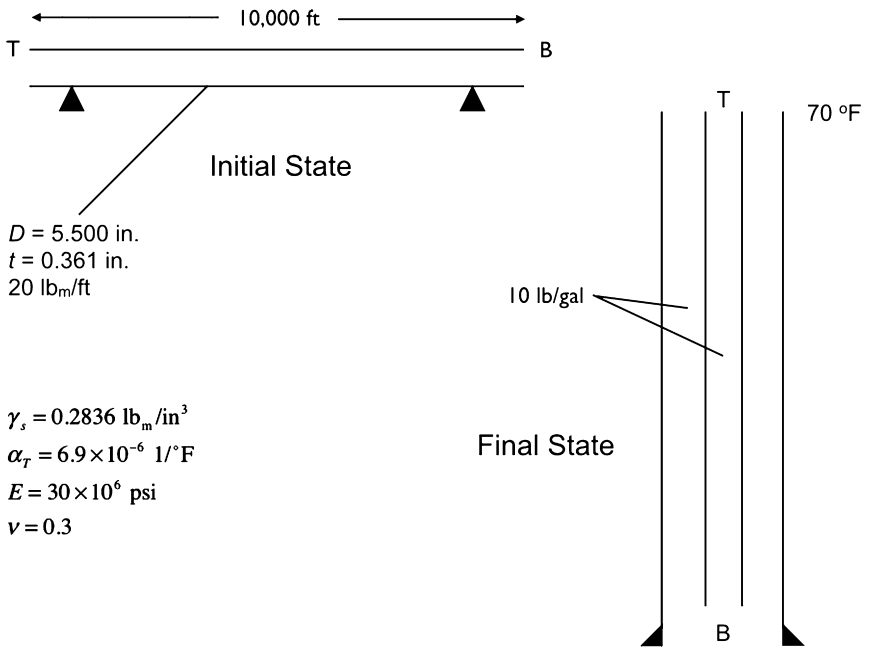

Figure 11.1 ***Schematic for length change example calculation.*** A tubing string originally lying horizontally at the well site is lowered into a vertical wellbore; T = top, B = bottom.

11.4.2 Length changes

The following length changes are pertinent to this problem.

11.4.2.1 Temperature change

The formula for length change associated with average change in temperature along the free length of the tubular is Eq. (11.8). For the example problem, from Table 11.1 we have

$$\Delta L_T = 6.9 \times 10^{-6} \frac{1}{°\text{F}} \times 55\,°\text{F} \times \left(12 \frac{\text{in}}{\text{ft}} \times 10\,000\,\text{ft}\right) = 45.5\,\text{in.} \tag{11.27}$$

11.4.2.2 Ballooning

The formula for length change associated with average change in internal and external pressure along the free length of the tubular is Eq. (11.10). For the example problem, the internal and external pressures are equal in both the initial and final states, so that $\overline{\Delta p_i} = \overline{\Delta p_o} = \overline{\Delta p}$ and Eq. (11.10) can be rewritten as

$$\Delta L_B = \frac{2\nu}{E} \overline{\Delta p} L. \tag{11.28}$$

From Table 11.1 we obtain

$$\Delta L_B = \frac{2 \times 0.3}{30 \times 10^6 \text{ psi}} \times 2600 \text{ psi} \times \left(12 \frac{\text{in}}{\text{ft}} \times 10\,000 \text{ ft}\right) = 6.24 \text{ in.} \tag{11.29}$$

11.4.2.3 Exposed shoulder at bottom of string

The formula for length change associated with the local change in a concentrated force acting on the tubular is Eq. (11.14). For the example problem, from Table 11.1 we have

$$\Delta L_S = -\frac{5200 \text{ psi} \times \left(12 \frac{\text{in}}{\text{ft}} \times 10\,000 \text{ ft}\right)}{30 \times 10^6 \text{ psi}} = -20.8 \text{ in.} \tag{11.30}$$

11.4.2.4 Buckling

In order for the tube to experience a length change due to buckling, the tube must be buckled. As illustrated in Section 10.2.4.1 of Chapter 10, an open-ended tube suspended vertically in a fluid will not buckle provided the material of the tube is denser than the fluid in which it is suspended. Therefore

$$\Delta L_{Bu} = 0. \tag{11.31}$$

11.4.2.5 Self-weight

The formula for length change associated with a tube's self-weight for a straight, vertical wellbore is Eq. (11.26). Since we have been provided no information on a connection, setting $w_a = \gamma_s A_s$ yields

$$\Delta L_W = \frac{\gamma_s L^2}{2E}. \tag{11.32}$$

For this example problem,

$$\Delta L_W = \frac{0.2836 \frac{\text{lb}_\text{m}}{\text{in}^3} \left(12 \frac{\text{in}}{\text{ft}} \times 10\,000 \text{ ft}\right)^2}{2 \times 30 \times 10^6 \text{ psi}} = 68.1 \text{ in.} \tag{11.33}$$

11.4.2.6 Net length change

The net length change of the tubing string due to stretch is the algebraic sum of the results of Eqs. (11.27), (11.29), (11.30) and (11.33), namely

$$\Delta L_{Total} = \Delta L_T + \Delta L_B + \Delta L_S + \Delta L_W = 45.5 + 6.24 - 20.8 + 68.1 = 99.0 \text{ in.} \tag{11.34}$$

The following observations are pertinent to this example stretch calculation:

- As suggested in Section 11.3.5, this is the sole time in this book that the length change due to self-weight ΔL_W will be calculated. In all other problems involving

changes in the pressure/temperature environment the initial condition will correspond to a time after the tubular has been run into the wellbore.

- The length changes due to temperature change and ballooning, ΔL_T and ΔL_B, respectively, accumulate effects that are occurring along the entire length of the string. Their values therefore depend on averages that account for ΔT's and Δp's occurring everywhere along the tubular.
- The ballooning length change is, at first view, slightly counterintuitive. If the same fluid density is both inside and outside the tubular, why is there a ballooning effect? A review of Eq. (11.10) indicates that changes in internal pressure are weighted by d^2, whereas external pressure changes are weighted by D^2. Equal pressure changes inside and outside the tubular will favor the external pressure change and result in a lengthening of the tubular.
- The shoulder length change ΔL_S accounts for the effects of a local external traction at the bottom of the string. It therefore uses the local pressure change at that location, not an average.
- Reviewing the formulas used in this calculation, Eqs. (11.8), (11.28), (11.14) and (11.32), respectively, none of these equations depends on the cross-sectional area of the tube. That is, the calculation is actually applicable, not only to a 5.500 in., 20 $\frac{\text{lb}_\text{m}}{\text{ft}}$ tubular, but to any tubular, provided the tubular is run in the same environment and is of the same material and length.[5]
- A stretch table or calculator may not include the effect of temperature. In this example calculation temperature change accounts for almost one-half the stretch of the tubular, which suggests temperature effects should not be ignored.

11.4.2.7 Excursion—computing intermediate axial force

It will often be necessary in design calculations to compute the axial force at a depth between the two ends of the tubular. For example, one may wish to compute axial load to check the integrity of a threaded connection or to adjust collapse resistance for the presence of tension. To illustrate the process, we will use the tubular in the current stretch problem. Assume we wish to know the tension in the tubular string at a depth of 7500 ft immediately after the string is run in the wellbore.

As preliminary calculations we need the cross-sectional area of the tube and its plain end weight per length. The cross-sectional area is

$$A_s = \frac{\pi}{4}\left[(5.500\,\text{in.})^2 - (5.500\,\text{in.} - 2 \times 0.361\,\text{in.})^2\right] = 5.828\,\text{in}^2.$$

[5] Often published stretch tables report a number denoted the "stretch constant" that is associated with a particular size and wall thickness. The stretch constant is usually an expression of Eq. (11.11), $\Delta L_S = \frac{f_t L}{EA}$, for example, in terms of inches stretched when a 1000 ft tubular is loaded with 1000 lb_f.

The plain end weight is[6]

$$w_a = \gamma_s A_s = 0.2836 \frac{\text{lb}_\text{f}}{\text{in}^3} \times 5.828\,\text{in}^2 \times 12 \frac{\text{in}}{\text{ft}} = 19.83 \frac{\text{lb}_\text{f}}{\text{ft}}.$$

Fig. 11.2 illustrates the calculation of intermediate axial force. We create a free body diagram using only the portion of the tubular string we wish to examine—in this instance, the lower 2500 ft. The three forces acting on the free body are:

- The force due to hydrostatic pressure acting on the shoulder (exposed area) at the bottom of the string f_{bot}. This is the same force used in the calculation above of length change due to a shoulder, and its value is

$$f_{bot} = p_{bot} A_s = 5200\,\text{psi} \times 5.828\,\text{in}^2 = 30\,306\,\text{lb}_\text{f}. \tag{11.35}$$

- The (air) weight of tubular hanging below the point of investigation

$$f_W = w_a L = 19.83 \frac{\text{lb}_\text{f}}{\text{ft}} \times 2500\,\text{ft} = 49\,575\,\text{lb}_\text{f}. \tag{11.36}$$

- The internal traction f_t exposed when we imaginarily cut the tubular at 7500 ft to produce the free body diagram.

Summing forces in the diagram, arbitrarily choosing up as positive, yields

$$f_t - f_W + f_{bot} = 0, \quad f_t = f_W - f_{bot} = 49\,575\,\text{lb}_\text{f} - 30\,306\,\text{lb}_\text{f} = 19\,269\,\text{lb}_\text{f}, \tag{11.37}$$

which is the axial force internal to the tubular but external to the free body diagram, supporting the portion of the string below 7500 ft.

The answer given in Eq. (11.37) is not the answer one would get by computing the buoyed weight of tubular string below the point of interest.[7] Archimedes' principle is not applicable when computing the intermediate internal axial force because the entire tubular of interest is not submerged in fluid. As indicated in Fig. 11.2, the location of f_t is internal to the tubular cross-section and therefore not exposed to fluid pressure. To convince oneself of this point, consider a location in the string that is just a fraction of an inch above the bottom of the tubular. We know that at that location the tubular is in compression and the axial force is very close in value to $-f_{bot}$. Yet if we were to calculate the axial force at that same point using the buoyancy factor, the answer would be a small

[6] The specified mass of a joint of 5.500 in. pipe with 0.361 in. wall thickness is 20.00 $\frac{\text{lb}_\text{m}}{\text{ft}}$. The specified value includes the weight removed to machine two pins on the tube and the weight added when a coupling is attached. Further, when the first calculations of specified mass were made, the length of a standard joint was 20 ft.

[7] The author was first exposed to the importance of this paragraph to tubular design calculations in a class taught by Charles M. Prentice of Prentice Training Company.

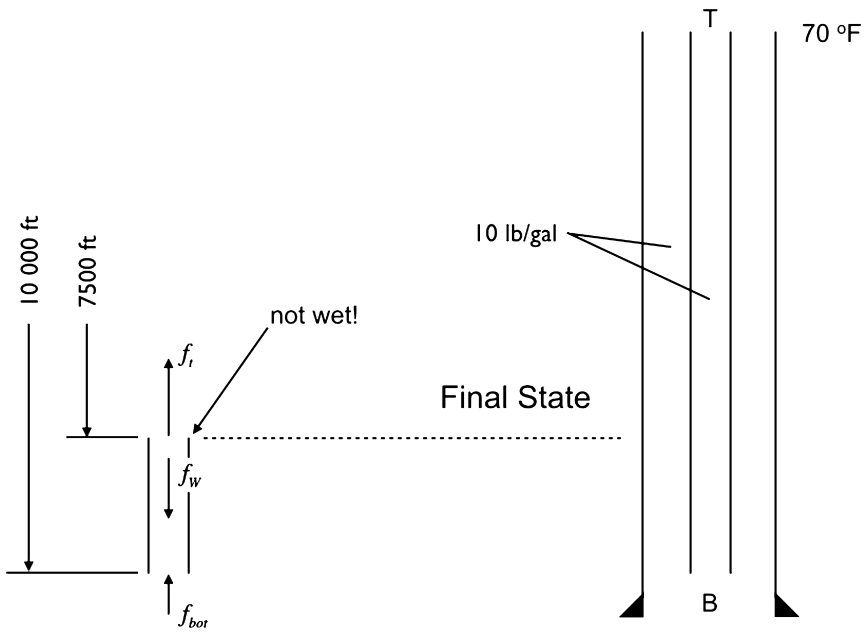

Figure 11.2 ***The importance of constructing a free body diagram to compute axial force.***

positive number. The only place in the string where a calculation using buoyancy factor will provide the correct answer is the top of the string, since there the "pressure" acting on the surface associated with f_t is zero.

11.5. EXAMPLE PROBLEM—HYDRAULIC-SET PACKER

Once landed in the wellhead, the tubing of Section 11.4 with internal diameter 4.778 in. is fixed at 9500 ft by activating the slips of a packer whose setting procedure is characterized as "hydraulic-set"—see Fig. 11.3. The pressure at which the slips engage the adjacent casing is 2500 psi; the final pressure of the packer setting sequence is 5000 psi. The plug at which the internal pressure acts is at 9700 ft. Determine the length change and associated increment in axial load associated with the packer setting sequence.

11.5.1 Preliminary calculations

A hydraulic setting sequence consists of setting a plug in the tubing at a depth greater than or equal to that of the packer. The tubing is then internally pressured, activating the packer slips and "attaching" the packer to the casing as the slips engage. Length changes associated with activating the slips induce an incremental axial force in the tubing that remains when the setting pressure is removed.

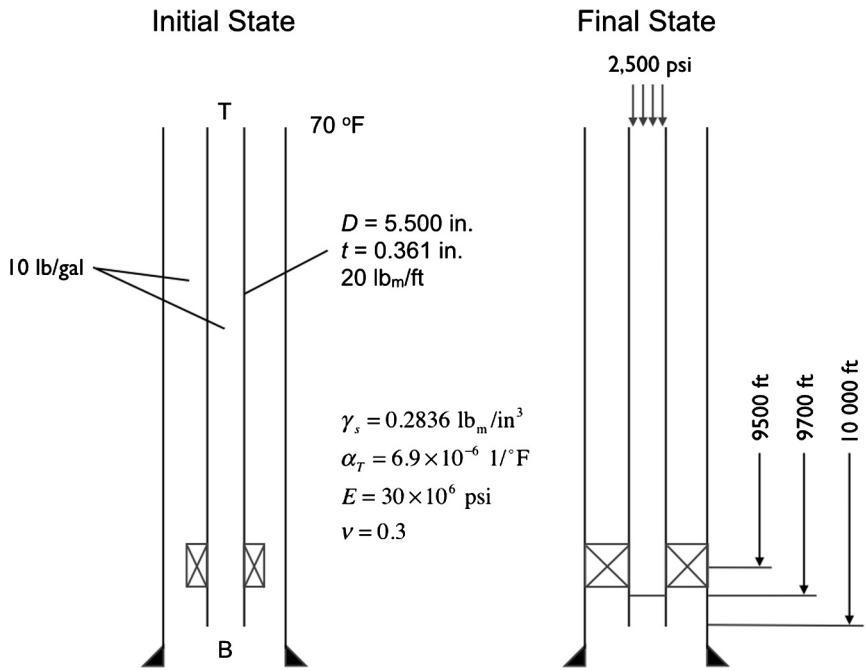

Figure 11.3 ***Schematic for hydraulic-set packer example calculation.***

For future reference, the internal cross-sectional area of the tubing is

$$A_i = \frac{\pi}{4} d^2 = \frac{\pi}{4} (4.778\,\text{in.})^2 = 17.930\,\text{in}^2, \tag{11.38}$$

and the external cross-sectional area of the tubing is

$$A_o = \frac{\pi}{4} D^2 = \frac{\pi}{4} (5.500\,\text{in.})^2 = 23.758\,\text{in}^2. \tag{11.39}$$

In this instance, we are only interested in the incremental changes in the state of the tubing since it was hung in the wellhead. The initial state is therefore equivalent to the final state in the stretch problem of Section 11.4. The final state corresponds to the initial engagement of the packer slips when the tubing stops moving relative to the casing. This implies that the final pressure in the packer setting sequence plays no role in the axial force induced in the tubing. Essentially, once the packer slips engage the tubing above the packer goes through a cycle—2500 psi → 5000 psi → 2500 psi—with the same initial and final states. Although force increments will be generated in the tubing above the packer during the excursion from 2500 psi to 5000 psi, those force and length changes will be lost as the pressure returns from 5000 psi to 2500 psi. Tubing above the packer regains the state associated with slip contact with the casing. Once

Table 11.2 Hydraulic-set packer example—initial and final states

Variable	Initial	Final[a]	Change (Δ)
T_{top}	70	70	0
T_{bot}	180	180	0
$\bar{T}$	125	125	0
p_{i-top}	0	2500	2500
p_{i-bot}	$0.052 \times 10 \times 9500 = 4940$	$4940 + 2500 = 7440$	2500
$\bar{p}_i$	2740	4970	2500
p_{o-top}	0	0	0
p_{o-bot}	$0.052 \times 10 \times 9500 = 4940$	4940	0
$\bar{p}_o$	2740	2740	0

[a] $0.052\ \frac{\text{psi}}{\text{ft ppg}}$ is a convenient conversion factor.

the setting pressure is removed, tubing below the packer returns to the state before the packer setting operation began.

The initial and final states for this problem are summarized as in Table 11.2. The common units chosen for this problem are lb_f, in. and °F. All entries in the table are expressed in these common units to ease substitution in the length change formulas. The "bottom" of the string is, for this problem, 9500 ft, the depth of the packer.

11.5.2 Length changes

The following length changes are pertinent to this problem.

11.5.2.1 Ballooning

The formula for length change associated with average change in internal and external pressure along the free length of the tubular is Eq. (11.10). From Table 11.2 we get

$$\Delta L_B = -\frac{2 \times 0.3}{30 \times 10^6\,\text{psi}} \times \frac{2500\,\text{psi} \times 17.930\,\text{in}^2}{23.758\,\text{in}^2 - 17.930\,\text{in}^2} \times \left(12\,\frac{\text{in}}{\text{ft}} \times 9500\,\text{ft}\right) = -17.536\,\text{in}. \tag{11.40}$$

11.5.2.2 Exposed shoulder at depth of plug

The formula for length change associated with the local change in a concentrated force acting on the tubular is Eq. (11.11). For the example problem, the only concentrated axial force is that due to the internal setting pressure acting on the plug at 9700 ft. From Table 11.2 we have

$$\Delta L_S = \frac{2500\,\text{psi} \times 17.930\,\text{in}^2 \times 12\,\frac{\text{in}}{\text{ft}} \times 9500\,\text{ft}}{30 \times 10^6\,\text{psi} \times \left(23.758\,\text{in}^2 - 17.930\,\text{in}^2\right)} = 29.227\,\text{in}. \tag{11.41}$$

Note that Eq. (11.41) uses 9500 ft for L, not 9700 ft.

11.5.2.3 Net length change

The net length change of the tubing string above the packer due to the packer setting procedure is the algebraic sum of the results of Eqs. (11.40) and (11.41), namely

$$\Delta L_{Total} = \Delta L_B + \Delta L_S = -17.536\,\text{in.} + 29.227\,\text{in.} = 11.691\,\text{in.} \tag{11.42}$$

11.5.2.4 Excursion—combining ballooning and exposed shoulder effects

Examination of Eqs. (11.10) and (11.11) indicates that for the case of the hydraulic-set packer

$$\Delta L_{hydraulic} = \Delta L_B + \Delta L_S = -\frac{2\nu}{E}\frac{\overline{\Delta p_i} A_i L}{A_o - A_i} + \frac{\Delta p_i A_i L}{E(A_o - A_i)} = \frac{1-2\nu}{E}\frac{\Delta p_i A_i}{A_o - A_i} L, \tag{11.43}$$

where we recognize that in this instance $\overline{\Delta p_i} = \Delta p_i$. Since $1 - 2\nu > 0$, one should expect an incremental tension associated with setting a hydraulic packer.

11.5.3 Incremental axial force

At this point in the packer setting sequence the internal pressure[8] has been applied with an ensuing length change of 11.691 in. As the internal pressure is lowered from 2500 psi to 0 psi the inclination of the tubing is to recover this length change. This is not possible, however, due to the restraint of the packer slips. The effect is identical to a scenario where, with an applied axial force, one stretches the tubing 11.691 in. This axial force is determined by solving Eq. (11.11) for Δf_t, where now Δf_t is an axial tension rather than a pressure applied at an internal plug

$$\Delta f_t = \frac{E A_s \Delta L_{Total}}{L}, \tag{11.44}$$

or

$$\Delta f_t = \frac{30 \times 10^6\,\text{psi} \times \left(23.758\,\text{in}^2 - 17.930\,\text{in}^2\right) \times 11.691\,\text{in.}}{12\,\frac{\text{in}}{\text{ft}} \times 9500\,\text{ft}} = 17\,930\,\text{lb}_\text{f}. \tag{11.45}$$

This incremental tension of 17 930 lb_f is a permanent prestress in the tubing applicable to the remainder of the life of the string.

[8] Recall that the net effect of the packer setting sequence can be fully realized by only considering the pressure necessary to initiate contact between the packer slips and the adjacent casing, i.e., restrain movement of the packer.

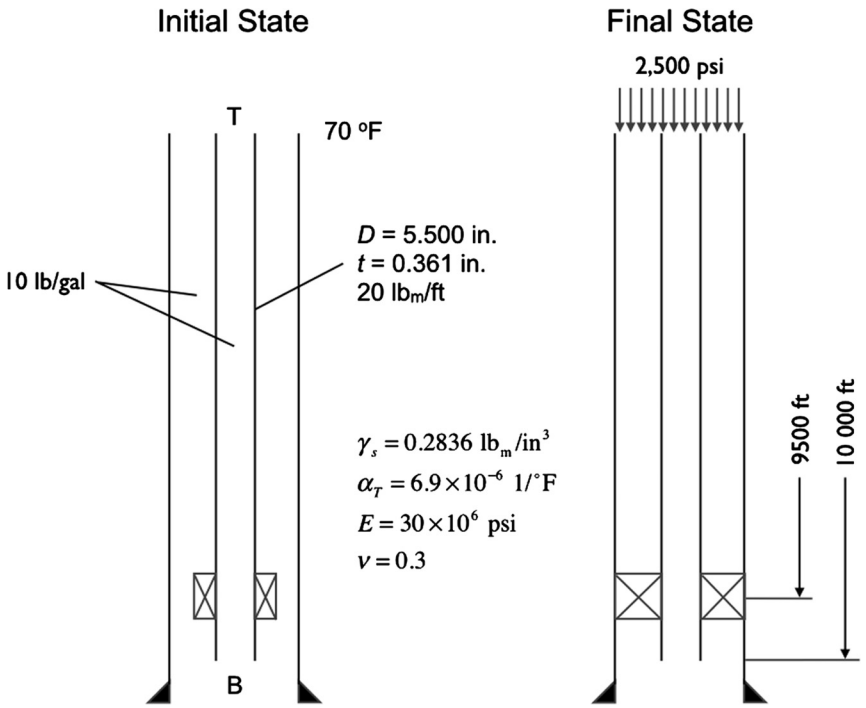

Figure 11.4 ***Schematic for hydrostatic-set packer example calculation.***

11.6. EXAMPLE PROBLEM—HYDROSTATIC-SET PACKER

We wish to work the same problem as Section 11.5, only this time the tubing is fixed at 9500 ft by activating the slips of a packer whose setting procedure is characterized as "hydrostatic-set"—see Fig. 11.4. The pressure at which the slips engage the adjacent casing is 2500 psi; the final pressure of the packer setting sequence is 5000 psi. Determine the length change and associated increment in axial load associated with the packer setting sequence.

11.6.1 Preliminary calculations

A hydrostatic setting sequence consists of pressuring the entire production tubing/production casing cavity, activating the packer slips and "attaching" the packer to the casing as the slips engage. No plug is required in the tubing. Once more, length changes associated with activating the slips induce an incremental axial force in the tubing that remains when the setting pressure is removed.

The internal and external cross-sectional areas of the tubing are identical to those in the calculation in Section 11.5, $A_i = 17.930\,\text{in}^2$, $A_o = 23.758\,\text{in}^2$.

Table 11.3 Hydrostatic-set packer example—initial and final states

Variable	Initial	Final[a]	Change (Δ)
T_{top}	70	70	0
T_{bot}	180	180	0
$\bar{T}$	125	125	0
p_{i-top}	0	2500	2500
p_{i-bot}	$0.052 \times 10 \times 9500 = 4940$	$4940 + 2500 = 7440$	2500
$\bar{p}_i$	2740	4970	2500
p_{o-top}	0	2500	2500
p_{o-bot}	$0.052 \times 10 \times 9500 = 4940$	$4940 + 2500 = 7440$	2500
$\bar{p}_o$	2740	4970	2500

[a] $0.052\ \frac{\text{psi}}{\text{ft ppg}}$ is a convenient conversion factor.

In this instance, we are only interested in the incremental changes in the state of the tubing since it was hung in the wellhead. The initial state is, as with the hydraulic-set packer, equivalent to the final state in the stretch problem of Section 11.4. The final state corresponds to the initial engagement of the packer slips when the tubing stops moving relative to the casing. In a manner similar (but not identical) to the hydraulic-set packer, portions of the string above and below the packer traverse a cycle from setting pressure to final pressure back to setting pressure, and any length change and axial force associated with the setting-to-final pressure cycle disappears. Tubing above the packer regains the state associated with slip first contact with the casing. Once the setting pressure is removed, tubing below the packer returns to the state before the packer setting operation began.

The initial and final states for this problem are summarized as in Table 11.3. The common units chosen for this problem are lb_f, in. and °F. All entries in the table are expressed in these common units to ease substitution in the length change formulas. The "bottom" of the string is, for this problem, 9500 ft, the depth of the packer.

11.6.2 Length changes

The following length changes are pertinent to this problem.

11.6.2.1 Ballooning

The formula for length change associated with average change in internal and external pressure along the free length of the tubular is Eq. (11.10). For the example problem, the average internal and external pressure increments are equal, so that $\overline{\Delta p_i} = \overline{\Delta p_o} = \overline{\Delta p}$ and Eq. (11.10) can be rewritten as

$$\Delta L_B = \frac{2\nu}{E}\overline{\Delta p} L. \tag{11.46}$$

From Table 11.3 we have

$$\Delta L_B = \frac{2 \times 0.3}{30 \times 10^6\,\text{psi}} \times 2500\,\text{psi} \times \left(12\,\frac{\text{in}}{\text{ft}} \times 9500\,\text{ft}\right) = 5.700\,\text{in.} \tag{11.47}$$

11.6.2.2 Exposed shoulder at bottom of tubing

The formula for length change associated with the local change in a concentrated force acting on the tubular is Eq. (11.11). For the example problem, the only concentrated incremental axial force is that due to the applied setting pressure[9] acting at the bottom of the tubing but transmitted undiminished to the depth of the packer, $f_t = -\Delta p_{bot} A_s$, a compression. Substituting this value of f_t in Eq. (11.11) yields

$$\Delta L_S = -\frac{\Delta p_{bot} L}{E}. \tag{11.48}$$

From Table 11.3 we get

$$\Delta L_S = -\frac{2500\,\text{psi} \times 12\,\frac{\text{in}}{\text{ft}} \times 9500\,\text{ft}}{30 \times 10^6\,\text{psi}} = -9.500\,\text{in.} \tag{11.49}$$

11.6.2.3 Net length change

The net length change of the tubing string above the packer due to the packer setting procedure is the algebraic sum of the results of Eqs. (11.47) and (11.49), namely

$$\Delta L_{Total} = \Delta L_B + \Delta L_S = 5.700\,\text{in.} - 9.500\,\text{in.} = -3.800\,\text{in.} \tag{11.50}$$

11.6.2.4 Excursion—combining ballooning and exposed shoulder effects

Examination of Eqs. (11.46) and (11.48) indicates that for the case of the hydrostatic-set packer

$$\Delta L_{hydrostatic} = \Delta L_B + \Delta L_S = \frac{2\nu}{E}\overline{\Delta p} L - \frac{\Delta p_{bot} L}{E} = -\frac{1 - 2\nu}{E}\Delta p L, \tag{11.51}$$

where $\Delta p = \overline{\Delta p} = \Delta p_{bot}$ is the applied surface pressure. Since $1 - 2\nu > 0$, one should expect an incremental compression associated with setting a hydraulic packer.

11.6.3 Incremental axial force

At this point in the packer setting sequence the pressure[10] has been applied with an ensuing length change of −3.800 in. As the pressure is lowered from 2500 psi to 0 psi the

[9] Here referred to as Δp_{bot}, where $\Delta p_{bot} = \Delta p_{i-bot} = \Delta p_{o-bot}$.

[10] Recall that the net effect of the packer setting sequence can be fully realized by only considering the pressure necessary to initiate contact between the packer slips and the adjacent casing, i.e., restrain movement of the packer.

inclination of the tubing is to recover this length change. This is not possible, however, due to the restraint of the packer slips. The effect is identical to a scenario where, with an applied axial force, one compresses the tubing 3.800 in. This axial force is determined by solving Eq. (11.11) for Δf_t, where now Δf_t is an axial tension rather than a pressure applied at an internal plug

$$\Delta f_t = \frac{EA_s \Delta L_{Total}}{L}, \tag{11.52}$$

or

$$\Delta f_t = \frac{30 \times 10^6\,\text{psi} \times \left(23.758\,\text{in}^2 - 17.930\,\text{in}^2\right) \times (-3.800)}{12\,\frac{\text{in}}{\text{ft}} \times 9500\,\text{ft}} = -5828\,\text{lb}_\text{f}. \tag{11.53}$$

This incremental compression of $-5828\,\text{lb}_\text{f}$ is a permanent prestress in the tubing applicable to the remainder of the life of the string.

11.6.3.1 Buckling check

The calculation in Eq. (11.53) assumes that the only length changes associated with response of the tubing as the setting pressure is released are those due to ballooning and shoulder force. It is important to recognize, however, that is it possible for the tubing above a hydrostatic-set packer to be buckled when the setting pressure is released.[11] The incremental, axial restrain force calculated in Eq. (11.53) may render the effective force at the depth of the packer negative and thus buckle the tubing.

The initial axial force at the packer depth in the tubing following landing, but prior to setting the packer is[12]

$$\begin{aligned} f_t = &-0.052\,\frac{\text{psi}}{\text{ft ppg}} \times 10.0\,\text{ppg} \times 10\,000\,\text{ft} \times \left(23.758\,\text{in}^2 - 17.930\,\text{in}^2\right) \\ &+ 20.00\,\frac{\text{lb}_\text{f}}{\text{ft}} \times (10\,000\,\text{ft} - 9500\,\text{ft}) = -20\,306\,\text{lb}_\text{f}. \end{aligned} \tag{11.54}$$

Including the incremental axial force from the installation of the hydrostatic-set packer, the axial force following packer installation is $-20\,306\,\text{lb}_\text{f} - 5828\,\text{lb}_\text{f} = -26\,134\,\text{lb}_\text{f}$ and the effective force is

$$\begin{aligned} f_{eff} &= -26\,134\,\text{lb}_\text{f} - 0.052\,\frac{\text{psi}}{\text{ft ppg}} \times 10.0\,\text{ppg} \times 9500\,\text{ft}\left(17.930\,\text{in}^2 - 23.758\,\text{in}^2\right) \\ &= 2656\,\text{lb}_\text{f}. \end{aligned} \tag{11.55}$$

[11] Although the lower end of the tubing will be in compression during the *application* of the setting pressure, the tubing will not buckle. At all times, the internal and external pressure at the bottom of the tubing are identical so that $f_{eff} = f_t - (p_i A_i - p_o A_o)$ is $f_{eff} = -p(A_o - A_i) - (pA_i - pA_o) = 0$, that is, the neutral point is at the bottom of the string.

[12] This calculation is identical to that discussed in Section 11.4.2.7.

Since f_{eff} is positive at the packer, following the setting sequence for this packer the production tubing will not be buckled. If the tubing were buckled at the packer, it would be necessary to perform a (possibly trial-and-error) calculation along the following lines:

1. From Eq. (11.55) and Section 11.3.4, calculate the length due to buckling.
2. Add this buckled length to the total length change in Eq. (11.50).
3. Compute a new axial force corresponding to this length change using Eq. (11.52).
4. Use the newly calculated axial force f_t to repeat the buckling check.

Repeat the above process until a suitable tolerance is reached between two successive calculations.

CHAPTER 12

Design Loads

12.1. INTRODUCTION

To this point the focus has been on the response and resistance of a tubular to imposed internal pressure, external pressure, temperature and axial force. Only brief attention has been paid to the origin of such loads in an oil or gas well. The purpose of this chapter is to bring closure to the issue of load definition by offering insight into the well operations or environment from which a set of pressure, temperature and force distributions may develop. Such a combination of loads is termed a load case.

Internal and external pressure are typically defined by either a surface or bottomhole pressure and the fluid gradient that is to be, respectively, either added or subtracted to yield a local pressure value. Both the absolute values of the internal and external pressures and the changes they represent from a defined initial state are important.

Similarly with temperature, both the absolute value of the temperature and its change from the initial state is considered. The former usually has a material effect, such as lowering the yield stress of the tubular or influencing the final strength of the cement sheath, whereas the latter is indirectly related to axial force through the tubular's attempt to change dimensions with the temperature change.

Axial loads may be distributed (gravity) or concentrated (e.g., overpull).

The sections to follow segregate the well tubulars into three categories—surface and intermediate casing, production casing or production tubing. These categories serve as boundaries in differentiating the types of loads one can expect in a tubular's service life. Some overlap and exceptions can be expected—for example, the lower end condition on tubing in a so-called "tubingless" completion—but the general segregation below seems reasonable.

The last section of the chapter discusses design and safety factors. For deterministic design, this factor is used to emulate uncertainty in either the load or resistance side of the design relation.

12.2. THE IMPORTANCE OF TRIAXIAL YIELD

Early designs, particularly those performed by hand, checked three tube body resistance values—minimum internal yield pressure, axial yield and collapse resistance—and the connection joint strength in tension. Corresponding load values of internal pressure, external pressure and axial load were constructed. Such an approach avoids the complexity of multidimensional stress analysis, purposing to keep the design simple at the cost of accuracy. Further, loads involving changes from an initial state were rarely calculated.

Elements of Oil and Gas Well Tubular Design
DOI: 10.1016/B978-0-12-811769-9.00012-8

From previous discussions (see Chapter 11), however, we know that changes in pressure and temperature affect the axial load, and in return the axial load affects both yield and collapse resistance. That is, the quantities of pressure, temperature and axial load cannot be so easily separated, either on the load or the resistance side of the design equation. As a consequence, with regard to the tube body, we may combine consideration of minimum internal yield pressure and axial yield into the single limit state of triaxial yield. This allows us to properly assess the resistance of the tubular to the interrelated loads to which it is subjected. We no longer ask if the tubular has fallen short of an internal pressure design requirement or of an axial design requirement, but rather we ask if any point in the tube cross section or along the tube's length exceeded a three-dimensional yield limit state. Our calculations are more involved but increase the fidelity of the design.

We mention in passing that the simultaneous consideration of internal pressure and axial load in collapse design is also important. In the case of collapse, however, the design calculations are significantly complicated by consideration of a multiaxial stress state. Solution using either a spreadsheet or special-purpose software is in order.

12.3. EXPLANATION OF LOAD CASE FIGURES

The chapter contains a table summary for each of the load cases described. In viewing the tables the following notes are pertinent:

- All tables contain a figure (cf. Table 12.1), with the left-hand diagram plotting the internal and external pressure profiles as a function of vertical depth.
- The right-hand diagram in each figure offers a schematic of the relative location in the well of the tubular in focus. The focus tubular is accompanied by at least one of its neighbors. For the production tubing, this is the production casing. For casings, usually the previous string is depicted. The focus tubular is distinguished by its wider, shaded thickness.
- The right-hand figure always depicts an offshore installation with, in most cases, all tubulars returning to a surface (platform) datum marked as the rotary kelly bushing (RKB).
  - For onshore wells the mean sea level (MSL) indicator should be ignored and the mudline (ML) should be treated as the local surface of the earth.
  - For subsea completions and platforms with surface wellheads, not all tubulars return to the surface datum but may be terminated in a wellhead at the mudline. In these instances, the hydrostatic pressure plotted in the left-hand figure is usually assumed to be trapped when the seal assembly in the subsea wellhead is activated while landing the tubular string. A similar comment applies when using the load case table figures to design liners—the pressure at the liner top is the hydrostatic head of a (running) fluid column from the surface datum to the top of the liner.

- The ordinate of the left-hand plots is simply labeled "Depth." The fluid gradients are depicted as constant implying the wellbore is vertical. The plots are applicable to deviated wellbores also, provided "Depth" is interpreted as vertical depth.
- The fluid densities indicated in the left-hand plots cover the majority of well scenarios but should not be taken as proscriptive. Further, most fluid pressure distributions are linear or piecewise linear implying a static fluid column. Proper adjustments should be made in the case of a dynamic fluid condition, for example, interior to the production tubing for the injection and production load cases.
- When possible the tubing load cases distinguish between completion fluid—the fluid used to perform final completion operations prior to placing the well on production—and packer fluid—the fluid which is placed in the production tubing annulus after the completion is installed and which remains for the life of that tubing installation.
- Particularly for tubing, the consideration of multiple versions of a load case is common. This is usually traced to scenarios which may occur at different times in the life of the reservoir. A tubing designer may work with tens of load cases.

12.4. DETERMINATION OF PRESSURE DISTRIBUTION

The pressure distributions plotted in the load case summary tables of this chapter depict the pressure as a piecewise linear function of vertical depth. Depending on the compressibility of the fluid(s) in the column, that simplification may not be accurate. When necessary the simple linear distributions of the tables should be replaced by the concepts of this section.

12.4.1 Hydrostatic pressure

A drilling fluid is a combination of (usually) water, oil and weighting solids,[1,2] where for each constituent the mass density is a function of pressure and temperature. The density of a hydrocarbon gas phase is likewise a function of p and T.

Fig. 12.1 depicts a fluid mass at rest in a larger body of fluid. The fluid mass has surface area S, volume V, and is exposed to traction $-p\mathbf{n}$ due to local pressure that is everywhere on S directed in the opposite sense of the local normal $\mathbf{n}$ and body force per unit mass $\mathbf{b}_f$ due to gravity. Static equilibrium requires that the vector sum of all forces acting on the fluid mass vanish

[1] Completion and packer fluids are usually single-phase and therefore special cases of the discussion to follow.

[2] One can also consider chemicals as an additional constituent [138,139]. Although chemicals are ignored here, their inclusion is a straightforward extension of the derivations presented.

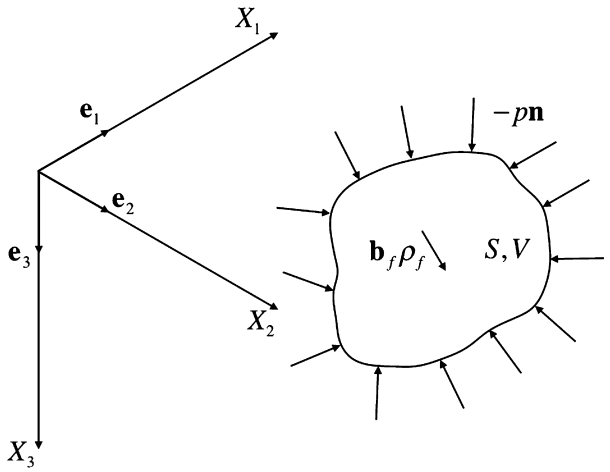

Figure 12.1 ***Equilibrium of a static fluid mass in a larger body of fluid.*** As the fluid has no shear rigidity all pressure forces are directed (in a negative sense) along the local normal to the surface of the mass. Although depicted with a single vector, the body force is distributed over the entire volume occupied by the mass.

$$\int_V \mathbf{b}_f \rho_f \, dV + \int_S p\,(-\mathbf{n})\, dS = \mathbf{0}. \tag{12.1}$$

Using Gauss's theorem for a scalar (see Footnote 11 in Chapter 5), we may convert the surface integral to a volume integral with the result

$$\int_V \mathbf{b}_f \rho_f \, dV - \int_V \nabla p \, dV = \int_V \left(\mathbf{b}_f \rho_f - \nabla p\right) dV = \mathbf{0}. \tag{12.2}$$

If Eq. (12.2) is to remain true for all volumes, its integrand must vanish, resulting in the partial differential equation

$$\mathbf{b}_f \rho_f - \nabla p = \mathbf{0}. \tag{12.3}$$

For the case when $\mathbf{b}_f$ is aligned with the X_3-axis, $\mathbf{b}_f = g\mathbf{e}_3$ and Eq. (12.3) can be written as an ordinary differential equation

$$\frac{dp}{dX_3} = \frac{g}{g_c}\rho_f, \tag{12.4}$$

where $\rho_f = \hat{\rho}_f(p, T)$ and g_c has been added for unit conversion (see Section 1.4.1 of Chapter 1). Provided the functional form of $\hat{\rho}_f$ is known, Eq. (12.4) can be (perhaps numerically) integrated to provide pressure distribution as a function of vertical depth.

12.4.1.1 Solids-laden liquids

For drilling and completion liquid mixtures, we will first consider variable density mixtures[3] and then derive the simpler model of a constant density mixture as a special case. Consider a mixture of oil, water and solids[4] that is defined by the volume percentages of the constituents at an initial state. From the conservation of mass the density/volume relation for the oil constituent is

$$\chi_{Oi} V \rho_{Oi} = (\chi_{Oi} V + \delta V_O) \rho_{Of}, \tag{12.5}$$

where χ is the volumetric fraction of constituent per volume V in the initial state and the subscripts O, i and f denote oil, the initial state and the final state, respectively. We can write similar expressions for the water (subscript W) and solid (subscript S) constituents, namely

$$\chi_{Wi} V \rho_{Wi} = (\chi_{Wi} V + \delta V_W) \rho_{Wf}, \tag{12.6}$$

$$\chi_{Si} V \rho_{Si} = (\chi_{Si} V + \delta V_S) \rho_{Sf}. \tag{12.7}$$

The initial density of the drilling fluid is its mass divided by its initial volume

$$\rho_i = \frac{\chi_{Oi} V \rho_{Oi} + \chi_{Wi} V \rho_{Wi} + \chi_{Si} V \rho_{Si}}{V} = \chi_{Oi} \rho_{Oi} + \chi_{Wi} \rho_{Wi} + \chi_{Si} \rho_{Si}. \tag{12.8}$$

The final drilling fluid density is, from Eqs. (12.5)–(12.7),

$$\rho_f = \frac{\rho_i V}{V + \delta V_O + \delta V_W + \delta V_S} = \frac{\rho_i}{1 + \frac{\delta V_O}{V} + \frac{\delta V_W}{V} + \frac{\delta V_S}{V}}. \tag{12.9}$$

Eq. (12.9) can also be written in terms of the volume fractions and densities of the constituents. Solving for the ratios $\frac{\delta V_O}{V}$, $\frac{\delta V_W}{V}$ and $\frac{\delta V_S}{V}$ in Eqs. (12.5)–(12.7), and then substituting these results into Eq. (12.9) produces

$$\rho_f = \frac{\rho_i}{1 + \chi_O \left(\frac{\rho_{Oi}}{\rho_{Of}} - 1 \right) + \chi_W \left(\frac{\rho_{Wi}}{\rho_{Wf}} - 1 \right) + \chi_S \left(\frac{\rho_{Si}}{\rho_{Sf}} - 1 \right)} = \frac{\rho_i}{\chi_O \frac{\rho_{Oi}}{\rho_{Of}} + \chi_W \frac{\rho_{Wi}}{\rho_{Wf}} + \chi_S \frac{\rho_{Si}}{\rho_{Sf}}}, \tag{12.10}$$

where we have used the fact that $\chi_O + \chi_W + \chi_S = 1$.

[3] This discussion closely follows the work of Sorelle et al. [140].

[4] We use oil, water and solids because they characterize a conventional drilling fluid. The derivation, however, is independent of the particulars on the individual constituents.

Using Eq. (12.10) in (12.4), we can determine the hydrostatic pressure between any two vertical depths Z_1 and Z_2 by

$$\int_{p_1}^{p_2}\left(\chi_O\frac{\rho_{Oi}}{\rho_{Of}}+\chi_W\frac{\rho_{Wi}}{\rho_{Wf}}+\chi_S\frac{\rho_{Si}}{\rho_{Sf}}\right)dp=\frac{g}{g_c}\int_{Z_1}^{Z_2}\rho_i dZ. \tag{12.11}$$

Integrating Eq. (12.11) and simplifying yields

$$\chi_O\rho_{Oi}\int_{p_1}^{p_2}\frac{dp}{\rho_{Of}}+\chi_W\rho_{Wi}\int_{p_1}^{p_2}\frac{dp}{\rho_{Wf}}+\chi_S\rho_{Si}\int_{p_1}^{p_2}\frac{dp}{\rho_{Sf}}=\frac{g}{g_c}\rho_i\left(Z_2-Z_1\right). \tag{12.12}$$

Eq. (12.12) readily lends itself to several special cases.

Incompressible solid

The solids normally used in drilling fluids are much less compressible than the constituent liquids. If we treat the solid component as incompressible, then $\rho_{Sf}=\rho_{Si}$ is constant, and the last integral in Eq. (12.12) becomes $\left(p_2-p_1\right)\chi_S$, which simplifies Eq. (12.12) to

$$\left(p_2-p_1\right)\left(1-\chi_O-\chi_W\right)+\chi_O\rho_{Oi}\int_{p_1}^{p_2}\frac{dp}{\rho_{Of}}+\chi_W\rho_{Wi}\int_{p_1}^{p_2}\frac{dp}{\rho_{Wf}}=\frac{g}{g_c}\rho_i\left(Z_2-Z_1\right). \tag{12.13}$$

This is the relation derived in [140]. The solid constituent still contributes to the relation, but only through (a) its volumetric fraction, $\chi_S=1-\chi_O-\chi_W$, and (b) ρ_i (see Eq. (12.8)).

Single fluid, no solids

For the case of a compressible packer fluid, we set $\chi_O=\chi_S=0$ (which implies $\chi_W=1$) and change the subscript W to PF (packer fluid) to avoid confusion with the previously discussed water constituent of a drilling fluid. Eq. (12.12) simplifies to

$$\int_{p_1}^{p_2}\frac{dp}{\rho_{PFf}}=\frac{g}{g_c}\left(Z_2-Z_1\right). \tag{12.14}$$

Eq. (12.14) is deceptively simple. The integral still involves the density function $\rho_{PFf}=\hat{\rho}_{PFf}(p,T)$, where both p and T are functions of X_3.

Incompressible constituents

If all of the fluid/solid mixture components are assumed to be incompressible, then $\rho_{Of}=\rho_{Oi}$, $\rho_{Wf}=\rho_{Wi}$ and $\rho_{Sf}=\rho_{Si}$ are all individual constants, and the three integrals take the form $\left(p_2-p_1\right)\chi_*$, where $*$ is O, W or S. Eq. (12.12) simplifies to

$$\left(p_2-p_1\right)\left(\chi_O+\chi_W+\chi_S\right)=p_2-p_1=\frac{g}{g_c}\rho_i\left(Z_2-Z_1\right). \tag{12.15}$$

That is, the difference in pressures across $Z_2 - Z_1$ is simply the vertical depth times the (constant) mixture density. The volumetric fractions of the constituents still contribute to the calculation through their role in the calculation of ρ_i (see Eq. (12.8)).

Single incompressible fluid

This is a special case of Eq. (12.15) where $\chi_O = \chi_S = 0$ (which implies $\chi_W = 1$). We again change the subscript W to PF (packer fluid) to avoid confusion with the water constituent. Eq. (12.15) simplifies to

$$p_2 - p_1 = \frac{g}{g_c}\rho_{PF}\,(Z_2 - Z_1)\,. \tag{12.16}$$

Eq. (12.16) is used extensively in this book. The assumption of a single, incompressible fluid allows us to retain the essence of the physics of the hydrostatic pressure calculation for a liquid without resorting to the complexities of a numerical solution.

12.4.1.2 Gases

The equations of state of gases are sufficiently different from liquids to require a separate treatment for the hydrostatic pressure of a gas column.

Ideal gas

Starting with the simplest equation of state—that for a perfect or ideal gas—we write

$$p\nu = \mathcal{R}T, \tag{12.17}$$

where the specific volume ν is the reciprocal of density, and the individual gas constant $\mathcal{R}$ has a value that depends on the units chosen (through its dependence on the universal gas constant $\mathcal{R}_u$—see Section 1.4.3 of Chapter 1) and the molecular mass $\mathcal{M}$ of the gas in question. For USC units, $\mathcal{R} = \mathcal{R}_u/\mathcal{M} = 1545.349\,\frac{\text{lb}_\text{f}\,\text{ft}}{\text{lb}_\text{m}\,\text{R}}/\mathcal{M}$, and for SI units, $\mathcal{R} = \mathcal{R}_u/\mathcal{M} = 8314.472\,\frac{\text{N}\,\text{m}}{\text{kg}\,\text{K}}/\mathcal{M}$.

If we multiply Eq. (12.17) by the mass m, then

$$pV = m\mathcal{R}T, \tag{12.18}$$

where V is the gas volume.

Substituting Eq. (12.17) into (12.4) and recalling that $\nu = 1/\rho$, we can write

$$\int_{p_1}^{p_2}\frac{dp}{p} = \ln p\Big|_{p_1}^{p_2} = \ln\frac{p_2}{p_1} = \frac{g}{g_c}\frac{1}{\mathcal{R}}\int_{Z_1}^{Z_2}\frac{1}{\hat{T}(Z)}\,dZ. \tag{12.19}$$

Given the temperature distribution as a function of vertical depth, Eq. (12.19) can be integrated to determine the pressure change between the vertical depths Z_1 and Z_2.

Example problem—ideal gas hydrostatic head

Derive expressions for the hydrostatic head of a gas column for (a) a constant temperature distribution and (b) a linear temperature distribution.

For a constant temperature distribution, $\hat{T}(Z) = \overline{T}$ in Eq. (12.19). Integrating gives

$$\ln \frac{p_2}{p_1} = \frac{g}{g_c} \frac{1}{\mathcal{R}\overline{T}} (Z_2 - Z_1), \quad p_2 = p_1 \exp\left[\frac{g}{g_c} \frac{1}{\mathcal{R}\overline{T}} (Z_2 - Z_1)\right]. \tag{12.20}$$

If the temperature distribution is linear, then

$$T = \hat{T}(Z) = T_1 + \gamma_T (Z - Z_1), \tag{12.21}$$

where γ_T is the temperature gradient with vertical depth. Substituting Eq. (12.21) into (12.19) yields

$$\begin{aligned} \ln \frac{p_2}{p_1} &= \frac{g}{g_c} \frac{1}{\mathcal{R}} \int_{Z_1}^{Z_2} \frac{1}{T_1 + \gamma_T (Z - Z_1)} dZ \\ &= \frac{g}{g_c} \frac{1}{\mathcal{R}\gamma_T} \ln \frac{T_1 + \gamma_T (Z_2 - Z_1)}{T_1}, \end{aligned} \tag{12.22}$$

or

$$p_2 = p_1 \left(1 + \frac{\gamma_T (Z_2 - Z_1)}{T_1}\right)^{\frac{g}{g_c} \frac{1}{\mathcal{R}\gamma_T}}. \tag{12.23}$$

If the temperature distribution in the gas column is piecewise liner, Eq. (12.23) can be used repeatedly for each linear temperature segment.

We now apply Eqs. (12.20) and (12.23) to a 15 000 ft vertical wellbore full of methane. The surface ($X_3 = Z_1$) pressure and temperature are 5000 psi and 80 °F, respectively, and the geostatic temperature gradient is 1.4 $\frac{°\text{F}}{100\,\text{ft}}$.

The molecular mass of methane is 16.04, so $\mathcal{R} = 1545.349 \frac{\text{lb}_\text{f}\,\text{ft}}{\text{lb}_\text{m}\,\text{R}} / 16.04 = 96.34 \frac{\text{lb}_\text{f}\,\text{ft}}{\text{lb}_\text{m}\,\text{R}}$. Using Eq. (1.11), $T_1 = 539.67\,\text{R}$ and, since Fahrenheit and Rankine temperature units have equal increments, $T_2 = 539.67\,\text{R} + 1.4 \frac{\text{R}}{100\,\text{ft}} \times 150\,100\,\text{ft} = 749.67\,\text{R}$.

For the case of a constant temperature distribution, we can take the average temperature as a reasonable substitute, that is, $\overline{T} = \frac{539.67 + 749.67}{2} = 644.67\,\text{R}$. Substituting the input values into Eq. (12.20) gives

$$\begin{aligned} p_2 &= 5000\,\text{psi} \times \exp\left[\frac{32.1740 \frac{\text{ft}}{\text{s}^2}}{32.1740 \frac{\text{lb}_\text{m}\,\text{ft}}{\text{lb}_\text{f}\,\text{s}^2}} \frac{1}{96.34 \frac{\text{lb}_\text{f}\,\text{ft}}{\text{lb}_\text{m}\,\text{R}} \times 644.67\,\text{R}} \times (15\,000 - 0)\,\text{ft}\right] \\ &= 6366\,\text{psi}. \end{aligned} \tag{12.24}$$

For the case of a linear temperature distribution, we can substitute directly into Eq. (12.23) to obtain

$$p_2 = 5000\,\text{psi} \times \left(1 + \frac{0.014\,\frac{\text{R}}{\text{ft}} \times (15\,000 - 0)\,\text{ft}}{539.67\,\text{R}}\right)^{\frac{32.1740\,\frac{\text{ft}}{\text{s}^2}}{32.1740\,\frac{\text{lb}_\text{m}\,\text{ft}}{\text{lb}_\text{f}\,\text{s}^2}}\,\frac{1}{96.34\,\frac{\text{lb}_\text{f}\,\text{ft}}{\text{lb}_\text{m}\,\text{R}} \times 0.014\,\frac{\text{R}}{\text{ft}}}}$$
$$= 6380\,\text{psi}. \tag{12.25}$$

In this particular example the difference between the constant and linear temperature distribution assumptions is small. Depending on the specific input variable, however, the difference could be significant.

Real gas

Eq. (12.17) is, as one might expect, not necessarily accurate for real gases. As a measure of its inaccuracy we can introduce the so-called compressibility factor[5] Z_c defined by the equation

$$Z_c = \frac{pv}{\mathcal{R}T}. \tag{12.26}$$

The compressibility factor has a value of 1 for an ideal gas and otherwise provides a measure of deviation from ideal behavior.

Fig. 12.2 summarizes the behavior of Z_c as a function of pseudoreduced pressure p_{pr} and temperature T_{pr}. The reduced properties[6] of a fluid are state variables normalized by the state variables of the fluid at its critical point. For pressure and temperature

$$p_{pr} = \frac{p}{p_{cr}}, \tag{12.27}$$

$$T_{pr} = \frac{T}{T_{cr}}, \tag{12.28}$$

where p_{cr} and T_{cr}, respectively, are the critical[7] pressure and temperature which, given

[5] The conventional symbol fort the compressibility factor is Z. Since this symbol is already used for the depth/axial coordinate in a cylindrical coordinate system, the compressibility factor is denoted Z_c.

[6] Hereafter we will refer to the reduced pressure and temperature as the pseudoreduced pressure and temperature. The term "reduced" is appropriate for a single fluid. In the case of hydrocarbons, however, the fluid in question is usually a mixture of a number of components. The "pseudo" reduced pressure and temperature are calculated from an average of the component reduced pressures and temperatures, where each component in the mixture is weighted by its mole fraction.

[7] In a pressure–temperature phase diagram, phase equilibrium, for example, between liquid and gas phases, is represented by a curve—the vapor-pressure curve—separating the coexisting liquid and gas phases. The point in the diagram at which that curve terminates is the critical point, and the corresponding pressure

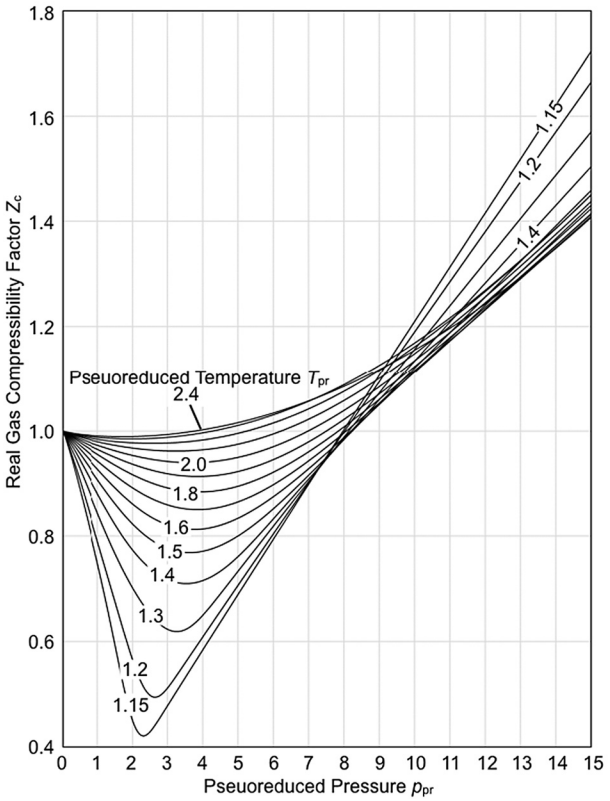

Figure 12.2 ***Compressibility factor for a real gas.*** Individual curves are lines of constant pseudoreduced temperature. The particular correlation displayed is from an explicit correlation by Beggs and Brill [141] and is plotted only for its recommended range of applicability, $1.15 \leq T_{pr} \leq 2.4$, $0.2 \leq p_{pr} \leq 15.0$.

the specific gravity of the gas, can be calculated (at least in their pseudocritical forms p_{pc} and T_{pc}—see Footnote 6) from the correlations [143] as

$$p_{pc} = 756.8 - 131.07SG - 3.6SG^2, \tag{12.29}$$

$$T_{pc} = 169.2 + 349.5SG - 74.0SG^2, \tag{12.30}$$

where SG is the gas specific gravity, and the units of p_{pc} and T_{pc} are psi and R, respectively. The temperature T_{pc}, as well as T and T_{cr} in Eqs. (12.26) and (12.28), are absolute temperatures.

and temperature are the critical pressure and critical temperature. At the critical point the saturated-liquid and saturated-vapor phases are identical [142].

Example problem—real gas hydrostatic head

Recompute the hydrostatic head of methane for the well conditions provided in section 'Example problem—ideal gas hydrostatic head'.

We will only perform the calculation for the case of a constant temperature distribution. Reviewing the derivation of Eq. (12.20), if Z_c is assumed constant over the calculation depth interval, we may immediately write

$$p_2 = p_1 \exp\left[\frac{g}{g_c}\frac{1}{Z_c \mathcal{R}\overline{T}}(Z_2 - Z_1)\right]. \tag{12.31}$$

The problem is still difficult since an average value of Z_c depends on p_2, the unknown pressure. A spreadsheet solution would not be overwhelming, but to illustrate the procedure with hand calculations we will simply use the value of Z_c at p_1 and $\overline{T}$.

The specific gravity of methane compared to air is $SG = \frac{16.04}{28.95} = 0.554$. Using Eqs. (12.29) and (12.30) gives

$$p_{pc} = 756.8 - 131.07\,(0.554) - 3.6\,(0.554)^2 = 683.1\,\text{psi}, \tag{12.32}$$

$$T_{pc} = 169.2 + 349.5\,(0.554) - 74.0\,(0.554)^2 = 340.1\,\text{R}, \tag{12.33}$$

so that, from Eqs. (12.27) and (12.28),

$$p_{pr} = \frac{5000}{683.1} = 7.32, \tag{12.34}$$

$$T_{pr} = \frac{644.67}{340.1} = 1.90. \tag{12.35}$$

The correlation [141] used to generate[8] Fig. 12.2 is an explicit function of p_{pr} and T_{pr} and proceeds as follows:

$$A = 1.39\left(T_{pr} - 0.92\right)^{0.5} - 0.36\,T_{pr} - 0.101, \tag{12.36}$$

$$E = 9\left(T_{pr} - 1\right), \tag{12.37}$$

$$B = \left(0.62 - 0.23\,T_{pr}\right)p_{pr} + \left(\frac{0.066}{T_{pr} - 0.86} - 0.037\right)p_{pr}^2 + \frac{0.32\,p_{pr}^6}{10^E}, \tag{12.38}$$

$$C = 0.132 - 0.32\frac{\ln T_{pr}}{2.303}, \tag{12.39}$$

$$F = 0.3106 - 0.49\,T_{pr} + 0.1824\,T_{pr}^2, \tag{12.40}$$

[8] The Beggs and Brill correlation [141] is one of several proposed to fit a figure originally generated by Standing and Katz [144,145]. Alternatives include both implicit and explicit solutions [146]. The Beggs and Brill correlation was chosen here because of its accuracy and the explicit nature of its solution.

$$D = 10^F, \tag{12.41}$$

$$Z_c = A + (1 - A)\exp(-B) + Cp_{pr}^D. \tag{12.42}$$

Carrying out the indicated operations in Eqs. (12.36)–(12.42), we get

$$A = 1.39\,(1.90 - 0.92)^{0.5} - 0.36 \times 1.90 - 0.101 = 0.589, \tag{12.43}$$

$$E = 9\,(1.90 - 1) = 8.06 \tag{12.44}$$

$$B = (0.62 - 0.23 \times 1.90)\,7.32 + \left(\frac{0.066}{1.90 - 0.86} - 0.037\right)(7.32)^2 + \frac{0.32\,(7.32)^6}{10^E}$$

$$= 2.781, \tag{12.45}$$

$$C = 0.132 - 0.32\frac{\ln 1.90}{2.303} = 0.0432, \tag{12.46}$$

$$F = 0.3106 - 0.49 \times 1.90 + 0.1824\,(1.90)^2 = 0.0371, \tag{12.47}$$

$$D = 10^F = 1.089, \tag{12.48}$$

$$Z_c = 0.591 + (1 - 0.591)\exp(-2.758) + 0.0428\,(7.32)^{1.092} = 0.992. \tag{12.49}$$

With knowledge of Z_c we may now use Eq. (12.31) to calculate the pressure at depth Z_2 for methane as a real gas, namely

$$p_2 = 5000\,\text{psi} \times \exp\left[\frac{32.1740\,\frac{\text{ft}}{\text{s}^2}}{32.1740\,\frac{\text{lb}_\text{m}\,\text{ft}}{\text{lb}_\text{f}\,\text{s}^2}} \frac{1}{0.992 \times 96.34\,\frac{\text{lb}_\text{f}\,\text{ft}}{\text{lb}_\text{m}\,\text{R}} \times 644.67\,\text{R}} \times (15000 - 0)\,\text{ft}\right]$$

$$= 6378\,\text{psi}, \tag{12.50}$$

which is to be compared to the value 6366 psi assuming an ideal gas. As was the case with the example problem in section 'Example problem—ideal gas hydrostatic head', no conclusion regarding the closeness of answers for the real and ideal gas calculations can be inferred from this example. A different gas, or the same gas at different conditions can alter the calculations significantly. In this particular problem the primary differentiator (compare Eqs. (12.20) and (12.31)) between the real and ideal gas models—the compressibility factor Z_c—has a value close to unity.

12.4.2 Flowing pressure

A complete treatment of flowing pressure is beyond the scope of this book. For single phase systems—circulating mud or cement, water injection, some treatment operations—the problem is amenable to reasonably simple hand calculations. For multiphase system, in particular produced hydrocarbons, the description of flow is sufficiently complicated to warrant a separate text [147–149].

12.5. PREINSTALLATION LOADS

Preinstallation includes all activities prior to activation of the initial state or condition. Installing the tubular string, including accounting for potential difficulties such as a stuck condition requiring overpull, dominates the preinstallation period. This segment of tubular life ends when either the cement is displaced and allowed to thicken (casing) or a packer is set (tubing).

12.5.1 All casing

Tables 12.1–12.2 define preinstallation loads for casing.

12.5.1.1 Running in hole

Running in hole (see Table 12.1) is usually performed with the tubular open-ended with a single wellbore fluid. Floating casing may be necessary, however, due to rig limitations or hole tortuosity. In such instances, care should be taken in to keep the casing sufficiently full to avoid an external pressure differential that approaches the tube's collapse resistance.

Running in hole is typically modeled ignoring frictional drag, usually a conservative assumption inasmuch as drag during RIH reduces the axial tension. This results in the same axial load distribution as one would observe if the casing were rotated off bottom.

If desired, drag can be modeled for both running in hole and pulling out of hole with currently available software:

- Simpler software typically employs the so-called soft-string model [34] and assumes that all portions of the tubular are moving simultaneously.
- More complicated numerical software includes the bending stiffness of the tubular [150,37] and can model stick/slip conditions everywhere along the string.

It is not uncommon to include a dynamic or shock load increment to the axial force. The load is intended to model an instance where, while the tubular string is being lowered, the slips are inadvertently activated causing the string to abruptly stop. Ignoring the ramp up to and down from the running speed, typical values [17] for running a tubular joint are on the order of 2–6 $\frac{\text{ft}}{\text{s}}$ (1–2 $\frac{\text{m}}{\text{s}}$). A detailed example addressing the shock load is presented in subsection 'Example problem—computing shock load' in Section 4.2.6.2 of Chapter 4.

12.5.1.2 Overpull

Casing overpull (see Table 12.2) can be modeled incrementally, as the string is assembled and run in the well, or as one or more checks at depths of concern. A common worst case analysis considers the possibility of the string being stuck just as it reaches the bottom of the hole, and computes the overpull load as an increment above the buoyed weight of the string.

Typical values for casing overpull are in the range 150–200 000 lb_f.

Table 12.1 Preinstallation—all casing: running in hole[a, b]

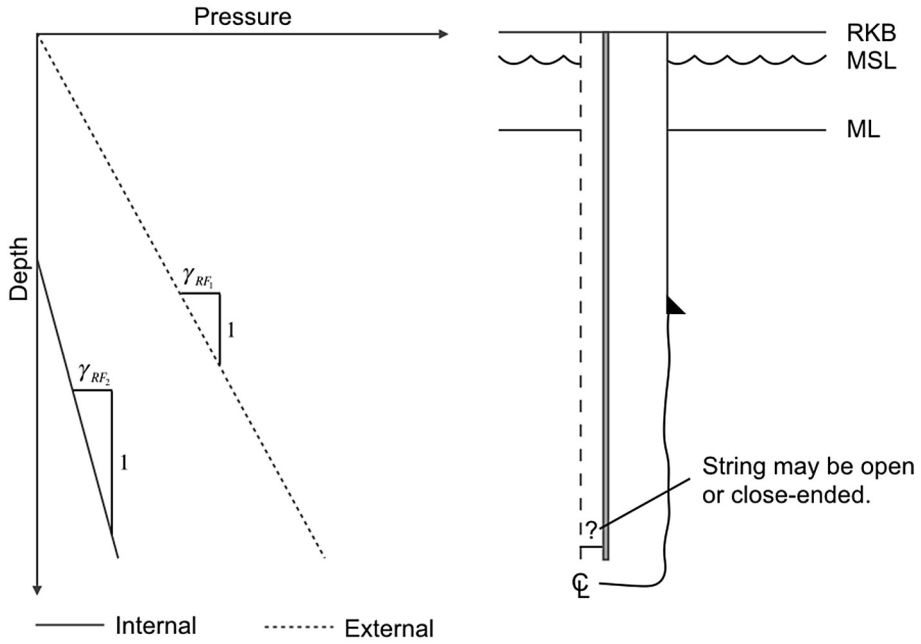

Internal pressure	External pressure	Temperature
Normally, RF. If casing is floated-in the internal profile could be a column of air over the fluid being intermittently pumped to fill the casing.	RF. Density may be different from internal fluid.	G

Comments:

- Take care when floating a string into the hole to fill at proper intervals. If the string becomes too light, it could buckle at the top, adding to the resistance going into the wellbore. For large D/t ratios, a sufficiently empty string can collapse.
- A "dynamic" load may be included as an additional increment to the axial force.
- String can be open or close-ended.

[a] Design string has shaded cross-section.
[b] RF = running fluid, G = local geostatic.

12.5.2 Production tubing

Tables 12.3–12.4 define preinstallation loads for tubing.

12.5.2.1 Running in hole

Running in hole is typically modeled ignoring frictional drag, usually a conservative assumption inasmuch as drag during RIH reduces the axial tension. See the detailed discussion in Section 12.5.1.1.

Table 12.2 Preinstallation—all casing: overpull[a, b]

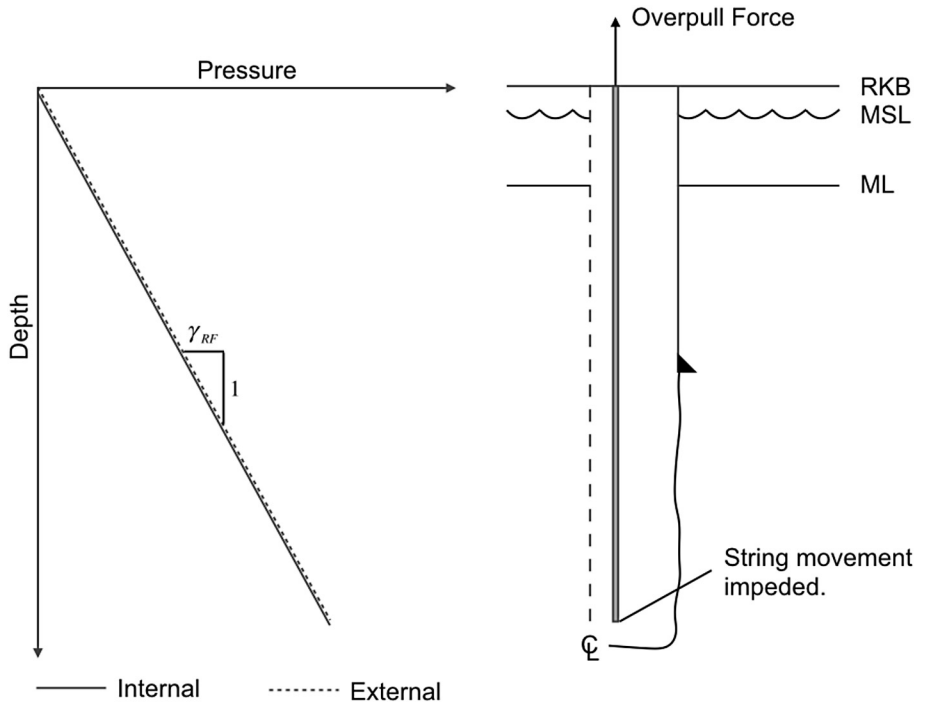

Internal pressure	External pressure	Temperature
RF	RF	G

Comments:

- An additional increment of tension equal to the design overpull force is applied at the surface.
- String is usually assumed to be open-ended, but fixed at the bottom.

[a] Design string has shaded cross-section.
[b] RF = running fluid, G = local geostatic.

12.5.2.2 Overpull

Overpull for tubing is more likely to be associated with shearing a pin associated with the installation or retrieval of an accessory [151]. Typical values for tubing overpull (see Table 12.4) are in the range 100–150 000 lb_f.

12.6. THE INITIAL STATE FOR DESIGN CALCULATIONS

Prior to cementing (casing) or setting the packer (tubing) the individual axial loads can be modeled as either incremental (e.g., Load Case $I + 1$ follows Load Case I) or total (e.g., each load case follows an unloaded condition). Once at least one end of the

Table 12.3 Preinstallation—tubing: running in hole[a, b]

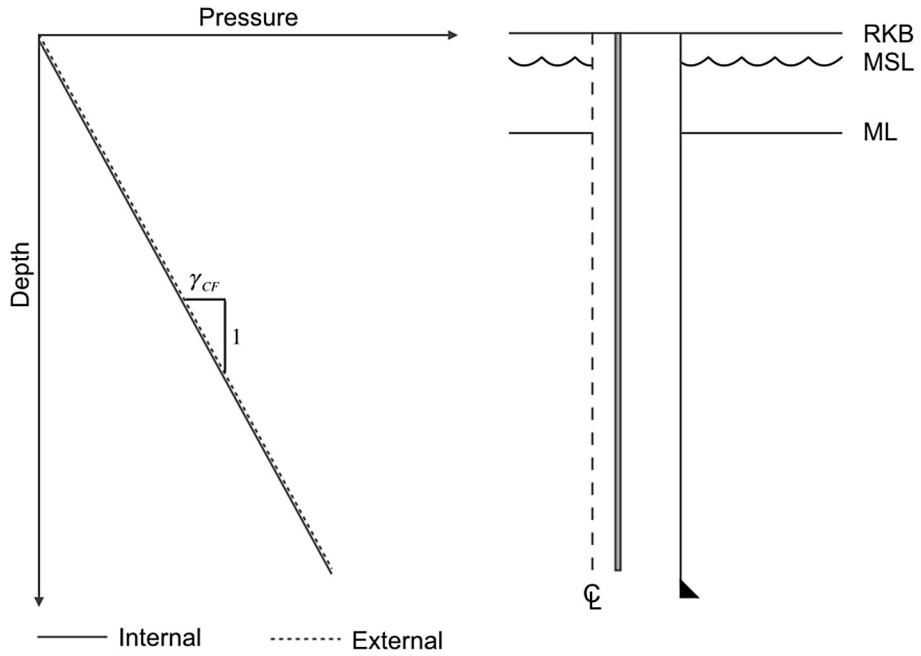

Internal pressure	External pressure	Temperature
CF	CF	G

Comments:

- A "dynamic" load may be included as an additional increment to the axial force.
- String is usually open-ended.

[a] Design string has shaded cross-section.
[b] CF = completion fluid, G = local geostatic.

string is fixed, however, an initial state or initial condition is defined which replaces the unloaded condition. One may still treat loads as incremental, but more common practice is to refer all load cases back to the initial state or condition. Answers worked either way should be equivalent provided frictionless elastic behavior is analyzed. If either friction or inelastic behavior is included, the problem becomes path dependent and the answers from an incremental solution and a total solution will no longer coincide, with the former approach being correct.

The importance of the initial state is its use as a datum from which length changes, or potential length changes, are calculated. At any point in the history of the tubular its pressure and temperature environments are usually treated as input or independent variables. The axial load, on the other hand, is dependent and fluctuates with changes in pressure and temperature (see Chapter 11) due to the following actions:

- thermal expansion/contraction;

Table 12.4 Preinstallation—tubing: overpull[a, b]

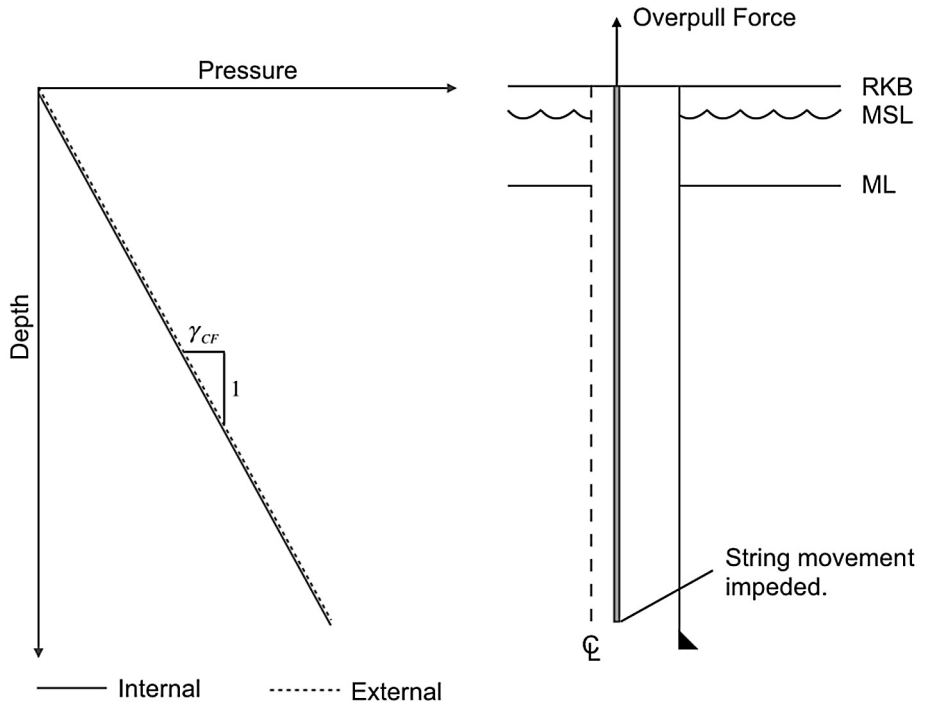

Internal pressure	External pressure	Temperature
CF	CF	G

Comments:

- An additional increment of tension equal to the design overpull force is applied at the surface.
- String is usually assumed to be open-ended, but fixed at the bottom.

[a] Design string has shaded cross-section.
[b] CF = completion fluid, G = local geostatic.

- ballooning;
- pressure forces on exposed shoulders;
- column buckling.

The change in axial load with changes in pressure and temperature requires a datum, and that datum is the initial state. One first calculates the initial axial force distribution in the tubular corresponding to the initial state (see Table 12.5 for casing and Tables 12.6–12.8 for tubing). The axial force distribution for any load case is then the initial axial force distribution plus the distribution of change in axial force due to the change in the pressure and temperature environment from the initial state to the load case in question.

With the introduction of concern regarding incremental loads associated with annular pressure build-up (APB) (See Section 15.2 of Chapter 15) there now exist two types of initial state with which one must be concerned:

- For conventional load cases in which APB is not an issue, the initial state is defined as the moment at which the cement/packer sets preventing further axial expansion/contraction of the tubular. If the completion is packerless, the initial state for the production tubing is defined by the moment at which the string is landed in the wellhead.
- For APB calculations the initial state is defined as the time at which the annulus in question becomes sealed.

For many wells the above two conditions coincide. For some wells, however, venting an annulus as a well is produced may delay sealing (or constitute resealing) of an annulus and therefore redefine the state at which an APB calculation begins.

12.6.1 Conventional design

The initial condition in conventional design is primarily tied to axial movement and usually represents the moment in the tubular's life at which unimpeded length change is no longer possible. For casing this moment is fairly well defined (see Section 12.6.2). For tubing (Section 12.6.3), the issue is less clear if the lower end of the tubing is allowed movement, as in the case of a tubing string whose lower end consists of a seal stem inserted into a seal bore. Even if later movement is restricted—for example, by an initial offset from a no-go shoulder—it may be appropriate to define the tubing hang-off in the wellhead as the initial state.

12.6.2 All casing

Inasmuch as almost all casing is cemented at its lower end, the initial condition for casing is taken to be the moment during cement displacement at which the top cement plug bumps,[9] indicating the end of cement circulation. This definition ignores important factors:

- Cement thickening time. The time between the end of circulation and the moment at which the cement reaches a predefined, solid-like constitution may be hours. During that time, and depending on the local environment (open or cased hole, local temperature and/or pore pressure and formation permeability), the hydrostatic head of pressure supplied by the cement column may vary. Further, there is evidence that, at least opposite a permeable formation, the local pressure in the cement column can with time approach local pore pressure [153].

[9] Often two cement plugs are used to surround and isolate the cement slurry during placement—a bottom plug pumped ahead of the slurry and containing a diaphragm that ruptures when it reaches the float shoe, and a top plug that is solid [152]. The plug referred to here is the latter.

- Temperature. The chemical reaction by which the cement slurry becomes a solid sheath is exothermic [61]. Although cement solidification is not impossible to model, the vagaries of input variables can affect the fidelity of such an analysis.

Given the above unknowns, it is common practice to ignore the bulleted items and define the initial condition in the casing by the undisturbed formation temperature and a hydrostatic calculation of pressure forces based on the fluids in the hole at the instant cement circulation ceases.

12.6.2.1 Example problem—initial axial force in cemented casing

A 12 000 ft string of casing is run in 12 ppg drilling fluid and then cemented up to 9500 ft with 15.2 ppg cement that is separated from the drilling fluid by 500 ft of a 13 ppg spacer. The cement column is pumped down the casing with 13 ppg drilling fluid in anticipation of drilling out and beginning the next hole section. Calculate the initial state of axial force in the casing at its bottom, assumed to be the (approximate) location of the float collar. The casing is 9.625 in. with a wall thickness of 0.545 in.

The internal area of the casing at its lower end is

$$A_i = \frac{\pi}{4}(D - 2t)^2 = \frac{\pi}{4}(9.625\,\text{in.} - 2 \times 0.545\,\text{in.})^2 = 57.213\,\text{in}^2, \tag{12.51}$$

and its external area is

$$A_o = \frac{\pi}{4}D^2 = \frac{\pi}{4}(9.625\,\text{in.})^2 = 72.760\,\text{in}^2. \tag{12.52}$$

Assuming constant densities for all fluids, the internal and external pressures acting at the bottom of the string are, respectively,

$$p_i = 0.051\,948\,\frac{\text{psi}}{\text{ft ppg}}\,13\,\text{ppg} \times 12\,000\,\text{ft} = 8104\,\text{psi}, \tag{12.53}$$

$$p_o = 0.051\,948\,\frac{\text{psi}}{\text{ft ppg}}\,(12\,\text{ppg} \times 9000\,\text{ft} + 13\,\text{ppg} \times 500\,\text{ft} + 15.2\,\text{ppg} \times 2500\,\text{ft}) = 7922\,\text{psi}. \tag{12.54}$$

The net axial force at the bottom of the casing (see Fig. 12.3) is therefore

$$f_z = 8104\,\text{psi} \times 57.213\,\text{in}^2 - 7922\,\text{psi} \times 72.760\,\text{in}^2 = -112\,751\,\text{lb}_\text{f}. \tag{12.55}$$

12.6.3 Production tubing

Three possibilities present themselves for a tubing string containing at least one packer—mechanically-set, hydraulic-set or hydrostatic-set.

The following comments are applicable to the initial conditions for production tubing:

Table 12.5 Initial condition—casing[a, b]

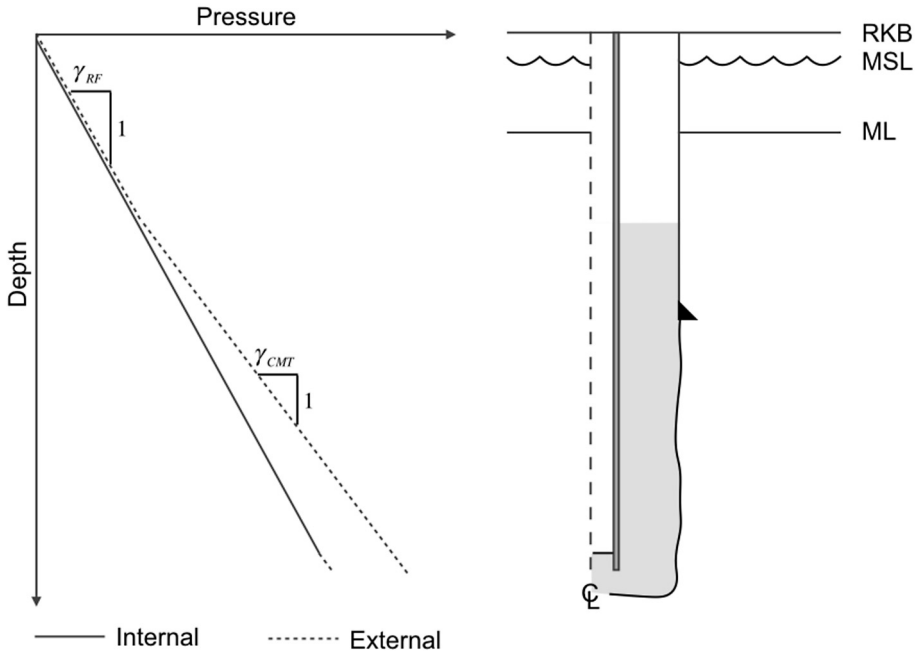

Internal pressure	External pressure	Temperature
RF	RF + SP + CMT[c]	G

Comments:

- RF is a general designation for both the external and internal drilling fluids used to install the casing (external) and chase the top cementing plug (internal). Although not depicted in the figure, the densities of these fluids may differ.
- A spacer may be used to separate the cement from the external drilling fluid.
- All fluids in the wellbore at the moment the cement plug bumps are used in the calculation of the initial axial force at the bottom of the casing.
- Application of surface pressure may be necessary, for example, to prevent U-tubing of fluids if the cement float fails to hold. Since this condition is indeterminate at the time of design, it is usually only considered as a contingency.

[a] Design string has shaded cross-section.
[b] RF = running fluid, SP = spacer, CMT = cement, G = local geostatic.
[c] External fluid occupies the casing below the cement float shoe.

- As they affect tubular initial conditions, packers have two components—the slips used to anchor the packer to the adjacent production casing and a seal element to isolate the tubing annulus from lower portions of the completion and/or the tubing interior. The manner in which the slips and seal element are activated can be mechanical or by two different pressurization alternatives.

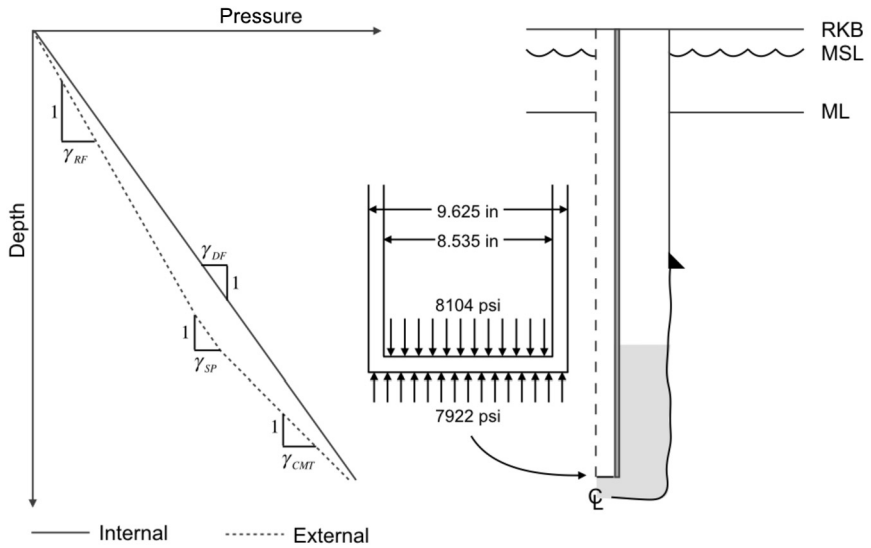

Figure 12.3 ***Fluids and forces used in example calculation of cemented casing initial force.*** $\gamma_{RF} = 12\,\text{ppg}$, $\gamma_{SP} = 13\,\text{ppg}$, $\gamma_{CMT} = 15.2\,\text{ppg}$, $\gamma_{DF} = 13\,\text{ppg}$.

- Only one of the initial conditions—mechanical, hydraulic- or hydrostatic-set packer should be modeled (Tables 12.6–12.8).
- Tubingless completions—where the production tubing and production casing are the same tubular string—have their initial conditions computed in a manner identical to that of production casing—see Section 12.6.2.

12.6.3.1 Mechanically-set packers

Mechanically-set packers (see Table 12.6) depend on a control line, axial force or rotation to activate the slips and seal element. Once the slips and seal are activated, the tubing may be landed in a variety of stress states. Typically, however, the act of installing the packer in the casing does not in itself impose a permanent stress in the tubing.

12.6.3.2 Hydraulic-set packers

Hydraulic-set packers (see Table 12.7) depend on a plug set below the packer to render the tubing a pressure chamber and allow the slips and seal element to be activated. The setting process induces a permanent, net axial extension of the tubing which results in an incremental axial tension associated with installation:

1. A temporary plug or dropped ball seals the tubing to internal pressure in the tail pipe below the packer.
2. Surface tubing pressure is increased, the first landmark being the pressure necessary to initiate contact between the slips (forced outward by the axial motion of a piston

Table 12.6 Initial condition—tubing: mechanically-set packer[a, b]

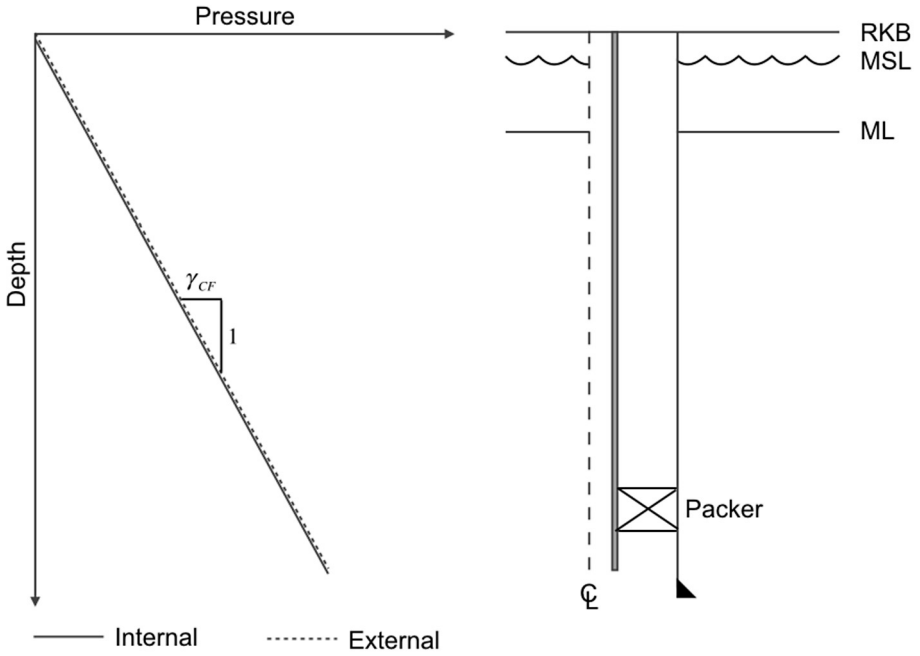

Internal pressure	External pressure	Temperature
CF/PF	CF/PF (above packer[c])	G

Comments:

- Incremental tension, compression or a zero axial force in the tubing may be associated with landing the tubing following the packer installation.
- The possibility of damaging the cement/production casing interface during a CF/PF fluid swap should be considered.

[a] Design string has shaded cross-section.
[b] CF = completion fluid, PF = packer fluid, G = local geostatic.
[c] Internal fluid occupies the tubing annulus below the packer.

internal to the packer) and the production casing. At the time the slips engage, the tubing down to the tailpipe plug has:

(a) elongated due to the axially directed force of pressure on the plug;

(b) shortened due to ballooning via Poisson's effect acting along the entire tubing length down to the plug.

The net effect is a lengthening of the tubing down to the packer and a lengthening of the tailpipe down to the plug. Tailpipe below the plug displaces downward but is not stretched.

3. As the surface pressure is increased further, the slips penetrate into the wall of the production casing. There is, however, no further downward movement of the tub-

ing above the packer. Below the packer, the tailpipe lengthens further—again, due to pressure on the plug minus ballooning. During this time the seal element is also expanding against the wall of the production casing to effect the seal.

4. With the slip elements firmly seated in the production casing and the seal element isolating the tubing annulus, the applied surface pressure is decreased to zero. In response the tailpipe above the plug loses the stretch associated with pressurization and returns to its length prior to the packer-setting operation.[10] No axial movement occurs above the packer.

The pressurization/depressurization cycle described above has consequences for design. As mentioned in the introduction of this section, the setting operation up to the moment of slip/casing contact results in a net length change—plug pressure force minus ballooning—of

$$\begin{aligned}\Delta L &= \frac{\Delta f_{t-plug} L}{E A_s} - \frac{2\nu}{E}\frac{\Delta p_i A_i}{A_s} L \\ &= (1-2\nu)\frac{\Delta p_i A_i L}{E A_s},\end{aligned} \tag{12.56}$$

or a permanently induced incremental tension of

$$\Delta f_t = (1-2\nu)\,\Delta p_i A_i, \tag{12.57}$$

where ν and E are Poisson's ratio and Young's modulus of the tubing material, respectively, and A_i and A_s are the tubing cross-sectional area based on inside diameter and cross-sectional area of tubing, respectively. Importantly, Δp_i is the setting pressure corresponding to step 2 of the outlined procedure, and L is the length of tubing above the packer. The tailpipe plays no role in this calculation as its deformation is completely recovered in the cycle. See Section 11.5 of Chapter 11 for a detailed discussion of Eqs. (12.56) and (12.57) and an example calculation.

12.6.3.3 Hydrostatic-set packers

Hydrostatic-set packers (see Table 12.8) require pressurization of the entire tubing-production casing chamber to allow the slips and seal element to be activated. The setting process induces a permanent, net axial contraction of the tubing which results in an incremental axial compression associated with installation:

1. Surface tubing and annulus pressure is increased, the first landmark being the pressure necessary to initiate contact between the slips (forced outward by the axial

[10] There is, of course, a small change in length of the tailpipe since it is, at the end of this process, slightly deeper than it was before, and therefore subjected to slightly higher hydrostatic pressure. This minor length change is ignored in the design calculation.

Table 12.7 Initial condition—tubing: hydraulic-set packer[a, b]

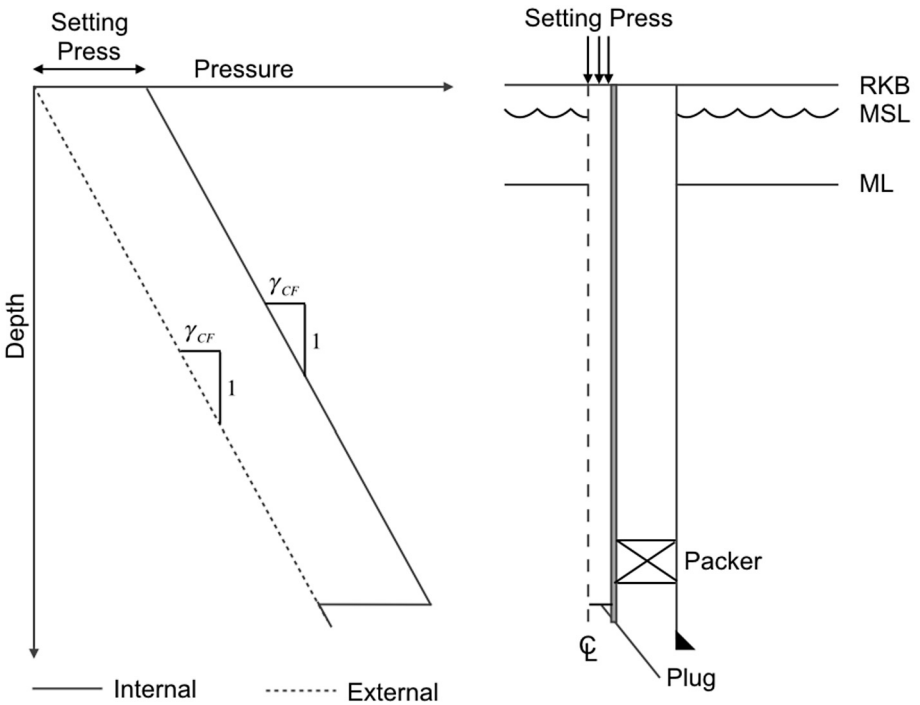

Internal pressure	External pressure	Temperature
Setting pressure + CF/PF	CF/PF (above packer[c])	G

Comments:

- An incremental tension will be induced in the tubing via the setting pressure.
- A tubing plug is required for installation.
- Hydrostatic-set packers are usually rated with two setting pressures. The lower pressure used to set the slip elements is the value required for this load case.
- The possibility of damaging the cement/production casing interface during a CF/PF fluid swap should be considered.

[a] Design string has shaded cross-section.
[b] CF = completion fluid, PF = packer fluid, G = local geostatic.
[c] Internal fluid occupies the tubing annulus below the packer.

motion of a piston internal to the packer) and the production casing. At the time the slips engage, the tubing has:

(a) shortened due to the axially directed upward force of pressure on the lowermost exposed cross section of the tailpipe;

(b) lengthened due to ballooning via Poisson's effect acting along the entire length of the tubing, both internally and externally.

The net effect is a shortening of the tubing down to the packer and a shortening of the tailpipe.

2. As the surface pressure is increased further, the slips penetrate into the wall of the production casing. There is, however, no further upward movement of the tubing above the packer. Below the packer, the tailpipe shortens further—again, due to pressure on the end of the tailpipe partially countered by ballooning. During this time the seal element is also expanding against the wall of the production casing to effect the seal.
3. With the slip elements firmly seated in the production casing and the seal element isolating the tubing annulus, the applied surface pressure is decreased to zero. In response the tailpipe loses the contraction associated with pressurization and returns to its length prior to the packer-setting operation.[11] No axial movement occurs above the packer.

The pressurization/depressurization cycle described above has consequences for design. As mentioned in the introduction of this section, the setting operation up to the moment of slip/casing contact results in a net length change—exposed lower end pressure force minus ballooning—of

$$\begin{aligned}\Delta L &= -\frac{\Delta f_{t-bot} L}{E A_s} + \frac{2\nu}{E}\frac{\Delta p A_s}{A_s} L \\ &= -(1-2\nu)\frac{\Delta p L}{E},\end{aligned} \tag{12.58}$$

or a permanently induced incremental compression of

$$\Delta f_t = -(1-2\nu)\,\Delta p A_s, \tag{12.59}$$

where ν and E are Poisson's ratio and Young's modulus of the tubing material, respectively, and A_s is the cross-sectional area of tube. Importantly, $\Delta p = \Delta p_i = \Delta p_o$ is the setting pressure corresponding to step 1 of the outlined procedure, and L is the length of tubing above the packer. The tailpipe plays no role in this calculation as its deformation is completely recovered in the cycle. See Section 11.6 of Chapter 11 for a detailed discussion of Eqs. (12.58) and (12.59) and an example calculation.

The fact that Δf_t for a hydrostatic-set packer is negative also means that the effective force in the tubing is lowered due to the setting operation. With hydrostatic-set packers it is important to perform a check on the post-installation state of the tubing to determine if installation results in tubing that is buckled prior to production. Again, see Section 11.6 of Chapter 11 for a detailed discussion and example calculation.

[11] There is, of course, a small change in length of the tailpipe since it is, at the end of this process, slightly shallower than it was before, and therefore subjected to slightly lower hydrostatic pressure. This minor length change is ignored in the design calculation.

Table 12.8 Initial condition—tubing: hydrostatic-set packer[a, b]

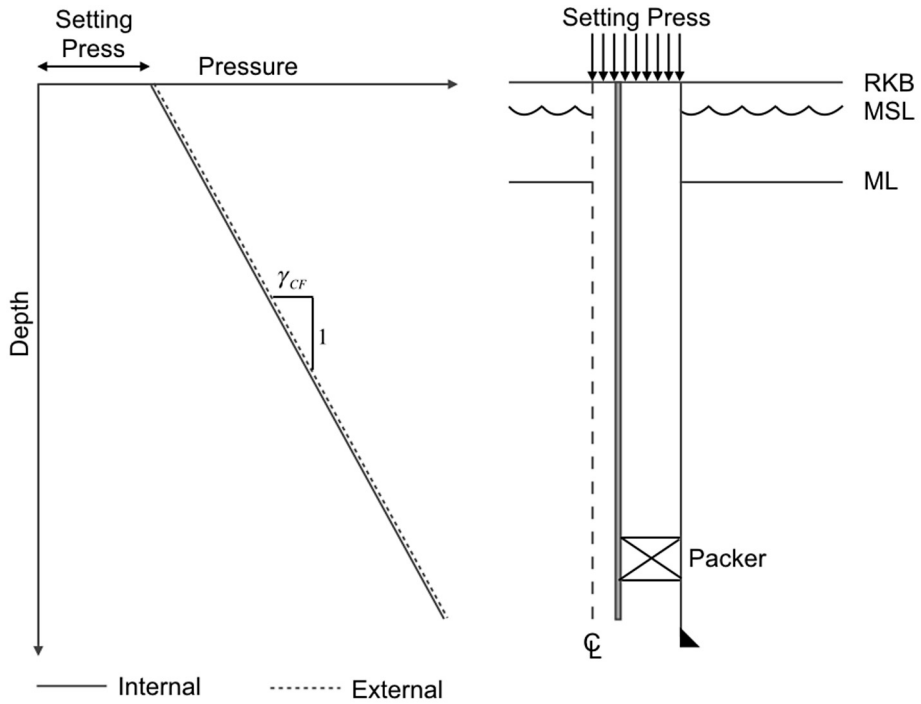

Internal pressure	External pressure	Temperature
Setting pressure + CF/PF	Setting pressure + CF/PF	G

Comments:

- An incremental compression will be induced in the tubing via the setting pressure.
- Hydrostatic-set packers are usually rated with two setting pressures. The lower pressure used to set the slip elements is the value required for this load case.
- Residual buckling can be a by-product of installation.
- The setting pressure can represent a significant load on the production casing.
- The possibility of damaging the cement/production casing interface during a CF/PF fluid swap should be considered.

[a] Design string has shaded cross-section.
[b] CF = completion fluid, PF = packer fluid, G = local geostatic.

12.7. INTERNAL PRESSURE DOMINANT LOADS

It is common design practice when addressing internal pressure dominant loads to work with a single external pressure distribution and create the internal pressure differential by applying various scenarios to the internal pressure distribution.

For casing, external pressure distributions vary across the industry and include the following:

- Pore pressure. Using pore pressure as the external fluid is a fairly conservative choice. Even for the portions of the casing annulus that are not directly exposed to pore pressure (e.g., above the shoe of the previous casing string), the annulus would normally be filled with the drilling fluid used in the current casing's hole section, which should be of higher density than the pore pressure gradient.[12] An exception to this statement is the next bullet.

  One scenario where pore pressure may be overly conservative is in the design of a well drilled through a depleted reservoir. Particularly if the depleted reservoir contained gas, the pore pressure at which the reservoir is abandoned for deeper prospects can be extremely low.
- Degraded drilling fluid. Depending on a number of factors such as fluid chemistry, annular clearance and temperature, the solid weighting particles in a drilling fluid may settle with time. The degree to which this degradation occurs is, for the most part, unknown. The most conservative form of this design assumption is to model the drilling fluid with all solids settled, using the density of the base fluid as the final annulus fluid density. Alternately, one might choose a reasonably low value of degraded fluid density that is intermediate to either the initial or fully settled values. Industry practice varies significantly on this subject.
- Combination fluid columns. It is not unusual to encounter an external fluid density distribution that is a combination of the above. As an example, one might choose to use pore pressure in the open hole below the previous casing shoe, and then tie the pore pressure value at the shoe to an original fluid density column from the previous shoe to the top of the designed string's annulus.
- The proper external pressure to use in the cemented portion of a tieback is unclear. In addition to variations on the options already listed, a viable, fairly conservative option below the tieback cement top is a column of cement mix water tied to whatever pressure has been assumed in the uncemented portion of the tieback just above its top of cement.

For production tubing the fluid column is taken to be the packer fluid down to the packer.

12.7.1 Surface and intermediate casing

Internal pressure dominant loads for surface and intermediate casing vary from well-defined, controlled loads (pressure test) to loads which may depend on both subsurface conditions and crew capabilities (well control).

[12] A possible exception is underbalanced drilling.

12.7.1.1 Pressure test

The internal surface pressure test load (see Table 12.9), although under fairly stable operational control by the rig crew, varies widely in value and philosophic origin across the industry for the same well conditions. Some practices target a percentage of the minimum internal yield pressure rating of the tubular—usually between 70% and 80%—based on the related notions that (a) a load this high is sufficient to detect any manufacturing or transportation flaws, and (b) modern tubulars are of sufficient ductility to mitigate minor flaws. Other practices tie the pressure test load to the worst of the other anticipated internal pressure dominant load cases—usually the well control load case—with the reasoning that, as a pressure vessel, the tubular should be tested to the highest anticipated load to which it will be subjected.[13]

A crucial assumption in formulating the pressure test load is the nature/density assumed for the annulus fluid. If the density of the annulus fluid is less than that of the internal fluid, the internal pressure differential will increase with depth and have the following two consequences:

- A tubular tested to the appropriate test pressure at the top of the string will be overloaded at the bottom of the string.
- A tubular tested to the appropriate test pressure at the bottom of the string will be under-tested at the top of the string.

There is no simple way out of this dilemma short of testing the string in intervals using packers to isolate each tested zone.

An additional complication in pressure testing is the presence of liners and their effect on the exposure of previous strings to pressure test loads (see Fig. 12.4). In most instances, pressure testing a liner will also pressurize any strings above the liner that have not been isolated. The need to pressure test a liner without endangering previous, intermediate casings and/or liners may influence the timing of running a tieback. With the tieback in place, possibly weaker upper strings may no longer be exposed to the rigors of the test pressure applied to deeper tubulars.

12.7.1.2 Well control

Usually the determinant internal pressure dominant load case for surface and intermediate casing is that of (loss of) well control (see Table 12.10). For the most severe case, typically applied when little is known of the target overburden and reservoir, one assumes the following:

- A gas kick has been experienced and due to unforeseen detection and crew circumstances total loss of control of flow from the source reservoir is experienced. The

[13] Such a practice does not necessarily test the tubular to its internal yield pressure, as the tubular should have been designed with a design factor that keeps the tubular's stress state below yield.

Table 12.9 Burst—all casing: pressure test[a, b]

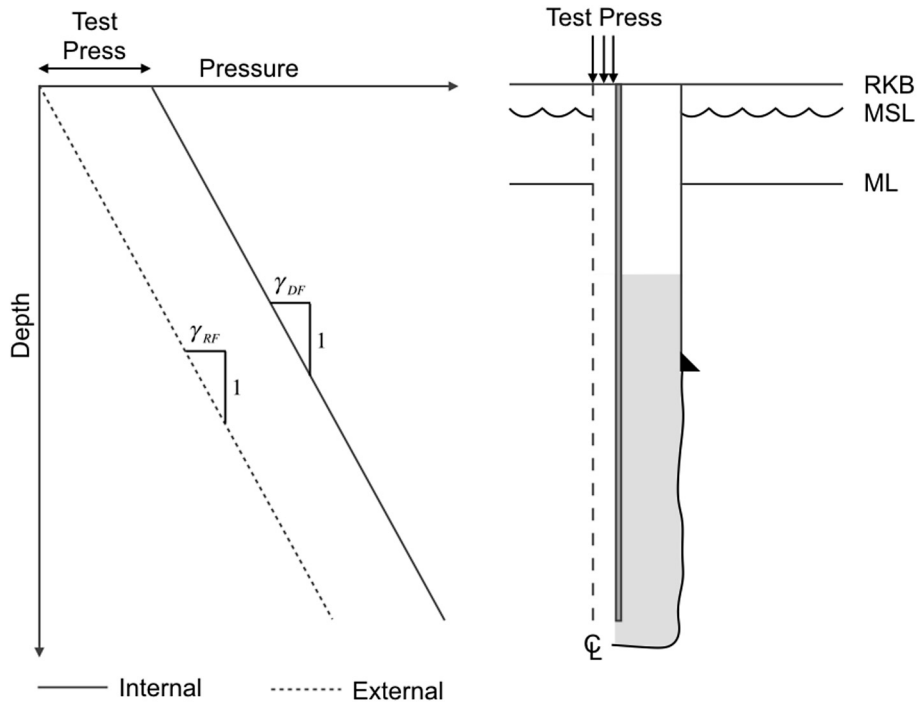

Internal pressure	External pressure	Temperature
Test pressure + DF	RF	G

Comments:

- Top of cement can be above or below previous casing shoe.
- When the pressure test occurs during the infancy of the string (i.e., shortly after waiting-on-cement) it is reasonable to counter the normal assumption for the external pressure distribution and assume the RF to still possess its original density.
- It is extremely easy to fracture the cement sheath during a pressure test.
- DF usually equals RF for production casing.

[a] Design string has shaded cross-section.
[b] DF = drilling fluid for next hole section, RF = running fluid, G = local geostatic.

reservoir fluid is (default methane) gas which has totally filled both the open hole above the source formation and the casing string being drilled through/designed.

- The pressure of the gas is limited by that pressure required to fracture the formation at the shoe of the casing string being drilled through/designed.[14]

[14] It is possible that formation fracture could occur at any depth in the open hole. Usually, however, the current shoe is (a) a good candidate for having the lowest fracture pressure, and (b) the only depth in the open hole where the fracture pressure is at least approximately known.

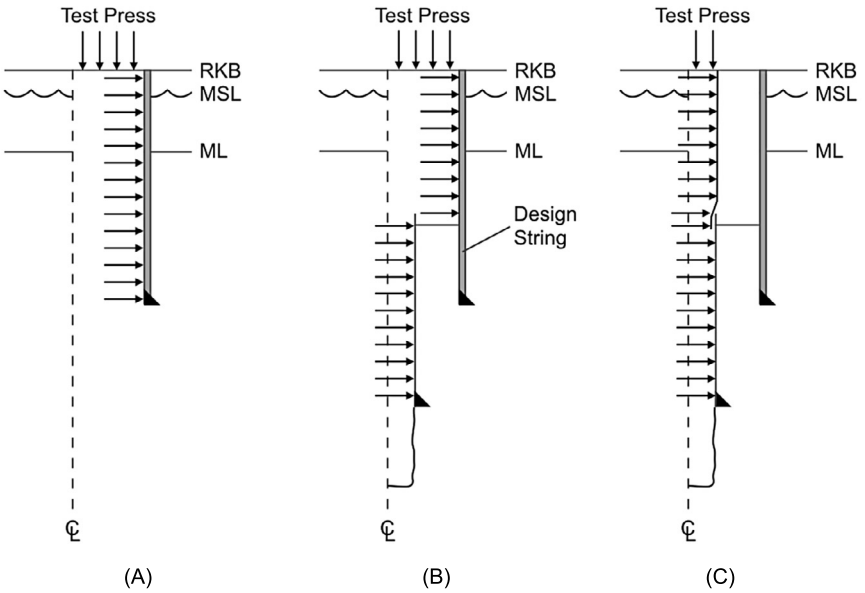

Figure 12.4 ***Exposure to pressure test in the presence of a liner.*** In scenario (A) the casing is designed only for its own pressure test—the next string is a full casing string which isolates the tested string from future loads. In scenario (B) the presence of a liner (only) means that the original casing is exposed during the liner pressure test. In scenario (C) a tieback is run before testing the liner, and the original casing is not exposed to the liner pressure test.

- The pressure inside the casing string being drilled through/designed is therefore the fracture pressure at its shoe minus a gas gradient to the surface.

The scenario described above is termed "Frac at shoe, gas to surface" or words to that effect.

Frac at shoe, gas to surface is indeed a severe load case, but the consequences of a total loss of well control often warrant its use. Nevertheless, in circumstances where ample data is available to justify relaxing this condition, other reasonable alternatives include the following (see Fig. 12.5):

- Pore pressure at source, gas to surface. If it can be demonstrated that none of the formations in the open hole below the casing being designed has sufficient pressure to fracture the formation adjacent to the casing's shoe, then an acceptable design alternative is to project the gas gradient from the source formation to the surface.
- Frac at shoe, liquid to surface. If it can be demonstrated that none of the formations in the open hole below the casing being designed is gas bearing (e.g., liquid hydrocarbon, formation brine), then an acceptable design alternative is to project a worst case liquid gradient from the casing's shoe to the surface.

Table 12.10 Burst—surface and intermediate casing: well control[a, b]

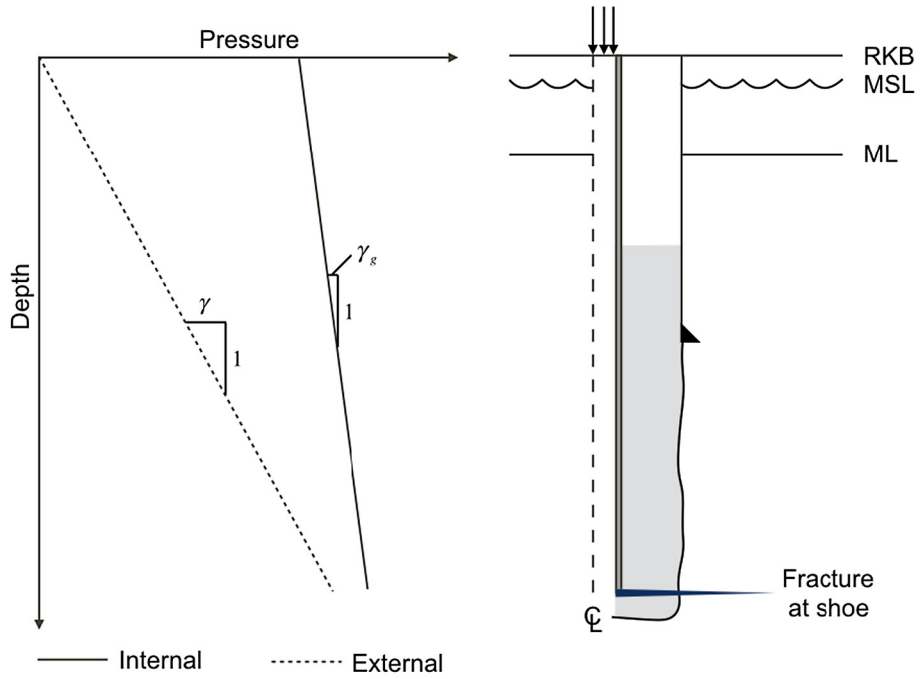

Internal pressure	External pressure	Temperature
Fracture pressure at shoe – gas gradient above	One of several[c]	C

Comments:

- Top of cement can be above or below previous casing shoe.
- A conservative choice for kick gas is methane.
- If this load case is modeled as a dynamic condition a suitable flow simulator should be implemented.

[a] Design string has shaded cross-section.
[b] DF = drilling fluid for next hole section, RF = running fluid, C = circulating.
[c] See the discussion at the beginning of Section 12.7 for external fluid alternatives.

- Pore pressure at source, liquid to surface. If it can be demonstrated that (a) none of the formations in the open hole below the casing being designed is gas bearing, and (b) none of the formations in the open hole below the casing being designed has sufficient pressure with a worst case liquid gradient to fracture the formation adjacent to the casing's shoe, then an acceptable design alternative is to project that liquid's gradient from the source formation to the surface.
- Well control procedural models. With currently available software it is possible to model the circulation of a kick out of the wellbore, tracing the maximum pressure

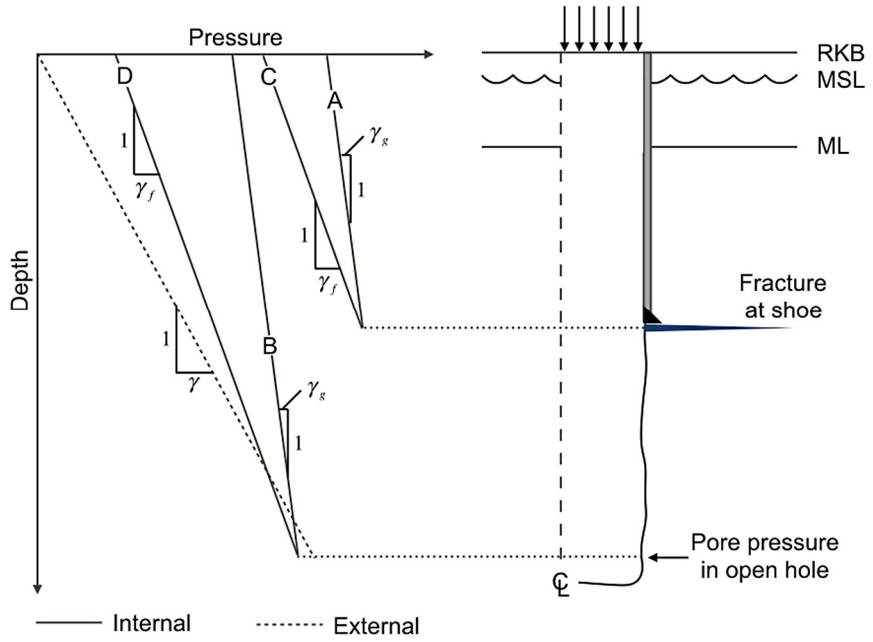

Figure 12.5 ***Alternative internal pressure scenarios for well control load case.*** Scenario A is the "Frac at shoe, gas to surface" load case, usually the most reasonable worst case scenario, especially in the absence of information on the overburden in the next hole section. Scenario B also uses a gas gradient upward from the influx horizon, but the source pore pressure is insufficient to fracture the shoe of the casing string under design. Scenario C depends on the knowledge that no gas-bearing hydrocarbon zones exist in the next hole section, so that the kick fluid is brine or oil. Scenario D adds to scenario C the fact that the lightest of the liquid gradients that might be projected upward from the liquid's influx horizon is insufficient to fracture the shoe of the casing string under design.

seen by the casing being designed as the kick migrates to the surface. Using this alternative is best a product of a detailed conversation with one's well control team to ensure that worst case conditions are still properly honored.

- Well control model alternatives. Again tending toward worst case conditions, certain scenarios involving portions of the wellbore full of either gas or drilling fluid to roughly simulate kick migration are also used, particularly when other modeling alternatives are not available.

As was the case with pressure testing (Section 12.7.1.1), the installation of a liner below a previous string may influence the shoe from which the fracture pressure and gas column depth are selected for the well control calculation. The safe alternative is to analyze well control events for the open hole section below the casing being designed and for all liners below that string. Again, the timing of tieback installations can affect this calculation.

12.7.1.3 Drill ahead

The drill ahead load (see Table 12.11) is not intended to be a determinant of either the geometry or grade of the tube body and connection. The sole purpose of this load case is to investigate whether the surface/intermediate casing will buckle while drilling the next hole section due to the following:

- positive internal pressure change due to increased drilling fluid density when drilling lower hole sections;
- positive potential (but not realized) length change due to increased circulating temperature while circulating drilling fluid from greater depths.

The intent is to model actual drilling conditions in the next hole section, so the best estimates of the density of the drilling fluid for the next hole section, the drilling fluid in which the casing was run and the circulating temperature should be used, as opposed to speculating on worst case values for these variables.

Should the drill ahead load case indicate the casing will buckle (usually in the vicinity of the top of cement), a wear analysis should be performed by superimposing the curvature due to buckling on any curvature due to wellbore trajectory (see Section 15.3.3 of Chapter 15). Usually this incremental curvature will be small—on the order of tenths of a $\frac{^\circ}{100\text{ ft}}$ ($\frac{^\circ}{30\text{ m}}$)—due to the small radial clearance between the casing and its next outer neighbor(s). Even this small amount, however, is sufficient to initiate or aggravate casing wear, particularly if the interval requires extended drilling time.

As was the case with pressure testing (Section 12.7.1.1), the installation of a liner below a previous string may influence the duration of exposure of a particular casing string. Further, subsequent liners and their associated next hole sections[15] will probably involve increased drilling fluid densities and circulating temperatures. Again, the timing of tieback installations can affect this calculation.

12.7.2 Production casing

12.7.2.1 Pressure test

Production casing is pressure tested. See the pressure test load case described in Section 12.7.1.1 and Table 12.9.

12.7.2.2 Tubing leak

The tubing leak (see Table 12.12) is assumed to occur early in the productive life of the well and near the surface. The latter assumption is not essential, as a deeper tubing leak will migrate to the surface in a relatively rigid annulus. Both hot and cold (shut-in) scenarios are possible as the leak could occur during a time of prolonged inactivity.

[15] Liners further complicate the problem in that (a) for each liner the buckling check will have to be performed with a new set of drilling parameters, and (b) the drilling parameters for the wear calculation will also change for the liner's next hole section.

Table 12.11 Burst—surface and intermediate casing: drill ahead[a, b]

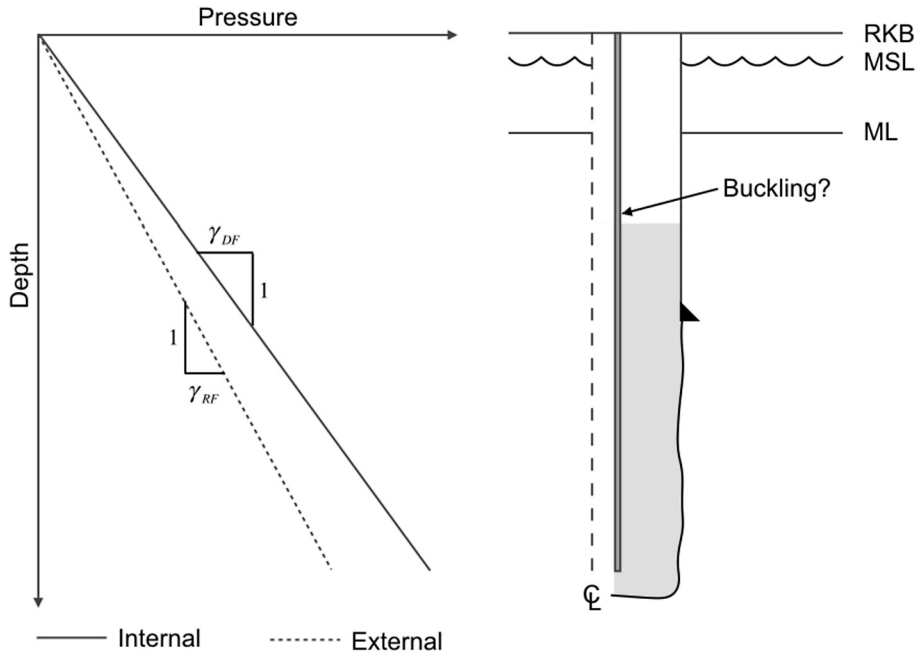

Internal pressure	External pressure	Temperature
DF	RF	C

Comments:

- Top of cement can be above or below previous casing shoe.
- This is a column buckling check, not a design load that would affect tubular or connection dimensions and grade.
- Use best estimate for DF, RF and C, not extremes.

[a] Design string has shaded cross-section.
[b] DF = drilling fluid for next hole section, RF = running fluid, C = circulating.

Below the packer the production casing is not endangered by this load case as the perforations introduce only a minor differential internal pressure, if any.

12.7.2.3 Possible additional loads

Production casing may be exposed to loads associated with other tubulars, particularly the production tubing:

- Hydrostatic-set packers (see Section 12.6.3.3 and the loads illustrated in Table 12.8) are installed by pressurizing the entire tubing/production casing chamber. Depending on the particular packer, the production casing can be exposed to significant internal pressure.

Table 12.12 Burst—production casing: tubing leak[a, b]

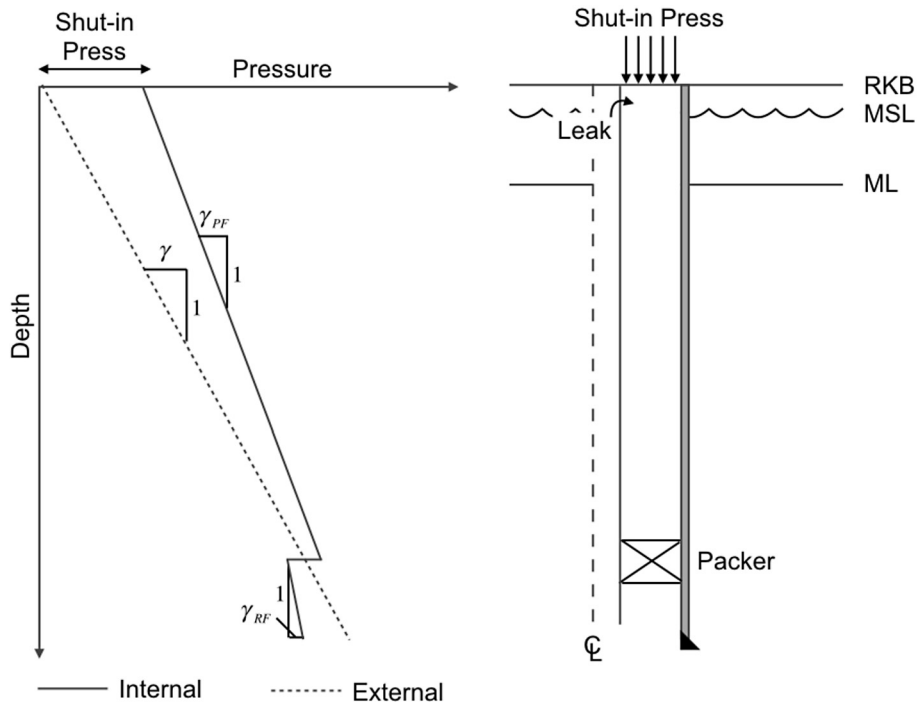

Internal pressure	External pressure	Temperature
Shut-in tubing pressure + PF	One of several[c]	G or P

Comments:

- Top of cement can be above or below previous casing shoe.

[a] Design string has shaded cross-section.
[b] PF = packer fluid, G = local geostatic, P = producing.
[c] See the discussion at the beginning of Section 12.7 for external fluid alternatives.

- Tubing annulus pressure tests (see Section 12.8.3.1 and the loads illustrated in Table 12.21) can also load the production casing with a sizable pressure, on the order of that associated with a tubing leak (see Section 12.7.2.2). In this case the temperature is probably near geostatic so ballooning-induced tension loads may be of particular concern.
- Tubing leaks during injection or stimulation. This load is similar to the tubing leak load case (see Section 12.7.2.2), the primary differences being (a) the shut-in surface pressure is replaced by the tubing surface injection or treating pressure, and (b) the temperature distribution is that due to injection or the treatment.
- Hydraulic horsepower concerns associated with friction losses during hydraulic fracturing may suggest the production casing as the primary conduit for fracturing fluids

Table 12.13 Burst—tubing: pressure test[a, b]

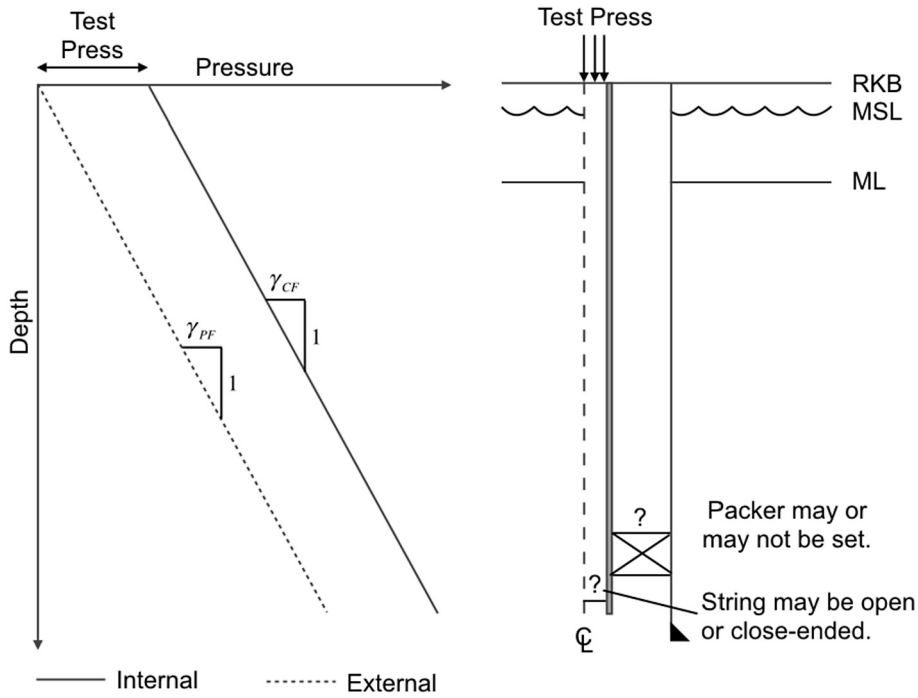

Internal pressure	External pressure	Temperature
Test pressure + CF	PF	G

Comments:

- Either the CF or the PF may be both internal and external to the tubing during the test.

[a] Design string has shaded cross-section.
[b] CF = completion fluid, PF = packer fluid, G = local geostatic.

during a treatment. Here the production casing will be affected by both ballooning- and temperature-induced tension increments.

12.7.3 Production tubing

Internal pressure dominant loads assume importance for production tubing design as (a) the tubing is usually a component of the primary barrier envelope, and (b) internal pressure loads are often highest near the top of the tubing string.

12.7.3.1 Pressure test

See the pressure test load case comments in Section 12.7.1.1 and Table 12.13. Tubing is usually tested to a higher relative value than casing, especially if it is a component of the primary barrier envelope.

Table 12.14 Burst—tubing: injection[a, b]

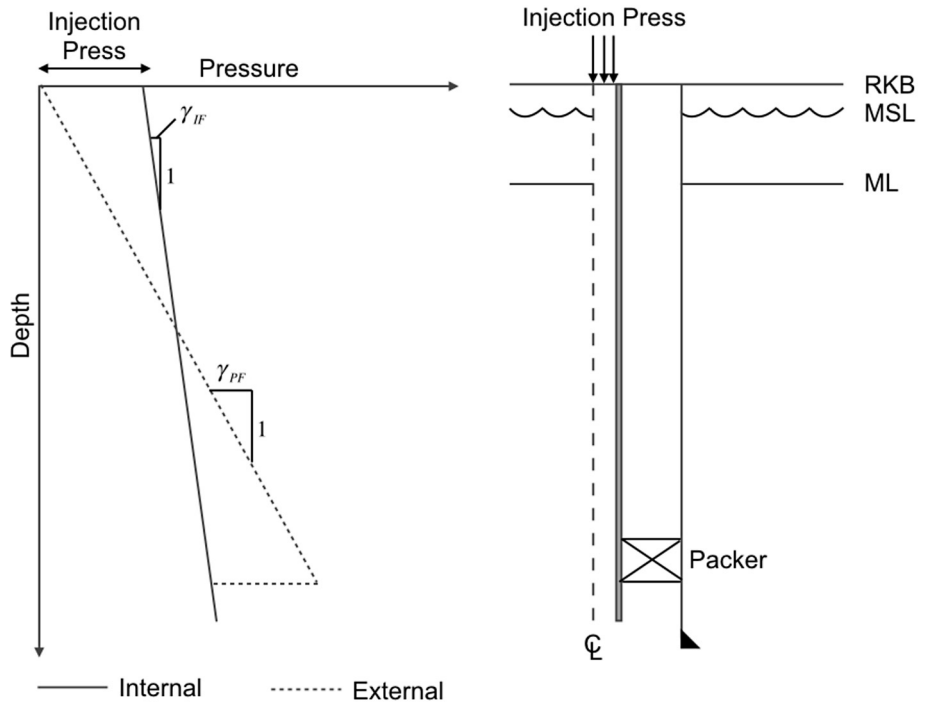

Internal pressure	External pressure	Temperature
Injection wellhead pressure + IF	PF (above packer[c])	I

Comments:

- Check for excessive tubing length change in completions involving a seal bore allowing tubing movement.
- When appropriate and available, a fluid flow simulator should be used to determine both the internal tubing pressure and complete wellbore temperature distributions.

[a] Design string has shaded cross-section.
[b] IF = injection fluid, PF = packer fluid, I = injecting.
[c] Internal fluid occupies the tubing annulus below the packer.

12.7.3.2 Injection

Injection (see Table 12.14) should be checked at its initiation (wellbore is cold) and at a condition of steady state. Movement (in the presence of a seal assembly allowing motion) or attempted movement of the tubing in the vicinity of the packer can either unseat the tubing or damage the packer, respectively.

12.7.3.3 Production

Production (see Table 12.15) should be checked for all landmark flow conditions in the life of the well. Of particular importance is the possibility of buckling as:

Table 12.15 Burst—tubing: production[a, b]

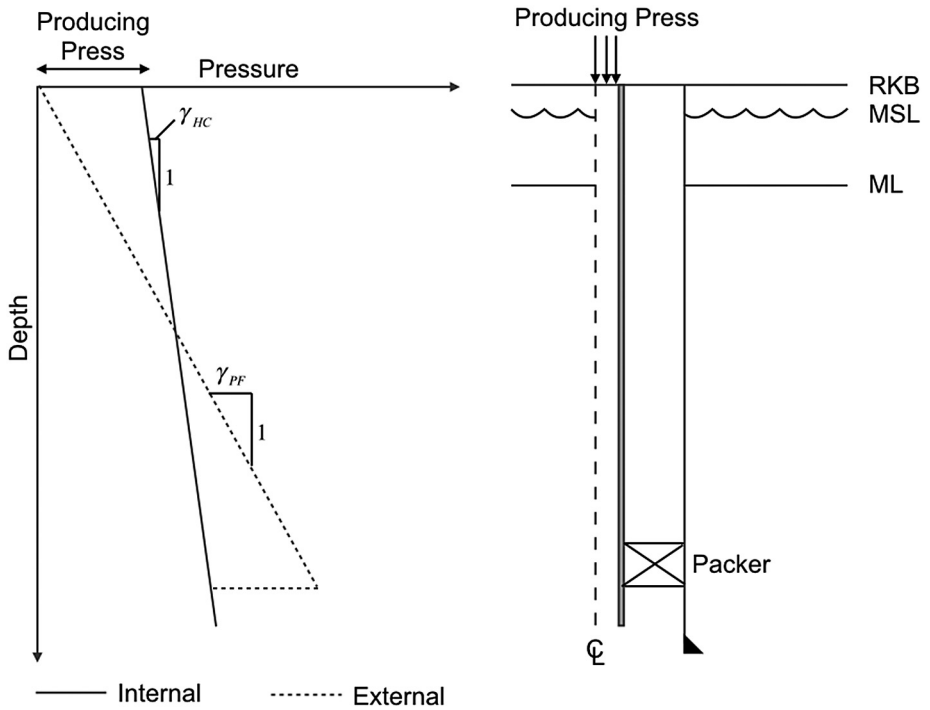

Internal pressure	External pressure	Temperature
Flowing wellhead pressure + HC	PF (above packer[c])	P

Comments:

- This scenario should be modeled for several landmarks in the life of the reservoir—initial production, first water.
- When available, a software multiphase flow simulator should be used to determine both the internal tubing pressure and complete wellbore temperature distributions.
- Check for excessive tubing length change in completions involving a seal bore allowing tubing movement.

[a] Design string has shaded cross-section.
[b] PF = packer fluid, HC = reservoir fluid, P = producing.
[c] Internal fluid occupies the tubing annulus below the packer.

- The additional bending stresses associated with the postbuckled configuration can yield the tubing leading to a condition of so-called "permanent corkscrewing" wherein the tubing does not return to its original configuration when the well is shut-in.
- Movement (in the presence of a seal assembly allowing motion) or attempted movement of the tubing in the vicinity of the packer can either unseat the tubing or damage the packer or tubing, respectively.

Production assisted by artificial lift can complicate this load case as annulus pressure (gas lift) or possible tubing wear (rod pump [154]) can modify the description of loads to which the tubing is subjected.

12.7.3.4 Pump in to kill well

Killing a well through the production tubing (see Table 12.16) should be checked for at least two operational states:

- At the beginning of the operation when the tubing temperature can be cold (depending on the well operations prior to the kill) and tubing internal pressure its highest. The combination of high internal pressure (ballooning) and low temperature may significantly affect either tubing movement or, if movement is not possible, tubing stress.
- At the end of the operation when the pump pressure may be lower, but the wellbore significantly cooler, particularly in its lower regions.

12.7.3.5 Shut-in

Both the hot and cold shut-in conditions are usually modeled, as both represent potential load environments in a well (see Table 12.17).

12.8. EXTERNAL PRESSURE DOMINANT LOADS

As was the case with internal pressure dominant load cases, most designers work with a single external pressure profile and create the external pressure differential by applying various scenarios to the internal pressure distribution.

For all casing the external fluid is usually taken to be a column of the drilling fluid in which the casing was run. This column extends from the top of the string to the casing shoe. That is, we assume the cement sheath to be channeled and of dual quality:

- For the purpose of arresting axial movement, the cement sheath is presumed to be of sufficient bond with the casing that axial casing displacement is prohibited.
- For the purpose of imposing a collapse load, the cement sheath is assumed to be channeled to such a great extent that a continuous column of the drilling fluid in which the casing was run exists along the entire length of the string, including that portion of the string below the top of cement.

These two seemingly contradictory assumptions—an adequate sheath to restrict axial movement, a practically nonexistent sheath for defining a continuous collapse fluid column—can both be reasonably pictured. Particularly for the case of axial movement restriction, consider the experimentally verified rule-of-thumb which states that the shear bond between the casing and cement sheath is roughly one-tenth the unconfined compressive strength of the cement. As an example, for 9-5/8 in. casing, the surface area for one foot of casing is $\pi \times 9.625 \times 12$, or 363 in^2. Given a relatively weak cement with 1000 psi unconfined compressive strength, the shear bond on one foot of casing

Table 12.16 Burst—tubing: pump in to kill well[a, b]

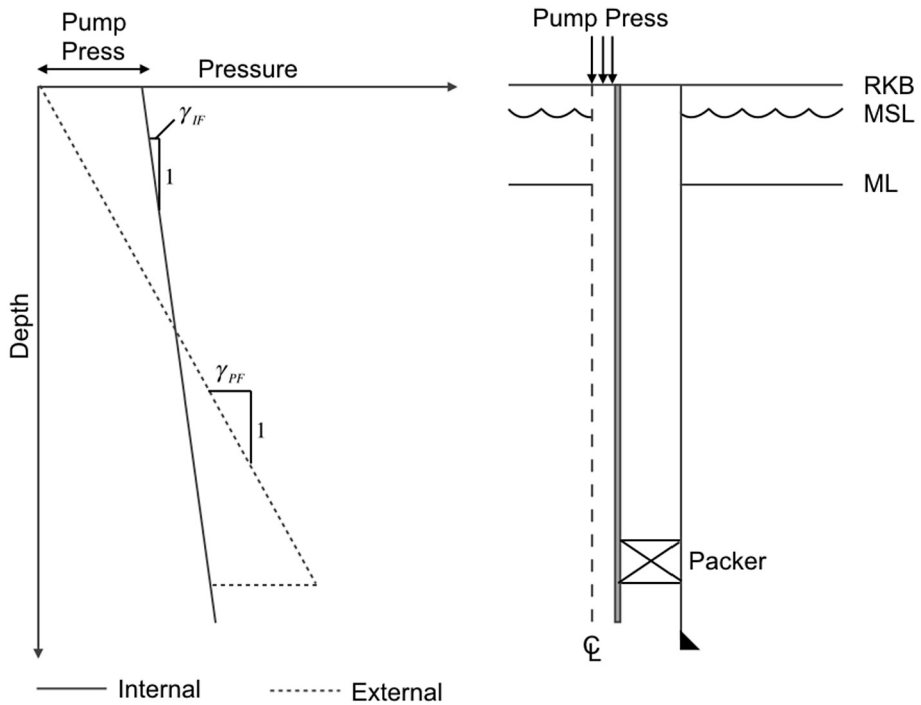

Internal pressure	External pressure	Temperature
Shut-in tubing pressure + kill margin + IF (start kill), steady state pump pressure + IF (end kill)	PF (above packer[c])	I

Comments:

- Check for excessive tubing length change in completions involving a seal bore allowing tubing movement.
- When appropriate and available, a fluid flow simulator should be used to determine both the internal tubing pressure and complete wellbore temperature distributions.

[a] Design string has shaded cross-section.
[b] IF = injection fluid, PF = packer fluid, I = injecting.
[c] Internal fluid occupies the tubing annulus below the packer.

is 100×363, or $36\,300\,\text{lb}_\text{f}$. The conclusion we reach is that severely channeled cement can still prevent axial movement.

Regarding channeling and its effect on casing collapse resistance, an experimental[16] and numerical study by Jammer et al. [73] indicates that imperfect, but sufficient ce-

[16] See also earlier work by Evans and Harriman [155].

Table 12.17 Burst—tubing: shut-in[a, b]

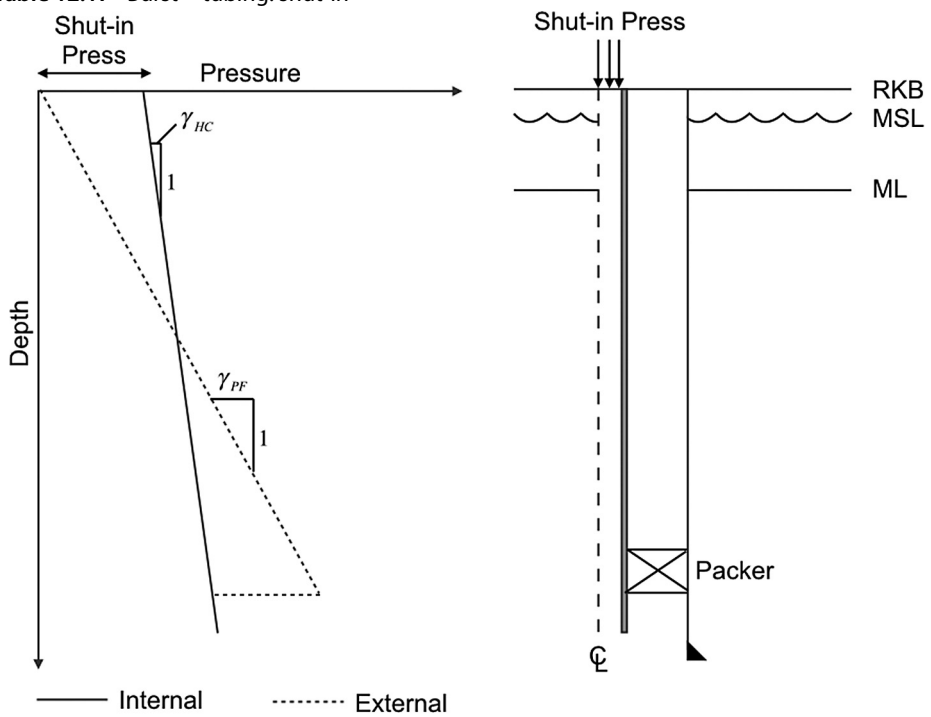

Internal pressure	External pressure	Temperature
Shut-in pressure + HC	PF (above packer[c])	G (cold shut-in) or P (hot shut-in)

Comments:

- Hot shut-in represents a short term condition immediately after the well flow is arrested.
- Cold shut-in models a well shut-in for a long period of time.
- The internal pressure determination can either proceed from the wellhead, down, or from the perforations, up. The latter is the more natural path.

[a] Design string has shaded cross-section.
[b] PF = packer fluid, HC = reservoir fluid, G = local geostatic, P = producing.
[c] Internal fluid occupies the tubing annulus below the packer.

ment circumferential coverage can alter the buckling mode of the casing cross section, thus increasing its resistance to external pressure. This increase, however, is diminished by increasing cement void angle (particularly if the void angle exceeds 90° and/or a micro-annulus exists between the cement and casing. A common, conservative assumption in line with the second bullet above is to ignore any beneficial increase in collapse resistance due to the cement sheath.

One could, of course, avoid the above bulleted conundrum by assuming the density of the cement slurry as the external fluid below the cement top. This author judges this choice to be a bit too conservative. Further, the presence of liquid cement during the life of a string suggests a problem that needs to be solved before this string's installation is considered complete.

In addition to the drilling fluid column, the casing external pressure distribution may include a surface pressure due to annular pressure build-up. Liners and other tubulars not hung from the surface assume the local hydrostatic pressure at the top of the string to be trapped when the liner top packer is set, plus any potential APB pressure.

For production tubing the fluid column is taken to be the packer fluid down to the packer. In addition, some tubing loads will assume a surface pressure applied to the tubing, typical sources being a tubing leak and annular pressure build-up.

12.8.1 Surface and intermediate casing

Particularly for larger diameter casing, the initial condition (see Section 12.6.2 and Table 12.5) should always be checked for collapse. The resistance of some large diameter tubulars is so low that the external pressure differential of the cement column itself can be sufficient to collapse the casing.

12.8.1.1 Lost circulation

The primary external pressure load for casing set in the overburden is that of lost circulation (see Table 12.18). We assume that while drilling the hole section below the casing to be designed we encounter a zone of lower than normal pore pressure. Drilling fluid begins to exit the wellbore, lowering the internal pressure inside the casing and creating an external differential pressure load.

In theory, and it is this worst case that is assumed, the drilling fluid level inside the casing can drop until it reaches hydrostatic equilibrium with the pore pressure at the point fluid is exiting the wellbore. That is, the height of the fluid column inside the casing will be

$$h_{LC} = \frac{\hat{p}_p(Z)}{\gamma_f}, \tag{12.60}$$

where h_{LC} is the height of the drilling fluid (with weight density γ_f) column at equilibrium and $p_p = \hat{p}(Z)$ is the pore pressure as a function of vertical depth.

In reality, the fluid level will seldom drop as low as predicted for the following reasons:

- With drilling fluid flow to the formation, the near-wellbore pore pressure will increase. Assuming a Darcy-like fluid flow into the formation from the wellbore, with the flow rate proportional to pressure gradient [156], the flow rate will decrease with time as the pressure gradient at the wellbore wall decreases.

Table 12.18 Collapse—surface and intermediate casing: lost circulation[a, b]

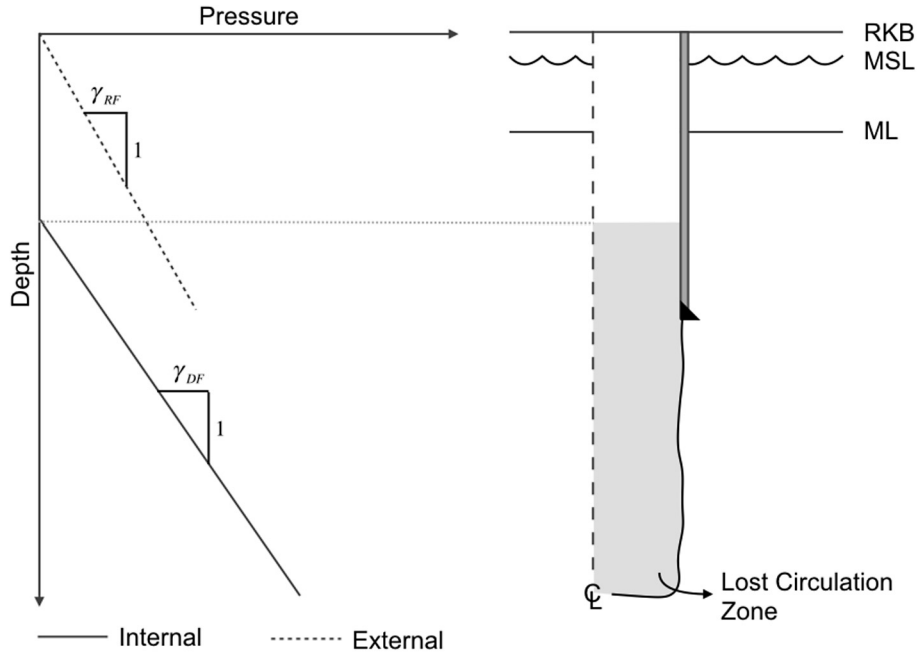

Internal pressure	External pressure	Temperature
Empty to top of DF, then DF	RF	G or C

Comments:

- Top of DF is determined by a hydrostatic balance between the DF column and pore pressure at the lost circulation vertical depth.
- Conditions can be such that this load case is the same as full evacuation.

[a] Design string has shaded cross-section.
[b] DF = drilling fluid, RF = running fluid, G = local geostatic, C = circulating.

- As the height of the drilling fluid column drops, the wellbore pressure contribution to the pressure gradient at the wellbore wall will decrease.
- Depending on the permeability of the formation and the fluid constitution, solids in the drilling fluid will be filtered out at the wellbore wall, creating a region of "damaged permeability", further lowering fluid flow/loss rate.
- The factors above that lower the loss rate imply a long period of time with no one on the rig floor detecting the loss.

The counter to the above argument is that the loss zone may be fractured, so that Darcy flow is not the governing relation for the fluid loss rate.

As was the case with pressure testing (Section 12.7.1.1) and well control (Section 12.7.1.2), the installation of a liner below a previous string may influence the depth of the lost circulation zone being analyzed (see Fig. 12.6). The safe alternative is

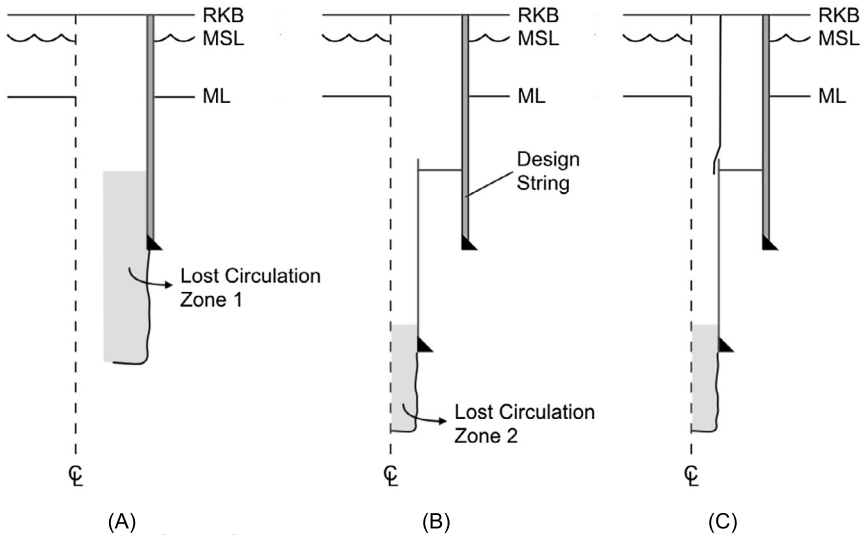

Figure 12.6 ***Calculating lost circulation in the presence of a liner.*** In scenario (A) the casing is designed only for lost circulation while drilling the open hole immediately below that casing's shoe. In scenario (B) the presence of a liner (only) means that the original casing is still exposed should Lost Circulation Zone 2 be encountered. In scenario (C) a tieback is run before drilling out the liner, and the original casing is not exposed to the lost circulation event associated with Lost Circulation Zone 2.

to analyze lost circulation for the open hole section below the casing being designed and for all liners below that string. As before, the timing of tieback installations can affect this calculation.

Example problem—lost circulation load case

While drilling ahead out of 9-5/8 casing with 11.5 ppg fluid, a lost circulation zone having a pore pressure of 5000 psi is encountered at 18 000 ft. In the worst case, how far will the fluid level inside the casing drop?

From Eq. (12.60) the height of the fluid column will be

$$h_{LC} = \frac{5000\,\text{psi}}{11.5\,\text{ppg} \times 0.051\,948\,\frac{\text{psi}}{\text{ft ppg}}} = 8370\,\text{ft}, \tag{12.61}$$

where we have assumed that the local acceleration of gravity is such that $1\,\text{lb}_\text{m}$ has a weight of $1\,\text{lb}_\text{f}$. For the load case, the casing is assumed evacuated down to $18\,000 - 8370 = 9630\,\text{ft}$, with 11.5 ppg drilling fluid below that depth.

Table 12.19 Collapse—surface and intermediate casing: riser margin[a, b]

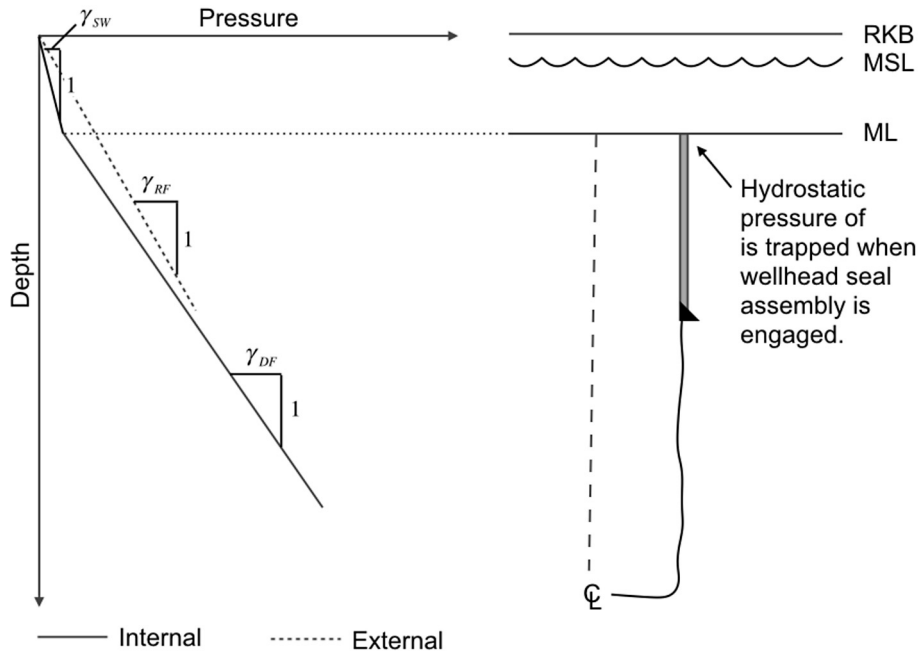

Internal pressure	External pressure	Temperature
SW to mudline, then DF	RF	G or C

Comments:

- This load case is usually pertinent to deepwater wells only.

[a] Design string has shaded cross-section.
[b] DF = drilling fluid, RF = running fluid, SW = sea water, G = local geostatic, C = circulating.

12.8.1.2 Riser margin

This load case (see Table 12.19) is applicable only to offshore wells drilled with a riser, and usually only to wells in deepwater. The scenario assumes that during drill ahead the drilling riser parts near the mudline. What was previously a column of drilling fluid to the surface now becomes a mixed column of sea water to the mudline with drilling fluid below. The severity of this load case depends on the current drilling fluid density and the water depth. For a more detailed description of riser margin, see Section 13.3.2.5 of Chapter 13.

12.8.2 Production casing

12.8.2.1 Riser margin

Production casing may also be affected by a parted riser. See the riser margin load case described in Section 12.8.1.2 and Table 12.19.

Table 12.20 Collapse—production casing: packer leak[a, b]

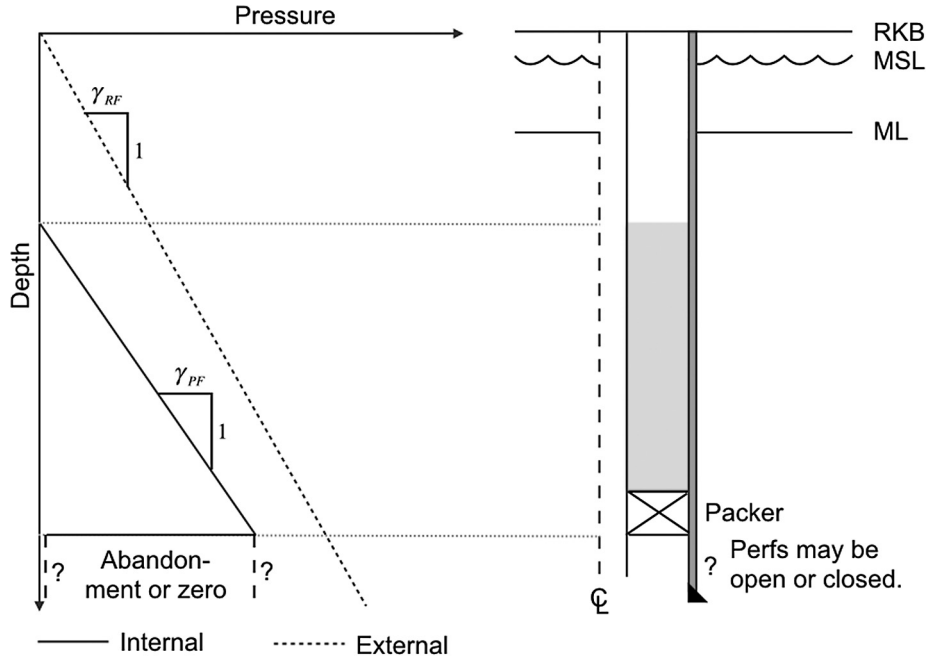

Internal pressure	External pressure	Temperature
Empty to top of PF, then PF	RF	G

Comments:

- Top of PF is determined by a hydrostatic balance between the PF column and reservoir abandonment pressure.
- Conditions can be such that this load case is the same as full evacuation.

[a] Design string has shaded cross-section.
[b] PF = packer fluid, RF = running fluid, G = local geostatic.

12.8.2.2 Packer leak

The packer leak load case for production casing (see Table 12.20) is similar to the lost circulation load case for surface and intermediate casing. One imagines that late in the life of the well the packer develops a leak. The level of packer fluid in the tubing annulus can drop until it reaches a hydrostatic balance with the pressure below the packer, which is essentially perforation pressure. The production casing therefore undergoes a loss in internal pressure.

How low can the packer fluid level drop? As was the case with lost circulation (see discussion in Section 12.8.1.1), this drop will depend on a number of factors related to the elapsed time and the flow properties of the reservoir. Engineers who use this load case assume the late-life perforation pressure to be abandonment pressure. Even for a gas

well, whose abandonment pressure can be just hundreds of psi (a few MPa), accounting for abandonment pressure may save one wall thickness increment in the design.

Engineers who do not consider the abandonment pressure usually design the production casing for evacuation. This option is defendable for at least the following reasons:

- A late-life condition of plugged perforations, if not immediately countered, can essentially leave at least the subpacker portion of the production casing in a state of near evacuation.
- Similarly, the use of small (able to be run inside the tubing) strings to inject nitrogen for the purpose of gas-lifting older wells to a producing gradient has been known to be uncontrolled to the point that the tubing and subpacker casing can be essentially evacuated.

Either of the above scenarios, when coupled with a questionable seal at the packer, can endanger all or at least the deeper portions of the production casing.

12.8.3 Production tubing

12.8.3.1 Annulus pressure test

The annulus pressure test (see Table 12.21) is used to test the packer and/or tubing hanger [151]. The pressures associated with this test should also be used to generate an internal pressure load case for the production casing. Depending on that casing's cement top, this test could damage the production casing cement sheath.

12.8.3.2 Production from long term shut-in

This scenario (see Table 12.22) imagines a well shut-in for a long period with a slow tubing-to-annulus leak (tubing connection, expansion joint). Reservoir pressure is allowed to migrate from the tubing to the top of the tubing annulus. The well is now inoperative with essentially shut-in pressure on both sides of the tubing. Should the well then be placed on production without first checking the tubing annulus pressure the following loads immediately develop:

- the internal pressure at the top of the tubing decreases as the well is opened to production;
- the well is relatively cool, implying maximum tension at the top of the tubing;
- the tension in the tubing reduces its collapse resistance;
- the exterior of the tubing is loaded by shut-in pressure from the leak.

This load case could, presumably, be eliminated by proper adherence to operating procedures but has, nevertheless, occurred.

12.8.3.3 Safety valve leak

This load case (see Table 12.23) is applicable to offshore wells. One envisions the well shut-in, with the tubing above the closed subsurface safety value (SSSV) bled to a low

Table 12.21 Collapse—tubing: annulus pressure test[a, b]

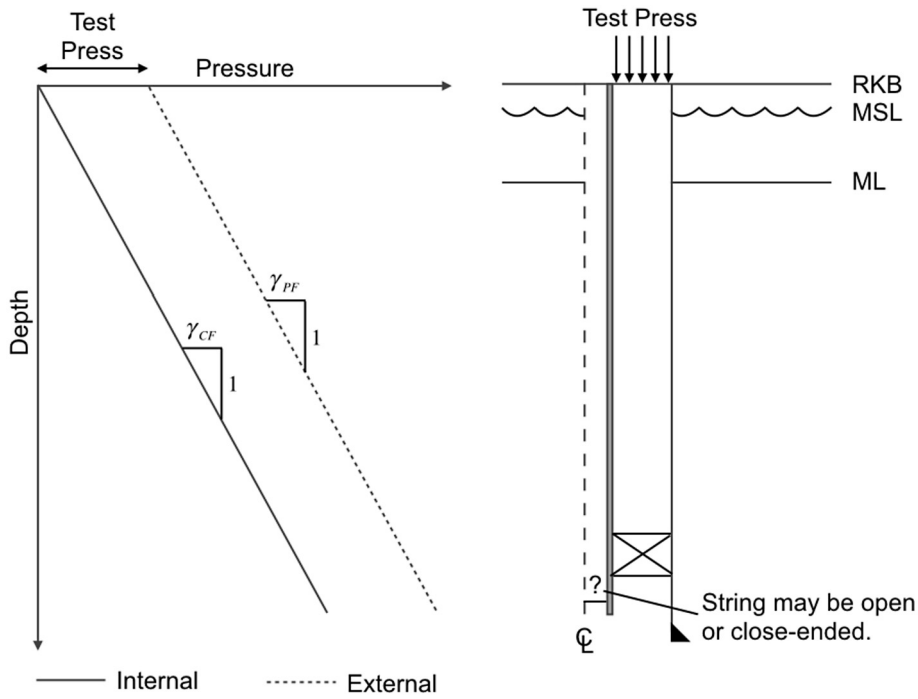

Internal pressure	External pressure	Temperature
CF	Test pressure + PF	G

Comments:

- Either the CF or the PF may be both internal and external to the tubing during the test.
- A surface pressure may also be applied internally to the tubing to mitigate possible collapse.

[a] Design string has shaded cross-section.
[b] CF = completion fluid, PF = packer fluid, G = local geostatic.

pressure (or evacuation). The tubing develops a leak below the SSSV that can flow until the tubing and annulus pressure equalize at the location of the leak. Above the leak the pressure is determined by subtracting the gradient of the packer fluid. This load case particularly endangers portions of the tubing above the SSSV.

12.8.3.4 Evacuation

The discussion of the packer leak load case for production casing (see Section 12.8.2.2) suggests instances where the production tubing may be at or near evacuation (see Table 12.24).

Table 12.22 Collapse—tubing: production from long term shut-in[a, b]

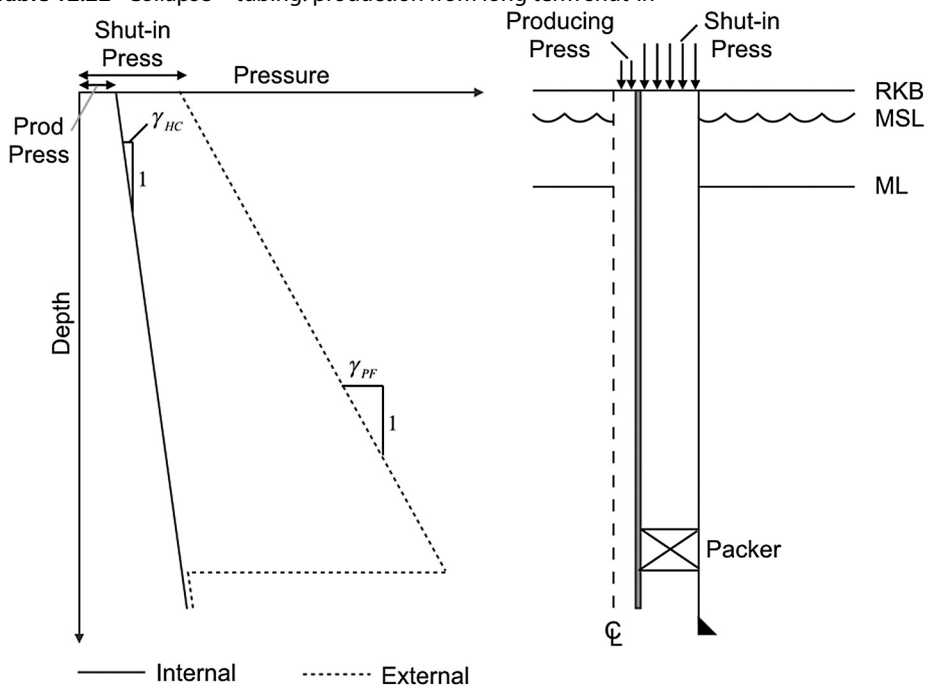

Internal pressure	External pressure	Temperature
Flowing tubing pressure + HC	Shut-in pressure + PF	G

Comments:

- This load case is assumed to happen too early for the well to deviate from geostatic temperature.
- When appropriate and available, a fluid flow simulator should be used to determine the internal tubing pressure distribution.

[a] Design string has shaded cross-section.
[b] PF = packer fluid, HC = reservoir fluid, G = local geostatic.

12.9. DESIGN AND SAFETY FACTORS

Terminology is this area is author-dependent. In this book we will use a fairly common practice and differentiate between design factor and safety factor. Consider the ratio of resistance to load for the design equation of a particular limit state. The minimum value of that ratio that is acceptable is the design factor. The actual value we calculate when we compute a tubular's resistance (given a limit state) to the imposed load (as defined by the tables in this chapter) is the safety factor.[17]

[17] An alternative measure to the safety factor (Resistance / Load) is safety margin defined as Resistance minus Load.

Table 12.23 Collapse—tubing: SSSV leak[a, b]

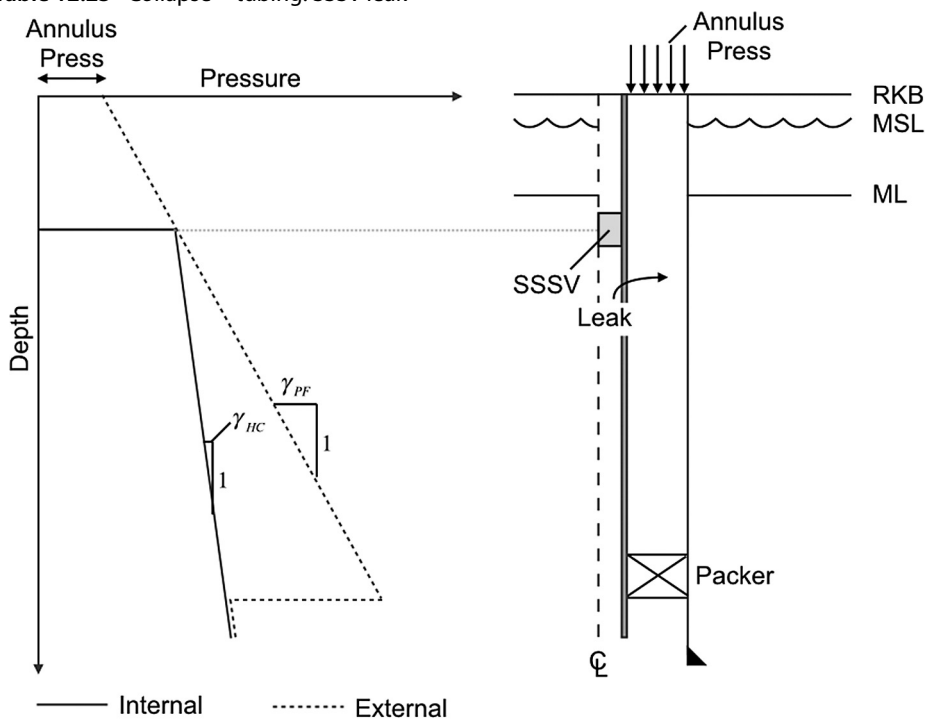

Internal pressure	External pressure	Temperature
Shut-in reservoir pressure at perforations – HC	Annulus pressure + PF (above packer)	G or P

Comments:

- Pressure under SSSV is determined by calculating from the perforations (at shut-in conditions) up to the SSSV using a column of (shut-in) reservoir fluid.
- The pressures inside and outside the tubing at the leak location are equal.
- Above the leak the pressure, including the annulus surface pressure, is determined by subtracting the gradient of the packer fluid.
- The pressure above the SSSV can either be determined by a vented column of reservoir fluids, or that portion of the tubing can be assumed evacuated.

[a] Design string has shaded cross-section.
[b] PF = packer fluid, HC = reservoir fluid, G = local geostatic, P = producing.
[c] Internal fluid occupies the tubing annulus below the packer.

The design factor is a measure of uncertainty in a number of factors including the following [157,158]:

- material properties (E, ν, f_y, f_u, degree of anisotropy);
- load values (p_p, p_{fr}, γ_f, detection and crew capabilities);
- tubular, connection and accessory dimensions (D, t, thread form, tolerances);

Table 12.24 Collapse—tubing: evacuation[a, b]

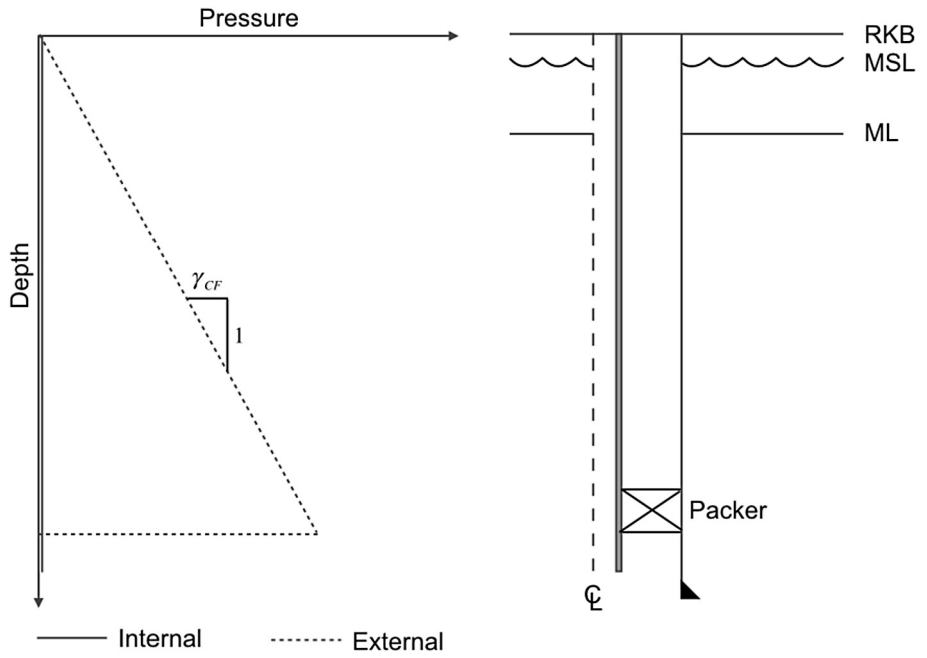

Internal pressure	External pressure	Temperature
Empty	PF (above packer)	G or P

Comments:

- Possible causes are plugged perforations and over displacement of tubing via a nitrogen string.

[a] Design string has shaded cross-section.
[b] PF = packer fluid, G = local geostatic, P = producing.
[c] Internal fluid occupies the tubing annulus below the packer.

- models used to describe both load and resistance.

Embedded in design factors are significant company historical experiences that should be given due weight when considering a design factor change or dispensation.

There are two forms of a equation defining a limit state or failure mode. The limit state equation itself is defined by the tubular subcommittees of the API as an "equation which, when used with the measured geometry and material properties of a sample, produces an estimate of the failure value of that sample" [51]. This equation purports to be an accurate predictor of the resistance of a sample given the actual dimensions and material of that sample. Closely related to the limit state equation is the design equation defined as an "equation which, based on production measurements or specifications, provides a performance property useful in design calculations" [51]. The design equation is derived from the limit state equation by choosing reasonably severe extremes

of the dimensions and material constitution and substituting them for the otherwise measured quantities.[18]

12.9.1 Conventional design and safety factors

As an example of a conventional design and safety factor, consider triaxial yield. The limit state is defined by Eq. (6.34). In that equation (see below) the resistance is represented by the yield stress f_y, and the load is measured by the von Mises equivalent stress defined in Eq. (6.58). We render Eq. (6.34) a design equation by (a) assuming the thinnest reasonable wall thickness from the manufacturing process and (b) using the minimum acceptable yield strength for the material (see discussion in Section 6.3.6 in Chapter 6). The resulting design equation is Eq. (6.95), reproduced here for further discussion as

$$\hat{f}_{des}(r) = \underbrace{\left(\Sigma_{zz} - \frac{p_i d_{wall}^2 - p_o D^2}{D^2 - d_{wall}^2}\right)^2 + \frac{3}{16r^4}\left(\frac{(p_i - p_o)\, d_{wall}^2 D^2}{D^2 - d_{wall}^2}\right)^2}_{\text{Load, } \Sigma_e^2} - \underbrace{f_{ymn}^2}_{\text{Resistance}} = 0. \quad (12.62)$$

As indicated in Eq. (12.62), the left-most portion of the relation is the von Mises equivalent stress (squared) for the case of no torsion or other shear,[19] where the radial and hoop components of Σ_e have been evaluated at a point on the tubular where the wall thickness is d_{wall}, the thinnest reasonable wall thickness. The von Mises equivalent stress is a measure of the load as applied to this location in the tube and assumes a maximum value at a radius r that depends on the presence of bending. The minimum yield stress f_{ymn} represents a portion of the tube with minimum strength constitution. Further, the minimum wall thickness (maximum Σ_e) and minimum yield stress are assumed to be collocated.

In the absence of bending we can evaluate Eq. (12.62) at $r = \frac{d_{wall}}{2}$ and get

$$\hat{f}_{des}\left(\frac{d_{wall}}{2}\right) = \underbrace{\left(\Sigma_{zz} - \frac{p_i d_{wall}^2 - p_o D^2}{D^2 - d_{wall}^2}\right)^2 + 3\left(\frac{(p_i - p_o)\, D^2}{D^2 - d_{wall}^2}\right)^2}_{\text{Load, } \Sigma_e^2} - \underbrace{f_{ymn}^2}_{\text{Resistance}} = 0. \quad (12.63)$$

[18] The design equation described here is for deterministic design. For probabilistic design, the design equation is derived statistically and represents a chosen lower percentage of the probability distribution curve of the tubular's resistance.

[19] Compare Eq. (6.35) with Eq. (6.23) and the narrative in Section 6.3.6 of Chapter 6.

For triaxial design it is typical practice to compare the square roots of the load and resistance terms in Eq. (12.63). The safety factor for triaxial yield is therefore

$$SF_{Triaxial} = \frac{\text{Resistance}}{\text{Load}} = \frac{f_{ymn}}{\sqrt{\left(\Sigma_{zz} - \frac{p_i d_{wall}^2 - p_o D^2}{D^2 - d_{wall}^2}\right)^2 + 3\left(\frac{(p_i - p_o)D^2}{D^2 - d_{wall}^2}\right)^2}}. \tag{12.64}$$

This relation would, of course, be more complicated if we had included bending in the calculation of Σ_{zz}.

In applying Eq. (12.64) to any of the load cases in this chapter, one uses:

- the pessimistic dimensions (D, d_{wall}) and strength (f_{ymn}) of the tube being evaluated;
- local values of Σ_{zz}, p_i and p_o of the selected load case at the depth of investigation.

The resulting value for the triaxial safety factor $SF_{Triaxial}$ is compared to a minimum acceptable value of $SF_{Triaxial}$ which is the triaxial design factor $DF_{Triaxial}$, that is, for an acceptable design we require

$$SF_{Triaxial} \geq DF_{Triaxial}. \tag{12.65}$$

Typical values of $DF_{Triaxial}$ are in the range 1.15–1.25, with the many operators leaning toward the lower side of this range.[20]

The condition for collapse resistance is similar to that discussed for triaxial yield with the following exceptions:

- Resistance is measured by the API minimum collapse resistance of the tube (or a minimum value supplied by the manufacturer for proprietary tubes), suitably adjusted for the presence of Σ_{zz} and p_i as described in Section 8.2.4 of Chapter 8;
- The material strength is still pessimistic (f_{ymn}), but the dimensions of the tube are considered to be as specified (D, t);
- The safety factor is defined by

$$SF_{Collapse} = \frac{\Delta p_c \quad \text{(Section 8.2.4 of Chapter 8)}}{p_o - p_i \quad \text{(Load case)}}. \tag{12.66}$$

Typical values of $DF_{Collapse}$ are in the range 1.00–1.10, with the many operators leaning toward the lower side of this range. The statistics of mapping average collapse resistance to minimum collapse resistance are, for the most part, sufficiently conservative that a large design factor has proven unnecessary.

[20] Prior to the release of a version of API TR 5C3 [51] using d_{wall} in design Eq. (12.63), the diameter calculated using specified D and t ($d = D - 2t$) was used. In that previous era, triaxial design factors tended toward the upper side of the indicated range.

12.9.1.1 Example problem—collapse safety factor

Given the tube and axial stress and internal pressure conditions of the example collapse calculation in Section 8.2.4.6 of Chapter 8, compute the collapse safety factor when the external pressure is 8000 psi.

From Section 8.2.4.6 of Chapter 8, $\Sigma_{zz} = 20\,000$ psi, $p_i = 1000$ psi, and the resulting value of $\Delta p_c = 7474$ psi. From Eq. (12.66) we get

$$SF_{Collapse} = \frac{7474\,\text{psi}}{8000 - 1000\ \text{psi}} = 1.07, \tag{12.67}$$

which for most engineers would be acceptable when compared to the collapse resistance design factor range of 1.00–1.10.

12.9.2 Radial design and safety factors

When considering threaded connections one can follow a procedure similar to Section 12.9.1 for the joint strength, compressive strength and even internal and external pressure ratings. Increasingly, however, the popularity of casing design software and the availability of results from sophisticated test procedures [56] have led to a multidimensional approach to expressing connection resistance.

The approach is similar to that used for triaxial yield. An envelope constructed by the manufacturer in axial force/stress × differential pressure space (see Section 6.3.4.3 of Chapter 6) is used to display the resistance of the connection to combined loading. The difference between the character of the connection envelope and the von Mises yield surface for the tube body is that not all penetrations of the envelope necessarily represent connection yield. Some portions of the connection envelope may be governed by connection-specific considerations such as leak integrity.[21] Other portions of the envelope may address yield of internal shoulders rather than the critical section areas of the pin and box members. For this reason, it is not unusual to see a connection envelope that is continuous, but not necessarily smooth, with abrupt corners signifying the juncture of limit states from different portions of the connection geometry.

Parallel to the advancement in connection envelopes are similar performance envelopes used to describe the capacity of accessories such as hangers and packers [55]. Frequently the axes are reversed—differential pressure becomes the abscissa, axial force/stress becomes the ordinate—but the underlying principle is the same. An attempt is being made to characterize the resistance of the part in multidimensional load space.

[21] Even in the case of leak integrity, the underlying limit state may be yield of an internal shoulder in the connection.

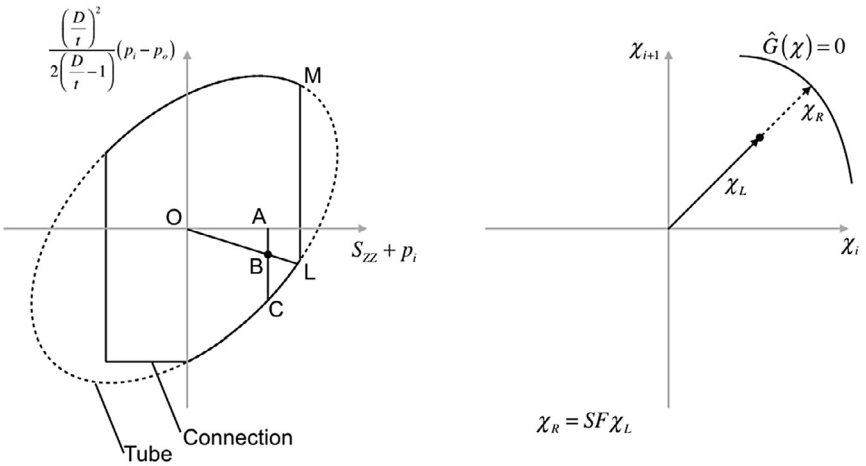

Figure 12.7 ***Specific connection envelope and general illustrations of radial safety factor.*** The left-hand diagram could, alternatively, be an accessory performance envelope, or triaxial yield or collapse resistance of a tube. (A) Connection envelope; (B) general envelope.

Pertinent to the above envelopes is a new view of safety factor,[22] termed by Liu and coworkers the radial safety factor [158]. The radial safety factor is an attempt to better describe the closeness of a combined load to a multidimensional stress limit state. Consider the two diagrams in Fig. 12.7. The left-hand diagram follows the collapse example of [158] and illustrates the radial safety factor concept concretely in terms of collapse of a tube body. The right-hand diagram is a generalization to other failure modes and to other, nontubular components of a tubing or casing string.

In the left-hand diagram a performance envelope for a generic connection (solid envelope) is compared to the von Mises yield surface for the tube body (dashed ellipse). The connection is roughly eighty percent efficient in tension, 60% efficient in compression, and over most of its upper and lower extremities displays internal and external pressure resistance equal to the tube body.

Assume that at some location in the tubular string of which this tube-connection combination is a part, the connection is subjected to a load with Σ_{zz}, p_i and p_o values corresponding to point B. If we were to approach this problem in terms of conventional safety factors, the external pressure safety factor for the connection would be $\overline{AC}/\overline{AB}$, which appears to be approximately 40% of the way to penetrating the connection envelope at point C. On the other hand, if we reasonably assume that all of the loads are

[22] Thanks to Frans J. Klever, a coauthor of [158], for an informative email interchange regarding radial safety factor.

being applied proportionally, then it is more likely that increasing load will penetrate the connection envelope at point L. Further, if this is the case, comparing line $\overline{OB}$ with line $\overline{OL}$ would imply that the current load is approximately two-thirds of the way to penetrating the connection envelope at L. The conclusion to be reached from the left-hand diagram in Fig. 12.7 is that a conventional safety factor calculation will render a mistaken impression of the closeness of the connection to its limit state. A safety factor measure of $\overline{OL}/\overline{OB}$ is a more meaningful measure of the connection's loading relative to its capacity.

The right-hand side of Fig. 12.7 generalizes the concepts presented for the connection envelope. We introduce a limit state equation $\hat{G}(\chi) = 0$ to define the condition of our tubular structure, with $\hat{G}(\chi) < 0$ being an unacceptable state.[23] The dimension of the vector χ can, depending on the functions describing load and resistance, be large. For this reason, only two of the coordinate axes for the limit state, χ_i and χ_{i+1}, have been indicated in Fig. 12.7.

In the generalization for radial safety factor, the safety factor is expressed as $\chi_R = SF\chi_L$. The vector χ_L is that portion of χ that defines the load; the vector χ_R is the extension of χ_L out to the limit state. Both χ_R and χ_L begin at the origin.

12.9.2.1 Example problem—radial safety factor for triaxial yield

Apply the concept of radial safety factor to triaxial yield in the absence of bending.

The limit state equation is (see Eq. (12.62) with $r = d_{wall}/2$)

$$\hat{G}(\Sigma_{zz}, p_i, p_o, D, t, k_{wall}, f_{ymn}) = \left(\Sigma_{zz} - \frac{p_i d_{wall}^2 - p_o D^2}{D^2 - d_{wall}^2}\right)^2 + 3\left(\frac{(p_i - p_o)\, D^2}{D^2 - d_{wall}^2}\right)^2 - f_{ymn}^2$$
$$= \Sigma_e^2 - f_{ymn}^2 = 0, \tag{12.68}$$

where $d_{wall} = D - 2k_{wall}t$, $\chi_L = \begin{bmatrix} \Sigma_{zz} & p_i & p_o \end{bmatrix}^T$ and $\chi_S = \begin{bmatrix} D & t & k_{wall} & f_{ymn} \end{bmatrix}^T$, where $\chi = \begin{bmatrix} \Sigma_{zz} & p_i & p_o & D & t & k_{wall} & f_{ymn} \end{bmatrix}^T$. The example problem in Section 6.3.6.1 of Chapter 6 reinforces the substitution of Σ_e (evaluated using $d = d_{wall}$) for the first two terms on the right-hand side of Eq. (12.68).

At a certain location s along the tubular string, $\chi_L(s) = \begin{bmatrix} \Sigma_{zz}(s) & p_i(s) & p_o(s) \end{bmatrix}^T$. At this location we can determine that

$$\chi_R(s) = SF\chi_L(s), \tag{12.69}$$

[23] The function $\hat{G}$ is sometime written as $\hat{G} = \hat{R} - \hat{S}$ where $\hat{R}$ is the resistance portion of the equation and $\hat{S}$ is the load. We have chosen to use the more general expression $\hat{G}$ to account for the frequent circumstance when $\hat{R}$ and $\hat{S}$ may depend on some of the same variables. If load and resistance are separated, then the limit state equation is $\hat{R} - \hat{S} = 0$.

where SF is the radial safety factor for triaxial yield. The equation implies that multiplying all the elements of $\chi_L(s)$ by SF will render $\hat{G}(\Sigma_{zz}, p_i, p_o, D, t, k_{wall}, f_{ymn}) = 0$. But from Eq. (12.68) this is the same as saying $\Sigma_e = f_{ymn}$. Further, from Eq. (12.63), multiplying all the elements of $\chi_L(s)$ by SF is identical to multiplying Σ_e by SF. We conclude that the conventional safety factor for triaxial yield is, in fact, an application of the radial safety factor, and therefore the safety factors computed from Eqs. (12.64) and (12.69) are identical. This result lends credence to the conventional triaxial yield safety factor as a credible means of measuring a tubular design for yield.

Liu et al. [158] also present an iterative calculation procedure for the radial safety factor for collapse.

12.9.3 Extensions of the radial safety factor concept

Several extensions to the radial safety factor concept exist regarding both the limit state and the definition of the radius vector.

12.9.3.1 Multiple limit states

A threaded connection or tubing accessory may have a suite of limit states to be checked, depending on the part's internal geometry (connection) or collection of subparts (accessory). In either case a useable generalization to the preceding discussion would be to plot the multiple limit states and then, by projecting the load point radius, determine which limit state surface is penetrated. The concept is visualized in the left-hand diagram of Fig. 12.8.

This concept is an extension of the calculation presented by Liu et al. [158] for threaded connections, where the straight lines connecting individual points defining the connection service envelope can be considered individual limit state lines/surfaces.

12.9.3.2 Nonradial load lines

Underlying the concept of radial safety factor is the assumption that between the current load point and the resistance point, or intersection of the radial load line with the limit state surface, the loading is increased proportionally. This assumption is reasonable. In most instances, however, the proportionality of an individual load case has its origin not at a state of zero load, but at the initial state for the tubular.[24] Contra the implementation of nonradial load lines is that the initial state, although usually a benign state of stress, is not a datum of zero stress.

[24] In a truly nonlinear analysis—for example, and analysis involving friction—one could argue that a better candidate than either the state of zero load or the initial state for the tubular would be the state corresponding to the previous load case. Most casing and tubing designs, however, do not consider this degree of nonlinearity.

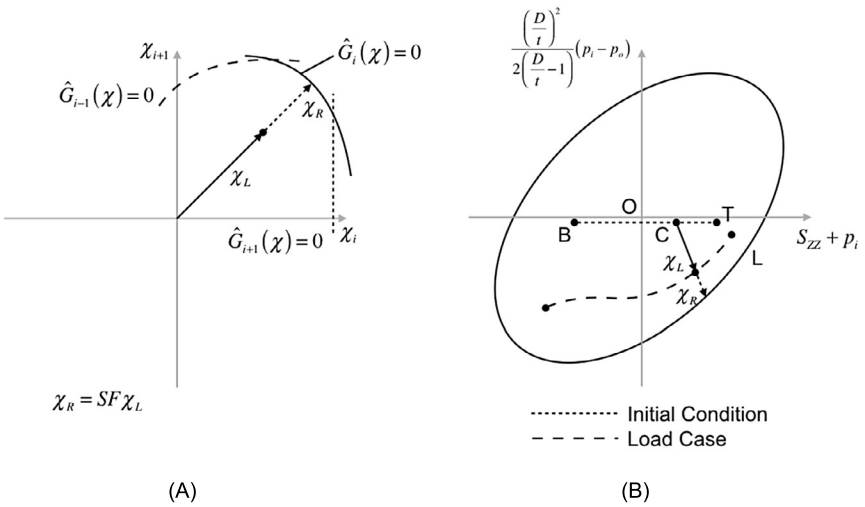

Figure 12.8 ***Possible extensions to the concept of radial safety factor.*** The left-hand diagram illustrates multiple limit states. In the diagram the load line, if extended proportionally, will intersect the *i*th limit state. The right-hand diagram illustrates nonradial load lines. The base of the load line is the tubular string's initial condition instead of the origin; T = top of string, B = bottom of string, C = current location of interest in tubular string.

The right-hand diagram in Fig. 12.8 illustrates an implementation of nonradial load lines. The dashed curve represents the initial state of the tubular in a space pertinent to the current limit state. The solid curve is the state of the tubular under a particular load case.

CHAPTER 13

Casing Seat Selection and Sizing

13.1. INTRODUCTION

Determination of both the lengths and diameters of the well tubular constituents is required prior to stress analysis. Length determination is the more complicated issue and is usually approached first.

The setting depths of various casing strings are predicated on a desire to maintain a stable wellbore throughout well construction. Drilling fluid density helps mechanically support the wellbore but is limited in selection both from above and below by considerations related to the nature of the rock through which drilling and completion operations must be performed. As these bounds vary continuously, a suitable drilling fluid density at one depth may prove unacceptable elsewhere in the well trajectory. It therefore becomes necessary to replace the porous formation wall with something more substantial—a metal (usually steel) casing. The factors guiding the decision of casing placement are the subject of Sections 13.2 and 13.3.

With the setting depths for the various casing strings determined, diametric sizing becomes important (see Section 13.4). Sizing tubulars proceeds from the innermost string (production tubing), outward. Sizing the tubing is the most complicated and economically important task, followed by the sizing of the production casing. Subsequent tubulars are primarily sized with an eye on standardization of bits and tubulars, with due consideration given to wellbore hydraulics.

13.2. CASING SEAT SELECTION

Why is casing necessary at all? The rock formations that overlay petroleum reservoirs possess certain weaknesses that, in the end, dictate the use of tubulars. Attempting to overcome the inadequacies of rock as a structural component of the well by means of a drilling fluid-filled hole leads one to address the issue of tubular string length.

13.2.1 Deficiencies of rock

It is not possible to drill a hole from the surface to the depth of a typical petroleum reservoir in the absence of formation structural and flow considerations. Rock constitution renders it undesirable as a structural component at depth. The weaknesses of rock fall into three categories, all of which are addressed by casing.

Elements of Oil and Gas Well Tubular Design
DOI: 10.1016/B978-0-12-811769-9.00013-X

13.2.1.1 Permeability

Subsurface rock contains interconnected pores through which interstitial fluids can flow when subjected to a pressure gradient. When drilling operations first penetrate a subsurface formation, an equilibrium established by deposition and time is disturbed. Flow either to or from the wellbore ensues. Under normal circumstances,[1] the local pressure in the wellbore will be slightly higher than the pressure in adjacent rock pores, and, if anything, there is a loss of fluid to the formation.[2]

The presence of a filter cake associated with wellbore fluid loss to an adjacent formation can result in the phenomenon of differential sticking. If casing or a drilling tubular comes to rest against the wellbore wall and, with time, embeds in the filter cake, the majority of the tubular circumference will be exposed to drilling fluid hydrostatic pressure from the wellbore while the embedded portion is subjected to, at best, formation pore pressure. A net, radially outwardly directed pressure force reinforces contact between the tubular and the wellbore wall. The tubular can become stuck due to this differential (wellbore vs. formation) pressure, or differentially stuck.

Aside from formation fluid interaction with the drilling fluid, introduction of the wellbore can also initiate interaction between formations—higher pressure formations flowing into lower pressure formations—and the exchange of (possibly) hydrocarbon and nonhydrocarbon fluids between formations. In some instances—for example, cross-flow between various formations in a multilayered reservoir—the fluid exchange may be manageable. In other instances, relative permeability effects may either damage the flow characteristics of an otherwise productive formation or, if flow is from the reservoir, result in a loss of reserves.

If cross-flow between formations does not occur, one still must deal with the possibility of formation fluids unintentionally flowing up the wellbore. Responding to loss of well control can consume productive time that might be spent drilling. More serious loss of well control can result in a blow-out.

The permeability of rock leading to the flow issues outlined above suggests that a barrier to unintended flow to/from a formation is desirable, particularly for the long-term integrity of the wellbore as a conduit for reservoir hydrocarbons. Casing,

[1] Underbalanced drilling is an exception.

[2] Fluid loss to the formation can be slow or decrease with time. The majority of formations overlying petroleum reservoirs are shale, which typically has extremely low permeability. If the formation is more permeable (sandstone, for example), loss of drilling fluid to the formation usually involves deposition of solids in the fluid on the wall of the wellbore. This so-called filter cake has low permeability and progressively slows fluid loss to the formation. Further, and regardless of the formation permeability, fluid loss from the wellbore serves to lower the radial pressure gradient at the wellbore wall, thereby reducing flow potential. Exceptions to the above scenarios include formations with large cavities to which Darcy flow is not applicable and drilling fluid densities that are so high (or local, total rock stresses that are so low) that the wellbore wall is fractured.

in conjunction with an annular seal—typically cement or, less commonly, an open-hole packer—is essential for contained hydrocarbon extraction.

13.2.1.2 Weakness under certain loads

Given the occurrences of casing deformation opposite mobile formations [95,159,160, 82,91], characterizing rock as weak seems to counter experience. The deformation of casing by an adjacent, deforming formation is strongly tied to the manner in which the casing is loaded (see Section 8.3 of Chapter 8) and not necessarily the inherent strength of the rock itself.

Tension

Most rocks are weak in tension—thus the inception of the hydraulic fracturing productivity enhancement technique. Should a particularly weak or shallow formation be exposed to pressures from either the wellbore drilling fluid or another zone, tensile fracture at the wall of the wellbore can result in loss of containment of wellbore fluids.

Knowledge of the fracture pressure distribution with depth is drawn from both unintended (lost circulation due to fracture in offset wells) and deliberate (hydraulic fracture treatments and minifracture measurements in offset wells, leak-off tests, regional correlations) sources, all of which require subject matter expert input to be used and interpreted properly [161]. Deliberate formation fracturing at overburden depths far removed from a casing seat is rare.

Creep

The most pervasive instance of creep related to casing damage is the flow of a mobile salt. Salt creep has plagued the industry worldwide [80,95,162,81,82]. Engineered solutions vary but often involve reinforcing a conventional string either with augmented wall thickness, or with the presence of a second string interior and cemented to the first. Installing such solutions can impact both the length and diameter of adjacent tubulars.

In addition to mobile salts, even rock formations with substantial strength can creep in the presence of sufficient tectonic stress [91].

Formation compaction

Particularly regarding the producing formation, pore pressure depletion during hydrocarbon extraction can, given sufficiently weak formation rock, induce compaction and, in severe cases, translate that compaction to the mudline, causing subsidence [163,164,159,160,165–170,86,88,89,171]. Formation response—in the reservoir, at the reservoir/overburden boundary, and in the overburden—can require special considerations in design of both the wellbore trajectory and associated tubulars.

13.2.1.3 Chemical sensitivity

Later discussion of the role of rock mechanics in casing seat determination will focus on the mechanical aspects of wellbore stability. Inasmuch as the majority of overburden rock is shale, well design is further complicated by the sensitivity of some shales to water in the drilling fluid. Both the load and resistance sides of design are affected by this interplay—the presence of the wellbore and the drilling fluid it contains alter the effective stress state to which the shale is subjected, while simultaneously the reaction of the shale to the presence of water reduces its strength [172].

13.2.2 Strategy

The intent of a drilling program is to devise a schedule of drilling fluid densities to overcome the above-mentioned deficiencies of subsurface rock. In some instances solutions to the variety of challenges rock offers may conflict. For example, underbalanced drilling, where the drilling fluid density is purposely targeted below the adjacent pore pressure, is an example of a solution that violates one desire (preventing pore fluids from entering the wellbore) in order to satisfy another (counter rock constitution). The majority of drilling activity, however, intends to counter the three deficiencies of rock—permeability, weakness under certain loads, and chemical sensitivity. It is this strategy that leads to the necessity of running casing.

13.3. DRILLING FLUID DENSITY CONSTRAINTS

The blank plot of Fig. 13.1 illustrates the first step in the casing seat selection process—choosing convenient coordinate axes with which to work. In the figure, the horizontal axis conforms to the accepted procedure of using pressure gradient, rather than pressure, to record fluid and formation effects. Typical units for the abscissa are ppg, psi/ft, and specific gravity (SG). The vertical axis is true vertical depth as many of the factors affecting casing seat selection have some relation to a fluid column.

The drilling fluid density,[3] pore pressure gradient and fracture pressure gradient are all secant (average) gradients, as opposed to tangent (local) gradients. The drilling fluid density (or drilling fluid pressure gradient) γ_f at a vertical depth of interest is the wellbore pressure $p_f(Z)$ divided by the selected vertical depth, as measured from a reference datum

$$\gamma_f = \frac{p_f(Z)}{Z - Z_0}, \tag{13.1}$$

[3] In this discussion we use weight density γ rather than mass density ρ. In any of the ensuing equations the formula $\gamma = (g/g_c)\,\rho$, where g is the local acceleration of gravity and g_c is the gravitational constant, provides a proper conversion between ρ and γ.

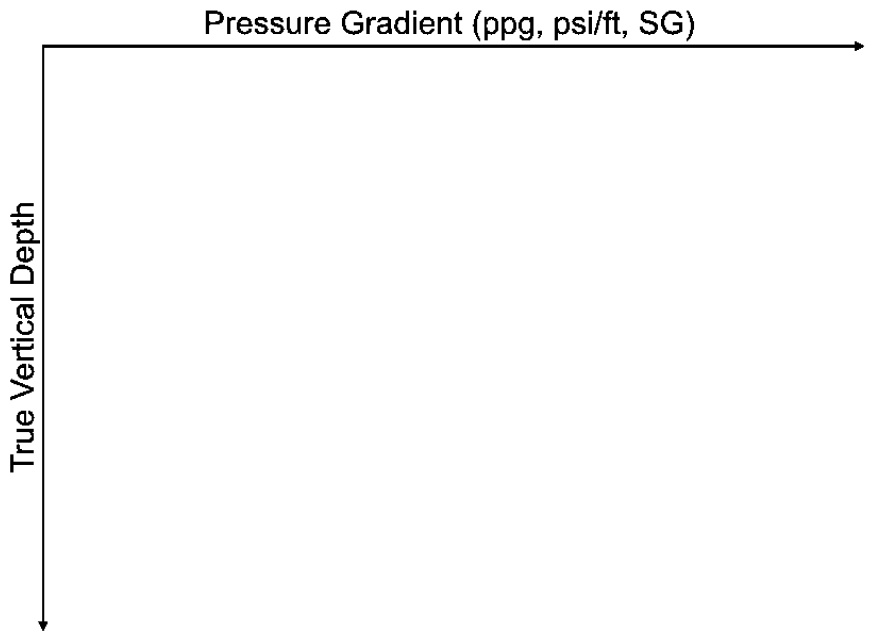

Figure 13.1 ***Casing seat selection—choosing axes.***

where Z is vertical depth and Z_0 is the vertical depth to the datum. In most instances the datum is the drill floor or rotary kelly bushing.

Similarly, the gradient of pore pressure (fracture pressure) at a vertical depth of interest is the local pore pressure (fracture pressure) divided by the selected vertical depth, as measured from a reference datum

$$\gamma_p = \frac{p_p(Z)}{Z - Z_0}, \tag{13.2}$$

$$\gamma_{fr} = \frac{p_{fr}(Z)}{Z - Z_0}. \tag{13.3}$$

The variables γ_f, γ_p and γ_{fr} have units of force per volume (e.g., ppg) or, equivalently, pressure gradient (e.g., psi/ft).

13.3.1 Pore and fracture pressure gradients

At this point in the discussion, any drilling fluid density is acceptable at any depth. We wish to search for constraints to the selection of fluid density based on the discussion in Section 13.2.1 of overburden and reservoir rock. Selecting a candidate depth in

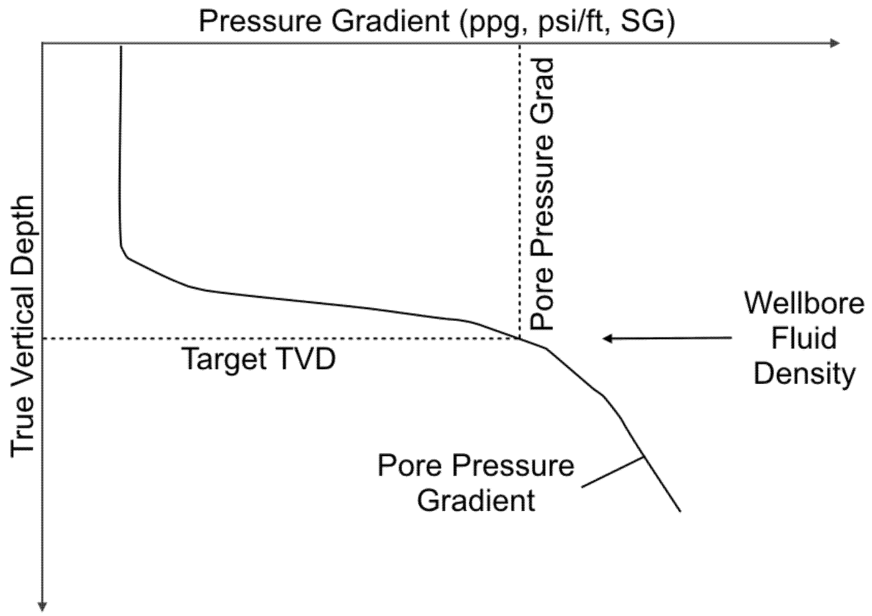

Figure 13.2 ***Casing seat selection—minimum drilling fluid density constraint.*** At each vertical depth, a wellbore fluid density less than the local pore pressure gradient will induce entry of formation fluid into the wellbore.

the wellbore,[4] and beginning with a high drilling fluid density, we gradually lower the density searching for a minimum fluid density with which we are comfortable as indicated in Fig. 13.2. Moving to the left on the abscissa, we encounter no difficulty until our fluid density reaches a value equal to the local pressure of the fluid in the pores of the adjacent formation. Lowering the drilling fluid density below the pore pressure gradient creates an unfavorable pressure difference that would allow formation fluid to enter the wellbore—under most circumstances an undesirable situation.[5] We have therefore found a minimum constraint for the wellbore fluid density. At each depth, values of wellbore fluid density to the left of, or less than, the curve labeled "Pore Pressure Gradient" are now unacceptable.

Given the importance of the pore pressure gradient, from where does this curve originate? For the drilling engineer in the planning phase of a well, the source of the pore pressure gradient curve is usually the subsurface scientist assigned to the well in question. Depending on the locale and the age of the field in which the well is being drilled, the following are sources and tools the subsurface scientist may use in determining the pore pressure gradient:

[4] For the moment, consider the wellbore to be onshore, vertical and straight.
[5] An obvious exception to this statement would be underbalanced drilling.

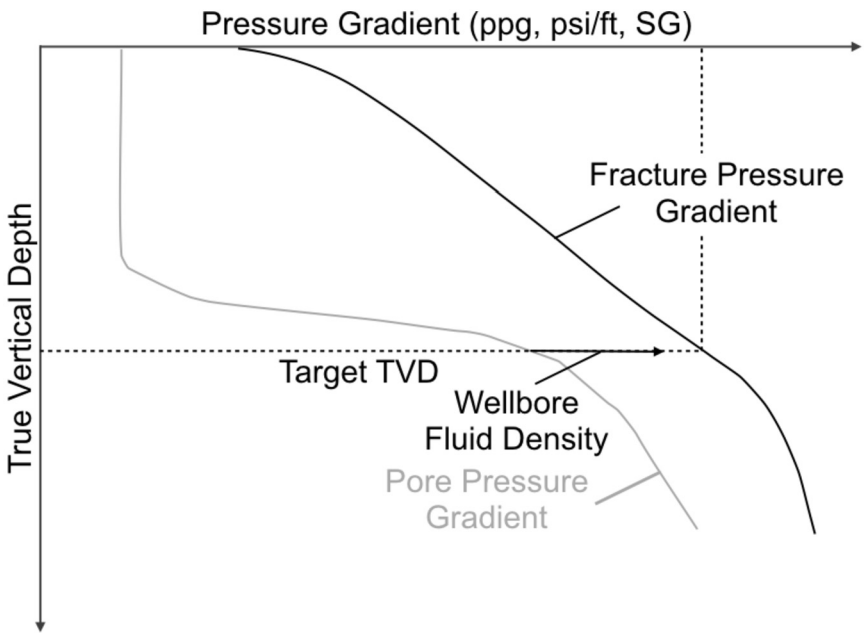

Figure 13.3 ***Casing seat selection—maximum drilling fluid density constraint.*** At each vertical depth, a wellbore fluid density greater than the local fracture pressure gradient will fracture the formation and induce loss of wellbore fluid to the formation.

- empirical correlations for the region and type of deposition,
- seismic surveys, and
- drilling and production history of offset wells.

Reversing the process at the candidate depth in our wellbore, and now beginning with a drilling fluid density equal to the acceptable minimum of the local pore pressure gradient, we gradually increase the density searching for a maximum fluid density with which we are comfortable, as indicated in Fig. 13.3. Moving to the right on the abscissa, we encounter no difficulty until our fluid density reaches a value equal to the local fracture pressure gradient of the adjacent formation. Increasing the drilling fluid density above the fracture pressure gradient creates an unfavorable pressure difference that would induce a (usually) vertical tensile fracture in the formation and cause loss of wellbore fluid. We have therefore found a maximum constraint for the wellbore fluid density. At each depth, values of wellbore fluid density to the right of, or greater than, the curve labeled "Fracture Pressure Gradient" are now unacceptable.

The drilling engineer's source of fracture pressure gradient is also the subsurface scientist. As was the case with pore pressure gradient, the scientist has a number of tools with which to construct the fracture pressure gradient curve:

- empirical correlations for the region and type of deposition,

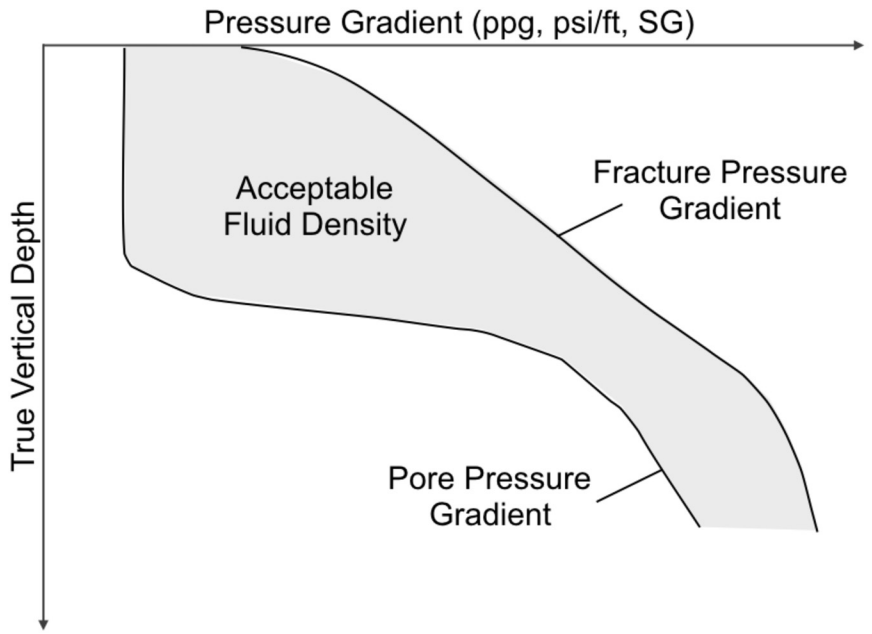

Figure 13.4 ***Casing seat selection—acceptable fluid density range.*** At each vertical depth, the acceptable fluid density range is bounded below by the pore pressure gradient and above by the fracture pressure gradient.

- formation fracturing tests (see the discussion of "Tension" in Section 13.2.1.2) from offset wells, and
- drilling and production history of offset wells.

Our knowledge at this point is summarized in Fig. 13.4. At each subsurface depth, and according to our desire in this well to have neither entry of formation pore fluid nor loss of wellbore fluid, we have arrived at an acceptable range of drilling fluid density. The acceptable drilling fluid density range at each vertical depth is

$$\gamma_p(Z) \le \gamma_f(Z) \le \gamma_{fr}(Z), \quad \text{base constraint.} \tag{13.4}$$

Fig. 13.4 and Eq. (13.4), along with the extensions to follow in Section 13.3.2, express local constraints. That is, at vertical depth Z the acceptable limits of the drilling fluid are stated in terms of constraints at that depth. These local constraints do not mean that the entire wellbore above depth Z is capable of supporting a column of drilling fluid with density in the acceptable range without issue.

13.3.2 Additional constraints

Pore and fracture pressure gradients are fundamental considerations for practically all discussions of drilling fluid density. There exist, however, additional issues that can further restrict the drilling fluid density, several of which are discussed below.

13.3.2.1 Uncertainty

Even if one discounts measurement and correlation error, the anticipated pore and fracture pressure gradients will vary from wellbore to wellbore, resulting in a distribution of values at each depth. This uncertainty can be addressed with statistics, an increasingly popular approach aligned with design using probabilistic concepts. A less sophisticated but popular alternative is to apply what amounts to a design factor to both pore and fracture pressure gradient, thus narrowing the acceptable range of drilling fluid density. Typically, either method results in shifts of the "expected value" curve by tenths of a ppg (0.012 SG).

13.3.2.2 Surge and swab margins

The mental exercise used to construct Figs. 13.1–13.4 compares static columns of wellbore fluid to formation pore and fracture pressure gradients. In reality, there exist times when the fluid in the wellbore is moving, this motion being due to drilling fluid circulation or, our concern in this section, pipe movement in the wellbore. The increments in pressure above and below hydrostatic are termed surge and swab pressure, respectively. The phenomenon has been studied extensively [17–20,173].

During well planning a drilling engineer may use one of several commercially available software tools to perform simulations of either running in hole (RIH) or pulling out of hole (POOH) with a drill string. These modeling exercises will result in adjustments to the hydrostatic fluid column on the order of tenths of a ppg (0.012 SG). It is common practice to combine the surge and swab values with the design factor of Section 13.3.2.1, this net shift in the pore and fracture pressure gradient curves being on the order of 0.5 ppg (0.06 SG). Fig. 13.5 illustrates the impact of uncertainty and surge/swab on the acceptable fluid density range.

Including uncertainty and the surge and swab margins alters the base constraint of Eq. (13.4) to the following:

$$\gamma_p(Z) + \gamma_{sb}(Z) \le \gamma_f(Z) \le \gamma_{ft}(Z) - \gamma_{su}(Z), \qquad \begin{matrix}\text{base constraint} \\ + \text{ surge and swab margins,}\end{matrix} \tag{13.5}$$

where the swab margin $\gamma_{sb}(Z)$ and the surge margin $\gamma_{su}(Z)$ are, respectively, the surge and swab pressures divided by the vertical depth from the datum.

Although the surge and swab margins are, in general, functions of vertical depth, in practice these two margins are often treated as (not necessarily equal) constant values.

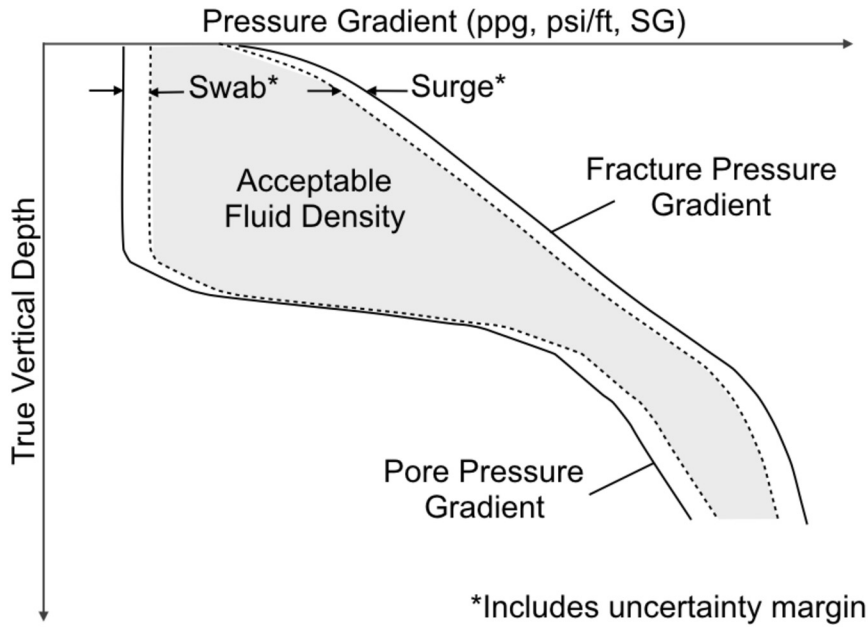

Figure 13.5 ***Casing seat selection—adjustment of acceptable fluid density range for uncertainty and surge/swab.***

Similarly, it is not necessary that the margin of uncertainty on the pore pressure curve be identical to its counterpart on the fracture pressure curve.

13.3.2.3 Differential sticking

From Section 13.2.1.1 the presence of a filter cake introduces the potential for differential sticking, particularly if a tubular string is maintained in a static state in the wellbore for some length of time. There usually exists some differential sticking limit beyond which experience in a locale has shown differential sticking to be prevalent. The differential sticking limit is expressed as a pressure difference between the local wellbore and pore pressures. This number can be location sensitive and is usually on the order of 2000 psi to 4000 psi (13.8 MPa to 27.6 MPa).

In accounting for differential sticking the following facts are pertinent:

- The abscissa for the pore and fracture gradient plot is pressure *gradient*, whereas the differential sticking criterion is a pressure value. The adjustment to account for differential sticking will therefore vary with vertical depth, even if the differential sticking limit is constant.
- When comparing differential sticking to pore pressure, the unfactored (no uncertainty, no swab margin) pore pressure curve is the appropriate datum. Differential sticking and swab pressure are unrelated phenomena. One could opt to include

the margin for uncertainty (Section 13.3.2.1), but typically the differential sticking limit is not known that precisely. Further, using unfactored pore pressure will be conservative, as the difference between wellbore pressure and pore pressure will be greater.

- The potential for differential sticking is difficult to anticipate without performing the calculation. A smaller difference between drilling fluid density and pore pressure gradient may be outweighed by the fact that the difference occurs at greater depth—the differential sticking limit is based on pressure.
- In some instances, the potential for differential sticking must be tolerated, and the differential sticking limit ignored. If, for example, a portion of the wellbore passes through a depleted reservoir, it may not be possible to lower the drilling fluid density sufficiently to prevent an unfavorable difference between wellbore pressure and pore pressure.[6] Depleted zones are particularly challenging when designing for differential sticking as pore pressure depletion affects not only the pore pressure gradient but also the fracture gradient. According to the effective stress principle (see Section 13.3.2.4 to follow, along with Appendix C), and assuming the depleting formation behaves as a poroelastic material with constant[7] overburden stress, a decrease in pore pressure will result in a corresponding decrease[8] in fracture pressure.[9] The effect of pore pressure depletion on the original pore and fracture pressure gradients is illustrated in Fig. 13.6.

Although the pressure differential of concern is wellbore minus pore pressure, the differential sticking limit manifests itself as a reduction in the upper limit of acceptable fluid density. At each depth of concern, starting with the pore pressure one asks, "How high can the drilling fluid density be without exceeding the differential sticking limit?" This value, converted to a pressure gradient for the depth of concern, can be less than the fracture pressure gradient at that depth, and if so, the upper limit of acceptable drilling fluid density should be adjusted downward.

An example is shown in Fig. 13.7. At each depth, the dotted line is a calculation of the maximum wellbore fluid pressure that, when compared to the pore pressure, is less than the differential sticking limit.

[6] Further, lowering the drilling fluid density in order to lower the risk of differential sticking may increase the risk of a pore fluid influx when exiting the depleted zone and penetrating a formation with higher pore pressure gradient. The potential for differential sticking, and a possible sidetrack, usually has lower consequence than that of a well control incident, particularly in the vicinity of hydrocarbon-bearing formations.

[7] Partial support of the overburden by "arching" will lessen but not eliminate the change in total horizontal stress.

[8] The horizontal stress is negative—with pore pressure depletion it assumes a smaller negative value.

[9] If the overburden stress is S_V, a decrease in pore pressure of Δp_p will result in a corresponding decrease in fracture pressure of (see Section C.3.1 of Appendix C) $-[(1-2\nu)/(1-\nu)] \times \alpha \Delta p_p$, where $0 \le \nu \le 0.5$ is Poisson's ratio and $0 \le \alpha \le 1$ is the Biot parameter.

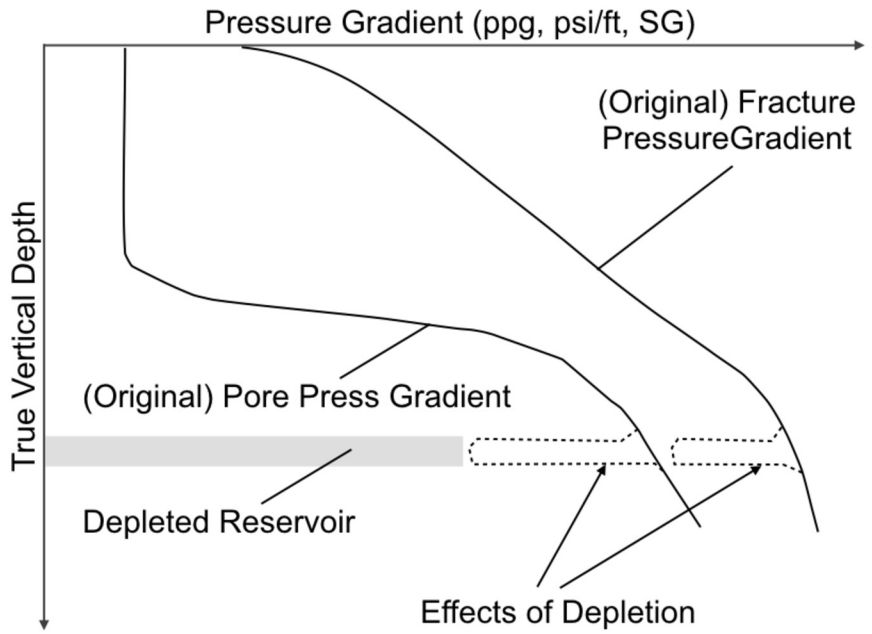

Figure 13.6 ***Casing seat selection—effect of pore pressure depletion on pore and fracture pressure gradients.***

Incorporating the differential sticking limit, the range of acceptable drilling fluid density at any vertical depth becomes

$$\gamma_p(Z) + \gamma_{sb}(Z) \le \gamma_f(Z) \le \min \begin{cases} \gamma_{fr}(Z) - \gamma_{su}(Z) \\ \gamma_{ds}(Z) \end{cases}, \quad \begin{array}{l} \text{base constraint} \\ + \text{ surge and swab margins} \\ + \text{ differential sticking limit,} \end{array} \tag{13.6}$$

where

$$\gamma_{ds}(Z) = \frac{\gamma_p(Z)\,(Z - Z_0) + p_{ds}}{Z - Z_0}, \tag{13.7}$$

with p_{ds} being the differential sticking limit.

13.3.2.4 Wellbore stability

Wellbore stability is an investigation of the structural integrity of near wellbore formations under the action of initial stresses and pore pressure, and as influenced by the drilled wellbore. Wellbore stability is also influenced by both the mechanical and chemical constitution of the formation rock. Wellbore stability considerations, even for a

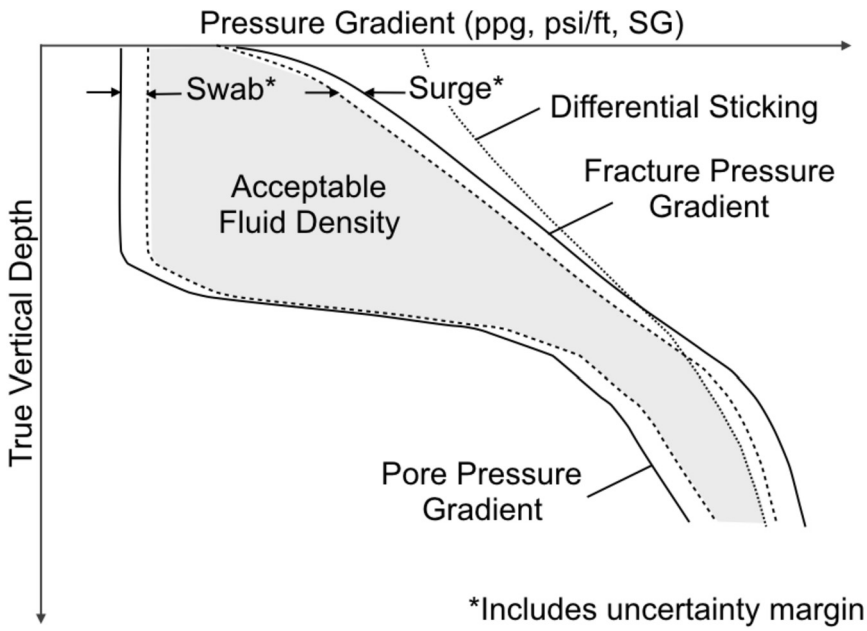

Figure 13.7 ***Casing seat selection—adjustment of acceptable fluid density range for differential sticking.*** The uncertainty and surge/swab margins (dashed lines) have been ignored for this calculation, except when determining if the upper limit of the acceptable range should be adjusted downward.

straight, vertical wellbore, can dominate the determination of an acceptable drilling fluid density schedule.

A wealth of rock mechanical literature addresses wellbore stability in the context of the petroleum industry and other mining-related activities [174–178]. Here, we will use simple models to discuss the underlying principles in a wellbore stability calculation, recognizing that the acceptable drilling fluid density range resulting from such a calculation is usually performed for the drilling engineer by a rock mechanist well-versed in both the subject and applicable modeling software.

Fig. 13.8 illustrates the stress state of a rock sample in a laboratory triaxial compression[10] test.[11] The sample is jacketed (lateral surface) and sealed (end surfaces[12]). The

[10] Rock mechanists conventionally designate compressive stresses as positive. In keeping with the rest of this text, we shall treat tensile stresses as positive, which will cause some plots to appear as axis reflections when compared to the standard rock mechanics literature.

[11] Although termed "triaxial", the two lateral stresses are equal throughout the loading.

[12] The sample ends are sealed in a so-called undrained test. If the test is executed in a drained condition, one sample end may be vented to a constant pressure reservoir to maintain original sample pore pressure.

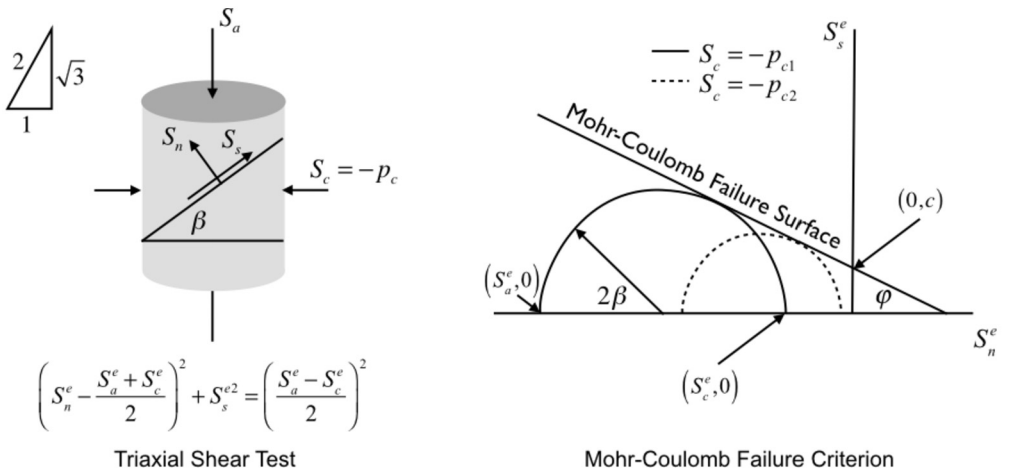

Figure 13.8 ***Triaxial compression rock mechanical test.*** The left-hand figure introduces the test variables; the right-hand figure uses the results of two tests with different confining pressures to construct a Mohr–Coulomb failure envelope. S_a^e and S_c^e as indicated are for the test with confining pressure p_{c1}.

sample is first loaded hydrostatically ($S_a = S_c$)[13] to a desired confining (lateral) stress. Typically, but not necessarily,[14] the sample is loaded in a drained condition, where the loading rate is sufficiently slow to allow dissipation of any pressure generated in the pores of the sample.

Once the desired confining pressure is reached, this pressure is held constant while the sample is loaded axially (S_a increased in a compressive sense) by an end platen through states of either inelastic deformation, if the confining stress is high, or brittle failure, if the confining stress is low. In many instances related to the integrity of the wellbore wall, the stress state is such that the confining stress is low, and the rock fails in a brittle manner.

One of the many mathematical models used to describe the limit state of a rock loaded at low confining stress is the Mohr–Coulomb model. The model's name originates from the following:

- The relation between shear and normal stress on the failure plane is described by a Coulomb-like friction model

$$S_s^e = -\mu S_n^e + c, \tag{13.8}$$

[13] We maintain the previously introduced convention (see Section 6.1 of Chapter 6) of using the Piola–Kirchhoff (engineering) stress for stress–strain curves.

[14] In a properly instrumented experiment, the pore pressure in the sample can be monitored and, if desired, controlled, even at a value other than zero.

where $\mu = \tan\phi$, ϕ being the angle of internal friction. Unlike the classic Coulomb friction model, however, the rock has a nonzero strength when the normal stress vanishes—this is the cohesion c.

- Mohr's circle (see Section 4.2.7.2 of Chapter 4) is used to determine the angle of the failure plane. Executing several tests (two are shown in Fig. 13.8) at different confining stresses, one can plot a series of Mohr's circles and then, usually to a reasonable approximation, draw a straight line simultaneously tangent to all the test circles. This is the Mohr–Coulomb failure surface.

The presence of the superscript 'e' on the stress terms in Eq. (13.8) signifies that rock mechanics actually deals with two types of stresses—total stresses and effective stresses. Total stresses, usually used when defining tractions, represent the traction one would observe if the exterior surface of the rock element in question were wrapped in a thin membrane. The total stress therefore is a measure of the force intensity over an entire rock surface area, including any exposed pore space. An example of total stress is the closure stress attributed to a formation in the context of hydraulic fracturing.

Effective stresses, usually appearing in constitutive equations, are measures of the force intensity on the granular structure of an exposed surface. Particularly for elastic behavior, the relation between effective stress and total stress is [179]

$$\mathbf{S}^e = \mathbf{S} + \alpha p_p \mathbf{I}, \quad S^e_{IJ} = S_{IJ} + \alpha p_p \delta_{IJ}, \tag{13.9}$$

where

$$\alpha = 1 - \frac{K_b}{K_s}, \tag{13.10}$$

with K_b being the bulk modulus of the porous matrix and K_s being the bulk modulus of the solid constituent of the matrix. In many applications, and particularly for inelastic deformation, $K_b \ll K_s$ so that $\alpha \approx 1$.

In order to transfer the discussion from the laboratory to a well, consider the state of stress in the formation at the wellbore wall. The elastic solution to this problem, assuming material isotropy of the formation and plane strain to be a suitable approximation of the local stress state,[15] is detailed in Appendix C. An example problem in the appendix (Section C.3) illustrates that the shear stress gradient, as a function of the density of the drilling fluid, can have two maxima—one each for low and high fluid density. Superimposing such behavior on the plot in Fig. 13.8 suggests that the Mohr–Coulomb failure surface can be penetrated twice, with drilling fluid densities between

[15] The plane strain assumption essentially models the wellbore as penetrating an infinite solid possessing a uniform stress state far from the hole. Major determinants—the angle of the wellbore centerline with respect to the far field stress state, the prewellbore far field stress state itself—are assumed constant along the wellbore.

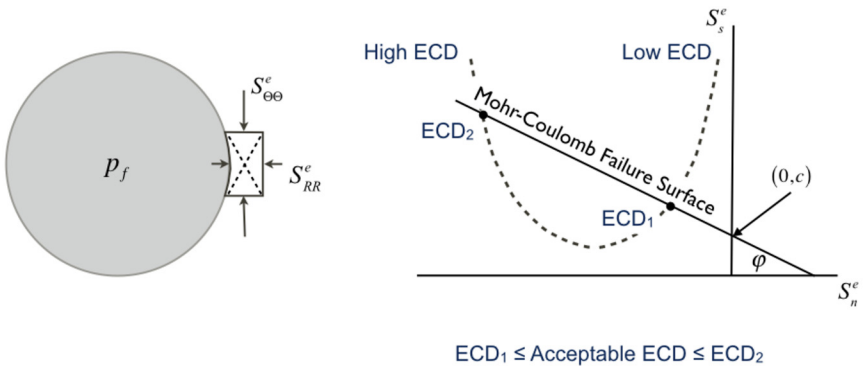

Figure 13.9 ***Stability of the wellbore wall.*** Within the equivalent circulating density (ECD) range $ECD_1 \leq$ Acceptable ECD $\leq ECD_2$ the stress state at the wellbore wall falls below the Mohr–Coulomb failure surface indicating wellbore stability. ECD values outside this range will theoretically result in spalling of the formation, that is, wellbore instability. S^e_{RR} and $S^e_{\Theta\Theta}$ are, respectively, the effective radial and hoop stress at the wellbore wall.

the two penetration values representing acceptable values from the wellbore stability perspective.

This concept is illustrated in Fig. 13.9. The right-hand portion of the figure illustrates the change in effective stress state at the wellbore wall (S^e_n, S^e_s) with drilling fluid density, here represented by the more general concept of equivalent circulating density[16] (ECD). The dashed line representing stress state starts unacceptably outside the boundary of the Mohr–Coulomb failure surface for some low value of ECD. As the drilling fluid density is increased, eventually the stress state penetrates and then falls below the Mohr–Coulomb boundary—the stress state is acceptable. As the drilling fluid density is further increased, the stress state may again penetrate the Mohr–Coulomb boundary, signaling the maximum acceptable ECD value for the current formation and drilling conditions. Wellbore structural integrity has therefore provided a window of drilling fluid densities to be included in the search for an overall acceptable fluid density range.

Returning to the two ECD values bounding the acceptable range, these two values also signify the type of failure one would expect at the wellbore wall. The example problem in Section C.3.1 of Appendix C illustrates a vertical well in a formation whose far field principal stresses align with the wellbore axis and its cross-section. For this case, the left-hand portion of Fig. 13.9 illustrates one failure mode. At the wellbore wall, the effective hoop stress will usually be greater, in a compressive sense, than

[16] Equivalent circulating density is the fluid column pressure gradient that, in addition to drilling fluid density, includes such factors as fluid wall friction.

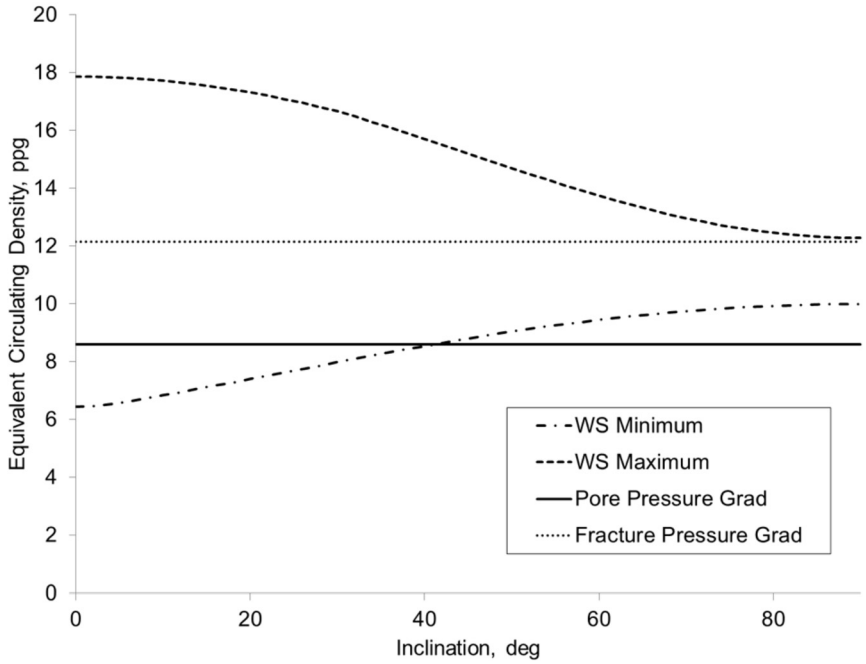

Figure 13.10 ***Effect of inclination on acceptable drilling fluid density range for inclined wellbore example problem variables.*** The calculation procedure leading to this graph is discussed in Section C.3.2 of Appendix C.

the effective radial stress. The stresses acting on an element of rock at the wellbore can be compared to the laboratory sample in Fig. 13.8. If the effective stress state excedes the Mohr–Coulomb failure surface the rock element will fail. The dashed lines crossing in the rock element indicate (see Fig. 13.8) planes along which failure will occur. Rock will separate from the wellbore wall, eventually leading to an elliptically shaped hole. The spalled rock losses on the wellbore wall are termed "breakouts."

Given an initial in situ stress state, an important determinant of the severity of the stress state is the inclination of the wellbore. The example problem in Section C.3.2 of Appendix C extends the concept presented for a vertical well in Fig. 13.9 to investigate inclination dependence. In a sample calculation summarized in Fig. C.4, reproduced here as Fig. 13.10, the curves labeled "WS Minimum" and "WS Maximum" represent, respectively, points ECD_1 and ECD_2 in Fig. 13.9. For the specific input parameters of the sample, wellbore stability considerations replace pore pressure as the determinant of the lower bound of the acceptable drilling fluid density range for inclinations greater than 40°.

With the safe drilling fluid density range for wellbore stability included, the range of acceptable drilling fluid density at any vertical depth becomes

$$\max\left\{\begin{array}{l}\gamma_p(Z)+\gamma_{sb}(Z)\\ \gamma_{wn}(Z)\end{array}\right. \leq \gamma_f(Z) \leq \min\left\{\begin{array}{l}\gamma_{fr}(Z)-\gamma_{su}(Z)\\ \gamma_{ds}(Z)\\ \gamma_{wx}(Z)\end{array}\right. , \quad \begin{array}{l}\text{base constraint}\\ +\text{ surge and swab margins}\\ +\text{ differential sticking limit}\\ +\text{ wellbore stability,}\end{array} \tag{13.11}$$

where γ_{wn} and γ_{wx} are, respectively, the minimum and maximum limits of the acceptable ECD/drilling fluid density range from the perspective of wellbore stability.

13.3.2.5 Riser margin

Riser margin is an adjustment to the lower bound of acceptable drilling fluid density to account for the possibility of a loss of riser integrity during offshore drilling. Fig. 13.11 illustrates the problem schematically. Pictured is an offshore drilling operation having the pore and fracture pressure gradients and drilling fluid density illustrated in the left-hand portion of the figure. At the vertical depth illustrated (see the dot in the figure), the local wellbore pressure is due to a column of drilling fluid from that vertical depth to the drill floor via the wellbore and drilling riser.

Should the drilling riser part [180], and assuming either the initial failure or subsequent damage as the riser falls causes a loss of pressure integrity in the vicinity of the mudline (ML), the portion of the drilling fluid column above the mudline is replaced by a column of air and sea water. This reduced-density fluid column will now produce a lower hydrostatic pressure at the target depth, introducing the possibility that the local wellbore pressure may fall below the value of the local pore pressure. Formation fluid entry into the wellbore would ensue, control of which is compounded by the lack of fluid control from the drill floor to the mudline. Substantial responsibility falls on the blowout preventer (BOP) to operate as intended.

The riser margin calculation (see Aadnøy et al. [181,182]) anticipates the above scenario and computes the drilling fluid density necessary to maintain a positive pressure differential between the wellbore and adjacent pore pressure. Ignoring the pressure associated with the air column from the datum to mean sea level (MSL), the proper balance between local pore pressure and the pressure in the wellbore following the riser break is

$$\gamma_p\,(Z-Z_0)=\gamma_{sw}\,(Z_{wh}-Z_{MSL})+\gamma_f\,(Z-Z_{wh})\,. \tag{13.12}$$

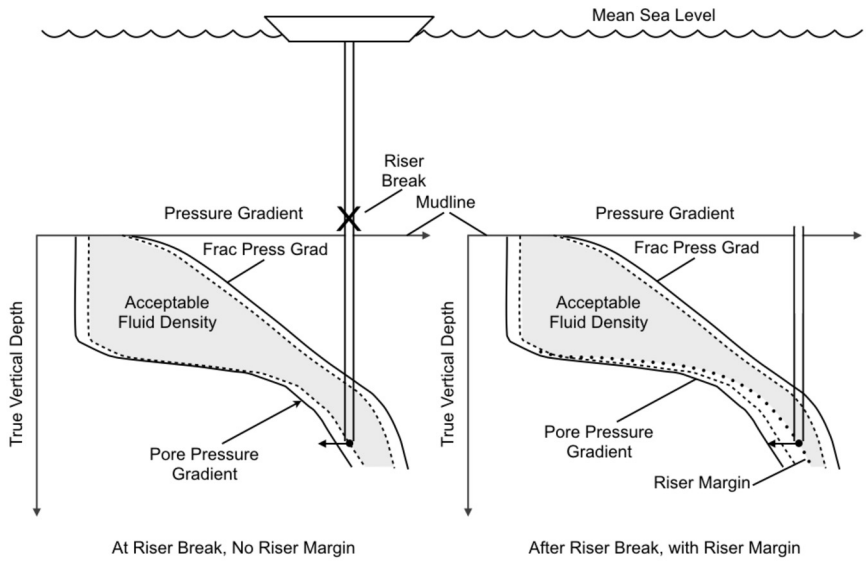

Figure 13.11 ***Casing seat selection—adjustment of acceptable fluid density range for riser margin.*** Before the riser break (left schematic) the local wellbore pressure gradient at a vertical depth (indicated by a dot at the lower end of the drill string) is calculated from the drilling fluid hydrostatic pressure measured with the drill floor as a datum. Even with a swab margin, this pressure gradient could fall below the local pore pressure gradient if the riser is lost. If a riser margin is calculated (dotted line in right schematic), the lower bound of the acceptable drilling fluid density range is adjusted upward so that the wellbore pressure gradient, including the air gap and sea water depth, is still acceptable. The uncertainty and surge/swab margins (dashed lines) have been ignored for this calculation, except when determining if the lower limit of the acceptable range should be adjusted upward.

We may use the post-riser break balance in Eq. (13.12) to express riser margin as an increment above the pore pressure

$$\begin{aligned}\gamma_{rm}(Z-Z_0) &= \left(\gamma_f-\gamma_p\right)(Z-Z_0)\\ &= \gamma_f(Z-Z_0)-\left[\gamma_{sw}(Z_{wh}-Z_{MSL})+\gamma_f(Z-Z_{wh})\right]\\ &= \gamma_f(Z_{wh}-Z_0)-\gamma_{sw}(Z_{wh}-Z_{MSL}),\end{aligned} \tag{13.13}$$

where γ_p, γ_f and γ_{rm} are functions of Z. Reexpressing Eq. (13.13) as a gradient[17] gives

$$\gamma_{rm}=\gamma_f-\gamma_p=\frac{\gamma_f(Z_{wh}-Z_0)-\gamma_{sw}(Z_{wh}-Z_{MSL})}{Z-Z_0}. \tag{13.14}$$

[17] In Fig. 13.11 the dotted line corresponding to riser margin does not start at the mudline, as values of riser margin in the vicinity of the wellhead, although physically correct, are unusably large. This feature will decrease exponentially as the depth increases and eventually, as illustrated in the figure, may be overtaken by the pore pressure gradient.

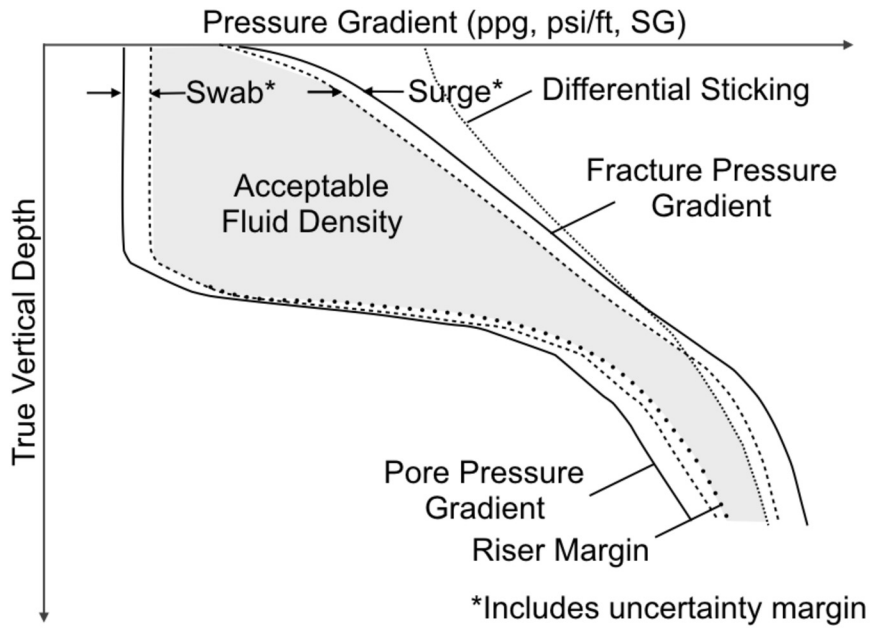

Figure 13.12 ***Casing seat selection—adjustment of acceptable fluid density range for riser margin.*** The uncertainty and surge/swab margins (dashed lines) have been ignored for this calculation, except when determining if the lower limit of the acceptable range should be adjusted upward.

With riser margin incorporated (see Fig. 13.12), the range of acceptable drilling fluid density at any vertical depth becomes

$$\max \begin{Bmatrix} \gamma_p(Z) + \gamma_{sb}(Z) \\ \gamma_{wn}(Z) \\ \gamma_p(Z) + \gamma_{rm}(Z) \end{Bmatrix} \leq \gamma_f(Z) \leq \min \begin{Bmatrix} \gamma_{fr}(Z) - \gamma_{su}(Z) \\ \gamma_{ds}(Z) \\ \gamma_{wx}(Z) \end{Bmatrix}, \quad \begin{array}{l} \text{base constraint} \\ + \text{ surge and swab margins} \\ + \text{ differential sticking limit} \\ + \text{ wellbore stability} \\ + \text{ riser margin.} \end{array} \tag{13.15}$$

Practically, riser margin is applicable to intermediate water depths. For shallow water depths the correction is minor; for deepwater, the correction can be so great the concept is often neglected.

13.3.2.6 Formation idiosyncrasies

The topics of this section are difficult to express in equation form and are usually part of either (a) boundary constraints placed on the rest of the design or (b) amendments to the design once an initial pass is completed.

Mobile formation

Formation movement—salt creep, tectonic displacement, compaction—that loads adjacent casing in a nonuniform manner usually necessitates an abrupt change in wall thickness to increase resistance. This change often entails either a thick-walled tubular or a concentric casing configuration employing either a scab liner or a long liner lap. Such an abrupt change in cross-section may affect adjacent casing setting depths.

Chemical sensitivity

Due to the sensitivity of some (particularly shale) rocks, it may be necessary to case the open hole as soon as the subject formation is drilled. Typical drivers include wellbore stability concerns and/or altering the drilling fluid to optimally drill subsequent hole. Such a casing seat may, as was the case with mobile formations, alter the conventional casing program.

13.3.2.7 Regulatory requirements

Regardless of the geomechanical and pore fluid environment, local regulatory requirements may specify that shallow conductor and/or surface casing strings be installed to a certain depth for such purposes as protecting fresh water aquifers. These requirements do not enter the constraint equation on pore and fracture pressure gradients but are usually treated either as (a) an initial, fixed casing seat from which other calculations begin or (b) an override, once all other casing seats have been determined.

13.3.3 Application of constraints

Once all constraints to the available drilling fluid density have been assembled, the resulting region of acceptable fluid density—excepting the considerations of Sections 13.3.2.6 and 13.3.2.7—will appear in the form illustrated in Fig. 13.13.

First, consider the so-called "bottom-up" method of seat determination. Starting at the bottom of the wellbore, any of the drilling fluid densities in the range determined by—*in this particular case*—the curves for riser margin and differential sticking are acceptable. Other concerns—for example, the fact that lower fluid densities usually correspond to higher rate-of-penetration—will, however, suggest that the optimum drilling fluid density will be on the low side of the acceptable range, that is, Point 0. Selecting Point 0 means that when the last increment of the hole is drilled the wellbore is filled with a fluid of density corresponding to Point 0. If that is the case, however, the

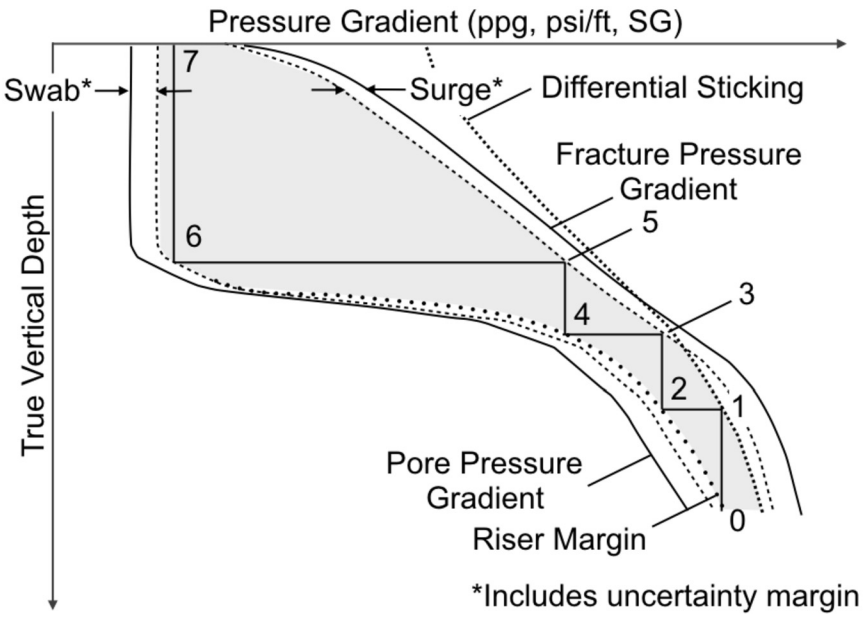

Figure 13.13 ***Casing seat selection—illustration of the "bottom-up" design philosophy.*** The acceptable drilling fluid density range is generated with the components of Eq. (13.15).

intersection at Point 1 suggests that at Point 1, and for some distance above that point,[18] we open the possibility of becoming differentially stuck. To avoid that possibility, the formation above Point 1 should be isolated from the wellbore. That is, we should run casing, and Point 1 becomes a casing seat depth.

The same logic can be followed up the wellbore. For example, think of drilling the last increment of the hole section in which the casing for the seat at Point 1 will be run. Now considering the drilling fluid density corresponding to Point 2 to be the fluid density,[19] a column of fluid with density corresponding to Point 2 would, if it filled the wellbore to the surface, fracture the formation at Point 3. Point 3 then becomes another casing seat depth.

The above line of reasoning can be followed to the surface, in the case of Fig. 13.13 resulting in another casing seat at Point 5, again to avoid formation fracture. With this initial set of seats, one is then prepared to consider the effects of Sections 13.3.2.6 and 13.3.2.7 on possible adjustments to the casing seats at Points 0, 1, 3 and 5.

[18] The potential of becoming differentially stuck exists from Point 1 upward, until the "Differential Sticking" curve is no longer the determinant of the maximum acceptable drilling fluid density.

[19] As was the case at the well depth (Point 0), any drilling fluid density between those densities corresponding to Points 2 and 1 is acceptable. We favor the density at Point 2 for reasons of drilling efficiency.

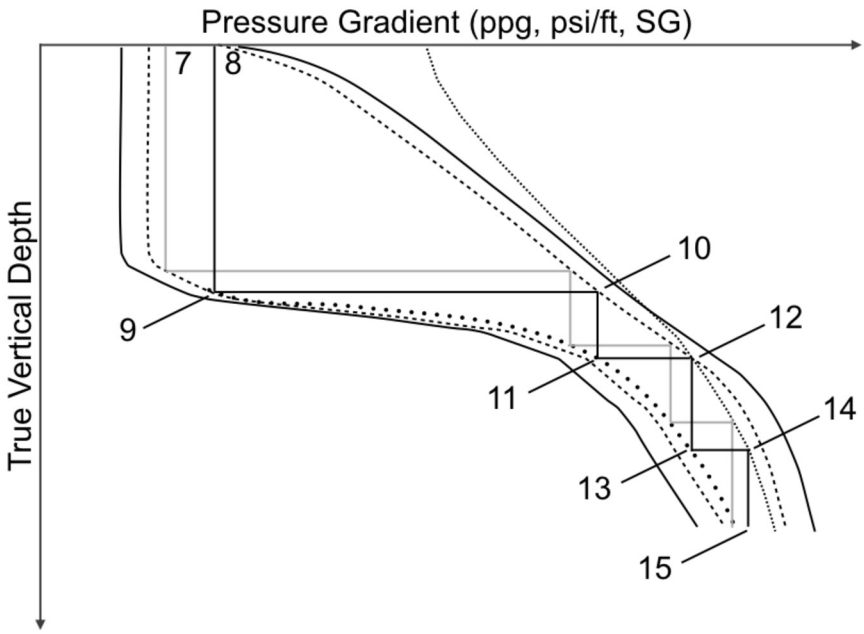

Figure 13.14 ***Casing seat selection—illustration of the "top-down" design philosophy.*** The acceptable drilling fluid density range is generated with the components of Eq. (13.15). For comparison, the results of the "bottom-up" design philosophy (Fig. 13.13) are included in gray.

There also exists a "top-down" approach to casing seat selection, illustrated here in Fig. 13.14. Starting at the top of the wellbore, any of the drilling fluid densities in the range corresponding to the uppermost vertical depth are acceptable. In this case, one imagines starting the hole section with a fluid density corresponding to the low end of the acceptable density range, but gradually increasing drilling fluid density with depth. From Fig. 13.14, however, the fluid density can only be increased to a density corresponding to Points 8 and 9 before formation fracture becomes a concern. At the depth corresponding to Point 9 one must then set a casing string before drilling deeper. This logic continues down the wellbore, with, in the case of Fig. 13.14, casing seats appearing at Points 10, 12, 14 and 15 (the bottom of the wellbore).

Neither the "bottom-up" nor the "top-down" philosophy has an indisputable advantage. Both methods will often result in the same number of casing seats. It is common, however, for the "top-down" philosophy to produce deeper casing seats, which some engineers feel is an advantage in flexibility.

13.3.3.1 Example problem—casing seat selection

Given the pore pressure and fracture gradients of Table 13.1 and the values of 0.3, 0.2 and 0.2 ppg, respectively, for the swab margin, surge margin and design factor, do the following:

Table 13.1 Casing seat selection—example problem input data

Vertical depth[a], ft	Pore pressure gradient, ppg	Fracture gradient, ppg
0	8.6	10.5
2000	8.6	11.5
4000	8.6	12.4
6000	8.6	13.2
8000	8.6	13.8
10 000	8.6	14.4
11 000	9.0	14.6
12 000	10.0	14.9
14 000	12.0	15.5
16 000	12.8	16.0
18 000	13.5	16.4
20 000	13.7	16.5
22 000	13.8	16.6

[a] Onshore well, negligible elevation.

1. Plot the data, both the base curves and marginal curves;
2. Perform a first pass design using the bottom-up reasoning;
3. Where appropriate, include the differential sticking limit, using 2,000 psi as a limit on acceptable differential pressure.

Fig. 13.15 completes the work requested in item 1. The "Pore Pressure Gradient" and "Fracture Pressure Gradient" curves are straightforward plots of the data as presented in Table 13.1. The related curves including surge and swab margin and the design factor representing uncertainty follow by adding 0.5 ppg to the pore pressure gradient and subtracting 0.4 ppg from the fracture pressure gradient at each vertical depth data point.

The "Differential Sticking" curve follows from Eq. (13.7), again evaluated at each vertical depth for which a data point is provided. For example, at 12 000 ft, the calculation is

$$\begin{aligned}\gamma_{ds}(Z)\text{ppg} &= \frac{\gamma_p(Z)\text{ppg} \times 0.051\,948\,\frac{\text{psi}}{\text{ft ppg}}\,(Z\text{ft} - Z_0\text{ft}) + p_{ds}\text{psi}}{Z\text{ft} - Z_0\text{ft}} \times \frac{1}{0.051\,948\,\frac{\text{psi}}{\text{ft ppg}}} \\ &= \frac{10.0 \times 0.051\,948\,(12\,000 - 0) + 2000}{12\,000 - 0} \times \frac{1}{0.051\,948} \\ &= 13.21\,\text{ppg},\end{aligned} \tag{13.16}$$

where the value for $\gamma_p(Z)$ is taken from the "Pore Pressure Gradient" curve and not the adjustment to pore pressure for swab margin and uncertainty (see the discussion in Section 13.3.2.3).

The acceptable fluid density region is shown shaded. The upper bound of acceptable drilling fluid density is governed by the lesser of (factored) fracture pressure gradient and

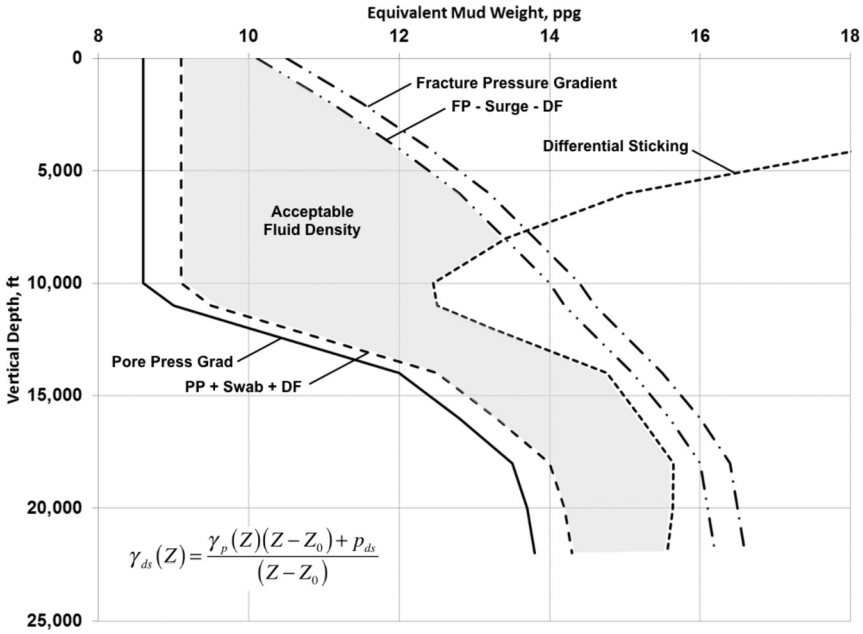

Figure 13.15 ***Casing seat example—determination of the region of acceptable fluid density.*** The acceptable drilling fluid density range is generated with the components of Eq. (13.6). The "Differential Sticking" curve was generated with Eq. (13.7).

the differential sticking limit, depending on the depth. This completes items 1 and 3 of the problem statement.

To execute a bottom-up design (see Fig. 13.16), begin at point (14.3, 22 000), the lowest acceptable drilling fluid density at the bottom of the wellbore. Drawing a vertical construction line from that point, we discover that drilling with that fluid density at or above 13 406 ft does not fracture the wellbore but does jeopardize pipe-in-hole, either drill pipe or casing, becoming differentially stuck. While drilling from 13 406 ft to 22 000 ft therefore, wellbore above that depth should be isolated. The vertical depth 13 406 ft corresponds to a casing point.

Determining 13 406 ft as the depth of intersection of the vertical construction line with the "Differential Sticking" curve can be accomplished by linear interpolation.[20] Comparison of the abscissa of point (14.3, 22 000) with data used to generate the "Differential Sticking" curve will determine between which two points the intersection lies. For this problem, the two points on the "Differential Sticking" curve are (13.22, 12 000) and (14.76, 14 000), where in each case the abscissa value of pressure gradient was de-

[20] Usually, any character of the pore pressure gradient or fracture pressure gradient curve between data points is sufficiently questionable to preclude any more sophisticated model of interpoint curve behavior.

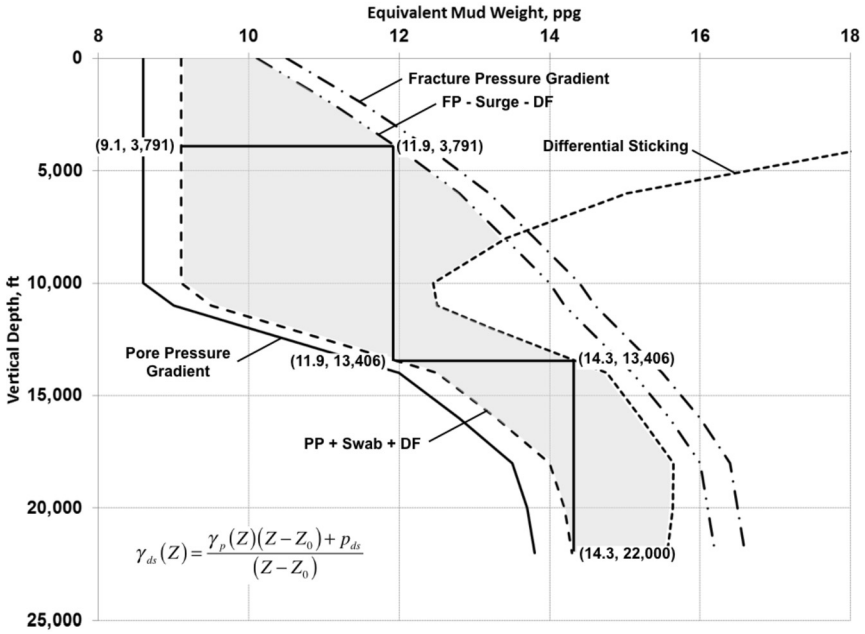

Figure 13.16 ***Casing seat example—illustration of the bottom-up design philosophy including a differential sticking limit.*** The acceptable drilling fluid density range is generated with the components of Eq. (13.6).

termined in the manner of Eq. (13.16). By linear interpolation,

$$\begin{aligned} Z &= Z_1 + \frac{Z_2 - Z_1}{\gamma_2 - \gamma_1} \times (\gamma - \gamma_1) \\ &= 12\,000 + \frac{14\,000 - 12\,000}{14.76 - 13.22} \times (14.3 - 13.22) \\ &= 13\,403, \end{aligned} \tag{13.17}$$

which differs only slightly from the value 13 406 ft, which was generated by a spreadsheet carrying more significant digits in its internal calculations. A similar procedure, tailor-made for a spreadsheet, can be used to determine other points of intersection in the discussion to follow.

How is drilling conducted down to 13 406 ft? We consider the acceptable drilling fluid density range and discover a horizontal line at 13 406 ft intersects the factored pore pressure gradient at a fluid density of 11.9 ppg. If a column of fluid of this density extends to the surface, a vertical construction line from point (11.9, 13 406 ft) intersects the factored fracture pressure gradient curve at 3791 ft. As formations above this depth

Table 13.2 Casing seat selection—example problem, summary of casing seats following bottom-up exercise

Vertical depth[a], ft	Drilling fluid density, ppg	Reason
3791	9.1–10.1	Formation fracture
13 406	Variable–11.9	Differential sticking
22 000	Variable–14.3	Well depth

[a] Onshore well, negligible elevation.

must be isolated when drilling the hole section below, this depth becomes an additional casing point.

Finally, a horizontal line at 3791 ft will intersect the factored pore pressure gradient at a fluid density of 9.1 ppg. A construction above this depth encounters no additional intersections with the bounds of acceptable fluid density—the bottom-up analysis is complete.

Table 13.2 summarizes the results of the exercise, offering the reason for each selected casing seat. The second column in the table reports the acceptable fluid density range for that hole section. The minimum acceptable fluid density varies through each hole section and is limited by the factored pore pressure gradient curve or, more generally, whatever mechanism in Eq. (13.15) determines the lower bound of acceptable drilling fluid density. The maximum acceptable fluid density in each section is either (a) the factored fracture pressure gradient at the top of the hole section or (b) the drilling fluid density at the previous shoe as determined by the differential sticking limit or, more generally, whatever mechanism in Eq. (13.15) determines the upper bound of acceptable drilling fluid density.

Table 13.2 in its present form represents a "first draft" of proposed casing seats. In particular, the contents of Sections 13.3.2.6 and 13.3.2.7 may require additional seats, causing the results of Table 13.2 to be revisited in the spirit of optimization.

Returning to Fig. 13.15, how would a top-down "first draft" design differ from the results of Table 13.2? The result is shown graphically in Fig. 13.17.

To execute a top-down design (see Fig. 13.17), begin at point (10.1, 0), the highest acceptable drilling fluid density at the top of the wellbore. Drawing a vertical construction line from that point, we discover that drilling with that fluid density at or above 11 600 ft (a) will not fracture shallow formations and (b) will not induce formation pore fluid influx. Wellbore above 11,600 ft must, however, be isolated before using higher drilling fluid densities to drill deeper. The vertical depth 11 600 ft corresponds to a casing point.

Our attention now focuses on the hole section below the casing seat at 11 600 ft. Drawing a horizontal construction line from the point (10.1, 11 600), the maximum acceptable drilling fluid density in this section is dictated by the possibility of differential sticking with a fluid density above 12.9 ppg. With this fluid density, a vertical con-

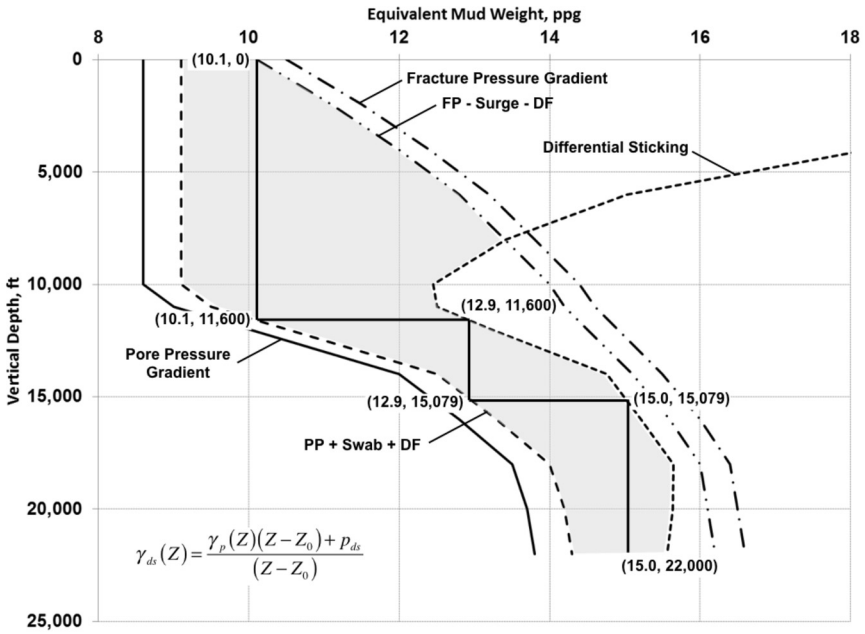

Figure 13.17 ***Casing seat example—illustration of the top-down design philosophy including a differential sticking limit.*** The acceptable drilling fluid density range is generated with the components of Eq. (13.6).

struction line indicates we may drill to 15 079 ft before the fluid column in the wellbore becomes insufficient to prevent influx of formation pore fluids. The depth 15 079 ft becomes the next casing point.

Repeating the process of the preceding paragraph, the maximum drilling fluid density for the next hole section is 15.0 ppg, a fluid density sufficient to complete the well.

Table 13.3 summarizes the results of the top-down design exercise, offering the reason for each selected casing seat. The second column in the table reports the maximum acceptable fluid density for that hole section. As before, and for the mechanisms considered in this example, the minimum acceptable fluid density varies through each hole section and is limited by the factored pore pressure gradient curve. The maximum acceptable fluid density in each section is either (a) the factored fracture pressure gradient at the top of the hole section or (b) the drilling fluid density at the previous shoe as determined by the differential sticking limit.

13.3.4 Kick tolerance

Having selected the casing seats based on the constraints on drilling fluid density, one calculation remains—kick tolerance. Kick tolerance is a measure of the volume of gas,

Table 13.3 Casing seat selection—example problem, summary of casing seats following top-down exercise

Vertical depth[a], ft	Drilling fluid density, ppg	Reason
11 600	9.1–10.1	Pore fluid influx
15 079	Variable–12.9	Pore fluid influx
22 000	Variable–15.0	Well depth

[a] Onshore well, negligible elevation.

measured at downhole conditions, that can be circulated out of a wellbore without fracturing the formation at the weakest point in the open hole. That is, how strong is the open hole below the current casing seat with regard to containing a kick?

Fig. 13.18 summarizes the concept of kick tolerance in a straight, vertical wellbore. Consider first the diagram labeled "Case 1." We envision a kick of height h entering the wellbore at the depth of the bit. The influx might occur at positive kick intensity,[21] or it might happen at zero or small negative kick intensity. In the latter case, the influx could be due to a swab pressure increment associated with pipe movement out of the hole. The influx increases the pressure in the wellbore as it has density less than that of the drilling fluid. A previously benign drilling environment might now threaten the integrity of the wellbore as the increased wellbore pressure fractures the wellbore wall at its weakest location. This site of weakness can be anywhere in the open hole section but is usually taken to be just below the previous casing shoe, as this is the only location for which one usually has a measure of formation strength (see subsection 'Tension' in Section 13.2.1.2). The kick tolerance calculation determines the size of the kick for which formation fracture can occur.

Now consider the diagram labeled "Case 2." This figure illustrates an alternate scenario when an influx originally at the bit has expanded and just reached the open hole weak point, taken in the figure to be the previous casing shoe. It is important to recognize that Case 2 is an entirely different problem from Case 1—Case 2 is not a snapshot of the influx from Case 1 when that influx reaches the open hole weak point. To emphasize this caution, the Case 2 influx is included in its diagram, illustrating that, at the bit, the two influxes differ.

The only common feature between the Case 1 and Case 2 influxes is that they have the same height at the time their respective models are evaluated. A graphical explanation for this equality is presented in Fig. 13.19. The graph on the right-hand portion of the figure indicates the following:

- Both scenarios are targeted at the same weak point, Point A in the figure;
- Both scenarios have an influx entering at the same pressure, Point B in the figure;

[21] Kick intensity is the difference between local formation pore pressure gradient and the drilling fluid density in the wellbore, measured in the same units as fluid density.

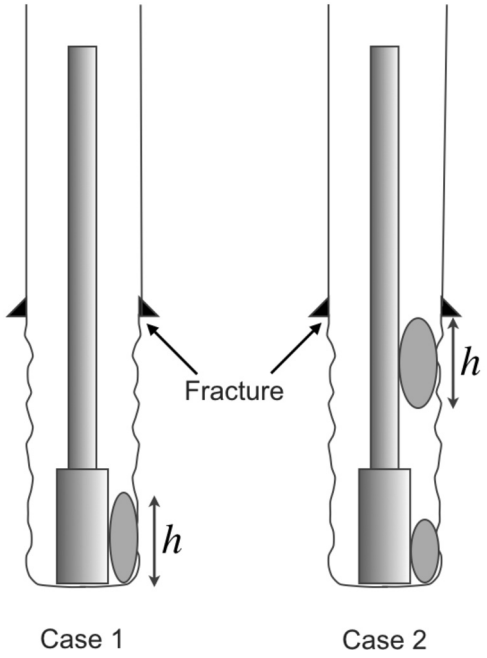

Figure 13.18 ***The concept of kick tolerance.*** Cases 1 and 2 are two scenarios, not two time snapshots of the same scenario.

- Both scenarios have the same drilling fluid density and influx density—this fixes the slopes of the "MW" lines and the near-vertical dashed lines representing the influx.

Constructing the "MW" and influx lines from Points A and B, the intersections of the lines must[22] produce the same influx height h. In fact, one could construct an infinite number of scenarios, each with its influx analyzed at a particular depth, and in all these scenarios, provided the wellbore pressure is just sufficient to fracture the formation at the open hole section's weak point, the influx height will be the same.

13.3.4.1 Kick tolerance calculation

The kick tolerance calculation proceeds in the following steps.

Influx height

Consider Case 1 in Fig. 13.18, recognizing that one could select Case 2 and calculate the same height. For Case 1, there exist two ways of expressing the pressure at the open

[22] The term "must" is only true in the context of the assumptions of this simple model. In actuality, both the drilling fluid density and influx density will vary with depth in the two scenarios. Within the assumptions of the model, however, "must" is appropriate.

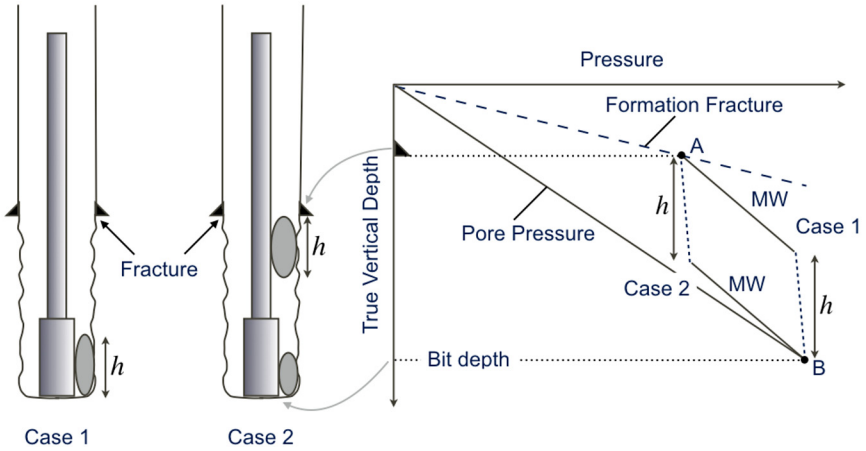

Figure 13.19 ***Both kick tolerance scenarios have the same influx height.***

hole section weak point. First, we may simply realize that at the weak point

$$p_{max} = p_{fr} - p_{DF}, \tag{13.18}$$

that is, the maximum realizable pressure at the weak point is the local formation fracture pressure p_{fr} diminished by a design factor p_{DF}. The design factor accounts for such issues as rig crew response time.

Alternately, we may start at the bit and work our way up to the weak point

$$p_{max} = p_p - \gamma_g h - \gamma_f \left(Z_{bit} - h - Z_{wp}\right). \tag{13.19}$$

Starting with the pressure of the influx at the bit p_p, we subtract the pressure loss through the gas column, assuming a constant gas density γ_g and then the pressure loss through the column of drilling fluid of weight density γ_f.

Since Eqs. (13.18) and (13.19) are both calculating p_{max}, we may equate the two and solve for the unknown height

$$h = \frac{p_{fr} - p_{DF} - p_p + \gamma_f \left(Z_{bit} - Z_{wp}\right)}{\gamma_f - \gamma_g}. \tag{13.20}$$

As discussed above, this value of h applies to both Case 1 and Case 2.

Influx volume

As kick tolerance is expressed as a volume, the next calculation step is to convert the influx height to a volume. Let C_{BHA} be the annular capacity of the bottom hole assembly

and C_{DP} be the annular capacity of the drill pipe, both expressed in units of volume per length. For Case 1,

$$V_{bit} = C_{BHA}h, \tag{13.21}$$

and for Case 2,

$$V_{wp} = C_{DP}h. \tag{13.22}$$

It may be that the influx in either case straddles the crossover between the BHA and drill pipe. This complicates the calculation shown here, but the underlying principle remains unchanged.

The volumes in Eqs. (13.21) and (13.22) are incompatible in that they reference different depths. Common practice is to "move" the volume at the weak point to the bit (its origin) so that both volumes have a common reference. We do this using Boyle's law

$$V_{wp}\big|_{bit} = V_{wp}\frac{p_{max}}{p_p}. \tag{13.23}$$

Comparison of volumes

With both influx scenario volume values now available at the bit, the kick tolerance calculation can be completed by selecting the smaller of the two influx values, namely

$$\text{Kick Tolerance} = \min\begin{Bmatrix} V_{wp}\big|_{bit} \\ V_{bit} \end{Bmatrix}. \tag{13.24}$$

Kick tolerance is an evaluation of the structural capacity of the current open hole environment. If the kick tolerance is small, prudence may dictate altering a current casing seat to seek a more competent environment in which to drill. Typically, an operator's drilling policy will specify increasing levels of drilling management approval for decreasing values of an open hole section's kick tolerance.

Example problem—kick tolerance

Consider the 12.25 in. open hole below the shoe of 13.375 in. casing at 15 000 ft (4572 m). The fracture gradient at the shoe (which happens to be the weak point) is 12.7 ppg (1.52 SG).

While drilling ahead at 18 000 ft (5486 m) with 11 ppg (1.32 SG) mud, a pore pressure gradient of 12 ppg (1.44 SG) is encountered.

Assume a choke operator error of 200 psi and a gas gradient for the kick of 0.15 $\frac{\text{psi}}{\text{ft}}$. Use 5.5 in. as the drill pipe diameter and assume 8 in. collars. The formula for annular clearance in $\frac{\text{bbl}}{\text{ft}}$ is 0.0009714 × (Hole d^2 – Pipe D^2) if the pipe dimensions are in inches.

Compute the following:

- the kick tolerance;
- the kick tolerance if the mud weight equals the pore pressure (swab kick);
- qualitatively, what is the effect on kick tolerance if the hole is inclined rather than vertical?

At the weak point, p_{max} is calculated from Eq. (13.18) as

$$p_{max} = 0.051\,948\,\frac{\text{psi}}{\text{ft ppg}} \times 12.7\,\text{ppg} \times 15\,000\,\text{ft} - 200\,\text{psi} = 9696\,\text{psi}. \tag{13.25}$$

For future reference, the pore pressure at the bit is

$$p_p = 0.051\,948\,\frac{\text{psi}}{\text{ft ppg}} \times 12\,\text{ppg} \times 18\,000\,\text{ft} = 11\,221\,\text{psi}. \tag{13.26}$$

With care to maintain unit consistency, h is calculated from Eq. (13.20) as

$$h = \frac{9696\,\text{psi} - 11\,221\,\text{psi} + 0.051\,948\,\frac{\text{psi}}{\text{ft ppg}} \times 11\,\text{ppg} \times (18\,000 - 15\,000)\,\text{ft}}{0.051\,948\,\frac{\text{psi}}{\text{ft ppg}} \times 11\,\text{ppg} - 0.15\,\frac{\text{psi}}{\text{ft}}} = 449\,\text{ft}. \tag{13.27}$$

The annular capacities opposite the collars and the drill pipe are, respectively,

$$C_{BHA} = 0.000\,971\,4\left(12.25^2 - 8.0^2\right) = 0.0836\,\frac{\text{bbl}}{\text{ft}}, \tag{13.28}$$

$$C_{DP} = 0.000\,971\,4\left(12.25^2 - 5.5^2\right) = 0.1164\,\frac{\text{bbl}}{\text{ft}}. \tag{13.29}$$

The respective volumes corresponding to the kick are therefore

$$V_{bit} = 0.0836\,\frac{\text{bbl}}{\text{ft}} \times 449\,\text{ft} = 37.5\,\text{bbl} \tag{13.30}$$

at the bit, and

$$V_{wp} = 0.1164\,\frac{\text{bbl}}{\text{ft}} \times 449\,\text{ft} = 52.3\,\text{bbl} \tag{13.31}$$

at the weak point, which must be "moved" to the bit

$$V_{wp}\big|_{bit} = 52.3\,\text{bbl} \times \frac{9696\,\text{psi}}{11\,221\,\text{psi}} = 45.2\,\text{bbl}. \tag{13.32}$$

Comparison of Eqs. (13.30) and (13.32) yields a kick tolerance of 37.5 bbl.

The second part of the problem changes the drilling fluid density to equal that of the pore pressure. Recalculating the pertinent equations with $\gamma_m = 12$ ppg gives

$$h = \frac{9696\,\text{psi} - 11\,221\,\text{psi} + 0.051\,948\,\frac{\text{psi}}{\text{ft ppg}} \times 12\,\text{ppg} \times (18\,000 - 15\,000)\,\text{ft}}{0.051\,948\,\frac{\text{psi}}{\text{ft ppg}} \times 12\,\text{ppg} - 0.15\,\frac{\text{psi}}{\text{ft}}}$$

$$= 729\,\text{ft}, \tag{13.33}$$

$$V_{bit} = 0.0836\,\frac{\text{bbl}}{\text{ft}} \times 729\,\text{ft} = 60.9\,\text{bbl}, \tag{13.34}$$

$$V_{wp} = 0.1164\,\frac{\text{bbl}}{\text{ft}} \times 729\,\text{ft} = 84.9\,\text{bbl}, \tag{13.35}$$

$$V_{wp}\big|_{bit} = 84.9\,\text{bbl} \times \frac{9696\,\text{psi}}{11\,221\,\text{psi}} = 73.4\,\text{bbl}. \tag{13.36}$$

Comparison of Eqs. (13.34) and (13.36) yields a kick tolerance of 60.9 bbl.

Finally, for the case of an inclined wellbore, the height calculation, as it depends on fluid hydrostatic heads, remains unchanged. When the height is converted to volume, however, we must now use $h/\cos(\text{inclination})$ instead of height to determine the length component of the volume (Eqs. (13.30) and (13.31)). This value will always be greater than or equal to h. For this reason, most workers treat the wellbore as vertical to introduce a bit of conservatism into the calculation.

13.4. TUBULAR SIZING

With the casing seats now having been determined (Sections 13.3–13.3.3), including an evaluation of the ability of the wellbore as planned to contain a kick (Section 13.3.4), the remaining preamble to the design is diametric sizing. The well tubulars should be sized from the inside, progressing outward.

13.4.1 Tubing sizing

The most important well tubular in the sizing exercise is the production tubing. Fig. 13.20 illustrates the condition at the perforations where the intersection of two curves:

- the inflow performance relation (IPR) of the reservoir, determined by the properties of both the reservoir rock and the interstitial fluid—the flow rate increases as the pressure at the perforations is lowered;

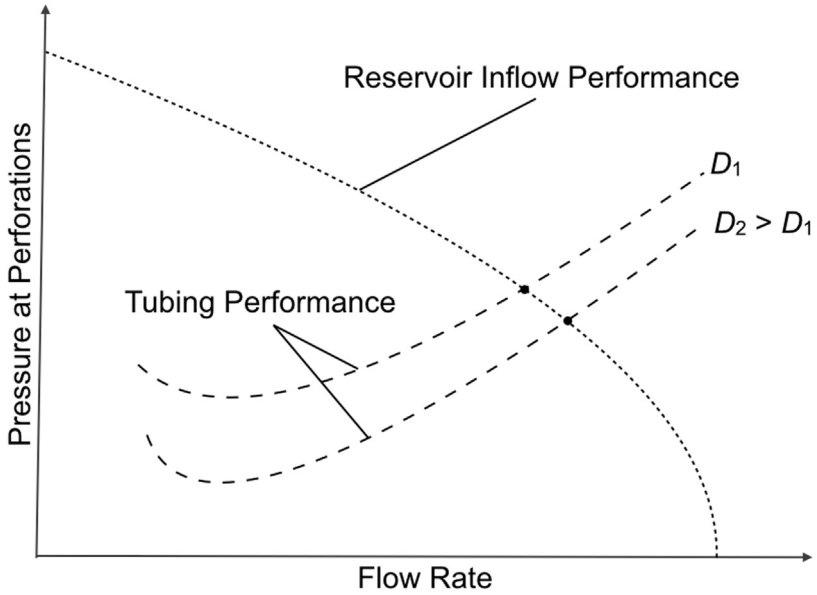

Figure 13.20 ***Reservoir inflow performance relation.*** The dots in the figure indicate locations of well operation based on the intersection of the reservoir inflow performance relation and the tubing performance curve.

- the flow performance of the tubing, determined by the geometry of the tubing and the produced fluid—above a certain minimum flow rate,[23] the flow rate increases as the pressure at the perforations increases;

determines the operating condition. In particular, all other variables being fixed, varying the diameter of the tubing can affect this intersection and therefore the flow rate to be expected from the well. Properly sized tubing can significantly affect the economics of hydrocarbon recovery [151].

Tubing sizing with respect to flow economics is not normally the responsibility of the drilling engineer. The completion engineer, on the other hand, may have significant input, particularly if the reservoir requires artificial lift to aid production.

13.4.2 Production casing sizing

Once the production tubing is sized, communication between the drilling and completion engineers increases. A number of considerations affect the clearance between the production tubing and production casing:

[23] For low flow rates, e.g., less than that corresponding to the curve minimum, the gravitational component of the energy balance dominates; for high flow rates, e.g., greater than that corresponding to the curve minimum, the friction loss term in the energy balance dominates [151,183].

- Completion accessories. Artificial lift—gas lift, electric submersible pump—may require annular space for mandrels, power fluids and power cables [151]. In deepwater completions, the size of the subsurface safety valve often dictates the size of the production casing at and above the valve. Control lines, chemical injection lines, gauge lines or possible dedicated lines for fiber optics [184], along with the associated cross-coupling protectors, are common in current well completions.
- Multiple completion. The number of tubing strings run in the production casing, perhaps to drain stacked reservoirs, can affect the clearance to be provided by the production casing.
- Tubing recovery. Depending on the location, providing sufficient annular space to accommodate wash-over operations may be prudent.
- Future recompletion. It may be that the wellbore will initially be used to drain one reservoir horizon and then, at a later date, be side-tracked to exploit another horizon. Retention of the original production casing may be important to the economics of the future completion. It may therefore be necessary to anticipate having to drill through the production casing with appropriate allowance for wear, and therefore increased wall thickness, affecting the annular clearance of the initial completion. Such forecasting may be complicated by unknowns such as external corrosion to the production casing during its use for the initial wellbore.

13.4.3 Surface and intermediate casing sizing

With the production casing having been sized with the types of discussion topics mentioned above, the sizing of the remainder of the well tubulars assumes a more proscripted form, the two major concerns being standardization of sizes—both casing and drill bits—and adequate cement sheath thickness. Such standardization will not result in the least expensive well, at least not when considered in isolation. When considered in the context of global company standardization, however, where tubulars and accessories may be shared between different operating regions, standardization almost always results in savings for the enterprise.

Starting with the production casing and working outward, a typical sizing exercise next determines the appropriate hole size to contain the production casing while providing adequate annular clearance for placement and solidified strength of the cement sheath outside the production casing. This hole diameter will be adjusted slightly such that it corresponds to a standard bit size. One then searches for a casing diameter—destined to be the outside tubular neighbor of the production casing—for which reasonable wall thicknesses will accommodate the bit necessary to drill the wellbore for the production casing. The above steps are then repeated for each successive new casing size, proceeding from inner tubulars, outward.

Deviations from the above procedure include the following:

- Less than standard clearance [185]. Well designs[24] requiring a large number of casing strings may approach handling limits of available rigs and/or rig equipment. Maintenance of reasonable hole and tubular size—too small may limit flow rates for produced fluids; too large may reduce drilling efficiency—can be achieved by reducing the annular clearance between strings while still using standard casing and drill bits.
- Nonstandard tubulars[25] [186]. Contra the comments on standardization above, using nonstandard tubular sizes in a major project or basin may be justified. Design of a nonstandard tubular string is identical to that of a standard tubular size. The challenge usually arises with respect to related activities such as cement placement and cement sheath integrity. Further, the design of a close tolerance liner hanger may prove difficult, and the qualification of specially designed clearance connections may be required.
- Well economics. Particularly in developed basins, continuous improvement of well designs can gravitate toward smaller holes for outer strings. In such instances, and again, with due regard for the effects on cement placement and cement sheath integrity, permitting less than standard clearance may be appropriate.
- Annular pressure build-up (APB) mitigation. Depending on the type of mitigation selected to alleviate thermally induced pressure in a trapped annulus, more or less annular clearance between casing strings may be necessary. Such consideration may not only affect installation of the mitigator but may also influence the probability that a previous casing shoe may be deemed open or closed. See Section 15.2 of Chapter 15 for a discussion of APB mitigation.

A chart[26] for selecting casing and bit/open hole sizes for commonly used tubulars and bits is provided in Table 13.4. The left-most column of the table lists casing outside diameters. The title rows of the remaining columns list common bit sizes or, equivalently, confining open hole sizes. Starting with the production casing diameter

[24] The pore and fracture pressure profiles for deepwater locations may require more than a half-dozen casing strings to accommodate the narrow range of acceptable drilling fluid density. Deepwater wells are further restricted by the usual necessities of:

- a relatively large final hole size (~8-1/2 in. (215.95 mm)) to accommodate high volume production and/or injection and large subsurface safety valves (~9 in. (228.6 mm));
- a current maximum 18-3/4 in. (476.25 mm) diameter bore on the high pressure wellhead.

Most of the well tubulars must fit within these diametral limits.

[25] Other alternatives to nonstandard tubulars include riserless drilling to delay the running of the high pressure wellhead with its (current) maximum 18-3/4 in. (476.25 mm) bore, solid expandable liners and managed pressure drilling [186].

[26] A common alternative to the selection chart presented here is a graphical diagram on which the user follows a connecting path from casing to bit to casing. Both the graphical diagram and the selection chart provide identical information.

as selected according to the criteria outlined previously,[27] the procedure for using the sizing selection chart is as follows:

1. Locate the production casing diameter in the left-most column. Searching to the right along this row, find the designations "C" and "SC" to determine an appropriate bit or confining open hole size in which the production casing will be installed.
   - "C" designates a bit size that provides adequate clearance for running the casing and for achieving a cement sheath of recommended thickness to provide an isolating seal in the casing/confining hole annulus.
   - "SC" designates a bit size that provides less than normal clearance for running and cementing the casing. Special attention should be paid to cement placement hydraulics, cement sheath integrity and sizable doglegs [185].
2. Having selected a hole size for the current casing, search the column for that bit to determine what (previous) casing string diameters can drift that bit size while still having adequate wall thickness to provide resistance to design loads.
   - "B" designates a casing diameter which can drift the selected bit and still have sufficient wall thickness to withstand typical design loads. The actual design process may suggest a thicker than ordinary wall, but the "B" selection should be adequate for most well applications.
   - "SB" designates a casing diameter which, in order to drift the current bit, may be thinner than typical inventory. Such casing may be selected if the load environment is benign. Alternately, it may be possible to increase wall thickness by moving to a larger outside diameter (from 13-3/8 to 13-5/8, for example).
3. The previous step results in an appropriate diameter for the next outer casing string. At this point, the process returns to Step 1 and is repeated.

13.4.4 Example problem—tubular sizing

Assume that a sizing exercise on the production tubing, coupled with adequate consideration of production tubing to production casing annular clearance, has resulted in the decision to run 4 in. production casing. Further, assume the well in question requires four casing seats. Using the selection chart of Table 13.4, and requiring standard clearance for running and cementing all casing strings, determine the bit and casing sizes for all strings above the production casing.

Fig. 13.21 reproduces Table 13.4, overlaying the procedure used to select the remaining bit and casing sizes. The table has been grayed to emphasize the size selection procedure. The numbered items below correspond to the numbered decision paths in the figure:

1. Starting with the row for 4 in. production casing, search arrow 1 locates a cell containing "C" and designating a bit size for the 4 in. casing of 5.875 in., a hole size

[27] A properly size production casing string assumes the production tubing has already been sized.

Table 13.4 Casing diametric sizing—selection chart[a, b]

Casing[c]	Bit or confining open hole size (in.)															
	4-3/4	5-7/8	6-1/8	6-1/2	7-7/8	8-1/2	8-3/4	9-1/2	10-5/8	12-1/4	14-3/4	17-1/2	20	22	26	33
3-1/2	C															
4	SC	C														
4-1/2		SC	C													
5			SC	C												
5-1/2	SB			SC	C											
6-5/8	B	SB			SC	C										
7		B	SB			C	C									
7-5/8			B	B		SC	SC	C								
7-3/4			B	B		SC	SC	C								
8-5/8				B	SB			SC	C							
9-5/8					B	B	SB		SC	C						
9-7/8					B	B	SB		SC	C						
10-3/4							B	B		SC	C					
11-3/4									B		C					
11-7/8									B		C					
13-3/8										B	SC	C				
13-5/8										B	SC	C				
14										B	SC	C				
16											B	SC	C	C	C	
18-5/8													SC	SC	C	
20												B			C	
24													B	B	C	
26																C
30															B	C
36																B

[a] C = standard clearance for running and cementing casing, SC = nonstandard casing clearance, B = standard bit inside casing, SB = thinner casing wall to accommodate bit.

[b] Starting with the production casing size, search horizontally for a "C" or "SC", according to the desired annular clearance between the casing and its confining open hole. Then read the corresponding column heading to determine the bit/confining open hole size for this casing. Search vertically in this same column for previous casing sizes that can accommodate this bit, with either popular wall thicknesses ("B") or thinner walls ("SB"). Having selected a previous casing size, repeat the process to determine its bit/hole size. Continue until all casing sizes have been determined.

[c] Label 1 designation or outside diameter in inches.

Casing[c]	Bit or confining open hole size (in.)															
	4-3/4	5-7/8	6-1/8	6-1/2	7-7/8	8-1/2	8-3/4	9-1/2	10-5/8	12-1/4	14-3/4	17-1/2	20	22	26	33
3-1/2	C															
4	SC	C														
4-1/2		SC	C													
5			SC	C												
5-1/2	SB			SC	C											
6-5/8	B	SB			SC	C										
7		B	SB			C	C									
7-5/8			B	B		SC	SC	C								
7-3/4			B	B		SC	SC	C								
8-5/8				B	SB			SC	C							
9-5/8					B	B	SB		SC	C						
9-7/8					B	B	SB		SC	C						
10-3/4							B	B		SC	C					
11-3/4									B		C					
11-7/8									B		C					
13-3/8										B	SC	C				
13-5/8										B	SC	C				
14										B	SC	C				
16											B	SC	C	C	C	
18-5/8													SC	SC	C	
20												B			C	
24													B	B	C	
26																C
30															B	C
36																B

[a] C = standard clearance for running and cementing casing, SC = nonstandard casing clearance, B = standard bit inside casing, SB = thinner casing wall to accommodate bit.

[b] Starting with the production casing size, search horizontally for a "C" or "SC", according to the desired annular clearance between the casing and its confining open hole. Then read the corresponding column heading to determine the bit/confining open hole size for this casing. Search vertically in this same column for previous casing sizes that can accommodate this bit, with either popular wall thicknesses ("B") or thinner walls ("SB"). Having selected a previous casing size, repeat the process to determine its bit/hole size. Continue until all casing sizes have been determined.

[c] Label 1 designation or outside diameter in inches.

Figure 13.21 ***Casing diametric sizing—example use of selection chart.*** All selections use standard clearances for running and cementing casing and standard bits that will drift normal wall thicknesses.

adequate to obtain a competent cement sheath for the near-reservoir portion of the wellbore.

2. Knowing that the confining hole for the production casing will be drilled with a 5.875 in. bit, search arrow 2 locates a "B" in the row corresponding to 7 in. casing, indicating that this casing can pass (drift) a 5.875 in. bit, while still retaining sufficient wall thickness (yet to be proved by the design calculations) to meet all design loads.
3. The 7 in. casing is now the focus of the sizing exercise. Repeating the procedure in Step 1, search arrow 3 locates a cell containing "C" and designating a bit size for the 7 in. casing of 8.5 in.
4. In the column for the 8.5 in. bit, search arrow 4 locates a "B" in the rows corresponding to both 9.625 in. and 9.875 in. casing. Both drilling efficiency and economics suggest that 9.625 in. casing is the better choice. However, should anticipated drilling wear or unusually high design loads dictate, the 9.875 in. alternative may provide more design flexibility.
5. The 9.625 in. casing is now in focus. Repeating the procedure in Step 1, search arrow 5 locates a cell containing "C" and designating a bit size for the 9.625 in. casing of 12.25 in.

6. Finally, in the column for the 12.25 in. bit, search arrow 6 locates a "B" in the rows corresponding to 13.375 in. through 14 in. casing. The smaller 13.375 in. casing may again be the better choice, with other factors possibly suggesting the larger diameter alternatives.

CHAPTER 14

Example Design

14.1. INTRODUCTION

This chapter is intended as a companion to Chapter 2, supplementing the formality of the outlined design procedure with commentary on a typical design.

14.2. DESIGN PROBLEM—TUBINGLESS CASING DESIGN

A tubingless completion[1] consisting of 8.625 in., 36.0 $\frac{\text{lb}_\text{m}}{\text{ft}}$ (0.400 in. wall) N80 surface casing[2] (9.875 in. hole) to 1600 ft and 4.500 in. casing (6.250 in. hole) to 11 500 ft is to be designed with three major loads (see Fig. 14.1) in mind:

1. Internal pressure loading from the sand-out or screen-out conditions of a hydraulic fracturing treatment where the maximum surface pressure is 9000 psi with fracture fluid density of 8.5 $\frac{\text{lb}_\text{m}}{\text{gal}}$—see Section 12.7.3.2 of Chapter 12 and Table 12.14[3];
2. External pressure loading assuming plugged perforations resulting in a column of gas to atmospheric pressure at the surface—see Section 12.8.3.4 of Chapter 12 and Table 12.24;
3. Steady state production of gas at 2000 psi surface "tubing" pressure—see Section 12.7.3.3 of Chapter 12 and Table 12.15.

The collapse load (i.e., plugged perforations, gas to surface) is to be simplified by assuming complete internal evacuation.[4] The production load is to be simplified by assuming a constant internal pressure profile of 2000 psi along the entire string.[5]

These are not the only loads one would normally apply to this string—see Tables 2.7 and 2.8—but are the design-governing loads for this string and should be sufficient to illustrate the design principles.

[1] The production tubing and production casing are the same tubular string. There is no packer.

[2] Assume the surface casing is run in fresh water and cemented to the surface with 15.6 $\frac{\text{lb}_\text{m}}{\text{gal}}$ cement. The sole purpose of the surface casing in this problem is to provide an element of the confining hole. The surface casing will not be stress analyzed.

[3] Alternately, Section 12.7.3.1 of Chapter 12 and Table 12.13.

[4] For examples of calculating the pressure of a gas column, see subsections 'Example problem—ideal gas hydrostatic head' (ideal gas) and 'Example problem—real gas hydrostatic head' (real gas) in Section 12.4.1 of Chapter 12.

[5] Normally this pressure profile, along with the temperature profile, would be the output of a (multi- or single-phase) flow simulator.

Elements of Oil and Gas Well Tubular Design
DOI: 10.1016/B978-0-12-811769-9.00014-1

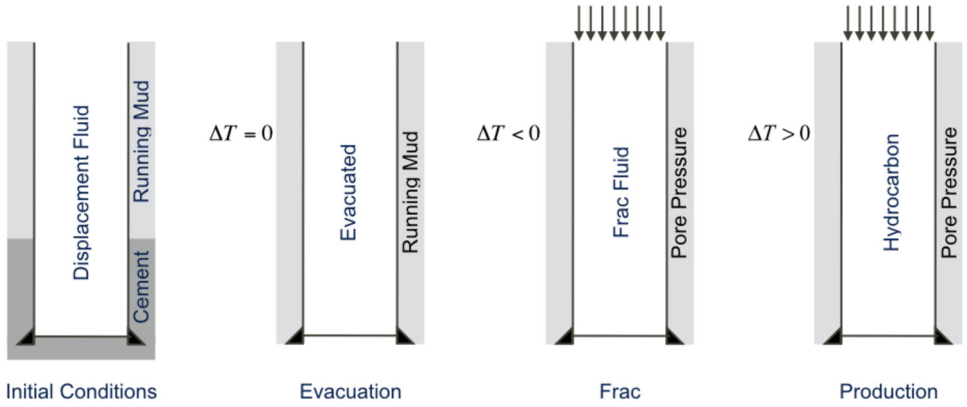

Figure 14.1 ***Load cases for tubingless design.***

The 4.500 in. production casing/tubing is run in a 10.5 $\frac{\text{lb}_\text{m}}{\text{gal}}$ water base fluid and then cemented to 10 200 ft with a 15.6 $\frac{\text{lb}_\text{m}}{\text{gal}}$ slurry. The pore pressure gradient for this well is a constant 8.6 $\frac{\text{lb}_\text{m}}{\text{gal}}$ from the surface.

The initial temperature profile consists of 60 °F at the surface with a 1.1 $\frac{^\circ\text{F}}{100\text{ ft}}$ temperature gradient below. During the hydraulic fracture treatment it is assumed that the entire production casing/tubing cools to the surface temperature. During production the temperature everywhere in the production casing/tubing is assumed equal to the bottomhole temperature.

Check the three load cases for the production casing assuming a proposed string of 4.500 in., 13.5 $\frac{\text{lb}_\text{m}}{\text{ft}}$ (0.290 in. wall) P110 casing. Determine relevant *tube body* axial, triaxial and collapse safety factors at (a) the top of the string and (b) the top of cement. Investigate the selection of a threaded connection for the string.

The API minimum internal yield pressure of 4.500 in., 13.5 $\frac{\text{lb}_\text{m}}{\text{ft}}$ P110 casing is 12 410 psi; the API minimum collapse resistance is 10 680 psi. Do not include temperature deration of yield strength.

For steel, $\rho_s = 0.2836\ \frac{\text{lb}_\text{m}}{\text{in}^3}$, $\alpha_T = 6.9 \times 10^{-6}\ \frac{1}{^\circ\text{F}}$, $E = 30 \times 10^6$ psi and $\nu = 0.3$.

The following comments are pertinent to this design problem statement:

- The pore and fracture pressure gradients for this type of well are usually benign—normally pressured at roughly 8.6 $\frac{\text{lb}_\text{m}}{\text{gal}}$, as stated, and with an at-depth fracture gradient of approximately 17–18 $\frac{\text{lb}_\text{m}}{\text{gal}}$. The well can usually be drilled with one fluid density in approximately one week of calendar time. Because of the simplicity of the subsurface pressure environment, this example skips the casing seat determination summarized in Section 2.3 of Chapter 2 and detailed in Section 13.3 of Chapter 13. For a detailed example of this calculation with a more complicated subsurface environment, see Section 13.3.3.1 of Chapter 13, along with subsection 'Example

Table 14.1 Tubingless casing design—initial and final states (temperature in °F, pressure in psi)

Variable	MD	Initial	Frac	Δ	Evac	Δ	Prod	Δ
T_{top}	0	60	60	0	60	0	186.5	126.5
T_{TOC}	10 200	172.2	60	−112.2	172.2	0	186.5	14.3
T_{bot}	11 500	186.5	60	−126.5	186.5	0	186.5	0
$\overline{T}$[a]	N/A	116.1	60	−56.1	116.1	0	186.5	70.4
p_{i-top}	0	0	9000	9000	0	0	2000	2000
p_{i-TOC}	10 200	5569.2	13 508	7939.2	0	−5569.2	2000	−3569.2
p_{i-bot}	11 500	6279.0	14 083	7804.0	0	−6279.0	2000	−4279.0
$\overline{p_i}$[a]	N/A	2784.6	11 254	8469.6	0	−2784.6	2000	−784.6
p_{o-top}	0	0	0	0	0	0	0	0
p_{o-TOC}	10 200	5569.2	4561.4	−1007.8	5569.2	0	4561.4	−1007.8
p_{o-bot}	11 500	6623.8	5142.8	−1481.0	6279.0	−344.8	5142.8	−1481.0
$\overline{p_o}$[a]	N/A	2784.6	2280.7	−503.9	2784.6	0	2280.7	−503.9

[a] Average values are average above cement top.

problem—kick tolerance' in Section 13.3.4.1 of Chapter 13 for calculating kick tolerance.

- Sizing of the tubulars for this type of well (see Section 2.4 of Chapter 2 or the more detailed discussion in Section 13.4 of Chapter 13) is a balance between managing hydraulic horsepower during the hydraulic fracturing treatment and optimizing subsequent production. The resulting size for the production casing/tubing is usually 3.500 in. or 4.500 in., with wall thickness and grade governed by the design loads.
- Use of a spreadsheet or similar tool is recommended for even a design as simple as the current example. If, for example, after all preliminary calculations and load case definitions the selected wall thickness or grade of tubular results in an inadequate safety factor(s), having to only change the offending parameter with an automatic recalculation will prove convenient.

14.2.1 Preliminary calculations

Important geometric variables for the production casing tube include $A_i = 12.069\,\text{in}^2$, $A_o = 15.904\,\text{in}^2$, $A_s = A_o - A_i = 3.836\,\text{in}^2$, $I = 8.538\,\text{in}^4$, $k_{wall} = 0.875$ (assumed) and $r_c = \frac{6.250\,\text{in.} - 4.500\,\text{in.}}{2} = 0.875\,\text{in.}$ in the open hole.

We construct a spatial cylindrical coordinate system aligned with the axis of the tubular such that (see Fig. 3.1) $\mathbf{g}_3 = \mathbf{e}_3$, $\mathbf{g}_1 = \mathbf{e}_1$, and the cylindrical angle is measured from the positive x_1-axis. The only possible bending in this problem will be column buckling where the bending is so slight that an s coordinate along the axis of the helix will essentially be equal to the $x_3 = z$ coordinate in the spatial system we have chosen.

Table 14.1 summarizes the pressure and temperature environment during the initial (post-WOC) state and the three final states of interest.

The first column lists the variable names for temperature, internal pressure and external pressure that will be used in the work to follow. In addition to the top and bottom of the string, the cement top is chosen as a significant depth since it serves as a boundary between different constraint mechanisms in the string. The second column records the depth (in this case, only measured depth since the well is vertical). The third column in Table 14.1 lists the values of the variables in the initial state, immediately after the cement has thickened sufficiently to prevent axial movement.

Columns 4 and 5 in Table 14.1 summarize both the value of each problem variable for the "Frac" load case and its change in value (Δ) from the initial state. For the "Frac" load case the internal pressure is the surface pressure experienced during the sand out over a column of the fracture fluid. The external pressure gradient is taken everywhere to be pore pressure.

Columns 6 and 7 in Table 14.1 summarize both the value of each problem variable for the "Evac" load case and its change in value from the initial state. For the evacuation load case the internal pressure is nil, and the external pressure is taken as a full column of the drilling fluid in which the casing was run—channeled cement is assumed.

Columns 8 and 9 in Table 14.1 summarize both the value of each problem variable for the "Prod" load case and its change in value from the initial state. For the production load case the internal pressure is 2000 psi everywhere, and the external pressure is taken everywhere to be pore pressure.

Figs. 14.2–14.4 summarize the design temperature and pressure profiles in graphical form.

14.2.2 Length changes

The length changes pertinent to this problem are summarized in Table 14.2. There is a shoulder in this string—the bottom of the string—but by the time it is exposed to the environmental changes of a load case from Table 14.1 it has been permanently fixed beneath the cement top, so no length change will occur due to a shoulder.[6]

The question marks in the ΔL_{Bu} signify the following:

- We do not know if there will be a length change due to buckling because we do not know if the string will buckle under this load case.
- To determine buckling in a load case, we must know f_{eff}, which depends on the axial load f_z. But f_z depends on the length changes.
- The resulting strategy is as follows:
  - We begin by assuming the string does not buckle under this load case.

[6] This is typically true of casing designs. Unless there is a cross-over above the cement top there will not be a length change due to a shoulder. Tubing designers, on the other hand, are continually confronted with shoulders—cross-overs, polished bore receptacles and accessories can create a multitude of shoulders with which the engineer must contend.

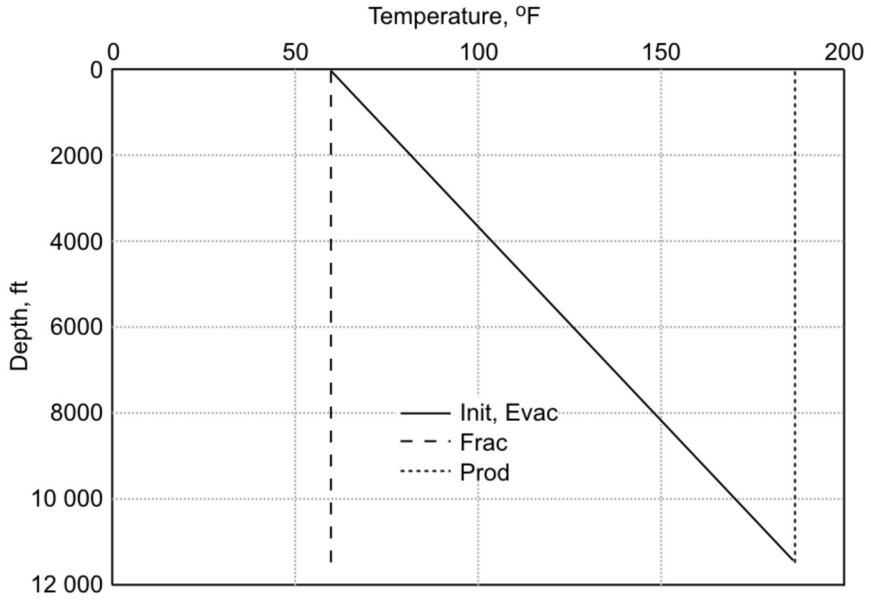

Figure 14.2 ***Load case temperatures for tubingless design.***

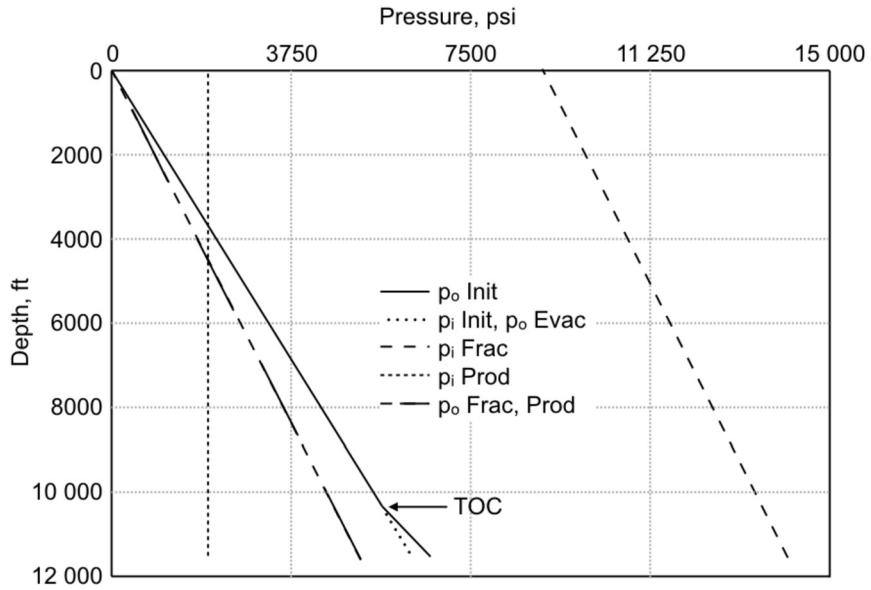

Figure 14.3 ***Load case pressures for tubingless design.*** The internal pressure for the "Evac" load case is zero and is not shown in the graph.

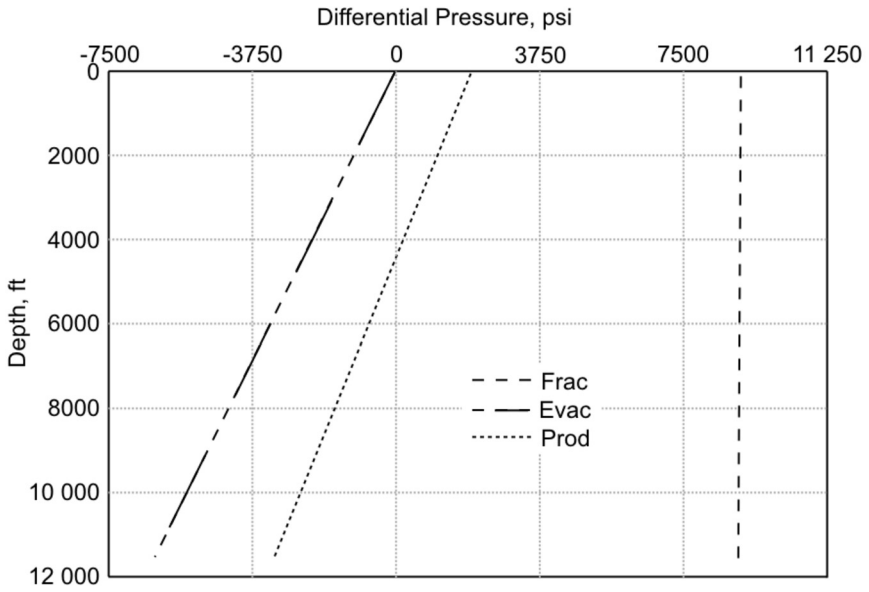

Figure 14.4 ***Load case differential pressures for tubingless design.*** The cementing condition should always be considered as a collapse load case but is omitted here as the "Evac" load case is obviously worse.

Table 14.2 Length change calculations necessary for current design

Load case	Temperature,[a] ΔL_T	Ballooning,[b] ΔL_B	Shoulder(s),[c] ΔL_S	Buckling,[d] ΔL_{Bu}
Frac	✓	✓		?
Evac		✓		?
Prod	✓	✓		?

[a] Section 11.3.1 of Chapter 11.
[b] Section 11.3.2 of Chapter 11.
[c] Section 11.3.3 of Chapter 11.
[d] Section 11.3.4 of Chapter 11.

- We calculate the length changes between the initial condition and this load case. From the length changes we can calculate the change (from its value in the initial condition) in axial force and update the initial value of the axial force.
- This now allows us to determine the effective force and discover if the tubular has buckled.
  - If the tubular has not buckled, the axial load calculation for this load case is complete.
  - If the tubular has buckled, we enter a trial-and-error procedure[7] where we

[7] Technically, the solution should be trial-and-error for all length changes. A length change implies the positions of all points in the string experience associated changes in pressure and temperature loading.

first calculate ΔL_{Bu} and include it in the calculation of change in axial force, then update the axial force, then redetermine the effective force. A new value of effective force generates a new value of ΔL_{Bu}.

– The process is repeated until two successive answers fall within a suitable tolerance.

For the purposes of this example problem only the calculations pertinent to the production load case will be performed—all calculations are summarized in Table 14.3.

14.2.2.1 Temperature change

From the last column of Table 14.1 and Eq. (11.8) we get

$$\Delta L_T = \alpha_T \overline{\Delta T} L = 6.9 \times 10^{-6} \frac{1}{\text{°F}} \times 70.4\,\text{°F} \times 10\,200\,\text{ft} = 4.95\,\text{ft}. \tag{14.1}$$

Below the cement top there is no length change due to temperature—a local axial force change is generated.

14.2.2.2 Ballooning

From the preliminary calculations of area and Eq. (11.10) we have

$$\begin{aligned}\Delta L_B &= -\frac{2\nu}{E}\frac{\overline{\Delta p_i} d^2 - \overline{\Delta p_o} D^2}{D^2 - d^2} L \\ &= -\frac{2 \times 0.3}{30 \times 10^6\,\text{psi}} \frac{-784.6\,\text{psi} \times (3.920\,\text{in.})^2 - (-503.9\,\text{psi}) \times (4.500\,\text{in.})^2}{(4.500\,\text{in.})^2 - (3.920\,\text{in.})^2} 10\,200\,\text{ft} \\ &= 0.08\,\text{ft}.\end{aligned} \tag{14.2}$$

14.2.2.3 Exposed shoulder(s)

As mentioned above in the discussion of Table 14.2, there is no length change due to a shoulder in this design. Eq. (11.11) will be used later in this problem but not in relation to force change at a shoulder (see Section 14.2.3.1).

14.2.2.4 Column buckling

Assuming the tubular is not so severely buckled that the neutral point is above the top of the casing string (i.e., entire string is buckled), the formula for length change associated with column buckling is Eq. (11.20). There is, of course, no length change due to buckling unless there is buckling. Whether or not the (vertical) string is partially

Within the bounds of the assumption of infinitesimal deformation, however, these small load changes are usually ignored. We are required to pursue trial-and-error for buckling because even under the assumption of infinitesimal deformation f_z and f_{eff} are unknown.

Table 14.3 Tubingless casing design—length changes (temperature in °F, pressure in psi, length change in foot)

Variable	Frac	Evac	Prod
$\overline{\Delta T}$[a]	−56.1[b]	0[b]	70.4[b]
$\overline{\Delta p_i}$[a]	8469.6[b]	−2784.6[b]	−784.6[b]
$\overline{\Delta p_o}$[a]	−503.9[b]	0[b]	−503.9[b]
ΔL_T	−3.95	0	4.95
ΔL_B	−5.86	1.79	0.08
ΔL_{Total}	−9.81	1.79	5.03

[a] Average values are average above cement top.
[b] From Table 14.1.

buckled can be determined by checking the value of the effective force at the cement top. For the moment we assume no buckling has occurred and return to this issue after the first-pass calculation of f_z.

14.2.2.5 Net potential length change

The net potential length change of the production casing/tubing string is the algebraic sum of the results of Sections 14.2.2.1–14.2.2.4, namely

$$\Delta L_{Total} = \Delta L_T + \Delta L_B + \Delta L_S + \Delta L_{Bu} = \Delta L_T + \Delta L_B + \Delta L_{Bu}. \tag{14.3}$$

Table 14.3 summarizes the length changes associated with the three load cases under the assumption that no buckling has occurred.

14.2.3 Axial force distribution

The cement top distinguishes tubulars above and below with regard to how their change in axial force is computed.

We can, however, compute the axial force for the initial condition as a single procedure since this axial load is determined by the fluids in the wellbore immediately after cement displacement. At the bottom of the string the axial force is determined by the differential pressures of the displaced fluids on the close-ended tube (cf. Table 12.5 and the example problem in Section 12.6.2.1 of Chapter 12, especially Fig. 12.3). With the information provided in Table 14.1,

$$f_z = 6279.0\,\text{psi} \times 12.069\,\text{in}^2 - 6623.8\,\text{psi} \times 15.904\,\text{in}^2 = -29\,567\,\text{lb}_\text{f}. \tag{14.4}$$

To the above value we add the air weight of the tubular to determine[8]:

[8] The factor $\frac{g}{g_c}$ to convert lb_m to lb_f is $\frac{32.1740\ \frac{\text{ft}}{\text{s}^2}}{32.1740\ \frac{\text{lb}_\text{m}\,\text{ft}}{\text{lb}_\text{f}\,\text{s}^2}}$ or $1\ \frac{\text{lb}_\text{f}}{\text{lb}_\text{m}}$.

- the axial force at the cement top, $-29\,567\,\text{lb}_\text{f} + \frac{g}{g_c} 13.5\,\frac{\text{lb}_\text{m}}{\text{ft}} \times 1300\,\text{ft} = -12\,017\,\text{lb}_\text{f}$.
- the axial force at the string top, $-29\,567\,\text{lb}_\text{f} + \frac{g}{g_c} 13.5\,\frac{\text{lb}_\text{m}}{\text{ft}} \times 11\,500\,\text{ft} = 125\,683\,\text{lb}_\text{f}$.

These values have been recorded in the second column of Table 14.4.

14.2.3.1 Above cement top

Given the values of ΔL_{Total} without buckling, we may now determine the associated increment in axial load by the following reasoning (see Fig. 14.5 and detailed discussion in Section 11.2 of Chapter 11). First, we recognize that both ends of the tubular string are constrained in the axial direction—by the wellhead at the surface[9] and by the cement top below the surface—such that ΔL_{Total} is actually a *potential* length change. That is, it is the length change that would occur if one end of the tubular were free to move. Since the cemented tubular is actually not free to move at either end, we imagine one end of the tubular to be free so that ΔL_{Total} is realized, and then apply a separate, incremental axial force at the unrestrained end that is sufficient to produce a length change equal and opposite to ΔL_{Total}. This incremental axial force is exactly the force generated by the *potential* length change and is given by solving Eq. (11.11) for the incremental axial force corresponding to $-\Delta L_{Total}$. This incremental axial force is given by

$$\Delta f_z = -\frac{EA_s \Delta L_{Total}}{L}. \tag{14.5}$$

For the "Frac" load case,

$$\Delta f_z = -\frac{30 \times 10^6\,\text{psi} \times 3.836\,\text{in}^2 \times (-9.81\,\text{ft})}{10\,200\,\text{ft}} = 110\,680\,\text{lb}_\text{f}. \tag{14.6}$$

For the "Evac" load case,

$$\Delta f_z = -\frac{30 \times 10^6\,\text{psi} \times 3.836\,\text{in}^2 \times (1.79\,\text{ft})}{10\,200\,\text{ft}} = -20\,164\,\text{lb}_\text{f}. \tag{14.7}$$

For the "Prod" load case,

$$\Delta f_z = -\frac{30 \times 10^6\,\text{psi} \times 3.836\,\text{in}^2 \times (5.03\,\text{ft})}{10\,200\,\text{ft}} = -56\,768\,\text{lb}_\text{f}. \tag{14.8}$$

Table 14.4 summarizes the axial force during the initial (post-WOC) state and the three final states of interest. For each load case, all points in the tubular string above the cement top experience the same increment in axial force—see Fig. 14.5.

Fig. 14.6 summarizes the axial force profiles in graphical form.

[9] In this problem we ignore wellhead movement.

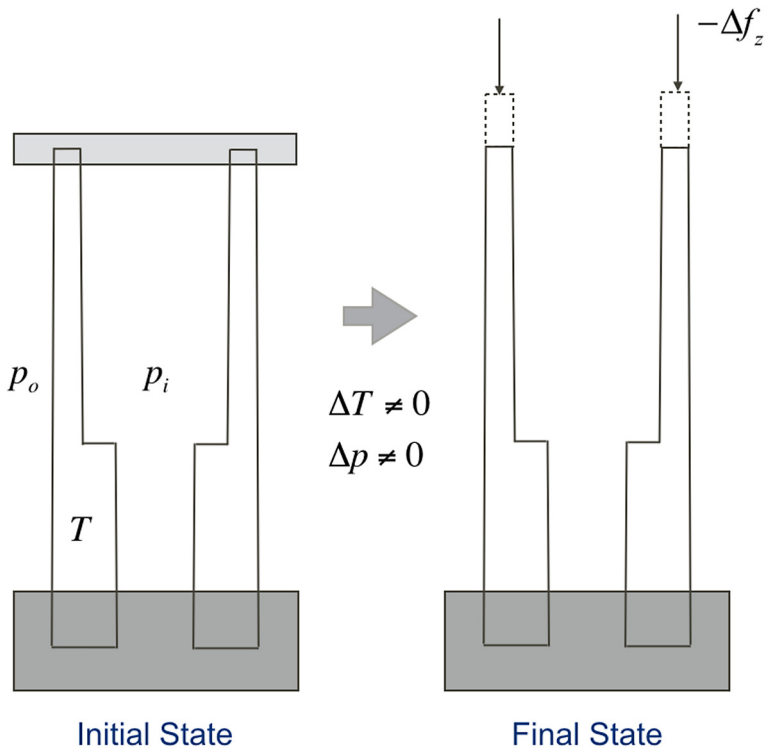

Figure 14.5 ***Concept used to determine axial force change.***

Table 14.4 Tubingless casing design—initial and final states of axial force ($1000\,\mathrm{lb_f}$)

Location	Initial	Frac		Evac		Prod	
		Increment	Total	Increment	Total	Increment	Total
Top[a]	125.68	110.68	236.36	−20.16	105.52	−56.77	68.91
TOC+[a]	−12.02	110.68	98.66	−20.16	−32.18	−56.77	−68.79
TOC-[b]	−12.02	156.19	144.17	−40.32	−52.34	−27.58	−39.60
Bottom[b]	−29.57	171.08	141.51	−42.18	−71.74	−16.85	−46.42

[a] Use Section 14.2.3.1 for load case calculations.
[b] Use Section 14.2.3.2 for load case calculations.

14.2.3.2 Below cement top

Below the top of cement the calculation of axial force is similar, with the exception that local, rather than average, length change potentials are important. Consider, for example, the axial force in Eq. (14.5). The variables E and A_s retain their previous meanings. The variable ΔL_{Total}, however, depends on $\overline{\Delta T}$, $\overline{\Delta p_i}$ and $\overline{\Delta p_o}$ which, in the limit as one considers smaller and smaller lengths of investigation, approach the local values of ΔT, Δp_i and Δp_o. Further, both ΔL_T and ΔL_B depend linearly on L, so that

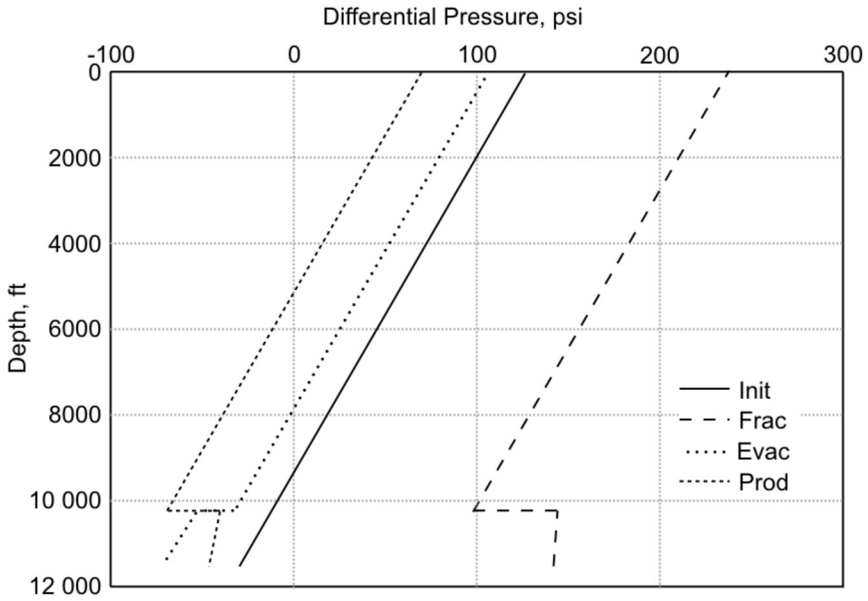

Figure 14.6 ***Load case axial forces for tubingless design.***

we may write

$$\Delta L_{Total} = \Delta L_T + \Delta L_B = \left[\alpha_T \overline{\Delta T} - \frac{2\nu}{E} \frac{\overline{\Delta p_i} A_i - \overline{\Delta p_o} A_o}{A_s} \right] L, \tag{14.9}$$

which, when substituted into Eq. (14.5) yields

$$\Delta f_z = -EA_s \alpha_T \Delta T + 2\nu \left(\Delta p_i A_i - \Delta p_o A_o \right), \tag{14.10}$$

where we now use local values of ΔT, Δp_i and Δp_o. In Eq. (14.9) ΔL_{Bu} is ignored as no further buckling can occur below the cement top once the cement has solidified. The length change due to a shoulder below the cement top (for example, a cross-over) has no meaning, as, at least theoretically, one can come infinitesimally close to the crossover and not experience the effect of the concentrated force.

The calculations of axial force increment below the top of cement summarized in Table 14.4 and Fig. 14.6 were performed using Eq. (14.10).

The break in axial force distribution at the cement top for the post-initial condition load cases is real and due to the manner in which the load is calculated above and below the top of cement. Imagine a load case in which the only change from the initial condition is temperature and consider two points just above and just below the cement top. In the equation for ΔL_{Total}, the main driver for change in axial force, the only

contributor is ΔL_T. Just above the cement top the tubular is responding to $\overline{\Delta T}$, the average of all temperature changes above the top of cement. Just below the cement top the tubular is responding to the local temperature change ΔT. Since these two temperature changes are rarely identical, we can expect a different Δf_z corresponding to each and therefore a discontinuity in axial load above and below the cement top.

14.2.3.3 Excursion: buckling above the cement top

Returning to the design procedure, we now have pressures and temperatures (Table 14.1) and axial forces (Table 14.4) corresponding to each of the load cases. The axial forces in particular were generated with an assumption of no buckling. It is now time to determine if that assumption was valid.

From Tables 14.1 and 14.4 we compute the effective force at the cement top for each load case using Eq. (10.1) and the current, local values of f_z, p_i and p_o:

For "Frac" load case,

$$\begin{aligned} f_{eff} &= f_z - (p_i A_i - p_o A_o) \\ &= 98\,660\,\text{lb}_\text{f} - (13\,508\,\text{psi} \times 12.069\,\text{in}^2 - 4561.4\,\text{psi} \times 15.904\,\text{in}^2) \\ &= 8181\,\text{lb}_\text{f}. \end{aligned} \tag{14.11}$$

For "Evac" load case,

$$\begin{aligned} f_{eff} &= -32\,180\,\text{lb}_\text{f} - (0\,\text{psi} \times 12.069\,\text{in}^2 - 5569.2\,\text{psi} \times 15.904\,\text{in}^2) \\ &= 56\,394\,\text{lb}_\text{f}. \end{aligned} \tag{14.12}$$

For "Prod" load case,

$$\begin{aligned} f_{eff} &= -68\,785\,\text{lb}_\text{f} - (2000\,\text{psi} \times 12.069\,\text{in}^2 - 4561.4\,\text{psi} \times 15.904\,\text{in}^2) \\ &= -20\,376\,\text{lb}_\text{f}. \end{aligned} \tag{14.13}$$

In two of the load cases—"Frac" and "Evac"—the effective force at the cement top during the load case is positive.[10] The "Prod" load case, however, has $f_{eff} < 0$ at the cement top, where zero is the critical buckling force for a vertical wellbore.

[10] Even though p_i is large for the "Frac" load case, so also is the tension associated with the low wellbore temperature. The "Evac" load case has $f_z < 0$ at the cement top, but this is balanced by the restoring nature of p_o.

From[11] Eq. (11.20) we get

$$\Delta L_{Bu} = -\frac{r_c^2\left(f_{eff2}^2 - f_{eff1}^2\right)}{8EIw_{eff}\cos\theta}$$
$$= -\frac{(0.875\,\text{in.})^2\left[(-20\,376\,\text{lb}_\text{f})^2 - 0\right]}{8\times 30\times 10^6\,\text{psi}\times 8.538\,\text{in}^4\times 6.388\,\frac{\text{lb}_\text{f}}{\text{ft}}} = -0.024\,\text{ft}, \tag{14.14}$$

where w_{eff} is given by Eq. (10.2) as

$$w_{eff} = \frac{g}{g_c}\left[13.5\,\frac{\text{lb}_\text{m}}{\text{ft}} + 0.052\,\frac{\text{psi}}{\text{ft}\,\text{p}_\text{m}\text{pg}}\left(0 - 8.6\,\text{p}_\text{m}\text{pg}\times 15.904\,\text{in}^2\right)\right]$$
$$= 6.388\,\frac{\text{lb}_\text{f}}{\text{ft}}. \tag{14.15}$$

We are confronted with the dilemma mentioned in Section 14.2.2. The length change due to buckling changes the axial force, which changes the effective force, which changes the length change due to buckling. Usually behavior of this sort requires a trial-and-error solution. In this particular example, however, the tubular string is simple enough that the problem may be solved directly. From Eqs. (14.3) and (14.5) we obtain

$$\Delta f_z = -\frac{EA_s\Delta L_{Total}}{L} = -\frac{EA_s\left(\Delta L_T + \Delta L_B - \frac{r_c^2 f_{eff}^2}{8EIw_{eff}}\right)}{L}, \tag{14.16}$$

or, solving for the value of f_z during the load case with $f_z = f_i + \Delta f_z$,

$$f_z - f_i = -\frac{EA_s\left(\Delta L_T + \Delta L_B - \frac{r_c^2\left[f_z - (p_iA_i - p_oA_o)\right]^2}{8EIw_{eff}}\right)}{L}, \tag{14.17}$$

and

$$f_z = -\frac{b}{2} \pm \sqrt{\left(\frac{b}{2}\right)^2 - c}, \tag{14.18}$$

where

$$b = -\left[\frac{8Iw_{eff}L}{r_c^2A_s} + 2\left(p_iA_i - p_oA_o\right)\right], \tag{14.19}$$

[11] Eq. (14.14) uses the open hole diameter as the confining hole size. Actually, the upper 1600 ft of confining hole is 7.825 in. corresponding to the inside diameter of the 8.625 in. surface casing. As will be demonstrated below, the neutral point in this calculation is below the surface casing seat, so the calculation is correct; with more severe buckling, however, it might be necessary to consider a confining hole of variable diameter.

$$c = \frac{8Iw_{eff}}{r_c^2}\left[\frac{f_i L}{A_s} - E(\Delta L_T + \Delta L_B)\right] + (p_i A_i - p_o A_o)^2. \tag{14.20}$$

For this example, and using consistent force and length units of lb_f and in., respectively,

$$\begin{aligned} f_z &= -\frac{-1\,418\,630}{2} - \sqrt{\left(\frac{-1\,418\,630}{2}\right)^2 - (-1.018\,97 \times 10^{11})} \\ &= -68\,518\,\text{lb}_\text{f}, \end{aligned} \tag{14.21}$$

where

$$\begin{aligned} b &= -\left[\frac{8 \times 8.538 \times 0.532 \times 122\,400}{0.875^2 \times 3.836} + 2(2000 \times 12.069 - 4561.4 \times 15.904)\right] \\ &= -1\,418\,630\,\text{lb}_\text{f}, \end{aligned} \tag{14.22}$$

$$\begin{aligned} c &= \frac{8 \times 8.538 \times 0.532}{0.875^2}\left[\frac{-12\,017 \times 122\,400}{3.836} - 30 \times 10^6\,(59.5 + 0.93)\right] + \\ &\quad (2000 \times 12.069 - 4561.4 \times 15.904)^2 \\ &= -1.018\,97 \times 10^{11}\,\text{lb}_\text{f}^2. \end{aligned} \tag{14.23}$$

The corresponding length change due to buckling is

$$\begin{aligned} \Delta L_{Bu} &= -\frac{(0.875)^2\,[-68\,518 - (2000 \times 12.069 - 4561.4 \times 15.904)]^2}{8 \times 30 \times 10^6 \times 8.538 \times 6.388} \\ &= -0.0237\,\text{ft}, \end{aligned} \tag{14.24}$$

and from Eq. (10.13) the distance above the cement top to the neutral point is

$$\begin{aligned} s_n &= \frac{f_{eff}}{w_{eff}} \\ &= \frac{-68\,518\,\text{lb}_\text{f} - (2000\,\text{psi} \times 12.069\,\text{in}^2 - 4561.4\,\text{psi} \times 15.904\,\text{in}^2)}{6.388\,\frac{\text{lb}_\text{f}}{\text{ft}}} \\ &= -3148\,\text{ft}, \end{aligned} \tag{14.25}$$

that is, 3148 ft upward.

The following observations are in order with regard to Eq. (14.18):

- As we now have a potential (negative) length change due to buckling for the "Prod" load case, the tension in the string has increased slightly—compare the value[12] of f_z in Eq. (14.21) with the axial force at the cement top in Table 14.4.

[12] For final reporting the value of f_z in Eq. (14.21) should replace the previous value at the cement top in Table 14.4.

Table 14.5 Tubingless casing design—load case safety factors

Location	Frac			Evac		Prod	
	Axial[a]	Triaxial	Collapse	Axial[a]	Triaxial	Axial[a]	Triaxial
Top	1.79	1.40	∞	4.00	4.00	6.15	5.76
TOC+	4.28	1.51	1.92	−13.1	2.26	−5.45[b]	5.06
TOC-	2.93	1.50	1.92	−8.06	2.34	−10.66	5.20
Bottom	2.98	1.50	1.70	−5.88	2.11	−9.09	4.23

[a] Negative sign indicates string is in axial compression.
[b] Includes a bending stress of −2318 psi assumed to act over the entire cross section.

- In this problem buckling alters the value of f_z only slightly. This is typical of problems involving casing buckling. The length change associated with column buckling is typically larger in tubing problems, primarily due to the larger radial clearance for tubing, which results in a larger ΔL_{Bu} and correspondingly larger effect on axial load.
- The fact that the neutral point is in the open hole justifies our use of hole diameter for the radial clearance in the calculation of length change due to buckling.
- The solution embodied in Eq. (14.18) rapidly gains complexity with tapered tubular strings or more complicated temperature and/or pressure profiles and is usually solved by less direct means than that demonstrated here.
- The fact that the production casing/tubing buckles during production does not necessarily signify a failure. The severity of the buckling will be determined in Section 14.2.4.

14.2.4 Safety factors

Sufficient load and resistance information is now available to calculate the safety factors in the current problem for the three load cases in the problem statement. The calculations are summarized in Table 14.5. Individual entries in the table are discussed in the sections to follow.

14.2.4.1 Collapse

The conventional collapse safety factor compares the API TR 5C3 [51] minimum collapse resistance to the external pressure differential. Although we will, in this example, skip the involved calculation of the effect of axial load on collapse,[13] this calculation is

[13] In this example design, the substantial calculation of the API minimum collapse resistance is not necessary since, from Table 14.4, all landmark depths except the surface are in compression. As discussed in Section 8.2.4.1 of Chapter 8 the API calculation procedure does not address corrections to the yield stress (Eq. (8.10) for cases where $\Sigma_{zz} + p_i < 0$. This aligns with common design practice—one hesitates to take advantage of a compression that may, when the string is installed, be eliminated by an operational difficulty.)

performed in standard tubular design software. The collapse safety factor is calculated from

$$SF_{Collapse} = \frac{\text{API minimum collapse resistance}}{\text{External pressure differential}}. \tag{14.26}$$

As an example calculation, the collapse safety factor at the cement top for the "Evac" load case is

$$SF_{Collapse} = \frac{10\,680\,\text{psi}}{5569.2\,\text{psi} - 0\,\text{psi}} = 1.92. \tag{14.27}$$

In general there may be a discontinuity in the collapse safety factor at the cement top, since this calculation does depend on the local axial tension.

14.2.4.2 Axial

Normally, this safety factor would not be calculated as it is embedded in the triaxial safety factor. Since, however, we were not provided a manufacturer's evaluation envelope for any connection to be run on the production casing/tubing, we calculate the axial safety factor as a rough, one-dimensional substitute for the envelope.

The conventional axial safety factor compares the API minimum pipe body yield force to the axial force. The axial safety factor is calculated from

$$SF_{Axial} = \frac{\text{API minimum pipe body yield}}{\text{Axial load}}. \tag{14.28}$$

As an example calculation, the axial safety factor at the string top for the "Frac" load case is

$$SF_{Axial} = \frac{110\,000\,\text{psi} \times 3.836\,\text{in}^2}{236\,360\,\text{lb}_\text{f}} = 1.79. \tag{14.29}$$

There may be a discontinuity in the axial safety factor at the cement top, since this calculation does depend on the local axial tension.

14.2.4.3 Triaxial

The triaxial safety factor—either conventional or radial (see Section 12.9.2.1 of Chapter 12)—compares the API minimum yield stress to the von Mises equivalent stress. Whereas the burst and axial safety factors are remnants of the early days of tubular design when hand calculations were prevalent, the triaxial safety factor properly recognizes the relation between the radial, hoop and axial stresses and includes their combined effect on yield. This renders the triaxial safety factor calculation a more complicated exercise.

The triaxial safety factor is calculated from

$$SF_{Triaxial} = \frac{\text{API minimum yield stress}}{\text{von Mises equivalent stress}} = \frac{f_{ymn}}{\Sigma_e}. \tag{14.30}$$

As an example calculation we will determine the triaxial safety factor at the cement top[14] for the "Prod" load case. Recall that in this load case the production casing/tubing is helically buckled at the cement top. The curved trajectory of the helix induces a bending stress in the tube that is given by Eq. (10.85) as

$$\Sigma_b = \pm\frac{Dr_c f_{eff}}{4I} = \pm\frac{4.500\,\text{in.} \times 0.875\,\text{in.} \times (-20\,109\,\text{lb}_\text{f})}{4 \times 8.538\,\text{in}^4} = \pm 2318\,\text{psi}, \tag{14.31}$$

where $-20\,109\,\text{lb}_\text{f}$ corresponds to the new value of effective force given in Eq. (14.21) (see the numerator in Eq. (14.25))

$$\begin{aligned} f_{eff} &= -68\,518\,\text{lb}_\text{f} - \left(2000\,\text{psi} \times 12.069\,\text{in}^2 - 4561.4\,\text{psi} \times 15.904\,\text{in}^2\right) \\ &= -20\,109\,\text{lb}_\text{f}. \end{aligned} \tag{14.32}$$

Since bending is present, we must calculate Σ_e four times[15]:

- $r = d_{wall}/2,\ \Sigma_{zz} = \frac{f_z}{A_s} + \Sigma_b = \Sigma_a + \Sigma_b$;
- $r = d_{wall}/2,\ \Sigma_{zz} = \Sigma_a - \Sigma_b$;
- $r = D/2,\ \Sigma_{zz} = \Sigma_a + \Sigma_b$;
- $r = D/2,\ \Sigma_{zz} = \Sigma_a - \Sigma_b$,

where the von Mises equivalent stress is calculated using

$$\Sigma_e = \sqrt{\Sigma_{rr}^2 + \Sigma_{\theta\theta}^2 + (\Sigma_a \pm \Sigma_b)^2 - \Sigma_{rr}\Sigma_{\theta\theta} - \Sigma_{\theta\theta}(\Sigma_a \pm \Sigma_b) - (\Sigma_a \pm \Sigma_b)\Sigma_{rr}}, \tag{14.33}$$

where

$$\Sigma_{rr} = \frac{p_i d_{wall}^2 - p_o D^2}{D^2 - d_{wall}^2} - \frac{(p_i - p_o) D^2 d_{wall}^2}{4r^2 (D^2 - d_{wall}^2)}, \tag{14.34}$$

$$\Sigma_{\theta\theta} = \frac{p_i d_{wall}^2 - p_o D^2}{D^2 - d_{wall}^2} + \frac{(p_i - p_o) D^2 d_{wall}^2}{4r^2 (D^2 - d_{wall}^2)}. \tag{14.35}$$

[14] In addition to the axial force at the cement top, the axial force at the top of the string will also change from its value in Table 14.4 and by the same amount. The new value of axial force at the top of the string is $68\,910 + (-68\,790 + 68\,518) = 68\,638\,\text{lb}_\text{f}$.

[15] In the absence of bending, the largest value of Σ_e always occurs at the inner radius ($r = d/2$), so only one calculation of Eqs. (14.33)–(14.38) need be made—see Section 6.3.4 of Chapter 6.

As an example, at $r = \frac{d_{wall}}{2} = \frac{4.500\,\text{in.} - 2 \times 0.875 \times 0.290\,\text{in.}}{2} = 3.9925\,\text{in.}$ with positive bending stress

$$\begin{aligned}\Sigma_{rr} &= \frac{2000\,\text{psi} \times (3.9925\,\text{in.})^2 - 4561.4\,\text{psi} \times (4.500\,\text{in.})^2}{(4.500\,\text{in.})^2 - (3.9925\,\text{in.})^2} \\ &\quad - \frac{(2000\,\text{psi} - 4561.4\,\text{psi}) \times (4.500\,\text{in.})^2 \times (3.9925\,\text{in.})^2}{4\left(\frac{3.9925\,\text{in.}}{2}\right)^2 \left[(4.500\,\text{in.})^2 - (3.9925\,\text{in.})^2\right]} \\ &= -2000\,\text{psi},\end{aligned} \tag{14.36}$$

$$\begin{aligned}\Sigma_{\theta\theta} &= \frac{2000\,\text{psi} \times (3.9925\,\text{in.})^2 - 4561.4\,\text{psi} \times (4.500\,\text{in.})^2}{(4.500\,\text{in.})^2 - (3.9925\,\text{in.})^2} \\ &\quad + \frac{(2000\,\text{psi} - 4561.4\,\text{psi}) \times (4.500\,\text{in.})^2 \times (3.9925\,\text{in.})^2}{4\left(\frac{3.9925\,\text{in.}}{2}\right)^2 \left[(4.500\,\text{in.})^2 - (3.9925\,\text{in.})^2\right]} \\ &= -26\,070\,\text{psi},\end{aligned} \tag{14.37}$$

and

$$\begin{aligned}\Sigma_e = \Bigg[&(-2000)^2 + (-26\,070)^2 + \left(\frac{-68\,518}{3.836} + 2318\right)^2 - (-2000)(-26\,070) \\ &- (-26\,070)\left(\frac{-68\,518}{3.836} + 2318\right) - \left(\frac{-68\,518}{3.836} + 2318\right)(-2000)\Bigg]^{\frac{1}{2}} \\ &= 20\,899\,\text{psi}.\end{aligned} \tag{14.38}$$

The four candidate values of Σ_e are 20 899 psi ($r = \frac{d_{wall}}{2}$, $\Sigma_b > 0$), 21 732 psi ($r = \frac{d_{wall}}{2}$, $\Sigma_b < 0$), 16 478 psi ($r = \frac{D}{2}$, $\Sigma_b > 0$) and 17 522 psi ($r = \frac{D}{2}$, $\Sigma_b < 0$), of which the second is the largest. The triaxial safety factor is therefore

$$SF_{Triaxial} = \frac{110\,000}{21\,732} = 5.06. \tag{14.39}$$

There may be a discontinuity in the triaxial safety factor at the cement top, since this calculation does depend on the local axial tension.

14.2.5 Connection selection

We have postponed consideration of the threaded connection until the tube body has been designed. Calculations for the tube body expose the differential pressures and axial loads associated with various load cases—key information for properly selecting a threaded connection.

When selecting a threaded connection, we use the procedure outlined in Section 2.7 of Chapter 2. Of the concerns listed, the primary drivers for the connection selection

Table 14.6 Tubingless casing design—load case coordinates for plot of von Mises yield surface with connection performance envelope

Init		Frac		Evac		Prod	
x	y	x	y	x	y	x	y
32 767	0	70 623	73 241	27 511	0	19 895[a]	16 276
2435	0	39 231	72 810	−8390	−45 322	−18 182[a]	−20 845
2435	0	51 096	72 810	−13 646	−45 322	−8324	−20 845
−1430	−2806	50 977	72 775	−18 704	−51 098	−10 103	−25 576

[a] Table 14.4 value adjusted for effect of buckling.

will be (a) the hydraulic fracturing surface pressure, (b) the necessity to seal gas and (c) cost. Regarding the last, wells of the type designed here are intended to be inexpensive, but because of the low permeability associated with the gas reservoir should be capable of performing for scores of years.

We were not provided with a manufacturer's performance envelope for any candidates so we shall build our own. Our simple envelope will consist of four ratings:

- The tube body yield stress in tension, decremented by a 1.3 design factor;
- The tube body yield stress in compression, decremented by a 1.0 design factor;
- The tube body triaxial internal yield pressure, decremented by a 1.25 design factor;
- The tube body triaxial external yield pressure, decremented by a 1.25 design factor.

Of the three expressions of yield presented in Sections 6.3.4.1, 6.3.4.2 and 6.3.4.3 in Chapter 6, we will use the presentation of Section 6.3.4.2. The abscissa for this plot is $\Sigma_{zz} + p_i$ and the ordinate is $\left(\frac{\left(\frac{D}{t}\right)^2}{2\left(\frac{D}{t}-1\right)} \left(p_i - p_o\right) \right)$. For our tube geometry, and replacing t with $k_{wall}t$ to align with the design limit state

$$\frac{\left(\frac{D}{k_{wall}t}\right)^2}{2\left(\frac{D}{k_{wall}t}-1\right)} = \frac{\left(\frac{4.500}{0.875\times 0.29}\right)^2}{2\left(\frac{4.500}{0.875\times 0.29}-1\right)} = 8.138. \tag{14.40}$$

Table 14.6, taken from data in Tables 14.1 and 14.4 (with updated values above the cement top for the "Prod" load case in the latter—see Section 14.2.4.3), provides the pertinent coordinates of the load cases.

Fig. 14.7 presents the results in graphical form. The load case coordinates[16] from Table 14.6 illustrate the state of the production casing/tubing for each case, with the

[16] Our work is eased by the fact that in this problem we are ignoring the effect of temperature on yield stress. Otherwise, we would have to plot a separate ellipse for each landmark depth and load case. One way of avoiding this problem is to move the effect of temperature on yield stress to the load side of the design equation (i.e., incorporate temperature effects in the load case coordinates) rather than to the resistance side of the design equation as represented by the ellipse.

point farthest to the right (highest tension) in each instance denoting the top of the string:

- Most of the "Init" curve lies along the abscissa as the initial condition has drilling fluid inside and out (i.e., no differential pressure), except near the bottom where the external fluid is cement.
- The "Frac" load case is distinguished by its high internal pressure differential. The high internal pressure and low (relative to the initial condition) temperature both induce incremental tension in the tubular.
- In contrast to "Frac", the "Evac" load case is characterized by a high external pressure differential. The incremental compression experienced in this load case is due to (negative) ballooning.
- The "Prod" curve illustrates the effect of its relatively high temperature by the higher compression increment from the initial condition, particularly at the top of the string.

Superimposed on the same graph are also four envelopes:

- The outermost dashed, closed ellipse is the unfactored von Mises yield criterion, identical to Fig. 6.13 with the exception that this is a design yield surface that uses f_{ymn} instead of f_y on the abscissa and, on the ordinate, $k_{wall}t$ instead of t.
- Overlaying most of the tube body yield ellipse is the connection design envelope based on our bullet-listed criteria at the beginning of this section.
- Companions to the two unfactored envelopes are also shown on the graph:
  - The dashed inner ellipse is the outer ellipse diminished by a design factor of 1.25.
  - The solid inner connection envelope is the design envelope diminished by the factors presented at the beginning of this section.

The conclusion we reach is that (a) the tube body is adequate for all load cases according to a factored von Mises triaxial design limit state, and (b) the connection is also adequate.

14.2.6 Comments on the example design

A number of simplifications were made to this example in order to focus on the fundamentals of the design procedure:

- Simple profiles for pressures and temperature. More complicated environmental distributions will add complexity to the calculation, primarily by increasing the number of landmark depths and requiring that some calculations, such as length change, be done on a per-segment basis, where a segment is the section of tubular between two landmarks.
- Vertical wellbore. Equating the measured and vertical depth affects the following:
  - A deviated wellbore introduces bending stress into the calculation of all safety factors. For the triaxial safety factor bending is handled through Σ_b as was demonstrated in Section 14.2.4.3 for the case of bending due to buckling. If both wellbore curvature and buckling are present, the effects must be added.

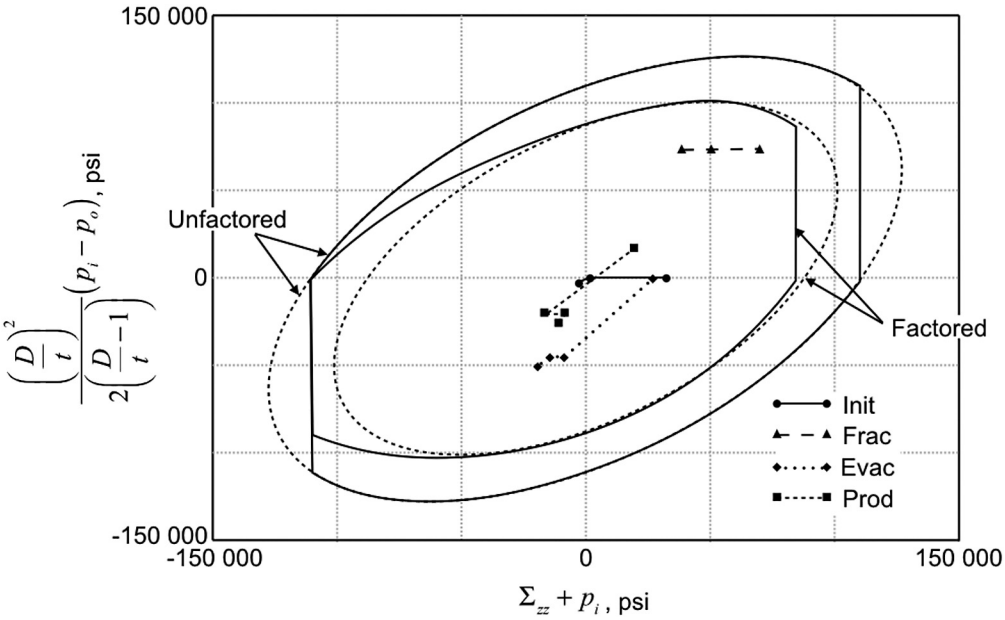

Figure 14.7 ***Load cases as compared to tube body (yield) and connection design envelopes.*** Both factored and unfactored envelopes are displayed.

- For collapse and axial yield (if needed), the following procedure is recommended:
  - Compute the maximum value of Σ_b in the cross-section, including contributions from both well trajectory and buckling.
  - Set the sign of the bending stress equal to the current sign of the axial force.
  - Presume the bending stress is actually acting across the entire cross-section; multiply Σ_b times A_s to arrive at an equivalent axial force for bending that is added to the axial force contributions from other sources.
  - Use the new axial force (all other sources + bending) in determining the collapse resistance adjusted for Σ_{zz} when computing the collapse safety factor and in determining the total axial force when computing the axial safety factor.

  The above procedure can cause anomalies—usually evidenced as a discontinuity—in the safety factor calculation at the depth in the string where f_z changes sign. We accept this small inconvenience, which is actually offering the correct answer under the stated assumptions, *in lieu* of having to resort to a three-dimensional approach to handling bending. This simplification is particularly inviting when considering the alternatives for analyzing the string's threaded connections.

CHAPTER 15

Special Topics

15.1. INTRODUCTION

The topics to follow often exist outside the bounds of conventional tubular design but nevertheless constitute key issues in a sizable number of wells. Further, a lack of appreciation of the physics associated with these topics can lead to unanticipated issues in wells with which they are anticipated:

- Annular pressure build-up (APB, see Section 15.2) is a failure mechanism possible in any well but primarily pertinent to deepwater completions where one or more annuli are inaccessible. The primary APB mitigator in onshore and shallow water platform wells is annulus venting via a surface wellhead valve, with rare APB incidents traced to lapses in operational procedure. In deepwater, an APB failure of a single string will usually lead to loss of the entire well.
- Casing wear (see Section 15.3) is typically associated with long drilling exposure, for example, in hard-rock locations, and with tortuous well paths. Ignoring wear instigators, however, can result in unanticipated wall loss in practically any drill through operation.

15.2. ANNULAR PRESSURE BUILD-UP

Annular pressure build-up[1] (APB) is an example of a low-probability, high-consequence event. As discussed below, even a well containing no APB mitigation can survive the production environment that might cause a failure. If, however, one or more APB-favorable events occur, the consequence is usually abandonment of the victim wellbore.

Annular pressure build-up occurs when a fluid-filled compartment in a well becomes closed and is subsequently heated. The increase in temperature acts on the contained fluid to cause a volume change greater than that which can be accommodated by the boundaries of the compartment (usually a tubular-by-tubular annulus). As the compartment's boundaries resist expansion, compressibility of the fluid results in an increase in fluid pressure. Should the induced pressure become large enough, failure of a component of the boundary envelope—usually a casing string—can occur.

[1] In the industry and literature the event described here assumes a number of names—annular pressure build-up (APB) [68,187,184,69,188,93,189,190], trapped annulus pressure (TAP) [191–193], annular fluid expansion (AFE) and annulus fluid heat-up [194,195], with the first two being the most common—all of which refer to the same well failure mechanism.

Elements of Oil and Gas Well Tubular Design
DOI: 10.1016/B978-0-12-811769-9.00015-3

Annular pressure build-up is usually associated with high rate production wells, that is, wells that approximately convey bottomhole reservoir temperature to the mudline/surface inside the tubing. The phenomenon can occur, however, in any trapped annulus, a documented example being an APB failure associated with circulating temperatures when drilling ahead from an intermediate casing string [69].

Annular pressure build-up depends on three source categories:

- the thermal and mechanical properties of the annulus fluid;
- the flexibility of the annulus boundary;
- the driving force—temperature change.

Mathematically, the interrelation of the three sources can be seen from the equation governing the annulus fluid[2]

$$\Delta V_f = \underbrace{V_f \left(3\alpha_{Tf} \underbrace{\Delta T}_{\text{Driving force}} - \underbrace{C_f \Delta p}_{\text{Stiffness of boundary}} \right)}_{\text{Unrestrained fluid volume change}}. \tag{15.1}$$

A change in temperature ΔT acts through the (volumetric) coefficient of thermal expansion of the fluid $3\alpha_{Tf}$ to produce a volume change ΔV_f. This volume change is resisted by the stiffness of the annulus boundary that, acting on the compressibility of the fluid C_f, produces a change in pressure Δp. Either a positive or negative pressure change is possible, depending on the sign of the temperature change.

Almost all APB failures studied by this author[3] have been collapse failures [68,187, 184,69,93], all of which appeared or have been proven to involve more than one tubular string. That is, an APB failure on an outer string sequentially point loads inner casings, creating a cascade that stops with the deformation of the production tubing. Particularly for subsea wells, the problem is complicated by the fact that the collapsing pressure initiates in an outer annulus which cannot be readily monitored. Regarding APB one should, at least initially, think "out and shallow." That is, the (outer) large

[2] Although Eq. (15.1) is convenient for discerning the individual contributors to APB, an alternate expression by Halal and Mitchell [191] is useful when modeling APB numerically. From the conservation of mass we can write

$$\int_{V_f} \left[\rho_f A_{oa} \right] ds = \int_{V_f} \left[\left(\rho_f + \Delta\rho_f \right) \left(A_{oa} + \Delta A_{oa} \right) \right] ds \quad \Rightarrow \quad \left(\rho_f + \Delta\rho_f \right) \Delta A_{oa} + \Delta\rho_f A_{oa} = 0.$$

Using the above relation, the net change of the fluid volume is

$$\Delta V_f = \int_{V_f} \Delta A_{oa} ds = \int_{V_f} \left[-\frac{\Delta\rho_f A_{oa}}{\rho_f + \Delta\rho_f} \right] ds,$$

which allows one to implicitly account for fluid thermal expansion and compressibility by tracking only the fluid density.

[3] A notable exception is [196].

diameter strings undergoing large temperature changes from their initial states (shallow) are particularly vulnerable to APB.

In well design, determination of APB in an annulus is complicated by the fact that the same phenomenon can also be occurring in adjacent annuli, the latter serving to change the effective stiffness of the target annulus' boundary. Such calculations involve a global numerical analysis of the well, allowing the various fluids, boundaries and temperatures to interact. The analysis is further complicated by nonlinear dependence of the annulus fluid thermal and mechanical properties on temperature and pressure. Numerical calculations are strongly recommended over a simple model.

15.2.1 Nonlinear fluid behavior

As mentioned above, one complicating factor in APB calculations is the nonlinear character of the fluids residing in a typical well annulus. Even fresh water possesses sufficient nonlinearity to render it beyond the bounds of a hand calculation.

To illustrate the nature of potential annulus fluids, consider the following simple example chosen to isolate fluid behavior. A small bench top experiment is supposed, consisting of a container that is rigid and capable of producing a constant, uniform pressure and temperature environment for a fluid sample. If the container is rigid, there is no change in volume; if the container maintains its seal there is no change in mass. Any change in the pressure and temperature environment of the sample will therefore occur along a path of constant density.

Fig. 15.1 presents the results of such an experiment on a fresh water sample. The behavior of the sample is modeled using the steam tables [197]. We consider the initial state of the fluid in our container (Point A) to be $p = 2000\,\text{psi}$, $T = 40\,°\text{F}$. For this condition, the initial density of the water is $8.40\,\frac{\text{lb}_\text{m}}{\text{gal}}$.

Now let the container be heated 50 °F to an intermediate temperature of 90 °F. Following a line of constant density, the pressure in the container increases by 1900 psi to a value of 3900 psi (Point B). As a second and final step, let the temperature of the container be increased another 50 °F to a final temperature of 140 °F. The pressure now increases by 4300 psi to a value of 8200 psi (Point C). Although the temperature change in the two load increments is identical, the pressure changes are dramatically different, illustrating the danger of attempting to perform an APB calculation by hand or with a simple spreadsheet that uses a constant value to characterize fluid behavior.

15.2.2 Low-probability, high-consequence

Fig. 15.2 illustrates a common challenge to annular pressure build-up design. The wellbore sketch in the left-hand diagram shows the near-mudline portion of a well whose A annulus is vented, but whose B and C annuli are closed. The design concern is possible collapse of the intermediate casing between the B and C annuli, the string marked with

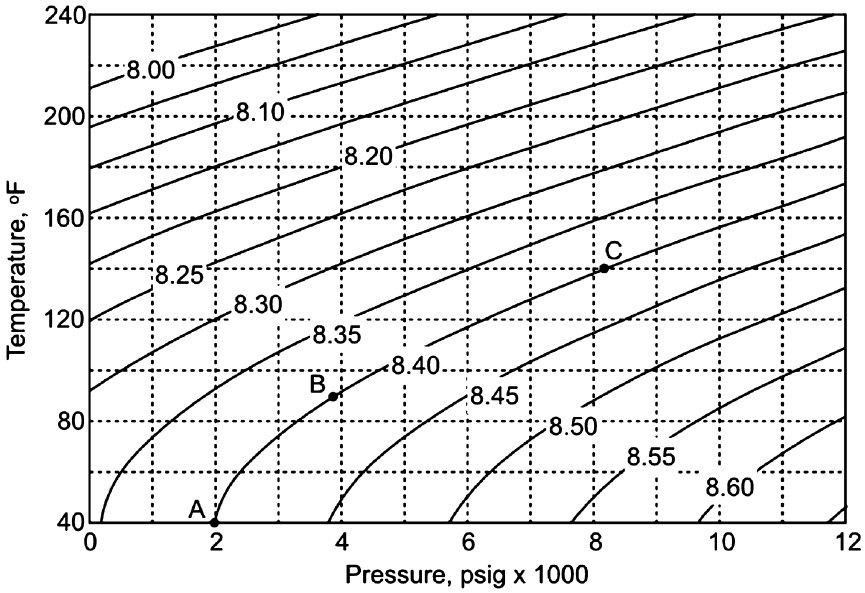

Figure 15.1 ***The consequences of nonlinear fluid behavior [187].*** Locations A, B and C are, respectively, the initial, interim and final states of an annulus being heated by fluid production through the tubing. Contours are in $\frac{\text{lb}_\text{m}}{\text{gal}}$. Copyright 2004, Society of Petroleum Engineers Inc. Reproduced with permission of SPE. Further reproduction prohibited without permission.

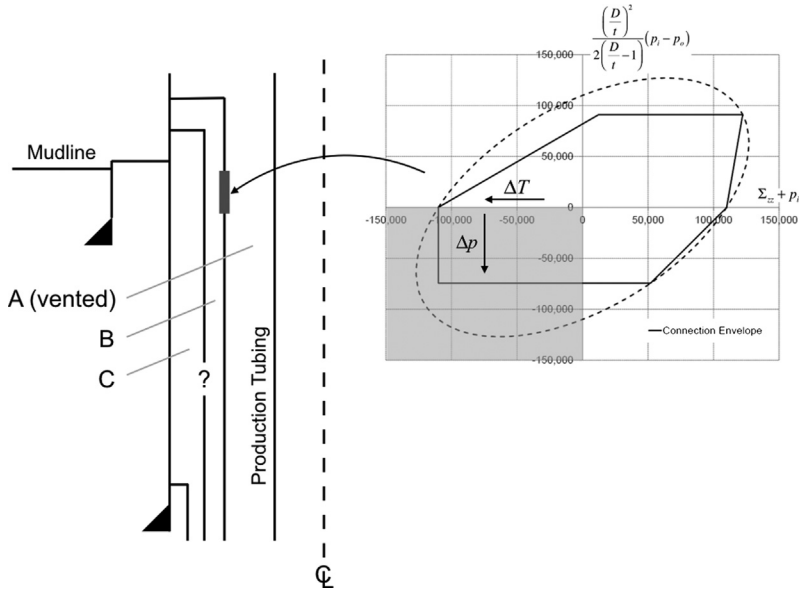

Figure 15.2 ***APB as a low-probability, high-consequence event.*** In the scenario depicted, both a closed annulus and a leak of the production casing connection are required for a failure.

a question. Production is expected to increase the temperature of the C annulus with corresponding increase in pressure, thus creating a collapse load on this casing.

The objection may be raised that the casing in question is in no danger. Accompanying the temperature and pressure increases in the C annulus will be similar increases in the B annulus, thus providing an internal pressure on this casing that will resist any collapse load from the C annulus. This objection is well-founded, were it not for the following conditions related to the A annulus:

- The A annulus is vented so it will not experience a pressure increase during production. There will be no additional backup for the tube or connection of the production casing.
- The connection (one such connection is shown) on the production casing is in jeopardy due to the additional loading accompanying APB:
  - Increasing pressure in the B annulus places an incremental external pressure on the connection;
  - Increasing temperature of the production casing places an incremental compression on the casing and its connection.

  Both of the above responses to APB serve to push the production casing connection into the third quadrant of its performance envelope, a quadrant in which it is difficult for some connections to maintain leak integrity.

We are still left with the fact that an APB failure in this scenario requires (a) that both the B and C annuli be closed and (b) the production casing connection leaks. The consequence of such a low-probability event occurring, however, is loss of what is probably a high-productivity well. At a minimum, design activities such as qualifying the production casing connection (particularly with load cycling between quadrants 1 (shut-in) and 3 (production)) and APB mitigation (see Section 15.2.4) are in order.

15.2.3 APB design principles

Analysis of failures has led to several design principles useful in designing a well for APB. All of the suggestions below will tilt the design analysis in favor of an APB failure and do therefore generate design controversy when they indicate a well needs mitigation. The decision to move forward with mitigation is risk-based, weighing the expense and collateral effects of mitigators on the completion versus the consequences of losing a well due to failure.

15.2.3.1 All shoes are closed

This principle states that, regardless of the location of the top of cement on the casing that serves as the inner boundary for a particular annulus, that annulus is assumed closed at the previous casing string. If the cement top has been deliberately planned to lie above the previous casing shoe (perhaps cementing a tieback or ensuring isolation of a hydrocarbon-bearing zone), then closure of the annulus is obvious. If, however, the

cement top has been targeted below the previous shoe, the principle assumes that mud settling or instability of the wellbore in the vicinity of the previous shoe will render the annulus "closed." Repeated informal surveys indicate that the incident rate of being unable to pump into an annulus that was supposedly open approaches 50%.

One exception to this rule is liners having short laps with the previous string. If the top of a liner is within 300 ft (100 m) of the previous casing shoe, this principle may be neglected, with the following caution. The impetus for this exception is that the author knows of no APB failure to have occurred with such short liner laps, a situation that may be attributed to the small fluid volume in such an annulus.

In a similar vein, cementing a tieback into a polished bore receptacle is often performed in such a manner that a trapped pocket of fluid could be left outside the PBR. Again, although a small number of collapsed PBRs have been reported, the number of incidents appears to be small and may not be directly attributable to APB.

15.2.3.2 Every annulus must stand alone

This design principle relates to the example discussed in Section 15.2.2. Consider a tubular string that serves as the outer boundary of one annulus and the inner boundary of another, with both annuli closed. As the well temperature increases due to production, the annulus outside this tubular will experience an increase in pressure, thereby exposing the tubular to a potential collapse failure. On the other hand, simultaneously the fluid inside the tubular will experience a pressure increase which counters the pressure building external to the tubular. The differential collapse pressure to which the tubular is exposed should be small. This optimistic picture assumes that both annuli boundaries are sufficiently robust that a leak—at a threaded connection or other seal, or perhaps by formation fracture or the failure of a rupture disk (see subsection 'Rupture disks' in Section 15.2.4.2 of this chapter)—will not occur.

The possibility of a scenario such as that described above leads a second design principle, namely, APB from an adjacent annulus is not allowed to provide such benefit as to reduce the differential load on a given tubular string.[4] In design practice, this principle means that when calculating the APB in one annulus the fluid column in the adjacent inside (for collapse calculations) or outside (for MIYP/triaxial calculations) annulus will be assumed vented so that no APB increase occurs in that annulus.

15.2.3.3 Use the hottest temperature

It is natural to assume that the hottest time in the life of the well is the first day of full production. It may be, however, that the hottest time in the life of the well is the first day of water production. Water has a high heat capacity and can carry significant temperature to the shallower portions of the tubing string and, coincidentally, adjacent

[4] This beneficial APB in the adjacent annulus is sometimes termed "sympathetic APB."

casings. When conducting an APB design, a conversation with the reservoir engineer, asking for flow rates corresponding to landmark events in the life of the well is in order. Each of these events should be tested in the APB simulator to ensure the most onerous conditions are applied to the well tubulars.

15.2.3.4 Use the proper initial conditions

Section 12.6 of Chapter 12 discusses this issue in some detail. The initial state for a conventional design calculation is usually the pressure and temperature state when the tubular being designed has its end conditions activated, be they wellhead and cement (casing) or wellhead and packer (tubing). By contrast, the initial state for a trapped annulus calculation is the pressure and temperature state when the annulus to be analyzed is closed. Any subsequent annulus venting or top-off of fluids that occurs necessitates a redefinition of the initial state for future APB calculations on the subject annulus.

Further, setting some (particularly secondary) seal assemblies in a subsurface wellhead open the possibility of a leak past the seal assembly during pressure energization and lock-down. Should a leak past the seal assembly occur, pressure above the normally trapped hydrostatic pressure can be imparted to the associated annulus. This pressure becomes part of the initial condition for that annulus [68].

15.2.3.5 Use a safety factor multiplier

As discussed in previous sections, APB prediction is a complex calculation that involves a wide variety of input:

- annular fluid properties as a function of pressure and temperature;
- tops of cement and other contributors to the stiffness of the annulus boundary;
- initial temperatures and temperature changes.

Some of the above inputs contain experimental error; other inputs rely on the accuracy of numerical simulation.

Once more appealing to these uncertainties in the context of a low-probability, high-consequence event, a prudent design practice is to increase all design factors using a 1.05–1.15 multiplier to anticipate such unknowns, with the exact multiplier value depending on one's confidence in the data to be submitted to the APB calculation software.

15.2.4 Mitigation

With the application of the APB design principles discussed in Section 15.2.3, at least one annulus in a high production rate wellbore will probably be at risk of a boundary failure—either collapse of the inner tubular boundary or triaxial yield to excess internal pressure on the outer tubular boundary. The design response is to in some way mitigate either the source or the effects of the pressure increment.

Recalling the list of APB sources in Section 15.2, we may categorize popular mitigation techniques into the same three categories—the thermal and mechanical properties of the annulus fluid, the flexibility of the boundary and the driving force, temperature change. Each of these categories will be considered in turn below. Before considering these alternatives, however, one other solution should be considered. In almost all instances, it is possible to conceive of a tubular wall thickness sufficient to resist the APB internal or external load. Unfortunately, at least in the case of deepwater completions most at risk to APB consequences, there usually is not enough space to implement this solution to more that one tubular string. The pore and fracture pressure gradients in deepwater are sufficiently narrow that a larger number of casing strings are in order. Further, one is limited on the innermost diameter by the size of the subsurface safety value—usually on the order of 9 in to 9.25 in. (228.6 mm to 234.95 mm)—and on the outermost diameter by the 18.750 in. (476.25 mm) diameter bore on the high pressure wellhead. Countering APB with wall thickness is a useful alternative, but one or more of the options below may also be necessary.

15.2.4.1 Altering annulus fluid properties

One's first thought with regard to countering APB via annulus fluid properties is to eliminate the problem by removing the fluid; that is, by cementing the annulus throughout and eliminating the possibility of fluid expansion. The notion is valid but carries the risk of creating the most vulnerable of annuli should the attempt to reach the surface not succeed. Consider Fig. 15.3 which depicts an endangered annulus (left-hand diagram) which we wish to totally cement. Also shown in the figure (right-hand diagram) are two temperature profiles—the undisturbed temperature profile which defines the initial state of the annulus and a later temperature profile corresponding to production. If the annulus is not cemented to surface (TOC_1), the average temperature change in the annulus driving APB is given by $\Delta\overline{T}_1$. If an attempt is made to cement the annulus back to the wellhead, but that attempt fails or there is cement settling in the early stages of thickening (TOC_2), then the shallowest portion of the annulus is left uncemented. This annulus will experience an average temperature change of $\Delta\overline{T}_2$ during production, resulting in a higher APB than shown previously. Depending on the properties of the fluid in the annulus and the actual values defining the initial and producing temperature distributions, the latter state of the annulus could be undesirably worse than the former.

Designer fluids

With the realization of the importance of fluid response to temperature increase some drilling fluid suppliers have formulated fluids specifically intended to possess a lower $\frac{dp}{dT}$ behavior. At an extreme end of such behavior has been the development of a fluid which, at a designed temperature, undergoes polymerization, shrinking on the order of 20% [198,193].

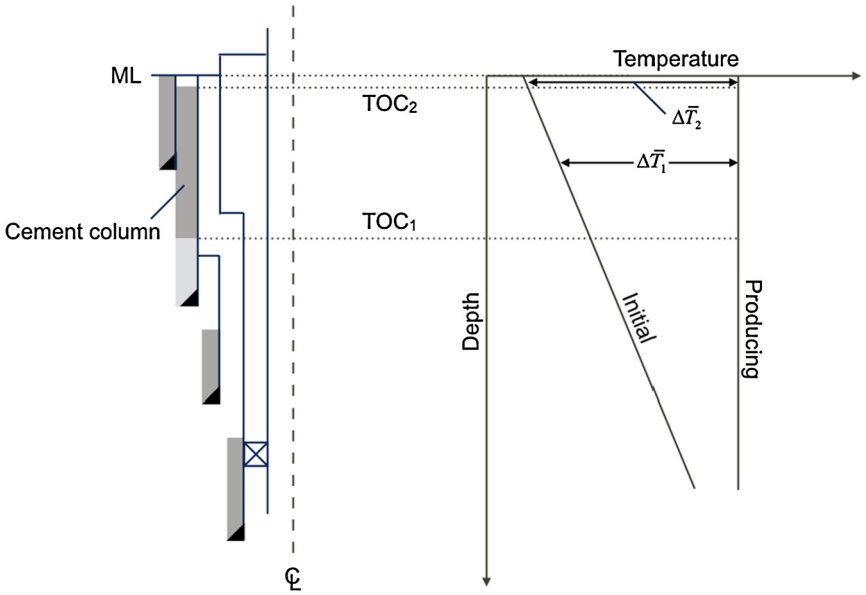

Figure 15.3 ***Cementing to surface.*** If an attempt to cement to surface (TOC_2) fails, the remaining portion of the annulus experiences an increased APB driving force due to the higher average temperature.

Foam spacer

This mitigation technique involves placing a nitrified foam spacer in the cement column ahead of the cement and pumping the spacer in place as part of the primary cementing operation. Once in place, the more compressible foam spacer serves as an accumulator allowing any heated fluid in the annulus to expand without creating a significant pressure increase. With time the foam destabilizes and the nitrogen can be expected to migrate up the annulus [199]. Except as noted below, however, the nitrogen should still be expected to compress accommodating fluid expansion.

Nitrified foam spacers have been successfully applied on a number of deepwater wells. Cautions on the use of this mitigation technique include the following:

- Placement of the nitrogen spacer carries with it the same risk that is always present in cementing. An ill conceived design, lost circulation or other issues may prevent the cement column from being situated as intended.
- A nitrified foam spacer that is initially placed deep in an annulus, may, under destabilization and subsequent migration, convey the higher pressure of the deep location up the annulus, thus placing a high pressure, less compressible gas bubble where it may be least desired.
- Shallow placement of a nitrified foam spacer may raise operational issues such as introducing gas into the riser past the BOP [200].

15.2.4.2 Altering annulus boundary flexibility

The most obvious means of altering the flexibility of the annulus boundary is to render the annulus infinitely flexible by venting. This is usually the solution for onshore and offshore shelf or shallow water platform wells where all annuli can be accessed from the surface wellhead. That is not to say, however, that the possibility of an APB failure can be eliminated [196,69]. Aside from wellhead venting, and particularly when the annulus is not accessible, the following alternatives have been used by the industry.

Formation fracture

An obvious candidate for APB mitigation is the formation below the shoe of the casing forming the outer boundary of the annulus of focus. Assuming this casing shoe to be open, and planning for such a state by adequate deep placement of the cement top for the next casing string, means that the casings forming the boundaries of the focus annulus need only be as strong as the formation. Otherwise, sufficient pressure will cause the formation to fracture at some point above the cement top, relieving the pressure due to temperature increase.

The primary disadvantage of this mitigation method is that it is in direct conflict with the design principle that "all shoes are closed" presented in Section 15.2.3.1. Nevertheless, relying on formation fracture to alleviate APB remains a popular means of dispensing with APB in design in some geographic locations.

Rupture disks

Rupture disks have served various parts of manufacturing for some time. Their application to APB mitigation takes the form of a small circular frame installed in the tube wall, and at the center of which is a machined, shallow dome-like disk intended to rupture within a suitably narrow pressure range. The disk may be oriented with its convex side outward (intended to rupture due to internal pressure) or inward (intended to rupture with external pressure).

The reasoning underlying rupture disk implementation is detailed in Fig. 15.4. Suppose that the well in the figure has been analyzed for the potential of an APB failure, and the analysis indicates the 16 in. annulus to be at risk. If the possibility of an APB failure cannot be eliminated, is it better to have the 20 in. casing rupture or the 16 in. casing collapse? Usually, the former is preferred. If the 16 in. casing collapses, it is likely that the collapse will cascade, successively loading interior strings and not stopping until the production tubing is damaged. On the other hand, if the 20 in. casing ruptures, a small amount of drilling fluid from the annulus will enter the adjacent formation, and the annulus pressure will be relieved.

With the above comments in mind, Fig. 15.4 illustrates a typical design. The wall thickness and grade of the 20 in. casing are chosen such that its minimum internal yield

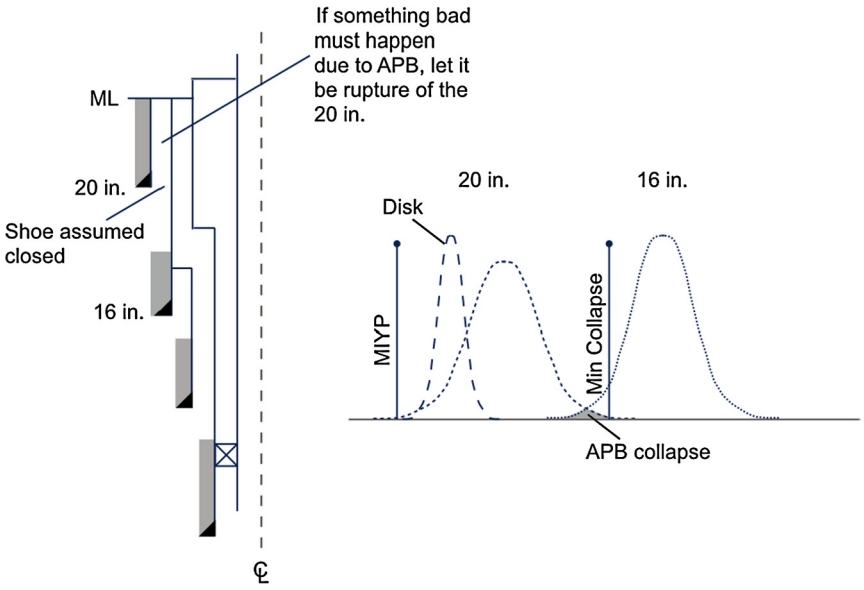

Figure 15.4 ***The strategy of a rupture disk.*** The disk serves to narrow the statistical distribution of the casing to which it is attached, thereby ensuring a controlled pressure and location of failure.

pressure[5] (MIYP) is less than the API minimum collapse resistance of the 16 in. casing. These two deterministic values are indicated by the ball-topped vertical lines in the figure.

Unfortunately, the statistics of manufacturing suggest that the actual MIYP and collapse resistance of the 20 in. and 16 in. casings, respectively, will more closely resemble the short dashed and dotted lines in Fig. 15.4. This leaves open the possibility—a small probability with large consequences—that, as indicated by the shaded region, the collapse resistance of the 16 in. casing could be less than the internal pressure resistance[6] of the 20 in., the result being an APB collapse failure.

Now consider the possibility of installing an outward-acting rupture disk in the 20 in. casing. The disk, which has a significantly smaller variation in rupture pressure than the internal pressure rating of the 20 in. tube, can be chosen with a rating higher than the MIYP of the 20 in. casing, thus not affecting the internal pressure design of the tube, but a more assured rating less than the collapse resistance of the 16 in. casing. The 16 in. casing is protected from collapse without altering the internal pressure safety

[5] We assume here that internal pressure design of the 20 in. casing is based on yield and not rupture.

[6] This possibility is compounded by the fact that actual rupture of the 20 in. casing can occur at a pressure significantly higher than MIYP. The 20 in. casing could yield, resulting in partial damage, but not rupture before collapse of the 16 in. casing.

factors of the 20 in. casing design. This feature of the rupture disk—a highly accurate rupture pressure—is its primary attribute applicable to APB mitigation.

Syntactic foam

Syntactic foam consists of hollow glass spheres encased in a polymer that fills the interstitial space. The resulting product is a solid, fairly hard structure capable of reasonable rigors of on site handling and transport downhole. For a specific application, the spheres are sized such that they will withstand the fluid pressure environment in which they are placed but will collapse at a specified increment in pressure above that corresponding to their installation state. The presence of the polymer carrier renders the foam composite a function of temperature.[7]

The syntactic foam is manufactured in curved panels that may be strapped or glued (or both) to the exterior of a casing joint, thus occupying that casing's annulus upon installation of the string. Usually a circumferential space is left vacant to provide an axial flow path past the foam modules. Further, the vicinity of the connection is left vacant to provide room for normal assembly tools.

The foam is intended to crush upon the application of sufficient external pressure, thus, in a manner similar to the nitrified foam spacer (see subsection 'Foam spacer' in Section 15.2.4.1 of this chapter), syntactic foam serves as an accumulator, allowing the less compressible annulus fluid to expand into the crushed volume with reduced impact on annular pressure build-up. Unlike the nitrified foam spacer, the placement of syntactic foam is more assured as it is conveyed to its target by the casing to which it is attached. There has been some evidence of foam chunks being detached from their panels during installation, an event that does not severely affect the performance of the foam but has caused concern with completion engineers with respect to plugging or interfering with downhole accessories.

Syntactic foam's disadvantage vis-à-vis a nitrified foam spacer is that its volume loss is irrecoverable. Imagine an instance of syntactic foam installed on intermediate casing above that casing's cement top, with the cement top located above the shoe of the previous casing string. As the well is placed on production, the annulus fluid pressure rises to the point that the foam crush pressure is reached. The foam crushes, maintaining the annulus pressure at a reduced level. Now, however, imagine that the casing's cement sheath has a small leak that, during a long period of shut-in, allows local pore fluid to slowly enter the cooled annulus, recharging it with fluid. If the well is now placed on production again, the crushed foam cannot respond to this second incident of pressure increase. Such a scenario as this suggests syntactic foam is used to best advantage when it

[7] Imagine a syntactic foam panel at room temperature. The solid polymeric structure will impede the transmission of applied pressure to the glass spheres. With increasing temperature, softening of the polymer at increased temperature facilitates the transmission of the pressure to the individual spheres.

is placed in an annulus for which there is near certainty of sealed annulus containment of fluids. A typical annulus of this nature would be that outside a production tieback. In this case, the leak described earlier in this paragraph is less likely due to (a) casing-in-casing cement placement behind the tieback and (b) the presence of a liner top packer. The use of syntactic foam for production casing also fortunately counters the fact that, as the production tieback may be part of the well's secondary barrier envelope, some alternatives such as rupture disks may be unacceptable.

15.2.4.3 Lowering annulus temperature change

In some instances[8] APB mitigation using the tools of the previous sections may not be possible or practical. There remains, nevertheless, one additional mitigation option—controlling the temperature (change) at its source (the production tubing) such that APB loads do not occur in outer annuli. The dominant alternative in this solution category is vacuum-insulated tubing.

Vacuum-insulated tubing

Vacuum-insulated tubing (VIT) consists of two standard tubular bodies welded together at either end, with a vacuum drawn on the annulus between the two tubes (see Fig. 15.5). The annulus may also contain foil to aid in minimizing radiant heat transfer and getter, a material to adsorb molecular hydrogen and maintain the vacuum. The tubes may also be separated by a centralizing mechanism, that mechanism being designed to work with low tube-to-tube contact so as to minimize conductive heat transfer.

One of the tubes will, at both ends, be longer than its counterpart to accommodate a standard threaded connection. VIT has been manufactured with both the internal tube and the external tube hosting the connection. The principal advantages of placing the connection on the inner tube are ease in obtaining a smooth-bored flow path for produced fluids and ease-of-access to the critical weld between the tubular bodies. The principal advantages of placing the connection on the outer tube are greater tensile capacity and the ease of connection assembly with standard tongs [201].

VIT mechanical design

The joining of two tubes that are separated by a vacuum presents a unique mechanical design situation wherein all of the following apply:

- The tubes are constrained to have the same displacement at the points of mutual attachment (i.e., the welds);
- The inner tube is thermally loaded by a temperature change that is normally much higher than the temperature change to which the outer tube is exposed;

[8] An example is the retrofitting of wells in the Marlin field following an APB failure in the first completed producer [184].

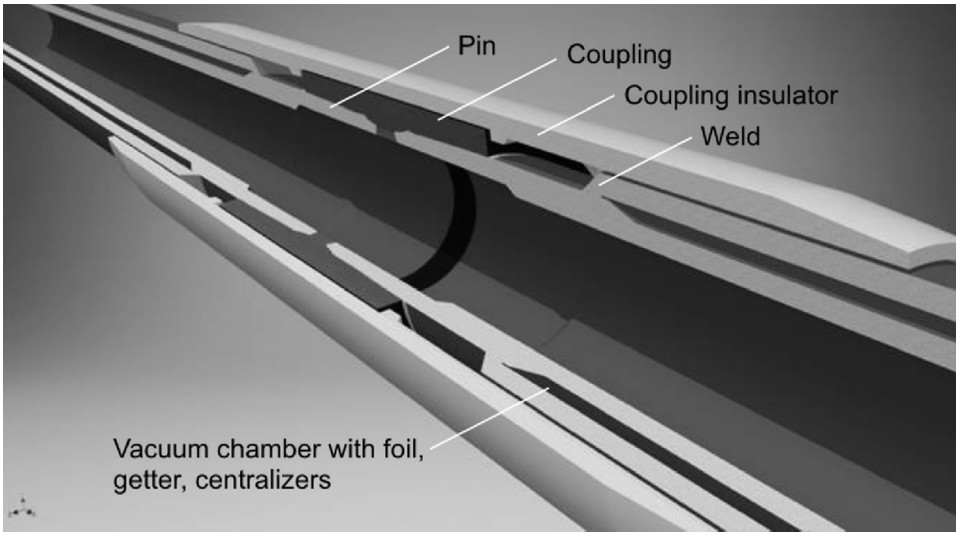

Figure 15.5 ***Sample VIT joint with threaded connection on outer tube.***

- The inner tube has no external pressure backup;
- The outer tube has no internal pressure backup.

With the above constraints, Pattillo et al. [201] have derived a set of relations between axial load and length change for VIT that are suitable for design calculations.

VIT thermal design

The threaded connection is a particularly sensitive and complex member of a VIT joint (cf. [202,203]). The approximately one foot of uninsulated joint at the connection can be the source of the preponderance of heat from the overall joint [187]. For this reason, VIT is usually installed with an insulating sleeve across each connection.

Thermal design of VIT can be clarified by treating the threaded connection as a fin [202,203] and giving due consideration for the properties of the annular fluid. Regarding the latter, Fig. 15.6 [184] exhibits two annular temperature profiles during steady production from Marlin Wells A-4 and A-6 having almost identical geometries and flow characteristics. The data was captured using a fiber-optic distributed temperature system. The temperature spikes every 40 ft correspond to the threaded connections that were both internally and externally insulated, an indication of the potential for heat loss outside the axial bounds of the VIT vacuum chamber.

At least for the (solid line) temperature profile labeled "Gelled Brine 1", however, the increase in temperature is confined to the vicinity of the connection. The annulus opposite the vacuum chamber is cooler, as the gel minimizes natural convection in the

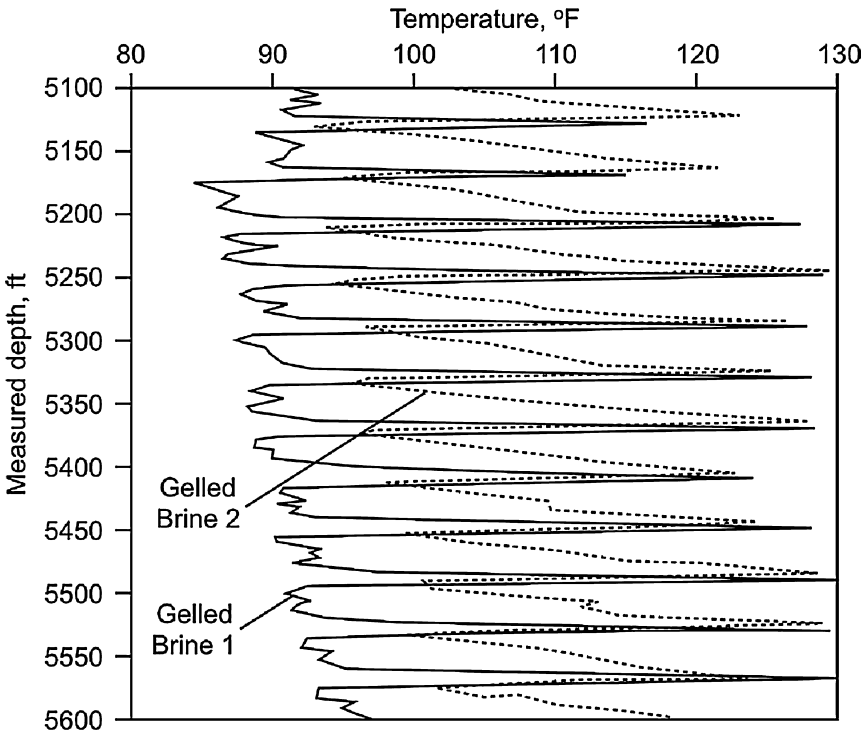

Figure 15.6 ***VIT annulus temperature profiles captured from Marlin Wells A-4 and A-6 [184].*** Well A-4 (Gelled Brine 2) experiences higher annular temperatures than Well A-6 (Gelled Brine 1) due to a lower gel-loading concentration in the former. Copyright 2004, Society of Petroleum Engineers Inc. Reproduced with permission of SPE. Further reproduction prohibited without permission.

annulus and limits heat transfer to conduction. The second (dashed line) temperature profile labeled "Gelled Brine 2" corresponds to a less concentrated annular gel. In this latter instance, heat transfer from the threaded connection mobilizes the annulus fluid, reducing both its density and viscosity. The density gradient between two connections creates a convection cell, transferring heat behind the vacuum chamber and partially defeating the VIT's ability to control annulus temperature. The well corresponding to "Gelled Brine 2" is passing more heat than its counterpart to the outer annuli, increasing APB.

The benefit gained from the use of a gelled annulus fluid comes at the cost of possible damage to the completion. The viscosity of the gelled fluid tends to promote transport of any debris in the flow path, again (see subsection 'Syntactic foam' in Section 15.2.4.2 of this chapter) increasing the possibility of plugging or interfering with downhole accessories.

15.3. WEAR

The most studied aspect of casing wear is the grooved wall loss associated with rotary drilling. The loss of wall thickness associated with wear can render a tubular string underdesigned following installation—a time when no small correction can usually be applied to remedy the integrity decrease.

The momentum behind casing wear technology has closely followed industry sponsored work conducted by Hall and coworkers [204–206] under the auspices of Maurer Engineering, Inc., and has led to adoption by the API of the primary experimental apparatus used to determine the all-important wear factor [207].

15.3.1 Governing equations of wear

We start with the fairly general premise that the volume per length V_w of steel removed from a casing string by contact with a rotating drill pipe tool joint is proportional to the frictional work done[9]

$$V_w = \frac{\mu_k \left|\mathbf{q}_c\right| L_c}{\varepsilon_w}, \tag{15.2}$$

where μ_k is the kinetic coefficient of friction, $\left|\mathbf{q}_c\right|$ is the magnitude of the contact force per length and ε_w is the specific energy of wear, i.e., the amount of energy necessary to remove a unit volume of material per length.

The variables μ_k and ε_w are similar in that they both depend on the two surfaces in contact and that neither is particularly easy to determine by means other than experiment. In that regard, a major distinction of the Maurer team was the decision to combine these two variables into a single variable denoted the wear factor

$$f_w = \frac{\mu_k}{\varepsilon_w}. \tag{15.3}$$

With the substitution of Eq. (15.3) into Eq. (15.2), the formula for material volume removed by wear becomes

$$V_w = f_w \left|\mathbf{q}_c\right| L_c. \tag{15.4}$$

Eq. (15.4) is both important and experimenter-friendly. If one builds an apparatus such that a tool joint can be rotated inside a length of casing with a measured contact force per length $\left|\mathbf{q}_c\right|$ while one simultaneously measures the volume of steel (per length) removed and the relative contact length L_c (rotary speed of tool joint times tool joint circumference), the only remaining unknown in Eq. (15.4) is f_w, the wear factor. Since its inception, the Maurer apparatus has been used to record the effect of casing material,

[9] See [206] for most of the equations to follow.

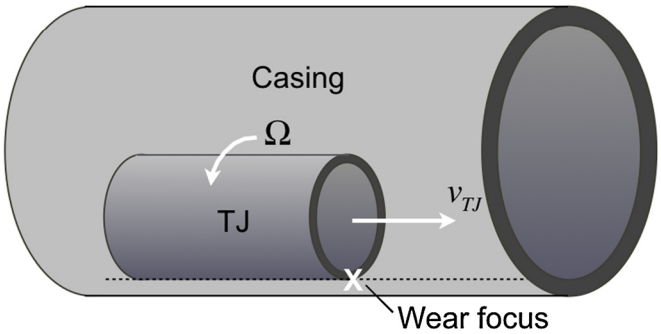

Figure 15.7 ***Residence time for a tool joint.*** At point × the tool joint is simultaneously rotating—the source of the wear groove—and advancing axially as new hole is drilled.

tool joint hard/soft banding and fluid environment on the wear factor, providing a wealth of information with which to design for wear.

Given a suite of experimentally determined wear factors, the prediction of wear requires two modeled pieces of information—the value of the contact force per length $|\mathbf{q}_c|$ and the time during which that force is resident at a particular casing location (used to determine L_c). The first item, contact force, is usually computed using equations identical or similar to those used in computing torque and drag. The second item, residence time, requires some method of accounting to record the history of drill string/casing contact. Both items have been discussed in the open literature, cf. [206]. Each of these contributors will be reviewed in the sections to follow.

15.3.1.1 Wear residence length

Consider Fig. 15.7 which examines a single tool joint rotating inside a casing string as the drill string advances. The × in the figure marks the location on the casing internal surface where wear is to be measured. Concerning length of circumferential sliding contact between the tool joint and the casing, one can state the following:

- The residence length corresponding to one rotation is πD_{TJ}, where D_{TJ} is the diameter of the tool joint;
- The number of rotations per unit time is Ω, usually expressed in revolutions per minute (RPM);
- The amount of time in residence is the length of the tool joint L_{TJ} divided by the forward speed of the tool joint v_{TJ} (i.e., rate of penetration).

With the above thoughts, the residence length of circumferential sliding contact of one tool joint at a specific location on the casing internal diameter is

$$(L_c)_{TJ} = \frac{\pi D_{TJ} \Omega L_{TJ}}{v_{TJ}}. \tag{15.5}$$

The residence length in Eq. (15.5) is for a single tool joint and has the following special cases:

- If the interval drilled is of measured length L_{dr} then the total number of tool joints passing the focus point $\times$ is $\frac{L_{dr}}{L_{dp}}$. The total residence length for all tool joints passing a casing point of focus is therefore

$$(L_c)_{TJ-total} = \frac{\pi D_{TJ} \Omega L_{TJ} L_{dr}}{v_{TJ} L_{dp}}, \quad \text{drill ahead.} \tag{15.6}$$

- If $v_{TJ} = 0$, for example, while milling inside casing or in a laboratory experiment to determine wear factor, then we replace the single tool joint residence time calculation $\tau_{TJ} = \frac{L_{TJ}}{v_{TJ}}$ with the residence time τ_{TJ} so that

$$(L_c)_{TJ} = \pi D_{TJ} \Omega \tau_{TJ}, \quad v_{TJ} = 0. \tag{15.7}$$

15.3.1.2 Contact force per length

At the high end of wear analysis one can explicitly model each joint of drill pipe and its corresponding tool joint. General purpose finite element software readily lends itself to this type of contact problem and can accommodate changes in geometry of both the drill string and bottom-hole assembly (BHA) and the confining hole. Alternately, simpler formulations such as the soft string model [34,42] have been successfully employed in wear calculations.

Depending on its degree of sophistication, the numerical model used to predict drill string behavior may not explicitly include tool joints. Alternately, as is the case with the soft string formulation, the model may be of such a nature that all portions of the tubular string are assumed to be in continuous contact with the confining hole, that is, the casing. If necessary, the simplicity of the model can be reconciled with the normal assumption that the drill pipe body is suspended between tool joints and not in contact with the confining hole by assuming the entire contact force over the length of a drill pipe joint is concentrated at the tool joint

$$(|\mathbf{q}_c|)_{TJ} = (|\mathbf{q}_c|)_{pipe} \frac{L_{dp}}{L_{TJ}}, \tag{15.8}$$

where L_{dp} is the average length of a joint of drill pipe, and L_{TJ} is the length of a tool joint. The justification of such an assumption should always be a prerequisite for its use. One can observe in severe instances, such as drilling through buckled casing, spiral polished patterns on the drill pipe body that are evidence of intra-tool joint contact.

15.3.1.3 Wear factor

Hall and Malloy [206] offer a detailed explanation of the experimental determination of wear factor. We simply note here that the laboratory data can be fit to a function of

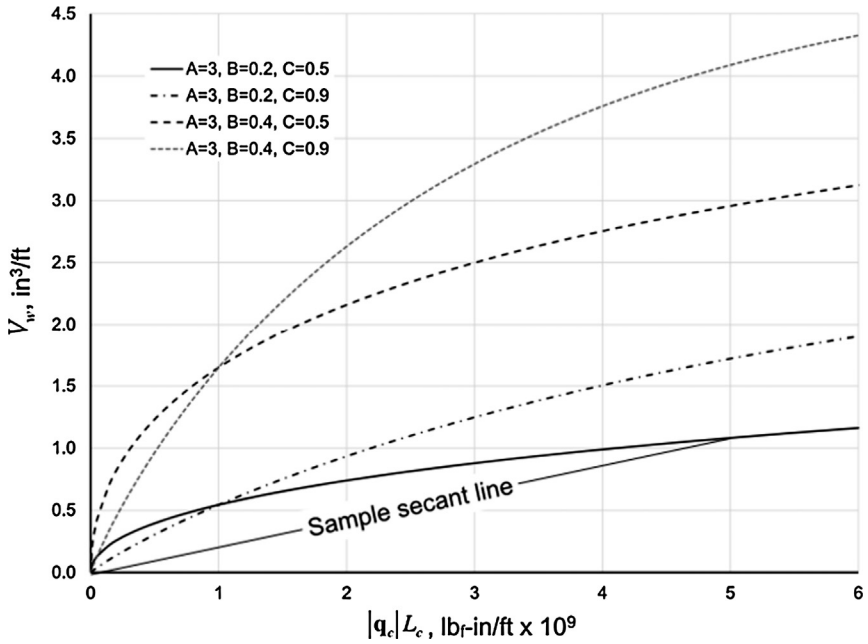

Figure 15.8 ***Curve fit to behavior of wear factor [206].*** The sample secant line is drawn from the origin to the point of interest on a curve.

the form

$$V_w = A\left(1 - e^{-B(|\mathbf{q}_c|L_c)^C}\right), \tag{15.9}$$

where A, B and C are curve fit parameters, and $|\mathbf{q}_c|$ and L_c are knowns from the experiment, with L_c calculated from Eq. (15.7).[10]

Representative plots of Eq. (15.9) are shown in Fig. 15.8. From Eq. (15.4) the wear factor f_w is the secant (line drawn from the origin to any point) on a V_w vs. $|\mathbf{q}_c| L_c$ curve. From Eq. (15.9) the wear factor is not a constant, being higher in the initial stages of wear.

For the examples illustrated in Fig. 15.8, Fig. 15.9 plots the wear factor itself as a function of the same abscissa as Fig. 15.8. With increased work, which implies increased wear, the wear factor approaches a constant value. Taking the limit as $|\mathbf{q}_c| L_c$ becomes large gives

$$\lim_{x\to\infty} \frac{V_w}{|\mathbf{q}_c| L_c} = \lim_{x\to\infty} \frac{A\left(1 - e^{-B(|\mathbf{q}_c|L_c)^C}\right)}{|\mathbf{q}_c| L_c}. \tag{15.10}$$

[10] Hall and Malloy [206] include the factor $\frac{L_{dp}}{L_{TJ}}$ (see Eq. (15.8)) explicitly in their definition of V_w.

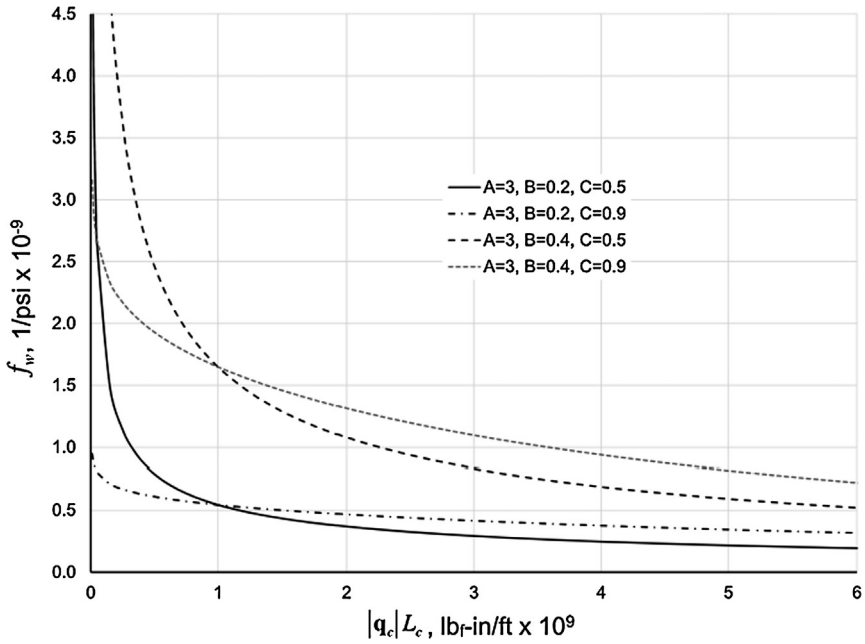

Figure 15.9 ***Wear factor from curve fit of experimental data.***

The additional wear associated with Eq. (15.9) renders the calculation nonlinear but should not be ignored. The increased wear factor in the early stages of tool joint groove development can represent a significant amount of metal loss.

15.3.2 Wear volume and wall loss

Presuming (a) the drill pipe is suspended on the tool joints[11] and (b) a soft string model or similar tool is supplying the average contact force $(|\mathbf{q}_c|)_{pipe}$ per length along a joint of drill pipe, Eqs. (15.4), (15.6) and (15.8) can be combined to yield

$$V_w = \frac{f_w(|\mathbf{q}_c|)_{pipe}\pi D_{TJ}\Omega L_{dr}}{v_{TJ}}, \quad \text{drill ahead,} \tag{15.11}$$

where f_w is determined by experiment, $(|\mathbf{q}_c|)_{pipe}$ is output from the soft string software, D_{TJ} reflects the tool joint geometry, and Ω, L_{dr} and v_{TJ} are drilling parameters. Eq. (15.11) could be used—with the drill string advanced on an incremental basis simulating drilling—to determine the accumulated wear at individual casing points for a particular hole interval.

[11] In the case of a casing-friendly "soft"-banding applied proud to the tool joint, one would assume the drill pipe is suspended on the soft-banding.

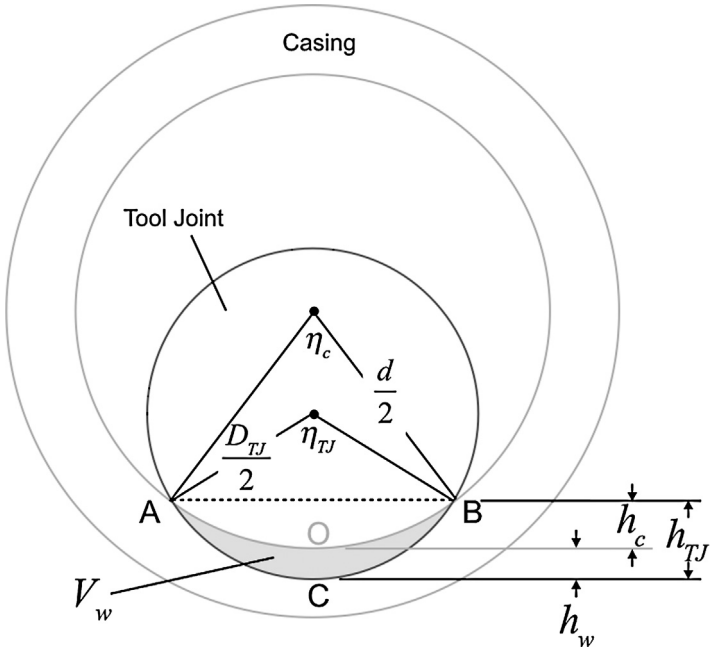

Figure 15.10 ***Calculation of wall thickness loss from wear volume.*** The lightly shaded area indicates the wear volume per length V_w. The straight line chord $\overline{AB}$ is common to both the casing and tool joint.

Eq. (15.11) is elegant in its simplicity. The difficulty with the relation is that wear is reported as a volume. For the purpose of tubular design our primary interest is loss of wall thickness. Conversion of wear volume to depth of wear groove is a geometry issue resolved by standard equations [208]. Fig. 15.10 illustrates the cross-section of a tool join as it wears an inner surface of casing. The following facts are at our disposal:

- The known quantity is the shaded region that is the wear volume per length V_w. Our desire is to know $h_w = h_{TJ} - h_c$, that is, the amount of wall thickness lost corresponding to V_w.
- In Fig. 15.10, the area of segment $\overline{\text{ABOA}}$ is [208]

$$A_{ABOA} = \frac{1}{2}\left(\frac{d}{2}\right)^2 (\eta_c - \sin\eta_c), \quad \eta_c = 2\sin^{-1}\frac{\overline{\text{AB}}}{2\left(\frac{d}{2}\right)}, \tag{15.12}$$

and the area of segment $\overline{\text{ABCA}}$ is

$$A_{ABCA} = \frac{1}{2}\left(\frac{D_{TJ}}{2}\right)^2 (\eta_{TJ} - \sin\eta_{TJ}), \quad \eta_{TJ} = 2\sin^{-1}\frac{\overline{\text{AB}}}{2\left(\frac{D_{TJ}}{2}\right)}, \tag{15.13}$$

where the known quantity V_w is

$$V_w = A_{ABCA} - A_{ABOA} = \frac{1}{2}\left(\frac{D_{TJ}}{2}\right)^2 (\eta_{TJ} - \sin\eta_{TJ}) - \frac{1}{2}\left(\frac{d}{2}\right)^2 (\eta_c - \sin\eta_c)$$
$$= \frac{1}{2}\left(\frac{D_{TJ}}{2}\right)^2 \left[(\eta_{TJ} - \sin\eta_{TJ}) - \left(\frac{d}{D_{TJ}}\right)^2 (\eta_c - \sin\eta_c)\right]. \tag{15.14}$$

- The unknown quantity h_w is

$$h_w = h_{TJ} - h_c = \left(\frac{D_{TJ}}{2}\right)\left(1 - \cos\frac{\eta_{TJ}}{2}\right) - \left(\frac{d}{2}\right)\left(1 - \cos\frac{\eta_c}{2}\right)$$
$$= \left(\frac{D_{TJ}}{2}\right)\left[\left(1 - \cos\frac{\eta_{TJ}}{2}\right) - \left(\frac{d}{D_{TJ}}\right)\left(1 - \cos\frac{\eta_c}{2}\right)\right]. \tag{15.15}$$

- The angles η_c and η_{TJ} can be related by their common defining factor $\overline{AB}$ (see Eqs. (15.12) and (15.13))

$$\eta_c = 2\sin^{-1}\left(\frac{D_{TJ}}{d}\sin\frac{\eta_{TJ}}{2}\right). \tag{15.16}$$

The three transcendental Eqs. (15.14)–(15.16) provide the desired relation between V_w and h_w. If we substitute Eq. (15.16) into Eq. (15.14), we can solve for η_{TJ}. With η_{TJ} known, we can solve Eq. (15.15). Or, as an alternative to the above trial-and-error procedure, one could start with Eq. (15.16) and increment η_{TJ}, successively solving for η_c (Eq. (15.16)), V_w (Eq. (15.14)) and h_w (Eq. (15.15)).

An example of the latter procedure is illustrated for 9.625 in., 53.50 $\frac{\text{lb}_\text{m}}{\text{ft}}$ (0.545 in. wall) casing being worn by a 6.25 in. tool joint. As was the case with wear factor (see Section 15.3.1.3), early wear exhibits noticeable nonlinearity which disappears for wear above approximately 30% of the wall thickness.

The calculations used to generate Fig. 15.11 can be used to address the issue of downrating cross-sectional resistance in the presence of tool joint wear. In previous chapters—Section 7.4 of Chapter 7 for internal pressure resistance and Section 8.4 of Chapter 8 for collapse resistance—we noted that for both internal and external pressure the loss in cross-sectional resistance is directly proportional to the percent of wall loss, i.e., 8% wear results in 8% loss of internal pressure resistance and 8% loss of collapse resistance.

We have not yet, however, addressed the effect of wear on axial resistance, particularly with regard to triaxial yield.[12] Insight into the reason most designers do not include

[12] The effect of wear on the radial and hoop stress contributions to triaxial resistance can be addressed by setting the factor k_{wall} equal to the fraction of remaining wall thickness. Whether one uses the wear

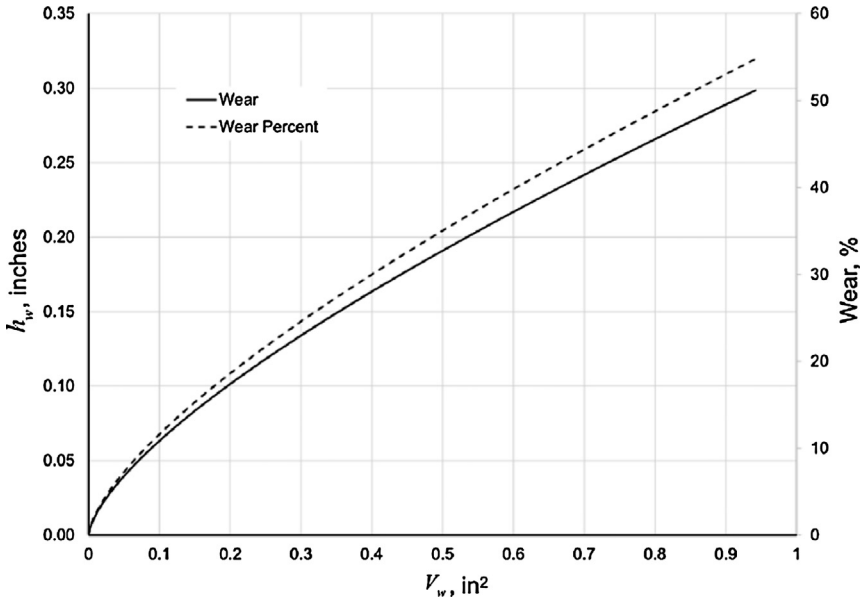

Figure 15.11 ***Relation between wear volume*** V_W ***and wall thickness loss*** h_W**,** $9.625\,\text{in}$**.,** $53.50\,\frac{\text{lb}_\text{m}}{\text{ft}}$ **(**$0.545\,\text{in}$**.** ***wall) casing being worn by a*** $6.25\,\text{in}$**.** ***tool joint.*** The left-hand ordinate measures absolute wall thickness loss at deepest point of wear grove. The right-hand ordinate measures h_W as a percent of original wall thickness. The maximum value of V_W corresponds to a wear groove with $\eta_{TJ} = 90°$.

a wear effect for axial resistance is presented in Fig. 15.12. For the casing and tool joint used in constructing the plot, a 50+% loss of wall thickness corresponds to only a 6% loss in cross-sectional area. The effect of wear on axial resistance is less marked than it is for the radial and hoop stress components.

The lower sensitivity of axial resistance to formation of a tool joint groove is primarily applicable to the tube body. Tool joint wear in the vicinity of a threaded connection can adversely affect the performance of a metal-to-metal seal as well as lower the critical section area on a pin-weak connection. The latter point is particularly pertinent to flush and nonflush clearance connections.

15.3.3 Wear of buckled casing during drill ahead

Designing casing for wear is relatively straightforward and illustrated in Fig. 15.13. As a first pass the casing is designed without regard to wear. The output of the design is a set

effect alone as the value of k_{wall} or multiplies the wear effect by the (normally) default 0.875 value of k_{wall} depends on the degree of conservatism one desires. Multiplying the wear effect by k_{wall} instead of unity implies that the wear groove aligns with the circumferential location of minimum wall thickness in the cross-section.

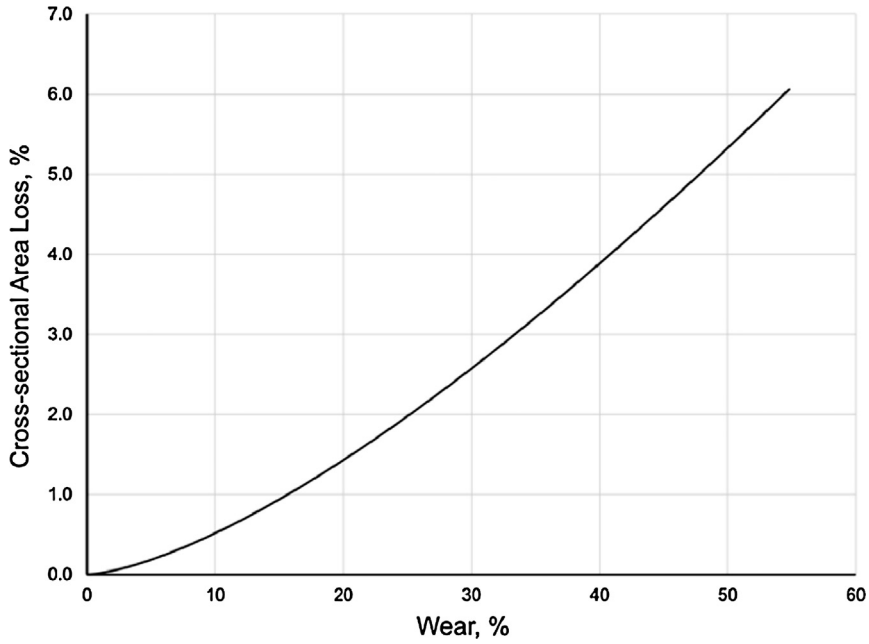

Figure 15.12 ***Relation between wear as a percentage of original wall thickness and loss of cross-sectional area,*** $9.625\,\text{in}$***.,*** $53.50\,\frac{\text{lb}_\text{m}}{\text{ft}}$ ***(***$0.545\,\text{in}$***. wall) casing being worn by a*** $6.25\,\text{in}$***. tool joint.*** The maximum value of wear percent corresponds to a wear groove with $\eta_{TJ} = 90°$.

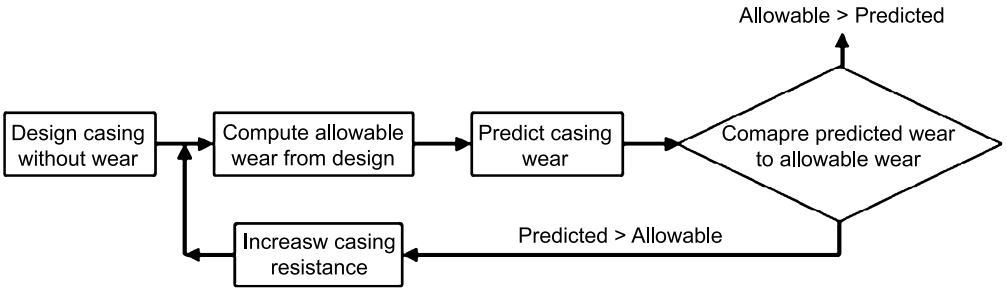

Figure 15.13 ***Wear work flow for casing design.***

of size, mass, grade combinations that are the constituents of the string in focus, along with computed safety factors for each load case.

Following the trial design, the individual load cases can be scanned to determine which load case is worst for the individual limit states of triaxial yield and collapse, with internal yield pressure being included in the triaxial limit state.[13] From these worst

[13] This assumes that minimum internal yield pressure, as opposed to ductile rupture, is the operable "burst" limit state.

case limit states, an estimate of allowable wear that would render the computed safety factor equal to the required design factor is determined. In both instances—collapse and triaxial yield—a reasonable estimate of allowable wear as wall thickness loss can be made by direct scaling of the wall thickness.

An estimate of wear can be obtained from a number of commercial software packages. Should the predicted wear exceed the allowable wear, then the following options are available:

- Increase the casing's resistance to wear, usually by increasing wall thickness[14];
- Change drilling parameters such as rotary speed or hole trajectory;
- Decrease the wear factor by applying casing-friendly soft-banding proud to the tool joint surface or otherwise altering the interface between the tool joint and casing (e.g., fluid additives, wear protectors).

A recalculation of allowable vs. predicted wear is then in order.

Usually the casing curvature is assumed to be identical to that of the wellbore. If, in addition, buckling is predicted, then the additional curvature due to the sinusoidal or helical nature of the tubular should be included in the determination of curvature. For the purpose of predicting wear, buckled casing in a straight wellbore will behave as if the postbuckled configuration presents a tortured well trajectory to the drill string.

[14] The increase in wall thickness may affect the outside rather than the inside diameter. For example, if it is important to maintain a 12.250 in. drift one can substitute 88.20 $\frac{\text{lb}_\text{m}}{\text{ft}}$ 13.625 in. casing for 72.00 $\frac{\text{lb}_\text{m}}{\text{ft}}$ 13.375 in. casing.

APPENDIX A

Tensors and Tensor Notation

A.1. INTRODUCTION

A tensor is a mathematical entity which obeys certain transformation rules. This appendix reviews elementary tensor concepts and describes the notation used throughout the main body of text.

An individual tensor component can be represented by the symbol $A_{abc\ldots xyz}$, where the number of subscripts necessary to distinguish the individual components[1] or elements of the tensor is its order. Here we consider the three orders of tensor most applicable to the study of tubulars—scalars (zeroth order tensors), vectors (first order tensors) and second order tensors.

A.2. ZEROTH ORDER TENSORS (SCALARS)

A scalar is a zeroth order tensor as it requires no indices to distinguish its components. Zeroth order tensors include temperature T, pressure p and time τ. Even though such quantities may be subscripted—p_i for internal pressure, p_o for external pressure—these identifying subscripts do not signify components or elements of a greater-than-zeroth tensor, but are merely identifiers to delineate different pressures.

A.3. FIRST ORDER TENSORS (VECTORS)

A vector is a first order tensor as it can distinguish its components by a single index. First order tensors include position $\mathbf{x}$ and displacement $\mathbf{u}$. In three-dimensional space, for example, the position in X_1–X_2–X_3 space has components along each of the coordinate axes, as does displacement.

The ith component of a vector is written v_i, and the vector itself can be written (see Fig. A.1)

$$\mathbf{v} = v_1\mathbf{e}_1 + v_2\mathbf{e}_2 + v_3\mathbf{e}_3 = \sum_{i=1}^{3} v_i\mathbf{e}_i, \tag{A.1}$$

where the $\mathbf{e}_i$s are unit (magnitude of 1) vectors aligned with the coordinate axes and v_i is the component of $\mathbf{v}$ along the ith coordinate axis.

[1] Almost exclusively in this manuscript the components of the tensor will, in some way, be related to a coordinate in Euclidean space, the space of all real numbers.

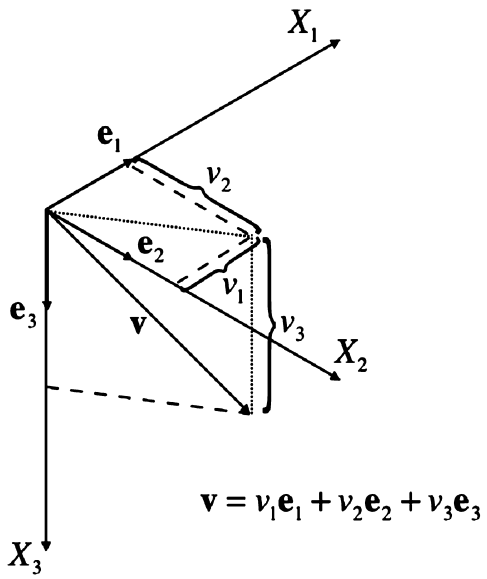

Figure A.1 ***Geometric interpretation of a vector.*** The intersections of the dashed lines with the coordinate axes indicate the individual components of the vector. The dotted lines are provided merely as aids in visualizing the three-dimensional figure.

A.3.1 Vector operations

Several operations on vectors are employed in the main text.

A.3.1.1 Vector addition

Addition of two vectors creates a new vector, each component of which is the sum of the corresponding components of the original vectors. If $\mathbf{w}$ is the sum of the vectors $\mathbf{u}$ and $\mathbf{v}$ then

$$\begin{aligned} &\mathbf{w} = \mathbf{u} + \mathbf{v} = (u_1 + v_1)\,\mathbf{e}_1 + (u_2 + v_2)\,\mathbf{e}_2 + (u_3 + v_3)\,\mathbf{e}_3, \\ &w_i = u_i + v_i, \quad i = 1, 2, 3. \end{aligned} \tag{A.2}$$

Vector addition is commutative (the order of the operands can be interchanged). Fig. A.2 illustrates vector addition graphically.

Eq. (A.2) illustrates a practice which, whenever appropriate, will be followed throughout this book. In the equation, two representations of the tensor relation are supplied:

1. Direct notation (i.e., $\mathbf{w} = \mathbf{u} + \mathbf{v}$), where the individual components of the tensor are hidden. Direct notation is clean and concise, focusing on the relation in its totality.
2. Index notation (i.e., $w_i = u_i + v_i$), where the focus is on individual components of the tensor(s).

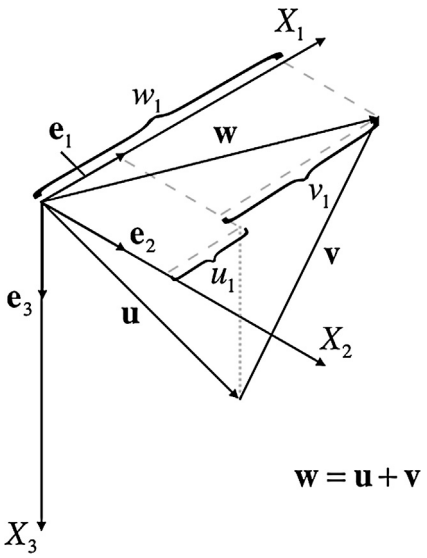

Figure A.2 ***Graphic illustration of vector addition.*** Only the operation on the "1" component is detailed.

The two extra expressions in Eq. (A.2)—$(u_1 + v_1)\,\mathbf{e}_1 + (u_2 + v_2)\,\mathbf{e}_2 + (u_3 + v_3)\,\mathbf{e}_3$ in the direct relation and $i = 1, 2, 3$ in the index relation—have been included for clarity in this early part of the discussion. They will soon be abandoned. For more on the notation conventions used throughout the book, see Section 1.5 of Chapter 1.

A.3.1.2 Scalar multiplication

Multiplication of a vector by a scalar multiplies each component of the vector by the scalar. If $\mathbf{w}$ is the product of the scalar c with the vector $\mathbf{v}$, then

$$\mathbf{w} = c\mathbf{v} = cv_1\mathbf{e}_1 + cv_2\mathbf{e}_2 + cv_3\mathbf{e}_3, \quad w_i = cv_i, \quad i = 1, 2, 3. \tag{A.3}$$

A.3.1.3 Dot product

The dot product[2] of two three-dimensional vectors $\mathbf{a}$ and $\mathbf{b}$ can be written as

$$\mathbf{a} \cdot \mathbf{b} = a_1b_1 + a_2b_2 + a_3b_3 = \sum_{i=1}^{3} a_ib_i, \quad \mathbf{a} \cdot \mathbf{b} = a_ib_i, \tag{A.4}$$

where repetition of indices indicates summation.

[2] An alternate name for this operation is *inner product*. Strictly speaking, the inner product is a generalization of the dot product to dimensions greater than three.

In the rightmost portion of Eq. (A.4) the summation sign has been discarded in favor of the abbreviated index notation. Here, repeated subscript indices such as the i in $a_i b_i$ indicate summation over the range of the indices—in this case from 1 to 3.

The following properties of the dot product can be derived from the definition in Eq. (A.4) [16]:

- it is commutative (the order of the operands can be interchanged)

$$\mathbf{a} \cdot \mathbf{b} = \mathbf{b} \cdot \mathbf{a}, \quad a_i b_i = b_i a_i; \tag{A.5}$$

- it is distributive over vector addition

$$\mathbf{a} \cdot (\mathbf{b} + \mathbf{c}) = \mathbf{a} \cdot \mathbf{b} + \mathbf{a} \cdot \mathbf{c}, \quad a_i (b_i + c_i) = a_i b_i + a_i c_i; \tag{A.6}$$

- it commutes with scaling of either of its factors (the grouping of the operands with a scalar constant k is arbitrary)

$$k(\mathbf{a} \cdot \mathbf{b}) = (k\mathbf{a}) \cdot \mathbf{b} = \mathbf{a} \cdot (k\mathbf{b}), \quad k(a_i b_i) = (k a_i) b_i = a_i (k b_i). \tag{A.7}$$

The dot product of a vector with itself is the square of the magnitude of the vector. From Eq. (A.4)

$$\mathbf{v} \cdot \mathbf{v} = v_1 v_1 + v_2 v_2 + v_3 v_3 = \sum_{i=1}^{3} v_i^2 = |\mathbf{v}|^2, \quad \mathbf{v} \cdot \mathbf{v} = v_i v_i = |\mathbf{v}|^2. \tag{A.8}$$

An alternate form of the dot product is

$$\mathbf{a} \cdot \mathbf{b} = |\mathbf{a}||\mathbf{b}| \cos\theta, \quad a_i b_i = \sqrt{a_i a_i}\sqrt{b_i b_i} \cos\theta, \tag{A.9}$$

where θ is the angle between the two vectors. This form of the dot product readily admits itself to geometric interpretation as the product of the projection of one of the vectors along the other and the magnitude of the unprojected vector—see Fig. A.3.

Example problem—vector components along axes

The geometric interpretation given Eq. (A.9) is particularly useful as a means of determining the components of a vector along coordinate axes. Recall Eq. (A.1) and assume we wish to determine the component of $\mathbf{v}$ along the X_2-axis. Using Eqs. (A.6) and (A.7) and recognizing that the unit vectors along the coordinate axes are orthogonal, $\mathbf{e}_i \cdot \mathbf{e}_j = 0$ if $i \neq j$, we get

$$\begin{aligned} \mathbf{e}_2 \cdot \mathbf{v} &= \mathbf{e}_2 \cdot (v_1 \mathbf{e}_1 + v_2 \mathbf{e}_2 + v_3 \mathbf{e}_3) \\ &= v_1 (\mathbf{e}_2 \cdot \mathbf{e}_1) + v_2 (\mathbf{e}_2 \cdot \mathbf{e}_2) + v_3 (\mathbf{e}_2 \cdot \mathbf{e}_3) \\ &= v_1 (0) + v_2 (1) + v_3 (0) \\ &= v_2. \end{aligned} \tag{A.10}$$

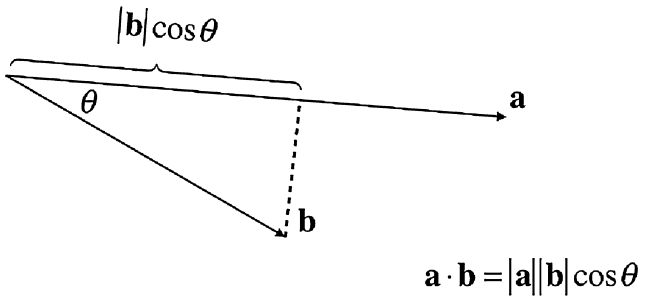

Figure A.3 ***Geometric interpretation of the dot product.***

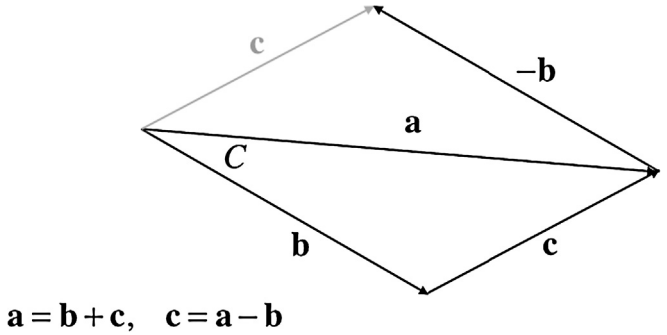

Figure A.4 ***Demonstration of the equivalence of Eqs.*** (A.4) ***and*** (A.9)**.** The angle C is designated θ in the main discussion—see Eq. (A.9).

Example problem—equivalence of Eqs. (A.4) and (A.9)

Recall from the law of cosines that if a, b and c are the lengths of the sides of a triangle and A, B and C are the corresponding angles opposite to the sides with lengths a, b and c, respectively, then

$$c^2 = a^2 + b^2 - 2ab\cos C. \tag{A.11}$$

If the sides of the triangle are actually vectors $\mathbf{a}$, $\mathbf{b}$, and $\mathbf{c}$ such that (see Fig. A.4) $\mathbf{a} = \mathbf{b} + \mathbf{c}$, then from Eq. (A.11)

$$\mathbf{c}\cdot\mathbf{c} = \mathbf{a}\cdot\mathbf{a} + \mathbf{b}\cdot\mathbf{b} - 2\,|\mathbf{a}|\,|\mathbf{b}|\cos C, \quad c_i c_i = a_i a_i + b_i b_i - 2\sqrt{a_i a_i}\sqrt{b_i b_i}\cos C. \tag{A.12}$$

Since (see Fig. A.4) $\mathbf{c} = \mathbf{a} - \mathbf{b}$, from the fact that the dot product is distributive over vector addition (Eq. (A.6)), we get

$$\begin{aligned} \mathbf{c}\cdot\mathbf{c} &= (\mathbf{a}-\mathbf{b})\cdot(\mathbf{a}-\mathbf{b}) = \mathbf{a}\cdot\mathbf{a} - 2\mathbf{a}\cdot\mathbf{b} + \mathbf{b}\cdot\mathbf{b}, \\ c_i c_i &= (a_i - b_i)(a_i - b_i) = a_i a_i - 2a_i b_i + b_i b_i. \end{aligned} \tag{A.13}$$

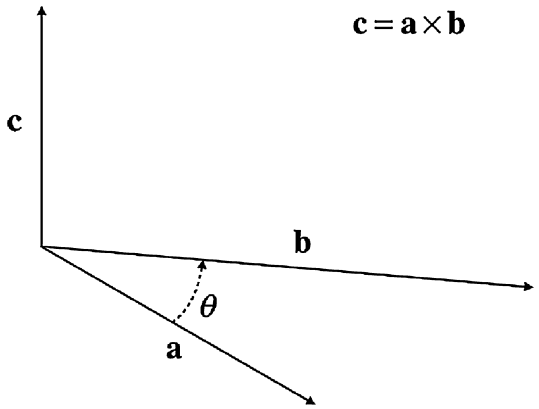

Figure A.5 ***Geometric interpretation of the cross product.***

Comparing Eqs. (A.12) and (A.13), and using Eq. (A.8),

$$|\mathbf{a}|^2 - 2\mathbf{a}\cdot\mathbf{b} + |\mathbf{b}|^2 = |\mathbf{a}|^2 + |\mathbf{b}|^2 - 2|\mathbf{a}||\mathbf{b}|\cos C, \quad \mathbf{a}\cdot\mathbf{b} = |\mathbf{a}||\mathbf{b}|\cos C,$$
$$a_i a_i - 2a_i b_i + b_i b_i = a_i a_i + b_i b_i - 2\sqrt{a_i a_i}\sqrt{b_i b_i}\cos C, \quad a_i b_i = \sqrt{a_i a_i}\sqrt{b_i b_i}\cos C. \quad \text{(A.14)}$$

Eq. (A.9) can be derived using Eq. (A.8), a special case of Eq. (A.4), the law of cosines and the distributive property of the dot product.

A.3.1.4 Cross product

The cross product of two three-dimensional vectors[3] $\mathbf{a} = a_i\mathbf{e}_i$ and $\mathbf{b} = b_i\mathbf{e}_i$ can be written as

$$\mathbf{a}\times\mathbf{b} = (a_2b_3 - a_3b_2)\,\mathbf{e}_1 + (a_3b_1 - a_1b_3)\,\mathbf{e}_2 + (a_1b_2 - a_2b_1)\,\mathbf{e}_3. \quad \text{(A.15)}$$

The cross product of two vectors produces a vector perpendicular to the plane containing the crossed vectors and with direction determined by applying the "right-hand rule."[4] Fig. A.5 illustrates the cross product geometrically, where $\mathbf{c} = \mathbf{a}\times\mathbf{b}$.

The following properties of the cross product can be derived from the definition in Eq. (A.15):

- it is distributive over vector addition

$$\mathbf{a}\times(\mathbf{b}+\mathbf{c}) = \mathbf{a}\times\mathbf{b} + \mathbf{a}\times\mathbf{c}. \quad \text{(A.16)}$$

[3] The vector cross product is only defined in three-dimensional space.

[4] In Fig. A.5, imagine your right wrist at the intersection/vertex of vectors **a** and **b** with your right fingers pointing in the direction of **a**. As you sweep your right hand from **a** to **b** your thumb points in the direction of $\mathbf{c} = \mathbf{a}\times\mathbf{b}$.

- it commutes with scaling of either of its factors (the grouping of the operands with a constant k is arbitrary)

$$k\left(\mathbf{a}\times\mathbf{b}\right)=\left(k\mathbf{a}\right)\times\mathbf{b}=\mathbf{a}\times\left(k\mathbf{b}\right). \tag{A.17}$$

Use of the distributive and scalar multiplication properties, along with the right-hand rule, illustrates that the definition of Eq. (A.15) follows from the cross products of the unit vectors along the coordinate axes:

$$\begin{aligned}\mathbf{a}\times\mathbf{b}&=\left(a_1\mathbf{e}_1+a_2\mathbf{e}_2+a_3\mathbf{e}_3\right)\times\left(b_1\mathbf{e}_1+b_2\mathbf{e}_2+b_3\mathbf{e}_3\right)\\&=a_1b_1\left(\mathbf{e}_1\times\mathbf{e}_1\right)+a_1b_2\left(\mathbf{e}_1\times\mathbf{e}_2\right)+a_1b_3\left(\mathbf{e}_1\times\mathbf{e}_3\right)\\&\quad+a_2b_1\left(\mathbf{e}_2\times\mathbf{e}_1\right)+a_2b_2\left(\mathbf{e}_2\times\mathbf{e}_2\right)+a_2b_3\left(\mathbf{e}_2\times\mathbf{e}_3\right)\\&\quad+a_3b_1\left(\mathbf{e}_3\times\mathbf{e}_1\right)+a_3b_2\left(\mathbf{e}_3\times\mathbf{e}_2\right)+a_3b_3\left(\mathbf{e}_3\times\mathbf{e}_3\right)\\&=a_1b_2\mathbf{e}_3+a_1b_3\left(-\mathbf{e}_2\right)+a_2b_1\left(-\mathbf{e}_3\right)+a_2b_3\mathbf{e}_1\\&\quad+a_3b_1\mathbf{e}_2+a_3b_2\left(-\mathbf{e}_1\right)\\&=\left(a_2b_3-a_3b_2\right)\mathbf{e}_1+\left(a_3b_1-a_1b_3\right)\mathbf{e}_2+\left(a_1b_2-a_2b_1\right)\mathbf{e}_3.\end{aligned} \tag{A.18}$$

The penultimate step in Eq. (A.18) illustrates a drastic reduction in terms from its predecessor due to the fact that $\mathbf{a}\times\mathbf{a}=0$ (see Eq. (A.15)). This step also illustrates the fact that the cross product is *not* commutative, that is, $\mathbf{a}\times\mathbf{b}=-\mathbf{b}\times\mathbf{a}\neq\mathbf{b}\times\mathbf{a}$ (again, a consequence of Eq. (A.15)).

The use of index notation in defining the vector cross product requires the introduction of the Levi-Civita symbol[5]

$$\varepsilon_{ijk}=\begin{cases}1 & \text{if } (i,j,k) \text{ is an even permutation of } (1,2,3),\\ 0 & \text{if two or more of the indices are equal,}\\ -1 & \text{if } (i,j,k) \text{ is an odd permutation of } (1,2,3),\end{cases} \tag{A.19}$$

where an even permutation is any one of (1, 2, 3), (2, 3, 1) or (3, 1, 2), and an odd permutation is any other combination of the three indices. The transition from the first step to the second step in Eq. (A.18) illustrates how the Levi-Civita symbol enters the index notation expression of cross product, since $\mathbf{e}_i=\varepsilon_{ijk}\mathbf{e}_j\times\mathbf{e}_k$.

Consider a right-handed coordinate system with base unit vectors $\mathbf{e}_1$, $\mathbf{e}_2$ and $\mathbf{e}_3$, such that a vector $\mathbf{v}$ is $\mathbf{v}=v_r\mathbf{e}_r$. Then the cross product of two vectors $\mathbf{a}$ and $\mathbf{b}$ can be written as

$$\mathbf{c}=\mathbf{a}\times\mathbf{b}=\left(a_s\mathbf{e}_s\right)\times\left(b_t\mathbf{e}_t\right)=a_sb_t\left(\mathbf{e}_s\times\mathbf{e}_t\right),\quad c_r=\varepsilon_{rst}a_sb_t. \tag{A.20}$$

[5] Also termed the permutation symbol or alternating symbol.

An alternate form of the cross product is

$$\mathbf{a} \times \mathbf{b} = |\mathbf{a}||\mathbf{b}| \sin\theta \, \mathbf{e}_{\mathbf{a}\times\mathbf{b}}, \tag{A.21}$$

where θ is the angle between the two vectors, and $\mathbf{e}_{\mathbf{a}\times\mathbf{b}}$ is a unit vector perpendicular to the two vectors and directed according to the right-hand rule.

Example problem—computing the cross product

Given the vectors $\mathbf{a} = 1\mathbf{e}_1 + 2\mathbf{e}_2 + 3\mathbf{e}_3$ and $\mathbf{a} = 4\mathbf{e}_1 - 5\mathbf{e}_2 - 6\mathbf{e}_3$, compute the cross product $\mathbf{a} \times \mathbf{b}$. From the definition given in Eq. (A.15),

$$\begin{aligned} \mathbf{a} \times \mathbf{b} &= \{[2 \times (-6)] - [3 \times (-5)]\}\,\mathbf{e}_1 + \{[3 \times 4] - [1 \times (-6)]\}\,\mathbf{e}_2 \\ &\quad + \{[1 \times (-5)] - [2 \times 4]\}\,\mathbf{e}_3 \\ &= 3\mathbf{e}_1 + 18\mathbf{e}_2 - 13\mathbf{e}_3. \end{aligned} \tag{A.22}$$

This vector is perpendicular to both $\mathbf{a}$ and $\mathbf{b}$. To illustrate, we compute the dot product of $\mathbf{a} \times \mathbf{b}$ with each of its parent vectors

$$\begin{aligned} (\mathbf{a} \times \mathbf{b}) \cdot \mathbf{a} &= (3\mathbf{e}_1 + 18\mathbf{e}_2 - 13\mathbf{e}_3) \cdot (1\mathbf{e}_1 + 2\mathbf{e}_2 + 3\mathbf{e}_3) \\ &= 3 + 36 - 39 = 0, \end{aligned} \tag{A.23}$$

and

$$\begin{aligned} (\mathbf{a} \times \mathbf{b}) \cdot \mathbf{b} &= (3\mathbf{e}_1 + 18\mathbf{e}_2 - 13\mathbf{e}_3) \cdot (4\mathbf{e}_1 - 5\mathbf{e}_2 - 6\mathbf{e}_3) \\ &= 12 - 90 + 78 = 0. \end{aligned} \tag{A.24}$$

Example problem—the Kronecker delta and the epsilon–delta identity

We first introduce a new symbol, the Kronecker delta

$$\delta_{ij} = \begin{cases} 1 & \text{if } i = j, \\ 0 & \text{if } i \neq j. \end{cases} \tag{A.25}$$

With repeated indices indicating summation, $\delta_{ii} = 1 + 1 + 1 = 3$.

The epsilon–delta identity relates the Kronecker delta to the Levi-Civita symbol through the equation

$$\varepsilon_{ijk}\varepsilon_{imn} = \delta_{jm}\delta_{kn} - \delta_{jn}\delta_{km}. \tag{A.26}$$

Consider the cross product $\mathbf{d} = \mathbf{a} \times (\mathbf{b} \times \mathbf{c})$, which in index notation can be written as

$$d_i = \varepsilon_{ijk} a_j \left(\varepsilon_{kmn} b_m c_n\right) = \varepsilon_{kij}\varepsilon_{kmn} a_j b_m c_n, \tag{A.27}$$

where we have taken advantage of an even permutation ($\varepsilon_{ijk} = \varepsilon_{kij}$) to rewrite the first ε_{ijk}. Applying the epsilon–delta identity (Eq. (A.26)),

$$\begin{aligned} d_i &= \left(\delta_{im}\delta_{jn} - \delta_{in}\delta_{jm}\right) a_j b_m c_n \\ &= a_j b_i c_j - a_j b_j c_i \\ &= b_i \left(a_j c_j\right) - c_i \left(a_j b_j\right), \end{aligned} \tag{A.28}$$

which is equivalent to the expression

$$\mathbf{d} = \mathbf{a} \times (\mathbf{b} \times \mathbf{c}) = \mathbf{b}(\mathbf{a} \cdot \mathbf{c}) - \mathbf{c}(\mathbf{a} \cdot \mathbf{b}). \tag{A.29}$$

Example problem—equivalence of Eqs. (A.15) and (A.21)

We know from the discussion following Eq. (A.15) and the definition of $\mathbf{e}_{\mathbf{a}\times\mathbf{b}}$ that both definitions produce vectors that are collinear. It only remains to show that the magnitudes of both vectors are identical. Starting with Eq. (A.21), the quantity $\sin\theta$ can be written in terms of the dot product of $\mathbf{a}$ and $\mathbf{b}$ using Eq. (A.9) as

$$\begin{aligned} \sin\theta &= \sqrt{1-\cos^2\theta} = \sqrt{1 - \left(\frac{|\mathbf{a}\cdot\mathbf{b}|}{|\mathbf{a}||\mathbf{b}|}\right)^2} = \frac{1}{|\mathbf{a}||\mathbf{b}|}\sqrt{|\mathbf{a}|^2|\mathbf{b}|^2 - |\mathbf{a}\cdot\mathbf{b}|^2}, \\ \sin\theta &= \sqrt{1-\cos^2\theta} = \sqrt{1 - \left(\frac{|a_i b_i|}{\sqrt{a_j a_j}\sqrt{b_k b_k}}\right)^2} = \frac{1}{\sqrt{a_j a_j}\sqrt{b_k b_k}}\sqrt{|a_i a_i|b_m b_m| - |a_n b_n|^2}. \end{aligned} \tag{A.30}$$

Applying this relation to Eq. (A.21) gives

$$\begin{aligned} |\mathbf{a}\times\mathbf{b}| &= |\mathbf{a}||\mathbf{b}|\left[\frac{1}{|\mathbf{a}||\mathbf{b}|}\sqrt{|\mathbf{a}|^2|\mathbf{b}|^2 - |\mathbf{a}\cdot\mathbf{b}|^2}\right] \\ &= \sqrt{|\mathbf{a}|^2|\mathbf{b}|^2 - |\mathbf{a}\cdot\mathbf{b}|^2} \\ &= \left[\left(a_1^2+a_2^2+a_3^2\right)\left(b_1^2+b_2^2+b_3^2\right) - \left(a_1b_1+a_2b_2+a_3b_3\right)^2\right]^{\frac{1}{2}} \\ &= \left[\left(a_1^2b_2^2 + a_2^2b_1^2 - 2a_1b_1a_2b_2\right) + \left(a_2^2b_3^2 + a_3^2b_2^2 - 2a_2b_2a_3b_3\right)\right. \\ &\qquad \left. + \left(a_3^2b_1^2 + a_1^2b_3^2 - 2a_1b_1a_3b_3\right)\right]^{\frac{1}{2}} \\ &= \sqrt{\left(a_2b_3 - a_3b_2\right)^2 + \left(a_3b_1 - a_1b_3\right)^2 + \left(a_1b_2 - a_2b_1\right)^2}, \end{aligned} \tag{A.31}$$

and similarly for the expression using index notation. Comparing this result to the expression for $|\mathbf{a}\times\mathbf{b}|$, derived using Eq. (A.15), indicates that the two definitions for cross product–Eqs. (A.15) and (A.21)–are identical.

A.4. SECOND ORDER TENSORS

A square matrix can be a second order tensor. Second order tensors include stress $\mathbf{S}$, S_{IJ}, and strain $\mathbf{E}$, E_{IJ}.

When using a matrix to manipulate tensor components, the first index of the tensor subscript is the row location, and the second index is the column location, as illustrated in Eq. (A.32),

$$\mathbf{T} = \begin{bmatrix} T_{11} & T_{12} & T_{13} \\ T_{21} & T_{22} & T_{23} \\ T_{31} & T_{32} & T_{33} \end{bmatrix}, \tag{A.32}$$

that is, the component of $\mathbf{T}$ in the ith row and the jth column of the matrix is T_{ij}.

The transpose of $\mathbf{T}$, designated $\mathbf{T}^T$, refers to the matrix representation of $\mathbf{T}$ and is obtained by exchanging the tensor indices

$$\mathbf{T}^T = \begin{bmatrix} T_{11} & T_{21} & T_{31} \\ T_{12} & T_{22} & T_{32} \\ T_{13} & T_{23} & T_{33} \end{bmatrix}, \tag{A.33}$$

that is, $\mathbf{T}^T_{ij} = \mathbf{T}_{ji}$. If a tensor is symmetric, $\mathbf{T}^T = \mathbf{T}$, or $\mathbf{T}^T_{ij} = \mathbf{T}_{ji} = \mathbf{T}_{ij}$.

A.4.1 Second order tensor operations

Consider the following second and first order[6] tensors:

$$\mathbf{A} = \begin{bmatrix} A_{11} & A_{12} & A_{13} \\ A_{21} & A_{22} & A_{23} \\ A_{31} & A_{32} & A_{33} \end{bmatrix}, \quad \mathbf{B} = \begin{bmatrix} B_{11} & B_{12} & B_{13} \\ B_{21} & B_{22} & B_{23} \\ B_{31} & B_{32} & B_{33} \end{bmatrix},$$
$$\mathbf{v} = \begin{bmatrix} v_1 \\ v_2 \\ v_3 \end{bmatrix}, \quad \mathbf{w} = \begin{bmatrix} w_1 \\ w_2 \\ w_3 \end{bmatrix}. \tag{A.34}$$

Several operations on such tensors are employed in the main text.

A.4.1.1 Tensor addition

Addition of two tensors creates a new tensor, each component of which is the sum of the corresponding components of the original tensors. If $\mathbf{T}$ is the sum of the tensors $\mathbf{A}$

[6] The matrix representation of a vector is a column. The matrix representation of the transpose of a vector is a row, $\mathbf{v}^T = \begin{bmatrix} v_1 & v_2 & v_3 \end{bmatrix}$.

and **B**, then

$$\mathbf{T} = \mathbf{A} + \mathbf{B} = \begin{bmatrix} A_{11} + B_{11} & A_{12} + B_{12} & A_{13} + B_{13} \\ A_{21} + B_{21} & A_{22} + B_{22} & A_{23} + B_{23} \\ A_{31} + B_{31} & A_{32} + B_{32} & A_{33} + B_{33} \end{bmatrix}, \quad T_{ij} = A_{ij} + B_{ij}. \tag{A.35}$$

Tensor addition is commutative (the order of the operands can be interchanged).

A.4.1.2 Scalar multiplication

Multiplication of a tensor by a scalar multiplies each component of the tensor by the scalar. If **T** is the product of the scalar c with the tensor **A** then

$$\mathbf{T} = c\mathbf{A} = \begin{bmatrix} cA_{11} & cA_{12} & cA_{13} \\ cA_{21} & cA_{22} & cA_{23} \\ cA_{31} & cA_{32} & cA_{33} \end{bmatrix}, \quad T_{ij} = cA_{ij}. \tag{A.36}$$

A.4.1.3 Tensor product

Seldom used in this book, but included here for completeness, the tensor product **C** of two vectors **v** and **w** is

$$\mathbf{C} = \mathbf{vw} = \begin{bmatrix} v_1 w_1 & v_1 w_2 & v_1 w_3 \\ v_2 w_1 & v_2 w_2 & v_2 w_3 \\ v_3 w_1 & v_3 w_2 & v_3 w_3 \end{bmatrix}, \quad C_{ij} = v_i w_j. \tag{A.37}$$

The tensor product of two vectors is also called a dyad.

The tensor product of two second order tensors also exists (as it does for two tensors of any order), but this product is not employed in this book and will not be covered here.

A.4.1.4 Tensor contraction product

Contraction is the operation by which two indices are set equal, followed by performing the resulting sum. For example, the trace[7] of **A** in Eq. (A.34) is

$$I_1 = \mathrm{tr}\{\mathbf{A}\} = A_{ii} = A_{11} + A_{22} + A_{33}. \tag{A.38}$$

The tensor contraction product has designation similar to the vector dot product (Section A.3.1.3). In index notation it corresponds to contracting the two adjacent indices of the affected matrices. The tensor contraction product **C** of **A** and **B** is

[7] The trace, or first invariant, of a second order tensor is the sum of its diagonal terms.

$$\begin{aligned}\mathbf{C} &= \mathbf{A}\cdot\mathbf{B}\\ &= \begin{bmatrix} A_{11}B_{11}+A_{12}B_{21}+A_{13}B_{31} & \dots & A_{11}B_{13}+A_{12}B_{23}+A_{13}B_{33}\\ A_{21}B_{11}+A_{22}B_{21}+A_{23}B_{31} & \dots & A_{21}B_{13}+A_{22}B_{23}+A_{23}B_{33}\\ A_{31}B_{11}+A_{32}B_{21}+A_{33}B_{31} & \dots & A_{31}B_{13}+A_{32}B_{23}+A_{33}B_{33}\end{bmatrix},\\ C_{ij} &= A_{ik}B_{kj},\end{aligned} \tag{A.39}$$

where the middle column $(A_{i1}B_{12}+A_{i2}B_{22}+A_{i3}B_{32}, i=1,2,3)$ has been omitted for reasons of space.

The tensor contraction product $\mathbf{w}$ of $\mathbf{A}$ and $\mathbf{v}$ is

$$\mathbf{w}=\mathbf{A}\cdot\mathbf{v}=\begin{bmatrix} A_{11}v_1+A_{12}v_2+A_{13}v_3\\ A_{21}v_1+A_{22}v_2+A_{23}v_3\\ A_{31}v_1+A_{32}v_2+A_{33}v_3\end{bmatrix},\quad w_i=A_{ik}v_k. \tag{A.40}$$

Care must be exercised, however, as the tensor contraction product of $\mathbf{v}$ and $\mathbf{A}$ is undefined. For the tensor contraction product to be valid, the contracted indices must be of the same dimension. Eq. (A.40) is valid since we are contracting a 3×3 tensor with a 3×1 tensor. The operation $\mathbf{v}\cdot\mathbf{A}$, on the other hand, attempts adjacent indices contraction of a 3×1 tensor with a 3×3 tensor. The second order tensor *can* be premultiplied by the first order tensor if, in the tensor contraction product we use the transpose of the latter, namely

$$\begin{aligned}\mathbf{w} &= \mathbf{v}^T\cdot\mathbf{A}\\ &= \begin{bmatrix}A_{11}v_1+A_{21}v_2+A_{31}v_3 & A_{12}v_1+A_{22}v_2+A_{32}v_3 & A_{13}v_1+A_{23}v_2+A_{33}v_3\end{bmatrix},\\ w_i &= v_k^T A_{ki}.\end{aligned} \tag{A.41}$$

The following properties of the tensor contraction product can be derived from the definition in Eq. (A.39) [16]:

- it is associative (the grouping of the operands can be interchanged)

$$\mathbf{A}\cdot(\mathbf{B}\cdot\mathbf{C})=(\mathbf{A}\cdot\mathbf{B})\cdot\mathbf{C},\quad A_{ij}\left(B_{jk}C_{kl}\right)=\left(A_{ij}B_{jk}\right)C_{kl}. \tag{A.42}$$

- it is distributive over vector addition

$$\mathbf{A}\cdot(\mathbf{B}+\mathbf{C})=\mathbf{A}\cdot\mathbf{B}+\mathbf{A}\cdot\mathbf{C},\quad A_{ij}\left(B_{jk}+C_{jk}\right)=A_{ij}B_{jk}+A_{ij}C_{jk}. \tag{A.43}$$

- it commutes with scaling of either of its factors (the grouping of the operands with a scalar constant (k) is arbitrary)

$$k\left(\mathbf{A}\cdot\mathbf{B}\right)=\left(k\mathbf{A}\right)\cdot\mathbf{B}=\mathbf{A}\cdot\left(k\mathbf{B}\right),\quad k\left(A_{ij}B_{jk}\right)=\left(kA_{ij}\right)B_{jk}=A_{ij}\left(kB_{jk}\right). \tag{A.44}$$

The tensor contraction product is not commutative.

Example problem—prove $(\mathbf{A}\cdot\mathbf{B})^T = \mathbf{B}^T\cdot\mathbf{A}^T$

We wish to prove that the transpose of a contraction product of two tensors is the contraction product of the two tensor transposes. Let $\mathbf{C} = \mathbf{A}\cdot\mathbf{B}$. Then, using index notation,

$$C_{ij} = A_{im}B_{mj}, \quad C^T_{ij} = C_{ji} = A_{jm}B_{mi}. \tag{A.45}$$

But $A^T_{mj} = A_{jm}$ and $B^T_{im} = B_{mi}$, which, when applied to the second expression in Eq. (A.45), implies

$$C^T_{ij} = B^T_{im}A^T_{mj}, \tag{A.46}$$

or $\mathbf{C}^T = (\mathbf{A}\cdot\mathbf{B})^T = \mathbf{B}^T\cdot\mathbf{A}^T$.

In Section A.4 we defined the transpose as the matrix representation of a second order tensor obtained by exchanging the tensor indices. To continue the current example, we introduce a stricter definition [6,209] of the transpose embodied in the equation

$$\mathbf{v}\cdot\left(\mathbf{T}^T\cdot\mathbf{w}\right) = (\mathbf{T}\cdot\mathbf{v})\cdot\mathbf{w}, \quad v_i T^T_{ij} w_j = T_{ij}v_j w_i, \tag{A.47}$$

where $\mathbf{T}$ is a second order tensor, and $\mathbf{v}$ and $\mathbf{w}$ are vectors.

Let $\mathbf{T} = \mathbf{A}\cdot\mathbf{B}$, $T_{ij} = A_{im}B_{mj}$. Then from Eq. (A.47),

$$\mathbf{v}\cdot\left[(\mathbf{A}\cdot\mathbf{B})^T\cdot\mathbf{w}\right] = (\mathbf{A}\cdot\mathbf{B}\cdot\mathbf{v})\cdot\mathbf{w}, \quad v_i\left(A_{im}B_{mj}\right)^T w_j = A_{im}B_{mj}v_j w_i. \tag{A.48}$$

If we apply Eq. (A.47) (twice) and the associative law (Eq. (A.42)) to the right-hand side of Eq. (A.48) (first, $\mathbf{B}\cdot\mathbf{v}$ replaces the vector $\mathbf{v}$ in Eq. (A.47), then $\mathbf{B}$ replaces the tensor $\mathbf{T}$ and $\mathbf{A}^T\cdot\mathbf{w}$ replaces the vector $\mathbf{w}$) and so

$$\begin{aligned}\left[\mathbf{A}\cdot(\mathbf{B}\cdot\mathbf{v})\right]\cdot\mathbf{w} = (\mathbf{B}\cdot\mathbf{v})\cdot\left(\mathbf{A}^T\cdot\mathbf{w}\right) = \mathbf{v}\cdot\left[\left(\mathbf{B}^T\cdot\mathbf{A}^T\right)\cdot\mathbf{w}\right],\\ A_{im}\left(B_{mj}v_j\right)w_i = \left(B_{mj}v_j\right)\left(A^T_{mi}w_i\right) = v_j\left[\left(B^T_{jm}A^T_{mi}\right)w_i\right].\end{aligned} \tag{A.49}$$

Combining Eqs. (A.48) and (A.49) yields

$$\mathbf{v}\cdot\left[(\mathbf{A}\cdot\mathbf{B})^T\cdot\mathbf{w}\right] = \mathbf{v}\cdot\left[\left(\mathbf{B}^T\cdot\mathbf{A}^T\right)\cdot\mathbf{w}\right], \quad v_i\left(A_{im}B_{mj}\right)^T w_j = v_j\left[\left(B^T_{jm}A^T_{mi}\right)w_i\right], \tag{A.50}$$

or, once more, $(\mathbf{A}\cdot\mathbf{B})^T = \mathbf{B}^T\cdot\mathbf{A}^T$.

A.4.1.5 Tensor and matrix operations

A word is in order before leaving this section. Particularly with regard to the tensor contraction product, the operations performed in Eqs. (A.39) and (A.41) are identical to the operations one would perform in multiplying matrices. Although the convenience of matrix manipulations can be used with tensors, not all matrices are tensors. Tensors

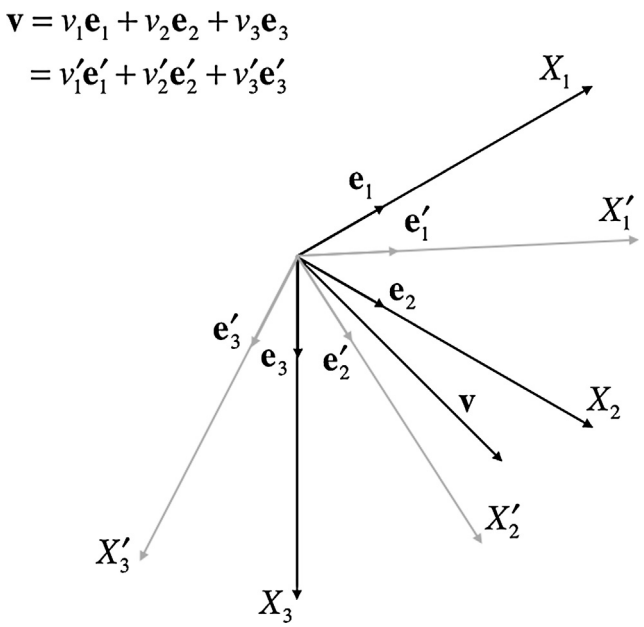

Figure A.6 ***Coordinate transformation of a vector.*** The primed axes and base unit vectors are shown gray to aid in distinguishing coordinates.

differ from matrices in that they obey transformation rules that a matrix may violate [15,210].

A.5. COORDINATE TRANSFORMATION

It frequently becomes necessary to reexpress the components of a tensor in one coordinate system in terms of a second coordinate system, where the relation between the two coordinate systems is known.

A.5.1 Transformation of vectors

Consider Fig. A.6 which illustrates a vector $\mathbf{v}$ and two distinct coordinate systems.

According to Eq. (A.1), we can write

$$\mathbf{v} = v_1\mathbf{e}_1 + v_2\mathbf{e}_2 + v_3\mathbf{e}_3 = v_i\mathbf{e}_i, \tag{A.51}$$

or

$$\mathbf{v} = v'_1\mathbf{e}'_1 + v'_2\mathbf{e}'_2 + v'_3\mathbf{e}'_3 = v'_i\mathbf{e}'_i. \tag{A.52}$$

In Eqs. (A.51) and (A.52) $\mathbf{v}$ refers to the same vector—it is simply being referenced to two separate coordinate systems.

To determine the components of $\mathbf{v}$ in the primed coordinate system in terms of the components of $\mathbf{v}$ in the unprimed system, we recall that the ith component of a vector is the dot product of the vector with the base unit vector of the ith axis (see Section A.4), i.e.,

$$v'_i = \mathbf{v} \cdot \mathbf{e}'_i = \left(v_j \mathbf{e}_j\right) \cdot \mathbf{e}'_i = v_j \left(\mathbf{e}'_i \cdot \mathbf{e}_j\right), \tag{A.53}$$

where we have used Eqs. (A.5) and (A.7), respectively, to reorder and regroup terms. Introducing the coordinate transformation matrix $\mathbf{L}$ gives

$$v'_i = \left(\mathbf{e}'_i \cdot \mathbf{e}_j\right) v_j = L_{ij} v_j, \quad L_{ij} = \mathbf{e}'_i \cdot \mathbf{e}_j. \tag{A.54}$$

The coordinate transformation matrix is not a (second order) tensor.[8]

Recognizing that Eq. (A.54) is valid for each component of $\mathbf{v}$ in the primed coordinate system, we can summarize

$$\mathbf{v}' = \mathbf{L} \cdot \mathbf{v}, \quad v'_i = L_{ij} v_j, \tag{A.55}$$

where $\mathbf{v}' = \mathbf{v}$, $\mathbf{v}'$ simply being $\mathbf{v}$ referred to in a different coordinate system. Explicitly

$$\begin{bmatrix} v'_1 \\ v'_2 \\ v'_3 \end{bmatrix} = \begin{bmatrix} L_{11} & L_{12} & L_{13} \\ L_{21} & L_{22} & L_{23} \\ L_{31} & L_{32} & L_{33} \end{bmatrix} \begin{bmatrix} v_1 \\ v_2 \\ v_3 \end{bmatrix} = \begin{bmatrix} \mathbf{e}'_1 \cdot \mathbf{e}_1 & \mathbf{e}'_1 \cdot \mathbf{e}_2 & \mathbf{e}'_1 \cdot \mathbf{e}_3 \\ \mathbf{e}'_2 \cdot \mathbf{e}_1 & \mathbf{e}'_2 \cdot \mathbf{e}_2 & \mathbf{e}'_2 \cdot \mathbf{e}_3 \\ \mathbf{e}'_3 \cdot \mathbf{e}_1 & \mathbf{e}'_3 \cdot \mathbf{e}_2 & \mathbf{e}'_3 \cdot \mathbf{e}_3 \end{bmatrix} \begin{bmatrix} v_1 \\ v_2 \\ v_3 \end{bmatrix}, \tag{A.56}$$

or, since the $\mathbf{e}_i$ and $\mathbf{e}'_i$ both have a magnitude of one, from Eq. (A.9)

$$\begin{bmatrix} v'_1 \\ v'_2 \\ v'_3 \end{bmatrix} = \begin{bmatrix} \cos\theta_{1'1} & \cos\theta_{1'2} & \cos\theta_{1'3} \\ \cos\theta_{2'1} & \cos\theta_{2'2} & \cos\theta_{2'3} \\ \cos\theta_{3'1} & \cos\theta_{3'2} & \cos\theta_{3'3} \end{bmatrix} \begin{bmatrix} v_1 \\ v_2 \\ v_3 \end{bmatrix}, \tag{A.57}$$

where θ_{ij} is the angle between the ith primed axis and jth unprimed axis.

The inverse transformation—from the primed to the unprimed system—follows directly from Eqs. (A.53) and (A.54) by exchanging primed and unprimed quantities, i.e.,

$$v_i = \left(\mathbf{e}_i \cdot \mathbf{e}'_j\right) v'_j = L_{ji} v'_j = L^T_{ij} v'_j, \tag{A.58}$$

where L_{ij} is defined in Eq. (A.54). Again, recognizing that Eq. (A.58) is valid for each component of $\mathbf{v}$ in the unprimed coordinate system,

$$\mathbf{v} = \mathbf{L}^T \cdot \mathbf{v}', \quad v_i = L^T_{ij} v'_j, \tag{A.59}$$

[8] The matrix $\mathbf{L}$ maps the components of a vector in one coordinate system into the component of the same vector in another coordinate system. The contraction product of a second order tensor and a vector $\mathbf{v}$ maps $\mathbf{v}$ into a different vector.

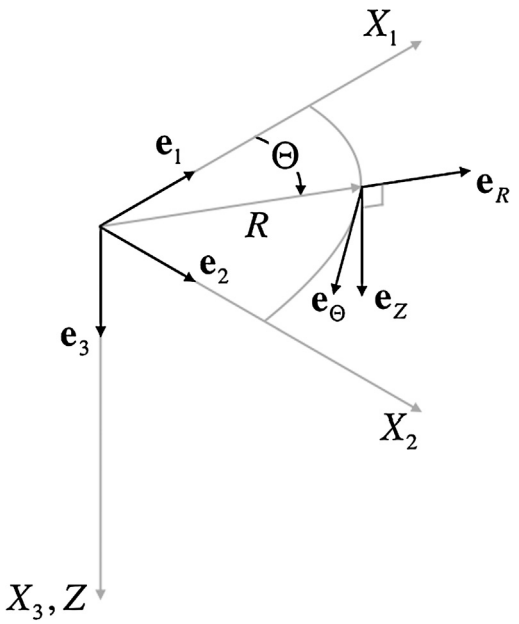

Figure A.7 ***A cylindrical coordinate system superimposed on the global coordinate system.***

or explicitly

$$\begin{bmatrix} v_1 \\ v_2 \\ v_3 \end{bmatrix} = \begin{bmatrix} \cos\theta_{1'1} & \cos\theta_{2'1} & \cos\theta_{3'1} \\ \cos\theta_{1'2} & \cos\theta_{2'2} & \cos\theta_{3'2} \\ \cos\theta_{1'3} & \cos\theta_{2'3} & \cos\theta_{3'3} \end{bmatrix} \begin{bmatrix} v'_1 \\ v'_2 \\ v'_3 \end{bmatrix}. \tag{A.60}$$

A.5.1.1 Example problem—vector components in cylindrical coordinates

Fig. A.7 is a duplicate of Fig. 3.6 in Chapter 3. We wish to express the cylindrical coordinate[9] (R, Θ, Z) components of a vector $\mathbf{v}$ in terms of its X_1, X_2 and X_3 components in the rectangular system.

Let the cylindrical coordinates be the primed system in this calculation. That is,

$$\mathbf{e}'_1 = \mathbf{e}_R, \quad \mathbf{e}'_2 = \mathbf{e}_\Theta, \quad \mathbf{e}'_3 = \mathbf{e}_Z. \tag{A.61}$$

From Fig. A.7 we get

$$\cos\theta_{1'1} = \cos\theta_{11'} = \mathbf{e}_R \cdot \mathbf{e}_1 = \cos\Theta,$$
$$\cos\theta_{1'2} = \cos\theta_{21'} = \mathbf{e}_R \cdot \mathbf{e}_2 = \sin\Theta,$$

[9] See Section 3.6 of Chapter 3 for a detailed description of the cylindrical coordinate system.

$$\begin{aligned}
\cos\theta_{1'3} &= \cos\theta_{31'} = \mathbf{e}_R \cdot \mathbf{e}_3 = 0,\\
\cos\theta_{2'1} &= \cos\theta_{12'} = \mathbf{e}_\Theta \cdot \mathbf{e}_1 = -\sin\Theta,\\
\cos\theta_{2'2} &= \cos\theta_{22'} = \mathbf{e}_\Theta \cdot \mathbf{e}_2 = \cos\Theta,\\
\cos\theta_{2'3} &= \cos\theta_{32'} = \mathbf{e}_\Theta \cdot \mathbf{e}_3 = 0,\\
\cos\theta_{3'1} &= \cos\theta_{13'} = \mathbf{e}_Z \cdot \mathbf{e}_1 = 0,\\
\cos\theta_{3'2} &= \cos\theta_{23'} = \mathbf{e}_Z \cdot \mathbf{e}_2 = 0,\\
\cos\theta_{3'3} &= \cos\theta_{33'} = \mathbf{e}_Z \cdot \mathbf{e}_3 = 1.
\end{aligned} \tag{A.62}$$

From Eq. A.57 therefore

$$\begin{bmatrix} v_R \\ v_\Theta \\ v_Z \end{bmatrix} = \begin{bmatrix} \cos\Theta & \sin\Theta & 0 \\ -\sin\Theta & \cos\Theta & 0 \\ 0 & 0 & 1 \end{bmatrix} \begin{bmatrix} v_1 \\ v_2 \\ v_3 \end{bmatrix}, \tag{A.63}$$

or

$$v_R = v_1\cos\Theta + v_2\sin\Theta, \quad v_\Theta = -v_1\sin\Theta + v_2\cos\Theta, \quad v_Z = v_3. \tag{A.64}$$

The appearance of the minus sign in Eqs. (A.62)–(A.64) is more clearly seen in Fig. A.8 which views the coordinate transformation from above, that is, along a line-of-sight parallel to the X_3, Z-axis.

The inverse transformation follows in similar fashion. From Eq. (A.60) we have

$$\begin{bmatrix} v_1 \\ v_2 \\ v_3 \end{bmatrix} = \begin{bmatrix} \cos\Theta & -\sin\Theta & 0 \\ \sin\Theta & \cos\Theta & 0 \\ 0 & 0 & 1 \end{bmatrix} \begin{bmatrix} v_R \\ v_\Theta \\ v_Z \end{bmatrix}, \tag{A.65}$$

or

$$v_1 = v_R\cos\Theta - v_\Theta\sin\Theta, \quad v_2 = v_R\sin\Theta + v_\Theta\cos\Theta, \quad v_Z = v_3. \tag{A.66}$$

A.5.1.2 Example problem—compute $\mathbf{L}^T \cdot \mathbf{L}$

For future use, we wish to evaluate the contraction product $L^T L$. We do so by noting from Eq. (A.55) that

$$\mathbf{L}^T \cdot \mathbf{v}' = \mathbf{L}^T \cdot \mathbf{L} \cdot \mathbf{v}, \quad L^T_{ki} v'_i = L^T_{ki} L_{ij} v_j, \tag{A.67}$$

but, from Eq. (A.59), $\mathbf{L}^T \cdot \mathbf{v}' = \mathbf{v}$, so

$$\mathbf{v} = \mathbf{L}^T \cdot \mathbf{L} \cdot \mathbf{v}, \quad v_k = L^T_{ki} L_{ij} v_j, \tag{A.68}$$

or

$$\left(\mathbf{I} - \mathbf{L}^T \cdot \mathbf{L}\right) \cdot \mathbf{v} = \mathbf{0}, \quad \left(\delta_{kj} - L^T_{ki} L_{ij}\right) v_j = 0, \tag{A.69}$$

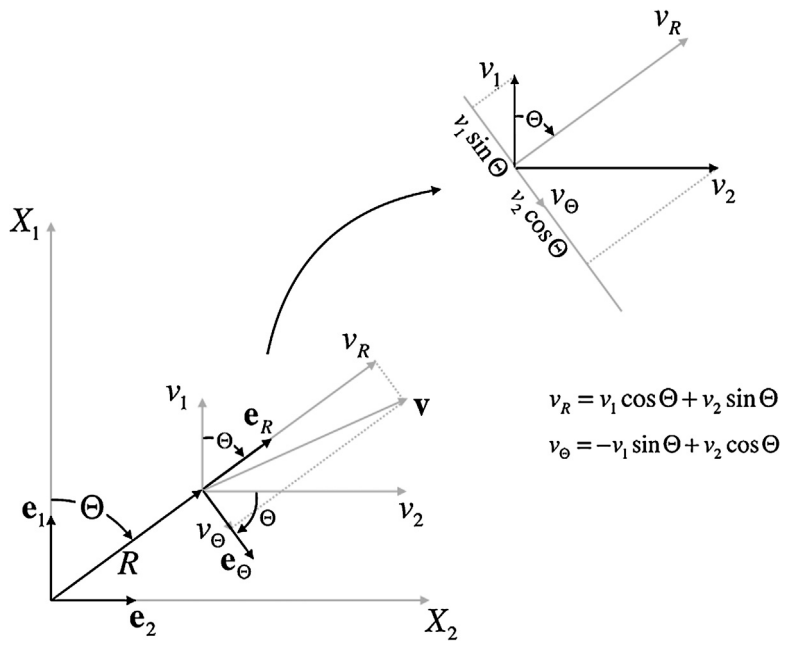

Figure A.8 ***A cylindrical coordinate system viewed down the*** X_3***, Z-axis .*** The v_R component of $\mathbf{v}$ is obtained by adding the v_1 and v_2 projections onto the R-axis. The v_Θ component of $\mathbf{v}$ is diminished by the v_1 projection along $\mathbf{e}_\Theta$.

where $\mathbf{I}$ is the identity matrix whose elements are 1 along its diagonal and 0 elsewhere. We conclude that

$$\mathbf{L}^T \cdot \mathbf{L} = \mathbf{I}, \quad L_{ki}^T L_{ij} = \delta_{kj}, \tag{A.70}$$

or, $\mathbf{L}^T = \mathbf{L}^{-1}$, where $\mathbf{L}^{-1}$ is the inverse of $\mathbf{L}$, that is, the matrix which, when multiplied by $\mathbf{L}$, equals $\mathbf{I}$. A matrix where $\mathbf{L}^T = \mathbf{L}^{-1}$ is termed orthogonal, as either its rows or its columns are orthogonal unit vectors.

The same line of reasoning allows us to write $\mathbf{v} = \mathbf{L}^T \mathbf{v}'$ from Eq. (A.59), or $\mathbf{L} \cdot \mathbf{v} = \mathbf{L} \cdot \mathbf{L}^T \cdot \mathbf{v}' = \mathbf{v}'$ implying

$$\mathbf{L} \cdot \mathbf{L}^T = \mathbf{I}, \quad L_{ki} L_{ij}^T = \delta_{kj}. \tag{A.71}$$

A.5.2 Transformation of second order tensors

Consider the contraction product

$$\mathbf{v} = \mathbf{T} \cdot \mathbf{w}, \quad v_i = T_{ij} w_j, \tag{A.72}$$

where $\mathbf{v}$ and $\mathbf{w}$ are vectors and $\mathbf{T}$ is a second order tensor. In a second, primed coordinate system, we can write

$$\mathbf{v}' = \mathbf{T}' \cdot \mathbf{w}', \quad v_i' = T_{ij}' w_j', \tag{A.73}$$

where $\mathbf{v}' = \mathbf{v}$ and $\mathbf{w}' = \mathbf{w}$. In order to relate $\mathbf{T}'$ to $\mathbf{T}$, we make use of Eq. (A.59) to rewrite Eq. (A.72) as

$$\mathbf{L}^T \cdot \mathbf{v}' = \mathbf{T} \cdot \mathbf{L}^T \cdot \mathbf{w}', \quad L_{ij}^T v_j' = T_{ij}' L_{jk} w_k', \tag{A.74}$$

where $\mathbf{L}$ is the coordinate transformation matrix defined in Eq. (A.54). Using Eq. (A.73) on the left-hand side of Eq. (A.74) yields

$$\mathbf{L}^T \cdot \mathbf{T}' \cdot \mathbf{w}' = \mathbf{T} \cdot \mathbf{L}^T \cdot \mathbf{w}', \quad L_{ij}^T T_{jl}' w_l' = T_{ij}' L_{jk}^T w_k'. \tag{A.75}$$

Premultiplying both sides of Eq. (A.75) by $\mathbf{L}$, we obtain

$$\mathbf{L} \cdot \mathbf{L}^T \mathbf{T}' \cdot \mathbf{w}' = \mathbf{L} \cdot \mathbf{T} \cdot \mathbf{L}^T \cdot \mathbf{w}', \quad L_{mi} L_{ij}^T T_{jl}' w_l' = L_{mi} T_{ij}' L_{jk}^T w_k', \tag{A.76}$$

and recalling (Section A.5.1.2) that $\mathbf{L}^T = \mathbf{L}^{-1}$ produces

$$\left(\mathbf{T}' - \mathbf{L} \cdot \mathbf{T} \cdot \mathbf{L}^T\right) \cdot \mathbf{w}' = \mathbf{0}, \quad \left(T_{mk}' - L_{mi} T_{ij} L_{jk}^T\right) w_k' = 0, \tag{A.77}$$

which leads to the conclusion

$$\mathbf{T}' = \mathbf{L} \cdot \mathbf{T} \cdot \mathbf{L}^T, \quad T_{mk}' = L_{mi} T_{ij} L_{jk}^T. \tag{A.78}$$

A similar argument could be used to arrive at the inverse transformation relating $\mathbf{T}$ to $\mathbf{T}'$. Alternately, and again recalling (Section A.5.1.2) that $\mathbf{L}^T = \mathbf{L}^{-1}$, we can premultiply both sides of Eq. (A.78) by $\mathbf{L}^T$ and postmultiply both sides by $\mathbf{L}$ with the result

$$\mathbf{T} = \mathbf{L}^T \cdot \mathbf{T}' \cdot \mathbf{L}, \quad T_{mk} = L_{mi}^T T_{ij}' L_{jk}. \tag{A.79}$$

A.5.2.1 Example problem—second order tensor physical components in cylindrical coordinates

The coordinate transformation matrix calculated in Section A.5.1.1 is unchanged. To express the cylindrical coordinate (R, Θ, Z) physical components of a second order tensor $\mathbf{T}$ in terms of its X_1, X_2 and X_3 components in the rectangular system, we may, due to Eq. (A.78), write

$$\begin{bmatrix} T_{RR} & T_{R\Theta} & T_{RZ} \\ T_{\Theta R} & T_{\Theta\Theta} & T_{\Theta Z} \\ T_{ZR} & T_{Z\Theta} & T_{ZZ} \end{bmatrix} = \begin{bmatrix} \cos\Theta & \sin\Theta & 0 \\ -\sin\Theta & \cos\Theta & 0 \\ 0 & 0 & 1 \end{bmatrix} \begin{bmatrix} T_{11} & T_{12} & T_{13} \\ T_{21} & T_{22} & T_{23} \\ T_{31} & T_{32} & T_{33} \end{bmatrix} \begin{bmatrix} \cos\Theta & -\sin\Theta & 0 \\ \sin\Theta & \cos\Theta & 0 \\ 0 & 0 & 1 \end{bmatrix}, \tag{A.80}$$

or, carrying out the indicated multiplications,

$$\begin{aligned}
T_{RR} &= T_{11}\cos^2\Theta + (T_{12}+T_{21})\sin\Theta\cos\Theta + T_{22}\sin^2\Theta,\\
T_{R\Theta} &= -(T_{11}-T_{22})\sin\Theta\cos\Theta + T_{12}\cos^2\Theta - T_{21}\sin^2\Theta,\\
T_{RZ} &= T_{13}\cos\Theta + T_{23}\sin\Theta,\\
T_{\Theta R} &= -(T_{11}-T_{22})\sin\Theta\cos\Theta - T_{12}\sin^2\Theta + T_{21}\cos^2\Theta,\\
T_{\Theta\Theta} &= T_{11}\sin^2\Theta - (T_{12}+T_{21})\sin\Theta\cos\Theta + T_{22}\cos^2\Theta,\\
T_{\Theta Z} &= -T_{13}\sin\Theta + T_{23}\cos\Theta,\\
T_{ZR} &= T_{31}\cos\Theta + T_{32}\sin\Theta,\\
T_{Z\Theta} &= -T_{31}\sin\Theta + T_{32}\cos\Theta,\\
T_{ZZ} &= T_{33}.
\end{aligned} \tag{A.81}$$

If $\mathbf{T}$ is symmetric ($\mathbf{T}^T = \mathbf{T},\ T_{ij} = T_{ji}$), Eq. (A.81) simplifies to

$$\begin{aligned}
T_{RR} &= T_{11}\cos^2\Theta + T_{12}\sin 2\Theta + T_{22}\sin^2\Theta,\\
T_{R\Theta} &= -(T_{11}-T_{22})\sin\Theta\cos\Theta + T_{12}\cos 2\Theta = T_{\Theta R},\\
T_{RZ} &= T_{13}\cos\Theta + T_{23}\sin\Theta = T_{ZR},\\
T_{\Theta\Theta} &= T_{11}\sin^2\Theta - T_{12}\sin 2\Theta + T_{22}\cos^2\Theta,\\
T_{\Theta Z} &= -T_{13}\sin\Theta + T_{23}\cos\Theta = T_{Z\Theta},\\
T_{ZZ} &= T_{33}.
\end{aligned} \tag{A.82}$$

The inverse transformation follows in a similar fashion. From Eq. (A.79),

$$\begin{bmatrix} T_{11} & T_{12} & T_{13}\\ T_{21} & T_{22} & T_{23}\\ T_{31} & T_{32} & T_{33}\end{bmatrix} = \begin{bmatrix} \cos\Theta & -\sin\Theta & 0\\ \sin\Theta & \cos\Theta & 0\\ 0 & 0 & 1\end{bmatrix}\begin{bmatrix} T_{RR} & T_{R\Theta} & T_{RZ}\\ T_{\Theta R} & T_{\Theta\Theta} & T_{\Theta Z}\\ T_{ZR} & T_{Z\Theta} & T_{ZZ}\end{bmatrix}\begin{bmatrix} \cos\Theta & \sin\Theta & 0\\ -\sin\Theta & \cos\Theta & 0\\ 0 & 0 & 1\end{bmatrix}, \tag{A.83}$$

or

$$\begin{aligned}
T_{11} &= T_{RR}\cos^2\Theta - (T_{R\Theta}+T_{\Theta R})\sin\Theta\cos\Theta + T_{\Theta\Theta}\sin^2\Theta,\\
T_{12} &= (T_{RR}-T_{\Theta\Theta})\sin\Theta\cos\Theta + T_{R\Theta}\cos^2\Theta - T_{\Theta R}\sin^2\Theta,\\
T_{13} &= T_{RZ}\cos\Theta - T_{\Theta Z}\sin\Theta,\\
T_{21} &= (T_{RR}-T_{\Theta\Theta})\sin\Theta\cos\Theta - T_{R\Theta}\sin^2\Theta + T_{\Theta R}\cos^2\Theta,\\
T_{22} &= T_{RR}\sin^2\Theta + (T_{R\Theta}+T_{\Theta R})\sin\Theta\cos\Theta + T_{\Theta\Theta}\cos^2\Theta,\\
T_{23} &= T_{RZ}\sin\Theta + T_{\Theta Z}\cos\Theta,\\
T_{31} &= T_{ZR}\cos\Theta - T_{Z\Theta}\sin\Theta,
\end{aligned} \tag{A.84}$$

$$T_{32} = T_{ZR}\sin\Theta + T_{Z\Theta}\cos\Theta,$$
$$T_{33} = T_{ZZ}.$$

If $\mathbf{T}$ is symmetric ($\mathbf{T}^T = \mathbf{T}$, $T_{R\Theta} = T_{\Theta R}$, $T_{\Theta Z} = T_{Z\Theta}$, $T_{ZR} = T_{RZ}$), Eq. (A.84) simplifies to

$$T_{11} = T_{RR}\cos^2\Theta - T_{R\Theta}\sin 2\Theta + T_{\Theta\Theta}\sin^2\Theta, \tag{A.85}$$
$$T_{12} = (T_{RR} - T_{\Theta\Theta})\sin\Theta\cos\Theta + T_{R\Theta}\cos 2\Theta = T_{21}, \tag{A.86}$$
$$T_{13} = T_{RZ}\cos\Theta - T_{\Theta Z}\sin\Theta = T_{31}, \tag{A.87}$$
$$T_{22} = T_{RR}\sin^2\Theta + T_{R\Theta}\sin 2\Theta + T_{\Theta\Theta}\cos^2\Theta, \tag{A.88}$$
$$T_{23} = T_{RZ}\sin\Theta + T_{\Theta Z}\cos\Theta = T_{32}, \tag{A.89}$$
$$T_{33} = T_{ZZ}. \tag{A.90}$$

A.5.2.2 Scalar invariants of second order tensors

Imagine a function of the components of a second order tensor that does not change with coordinate transformation. Then from Eq. (A.78) the operation $\mathbf{T}' = \mathbf{L}\mathbf{T}\mathbf{L}^T$ does not change the value of the function. Three such invariants are illustrated below.

The first scalar invariant—trace

The first invariant, or trace, of a second order tensor is the sum of the diagonal terms

$$I_1 = \mathrm{tr}\{\mathbf{T}\}, \quad I_1 = T_{jj}. \tag{A.91}$$

Consider the coordinate transformation of Eq. (A.78). Employing index notation and contracting the two indices of $\mathbf{T}$,

$$\delta_{mk}T'_{mk} = \delta_{mk}L_{mi}T_{ij}L^T_{jk}, \tag{A.92}$$

or, using Eq. (A.70),

$$T'_{kk} = L_{ki}T_{ij}L^T_{jk} = L^T_{jk}L_{ki}T_{ij} = \delta_{ji}T_{ij} = T_{ii}, \tag{A.93}$$

that is, following coordinate transformation, $T'_{kk} = T_{ii}$.

The second scalar invariant

The second scalar invariant of a second order tensor is defined by[10]

$$I_2 = \frac{1}{2}\left[T_{rs}T_{rs} - (T_{kk})^2\right]. \tag{A.94}$$

[10] As out-of-nowhere as this invariant appears, it plays a prominent role in the analysis of inelastic deformation. See Chapter 6.

Once more appealing to Eq. (A.78),

$$\frac{1}{2}\left[\delta_{mr}\delta_{ns}T'_{mn}T'_{rs}-I_1^2\right]=\frac{1}{2}\left[\delta_{mr}\delta_{ns}L_{mi}T_{ij}L^T_{jn}L_{rp}T_{pq}L^T_{qs}-I_1^2\right], \tag{A.95}$$

which uses the result of the previous section on I_1. Simplifying using Eq. (A.70) and the fact that $L_{ri}L_{rp}=L^T_{ir}L_{rp}=\delta_{ip}$ yields

$$\begin{aligned}\frac{1}{2}\left[T'_{rs}T'_{rs}-I_1^2\right]&=\frac{1}{2}\left[L_{ri}T_{ij}L^T_{js}L_{rp}T_{pq}L^T_{qs}-I_1^2\right]\\&=\frac{1}{2}\left[\delta_{ip}\delta_{jq}T_{ij}T_{pq}-I_1^2\right]\\&=\frac{1}{2}\left[T_{pq}T_{pq}-I_1^2\right].\end{aligned} \tag{A.96}$$

As was the case with I_1, the form and value of I_2 following a coordinate transformation are unchanged.

The third scalar invariant—determinant

Of the variety of ways the determinant can be expressed, the one which meets our current needs best is

$$I_3=\det\mathbf{T},\quad I_3=\frac{1}{6}\varepsilon_{ijk}\varepsilon_{pqr}T_{ip}T_{jq}T_{kr}, \tag{A.97}$$

where ε_{ijk}, the Levi-Civita or permutation symbol, is defined in Eq. (A.19). Using Eq. (A.78) to transform to the primed coordinate system,

$$\frac{1}{6}\varepsilon_{ijk}\varepsilon_{pqr}T'_{ip}T'_{jq}T'_{kr}=\frac{1}{6}\varepsilon_{ijk}\varepsilon_{pqr}L_{im}T_{mn}L^T_{np}L_{js}T_{st}L^T_{tq}L_{ku}T_{uv}L^T_{vr}, \tag{A.98}$$

the left-hand side of which can be simplified if we use the identity

$$\begin{aligned}\varepsilon_{ijk}\varepsilon_{lmn}&=\begin{vmatrix}\delta_{il}&\delta_{im}&\delta_{in}\\\delta_{jl}&\delta_{jm}&\delta_{jn}\\\delta_{kl}&\delta_{km}&\delta_{kn}\end{vmatrix}\\&=\delta_{il}\left(\delta_{jm}\delta_{kn}-\delta_{jn}\delta_{km}\right)-\delta_{im}\left(\delta_{jl}\delta_{kn}-\delta_{jn}\delta_{kl}\right)+\delta_{in}\left(\delta_{jl}\delta_{km}-\delta_{jm}\delta_{kl}\right).\end{aligned} \tag{A.99}$$

Using Eq. (A.99) in (A.98) gives

$$\begin{aligned}\frac{1}{6}\varepsilon_{ijk}\varepsilon_{pqr}T'_{ip}T'_{jq}T'_{kr}=\frac{1}{6}&\left[\delta_{ip}\left(\delta_{jq}\delta_{kr}-\delta_{jr}\delta_{kq}\right)-\delta_{iq}\left(\delta_{jp}\delta_{kr}-\delta_{jr}\delta_{kp}\right)\right.\\&\left.+\delta_{ir}\left(\delta_{jp}\delta_{kq}-\delta_{jq}\delta_{kp}\right)\right]T'_{ip}T'_{jq}T'_{kr}\end{aligned}$$

$$= \frac{1}{6}\left[T'_{ii}\left(T'_{jj}T'_{kk} - 3T'_{jk}T'_{kj}\right) + 2T'_{pq}T'_{qr}T'_{rp}\right]. \tag{A.100}$$
$$= \frac{1}{6}\left[I_1\left(I_1^2 - 3T'_{jk}T'_{kj}\right) + 2T'_{pq}T'_{qr}T'_{rp}\right].$$

Now, applying the coordinate transformation,

$$\begin{aligned}\frac{1}{6}\left[I_1\left(I_1^2 - 3T'_{jk}T'_{kj}\right) + 2T'_{pq}T'_{qr}T'_{rp}\right] &= \frac{1}{6}\left[I_1\left(I_1^2 - 3L_{jp}T_{pq}L^T_{qk}L_{kr}T_{rs}L^T_{sj}\right)\right. \\ &\quad \left. +2L_{pu}T_{uv}L^T_{vq}L_{qm}T_{mn}L^T_{nr}L_{rt}T_{tw}L^T_{wp}\right] \\ &= \frac{1}{6}\left[I_1\left(I_1^2 - 3\delta_{sp}\delta_{qr}T_{pq}T_{rs}\right)\right. \\ &\quad \left. +2\delta_{wu}\delta_{vm}\delta_{nt}T_{uv}T_{mn}T_{tw}\right] \\ &= \frac{1}{6}\left[I_1\left(I_1^2 - 3T_{sr}T_{rs}\right) + 2T_{wv}T_{vn}T_{nw}\right].\end{aligned} \tag{A.101}$$

Comparing left and right-hand sides of Eq. (A.101), the two relations are identical. The form and value of I_3 following a coordinate transformation are unchanged.

A.5.2.3 Eigenvectors of second order tensors

Consider a vector $\mathbf{v}$ and a transformation such that

$$\mathbf{A}\cdot\mathbf{v} = \lambda\mathbf{v}, \quad A_{jk}v_k = \lambda v_j, \tag{A.102}$$

where λ is a scalar. If, for example, $\mathbf{A}$ is a coordinate transformation, Eq. (A.102) implies that for that transformation there exists a vector $\mathbf{v}$ which only lengthens or contracts (by a factor λ) when the transformation is applied. Eq. (A.102) is called the characteristic equation of $\mathbf{A}$.

Rearranging Eq. (A.102),

$$(\mathbf{A} - \lambda\mathbf{I})\cdot\mathbf{v} = \mathbf{0}, \quad \left(A_{jk} - \lambda\delta_{jk}\right)v_k = 0, \tag{A.103}$$

where $\mathbf{0}$ is a vector, all of whose elements are zero, of the same dimension as $\mathbf{v}$. We have also used the fact that $\mathbf{Iv} = \mathbf{v}$, $\mathbf{I}$ being the identity matrix (see Section A.5.1.2).

Provided $\mathbf{v} \neq \mathbf{0}$, then one must have [16] $\det\{\mathbf{A} - \lambda\mathbf{I}\} = 0$, producing an nth order polynomial in λ, some roots of which may be imaginary. The λs solving the polynomial are termed characteristic values, or eigenvalues. When each λ is substituted into Eq. (A.103), the corresponding solution of $\mathbf{v}$ is termed an eigenvector.

In expanded form for a 3×3 tensor, Eq. (A.103) is

$$\begin{bmatrix} A_{11}-\lambda & A_{12} & A_{13} \\ A_{21} & A_{22}-\lambda & A_{23} \\ A_{31} & A_{32} & A_{33}-\lambda \end{bmatrix}\begin{bmatrix} v_1 \\ v_2 \\ v_3 \end{bmatrix} = \begin{bmatrix} 0 \\ 0 \\ 0 \end{bmatrix}, \tag{A.104}$$

which for the case of a 3 × 3 tensor results in a cubic equation for λ which can be written in terms of the invariants of Section A.5.2.2 [210][11]

$$\lambda^3 - I_1\lambda^2 - I_2\lambda - I_3 = 0. \tag{A.105}$$

[11] There is a sign difference between Eq. (A.105) and the equation appearing in Segel [210] as Segel's definition of I_2 is the negative of that given here in Eq. (A.94).

APPENDIX B

The Frenet–Serret Formulas

B.1. GOVERNING EQUATIONS

The recurring appearance of inclined and curved wellbore trajectories suggests the need for a local coordinate system aligned with the well path. We begin with a line (i.e., the centerline of the wellbore) whose path can be described by the continuous and differentiable function

$$\mathbf{p} = \hat{\mathbf{p}}(s), \quad p_i = \hat{p}_i(s), \tag{B.1}$$

where s is distance along the path. The instantaneous unit tangent vector to the path is (see Fig. B.1)

$$\mathbf{t} = \hat{\mathbf{t}}(s) = \frac{d\hat{\mathbf{p}}}{ds}, \quad t_i = \hat{t}_i(s) = \frac{d\hat{p}_i}{ds}. \tag{B.2}$$

The unit normal vector to the path is collinear with the rate of change of the unit tangent vector

$$\mathbf{n} = \hat{\mathbf{n}}(s) = \frac{\frac{d\hat{\mathbf{t}}}{ds}}{|\frac{d\hat{\mathbf{t}}}{ds}|} = \frac{1}{\kappa}\frac{d\hat{\mathbf{t}}}{ds}, \quad n_i = \hat{n}_i(s) = \frac{1}{\kappa}\frac{d\hat{t}_i}{ds}, \tag{B.3}$$

where the curvature κ is a measure of the rate of change of $\mathbf{t}$ and has units of [radians/length]. A useful expression for determining the magnitude of κ follows from combining Eqs. (B.2) and (B.3):

$$\kappa = \left|\frac{d\hat{\mathbf{t}}}{ds}\right| = \sqrt{\frac{d\hat{\mathbf{t}}}{ds}\cdot\frac{d\hat{\mathbf{t}}}{ds}} = \sqrt{\frac{d^2\hat{\mathbf{p}}}{ds^2}\cdot\frac{d^2\hat{\mathbf{p}}}{ds^2}}, \quad \kappa = \left|\frac{d\hat{t}_i}{ds}\right| = \sqrt{\frac{d\hat{t}_i}{ds}\cdot\frac{d\hat{t}_i}{ds}} = \sqrt{\frac{d^2\hat{p}_i}{ds^2}\cdot\frac{d^2\hat{p}_i}{ds^2}}. \tag{B.4}$$

The reciprocal of κ is the radius of curvature.

The vector triad is completed by the unit binormal vector, defined to be the third direction in a right-handed coordinate system, namely

$$\mathbf{b} = \hat{\mathbf{b}}(s) = \hat{\mathbf{t}} \times \hat{\mathbf{n}}, \quad b_i = \varepsilon_{ijk} t_j n_k. \tag{B.5}$$

The derivative of the unit tangent vector is given in Eq. (B.3). Computing the rate of change of $\mathbf{n}$, we use the fact that if $\mathbf{n}$ is a unit vector, $\mathbf{n}\cdot\mathbf{n} = 1$. Differentiating yields

$$\mathbf{n}\cdot\frac{d\mathbf{n}}{ds} = 0, \quad n_i\frac{dn_i}{ds} = 0, \tag{B.6}$$

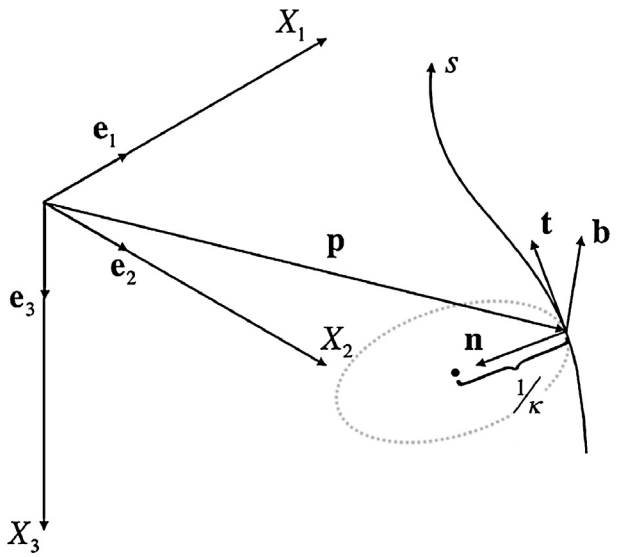

Figure B.1 ***Illustration of tangent, normal and binormal to a space curve.*** The independent variable defining the position vector $\mathbf{p}$ is s.

implying $\frac{d\mathbf{n}}{ds}$ is normal to $\mathbf{n}$ and can be written as a linear combination of unit vectors $\mathbf{t}$ and $\mathbf{b}$ as

$$\frac{d\mathbf{n}}{ds} = K\mathbf{t} + \tau\mathbf{b}, \quad \frac{dn_i}{ds} = Kt_i + \tau b_i, \tag{B.7}$$

where both K and τ are functions of s. For $\mathbf{b}$, differentiating Eq. (B.5) yields

$$\frac{d\mathbf{b}}{ds} = \frac{d}{ds}\left(\hat{\mathbf{t}} \times \hat{\mathbf{n}}\right) = \frac{d\hat{\mathbf{t}}}{ds} \times \hat{\mathbf{n}} + \hat{\mathbf{t}} \times \frac{d\hat{\mathbf{n}}}{ds} = \hat{\mathbf{t}} \times \frac{d\hat{\mathbf{n}}}{ds}, \tag{B.8}$$

since $\frac{d\hat{\mathbf{t}}}{ds} = \kappa\hat{\mathbf{n}}$ by Eq. (B.3). With Eq. (B.7) substituted into Eq. (B.8),

$$\frac{d\mathbf{b}}{ds} = \hat{\mathbf{t}} \times \frac{d\hat{\mathbf{n}}}{ds} = \hat{\mathbf{t}} \times \left(K\hat{\mathbf{t}} + \tau\hat{\mathbf{b}}\right) = \hat{\mathbf{t}} \times \tau\hat{\mathbf{b}} = -\tau\hat{\mathbf{n}}, \quad \frac{db_i}{ds} = -\tau n_i. \tag{B.9}$$

Finally, returning to the unspecified variable K in Eq. (B.7), we can write

$$\frac{d\mathbf{n}}{ds} = K\mathbf{t} + \tau\mathbf{b} = \frac{d}{ds}\left(\mathbf{b} \times \mathbf{t}\right) = \frac{d\mathbf{b}}{ds} \times \mathbf{t} + \mathbf{b} \times \frac{d\mathbf{t}}{ds}, \tag{B.10}$$

or, using Eqs. (B.3) and (B.9),

$$\frac{d\mathbf{n}}{ds} = -\tau\mathbf{n} \times \mathbf{t} + \mathbf{b} \times \kappa\mathbf{n} = -\kappa\mathbf{t} + \tau\mathbf{b}, \quad \frac{dn_i}{ds} = -\kappa t_i + \tau b_i, \tag{B.11}$$

from which, by comparing Eqs. (B.7) and (B.11), we conclude $K = -\kappa$.

The Frenet–Serret formulas consist of the definitions of **t**, **n** and **b** (Eqs. (B.2), (B.3) and (B.5), respectively) and their respective derivatives (Eqs. (B.3), (B.11) and (B.9)).

At any point along the curve $\mathbf{p} = \hat{\mathbf{p}}(s)$ there exists an instantaneous local plane defined by **t** and **n**. In that plane, the instantaneous curvature of the curve is κ; the radius of curvature is $1/\kappa$. The binormal vector **b** is normal to this **t**–**n** plane and, in general, is itself rotating at a rate measured by the torsion $-\tau$ whose units are [radians/length].

B.2. EXAMPLE PROBLEM—INDEX NOTATION

Using index notation, we repeat the derivation of db_i/ds as performed in Eqs. (B.8) and (B.9). In parallel with Eq. (B.8),

$$\frac{db_i}{ds} = \frac{d}{ds}\varepsilon_{ijk}t_j n_k = \varepsilon_{ijk}\left(\frac{dt_j}{ds}n_k + t_j\frac{dn_k}{ds}\right). \tag{B.12}$$

Since, however, $dt_i/ds = \kappa n_i$ (Eq. (B.3)), we have

$$\frac{db_i}{ds} = \varepsilon_{ijk}\left(\kappa n_j n_k + t_j\frac{dn_k}{ds}\right). \tag{B.13}$$

The first term on the right-hand side of Eq. (B.13) is the cross product of a vector with itself, which should vanish. Carrying out the indicated operations and ignoring terms where $j = k$ that are obviously zero, we find

$$\begin{aligned}\varepsilon_{ijk}n_j n_k = {} & \varepsilon_{i12}n_1 n_2 + \varepsilon_{i13}n_1 n_3 + \varepsilon_{i21}n_2 n_1 \\ & + \varepsilon_{i23}n_2 n_3 + \varepsilon_{i31}n_3 n_1 + \varepsilon_{i32}n_3 n_2.\end{aligned} \tag{B.14}$$

In Eq. (B.14), regardless of the value of i, four terms on the right-hand side vanish, and the remaining two contain an even and odd permutation that cancel, confirming that the cross product of a vector with itself is zero.

Using this result in Eq. (B.13) and recalling Eq. (B.7), we may write

$$\frac{db_i}{ds} = \varepsilon_{ijk}t_j\left(Kt_k + \tau b_k\right) = \tau\varepsilon_{ijk}t_j b_k = -\tau n_i, \tag{B.15}$$

where the last step recognizes that the cross product of **t** and **b** (i.e., $\varepsilon_{ijk}t_j b_k$) is $-\mathbf{n}$.

B.3. EXAMPLE PROBLEM—MINIMUM CURVATURE USING THE FRENET–SERRET FORMULAS

Consider a directional survey defining the trajectory of the wellbore. Each survey station is defined by its measured depth, its (inclination) angle with respect to downward vertical

and its (azimuth) angle with respect to North. The character of the wellbore between two survey points is unknown.

To describe a well trajectory as a continuous curve, a number of different models of the inter-station nature of the wellbore have been proposed. Currently, the preferred model is that of Minimum Curvature [211,212,37].

At each survey station, the tangent vector to the well trajectory can be written immediately from the local measurements as

$$\mathbf{t} = \sin\theta\cos\phi\mathbf{e}_1 + \sin\theta\sin\phi\mathbf{e}_2 + \cos\theta\mathbf{e}_3, \tag{B.16}$$

where the unit vectors $\mathbf{e}_1$, $\mathbf{e}_2$ and $\mathbf{e}_3$ are directed along the North, East and TVD (downward vertical) directions, respectively. The normal and binormal vectors cannot readily be determined, as these variables depend on the rates of change of the tangent vectors that, in turn, depend on a knowledge of the nature of the wellbore between successive survey stations. We introduce the Minimum Curvature model that posits a circular arc between two survey stations, the arc being defined by the tangent vectors at the two stations.[1]

Fig. B.2 illustrates the Minimum Curvature model when viewed perpendicular to the plane containing vectors $\mathbf{t}_1$ and $\mathbf{t}_2$. The binormal vector between survey stations 1 and 2 is constant and is given by

$$\mathbf{b} = \frac{\mathbf{t}_1 \times \mathbf{t}_2}{|\mathbf{t}_1 \times \mathbf{t}_2|} = \frac{\mathbf{t}_1 \times \mathbf{t}_2}{\sin\Delta\omega}, \quad b_i = \frac{\varepsilon_{ijk}t_{1j}t_{2k}}{\sin\Delta\omega}. \tag{B.17}$$

The normals at the two stations are respectively given by

$$\mathbf{n}_1 = -\mathbf{t}_1 \times \mathbf{b}, \quad n_{1i} = -\varepsilon_{ijk}t_{1j}b_k, \tag{B.18}$$

$$\mathbf{n}_2 = -\mathbf{t}_2 \times \mathbf{b}, \quad n_{2i} = -\varepsilon_{ijk}t_{2j}b_k, \tag{B.19}$$

or, from Eq. (B.17) (to eliminate $\mathbf{b}$) and the results of Section A.24 of Appendix A,[2]

$$\mathbf{n}_1 = -\cot\Delta\omega\mathbf{t}_1 + \csc\Delta\omega\mathbf{t}_2, \quad n_{1i} = -\cot\Delta\omega t_{1i} + \csc\Delta\omega t_{2i}, \tag{B.20}$$

[1] The Minimum Curvature model produces a well trajectory that is continuous, but not necessarily smooth. Consider three survey stations. Unless the three station tangent vectors are coplanar, the two Minimum Curvature arcs associated with the unit vector pairs $\mathbf{t}_1$–$\mathbf{t}_2$ and $\mathbf{t}_2$–$\mathbf{t}_3$ will not have a continuous space derivative ($d\mathbf{t}/ds$) at station 2, their point of intersection. Both the normal vector and the curvature are therefore undefined at this point.

[2] From Eqs. (B.17) and (B.18), $n_{1i} = -\frac{1}{\sin\Delta\omega}\varepsilon_{ijk}\varepsilon_{kmn}t_{1j}t_{1m}t_{2n}$. From an even permutation of ε_{ijk} and the epsilon–delta identity (Eq. (A.26)), $\varepsilon_{ijk}\varepsilon_{kmn} = \varepsilon_{kij}\varepsilon_{kmn} = \delta_{im}\delta_{jn} - \delta_{in}\delta_{jm}$, such that $n_{1i} = -\frac{1}{\sin\Delta\omega}\left(\delta_{im}\delta_{jn} - \delta_{in}\delta_{jm}\right)t_{1j}t_{1m}t_{2n}$. If we carry out the indicated operations with the Kronecker delta, $n_{1i} = -\frac{1}{\sin\Delta\omega}\left(t_{1j}t_{1i}t_{2j} - t_{1m}t_{1m}t_{2i}\right)$. Since $t_{1j}t_{2j} = \cos\Delta\omega$ and $t_{1m}t_{1m} = 1$, we conclude that $n_{1i} = -\cot\Delta\omega t_{1i} + \csc\Delta\omega t_{2i}$.

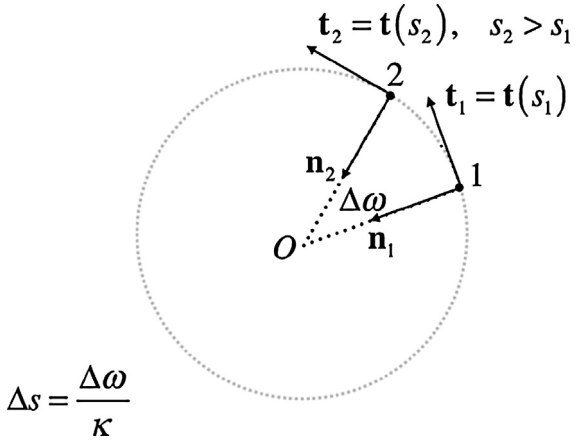

Figure B.2 ***The Minimum Curvature model applied between survey stations 1 and 2.*** The dashed gray circle is coplanar with tangent vectors $\mathbf{t}_1$ and $\mathbf{t}_2$. The segment of the wellbore trajectory *ds* between survey stations 1 and 2 subtends a circular arc whose angle at the center of the circle is $\Delta\omega$.

$$\mathbf{n}_2 = -\csc\Delta\omega\mathbf{t}_1 + \cot\Delta\omega\mathbf{t}_2, \qquad n_{2i} = -\csc\Delta\omega t_{1i} + \cot\Delta\omega t_{2i}. \tag{B.21}$$

Eqs. (B.17)–(B.21) are undefined if $\mathbf{t}_1$ and $\mathbf{t}_2$ are parallel, as $\mathbf{t}_1 \times \mathbf{t}_2$ and therefore $\sin\Delta\omega$ vanish. In this case, the two survey stations may be assumed collinear (a stronger constraint than simply parallel). The normal vectors $\mathbf{n}_1$ and $\mathbf{n}_2$ may be chosen from the infinite set of unit vectors perpendicular to $\mathbf{t}_1$ and $\mathbf{t}_2$, with the binormal vector following from Eq. (B.5).

We now know the tangent, normal and binormal ($\mathbf{b}_1 = \mathbf{b}_2 = \mathbf{b}$) at both ends of the Minimum Curvature circular arc between two successive survey stations. Further, we know[3] $\mathbf{p}_1$, the position vector from the survey datum to survey station 1. The torsion τ is zero, and the (constant) inter-station curvature is

$$\kappa = -\frac{\cos^{-1}(\mathbf{t}_1 \cdot \mathbf{t}_2)}{s_2 - s_1}. \tag{B.22}$$

By one final exercise we can develop a means of interpolating to determine the position of a trajectory point between two survey stations. Consider Fig. B.3 where the measured depth s is between two survey stations, $s_1 \le s \le s_2$, and, in the $\mathbf{t}_1$–$\mathbf{n}_1$ plane, the line $\overline{Os}$ makes an angle $\Delta\alpha$ with $\mathbf{n}_1$.

[3] The calculation is sequential, proceeding in a forward direction. The position vector of station $i+1$ is calculated using the position vector of station i, with the position vector of the first station being given.

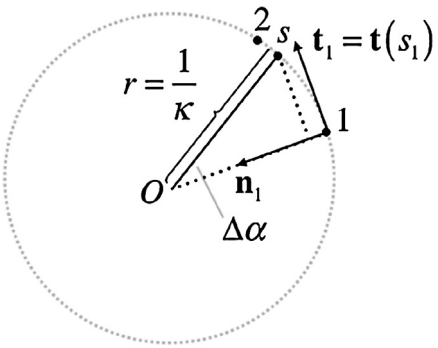

Figure B.3 ***Interpolating between two survey stations with the Minimum Curvature model.***

From Figs. B.2 and B.3, the position vector to s is (see [37])

$$\begin{aligned}\mathbf{p}_s &= \mathbf{p}_1 + \frac{1}{\kappa}\sin\Delta\alpha\mathbf{t}_1 + \frac{1}{\kappa}(1-\cos\Delta\alpha)\mathbf{n}_1 \\ &= \mathbf{p}_1 + \frac{1}{\kappa}[\sin[\kappa(s-s_1)]\mathbf{t}_1 + \{1-\cos[\kappa(s-s_1)]\}\mathbf{n}_1].\end{aligned} \tag{B.23}$$

Differentiating Eq. (B.23) with respect to s, we have

$$\mathbf{t}_s = \frac{\frac{d\mathbf{p}_s}{ds}}{\left|\frac{d\mathbf{p}_s}{ds}\right|} = \cos[\kappa(s-s_1)]\mathbf{t}_1 + \sin[\kappa(s-s_1)]\mathbf{n}_1, \tag{B.24}$$

and recognizing that $\mathbf{b}_s = \mathbf{b}$, we may write

$$\mathbf{n}_s = -\mathbf{t}_s \times \mathbf{b} = -\sin[\kappa(s-s_1)]\mathbf{t}_1 + \cos[\kappa(s-s_1)]\mathbf{n}_1. \tag{B.25}$$

APPENDIX C

Stress State Around a Wellbore

C.1. INTRODUCTION

The discussion below closely follows the work of Peska and Zoback [213] as outlined in Zoback [178]. We use $\mathbf{S}$ to denote the stress state in the global rectangular coordinate system and $\boldsymbol{\Sigma}$ to denote the near wellbore stress in a spatial coordinate system attached to the wellbore. The only transformations considered, however, are those between coordinate systems. This discussion is therefore only applicable to infinitesimal deformation.

We also discuss rock mechanical effective stress that should not be confused with either the von Mises equivalent stress Σ_e or the deviatoric stress $\boldsymbol{\Sigma}'$. We shall distinguish the rock mechanical effective stress by the symbol $\boldsymbol{\Sigma}^e$. For a discussion of the rock mechanical effective stress, see Section 13.3.2.4 of Chapter 13.

C.2. EQUATIONS FOR STRESS

Consider a global rectangular coordinate system where the X_1-axis is North, the X_2-axis is East and the X_3-axis is vertically down. Related to the global system is a second rectangular system defining the directions of the principal stresses, where the X_{p1}-axis aligns with the (algebraic) maximum principal stress,[1] the X_{p2}-axis aligns with the intermediate principal stress, and the X_{p3}-axis aligns with the minimum principal stress.

Finally, consider a cylindrical (r, θ, z) coordinate system aligned with the local tangent to the centerline of the wellbore.[2] The cylindrical coordinate system can be referenced to a third rectangular system, where in the third system the x_1-axis aligns with a radius from the wellbore centerline to the low side of the hole, the x_3-axis aligns with the wellbore centerline and the x_2-axis is such that, considering unit vectors along the three coordinate axes, $\mathbf{g}_1 \times \mathbf{g}_2 = \mathbf{g}_3$. In the (r, θ, z) coordinate system, θ lies in the x_1–x_2 plane and is measured from the x_1-axis to r. The complete set of $\mathbf{X}$, $\mathbf{X}_p$, $\mathbf{x}$ and cylindrical coordinate systems are depicted relative to each other in Fig. C.1.

[1] The maximum principal stress will be the minimum principal stress if, according to the normal convention of rock mechanics, compressive stresses are positive. Aligning the X_{p3}-axis with the minimum principal stress will, in most cases, imply that the X_{p3}-axis most closely conforms to the global X_3-axis.

[2] The discussion below only applies to locally straight wellbores.

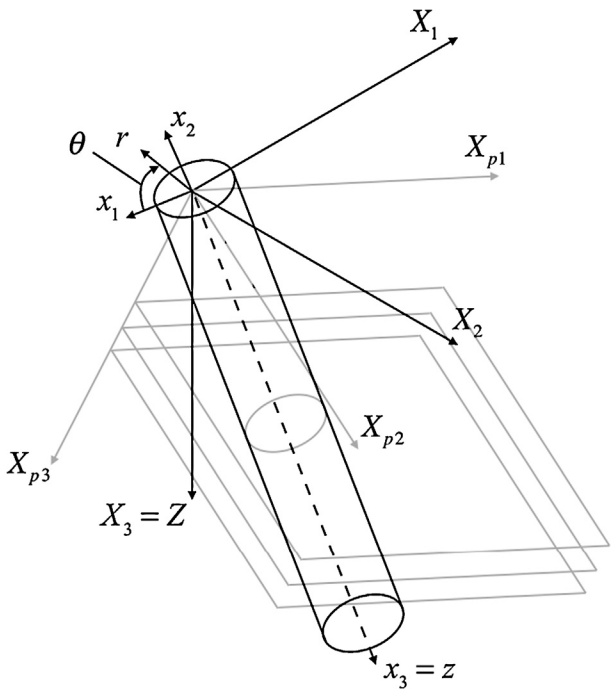

Figure C.1 ***Coordinate systems for analysis of formation stresses at wellbore wall.*** The **X** coordinate system is global and relative to the local surface of the earth. The $\mathbf{X}_p$ coordinate system aligns with the principal stresses in the formation at the depth of investigation. The **x** coordinate system aligns with the (assumed straight) wellbore, as does the (r, θ, z) coordinate system. The three "planes" suggest the planes of near-horizontal stress, and are only included to help interpret the relative orientation of the global and principal stress coordinate systems.

The far field total stress state $\mathbf{S}^p$ in the formation is defined[3] in the $\mathbf{X}_p$ coordinate system as

$$\mathbf{S}^p = \begin{bmatrix} S_1^p & 0 & 0 \\ 0 & S_2^p & 0 \\ 0 & 0 & S_3^p \end{bmatrix}, \tag{C.1}$$

where $0 \geq S_1^p \geq S_2^p \geq S_3^p$, that is, S_3^p is the maximum principal stress in a compressive sense. We first transform these stresses to the global coordinate system using Eq. (A.79)

$$\mathbf{S} = \mathbf{P}^T \cdot \mathbf{S}^p \cdot \mathbf{P}, \quad S_{Mk} = P_{MI}^T S_{Ij}^p P_{jk}. \tag{C.2}$$

[3] We retain the symbol $\mathbf{S}^p$ of the principle Piola–Kirchhoff stress of the first kind for stress states relative to the global $\mathbf{X}$ and $\mathbf{X}_p$ coordinate systems, while we use Cauchy stress $\boldsymbol{\Sigma}$ for the stress state in the spatial coordinate system attached to the wellbore. Recall from Section 4.3.3 of Chapter 4 that for infinitesimal deformations the two stress tensors are indistinguishable.

The transformation embodied in $\mathbf{P}$, and as used by Peska and Zoback [213] actually consists[4] of the following three transformations:

- a rotation[5] α $(0 \le \alpha \le 2\pi)$ about the global X_3-axis from the global (X_1, X_2, X_3) coordinate system to a global (X_1', X_2', X_3') coordinate system

$$\mathbf{P}^{\alpha} = \begin{bmatrix} \mathbf{e}_1' \cdot \mathbf{e}_1 & \mathbf{e}_1' \cdot \mathbf{e}_2 & \mathbf{e}_1' \cdot \mathbf{e}_3 \\ \mathbf{e}_2' \cdot \mathbf{e}_1 & \mathbf{e}_2' \cdot \mathbf{e}_2 & \mathbf{e}_2' \cdot \mathbf{e}_3 \\ \mathbf{e}_3' \cdot \mathbf{e}_1 & \mathbf{e}_3' \cdot \mathbf{e}_2 & \mathbf{e}_3' \cdot \mathbf{e}_3 \end{bmatrix} = \begin{bmatrix} \cos\alpha & \sin\alpha & 0 \\ -\sin\alpha & \cos\alpha & 0 \\ 0 & 0 & 1 \end{bmatrix}, \tag{C.3}$$

  where the $\mathbf{e}_i$ are unit vectors along axes in the global coordinate system, and the $\mathbf{e}_i'$ are unit vectors along axes in the $\mathbf{X}'$ coordinate system;
- a rotation β $(-\frac{\pi}{2} \le \beta \le \frac{\pi}{2})$ about the global X_2'-axis (i.e., the global X_2-axis after the previous rotation about the global X_3-axis) from the global (X_1', X_2', X_3') coordinate system to a global (X_1'', X_2'', X_3'') coordinate system

$$\mathbf{P}^{\beta} = \begin{bmatrix} \mathbf{e}_1'' \cdot \mathbf{e}_1' & \mathbf{e}_1'' \cdot \mathbf{e}_2' & \mathbf{e}_1'' \cdot \mathbf{e}_3' \\ \mathbf{e}_2'' \cdot \mathbf{e}_1' & \mathbf{e}_2'' \cdot \mathbf{e}_2' & \mathbf{e}_2'' \cdot \mathbf{e}_3' \\ \mathbf{e}_3'' \cdot \mathbf{e}_1' & \mathbf{e}_3'' \cdot \mathbf{e}_2' & \mathbf{e}_3'' \cdot \mathbf{e}_3' \end{bmatrix} = \begin{bmatrix} \cos\beta & 0 & -\sin\beta \\ 0 & 1 & 0 \\ \sin\beta & 0 & \cos\beta \end{bmatrix}, \tag{C.4}$$

  where the $\mathbf{e}_i'$ are unit vectors along axes in the $\mathbf{X}'$ coordinate system, and the $\mathbf{e}_i''$ are unit vectors along axes in the $\mathbf{X}''$ coordinate system;
- a rotation γ $(0 \le \gamma \le 2\pi)$ about the global X_1''-axis (i.e., the global X_1'-axis after the two previous rotations about the global X_3-axis and the global X_2'-axis) from the global (X_1'', X_2'', X_3'') coordinate system to the (X_{p1}, X_{p2}, X_{p3}) coordinate system

$$\mathbf{P}^{\gamma} = \begin{bmatrix} \mathbf{e}_1^p \cdot \mathbf{e}_1'' & \mathbf{e}_1^p \cdot \mathbf{e}_2'' & \mathbf{e}_1^p \cdot \mathbf{e}_3'' \\ \mathbf{e}_2^p \cdot \mathbf{e}_1'' & \mathbf{e}_2^p \cdot \mathbf{e}_2'' & \mathbf{e}_2^p \cdot \mathbf{e}_3'' \\ \mathbf{e}_3^p \cdot \mathbf{e}_1'' & \mathbf{e}_3^p \cdot \mathbf{e}_2'' & \mathbf{e}_3^p \cdot \mathbf{e}_3'' \end{bmatrix} = \begin{bmatrix} 1 & 0 & 0 \\ 0 & \cos\gamma & \sin\gamma \\ 0 & -\sin\gamma & \cos\gamma \end{bmatrix}, \tag{C.5}$$

  where the $\mathbf{e}_i''$ are unit vectors along axes in the $\mathbf{X}''$ coordinate system, and the $\mathbf{e}_i^p$ are unit vectors along axes in the principal stress coordinate system.

For the multiple transformations

$$\mathbf{P}^T = \mathbf{P}^{\alpha T} \cdot \mathbf{P}^{\beta T} \cdot \mathbf{P}^{\gamma T}, \tag{C.6}$$

[4] That is, the Peska and Zoback transformation is from the global coordinate system to the coordinate system aligned with the principal stresses, and is the transpose/inverse of the transformation matrix to express the principle stresses in the global coordinate system—compare Eq. (A.78) with Eq. (A.79). Also, review Section A.5.1.2 of Appendix A defining an orthogonal matrix.

[5] All three of the rotations discussed in this bulleted list are positive in the sense of the right-hand rule. For example, the α rotation appears counterclockwise in the X_1–X_2 plane.

or, carrying out the indicated contraction products and then taking the transpose,

$$\mathbf{P}^T = \begin{bmatrix} \cos\alpha\cos\beta & \cos\alpha\sin\beta\sin\gamma - \sin\alpha\cos\gamma & \cos\alpha\sin\beta\cos\gamma + \sin\alpha\sin\gamma \\ \sin\alpha\cos\beta & \sin\alpha\sin\beta\sin\gamma + \cos\alpha\cos\gamma & \sin\alpha\sin\beta\cos\gamma - \cos\alpha\sin\gamma \\ -\sin\beta & \cos\beta\sin\gamma & \cos\beta\cos\gamma \end{bmatrix}. \quad \text{(C.7)}$$

With the principal total stresses transformed to the global rectangular coordinate system, we may now transform the global expression of the stress state to the rectangular system aligned with the wellbore

$$\boldsymbol{\Sigma}^w = \mathbf{G}\cdot\mathbf{S}\cdot\mathbf{G}^T, \quad \Sigma^w_{mk} = G_{mI}S_{Ij}G^T_{jk}, \quad \text{(C.8)}$$

where

$$\mathbf{G} = \begin{bmatrix} \mathbf{g}_1\cdot\mathbf{e}_1 & \mathbf{g}_1\cdot\mathbf{e}_2 & \mathbf{g}_1\cdot\mathbf{e}_3 \\ \mathbf{g}_2\cdot\mathbf{e}_1 & \mathbf{g}_2\cdot\mathbf{e}_2 & \mathbf{g}_2\cdot\mathbf{e}_3 \\ \mathbf{g}_3\cdot\mathbf{e}_1 & \mathbf{g}_3\cdot\mathbf{e}_2 & \mathbf{g}_3\cdot\mathbf{e}_3 \end{bmatrix} = \begin{bmatrix} -\cos\theta'\cos\phi & -\cos\theta'\sin\phi & \sin\theta' \\ \sin\phi & -\cos\phi & 0 \\ \sin\theta'\cos\phi & \sin\theta'\sin\phi & \cos\theta' \end{bmatrix}, \quad \text{(C.9)}$$

where ϕ is the wellbore azimuth (i.e., the angle of the horizontal projection of the tangent to the wellbore trajectory and North), and θ' is the wellbore inclination (a singular exception to our normal unprimed notation for inclination). The $\mathbf{g}_i$ are unit vectors along axes in the wellbore coordinate system, with $\mathbf{g}_3$ directed along the local tangent to the centerline of the wellbore, $\mathbf{g}_1$ perpendicular to $\mathbf{g}_3$ and directed toward the low side of the wellbore and $\mathbf{g}_2$ such that $\mathbf{g}_1\times\mathbf{g}_2 = \mathbf{g}_3$. The unit base vector $\mathbf{g}_2$ is horizontal, lying in the $\mathbf{e}_1$–$\mathbf{e}_2$ plane.

Using Eq. (C.2) in Eq. (C.8),

$$\boldsymbol{\Sigma}^w = \mathbf{G}\cdot\mathbf{P}^T\cdot\mathbf{S}^p\cdot\mathbf{P}\cdot\mathbf{G}^T, \quad \Sigma^w_{rs} = G_{rM}P^T_{MI}S^p_{Ij}P_{jk}G^T_{ks}. \quad \text{(C.10)}$$

In the most general case this equation is unwieldy to evaluate, but lends itself readily to numerical evaluation.

At this point the far field total stress state $\mathbf{S}^p$—originally expressed in a rectangular coordinate system aligned with the directions of principal stress—has been re-expressed in terms of a rectangular coordinate system aligned with the local tangent of the wellbore. The far field total stress state is $\boldsymbol{\Sigma}^w$. Our objective, the total stress state at the wellbore wall, can be expressed in terms of components of $\boldsymbol{\Sigma}^w$ by the following relations (cf. [214,178]):

$$\begin{aligned} \Sigma_{rr} &= -p_f, \\ \Sigma_{\theta\theta} &= \Sigma^w_{11} + \Sigma^w_{22} - 2\left(\Sigma^w_{11} - \Sigma^w_{22}\right)\cos 2\theta - 4\Sigma^w_{12}\sin 2\theta + p_f, \\ \Sigma_{zz} &= \Sigma^w_{33} - \nu\left[2\left(\Sigma^w_{11} - \Sigma^w_{22}\right)\cos 2\theta + 4\Sigma^w_{12}\sin 2\theta\right], \end{aligned} \quad \text{(C.11)}$$

$$\Sigma_{\theta z} = 2\left(-\Sigma_{13}^{w}\sin\theta + \Sigma_{23}^{w}\cos\theta\right),$$
$$\Sigma_{r\theta} = \Sigma_{zr} = 0,$$

where θ is the azimuth in the x_1–x_2 plane measured from the direction of x_1 (see Fig. C.1).

The total stresses in Eq. (C.11) can be converted to effective stresses[6] via Eq. (13.9) in Chapter 13

$$\begin{aligned}
\Sigma_{rr}^{e} &= -p_f + \alpha p_p,\\
\Sigma_{\theta\theta}^{e} &= \Sigma_{11}^{w} + \Sigma_{22}^{w} - 2\left(\Sigma_{11}^{w} - \Sigma_{22}^{w}\right)\cos 2\theta - 4\Sigma_{12}^{w}\sin 2\theta + p_f + \alpha p_p,\\
\Sigma_{zz}^{e} &= \Sigma_{33}^{w} - \nu\left[2\left(\Sigma_{11}^{w} - \Sigma_{22}^{w}\right)\cos 2\theta + 4\Sigma_{12}^{w}\sin 2\theta\right] + \alpha p_p,\\
\Sigma_{\theta z}^{e} &= 2\left(-\Sigma_{13}^{w}\sin\theta + \Sigma_{23}^{w}\cos\theta\right),\\
\Sigma_{r\theta}^{e} &= \Sigma_{zr}^{e} = 0,
\end{aligned} \tag{C.12}$$

where α is the Biot parameter (see Eq. (13.10)), and p_f and p_p are the local pressures of the wellbore and pore fluid, respectively. We assume a filter cake on the wellbore wall may render $p_f \neq p_p$.

C.3. EXAMPLE PROBLEM—$\mathbf{P} = \mathbf{I}$

Assume a far field principle stress state that is aligned with the global coordinate system such that S_1^p and S_2^p align with the X_1-axis and the X_2-axis, respectively, and S_3^p aligns with the X_3-axis. Then $\mathbf{P} = \mathbf{I}$ and, from Eq. (C.2), $\mathbf{S} = \mathbf{S}^p$.

C.3.1 Vertical wellbore

If the wellbore is vertical, we may arbitrarily assign the low side of the hole such that the X_1 and x_1 axes coincide, implying $\mathbf{G} = \mathbf{I}$, and from Eq. (C.10), $\boldsymbol{\Sigma}^w = \mathbf{S}^p$. Further, let us consider the special case when the following assumptions apply:

[6] Some authors [213,178] prefer expressing both $\mathbf{S}$ and $\boldsymbol{\Sigma}^w$ in terms of their effective stress counterparts. In such a case, Eq. (C.12) becomes

$$\begin{aligned}
\Sigma_{rr}^{e} &= -p_f + \alpha p_p,\\
\Sigma_{\theta\theta}^{e} &= \Sigma_{11}^{we} + \Sigma_{22}^{we} - 2\left(\Sigma_{11}^{we} - \Sigma_{22}^{we}\right)\cos 2\theta - 4\Sigma_{12}^{we}\sin 2\theta + p_f - \alpha p_p,\\
\Sigma_{zz}^{e} &= \Sigma_{33}^{we} - \nu\left[2\left(\Sigma_{11}^{we} - \Sigma_{22}^{we}\right)\cos 2\theta + 4\Sigma_{12}^{we}\sin 2\theta\right],\\
\Sigma_{\theta z}^{e} &= 2\left(-\Sigma_{13}^{we}\sin\theta + \Sigma_{23}^{we}\cos\theta\right),\\
\Sigma_{r\theta}^{e} &= \Sigma_{zr}^{e} = 0.
\end{aligned}$$

- the Biot parameter $\alpha = 1$;
- the formation pore fluid has a pressure gradient of $0.45\ \frac{\text{psi}}{\text{ft}}$;
- the vertical principal stress is the smallest in an algebraic sense, $0 \geq S_1^p \geq S_2^p > S_3^p = S^V$, and S^V has a vertical gradient equal to $-1\ \frac{\text{psi}}{\text{ft}}$;
- the two horizontal principal stresses are equal, $0 \geq S_1^p = (S^{H1}) = S_2^p (= S^{H2}) > S_3^p = S^V$, and, assuming Poisson's ration has a value of 0.2, $S_{H1} = S_{H2}$ has a vertical gradient of [7] $[\nu/(1-\nu)] \times (S^V + \alpha p_p) - \alpha p_p = [0.2/0.8] \times (-1 + 0.45) - 0.45$ or $-0.5875\ \frac{\text{psi}}{\text{ft}}$.

Under the above simplifying assumptions, Eq. (C.12) reduces to

$$\begin{aligned}
\Sigma_{rr}^e &= -p_f + p_p, \\
\Sigma_{\theta\theta}^e &= 2S^H + p_f + p_p, \\
\Sigma_{zz}^e &= S^V + p_p, \\
\Sigma_{\theta z}^e &= \Sigma_{r\theta}^e = \Sigma_{zr}^e = 0,
\end{aligned} \tag{C.13}$$

where $S^H = S^{H1} = S^{H2}$. Substituting in the assumed numerical values, the stresses as vertical gradients become

$$\begin{aligned}
\Sigma_{rr}^e &= -p_f + 0.45, \\
\Sigma_{\theta\theta}^e &= -1.175 + p_f + 0.45 = p_f - 0.725, \\
\Sigma_{zz}^e &= -1 + 0.45 = -0.55, \\
\Sigma_{\theta z}^e &= \Sigma_{r\theta}^e = \Sigma_{zr}^e = 0.
\end{aligned} \tag{C.14}$$

Referencing the Mohr–Coulomb failure criterion (see Section 13.3.2.4 of Chapter 13), the shear stresses in the r–θ, θ–z and z–r planes will be given by the following equations (see Eq. (4.113) in Section 4.2.7.1 of Chapter 4):

$$\begin{aligned}
\left|(\mathbf{t_{(n)}})_s\right|_{r\theta} &= \left|\left(\Sigma_{rr}^e - \Sigma_{\theta\theta}^e\right)\cos\theta\sin\theta\right| = \left|-2S^H\cos\theta\sin\theta\right|, && r\text{–}\theta \text{ plane}, \\
\left|(\mathbf{t_{(n)}})_s\right|_{\theta z} &= \left|\left(\Sigma_{\theta\theta}^e - \Sigma_{zz}^e\right)\cos\theta\sin\theta\right| = \left|\left(2S^H - S^V\right)\cos\theta\sin\theta\right|, && \theta\text{–}z \text{ plane}, \\
\left|(\mathbf{t_{(n)}})_s\right|_{zr} &= \left|\left(\Sigma_{zz}^e - \Sigma_{rr}^e\right)\cos\theta\sin\theta\right| = \left|\left(S^V + p_f\right)\cos\theta\sin\theta\right|, && z\text{–}r \text{ plane}.
\end{aligned} \tag{C.15}$$

Fig. C.2 compares the three possible principal stress differences as gradients, eliminating depth as a variable. The differences, which are proportional to shear, are plotted as functions of drilling fluid density, and for each fluid density the maximum difference

[7] This formula for estimating the horizontal stress is derived from poroelasticity assuming the subsurface exists in a state created by burial with no lateral deformation. Assuming isotropic elasticity, $E_{11} = (1/E)[S_{11}^e - \nu(S_{22}^e + S_{33}^e)] = 0$, implying $(1-\nu)S_{11}^e - \nu S_{33}^e = 0$ if $S_{11}^e = S_{22}^e$, as is the case in this problem.

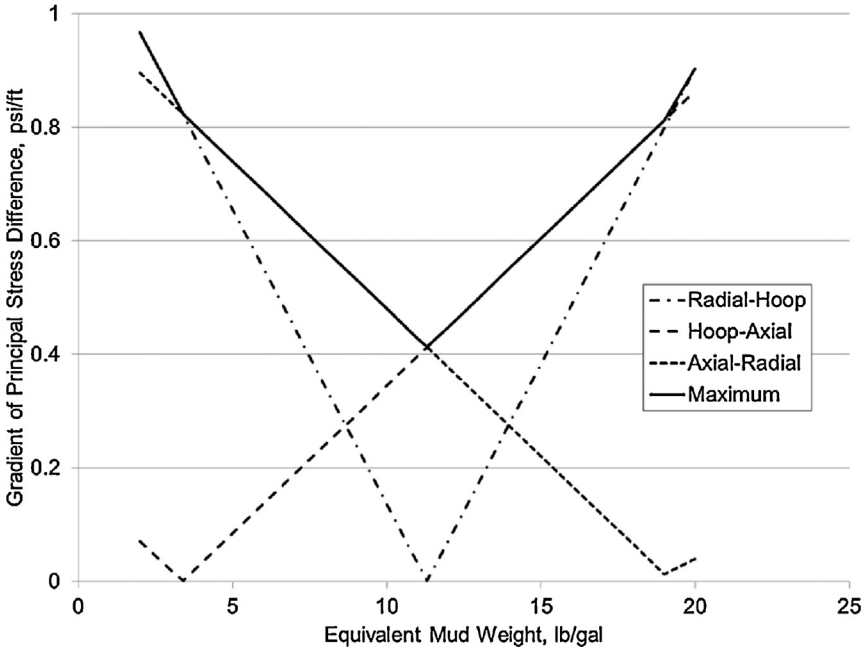

Figure C.2 ***Variation of principal stress difference gradients with drilling fluid density for vertical wellbore example problem variables.***

value is noted. An immediate conclusion from the graph is that there can be two maxima for the shear stress. Reviewing Fig. 13.9 of Chapter 13, this suggests that one might realize two penetrations of the Mohr–Coulomb failure surface, resulting in a range of acceptable drilling fluid densities associated with wellbore stress considerations. This consequence is discussed in Section 13.3.2.4 of Chapter 13.

C.3.2 Inclined wellbore

Consider now a straight (portion of a) wellbore inclined at an angle θ' with the global coordinate system. We further simplify the math by assuming the azimuth of the wellbore is north, that is, $\phi = 0$. As specified in the problem introduction, the far field principal stresses are aligned with the global coordinate system (i.e., $\mathbf{P} = \mathbf{I}$). For this trajectory, $\mathbf{G}$ is given by Eq. (C.9) for the special case when $\phi = 0$,

$$\mathbf{G} = \begin{bmatrix} -\cos\theta' & 0 & \sin\theta' \\ 0 & -1 & 0 \\ \sin\theta' & 0 & \cos\theta' \end{bmatrix}. \tag{C.16}$$

Using Eq. (C.16) in Eq. (C.10) yields

$$\boldsymbol{\Sigma}^{w} = \begin{bmatrix} S^H \cos^2\theta + S^V \sin^2\theta & 0 & \sin\theta\cos\theta\left(S^V - S^H\right) \\ 0 & S^H & 0 \\ \sin\theta\cos\theta\left(S^V - S^H\right) & 0 & S^H \sin^2\theta + S^V \cos^2\theta \end{bmatrix}. \tag{C.17}$$

Using the same bulleted assumptions as the vertical wellbore problem (Section C.3.1), Eq. (C.12) reduces to

$$\begin{aligned} \Sigma^e_{rr} &= -p_f + \alpha p_p, \\ \Sigma^e_{\theta\theta} &= S^H\left(1 + \cos^2\theta\right) + S^V \sin^2\theta - 2\sin^2\theta\left(S^V - S^H\right)\cos 2\theta + p_f + \alpha p_p, \\ \Sigma^e_{zz} &= S^H \sin^2\theta + S^V \cos^2\theta - 2\nu \sin^2\theta\left(S^V - S^H\right)\cos 2\theta + \alpha p_p, \\ \Sigma^e_{\theta z} &= -2\sin\theta\cos\theta\left(S^V - S^H\right)\sin\theta, \\ \Sigma^e_{r\theta} &= \Sigma^e_{zr} = 0, \end{aligned} \tag{C.18}$$

or, substituting in the assumed numerical values,

$$\begin{aligned} \Sigma^e_{rr} &= -p_f + 0.45, \\ \Sigma^e_{\theta\theta} &= -0.5875\left(1 + \cos^2\theta\right) - \sin^2\theta + 0.825\sin^2\theta\cos 2\theta + p_f + 0.45, \\ \Sigma^e_{zz} &= -0.5875\sin^2\theta - \cos^2\theta + 0.165\sin^2\theta\cos 2\theta + 0.45, \\ \Sigma^e_{\theta z} &= 0.825\sin\theta\cos\theta\sin\theta, \\ \Sigma^e_{r\theta} &= \Sigma^e_{zr} = 0. \end{aligned} \tag{C.19}$$

For a vertical wellbore ($\theta = 0$) Eq. (C.19) reduces to Eq. (C.14). For a horizontal wellbore ($\theta = \pi/2$), Eq. (C.19) reduces to

$$\begin{aligned} \Sigma^e_{rr} &= -p_f + 0.45, \\ \Sigma^e_{\theta\theta} &= -0.5875 - 1 + 0.825\cos 2\theta + p_f + 0.45 = -1.1375 + 0.825\cos 2\theta + p_f, \\ \Sigma^e_{zz} &= -0.5875 + 0.165\cos 2\theta + 0.45 = -0.1375 + 0.165\cos 2\theta, \\ \Sigma^e_{\theta z} &= \Sigma^e_{r\theta} = \Sigma^e_{zr} = 0. \end{aligned} \tag{C.20}$$

Fig. C.3 compares the three possible principal stress[8] differences as gradients, eliminating depth as a variable. The differences are plotted as functions of drilling fluid density, and for each fluid density the maximum difference value is noted. Comparing Fig. C.3 with Fig. C.2, the influence of the anisotropic far field stress state materializes. It also appears that for a horizontal wellbore penetrating a formation with this stress state the shear stresses are higher, particularly for lower drilling fluid densities. The integrity of the horizontal wellbore is less than that of its vertical counterpart.

[8] Since $\Sigma^e_{\theta z} = 0$ in Eq. (C.20) for a horizontal wellbore, all shear stresses vanish and the stress state is principal.

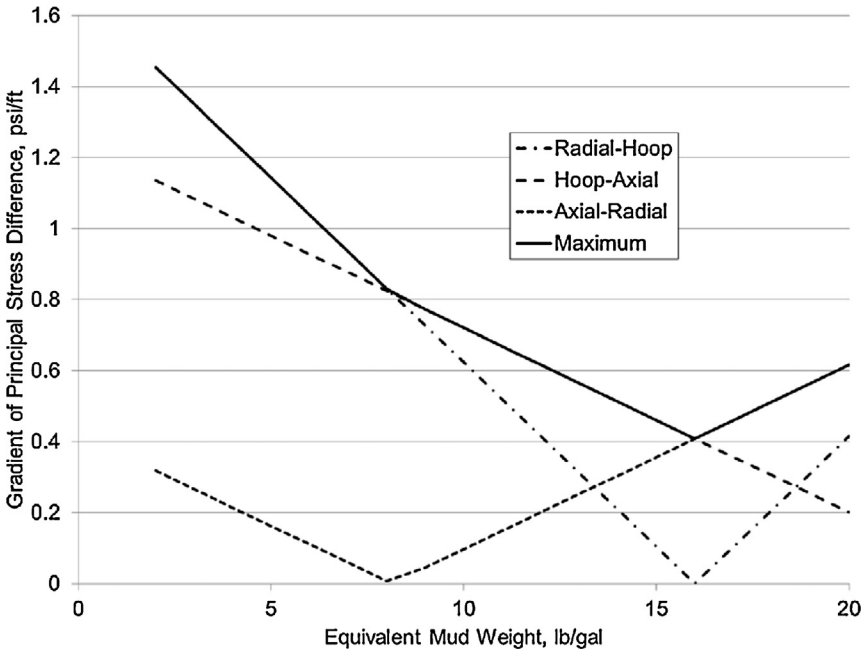

Figure C.3 ***Variation of principal stress difference gradients with drilling fluid density for inclined (horizontal) wellbore example problem variables.***

What was investigated by hand calculation in Fig. C.3 can be programmed to investigate a suite of inclinations. For a given set of inputs—here we will use the inputs for the current problem at a fixed vertical depth of 10 000 ft—one loops first on inclination, then on drilling fluid density, then around the circumference of the wellbore, to obtain the drilling fluid densities that place the stress state just inside a specified failure criterion. As suggested by the previous examination of Figs. C.2 and C.3, there will usually be two such densities bracketing a range of densities for which drilling may proceed without structural failure of the wellbore wall.

For this example problem, a Mohr–Coulomb failure surface having the form of Eq. (13.8) and repeated here

$$\Sigma_s^e = -\mu \Sigma_c^e + c, \tag{C.21}$$

the values of 0.839 and 2500 psi were chosen for μ and c, respectively.

The results are summarized in Fig. C.4. In viewing the figure, note the following:

- The calculation for suitable drilling fluid density is expressed on the ordinate as an equivalent circulating density to emphasize the effect of wellbore hydraulics on the stability of the borehole.
- Four curves are presented on the graph:

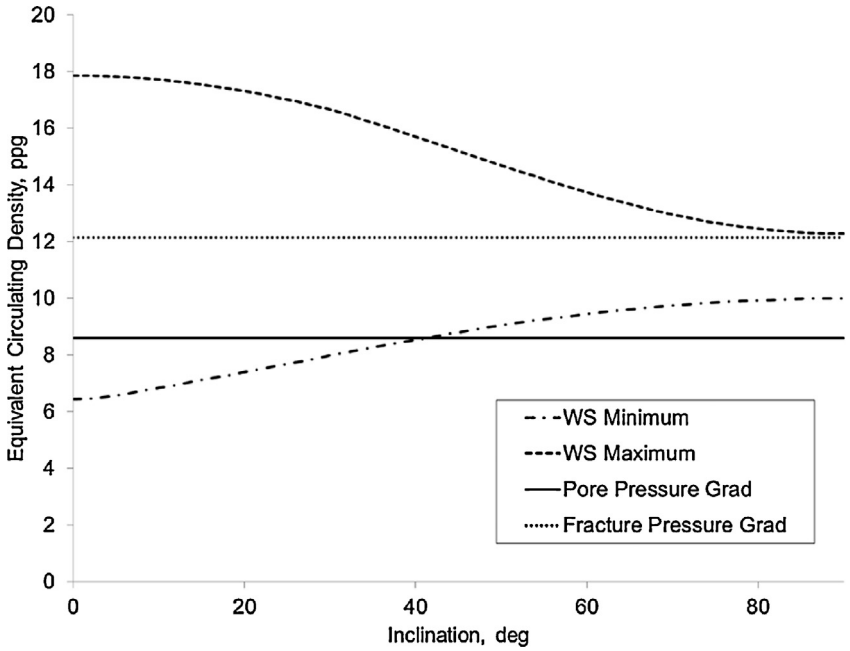

Figure C.4 ***Effect of inclination on acceptable drilling fluid density range for inclined wellbore example problem variables.***

  - Two lines—the pore and fracture pressure gradients—are included for reference, as it is often these two values that determine the acceptable drilling fluid density range. The solid line representing local pore pressure gradient is drawn horizontally, as inclination of the wellbore does not affect the pore pressure. The dotted line representing local fracture pressure gradient is also drawn horizontally, although this is not entirely correct. Inclination will have an effect on *initiation* of a fracture at the wellbore wall.
  - The remaining two curves on the graph represent the result of the programmed iteration discussed above to determine, for each inclination, the minimum and maximum values of drilling fluid density/ECD which can, from the perspective of wellbore stability, be used at the specified depth without inducing failure of the wellbore wall.
- For low values of wellbore inclination the acceptable drilling fluid density range is governed by the two innermost curves—pore pressure and fracture pressure gradient. Wellbore stability is not an issue.
- With increasing inclination the window of acceptable fluid densities to maintain a stable wellbore becomes smaller as the stress state of the wellbore wall is affected by wellbore inclination. Eventually, at an inclination of approximately 40°, the Mohr–

Coulomb failure model predicts that, with lower drilling fluid densities, the wellbore wall will become unstable before pore fluids enter the wellbore due to the pore pressure exceeding the pressure of the drilling fluid. Wellbore stability is therefore the determinant of the low end of the acceptable drilling fluid density range for inclinations greater than 40°.

- The behavior illustrated here is for this particular example problem. Results will change depending on both the formation and drilling parameters and the rock failure model selected.

Finally, and noting the character of the two wellbore stability curves in Fig. C.4, the question arises as to whether a combination of formation and drilling parameters could ever be such that the curves for the bounds of acceptable drilling fluid density could intersect, implying inclinations for which no fluid density will permit drilling the wellbore. This question must be answered in the affirmative, a published example being that of unsuccessful attempts to drill high-angle wellbores in the overburden of the Valhall Field in the Norwegian sector of the North Sea [215]. Due to a weak reservoir chalk, Valhall has undergone significant formation compaction with production-driven pore pressure depletion. Responding to this compaction, the overburden at Valhall has deformed, resulting in a degradation of strength of overburden formations thus reducing their failure envelopes. Two successive attempts to reach the flanks of the field with wells drilled from a platform at the reservoir crest failed to reach their objective. Eventually, platforms were installed on the flanks of the Valhall reservoir to exploit associated reserves.

APPENDIX D

Tables of Tubular Properties

D.1. INTRODUCTION

The tables to follow present selected tubular properties for tubes listed in the API tubing and casing lists [46]. Interpretation of the columns is as follows:

- D—specified outside diameter in in.;
- Linear Mass—specified mass per length in $\frac{\text{lb}_\text{m}}{\text{ft}}$;
- t—specified wall thickness in in.;
- Grade—API grade designation (see Table 6.1);
- $d = D - 2t$ in in.;
- Drift—API drift diameter in in.;
- D/t ratio of D to t;
- MIYP—the historical API one dimensional yield pressure design equation (see Eq. (7.12)) in psi;
- Δp_c—API minimum collapse resistance calculated per Section 8.2.4 of Chapter 8 in psi;
- Finish—the API threaded connection(s) for this tube.

Regarding the last column entry, the inventories to follow can also be obtained with a variety of proprietary threaded connections. When attempting to match the tube with a connection, wall thickness may be the most reliable link as the linear mass calculation can vary in the proprietary offerings.

Table D.1 Tubing dimensions and properties

D	**Linear mass**	t	**Grade**	d	**Drift**	D/t	**MIYP**[a]	Δp_c[b]	**Finish**[c]
in.	$\frac{\text{lb}_\text{m}}{\text{ft}}$	in.		in.	in.		psi	psi	
1.050	1.14	0.113	H40	0.824	0.730	9.29	7530	7680 (Y)	PN
1.050	1.20	0.113	H40	0.824	0.730	9.29	7530	7680 (Y)	PU
1.050	1.14	0.113	J55	0.824	0.730	9.29	10 360	10 560 (Y)	PN
1.050	1.20	0.113	J55	0.824	0.730	9.29	10 360	10 560 (Y)	PU
1.050	1.14	0.113	L80	0.824	0.730	9.29	15 070	15 370 (Y)	PN
1.050	1.20	0.113	L80	0.824	0.730	9.29	15 070	15 370 (Y)	PU
1.050	1.14	0.113	N80	0.824	0.730	9.29	15 070	15 370 (Y)	PN
1.050	1.20	0.113	N80	0.824	0.730	9.29	15 070	15 370 (Y)	PU
1.050	1.14	0.113	C90	0.824	0.730	9.29	16 950	17 290 (Y)	PN
1.050	1.20	0.113	C90	0.824	0.730	9.29	16 950	17 290 (Y)	PU
1.050	1.14	0.113	T95	0.824	0.730	9.29	17 890	18 250 (Y)	PN
1.050	1.20	0.113	T95	0.824	0.730	9.29	17 890	18 250 (Y)	PU
1.050	1.48	0.154	H40	0.742	0.648	6.82	10 270	10 010 (Y)	P
1.050	1.54	0.154	H40	0.742	0.648	6.82	10 270	10 010 (Y)	PU
1.050	1.48	0.154	J55	0.742	0.648	6.82	14 120	13 770 (Y)	P
1.050	1.54	0.154	J55	0.742	0.648	6.82	14 120	13 770 (Y)	PU
1.050	1.48	0.154	L80	0.742	0.648	6.82	20 530	20 020 (Y)	P
1.050	1.54	0.154	L80	0.742	0.648	6.82	20 530	20 020 (Y)	PU
1.050	1.48	0.154	N80	0.742	0.648	6.82	20 530	20 020 (Y)	P
1.050	1.54	0.154	N80	0.742	0.648	6.82	20 530	20 020 (Y)	PU
1.050	1.48	0.154	C90	0.742	0.648	6.82	23 100	22 530 (Y)	P
1.050	1.54	0.154	C90	0.742	0.648	6.82	23 100	22 530 (Y)	PU
1.050	1.48	0.154	T95	0.742	0.648	6.82	24 380	23 780 (Y)	P
1.050	1.54	0.154	T95	0.742	0.648	6.82	24 380	23 780 (Y)	PU
1.050	1.48	0.154	P110	0.742	0.648	6.82	28 230	27 530 (Y)	P
1.050	1.54	0.154	P110	0.742	0.648	6.82	28 230	27 530 (Y)	PU
1.315	1.70	0.133	H40	1.049	0.955	9.89	7080	7270 (Y)	PN
1.315	1.80	0.133	H40	1.049	0.955	9.89	7080	7270 (Y)	PU
1.315	1.72	0.133	H40	1.049	0.955	9.89	7080	7270 (Y)	PI
1.315	1.70	0.133	J55	1.049	0.955	9.89	9730	10 000 (Y)	PN
1.315	1.80	0.133	J55	1.049	0.955	9.89	9730	10 000 (Y)	PU
1.315	1.72	0.133	J55	1.049	0.955	9.89	9730	10 000 (Y)	PI
1.315	1.70	0.133	L80	1.049	0.955	9.89	14 160	14 550 (Y)	PN
1.315	1.80	0.133	L80	1.049	0.955	9.89	14 160	14 550 (Y)	PU

(continued on next page)

Table D.1 (*continued*)

D	**Linear mass**	t	**Grade**	d	**Drift**	D/t	**MIYP**[a]	Δp_c[b]	**Finish**[c]
in.	$\frac{lb_m}{ft}$	in.		in.	in.		psi	psi	
1.315	1.72	0.133	L80	1.049	0.955	9.89	14 160	14 550 (Y)	PI
1.315	1.70	0.133	N80	1.049	0.955	9.89	14 160	14 550 (Y)	PN
1.315	1.80	0.133	N80	1.049	0.955	9.89	14 160	14 550 (Y)	PU
1.315	1.72	0.133	N80	1.049	0.955	9.89	14 160	14 550 (Y)	PI
1.315	1.70	0.133	C90	1.049	0.955	9.89	15 930	16 360 (Y)	PN
1.315	1.80	0.133	C90	1.049	0.955	9.89	15 930	16 360 (Y)	PU
1.315	1.72	0.133	C90	1.049	0.955	9.89	15 930	16 360 (Y)	PI
1.315	1.70	0.133	T95	1.049	0.955	9.89	16 810	17 270 (Y)	PN
1.315	1.80	0.133	T95	1.049	0.955	9.89	16 810	17 270 (Y)	PU
1.315	1.72	0.133	T95	1.049	0.955	9.89	16 810	17 270 (Y)	PI
1.315	2.19	0.179	H40	0.957	0.863	7.35	9530	9410 (Y)	P
1.315	2.24	0.179	H40	0.957	0.863	7.35	9530	9410 (Y)	PU
1.315	2.19	0.179	J55	0.957	0.863	7.35	13 100	12 940 (Y)	P
1.315	2.24	0.179	J55	0.957	0.863	7.35	13 100	12 940 (Y)	PU
1.315	2.19	0.179	L80	0.957	0.863	7.35	19 060	18 810 (Y)	P
1.315	2.24	0.179	L80	0.957	0.863	7.35	19 060	18 810 (Y)	PU
1.315	2.19	0.179	N80	0.957	0.863	7.35	19 060	18 810 (Y)	P
1.315	2.24	0.179	N80	0.957	0.863	7.35	19 060	18 810 (Y)	PU
1.315	2.19	0.179	C90	0.957	0.863	7.35	21 440	21 170 (Y)	P
1.315	2.24	0.179	C90	0.957	0.863	7.35	21 440	21 170 (Y)	PU
1.315	2.19	0.179	T95	0.957	0.863	7.35	22 630	22 340 (Y)	P
1.315	2.24	0.179	T95	0.957	0.863	7.35	22 630	22 340 (Y)	PU
1.315	2.19	0.179	P110	0.957	0.863	7.35	26 200	25 870 (Y)	P
1.315	2.24	0.179	P110	0.957	0.863	7.35	26 200	25 870 (Y)	PU
1.660	2.10	0.125	H40	1.410	1.316	13.28	5270	5570 (Y)	PI
1.660	2.10	0.125	J55	1.410	1.316	13.28	7250	7660 (Y)	PI
1.660	2.30	0.140	H40	1.380	1.286	11.86	5900	6180 (Y)	PN
1.660	2.40	0.140	H40	1.380	1.286	11.86	5900	6180 (Y)	PU
1.660	2.33	0.140	H40	1.380	1.286	11.86	5900	6180 (Y)	PI
1.660	2.30	0.140	J55	1.380	1.286	11.86	8120	8490 (Y)	PN
1.660	2.40	0.140	J55	1.380	1.286	11.86	8120	8490 (Y)	PU
1.660	2.33	0.140	J55	1.380	1.286	11.86	8120	8490 (Y)	PI
1.660	2.30	0.140	L80	1.380	1.286	11.86	11 810	12 360 (Y)	PN
1.660	2.40	0.140	L80	1.380	1.286	11.86	11 810	12 360 (Y)	PU

(continued on next page)

Table D.1 (*continued*)

D	**Linear mass**	t	**Grade**	d	**Drift**	D/t	**MIYP**[a]	Δp_c[b]	**Finish**[c]
in.	$\frac{\text{lb}_\text{m}}{\text{ft}}$	in.		in.	in.		psi	psi	
1.660	2.33	0.140	L80	1.380	1.286	11.86	11 810	12 360 (Y)	PI
1.660	2.30	0.140	N80	1.380	1.286	11.86	11 810	12 360 (Y)	PN
1.660	2.40	0.140	N80	1.380	1.286	11.86	11 810	12 360 (Y)	PU
1.660	2.33	0.140	N80	1.380	1.286	11.86	11 810	12 360 (Y)	PI
1.660	2.30	0.140	C90	1.380	1.286	11.86	13 280	13 900 (Y)	PN
1.660	2.40	0.140	C90	1.380	1.286	11.86	13 280	13 900 (Y)	PU
1.660	2.33	0.140	C90	1.380	1.286	11.86	13 280	13 900 (Y)	PI
1.660	2.30	0.140	T95	1.380	1.286	11.86	14 020	14 670 (Y)	PN
1.660	2.40	0.140	T95	1.380	1.286	11.86	14 020	14 670 (Y)	PU
1.660	2.33	0.140	T95	1.380	1.286	11.86	14 020	14 670 (Y)	PI
1.660	3.03	0.191	H40	1.278	1.184	8.69	8050	8150 (Y)	P
1.660	3.07	0.191	H40	1.278	1.184	8.69	8050	8150 (Y)	PU
1.660	3.03	0.191	J55	1.278	1.184	8.69	11 070	11 200 (Y)	P
1.660	3.07	0.191	J55	1.278	1.184	8.69	11 070	11 200 (Y)	PU
1.660	3.03	0.191	L80	1.278	1.184	8.69	16 110	16 290 (Y)	P
1.660	3.07	0.191	L80	1.278	1.184	8.69	16 110	16 290 (Y)	PU
1.660	3.03	0.191	N80	1.278	1.184	8.69	16 110	16 290 (Y)	P
1.660	3.07	0.191	N80	1.278	1.184	8.69	16 110	16 290 (Y)	PU
1.660	3.03	0.191	C90	1.278	1.184	8.69	18 120	18 330 (Y)	P
1.660	3.07	0.191	C90	1.278	1.184	8.69	18 120	18 330 (Y)	PU
1.660	3.03	0.191	T95	1.278	1.184	8.69	19 130	19 350 (Y)	P
1.660	3.07	0.191	T95	1.278	1.184	8.69	19 130	19 350 (Y)	PU
1.660	3.03	0.191	P110	1.278	1.184	8.69	22 150	22 400 (Y)	P
1.660	3.07	0.191	P110	1.278	1.184	8.69	22 150	22 400 (Y)	PU
1.900	2.40	0.125	H40	1.650	1.556	15.20	4610	4920 (Y)	PI
1.900	2.40	0.125	J55	1.650	1.556	15.20	6330	6640 (P)	PI
1.900	2.75	0.145	H40	1.610	1.516	13.10	5340	5640 (Y)	PN
1.900	2.90	0.145	H40	1.610	1.516	13.10	5340	5640 (Y)	PU
1.900	2.76	0.145	H40	1.610	1.516	13.10	5340	5640 (Y)	PI
1.900	2.75	0.145	J55	1.610	1.516	13.10	7350	7750 (Y)	PN
1.900	2.90	0.145	J55	1.610	1.516	13.10	7350	7750 (Y)	PU
1.900	2.76	0.145	J55	1.610	1.516	13.10	7350	7750 (Y)	PI
1.900	2.75	0.145	L80	1.610	1.516	13.10	10 680	11 280 (Y)	PN
1.900	2.90	0.145	L80	1.610	1.516	13.10	10 680	11 280 (Y)	PU

(continued on next page)

Table D.1 (*continued*)

D	**Linear mass**	t	**Grade**	d	**Drift**	D/t	**MIYP**[a]	Δp_c[b]	**Finish**[c]
in.	$\frac{lb_m}{ft}$	in.		in.	in.		psi	psi	
1.900	2.76	0.145	L80	1.610	1.516	13.10	10 680	11 280 (Y)	PI
1.900	2.75	0.145	N80	1.610	1.516	13.10	10 680	11 280 (Y)	PN
1.900	2.90	0.145	N80	1.610	1.516	13.10	10 680	11 280 (Y)	PU
1.900	2.76	0.145	N80	1.610	1.516	13.10	10 680	11 280 (Y)	PI
1.900	2.75	0.145	C90	1.610	1.516	13.10	12 020	12 620 (P)	PN
1.900	2.90	0.145	C90	1.610	1.516	13.10	12 020	12 620 (P)	PU
1.900	2.76	0.145	C90	1.610	1.516	13.10	12 020	12 620 (P)	PI
1.900	2.75	0.145	T95	1.610	1.516	13.10	12 690	13 190 (P)	PN
1.900	2.90	0.145	T95	1.610	1.516	13.10	12 690	13 190 (P)	PU
1.900	2.76	0.145	T95	1.610	1.516	13.10	12 690	13 190 (P)	PI
1.900	3.65	0.200	H40	1.500	1.406	9.50	7370	7530 (Y)	P
1.900	3.73	0.200	H40	1.500	1.406	9.50	7370	7530 (Y)	PU
1.900	3.65	0.200	J55	1.500	1.406	9.50	10 130	10 360 (Y)	P
1.900	3.73	0.200	J55	1.500	1.406	9.50	10 130	10 360 (Y)	PU
1.900	3.65	0.200	L80	1.500	1.406	9.50	14 740	15 070 (Y)	P
1.900	3.73	0.200	L80	1.500	1.406	9.50	14 740	15 070 (Y)	PU
1.900	3.65	0.200	N80	1.500	1.406	9.50	14 740	15 070 (Y)	P
1.900	3.73	0.200	N80	1.500	1.406	9.50	14 740	15 070 (Y)	PU
1.900	3.65	0.200	C90	1.500	1.406	9.50	16 580	16 950 (Y)	P
1.900	3.73	0.200	C90	1.500	1.406	9.50	16 580	16 950 (Y)	PU
1.900	3.65	0.200	T95	1.500	1.406	9.50	17 500	17 890 (Y)	P
1.900	3.73	0.200	T95	1.500	1.406	9.50	17 500	17 890 (Y)	PU
1.900	3.65	0.200	P110	1.500	1.406	9.50	20 260	20 720 (Y)	P
1.900	3.73	0.200	P110	1.500	1.406	9.50	20 260	20 720 (Y)	PU
1.900	4.42	0.250	L80	1.400	1.306	7.60	18 420	18 280 (Y)	P
1.900	4.42	0.250	C90	1.400	1.306	7.60	20 720	20 570 (Y)	P
1.900	4.42	0.250	T95	1.400	1.306	7.60	21 880	21 710 (Y)	P
1.900	5.15	0.300	L80	1.300	1.206	6.33	22 110	21 270 (Y)	P
1.900	5.15	0.300	C90	1.300	1.206	6.33	24 870	23 930 (Y)	P
1.900	5.15	0.300	T95	1.300	1.206	6.33	26 250	25 260 (Y)	P
2.063	3.25	0.156	H40	1.751	1.657	13.22	5290	5590 (Y)	PI
2.063	3.25	0.156	J55	1.751	1.657	13.22	7280	7690 (Y)	PI
2.063	3.25	0.156	L80	1.751	1.657	13.22	10 590	11 180 (Y)	PI
2.063	3.25	0.156	N80	1.751	1.657	13.22	10 590	11 180 (Y)	PI

(continued on next page)

Table D.1 (*continued*)

D	**Linear mass**	t	**Grade**	d	**Drift**	D/t	**MIYP**[a]	Δp_c[b]	**Finish**[c]
in.	$\frac{\text{lb}_\text{m}}{\text{ft}}$	in.		in.	in.		psi	psi	
2.063	3.25	0.156	C90	1.751	1.657	13.22	11 910	12 420 (P)	PI
2.063	3.25	0.156	T95	1.751	1.657	13.22	12 570	12 980 (P)	PI
2.063	4.50	0.225	H40	1.613	1.519	9.17	7630	7770 (Y)	P
2.063	4.50	0.225	J55	1.613	1.519	9.17	10 500	10 690 (Y)	P
2.063	4.50	0.225	L80	1.613	1.519	9.17	15 270	15 550 (Y)	P
2.063	4.50	0.225	N80	1.613	1.519	9.17	15 270	15 550 (Y)	P
2.063	4.50	0.225	C90	1.613	1.519	9.17	17 180	17 490 (Y)	P
2.063	4.50	0.225	T95	1.613	1.519	9.17	18 130	18 460 (Y)	P
2.063	4.50	0.225	P110	1.613	1.519	9.17	20 990	21 380 (Y)	P
2.375	4.00	0.167	H40	2.041	1.947	14.22	4920	5230 (Y)	PN
2.375	4.00	0.167	J55	2.041	1.947	14.22	6770	7190 (Y)	PN
2.375	4.00	0.167	L80	2.041	1.947	14.22	9840	9980 (P)	PN
2.375	4.00	0.167	N80	2.041	1.947	14.22	9840	9980 (P)	PN
2.375	4.00	0.167	C90	2.041	1.947	14.22	11 070	10 940 (P)	PN
2.375	4.00	0.167	T95	2.041	1.947	14.22	11 690	11 410 (P)	PN
2.375	4.60	0.190	H40	1.995	1.901	12.50	5600	5890 (Y)	PN
2.375	4.70	0.190	H40	1.995	1.901	12.50	5600	5890 (Y)	PU
2.375	4.60	0.190	J55	1.995	1.901	12.50	7700	8100 (Y)	PN
2.375	4.70	0.190	J55	1.995	1.901	12.50	7700	8100 (Y)	PU
2.375	4.60	0.190	L80	1.995	1.901	12.50	11 200	11 780 (Y)	PN
2.375	4.70	0.190	L80	1.995	1.901	12.50	11 200	11 780 (Y)	PU
2.375	4.60	0.190	N80	1.995	1.901	12.50	11 200	11 780 (Y)	PN
2.375	4.70	0.190	N80	1.995	1.901	12.50	11 200	11 780 (Y)	PU
2.375	4.60	0.190	C90	1.995	1.901	12.50	12 600	13 250 (Y)	PN
2.375	4.70	0.190	C90	1.995	1.901	12.50	12 600	13 250 (Y)	PU
2.375	4.60	0.190	T95	1.995	1.901	12.50	13 300	13 980 (Y)	PN
2.375	4.70	0.190	T95	1.995	1.901	12.50	13 300	13 980 (Y)	PU
2.375	4.60	0.190	P110	1.995	1.901	12.50	15 400	16 130 (P)	PN
2.375	4.70	0.190	P110	1.995	1.901	12.50	15 400	16 130 (P)	PU
2.375	5.80	0.254	L80	1.867	1.773	9.35	14 970	15 280 (Y)	PN
2.375	5.95	0.254	L80	1.867	1.773	9.35	14 970	15 280 (Y)	PU
2.375	5.80	0.254	N80	1.867	1.773	9.35	14 970	15 280 (Y)	PN
2.375	5.95	0.254	N80	1.867	1.773	9.35	14 970	15 280 (Y)	PU
2.375	5.80	0.254	C90	1.867	1.773	9.35	16 840	17 190 (Y)	PN

(continued on next page)

Table D.1 (*continued*)

D	**Linear mass**	t	**Grade**	d	**Drift**	D/t	**MIYP**[a]	Δp_c[b]	**Finish**[c]
in.	$\frac{lb_m}{ft}$	in.		in.	in.		psi	psi	
2.375	5.95	0.254	C90	1.867	1.773	9.35	16 840	17 190 (Y)	PU
2.375	5.80	0.254	T95	1.867	1.773	9.35	17 780	18 150 (Y)	PN
2.375	5.95	0.254	T95	1.867	1.773	9.35	17 780	18 150 (Y)	PU
2.375	5.80	0.254	P110	1.867	1.773	9.35	20 590	21 010 (Y)	PN
2.375	5.95	0.254	P110	1.867	1.773	9.35	20 590	21 010 (Y)	PU
2.375	6.60	0.295	L80	1.785	1.691	8.05	17 390	17 410 (Y)	P
2.375	6.60	0.295	C90	1.785	1.691	8.05	19 560	19 580 (Y)	P
2.375	6.60	0.295	T95	1.785	1.691	8.05	20 650	20 670 (Y)	P
2.375	7.35	0.336	L80	1.703	1.609	7.07	19 810	19 430 (Y)	P
2.375	7.45	0.336	L80	1.703	1.609	7.07	19 810	19 430 (Y)	PU
2.375	7.35	0.336	C90	1.703	1.609	7.07	22 280	21 860 (Y)	P
2.375	7.45	0.336	C90	1.703	1.609	7.07	22 280	21 860 (Y)	PU
2.375	7.35	0.336	T95	1.703	1.609	7.07	23 520	23 080 (Y)	P
2.375	7.45	0.336	T95	1.703	1.609	7.07	23 520	23 080 (Y)	PU
2.875	6.40	0.217	H40	2.441	2.347	13.25	5280	5580 (Y)	PN
2.875	6.50	0.217	H40	2.441	2.347	13.25	5280	5580 (Y)	PU
2.875	6.40	0.217	J55	2.441	2.347	13.25	7260	7680 (Y)	PN
2.875	6.50	0.217	J55	2.441	2.347	13.25	7260	7680 (Y)	PU
2.875	6.40	0.217	L80	2.441	2.347	13.25	10 570	11 170 (Y)	PN
2.875	6.50	0.217	L80	2.441	2.347	13.25	10 570	11 170 (Y)	PU
2.875	6.40	0.217	N80	2.441	2.347	13.25	10 570	11 170 (Y)	PN
2.875	6.50	0.217	N80	2.441	2.347	13.25	10 570	11 170 (Y)	PU
2.875	6.40	0.217	C90	2.441	2.347	13.25	11 890	12 390 (P)	PN
2.875	6.50	0.217	C90	2.441	2.347	13.25	11 890	12 390 (P)	PU
2.875	6.40	0.217	T95	2.441	2.347	13.25	12 550	12 940 (P)	PN
2.875	6.50	0.217	T95	2.441	2.347	13.25	12 550	12 940 (P)	PU
2.875	6.40	0.217	P110	2.441	2.347	13.25	14 530	14 550 (P)	PN
2.875	6.50	0.217	P110	2.441	2.347	13.25	14 530	14 550 (P)	PU
2.875	7.80	0.276	L80	2.323	2.229	10.42	13 440	13 890 (Y)	PN
2.875	7.90	0.276	L80	2.323	2.229	10.42	13 440	13 890 (Y)	PU
2.875	7.80	0.276	N80	2.323	2.229	10.42	13 440	13 890 (Y)	PN
2.875	7.90	0.276	N80	2.323	2.229	10.42	13 440	13 890 (Y)	PU
2.875	7.80	0.276	C90	2.323	2.229	10.42	15 120	15 620 (Y)	PN
2.875	7.90	0.276	C90	2.323	2.229	10.42	15 120	15 620 (Y)	PU

(continued on next page)

Table D.1 (*continued*)

D	**Linear mass**	t	**Grade**	d	**Drift**	D/t	**MIYP**[a]	Δp_c[b]	**Finish**[c]
in.	$\frac{\text{lb}_\text{m}}{\text{ft}}$	in.		in.	in.		psi	psi	
2.875	7.80	0.276	T95	2.323	2.229	10.42	15 960	16 490 (Y)	PN
2.875	7.90	0.276	T95	2.323	2.229	10.42	15 960	16 490 (Y)	PU
2.875	7.80	0.276	P110	2.323	2.229	10.42	18 480	19 090 (Y)	PN
2.875	7.90	0.276	P110	2.323	2.229	10.42	18 480	19 090 (Y)	PU
2.875	8.60	0.308	L80	2.259	2.165	9.33	15 000	15 300 (Y)	PN
2.875	8.70	0.308	L80	2.259	2.165	9.33	15 000	15 300 (Y)	PU
2.875	8.60	0.308	N80	2.259	2.165	9.33	15 000	15 300 (Y)	PN
2.875	8.70	0.308	N80	2.259	2.165	9.33	15 000	15 300 (Y)	PU
2.875	8.60	0.308	C90	2.259	2.165	9.33	16 870	17 220 (Y)	PN
2.875	8.70	0.308	C90	2.259	2.165	9.33	16 870	17 220 (Y)	PU
2.875	8.60	0.308	T95	2.259	2.165	9.33	17 810	18 170 (Y)	PN
2.875	8.70	0.308	T95	2.259	2.165	9.33	17 810	18 170 (Y)	PU
2.875	8.60	0.308	P110	2.259	2.165	9.33	20 620	21 040 (Y)	PN
2.875	8.70	0.308	P110	2.259	2.165	9.33	20 620	21 040 (Y)	PU
2.875	9.35	0.340	L80	2.195	2.101	8.46	16 560	16 680 (Y)	P
2.875	9.45	0.340	L80	2.195	2.101	8.46	16 560	16 680 (Y)	PU
2.875	9.35	0.340	C90	2.195	2.101	8.46	18 630	18 770 (Y)	P
2.875	9.45	0.340	C90	2.195	2.101	8.46	18 630	18 770 (Y)	PU
2.875	9.35	0.340	T95	2.195	2.101	8.46	19 660	19 810 (Y)	P
2.875	9.45	0.340	T95	2.195	2.101	8.46	19 660	19 810 (Y)	PU
2.875	10.50	0.392	L80	2.091	1.997	7.33	19 090	18 840 (Y)	P
2.875	10.50	0.392	C90	2.091	1.997	7.33	21 470	21 200 (Y)	P
2.875	10.50	0.392	T95	2.091	1.997	7.33	22 670	22 370 (Y)	P
2.875	11.50	0.440	L80	1.995	1.901	6.53	21 430	20 740 (Y)	P
2.875	11.50	0.440	C90	1.995	1.901	6.53	24 100	23 330 (Y)	P
2.875	11.50	0.440	T95	1.995	1.901	6.53	25 440	24 630 (Y)	P
3.500	7.70	0.216	H40	3.068	2.943	16.20	4320	4630 (Y)	PN
3.500	7.70	0.216	J55	3.068	2.943	16.20	5940	5970 (P)	PN
3.500	7.70	0.216	L80	3.068	2.943	16.20	8640	7870 (P)	PN
3.500	7.70	0.216	N80	3.068	2.943	16.20	8640	7870 (P)	PN
3.500	7.70	0.216	C90	3.068	2.943	16.20	9720	8540 (P)	PN
3.500	7.70	0.216	T95	3.068	2.943	16.20	10 260	8850 (P)	PN
3.500	9.20	0.254	H40	2.992	2.867	13.78	5080	5380 (Y)	PN
3.500	9.30	0.254	H40	2.992	2.867	13.78	5080	5380 (Y)	PU

(continued on next page)

Table D.1 (*continued*)

D	**Linear mass**	t	**Grade**	d	**Drift**	D/t	**MIYP**[a]	Δp_c[b]	**Finish**[c]
in.	$\frac{lb_m}{ft}$	in.		in.	in.		psi	psi	
3.500	9.20	0.254	J55	2.992	2.867	13.78	6990	7400 (Y)	PN
3.500	9.30	0.254	J55	2.992	2.867	13.78	6990	7400 (Y)	PU
3.500	9.20	0.254	L80	2.992	2.867	13.78	10 160	10 540 (P)	PN
3.500	9.30	0.254	L80	2.992	2.867	13.78	10 160	10 540 (P)	PU
3.500	9.20	0.254	N80	2.992	2.867	13.78	10 160	10 540 (P)	PN
3.500	9.30	0.254	N80	2.992	2.867	13.78	10 160	10 540 (P)	PU
3.500	9.20	0.254	C90	2.992	2.867	13.78	11 430	11 570 (P)	PN
3.500	9.30	0.254	C90	2.992	2.867	13.78	11 430	11 570 (P)	PU
3.500	9.20	0.254	T95	2.992	2.867	13.78	12 070	12 080 (P)	PN
3.500	9.30	0.254	T95	2.992	2.867	13.78	12 070	12 080 (P)	PU
3.500	9.20	0.254	P110	2.992	2.867	13.78	13 970	13 530 (P)	PN
3.500	9.30	0.254	P110	2.992	2.867	13.78	13 970	13 530 (P)	PU
3.500	10.20	0.289	H40	2.922	2.797	12.11	5780	6060 (Y)	PN
3.500	10.20	0.289	J55	2.922	2.797	12.11	7950	8330 (Y)	PN
3.500	10.20	0.289	L80	2.922	2.797	12.11	11 560	12 120 (Y)	PN
3.500	10.20	0.289	N80	2.922	2.797	12.11	11 560	12 120 (Y)	PN
3.500	10.20	0.289	C90	2.922	2.797	12.11	13 010	13 640 (Y)	PN
3.500	10.20	0.289	T95	2.922	2.797	12.11	13 730	14 390 (Y)	PN
3.500	12.70	0.375	L80	2.750	2.625	9.33	15 000	15 310 (Y)	PN
3.500	12.95	0.375	L80	2.750	2.625	9.33	15 000	15 310 (Y)	PU
3.500	12.70	0.375	N80	2.750	2.625	9.33	15 000	15 310 (Y)	PN
3.500	12.95	0.375	N80	2.750	2.625	9.33	15 000	15 310 (Y)	PU
3.500	12.70	0.375	C90	2.750	2.625	9.33	16 880	17 220 (Y)	PN
3.500	12.95	0.375	C90	2.750	2.625	9.33	16 880	17 220 (Y)	PU
3.500	12.70	0.375	T95	2.750	2.625	9.33	17 810	18 180 (Y)	PN
3.500	12.95	0.375	T95	2.750	2.625	9.33	17 810	18 180 (Y)	PU
3.500	12.70	0.375	P110	2.750	2.625	9.33	20 630	21 050 (Y)	PN
3.500	12.95	0.375	P110	2.750	2.625	9.33	20 630	21 050 (Y)	PU
3.500	14.30	0.430	L80	2.640	2.515	8.14	17 200	17 240 (Y)	P
3.500	14.30	0.430	C90	2.640	2.515	8.14	19 350	19 400 (Y)	P
3.500	14.30	0.430	T95	2.640	2.515	8.14	20 430	20 480 (Y)	P
3.500	15.50	0.476	L80	2.548	2.423	7.35	19 040	18 800 (Y)	P
3.500	15.50	0.476	C90	2.548	2.423	7.35	21 420	21 150 (Y)	P
3.500	15.50	0.476	T95	2.548	2.423	7.35	22 610	22 330 (Y)	P
3.500	17.00	0.530	L80	2.440	2.315	6.60	21 200	20 560 (Y)	P
3.500	17.00	0.530	C90	2.440	2.315	6.60	23 850	23 130 (Y)	P
3.500	17.00	0.530	T95	2.440	2.315	6.60	25 180	24 410 (Y)	P

(continued on next page)

Table D.1 (*continued*)

D	**Linear mass**	t	**Grade**	d	**Drift**	D/t	**MIYP**[a]	Δp_c[b]	**Finish**[c]
in.	$\frac{lb_m}{ft}$	in.		in.	in.		psi	psi	
4.000	9.50	0.226	H40	3.548	3.423	17.70	3960	4050 (P)	PN
4.000	9.50	0.226	J55	3.548	3.423	17.70	5440	5110 (P)	PN
4.000	9.50	0.226	L80	3.548	3.423	17.70	7910	6590 (P)	PN
4.000	9.50	0.226	N80	3.548	3.423	17.70	7910	6590 (P)	PN
4.000	9.50	0.226	C90	3.548	3.423	17.70	8900	7080 (P)	PN
4.000	9.50	0.226	T95	3.548	3.423	17.70	9390	7310 (P)	PN
4.000	10.70	0.262	H40	3.476	3.351	15.27	4590	4900 (Y)	P
4.000	11.00	0.262	H40	3.476	3.351	15.27	4590	4900 (Y)	PU
4.000	10.70	0.262	J55	3.476	3.351	15.27	6300	6590 (P)	P
4.000	11.00	0.262	J55	3.476	3.351	15.27	6300	6590 (P)	PU
4.000	10.70	0.262	L80	3.476	3.351	15.27	9170	8800 (P)	P
4.000	11.00	0.262	L80	3.476	3.351	15.27	9170	8800 (P)	PU
4.000	10.70	0.262	N80	3.476	3.351	15.27	9170	8800 (P)	P
4.000	11.00	0.262	N80	3.476	3.351	15.27	9170	8800 (P)	PU
4.000	10.70	0.262	C90	3.476	3.351	15.27	10 320	9600 (P)	P
4.000	11.00	0.262	C90	3.476	3.351	15.27	10 320	9600 (P)	PU
4.000	10.70	0.262	T95	3.476	3.351	15.27	10 890	9980 (P)	P
4.000	11.00	0.262	T95	3.476	3.351	15.27	10 890	9980 (P)	PU
4.000	13.20	0.330	L80	3.340	3.215	12.12	11 550	12 110 (Y)	P
4.000	13.20	0.330	C90	3.340	3.215	12.12	12 990	13 620 (Y)	P
4.000	13.20	0.330	T95	3.340	3.215	12.12	13 720	14 380 (Y)	P
4.000	16.10	0.415	L80	3.170	3.045	9.64	14 530	14 880 (Y)	P
4.000	16.10	0.415	C90	3.170	3.045	9.64	16 340	16 740 (Y)	P
4.000	16.10	0.415	T95	3.170	3.045	9.64	17 250	17 670 (Y)	P
4.000	18.90	0.500	L80	3.000	2.875	8.00	17 500	17 500 (Y)	P
4.000	18.90	0.500	C90	3.000	2.875	8.00	19 690	19 690 (Y)	P
4.000	18.90	0.500	T95	3.000	2.875	8.00	20 780	20 780 (Y)	P
4.000	22.20	0.610	L80	2.780	2.655	6.56	21 350	20 680 (Y)	P
4.000	22.20	0.610	C90	2.780	2.655	6.56	24 020	23 260 (Y)	P
4.000	22.20	0.610	T95	2.780	2.655	6.56	25 350	24 560 (Y)	P

(continued on next page)

Table D.1 (*continued*)

D	Linear mass	t	Grade	d	Drift	D/t	MIYP[a]	Δp_c[b]	Finish[c]
in.	$\frac{lb_m}{ft}$	in.		in.	in.		psi	psi	
4.500	12.60	0.271	H40	3.958	3.833	16.61	4220	4490 (P)	PN
4.500	12.75	0.271	H40	3.958	3.833	16.61	4220	4490 (P)	PU
4.500	12.60	0.271	J55	3.958	3.833	16.61	5800	5730 (P)	PN
4.500	12.75	0.271	J55	3.958	3.833	16.61	5800	5730 (P)	PU
4.500	12.60	0.271	L80	3.958	3.833	16.61	8430	7500 (P)	PN
4.500	12.75	0.271	L80	3.958	3.833	16.61	8430	7500 (P)	PU
4.500	12.60	0.271	N80	3.958	3.833	16.61	8430	7500 (P)	PN
4.500	12.75	0.271	N80	3.958	3.833	16.61	8430	7500 (P)	PU
4.500	12.60	0.271	C90	3.958	3.833	16.61	9490	8120 (P)	PN
4.500	12.75	0.271	C90	3.958	3.833	16.61	9490	8120 (P)	PU
4.500	12.60	0.271	T95	3.958	3.833	16.61	10 010	8410 (P)	PN
4.500	12.75	0.271	T95	3.958	3.833	16.61	10 010	8410 (P)	PU
4.500	15.20	0.337	L80	3.826	3.701	13.35	10 480	11 080 (Y)	P
4.500	15.20	0.337	C90	3.826	3.701	13.35	11 800	12 220 (P)	P
4.500	15.20	0.337	T95	3.826	3.701	13.35	12 450	12 760 (P)	P
4.500	17.00	0.380	L80	3.740	3.615	11.84	11 820	12 370 (Y)	P
4.500	17.00	0.380	C90	3.740	3.615	11.84	13 300	13 920 (Y)	P
4.500	17.00	0.380	T95	3.740	3.615	11.84	14 040	14 690 (Y)	P
4.500	18.90	0.430	L80	3.640	3.515	10.47	13 380	13 830 (Y)	P
4.500	18.90	0.430	C90	3.640	3.515	10.47	15 050	15 560 (Y)	P
4.500	18.90	0.430	T95	3.640	3.515	10.47	15 890	16 420 (Y)	P
4.500	21.50	0.500	L80	3.500	3.375	9.00	15 560	15 800 (Y)	P
4.500	21.50	0.500	C90	3.500	3.375	9.00	17 500	17 780 (Y)	P
4.500	21.50	0.500	T95	3.500	3.375	9.00	18 470	18 770 (Y)	P
4.500	23.70	0.560	L80	3.380	3.255	8.04	17 420	17 430 (Y)	P
4.500	23.70	0.560	C90	3.380	3.255	8.04	19 600	19 610 (Y)	P
4.500	23.70	0.560	T95	3.380	3.255	8.04	20 690	20 700 (Y)	P
4.500	26.10	0.630	L80	3.240	3.115	7.14	19 600	19 260 (Y)	P
4.500	26.10	0.630	C90	3.240	3.115	7.14	22 050	21 670 (Y)	P
4.500	26.10	0.630	T95	3.240	3.115	7.14	23 280	22 880 (Y)	P

[a] Internal yield pressure according to Eq. (7.12) with $k_{wall} = 0.875$.
[b] Collapse mode: E = elastic, T = transition, P = plastic, Y = yield.
[c] Finish (API connections): P = plain end, N = NUE, E = EUE, I = IJ. A wide variety of proprietary thread vendors also offer threaded connections.

Table D.2 Casing dimensions and properties

D	**Linear mass**	t	**Grade**	d	**Drift**	D/t	**MIYP**[a]	Δp_c[b]	**Finish**[c]
in.	$\frac{\text{lb}_\text{m}}{\text{ft}}$	in.		in.	in.		psi	psi	
4.500	9.50	0.205	H40	4.090	3.965	21.95	3190	2760 (P)	PS
4.500	9.50	0.205	J55	4.090	3.965	21.95	4380	3310 (P)	PS
4.500	9.50	0.205	K55	4.090	3.965	21.95	4380	3310 (P)	PS
4.500	9.50	0.205	M65	4.090	3.965	21.95	5180	3600 (P)	PS
4.500	10.50	0.224	J55	4.052	3.927	20.09	4790	4010 (P)	PSB
4.500	10.50	0.224	K55	4.052	3.927	20.09	4790	4010 (P)	PSB
4.500	10.50	0.224	M65	4.052	3.927	20.09	5660	4430 (P)	PSB
4.500	11.60	0.250	J55	4.000	3.875	18.00	5350	4960 (P)	PSLB
4.500	11.60	0.250	K55	4.000	3.875	18.00	5350	4960 (P)	PSLB
4.500	11.60	0.250	M65	4.000	3.875	18.00	6320	5560 (P)	PLB
4.500	11.60	0.250	L80	4.000	3.875	18.00	7780	6350 (P)	PLB
4.500	11.60	0.250	N80	4.000	3.875	18.00	7780	6350 (P)	PLB
4.500	11.60	0.250	C90	4.000	3.875	18.00	8750	6820 (P)	PLB
4.500	11.60	0.250	R95	4.000	3.875	18.00	9240	7030 (P)	PLB
4.500	11.60	0.250	T95	4.000	3.875	18.00	9240	7030 (P)	PLB
4.500	11.60	0.250	P110	4.000	3.875	18.00	10 690	7580 (P)	PLB
4.500	13.50	0.290	M65	3.920	3.795	15.52	7330	7310 (P)	PLB
4.500	13.50	0.290	L80	3.920	3.795	15.52	9020	8540 (P)	PLB
4.500	13.50	0.290	N80	3.920	3.795	15.52	9020	8540 (P)	PLB
4.500	13.50	0.290	C90	3.920	3.795	15.52	10 150	9300 (P)	PLB
4.500	13.50	0.290	R95	3.920	3.795	15.52	10 710	9660 (P)	PLB
4.500	13.50	0.290	T95	3.920	3.795	15.52	10 710	9660 (P)	PLB
4.500	13.50	0.290	P110	3.920	3.795	15.52	12 410	10 690 (P)	PLB
4.500	15.10	0.337	P110	3.826	3.701	13.35	14 420	14 340 (P)	PLB
4.500	15.10	0.337	Q125	3.826	3.701	13.35	16 380	15 830 (P)	PLB
5.000	11.50	0.220	J55	4.560	4.435	22.73	4240	3060 (P)	PS
5.000	11.50	0.220	K55	4.560	4.435	22.73	4240	3060 (P)	PS
5.000	11.50	0.220	M65	4.560	4.435	22.73	5010	3290 (P)	PS
5.000	13.00	0.253	J55	4.494	4.369	19.76	4870	4140 (P)	PSLB
5.000	13.00	0.253	K55	4.494	4.369	19.76	4870	4140 (P)	PSLB
5.000	13.00	0.253	M65	4.494	4.369	19.76	5760	4590 (P)	PSLB
5.000	15.00	0.296	J55	4.408	4.283	16.89	5700	5560 (P)	PSLBE
5.000	15.00	0.296	K55	4.408	4.283	16.89	5700	5560 (P)	PSLBE
5.000	15.00	0.296	M65	4.408	4.283	16.89	6730	6280 (P)	PLB

(continued on next page)

Table D.2 (*continued*)

D	Linear mass	t	Grade	d	Drift	D/t	MIYP[a]	Δp_c[b]	Finish[c]
in.	$\frac{lb_m}{ft}$	in.		in.	in.		psi	psi	
5.000	15.00	0.296	L80	4.408	4.283	16.89	8290	7250 (P)	PLBE
5.000	15.00	0.296	N80	4.408	4.283	16.89	8290	7250 (P)	PLBE
5.000	15.00	0.296	C90	4.408	4.283	16.89	9320	7830 (P)	PLBE
5.000	15.00	0.296	R95	4.408	4.283	16.89	9840	8110 (P)	PLBE
5.000	15.00	0.296	T95	4.408	4.283	16.89	9840	8110 (P)	PLBE
5.000	15.00	0.296	P110	4.408	4.283	16.89	11 400	8850 (P)	PLBE
5.000	18.00	0.362	M65	4.276	4.151	13.81	8240	8730 (Y)	PLBE
5.000	18.00	0.362	L80	4.276	4.151	13.81	10 140	10 490 (P)	PLB
5.000	18.00	0.362	N80	4.276	4.151	13.81	10 140	10 490 (P)	PLBE
5.000	18.00	0.362	C90	4.276	4.151	13.81	11 400	11 520 (P)	PLBE
5.000	18.00	0.362	R95	4.276	4.151	13.81	12 040	12 030 (P)	PLB
5.000	18.00	0.362	T95	4.276	4.151	13.81	12 040	12 030 (P)	PLBE
5.000	18.00	0.362	P110	4.276	4.151	13.81	13 940	13 470 (P)	PLBE
5.000	18.00	0.362	Q125	4.276	4.151	13.81	15 840	14 820 (P)	PLBE
5.000	21.40	0.437	M65	4.126	4.001	11.44	9940	10 370 (Y)	PLBE
5.000	21.40	0.437	L80	4.126	4.001	11.44	12 240	12 760 (Y)	PLB
5.000	21.40	0.437	N80	4.126	4.001	11.44	12 240	12 760 (Y)	PLB
5.000	21.40	0.437	C90	4.126	4.001	11.44	13 770	14 360 (Y)	PLB
5.000	21.40	0.437	R95	4.126	4.001	11.44	14 530	15 150 (Y)	PLB
5.000	21.40	0.437	T95	4.126	4.001	11.44	14 530	15 150 (Y)	PLB
5.000	21.40	0.437	P110	4.126	4.001	11.44	16 820	17 550 (Y)	PLB
5.000	21.40	0.437	Q125	4.126	4.001	11.44	19 120	19 940 (Y)	PLB
5.000	23.20	0.478	L80	4.044	3.919	10.46	13 380	13 830 (Y)	PLB
5.000	23.20	0.478	N80	4.044	3.919	10.46	13 380	13 830 (Y)	PLB
5.000	23.20	0.478	C90	4.044	3.919	10.46	15 060	15 560 (Y)	PLB
5.000	23.20	0.478	R95	4.044	3.919	10.46	15 890	16 430 (Y)	PLB
5.000	23.20	0.478	T95	4.044	3.919	10.46	15 890	16 430 (Y)	PLB
5.000	23.20	0.478	P110	4.044	3.919	10.46	18 400	19 020 (Y)	PLB
5.000	23.20	0.478	Q125	4.044	3.919	10.46	20 910	21 620 (Y)	PLB
5.000	24.10	0.500	L80	4.000	3.875	10.00	14 000	14 400 (Y)	PLB
5.000	24.10	0.500	N80	4.000	3.875	10.00	14 000	14 400 (Y)	PLB
5.000	24.10	0.500	C90	4.000	3.875	10.00	15 750	16 200 (Y)	PLB
5.000	24.10	0.500	R95	4.000	3.875	10.00	16 630	17 100 (Y)	PLB
5.000	24.10	0.500	T95	4.000	3.875	10.00	16 630	17 100 (Y)	PLB
5.000	24.10	0.500	P110	4.000	3.875	10.00	19 250	19 800 (Y)	PLB

(continued on next page)

Table D.2 (*continued*)

D	**Linear mass**	t	**Grade**	d	**Drift**	D/t	**MIYP**[a]	Δp_c[b]	**Finish**[c]
in.	$\frac{\text{lb}_\text{m}}{\text{ft}}$	in.		in.	in.		psi	psi	
5.000	24.10	0.500	Q125	4.000	3.875	10.00	21 880	22 500 (Y)	PLB
5.500	14.00	0.244	H40	5.012	4.887	22.54	3110	2620 (P)	PS
5.500	14.00	0.244	J55	5.012	4.887	22.54	4270	3120 (P)	PS
5.500	14.00	0.244	K55	5.012	4.887	22.54	4270	3120 (P)	PS
5.500	14.00	0.244	M65	5.012	4.887	22.54	5050	3360 (P)	PS
5.500	15.50	0.275	J55	4.950	4.825	20.00	4810	4040 (P)	PSLBE
5.500	15.50	0.275	K55	4.950	4.825	20.00	4810	4040 (P)	PSLBE
5.500	15.50	0.275	M65	4.950	4.825	20.00	5690	4470 (P)	PS
5.500	17.00	0.304	J55	4.892	4.767	18.09	5320	4910 (P)	PSLB
5.500	17.00	0.304	K55	4.892	4.767	18.09	5320	4910 (P)	PSLBE
5.500	17.00	0.304	M65	4.892	4.767	18.09	6290	5500 (P)	PSLBE
5.500	17.00	0.304	L80	4.892	4.767	18.09	7740	6290 (P)	PLBE
5.500	17.00	0.304	C90	4.892	4.767	18.09	8710	6740 (P)	PLBE
5.500	17.00	0.304	R95	4.892	4.767	18.09	9190	6940 (P)	PLBE
5.500	17.00	0.304	T95	4.892	4.767	18.09	9190	6940 (P)	PLBE
5.500	17.00	0.304	P110	4.892	4.767	18.09	10 640	7480 (P)	PLBE
5.500	20.00	0.361	M65	4.778	4.653	15.24	7470	7540 (P)	PSLB
5.500	20.00	0.361	L80	4.778	4.653	15.24	9190	8830 (P)	PLB
5.500	20.00	0.361	N80	4.778	4.653	15.24	9190	8830 (P)	PLBE
5.500	20.00	0.361	C90	4.778	4.653	15.24	10 340	9630 (P)	PLBE
5.500	20.00	0.361	R95	4.778	4.653	15.24	10 910	10 020 (P)	PLB
5.500	20.00	0.361	T95	4.778	4.653	15.24	10 910	10 020 (P)	PLBE
5.500	20.00	0.361	P110	4.778	4.653	15.24	12 640	11 100 (P)	PLBE
5.500	23.00	0.415	M65	4.670	4.545	13.25	8580	9070 (Y)	PLB
5.500	23.00	0.415	L80	4.670	4.545	13.25	10 560	11 160 (Y)	PLBE
5.500	23.00	0.415	N80	4.670	4.545	13.25	10 560	11 160 (Y)	PLBE
5.500	23.00	0.415	C90	4.670	4.545	13.25	11 880	12 380 (P)	PLBE
5.500	23.00	0.415	R95	4.670	4.545	13.25	12 540	12 930 (P)	PLBE
5.500	23.00	0.415	P110	4.670	4.545	13.25	14 530	14 540 (P)	PLBE
5.500	23.00	0.415	Q125	4.670	4.545	13.25	16 510	16 060 (P)	PLBE
5.500	26.80	0.500	C90	4.500	4.375	11.00	14 320	14 880 (Y)	PLBE
5.500	26.80	0.500	T95	4.500	4.375	11.00	15 110	15 700 (Y)	P
5.500	29.70	0.562	C90	4.376	4.251	9.79	16 090	16 510 (Y)	P
5.500	29.70	0.562	T95	4.376	4.251	9.79	16 990	17 430 (Y)	P

(continued on next page)

Table D.2 (*continued*)

D	**Linear mass**	t	**Grade**	d	**Drift**	D/t	**MIYP**[a]	Δp_c[b]	**Finish**[c]
in.	$\frac{lb_m}{ft}$	in.		in.	in.		psi	psi	
5.500	32.60	0.625	C90	4.250	4.125	8.80	17 900	18 130 (Y)	P
5.500	32.60	0.625	T95	4.250	4.125	8.80	18 890	19 140 (Y)	P
5.500	35.30	0.687	C90	4.126	4.001	8.01	19 670	19 680 (Y)	P
5.500	35.30	0.687	T95	4.126	4.001	8.01	20 770	20 770 (Y)	P
5.500	38.00	0.750	C90	4.000	3.875	7.33	21 480	21 200 (Y)	P
5.500	38.00	0.750	T95	4.000	3.875	7.33	22 670	22 380 (Y)	P
5.500	40.50	0.812	C90	3.876	3.751	6.77	23 250	22 650 (Y)	P
5.500	40.50	0.812	T95	3.876	3.751	6.77	24 540	23 910 (Y)	P
5.500	43.10	0.875	C90	3.750	3.625	6.29	25 060	24 080 (Y)	P
5.500	43.10	0.875	T95	3.750	3.625	6.29	26 450	25 420 (Y)	P
6.625	20.00	0.288	H40	6.049	5.924	23.00	3040	2520 (P)	PS
6.625	20.00	0.288	J55	6.049	5.924	23.00	4180	2970 (P)	PSLB
6.625	20.00	0.288	K55	6.049	5.924	23.00	4180	2970 (P)	PSLB
6.625	20.00	0.288	M65	6.049	5.924	23.00	4940	3190 (P)	PSLB
6.625	24.00	0.352	J55	5.921	5.796	18.82	5110	4560 (P)	PSLBE
6.625	24.00	0.352	K55	5.921	5.796	18.82	5110	4560 (P)	PSLBE
6.625	24.00	0.352	M65	5.921	5.796	18.82	6040	5080 (P)	PLB
6.625	24.00	0.352	L80	5.921	5.796	18.82	7440	5760 (P)	PLBE
6.625	24.00	0.352	N80	5.921	5.796	18.82	7440	5760 (P)	PLBE
6.625	24.00	0.352	C90	5.921	5.796	18.82	8370	6140 (P)	PLBE
6.625	24.00	0.352	R95	5.921	5.796	18.82	8830	6310 (P)	PLBE
6.625	24.00	0.352	T95	5.921	5.796	18.82	8830	6310 (P)	PLBE
6.625	24.00	0.352	P110	5.921	5.796	18.82	10 230	6730 (P)	PLBE
6.625	28.00	0.417	M65	5.791	5.666	15.89	7160	7010 (P)	PLB
6.625	28.00	0.417	L80	5.791	5.666	15.89	8810	8170 (P)	PLBE
6.625	28.00	0.417	N80	5.791	5.666	15.89	8810	8170 (P)	PLBE
6.625	28.00	0.417	C90	5.791	5.666	15.89	9910	8880 (P)	PLBE
6.625	28.00	0.417	R95	5.791	5.666	15.89	10 460	9220 (P)	PLBE
6.625	28.00	0.417	T95	5.791	5.666	15.89	10 460	9220 (P)	PLBE
6.625	28.00	0.417	P110	5.791	5.666	15.89	12 120	10 160 (P)	PLBE
6.625	32.00	0.475	L80	5.675	5.550	13.95	10 040	10 320 (P)	PLBE
6.625	32.00	0.475	N80	5.675	5.550	13.95	10 040	10 320 (P)	PLBE
6.625	32.00	0.475	C90	5.675	5.550	13.95	11 290	11 330 (P)	PLBE
6.625	32.00	0.475	R95	5.675	5.550	13.95	11 920	11 820 (P)	PLBE

(continued on next page)

Table D.2 (*continued*)

D	**Linear mass**	t	**Grade**	d	**Drift**	D/t	**MIYP**[a]	Δp_c[b]	**Finish**[c]
in.	$\frac{\text{lb}_\text{m}}{\text{ft}}$	in.		in.	in.		psi	psi	
6.625	32.00	0.475	T95	5.675	5.550	13.95	11 920	11 820 (P)	PLBE
6.625	32.00	0.475	P110	5.675	5.550	13.95	13 800	13 220 (P)	PLBE
6.625	32.00	0.475	Q125	5.675	5.550	13.95	15 680	14 540 (P)	PLBE
7.000	17.00	0.231	H40	6.538	6.413	30.30	2310	1420 (T)	PS
7.000	20.00	0.272	H40	6.456	6.331	25.74	2720	1970 (P)	PS
7.000	20.00	0.272	J55	6.456	6.331	25.74	3740	2270 (T)	PS
7.000	20.00	0.272	K55	6.456	6.331	25.74	3740	2270 (T)	PS
7.000	20.00	0.272	M65	6.456	6.331	25.74	4420	2480 (T)	PS
7.000	23.00	0.317	J55	6.366	6.250	22.08	4360	3270 (P)	PSLBE
7.000	23.00	0.317	K55	6.366	6.250	22.08	4360	3270 (P)	PSLBE
7.000	23.00	0.317	M65	6.366	6.250	22.08	5150	3540 (P)	PLB
7.000	23.00	0.317	L80	6.366	6.250	22.08	6340	3830 (P)	PLBE
7.000	23.00	0.317	N80	6.366	6.250	22.08	6340	3830 (P)	PLBE
7.000	23.00	0.317	C90	6.366	6.250	22.08	7130	4030 (T)	PLBE
7.000	23.00	0.317	R95	6.366	6.250	22.08	7530	4140 (T)	PLBE
7.000	23.00	0.317	T95	6.366	6.250	22.08	7530	4140 (T)	PLBE
7.000	26.00	0.362	J55	6.276	6.151	19.34	4980	4330 (P)	PLBE
7.000	26.00	0.362	K55	6.276	6.151	19.34	4980	4330 (P)	PSLBE
7.000	26.00	0.362	M65	6.276	6.151	19.34	5880	4810 (P)	PSLBE
7.000	26.00	0.362	L80	6.276	6.151	19.34	7240	5410 (P)	PLB
7.000	26.00	0.362	N80	6.276	6.151	19.34	7240	5410 (P)	PLBE
7.000	26.00	0.362	C90	6.276	6.151	19.34	8150	5740 (P)	PLBE
7.000	26.00	0.362	R95	6.276	6.151	19.34	8600	5890 (P)	PLB
7.000	26.00	0.362	T95	6.276	6.151	19.34	8600	5890 (P)	PLBE
7.000	26.00	0.362	P110	6.276	6.151	19.34	9960	6230 (P)	PLBE
7.000	29.00	0.408	M65	6.184	6.059	17.16	6630	6100 (P)	PLB
7.000	29.00	0.408	L80	6.184	6.059	17.16	8160	7030 (P)	PLBE
7.000	29.00	0.408	N80	6.184	6.059	17.16	8160	7030 (P)	PLBE
7.000	29.00	0.408	C90	6.184	6.059	17.16	9180	7580 (P)	PLBE
7.000	29.00	0.408	R95	6.184	6.059	17.16	9690	7840 (P)	PLBE
7.000	29.00	0.408	T95	6.184	6.059	17.16	9690	7840 (P)	PLBE
7.000	29.00	0.408	P110	6.184	6.059	17.16	11 220	8530 (P)	PLBE
7.000	32.00	0.453	M65	6.094	6.000	15.45	7360	7360 (P)	PLB
7.000	32.00	0.453	L80	6.094	6.000	15.45	9060	8600 (P)	PLBE

(continued on next page)

Table D.2 (*continued*)

D	**Linear mass**	t	**Grade**	d	**Drift**	D/t	**MIYP**[a]	Δp_c[b]	**Finish**[c]
in.	$\frac{lb_m}{ft}$	in.		in.	in.		psi	psi	
7.000	32.00	0.453	N80	6.094	6.000	15.45	9060	8600 (P)	PLBE
7.000	32.00	0.453	C90	6.094	6.000	15.45	10 190	9380 (P)	PLBE
7.000	32.00	0.453	R95	6.094	6.000	15.45	10 760	9740 (P)	PLBE
7.000	32.00	0.453	T95	6.094	6.000	15.45	10 760	9740 (P)	PLBE
7.000	32.00	0.453	P110	6.094	6.000	15.45	12 460	10 780 (P)	PLBE
7.000	35.00	0.498	L80	6.004	5.879	14.06	9960	10 180 (P)	PLBE
7.000	35.00	0.498	N80	6.004	5.879	14.06	9960	10 180 (P)	PLBE
7.000	35.00	0.498	C90	6.004	5.879	14.06	11 210	11 170 (P)	PLBE
7.000	35.00	0.498	R95	6.004	5.879	14.06	11 830	11 650 (P)	PLBE
7.000	35.00	0.498	T95	6.004	5.879	14.06	11 830	11 650 (P)	PLBE
7.000	35.00	0.498	P110	6.004	5.879	14.06	13 700	13 030 (P)	PLBE
7.000	35.00	0.498	Q125	6.004	5.879	14.06	15 560	14 310 (P)	PLBE
7.000	38.00	0.540	L80	5.920	5.795	12.96	10 800	11 390 (Y)	PLBE
7.000	38.00	0.540	N80	5.920	5.795	12.96	10 800	11 390 (Y)	PLBE
7.000	38.00	0.540	C90	5.920	5.795	12.96	12 150	12 810 (Y)	PLBE
7.000	38.00	0.540	R95	5.920	5.795	12.96	12 830	13 430 (P)	PLBE
7.000	38.00	0.540	T95	5.920	5.795	12.96	12 830	13 430 (P)	PLBE
7.000	38.00	0.540	P110	5.920	5.795	12.96	14 850	15 130 (P)	PLBE
7.000	38.00	0.540	Q125	5.920	5.795	12.96	16 880	16 740 (P)	PLBE
7.000	42.70	0.625	C90	5.750	5.625	11.20	14 060	14 640 (Y)	PLBE
7.000	42.70	0.625	T95	5.750	5.625	11.20	14 840	15 450 (Y)	P
7.000	46.40	0.687	C90	5.626	5.501	10.19	15 460	15 930 (Y)	P
7.000	46.40	0.687	T95	5.626	5.501	10.19	16 320	16 820 (Y)	P
7.000	50.10	0.750	C90	5.500	5.375	9.33	16 880	17 220 (Y)	P
7.000	50.10	0.750	T95	5.500	5.375	9.33	17 810	18 180 (Y)	P
7.000	53.60	0.812	C90	5.376	5.251	8.62	18 270	18 460 (Y)	P
7.000	53.60	0.812	T95	5.376	5.251	8.62	19 290	19 480 (Y)	P
7.000	57.10	0.875	C90	5.250	5.125	8.00	19 690	19 690 (Y)	P
7.000	57.10	0.875	T95	5.250	5.125	8.00	20 780	20 780 (Y)	P
7.625	24.00	0.300	H40	7.025	6.900	25.42	2750	2030 (P)	PS
7.625	26.40	0.328	J55	6.969	6.844	23.25	4140	2900 (P)	PSLBE
7.625	26.40	0.328	K55	6.969	6.844	23.25	4140	2900 (P)	PSLBE
7.625	26.40	0.328	M65	6.969	6.844	23.25	4890	3100 (P)	PSLB
7.625	26.40	0.328	L80	6.969	6.844	23.25	6020	3400 (T)	PLBE

(continued on next page)

Table D.2 (*continued*)

D	**Linear mass**	t	**Grade**	d	**Drift**	D/t	**MIYP**[a]	Δp_c[b]	**Finish**[c]
in.	$\frac{\text{lb}_\text{m}}{\text{ft}}$	in.		in.	in.		psi	psi	
7.625	26.40	0.328	N80	6.969	6.844	23.25	6020	3400 (T)	PLBE
7.625	26.40	0.328	C90	6.969	6.844	23.25	6780	3610 (T)	PLBE
7.625	26.40	0.328	R95	6.969	6.844	23.25	7150	3710 (T)	PLBE
7.625	26.40	0.328	T95	6.969	6.844	23.25	7150	3710 (T)	PLBE
7.625	29.70	0.375	M65	6.875	6.750	20.33	5590	4310 (P)	PLB
7.625	29.70	0.375	L80	6.875	6.750	20.33	6890	4790 (P)	PLBE
7.625	29.70	0.375	N80	6.875	6.750	20.33	6890	4790 (P)	PLBE
7.625	29.70	0.375	C90	6.875	6.750	20.33	7750	5030 (P)	PLBE
7.625	29.70	0.375	R95	6.875	6.750	20.33	8180	5130 (P)	PLBE
7.625	29.70	0.375	T95	6.875	6.750	20.33	8180	5130 (P)	PLBE
7.625	29.70	0.375	P110	6.875	6.750	20.33	9470	5350 (P)	PLBE
7.625	33.70	0.430	M65	6.765	6.640	17.73	6410	5720 (P)	PLB
7.625	33.70	0.430	L80	6.765	6.640	17.73	7900	6560 (P)	PLBE
7.625	33.70	0.430	N80	6.765	6.640	17.73	7900	6560 (P)	PLBE
7.625	33.70	0.430	C90	6.765	6.640	17.73	8880	7050 (P)	PLBE
7.625	33.70	0.430	R95	6.765	6.640	17.73	9380	7280 (P)	PLBE
7.625	33.70	0.430	T95	6.765	6.640	17.73	9380	7280 (P)	PLBE
7.625	33.70	0.430	P110	6.765	6.640	17.73	10 860	7870 (P)	PLBE
7.625	39.00	0.500	L80	6.625	6.500	15.25	9180	8820 (P)	PLBE
7.625	39.00	0.500	N80	6.625	6.500	15.25	9180	8820 (P)	PLBE
7.625	39.00	0.500	C90	6.625	6.500	15.25	10 330	9620 (P)	PLBE
7.625	39.00	0.500	R95	6.625	6.500	15.25	10 900	10 000 (P)	PLBE
7.625	39.00	0.500	T95	6.625	6.500	15.25	10 900	10 000 (P)	PLBE
7.625	39.00	0.500	P110	6.625	6.500	15.25	12 620	11 080 (P)	PLBE
7.625	39.00	0.500	Q125	6.625	6.500	15.25	14 340	12 060 (P)	PLBE
7.625	42.80	0.562	L80	6.501	6.376	13.57	10 320	10 810 (P)	PLB
7.625	42.80	0.562	N80	6.501	6.376	13.57	10 320	10 810 (P)	PLB
7.625	42.80	0.562	C90	6.501	6.376	13.57	11 610	11 890 (P)	PLB
7.625	42.80	0.562	R95	6.501	6.376	13.57	12 250	12 410 (P)	PLB
7.625	42.80	0.562	T95	6.501	6.376	13.57	12 250	12 410 (P)	PLB
7.625	42.80	0.562	P110	6.501	6.376	13.57	14 190	13 930 (P)	PLB
7.625	42.80	0.562	Q125	6.501	6.376	13.57	16 120	15 350 (P)	PLB
7.625	45.30	0.595	L80	6.435	6.310	12.82	10 920	11 510 (Y)	PLB
7.625	45.30	0.595	N80	6.435	6.310	12.82	10 920	11 510 (Y)	PLB
7.625	45.30	0.595	C90	6.435	6.310	12.82	12 290	12 950 (Y)	PLB

(continued on next page)

Table D.2 (*continued*)

D	**Linear mass**	t	**Grade**	d	**Drift**	D/t	**MIYP**[a]	Δp_c[b]	**Finish**[c]
in.	$\frac{lb_m}{ft}$	in.		in.	in.		psi	psi	
7.625	45.30	0.595	R95	6.435	6.310	12.82	12 970	13 670 (Y)	PLB
7.625	45.30	0.595	T95	6.435	6.310	12.82	12 970	13 670 (Y)	PLB
7.625	45.30	0.595	P110	6.435	6.310	12.82	15 020	15 440 (P)	PLB
7.625	45.30	0.595	Q125	6.435	6.310	12.82	17 070	17 100 (P)	PLB
7.625	47.10	0.625	L80	6.375	6.250	12.20	11 480	12 040 (Y)	PLB
7.625	47.10	0.625	N80	6.375	6.250	12.20	11 480	12 040 (Y)	PLB
7.625	47.10	0.625	C90	6.375	6.250	12.20	12 910	13 540 (Y)	PLB
7.625	47.10	0.625	R95	6.375	6.250	12.20	13 630	14 300 (Y)	PLB
7.625	47.10	0.625	T95	6.375	6.250	12.20	13 630	14 300 (Y)	PLB
7.625	47.10	0.625	P110	6.375	6.250	12.20	15 780	16 550 (Y)	PLB
7.625	47.10	0.625	Q125	6.375	6.250	12.20	17 930	18 700 (P)	PLB
7.625	51.20	0.687	C90	6.251	6.126	11.10	14 190	14 760 (Y)	PLB
7.625	51.20	0.687	T95	6.251	6.126	11.10	14 980	15 580 (Y)	P
7.625	55.30	0.750	C90	6.125	6.000	10.17	15 490	15 960 (Y)	P
7.625	55.30	0.750	T95	6.125	6.000	10.17	16 350	16 850 (Y)	P
7.750	46.10	0.595	L80	6.560	6.500	13.03	10 750	11 340 (Y)	P
7.750	46.10	0.595	N80	6.560	6.500	13.03	10 750	11 340 (Y)	P
7.750	46.10	0.595	C90	6.560	6.500	13.03	12 090	12 750 (P)	P
7.750	46.10	0.595	R95	6.560	6.500	13.03	12 760	13 320 (P)	P
7.750	46.10	0.595	T95	6.560	6.500	13.03	12 760	13 320 (P)	P
7.750	46.10	0.595	P110	6.560	6.500	13.03	14 780	15 000 (P)	P
7.750	46.10	0.595	Q125	6.560	6.500	13.03	16 790	16 590 (P)	P
8.625	24.00	0.264	J55	8.097	7.972	32.67	2950	1370 (T)	PS
8.625	24.00	0.264	K55	8.097	7.972	32.67	2950	1370 (T)	PS
8.625	24.00	0.264	M65	8.097	7.972	32.67	3480	1420 (T)	PS
8.625	28.00	0.304	H40	8.017	7.892	28.37	2470	1610 (T)	PS
8.625	28.00	0.304	M65	8.017	7.892	28.37	4010	2020 (T)	PS
8.625	32.00	0.352	H40	7.921	7.875	24.50	2860	2200 (P)	PS
8.625	32.00	0.352	J55	7.921	7.875	24.50	3930	2530 (P)	PSLBE
8.625	32.00	0.352	K55	7.921	7.875	24.50	3930	2530 (P)	PSLBE
8.625	32.00	0.352	M65	7.921	7.875	24.50	4640	2740 (T)	PSLB
8.625	36.00	0.400	J55	7.825	7.700	21.56	4460	3450 (P)	PSLBE
8.625	36.00	0.400	K55	7.825	7.700	21.56	4460	3450 (P)	PSLBE

(continued on next page)

Table D.2 (*continued*)

D	**Linear mass**	t	**Grade**	d	**Drift**	D/t	**MIYP**[a]	Δp_c[b]	**Finish**[c]
in.	$\frac{\text{lb}_\text{m}}{\text{ft}}$	in.		in.	in.		psi	psi	
8.625	36.00	0.400	M65	7.825	7.700	21.56	5280	3760 (P)	PSLB
8.625	36.00	0.400	L80	7.825	7.700	21.56	6490	4100 (P)	PLBE
8.625	36.00	0.400	N80	7.825	7.700	21.56	6490	4100 (P)	PLBE
8.625	36.00	0.400	C90	7.825	7.700	21.56	7300	4250 (P)	PLBE
8.625	36.00	0.400	R95	7.825	7.700	21.56	7710	4350 (T)	PLBE
8.625	36.00	0.400	T95	7.825	7.700	21.56	7710	4350 (T)	PLBE
8.625	40.00	0.450	M65	7.725	7.625	19.17	5930	4900 (P)	PLBE
8.625	40.00	0.450	L80	7.725	7.625	19.17	7300	5520 (P)	PLB
8.625	40.00	0.450	N80	7.725	7.625	19.17	7300	5520 (P)	PLBE
8.625	40.00	0.450	C90	7.725	7.625	19.17	8220	5870 (P)	PLBE
8.625	40.00	0.450	R95	7.725	7.625	19.17	8670	6020 (P)	PLB
8.625	40.00	0.450	T95	7.725	7.625	19.17	8670	6020 (P)	PLBE
8.625	40.00	0.450	P110	7.725	7.625	19.17	10 040	6390 (P)	PLBE
8.625	44.00	0.500	L80	7.625	7.500	17.25	8120	6950 (P)	PLBE
8.625	44.00	0.500	N80	7.625	7.500	17.25	8120	6950 (P)	PLBE
8.625	44.00	0.500	C90	7.625	7.500	17.25	9130	7490 (P)	PLBE
8.625	44.00	0.500	R95	7.625	7.500	17.25	9640	7740 (P)	PLBE
8.625	44.00	0.500	T95	7.625	7.500	17.25	9640	7740 (P)	PLBE
8.625	44.00	0.500	P110	7.625	7.500	17.25	11 160	8420 (P)	PLBE
8.625	49.00	0.557	L80	7.511	7.386	15.48	9040	8570 (P)	PLBE
8.625	49.00	0.557	N80	7.511	7.386	15.48	9040	8570 (P)	PLBE
8.625	49.00	0.557	C90	7.511	7.386	15.48	10 170	9340 (P)	PLBE
8.625	49.00	0.557	R95	7.511	7.386	15.48	10 740	9700 (P)	PLBE
8.625	49.00	0.557	T95	7.511	7.386	15.48	10 740	9700 (P)	PLBE
8.625	49.00	0.557	P110	7.511	7.386	15.48	12 430	10 730 (P)	PLBE
8.625	49.00	0.557	Q125	7.511	7.386	15.48	14 130	11 660 (P)	PLBE
9.625	32.30	0.312	H40	9.001	8.845	30.85	2270	1370 (T)	PS
9.625	36.00	0.352	H40	8.921	8.765	27.34	2560	1720 (T)	PS
9.625	36.00	0.352	J55	8.921	8.765	27.34	3520	2020 (T)	PSLB
9.625	36.00	0.352	K55	8.921	8.765	27.34	3520	2020 (T)	PSLB
9.625	36.00	0.352	M65	8.921	8.765	27.34	4160	2190 (T)	PSLB
9.625	40.00	0.395	J55	8.835	8.750	24.37	3950	2570 (P)	PSLBE
9.625	40.00	0.395	K55	8.835	8.750	24.37	3950	2570 (P)	PSLBE
9.625	40.00	0.395	M65	8.835	8.750	24.37	4670	2770 (T)	PSLB

(continued on next page)

Table D.2 (*continued*)

D	**Linear mass**	t	**Grade**	d	**Drift**	D/t	**MIYP**[a]	Δp_c[b]	**Finish**[c]
in.	$\frac{lb_m}{ft}$	in.		in.	in.		psi	psi	
9.625	40.00	0.395	L80	8.835	8.750	24.37	5750	3090 (T)	PLBE
9.625	40.00	0.395	N80	8.835	8.750	24.37	5750	3090 (T)	PLBE
9.625	40.00	0.395	C90	8.835	8.750	24.37	6460	3260 (T)	PLBE
9.625	40.00	0.395	R95	8.835	8.750	24.37	6820	3330 (T)	PLBE
9.625	40.00	0.395	T95	8.835	8.750	24.37	6820	3330 (T)	PLBE
9.625	43.50	0.435	M65	8.755	8.599	22.13	5140	3530 (P)	PLB
9.625	43.50	0.435	L80	8.755	8.599	22.13	6330	3810 (P)	PLBE
9.625	43.50	0.435	N80	8.755	8.599	22.13	6330	3810 (P)	PLBE
9.625	43.50	0.435	C90	8.755	8.599	22.13	7120	4010 (T)	PLBE
9.625	43.50	0.435	R95	8.755	8.599	22.13	7510	4130 (T)	PLBE
9.625	43.50	0.435	T95	8.755	8.599	22.13	7510	4130 (T)	PLBE
9.625	43.50	0.435	P110	8.755	8.599	22.13	8700	4420 (T)	PLBE
9.625	47.00	0.472	M65	8.681	8.525	20.39	5580	4280 (P)	PLB
9.625	47.00	0.472	L80	8.681	8.525	20.39	6870	4750 (P)	PLBE
9.625	47.00	0.472	N80	8.681	8.525	20.39	6870	4750 (P)	PLBE
9.625	47.00	0.472	C90	8.681	8.525	20.39	7720	4990 (P)	PLBE
9.625	47.00	0.472	R95	8.681	8.525	20.39	8150	5090 (P)	PLBE
9.625	47.00	0.472	T95	8.681	8.525	20.39	8150	5090 (P)	PLBE
9.625	47.00	0.472	P110	8.681	8.525	20.39	9440	5300 (P)	PLBE
9.625	47.00	0.472	Q125	8.681	8.525	20.39	10 730	5630 (T)	PLBE
9.625	53.50	0.545	L80	8.535	8.500	17.66	7930	6620 (P)	PLBE
9.625	53.50	0.545	N80	8.535	8.500	17.66	7930	6620 (P)	PLBE
9.625	53.50	0.545	C90	8.535	8.500	17.66	8920	7110 (P)	PLBE
9.625	53.50	0.545	R95	8.535	8.500	17.66	9410	7340 (P)	PLBE
9.625	53.50	0.545	T95	8.535	8.500	17.66	9410	7340 (P)	PLBE
9.625	53.50	0.545	P110	8.535	8.500	17.66	10 900	7950 (P)	PLBE
9.625	53.50	0.545	Q125	8.535	8.500	17.66	12 390	8440 (P)	PLBE
9.625	58.40	0.595	L80	8.435	8.375	16.18	8650	7890 (P)	PLB
9.625	58.40	0.595	N80	8.435	8.375	16.18	8650	7890 (P)	PLB
9.625	58.40	0.595	C90	8.435	8.375	16.18	9740	8570 (P)	PLB
9.625	58.40	0.595	R95	8.435	8.375	16.18	10 280	8890 (P)	PLB
9.625	58.40	0.595	T95	8.435	8.375	16.18	10 280	8890 (P)	PLB
9.625	58.40	0.595	P110	8.435	8.375	16.18	11 900	9770 (P)	PLB
9.625	58.40	0.595	Q125	8.435	8.375	16.18	13 520	10 540 (P)	PLBE
9.625	59.40	0.609	C90	8.407	8.251	15.80	9970	8970 (P)	PLB

(continued on next page)

Table D.2 (*continued*)

D	**Linear mass**	t	**Grade**	d	**Drift**	D/t	**MIYP**[a]	Δp_c[b]	**Finish**[c]
in.	$\frac{\text{lb}_\text{m}}{\text{ft}}$	in.		in.	in.		psi	psi	
9.625	59.40	0.609	T95	8.407	8.251	15.80	10 520	9320 (P)	P
9.625	64.90	0.672	C90	8.281	8.125	14.32	11 000	10 800 (P)	P
9.625	64.90	0.672	T95	8.281	8.125	14.32	11 610	11 260 (P)	P
9.625	70.30	0.734	C90	8.157	8.001	13.11	12 010	12 600 (P)	P
9.625	70.30	0.734	T95	8.157	8.001	13.11	12 680	13 170 (P)	P
9.625	75.60	0.797	C90	8.031	7.875	12.08	13 040	13 670 (Y)	P
9.625	75.60	0.797	T95	8.031	7.875	12.08	13 770	14 430 (Y)	P
10.750	32.75	0.279	H40	10.192	10.036	38.53	1820	840 (T)	PS
10.750	40.50	0.350	H40	10.050	9.894	30.71	2280	1390 (T)	PS
10.750	40.50	0.350	J55	10.050	9.894	30.71	3130	1580 (T)	PSB
10.750	40.50	0.350	K55	10.050	9.894	30.71	3130	1580 (T)	PSB
10.750	40.50	0.350	M65	10.050	9.894	30.71	3700	1670 (T)	PSB
10.750	45.50	0.400	J55	9.950	9.875	26.88	3580	2090 (T)	PSBE
10.750	45.50	0.400	K55	9.950	9.875	26.88	3580	2090 (T)	PSBE
10.750	45.50	0.400	M65	9.950	9.875	26.88	4230	2270 (T)	PSB
10.750	51.00	0.450	J55	9.850	9.694	23.89	4030	2710 (P)	PSBE
10.750	51.00	0.450	K55	9.850	9.694	23.89	4030	2710 (P)	PSBE
10.750	51.00	0.450	M65	9.850	9.694	23.89	4760	2870 (T)	PSB
10.750	51.00	0.450	L80	9.850	9.694	23.89	5860	3220 (T)	PSBE
10.750	51.00	0.450	N80	9.850	9.694	23.89	5860	3220 (T)	PSBE
10.750	51.00	0.450	C90	9.850	9.694	23.89	6590	3400 (T)	PSBE
10.750	51.00	0.450	R95	9.850	9.694	23.89	6960	3480 (T)	PSBE
10.750	51.00	0.450	T95	9.850	9.694	23.89	6960	3480 (T)	PSBE
10.750	51.00	0.450	P110	9.850	9.694	23.89	8060	3660 (T)	PSBE
10.750	55.50	0.495	M65	9.760	9.625	21.72	5240	3690 (P)	PSB
10.750	55.50	0.495	L80	9.760	9.625	21.72	6450	4020 (P)	PSBE
10.750	55.50	0.495	N80	9.760	9.625	21.72	6450	4020 (P)	PSBE
10.750	55.50	0.495	C90	9.760	9.625	21.72	7250	4160 (T)	PSBE
10.750	55.50	0.495	R95	9.760	9.625	21.72	7660	4290 (T)	PSBE
10.750	55.50	0.495	T95	9.760	9.625	21.72	7660	4290 (T)	PSBE
10.750	55.50	0.495	P110	9.760	9.625	21.72	8860	4610 (T)	PSBE
10.750	60.70	0.545	C90	9.660	9.504	19.72	7980	5460 (P)	PSBE
10.750	60.70	0.545	T95	9.660	9.504	19.72	8430	5580 (P)	PSBE
10.750	60.70	0.545	P110	9.660	9.504	19.72	9760	5880 (P)	PSBE

(continued on next page)

Table D.2 (*continued*)

D	**Linear mass**	t	**Grade**	d	**Drift**	D/t	**MIYP**[a]	Δp_c[b]	**Finish**[c]
in.	$\frac{lb_m}{ft}$	in.		in.	in.		psi	psi	
10.750	60.70	0.545	Q125	9.660	9.504	19.72	11 090	6070 (T)	PSBE
10.750	65.70	0.595	C90	9.560	9.404	18.07	8720	6760 (P)	PSBE
10.750	65.70	0.595	T95	9.560	9.404	18.07	9200	6970 (P)	PSB
10.750	65.70	0.595	P110	9.560	9.404	18.07	10 650	7500 (P)	PSB
10.750	65.70	0.595	Q125	9.560	9.404	18.07	12 110	7920 (P)	PSB
10.750	73.20	0.672	C90	9.406	9.250	16.00	9850	8760 (P)	PSB
10.750	73.20	0.672	T95	9.406	9.250	16.00	10 390	9090 (P)	P
10.750	79.20	0.734	C90	9.282	9.126	14.65	10 750	10 370 (P)	P
10.750	79.20	0.734	T95	9.282	9.126	14.65	11 350	10 800 (P)	P
10.750	85.30	0.797	C90	9.156	9.000	13.49	11 680	12 010 (P)	P
10.750	85.30	0.797	T95	9.156	9.000	13.49	12 330	12 540 (P)	P
11.750	42.00	0.333	H40	11.084	11.000	35.29	1980	1040 (T)	PS
11.750	47.00	0.375	J55	11.000	10.844	31.33	3070	1510 (T)	PSB
11.750	47.00	0.375	K55	11.000	10.844	31.33	3070	1510 (T)	PSB
11.750	47.00	0.375	M65	11.000	10.844	31.33	3630	1590 (T)	PSB
11.750	54.00	0.435	J55	10.880	10.724	27.01	3560	2070 (T)	PSB
11.750	54.00	0.435	K55	10.880	10.724	27.01	3560	2070 (T)	PSB
11.750	54.00	0.435	M65	10.880	10.724	27.01	4210	2250 (T)	PSB
11.750	60.00	0.489	J55	10.772	10.625	24.03	4010	2670 (P)	PSB
11.750	60.00	0.489	K55	10.772	10.625	24.03	4010	2670 (P)	PSB
11.750	60.00	0.489	M65	10.772	10.625	24.03	4730	2840 (T)	PSB
11.750	60.00	0.489	L80	10.772	10.625	24.03	5830	3180 (T)	PSB
11.750	60.00	0.489	N80	10.772	10.625	24.03	5830	3180 (T)	PSB
11.750	60.00	0.489	C90	10.772	10.625	24.03	6550	3360 (T)	PSB
11.750	60.00	0.489	R95	10.772	10.625	24.03	6920	3440 (T)	PSB
11.750	60.00	0.489	T95	10.772	10.625	24.03	6920	3440 (T)	PSB
11.750	60.00	0.489	P110	10.772	10.625	24.03	8010	3610 (T)	PSB
11.750	60.00	0.489	Q125	10.772	10.625	24.03	9100	3680 (T)	PSB
11.750	65.00	0.534	L80	10.682	10.625	22.00	6360	3870 (P)	P
11.750	65.00	0.534	N80	10.682	10.625	22.00	6360	3870 (P)	P
11.750	65.00	0.534	C90	10.682	10.625	22.00	7160	4060 (T)	P
11.750	65.00	0.534	R95	10.682	10.625	22.00	7560	4170 (T)	P
11.750	65.00	0.534	T95	10.682	10.625	22.00	7560	4170 (T)	P
11.750	65.00	0.534	P110	10.682	10.625	22.00	8750	4480 (T)	P

(continued on next page)

Table D.2 (*continued*)

D	**Linear mass**	t	**Grade**	d	**Drift**	D/t	**MIYP**[a]	Δp_c[b]	**Finish**[c]
in.	$\frac{\text{lb}_\text{m}}{\text{ft}}$	in.		in.	in.		psi	psi	
11.750	65.00	0.534	Q125	10.682	10.625	22.00	9940	4690 (T)	P
11.750	71.00	0.582	L80	10.586	10.430	20.19	6930	4880 (P)	P
11.750	71.00	0.582	N80	10.586	10.430	20.19	6930	4880 (P)	P
11.750	71.00	0.582	C90	10.586	10.430	20.19	7800	5130 (P)	P
11.750	71.00	0.582	R95	10.586	10.430	20.19	8230	5240 (P)	P
11.750	71.00	0.582	T95	10.586	10.430	20.19	8230	5240 (P)	P
11.750	71.00	0.582	P110	10.586	10.430	20.19	9530	5470 (P)	P
11.750	71.00	0.582	Q125	10.586	10.430	20.19	10 840	5760 (T)	P
13.375	48.00	0.330	H40	12.715	12.559	40.53	1730	740 (T)	PS
13.375	54.50	0.380	J55	12.615	12.459	35.20	2730	1130 (T)	PSB
13.375	54.50	0.380	K55	12.615	12.459	35.20	2730	1130 (T)	PSB
13.375	54.50	0.380	M65	12.615	12.459	35.20	3230	1140 (E)	PSB
13.375	61.00	0.430	J55	12.515	12.359	31.10	3090	1540 (T)	PSB
13.375	61.00	0.430	K55	12.515	12.359	31.10	3090	1540 (T)	PSB
13.375	61.00	0.430	M65	12.515	12.359	31.10	3660	1620 (T)	PSB
13.375	68.00	0.480	J55	12.415	12.259	27.86	3450	1950 (T)	PSB
13.375	68.00	0.480	K55	12.415	12.259	27.86	3450	1950 (T)	PSB
13.375	68.00	0.480	M65	12.415	12.259	27.86	4080	2100 (T)	PSB
13.375	68.00	0.480	L80	12.415	12.259	27.86	5020	2260 (T)	PSB
13.375	68.00	0.480	N80	12.415	12.259	27.86	5020	2260 (T)	PSB
13.375	68.00	0.480	C90	12.415	12.259	27.86	5650	2320 (T)	PSB
13.375	68.00	0.480	R95	12.415	12.259	27.86	5970	2330 (T)	PSB
13.375	68.00	0.480	T95	12.415	12.259	27.86	5970	2330 (T)	PSB
13.375	68.00	0.480	P110	12.415	12.259	27.86	6910	2330 (E)	PSB
13.375	72.00	0.514	L80	12.347	12.250	26.02	5380	2670 (T)	PSB
13.375	72.00	0.514	N80	12.347	12.250	26.02	5380	2670 (T)	PSB
13.375	72.00	0.514	C90	12.347	12.250	26.02	6050	2780 (T)	PSB
13.375	72.00	0.514	R95	12.347	12.250	26.02	6390	2820 (T)	PSB
13.375	72.00	0.514	T95	12.347	12.250	26.02	6390	2820 (T)	PSB
13.375	72.00	0.514	P110	12.347	12.250	26.02	7400	2880 (T)	PSB
13.375	72.00	0.514	Q125	12.347	12.250	26.02	8410	2880 (E)	PSB
16.000	65.00	0.375	H40	15.250	15.062	42.67	1640	630 (E)	PS
16.000	75.00	0.438	J55	15.124	14.936	36.53	2630	1020 (T)	PSB

(continued on next page)

Table D.2 (*continued*)

D	**Linear mass**	t	**Grade**	d	**Drift**	D/t	**MIYP**[a]	Δp_c[b]	**Finish**[c]
in.	$\frac{\text{lb}_\text{m}}{\text{ft}}$	in.		in.	in.		psi	psi	
16.000	75.00	0.438	K55	15.124	14.936	36.53	2630	1020 (T)	PSB
16.000	75.00	0.438	M65	15.124	14.936	36.53	3110	1020 (E)	PSB
16.000	84.00	0.495	J55	15.010	14.822	32.32	2980	1410 (T)	PSB
16.000	84.00	0.495	K55	15.010	14.822	32.32	2980	1410 (T)	PSB
16.000	84.00	0.495	M65	15.010	14.822	32.32	3520	1460 (T)	PSB
16.000	109.00	0.656	J55	14.688	14.500	24.39	3950	2560 (P)	P
16.000	109.00	0.656	K55	14.688	14.500	24.39	3950	2560 (P)	P
16.000	109.00	0.656	L80	14.688	14.500	24.39	5740	3080 (T)	P
16.000	109.00	0.656	N80	14.688	14.500	24.39	5740	3080 (T)	P
16.000	109.00	0.656	R95	14.688	14.500	24.39	6820	3320 (T)	P
16.000	109.00	0.656	P110	14.688	14.500	24.39	7890	3470 (T)	P
16.000	109.00	0.656	Q125	14.688	14.500	24.39	8970	3520 (T)	P
18.625	87.50	0.435	H40	17.755	17.567	42.82	1630	630 (E)	PS
18.625	87.50	0.435	J55	17.755	17.567	42.82	2250	630 (E)	PSB
18.625	87.50	0.435	K55	17.755	17.567	42.82	2250	630 (E)	PSB
18.625	87.50	0.435	M65	17.755	17.567	42.82	2660	630 (E)	PSB
20.000	94.00	0.438	H40	19.124	18.936	45.66	1530	520 (E)	PSL
20.000	94.00	0.438	J55	19.124	18.936	45.66	2110	520 (E)	PSLB
20.000	94.00	0.438	K55	19.124	18.936	45.66	2110	520 (E)	PSLB
20.000	94.00	0.438	M65	19.124	18.936	45.66	2490	520 (E)	PSLB
20.000	106.50	0.500	J55	19.000	18.812	40.00	2410	770 (E)	PSLB
20.000	106.50	0.500	K55	19.000	18.812	40.00	2410	770 (E)	PSLB
20.000	106.50	0.500	M65	19.000	18.812	40.00	2840	770 (E)	PSLB
20.000	133.00	0.635	J55	18.730	18.542	31.50	3060	1500 (T)	PSLB
20.000	133.00	0.635	K55	18.730	18.542	31.50	3060	1500 (T)	PSLB

[a] Internal yield pressure according to Eq. (7.12) with $k_{wall} = 0.875$.
[b] Collapse mode: E = elastic, T = transition, P = plastic, Y = yield.
[c] Finish (API connections): P = plain end, S = STC, L = LTC, B = BTC, E = Extreme-line. A wide variety of proprietary thread vendors also offer threaded connections.

BIBLIOGRAPHY

[1] B.D. Craig, Practical Oil-Field Metallurgy, 1st ed., PennWell Publishing Company, Tulsa, Oklahoma, 1984.

[2] A.A. Rauf, Performance of fiberglass casing and tubing in highly corrosive environments, SPE 178729 presented at the SPE Annual Technical Conference and Exhibition, Houston, Texas, September 28–30, 2015.

[3] Norsk Sokkels Konkuranseposisjon, Well Integrity in Drilling and Well Operations, 4th ed., NORSOK, Oslo, Norway, 2013, NORSOK D-010:2013.

[4] C. Corley, J. Rike, Tubingless Completions, API-59-007, API Drilling and Production Practice, 1959.

[5] T. Butcher, L. Crown, R. Harshman, Specifications Tolerances, and Other Technical Requirements for Weighing and Measuring Devices, 2017 ed., National Institute of Standards and Technology, U.S. Department of Commerce, Washington, D.C., 2016, as adopted by the 101th National Conference on Weights and Measures 2016.

[6] P. Chadwick, Continuum Mechanics Concise Theory and Problems, 2nd ed., Dover Publications, Inc., Mineola, New York, 1976.

[7] A.C. Eringen, Mechanics of Continua, 1st ed., John Wiley & Sons, Inc., New York, 1967.

[8] L.E. Malvern, Introduction to the Mechanics of a Continuous Medium, Prentice-Hall, Inc., Englewood Cliffs, New Jersey, 1969.

[9] A.S. Khan, S. Huang, Continuum Theory of Plasticity, John Wiley & Sons, Inc., New York, 1995.

[10] K. Rektorys, Survey of Applicable Mathematics, MIT Press, Cambridge, Massachusetts, 1969.

[11] R. Abeyaratne, Lecture Notes on the Mechanics of Elastic Solids, Volume 1: A Brief Review of Some Mathematical Preliminaries, 1st ed., Department of Mechanical Engineering, MIT Press, Cambridge, Massachusetts, 2006, http://web.mit.edu/abeyaratne/lecture_notes.html.

[12] R. Abeyaratne, Lecture Notes on the Mechanics of Elastic Solids, Volume 2: Continuum Mechanics, 1st ed., Department of Mechanical Engineering, MIT, Cambridge, Massachusetts, 2012, http://web.mit.edu/abeyaratne/lecture_notes.html.

[13] A. McConnell, Applications of Tensor Analysis, Dover Publications, Inc., New York, 1957.

[14] Y.C. Fung, Foundations of Solid Mechanics, 1st ed., Prentice-Hall, Inc., Englewood Cliffs, New Jersey, 1965.

[15] Y.C. Fung, A First Course in Continuum Mechanics, 2nd ed., Prentice-Hall, Inc., Englewood Cliffs, New Jersey, 1977.

[16] R. Bellman, Introduction to Matrix Analysis, 2nd ed., McGraw-Hill Book Company, New York, 1970.

[17] J. Burkhardt, Wellbore pressure surges produced by pipe movement, Journal of Petroleum Technology 13 (6) (1961) 595–605.

[18] A. Lubinski, F. Hsu, K. Nolte, Transient pressure surges due to pipe movement in an oil well, Revue de L'Institut Français Du Pétrole 32 (3) (1977) 307–347.

[19] M. Lal, Surge and swab modeling for dynamic pressures and safe trip velocities, SPE 11412 presented at the IADC/SPE Drilling Conference, New Orleans, Louisiana, February 20–23, 1983.

[20] R.F. Mitchell, Dynamic surge/swab pressure predictions, SPE Drilling Engineering 3 (3) (1988) 325–333.

[21] S. Gibbs, Predicting the behavior of sucker-rod pumping systems, Journal of Petroleum Technology 15 (7) (1963) 769–778.

[22] S. Gibbs, Rod Pumping: Modern Methods of Design, Diagnosis and Surveillance, 1st ed., 2012.
[23] C. Wylie, Advanced Engineering Mathematics, 3rd ed., McGraw-Hill Book Company, New York, 1966.
[24] S.J. Farlow, Partial Differential Equations for Scientists and Engineers, 1st ed., Dover Publications, Inc., New York, 1993.
[25] W.F. Boyce, R.C. DiPrima, Elementary Differential Equations, 2nd ed., John Wiley & Sons, Inc., New York, 1969.
[26] A. Higdon, E. Olsen, W. Stiles, J. Weese, W. Riley, Mechanics of Materials, 3rd ed., John Wiles & Sons, Inc., New York, 1976.
[27] R.F. Mitchell, Forces on curved tubulars caused by fluid flow, SPE Production and Facilities 11 (1) (1996) 30–34.
[28] R.D. Blevins, Flow-Induced Vibration, 2nd ed., Krieger Publishing Company, Malabar, Florida, 2001.
[29] G. Kuiper, A. Metrikine, Effect of hydrodynamic drag on the stability of a cantilever pipe conveying fluid, WIT Transactions on the Built Environment 84 (2005) 175–184.
[30] G. Kuiper, A. Metrikine, J. Battjes, A new time-domain drag description and its influence on the dynamic behavior of a cantilever pipe conveying fluid, Journal of Fluids and Structures 23 (3) (2007) 429–445.
[31] G. Batchelor, An Introduction to Fluid Dynamics, 1st ed., Cambridge University Press, London, 1967.
[32] R.H. Pao, Fluid Dynamics, Charles E. Merrill Books, Inc., Columbus, Ohio, 1967.
[33] R.L. Daugherty, J.B. Franzini, Fluid Mechanics with Engineering Applications, sixth ed., McGraw-Hill Book Company, New York, 1965.
[34] C. Johancsik, D. Friesen, R. Dawson, Torque and drag in directional wells—prediction and measurement, Journal of Petroleum Technology 36 (6) (1984) 987–992.
[35] B.S. Aadnøy, K. Andersen, Friction analysis for long-reach wells, SPE 39391 presented at the IADC/SPE Drilling Conference, Dallas, Texas, March 3–6, 1998.
[36] I. Rezmer-Cooper, M. Chau, A. Hendricks, M. Woodfine, B. Stacey, N. Downton, Field data supports the use of stiffness and tortuosity in solving complex well design problems, SPE 52819 presented at the SPE/IADC Drilling Conference, Amsterdam, The Netherlands, March 9–11, 1999.
[37] R.F. Mitchell, R. Samuel, How good is the torque/drag model? SPE Drilling and Completion 24 (1) (2009) 62–71.
[38] V. Tikhonov, K. Valiullin, A. Nurgaleev, L. Ring, R. Gandikota, P. Chaguine, et al., Dynamic model for stiff-string torque and drag, SPE Drilling and Completion 29 (3) (2014) 279–294.
[39] R.F. Mitchell, A. Bjjørset, G. Grindhaug, Drillstring analysis with a discrete torque/drag model, SPE Drilling and Completion 30 (1) (2015) 5–16.
[40] R. Samuel, Friction factors: What are they for torque, drag, vibration, bottom hole assembly and transient surge/swab analyses, SPE 128059 presented at the IADC/SPE Drilling Conference and Exhibition, New Orleans, Louisiana, February 2–4, 2010.
[41] R.F. Mitchell, Simple frictional analysis of helical buckling of tubing, SPE Drilling Engineering 3 (3) (1986) 457–465.
[42] M. Sheppard, C. Wick, T. Burgess, Designing well paths to reduce drag and torque, SPE Drilling Engineering 2 (4) (1987) 344–350.
[43] P. Naghdi, J. Trapp, The significance of formulating plasticity theory with reference to loading surfaces in strain space, International Journal of Engineering Science 13 (9–10) (1975) 785–797.
[44] P. Pattillo, R. Boswell, Application of strain space plasticity theory to surface strain gage measurements, Journal of Energy Resources Technology 114 (1) (1992) 95–99.
[45] G. Dieter, Mechanical Metallurgy, 2nd ed., McGraw-Hill Series in Materials Science and Engineering, McGraw-Hill Book Company, New York, 1976.

[46] American Petroleum Institute, Specification for Casing and Tubing, eighth ed., API, Washington, D.C., 2005, API Specification 5CT.
[47] R. Hill, The Mathematical Theory of Plasticity, 1st ed., Oxford University Press, New York, 1950.
[48] J. Plàcido, P. Ademar, L. Paulo, I. Pasqualino, S. Estefen, Stress analysis of casing string submitted to cyclic steam injection, SPE 38978, presented at the Fifth Latin American and Caribbean Petroleum Engineering Conference and Exhibition in Rio de Janeiro, Brazil, August 30–September 3, 1997.
[49] A. Needleman, Post-bifurcation behavior and imperfection sensitivity of elastic-plastic circular plates, International Journal of Mechanical Sciences 17 (1975) 1–13.
[50] P. Ludwik, Elemente der Technologischen Mechanik, Springer-Verlag, Berlin, 1909.
[51] American Petroleum Institute, Technical Report on Equations and Calculations for Casing, Tubing, and Line Pipe Used as Casing or Tubing; and Performance Properties Tables for Casing and Tubing, 1st ed., API, Washington, D.C., 2008, ANSI/API Technical Report 5C3.
[52] R. von Mises, Mechanik der festen körper im plastisch deformablen zustand, Göttinger Nachrichten Math Phys 1 (1913) 582–592.
[53] H. Hencky, Zur theorie plastischer deformationen und der hierdurch im material hervorgerufenen nachspannngen, Zeitschrift für Angewandte Mathematik und Mechanik 4 (1924) 323–334.
[54] H. Tresca, Mémoire sur l'écoulement des corps solides soumis à de fortes pressions, Comptes Rendus de L'Académie des Sciences 59 (1864) 754.
[55] American Petroleum Institute, Packers and Bridge Plugs, 3rd ed., API, Washington, D.C., 2015, ANSI/API Specification 11D1.
[56] American Petroleum Institute, Procedures for Testing Casing and Tubing Connections, 4th ed., API, Washington, D.C., 2017, API Recommended Practice 5C5.
[57] F. Klever, T. Tamano, A new OCTG strength equation for collapse under combined loads, SPE Drilling & Completion 21 (3) (2006) 164–179.
[58] A. Lubinski, W. Althouse, J. Logan, Helical buckling of tubing sealed in packers, Journal of Petroleum Technology 14 (6) (1962) 655–670.
[59] D. Drucker, A more fundamental approach to plastic stress strain relations, in: Proceedings, First U.S. National Congress of Applied Mechanics (Chicago), 1951, pp. 487–491.
[60] P. Naghdi, Stress-strain relations in plasticity and thermoplasticity, in: E. Lee, P. Symonds (Eds.), Plasticity: Proceedings of the Second Symposium on Naval Structural Mechanics, Permagon Press, Chicago, 1960, pp. 121–169.
[61] B.S. Aadnøy, I. Cooper, S.Z. Miska, R.F. Mitchell, M.L. Payne, Advanced Drilling and Well Technology, 1st ed., Society of Petroleum Engineers, Richardson, Texas, 2009.
[62] F. Klever, Formulas for rupture, necking, and wrinkling of oil country tubular goods under combined loads, SPE Journal 15 (3) (2010) 834–855.
[63] F. Klever, G. Stewart, Analytical burst strength prediction of OCTG with and without defects, SPE 48329 presented at the SPE Applied Technology Workshop on Risk Based Design of Well Casing and Tubing, The Woodlands, Texas, May 7–8, 1998.
[64] G. Stewart, F. Klever, D. Ritchie, An analytical model to predict the burst capacity of pipelines, Presented at the 13th International Conference on Offshore Mechanics and Arctic Engineering, Houston, Texas, February 27–March 3, 1994.
[65] International Organization for Standardization, Petroleum, Petrochemical and Natural Gas Industries—Equations and Calculations for the Properties of Casing, Tubing, Drill Pipe and Line Pipe Used as Casing or Tubing, 1st ed., ISO, Geneva, Switzerland, 2007, ISO TR 10400:2007.
[66] W. Bradley, The effect of casing wear on the burst strength of casing, part 2: statistical burst strength of worn and unworn casing strings, Journal of Engineering for Industry 98 (2) (1976) 686–694.
[67] Z.P. Bažant, L. Cedolin, Stability of Structures, 1st ed., Dover Publications, Inc., Mineola, New York, 2003.
[68] D. Bradford, D. Fritchie Jr, D. Gibson, S. Gosch, P. Pattillo, J. Sharp, et al., Marlin failure analysis and redesign: Part 1—description of failure, SPE Drilling & Completion 11 (2) (2004) 104–111.

[69] P. Pattillo, B. Cocales, S. Morey, Analysis of an annular pressure buildup failure during drill ahead, SPE 89775 presented at the SPE Annual Technical Conference and Exhibition, Houston, Texas, September 26–29, 2004.
[70] S.P. Timoshenko, J.M. Gere, Theory of Elastic Stability, 2nd ed., McGraw-Hill Book Company, New York, 1961.
[71] W. Clinedinst, A rational expression for the critical collapsing pressure of pipe under external pressure, API Drilling and Production Practice 1939 (1940) 383–391.
[72] N. Huang, P. Pattillo, Collapse of oil well casing, Transactions of the ASME, Journal of Pressure Vessel Technology 104 (1982) 36–41.
[73] P. Jammer, H. Hariharan, F.J. Klever, Casing collapse strength enhancement due to cement and pipe support via modeling and testing, SPE 173069 presented at the SPE/IADC Drilling Conference and Exhibition, London, United Kingdom, March 17–19, 2015.
[74] A.P. Assanelli, G.L. Turconi, Effect of measurement procedures on estimating geometrical parameters of pipes, SPE 13051 presented at the Offshore Technology Conference, Houston, Texas, April 30–May 3, 2001.
[75] R.G. Toscano, L. Mantovano, E.N. Dvorkin, On the numerical calculation of collapse and collapse propagation pressure of steel deep-water pipelines under external pressure and bending: experimental verification of the finite element results, in: Proceedings of the Fourth International Conference on Pipeline Technology, 2004, pp. 1417–1428.
[76] J. Greenip, Collapse strength of casing subjected to combined load, SPE 178806 presented at the IADC/SPE Drilling Conference and Exhibition, Fort Worth, Texas, March 1–3, 2016.
[77] N. Huang, P. Pattillo, The effect of length: diameter ratio on collapse of casing, Transactions of the ASME, Journal of Pressure Vessel Technology 106 (1984) 160–165.
[78] P. Pattillo, Effect of length: diameter ratio on collapse test results and frame design, SPE 105602 prepared for presentation at the SPE/IADC Drilling Conference, Amsterdam, The Netherlands, February 20-22, 2007.
[79] J.L. Sanders Jr, Nonlinear theories for thin shells, Quarterly of Applied Mathematics 21 (1963) 21–36.
[80] J. Cheatham Jr, J. McEver, Behavior of casing subjected to salt loading, Journal of Petroleum Technology 16 (9) (1964) 1069–1075.
[81] F. Khalaf, Increasing casing collapse resistance against salt-induced loads, SPE 13712 presented at the Middle East Oil Technical Conference, Exhibition, Bahrain, March 11–14, 1985.
[82] S. Willson, A. Fossum, J. Fredrich, Assessment of salt loading on well casings, SPE Drilling and Completion 19 (1) (2003) 13–21.
[83] P. Pattillo, T. Kristiansen, Analysis of horizontal casing integrity in the Valhall field, SPE 78204 presented at the SPE/ISRM Rock Mechanics Conference, Irving, Texas, October 20–23, 2002.
[84] G.R. Wooley, W. Prachner, Reservoir compaction loads on casings and liners, SPE Production Engineering 3 (1) (1988) 96–102.
[85] E. Cernocky, F. Scholibo, Approach to casing design for service in compacting reservoirs, SPE 30322 presented at the SPE Annual Technical Conference and Exhibition, Dallas, Texas, October 22–25, 1995.
[86] J. Fredrich, J. Arguello, G. Detrick, E. de Rouffignac, Geomechanical modeling of reservoir compaction, surface subsidence, and casing damage at the Belridge diatomite field, SPE Reservoir Evaluation & Engineering 3 (4) (2000) 348–359.
[87] M. Bruno, Geomechanical and decision analyses for mitigating compaction-related casing damage, SPE Drilling & Completion (2002) 179–188.
[88] X. Li, F. Mitchum, M. Bruno, P. Pattillo, S. Willson, Compaction, subsidence, and associated casing damage and well failure assessment for the Gulf of Mexico shelf Matagorda Island 623 field, SPE 84533 presented at the SPE Annual Technical Conference and Exhibition, Denver, Colorado, October 5–8, 2003.

[89] C.M. Sayers, L.D. Boer, D.W. Lee, P.J. Hooyman, R.P. Lawrence, Predicting reservoir compaction and casing deformation in deepwater turbidites using a 3d mechanical earth model, SPE 103926 presented at the International Oil Conference and Exhibition, Cancun, Mexico, August 13–September 2, 2006.

[90] P. Pattillo, N. Last, W. Asbill, Effect of nonuniform loading on conventional casing collapse resistance, SPE Drilling and Completion 19 (3) (2004) 156–163.

[91] N. Last, S. Mujica, P. Pattillo, G. Kelso, Evaluation, impact, and management of casing deformation caused by tectonic forces in the Andean foothills, Colombia, SPE Drilling and Completion 21 (2) (2006) 116–124.

[92] M.B. Dusseault, M.S. Bruno, J. Barrera, Casing shear: causes, cases, cures, SPE Drilling & Completion 16 (2) (2001) 98–107.

[93] P. Pattillo, U. Sathuvalli, S. Rahman, H. Prewett, S. Carmichael, R. Wydrinski, Mad Dog W1 tubing deformation failure analysis, SPE 109882 presented at the SPE Annual Technical Conference and Exhibition, Anaheim, California, November 11–14, 2007.

[94] J. Nester, D. Jenkins, R. Simon, Resistances to failure of oil-well casing subjected to non-uniform transverse loading, API Drilling and Production Practice (1955) 374–378.

[95] J. Clegg, Casing failure study – Cedar Creek anticline, Journal of Petroleum Technology 23 (6) (1971) 676–684.

[96] P. Pattillo, Z. Moschovidis, M. Lal, An evaluation of concentric casing for nonuniform load applications, SPE Drilling and Completion 10 (3) (1995) 186–192.

[97] P. Pattillo, T. Rankin, How Amoco solved casing design problems in the Gulf of Suez, Petroleum Engineer International (1981) 86–112.

[98] E. Riks, An incremental approach to the solution of snapping and buckling problems, International Journal of Solids and Structures 15 (7) (1979) 529–551.

[99] P. Pattillo, R. Pruitt, A.A. Nakbi, J. Gent, K. Young, X. Zhang, Repair intervention of worn production casing in the Sajaa field, SPE 81537 prepared for presentation in: SPE 13th Middle East Oil Show & Conference, Bahrain, April 5–8, 2003.

[100] Y. Kuriyama, Y. Tsukano, T. Mimaki, T. Yonezawa, Effect of wear and bending on casing collapse strength, SPE 24597 presented at the SPE 67th Annual Technical Conference and Exhibition, Washington, DC, October 4–7, 1992.

[101] E. Klementich, Unraveling the mysteries of proprietary connections, Journal of Petroleum Technology 47 (12) (1995) 1055–1059.

[102] B. Schwind, M. Payne, G. Otten, P. Pattillo, Development of leak resistance in industry standard OCTG connections using finite element analysis and full scale testing, OTC 13050 presented at the Offshore Technology Conference, Houston, Texas, April 30–May 3, 2001.

[103] W. Asbill, P. Pattillo, W. Rogers, Investigation of 8 round casing connection performance – part I, introduction and method of analysis, Journal of Energy Resources Technology 106 (1984) 130–136.

[104] W. Asbill, P. Pattillo, W. Rogers, Investigation of 8 round casing connection performance – part II, stresses with criteria, Journal of Energy Resources Technology, Trans ASME 106 (1984) 137–143.

[105] W. Asbill, P. Pattillo, W. Rogers, Investigation of 8 round casing connection performance – part III, sealability and torque, Journal of Energy Resources Technology, Trans ASME 106 (1984) 144–154.

[106] L. Hilbert Jr, I. Kalil, Evaluation of premium threaded connections using finite-element analysis and full-scale testing, SPE 23904 presented at the SPE/IADC Drilling Conference, New Orleans, Louisiana, March 5–8, 1992.

[107] J. Xie, G. Tao, Analysis of casing connections subjected to thermal cycle loading, in: 2010 SIMULIA Customer Conference, Providence, Rhode Island, May 25–27, 2010, pp. 25–27.

[108] G. Tao, J. Xie, Analytical evaluation of casing connections for thermal well applications, SPE 165493 presented at the SPE Heavy Oil Conference, Canada, Calgary, Alberta, June 11–13, 2013.

[109] American Petroleum Institute, Specification for Threading, Gauging, and Thread Inspection of Casing, Tubing, and Line Pipe Threads, fifteenth ed., API, Washington, D.C., 2008, ANSI/API Specification 5B.
[110] M.J. Jellison, M.A. Davila, How to evaluate and select premium casing connectors, SPE 35037 presented at the IADC/SPE Drilling Conference, New Orleans, Louisiana, March 12–15, 1996.
[111] W. Clinedinst, Strength of threaded joints for steel pipe, Journal of Engineering for Industry 87 (2) (1965) 125–134.
[112] M. Payne, W. Asbill, H. Davis, P. Pattillo, Joint industry qualification test program for high-clearance casing connections, SPE Drilling Engineering 7 (4) (1992) 261–267.
[113] H.A. Reynolds, J.F. Greenip, Wedge thread tool joints: applications and economics, SPE 74567 presented at the IADC/SPE Drilling Conference, Dallas, Texas, February 26–28, 2002.
[114] M. Mayberry, Development of an API thread compound, API Drilling and Production Practice (1951).
[115] C. Bollfrass, Sealing tubular connections, Journal of Petroleum Technology 37 (6) (1985) 955–965.
[116] L. Hilbert Jr, J. Bergström, Evaluating pressure integrity of polymer ring seals for threaded connections in HP/HT wells and expandable casing, SPE 87214 presented at the IADC/SPE Drilling Conference, Dallas, Texas, March 2–4, 2004.
[117] G.A. Valigura, P. Cernocky, Shell exploration and production company list of connections tested for well service pressures > 8000 psi based on standardized API/ISO qualification testing procedures, SPE/IADC 97605 presented at the SPE High Pressure-High Temperature Sour Well Design Applied Technology Workshop, The Woodlands, Texas, May 17–19, 2005.
[118] J. Xie, C. Matthews, A. Hamilton, A study of sealability evaluation criteria for casing connections in thermal wells, SPE 180720 presented at the SPE Canada Heavy Oil Technical Conference, Calgary, Alberta, June 7–9, 2016.
[119] J. Xie, C. Matthews, Experimental investigation of metal-to-metal seal behavior in premium casing connections for thermal wells, SPE 184982 presented at the SPE Canada Heavy Oil Technical Conference, Calgary, Alberta, February 15–16, 2017.
[120] G. Murtagian, V. Fanelli, J. Villasante, D. Johnson, H. Ernst, Sealability of stationary metal-to-metal seals, Journal of Tribology 126 (2004) 591–596.
[121] International Organization for Standardization, Qualification of Casing Connections for Thermal Wells, 1st ed., ISO, Geneva, Switzerland, 2013, ISO/PAS 12835:2013.
[122] C. Sparks, The influence of tension, pressure and weight on pipe and riser deformations and stresses, Journal of Energy Resources Technology 106 (1) (1984) 46–54.
[123] H. Ziegler, Principles of Structural Stability, 1st ed., Blaisdell Publishing Company, Waltham, Massachusetts, 1968.
[124] D.W. Dareing, Drill collar length is a major factor in vibration control, Journal of Petroleum Technology 36 (4) (1984) 637–644.
[125] R.F. Mitchell, Tubing buckling—the state of the art, SPE Drilling and Completion 23 (4) (2008) 361–370.
[126] H.L. Langhaar, Energy Methods in Applied Mechanics, John Wiley and Sons, Inc., New York, 1962.
[127] A. Lubinski, A study of the buckling of rotary drill strings, in: S. Miska (Ed.), Developments in Petroleum Engineering, Collected Works of Arthur Lubinski, Vol. 1, Gulf Publishing Company, 1987, pp. 1–67.
[128] P. Paslay, D. Bogy, The stability of a circular rod laterally constrained to be in contact with an inclined circular cylinder, Journal of Applied Mechanics 31 (4) (1964) 605–610.
[129] R. Dawson, P. Paslay, Drillpipe buckling in inclined holes, Journal of Petroleum Technology 36 (10) (1984) 1734–1738.
[130] Y.C. Chen, Y.H. Lin, J. Cheatham Jr, Tubing and casing buckling in horizontal wells, Journal of Petroleum Technology 42 (2) (1990) 140–191.

[131] R. Mitchell, Effects of well deviation on helical buckling, SPE Drilling and Completion 12 (1) (1997) 63–70.
[132] N. Huang, P. Pattillo, Helical buckling of a tube in an inclined wellbore, International Journal of Non-Linear Mechanics 35 (5) (2000) 911–923.
[133] A. Kyllingstad, Buckling of tubular strings in curved wells, Journal of Petroleum Science and Engineering 12 (3) (1995) 209–218.
[134] X. He, A. Kyllingstad, Helical buckling and lock-up conditions for coiled tubing in curved wells, SPE Drilling & Completion 10 (1) (1995) 10–15.
[135] R.F. Mitchell, A buckling criterion for constant-curvature wellbores, SPE Journal 4 (4) (1999) 349–352.
[136] J. Cunha, Buckling of tubulars inside wellbores: a review on recent theoretical and experimental works, SPE 80944 presented at the SPE Production and Operations Symposium, Oklahoma City, Oklahoma, March 22–25, 2003.
[137] R. Mitchell, Buckling analysis in deviated wells: a practical method, SPE Drilling and Completion 14 (1) (1999) 11–20.
[138] L. Hoberock, D. Thomas, H. Nickens, Here's how compressibility and temperature affect bottomhole mud pressure, Oil and Gas Journal 80 (12) (1982) 159–164.
[139] E.J. Peters, M.E. Chenevert, C. Zhang, A model for predicting the density of oil-base muds at high pressures and temperatures, SPE Drilling Engineering 5 (1990) 141–148.
[140] R.R. Sorelle, R.A. Jardiolin, P. Buckley, Mathematical field model predicts downhole density changes in static drilling fluids, SPE 11118 presented at the 57th Annual Fall Technical Conference and Exhibition of the SPE of AIME, New Orleans, Louisiana, September 26–29, 1982.
[141] H.D. Beggs, J.P. Brill, A study of two-phase flow in inclined pipes, Journal of Petroleum Technology 25 (5) (1973) 607–617.
[142] G.J.V. Wylen, R.E. Sontag, Fundamentals of Classical Thermodynamics, 1st ed., John Wiley and Sons, Inc., New York, 1965.
[143] R. Sutton, Compressibility factors for high-molecular-weight reservoir gases, SPE 14265 presented at the SPE Annual Technical Conference, Exhibition, Las Vegas, Nevada, September 22–26, 1985.
[144] M. Standing, D. Katz, Density of natural gases, Transactions AIME 146 (1) (1942) 140–149.
[145] D. Katz, Handbook of Natural Gas Engineering, McGraw-Hill Book Company, Inc., New York, 1959.
[146] L.A. Kareem, T.M. Iwalewa, M. Al-Marhoun, New explicit correlation for the compressibility factor of natural gas: linearized z-factor isotherms, Journal of Petroleum Exploration and Production Technology 6 (3) (2016) 481–492.
[147] J.P. Brill, H.K. Mukherjee, Multiphase Flow in Wells, 1st ed., Henry L. Doherty Memorial Fund of AIME, Society of Petroleum Engineers, Richardson, Texas, 1999.
[148] A. Hasan, C. Kabir, Fluid Flow and Heat Transfer in Wellbores, 1st ed., Society of Petroleum Engineers, Richardson, Texas, 2002.
[149] O. Shoham, Mechanistic Modeling of Gas-Liquid Two-Phase Flow in Pipes, 1st ed., Society of Petroleum Engineers, Richardson, Texas, 2006.
[150] H.S. Hol, An improved modeling program for computing the torque and drag in directional and deep wells, SPE 18047 presented at the SPE Annual Technical Conference and Exhibition, Houston, Texas, October 2–5, 1988.
[151] J. Bellarby, Well Completion Design, 1st ed., Elsevier, Amsterdam, 2009.
[152] A.T. Bourgoyne Jr, K.K. Millheim, M.E. Chenevert, F. Young Jr, Applied Drilling Engineering, 1st ed., Society of Petroleum Engineers, Richardson, Texas, 1986.
[153] C. Cooke Jr, M. Kluck, R. Medrano, Field measurements of annular pressure and temperature during primary cementing, Journal of Petroleum Technology 35 (8) (1983) 1429–1438.
[154] A. Lubinski, K. Blenkarn, Buckling of tubing in pumping wells, its effects and means for controlling it, Petroleum Transactions, AIME 210 (1957) 73–88.

[155] G.W. Evans, D.W. Harriman, Laboratory tests on collapse resistance of cemented casing, SPE 4088 presented at the 47th Annual Fall Meeting of the Society of Petroleum Engineers of AIME, San Antonio, Texas, October 8–11, 1972.
[156] J. Bear, Dynamics of Fluids in Porous Media, Dover Publications, Inc., New York, 1972.
[157] R.E. Melchers, Structural Reliability Analysis and Prediction, John Wiley and Sons, New York, 1999.
[158] Z. Liu, F. Klever, R. Samuel, A. Gonzales, Y. King, The radial approach to safety factors for tubular design, SPE 181459 presented at the SPE Annual Technical Conference and Exhibition, Dubai, UAE, September 2016.
[159] I. Ruddy, M.A. Andersen, P. Pattillo, M. Bishlawi, N. Foged, Rock compressibility, compaction, and subsidence in a high-porosity chalk reservoir: a case study of Valhall field, Journal of Petroleum Technology 41 (7) (1989) 210–223.
[160] A. Yudovich, L. Chin, D. Morgan, Casing deformation in Ekofisk, Journal of Petroleum Technology 41 (7) (1989) 729–7341.
[161] T.G. Byrom, Casing and Liners for Drilling and Completion, 2nd ed., Elsevier, Amsterdam, 2015.
[162] R. Hackney, A new approach to casing design for salt formations, SPE 13431 presented at the SPE/IADC Drilling Conference, New Orleans, Louisiana, February 18–21, 1985.
[163] J. Geertsma, Land subsidence above compacting oil and gas reservoirs, Journal of Petroleum Technology 25 (6) (1973) 734–744.
[164] J. Geertsma, Some rock-mechanical aspects of oil and gas well completions, Society of Petroleum Engineers Journal 25 (6) (1985) 848–856.
[165] L. Teufel, D. Rhett, Geomechanical evidence for shear failure of chalk during production of the Ekofisk field, SPE 22755 presented at the SPE Annual Conference and Exhibition, Dallas, Texas, October 6–9, 1991.
[166] M. Bruno, Subsidence-induced well failure, SPE Drilling Engineering 7 (2) (1992) 148–152.
[167] L. Teufel, D. Rhett, Failure of chalk during waterflooding of the Ekofisk field, SPE 24911 presented at the SPE Annual Conference and Exhibition, Washington, D.C., October 4–7, 1992.
[168] C. Cook, M. Andersen, G. Halle, E. Gislefoss, G. Bowen, Simulating the effects of water-induced compaction in a North Sea reservoir, SPE 37992 presented at the SPE Reservoir Simulation Symposium, Dallas, Texas, June 8–11, 1997.
[169] P. Pattillo, T. Kristiansen, G. Sund, R. Kjelstadli, Reservoir compaction and seafloor subsidence at Valhall, SPE 47274 presented at SPE/ISRM Rock Mechanics in Petroleum Engineering, Trondheim, Norway, July 8–10, 1998.
[170] C. Kenter, T. Blanton, G. Schreppers, M. Baaijens, G. Ramos, Compaction study for Shearwater field, SPE 47280 presented at SPE/ISRM Rock Mechanics in Petroleum Engineering Conference, Trondheim, Norway, July 8–10, 1998.
[171] T.G. Kristiansen, B. Plischke, History matched full field geomechanics model of the Valhall field including water weakening and re-pressurisation, SPE 131505 presented at the SPE/EUROPE/EAGE Annual Conference and Exhibition, Barcelona, Spain, June 14–17, 2010.
[172] M. Lal, Shale stability: drilling fluid interaction and shale strength, SPE 54356 presented at the SPE Latin American and Caribbean Petroleum Engineering Conference, Caracas, Venezuela, April 21–23, 1999.
[173] R.F. Mitchell, Surge pressures in low-clearance liners, SPE 87181 presented at the IADC/SPE Drilling Conference, Dallas, Texas, March 2–4, 2004.
[174] P. Charlez, Rock Mechanics, Volume 1, Theoretical Fundamentals, 1st ed., Éditions Technip, Paris, 1991.
[175] P. Charlez, Rock Mechanics, Petroleum Applications, Vol. 2, 1st ed., Éditions Technip, Paris, 1997.
[176] J. Jaeger, N. Cook, R. Zimmerman, Fundamentals of Rock Mechanics, 4th ed., Blackwell Publishing, Malden, Massachusetts, 2007.

[177] E. Fjær, R. Holt, A. Raaen, R. Risnes, P. Horsrud, Petroleum Related Rock Mechanics, 2nd ed., Elsevier, Amsterdam, 2008.
[178] M.D. Zoback, Reservoir Geomechanics, 1st ed., Cambridge University Press, Cambridge, United Kingdom, 2010.
[179] A. Nur, J. Byerlee, An exact effective stress law for elastic deformation of rock with fluids, Journal of Geophysical Research 76 (26) (1971) 6414–6419.
[180] B. Kirton, G. Wulf, B. Henderson, Thunder Horse drilling riser break—the road to recovery, SPE 90628 presented at the SPE Annual Technical Conference and Exhibition, Houston, Texas, September 26–29, 2004.
[181] B.S. Aadnøy, Modern Well Design, 2nd ed., CRC Press, Boca Raton, Florida, 2010.
[182] B.S. Aadnøy, E. Kaarstad, M. Belayneh, Multiple criteria casing seat selection method, SPE 150931 presented at the IADC/SPE Drilling Conference and Exhibition, San Diego, California, March 6–8, 2012.
[183] Z. Gromotka, The Stability Region of the Tubing Performance Relation Curve, Masters Thesis, Delft University of Technology, September 2015.
[184] S. Gosch, D. Home, P. Pattillo, J. Sharp, P. Shah, Marlin failure analysis and redesign: part 3—VIT completion with real-time monitoring, SPE Drilling & Completion 11 (2) (2004) 120–128.
[185] J. Barker, Wellbore design with reduced clearance between casing strings, SPE 37615 presented at the SPE/IADC Drilling Conference, Amsterdam, The Netherlands, March 4–6, 1997.
[186] R.A. Miller, M.L. Payne, P. Erpelding, Designer casing for deepwater HPHT wells, SPE 97565 presented at the SPE Applied Technology Workshop on High Pressure/High Temperature Sour Well Design, The Woodlands, Texas, May 17–19, 2005.
[187] R. Ellis, D. Fritchie Jr, D. Gibson, S. Gosch, P. Pattillo, Marlin failure analysis and redesign: part 2—redesign, SPE Drilling & Completion 11 (2) (2004) 112–119.
[188] P. Oudeman, M. Kerem, Transient behavior of annular pressure build-up in HP/HT wells, SPE Drilling and Completion 21 (4) (2006) 234–241.
[189] R. Rizkiaputra, R. Siregar, T. Widow, S. Mabunga, A new method to mitigate annular pressure buildup by using sacrificial casing, case study: A deepwater well in Indonesia, SPE 178854 presented at the IADC/SPE Drilling Conference and Exhibition, Fort Worth, Texas, March 1–3, 2016.
[190] U. Sathuvalli, R.M. Pilko, A. Gonzalez, R. Psi, P. Sachdeva, P. Suryanarayana, Design and performance of annular-pressure-buildup mitigation techniques, SPE 178886, SPE Drilling and Completion preprint, May 2017.
[191] A. Halal, R. Mitchell, Casing design for trapped annular pressure buildup, SPE Drilling & Completion 9 (2) (1994) 107–114.
[192] L.F. Eaton, W.R. Reinhardt, J.S. Bennett, Liner hanger trapped annulus pressure issues at the Magnolia deepwater development, SPE 99188 presented at the IADC/SPE Drilling Conference, Miami, Florida, February 21–23, 2006.
[193] J.B. Bloys, M.E. Gonzalez, J. Lofton, R.B. Carpenter, S. Azar, D. Wiliams, et al., Trapped annular pressure mitigation: Trapped annular pressure—a spacer fluid that shrinks (update), SPE 112872 presented at the IADC/SPE Drilling Conference, Orlando, Florida, March 4–6, 2008.
[194] A. Adams, How to design for annulus fluid heat-up, SPE 22871 presented at the SPE Annual Technical Conference and Exhibition, Dallas, Texas, October 6–9, 1991.
[195] C. Leach, A. Adams, A new method for the relief of annular heat-up pressures, SPE 25497 presented at the SPE Production Operations Symposium, Oklahoma City, Oklahoma, March 21–23, 1993.
[196] Alaska Oil and Gas Conservation Commission, Investigation of Explosion and Fire at Prudhoe Bay Well A-22, North Slope, Alaska, August 16, 2002, Alaska Oil and Gas Conservation Commission Staff Report November 17, 2003.
[197] The International Association for the Properties of Water and Steam, Revised Release on the IAPWS Formulation 1995 for the Thermodynamic Properties of Ordinary Water Substance for General and Scientific Use, IAPWS, Doorwerth, The Netherlands, 2009, IAPWS95.

[198] J.B. Bloys, M.E. Gonzalez, R.E. Hermes, R.G. Bland, R.L. Foley, R. Tijerina, et al., Trapped annular pressure mitigation—a spacer fluid that shrinks, SPE 104698 presented at the SPE/IADC Drilling Conference, Amsterdam, The Netherlands, February 20–22, 2007.
[199] R.F. Vargo Jr, M. Payne, R. Faul, J. LeBlanc, J.E. Griffith, Practical and successful prevention of annular pressure buildup on the Marlin project, SPE 77473 presented at the SPE Annual Technical Conference and Exhibition, San Antonio, Texas, September 29–October 2, 2002.
[200] R.A. Miller, A. Coy, G. Frank, A. Dondale, Advancements in APB mitigation for Thunder Horse wells, SPE/IADC 184725 presented at the SPE/IADC Drilling Conference and Exhibition, The Hague, The Netherlands, March 14–16, 2017.
[201] P. Pattillo, J. Bellarby, G. Ross, S. Gosch, G. McLaren, Thermal and mechanical considerations for design of insulated tubing, SPE Drilling and Completion 19 (3) (2004) 181–188.
[202] J. Azzola, P. Pattillo, J. Richey, S. Segreto, The heat transfer characteristics of vacuum insulated tubing, SPE 90151 presented at the SPE Annual Technical Conference and Exhibition, Houston, Texas, September 26–29, 2004.
[203] J. Azzola, D. Tselepidakis, P. Pattillo, J. Richey, S. Tinker, R. Miller, et al., Application of vacuum insulated tubing to mitigate annular pressure buildup, SPE Drilling & Completion 22 (1) (2007) 46–51.
[204] R. Hall Jr, A. Garkasi, G. Deskins, J. Vozniak, Recent advances in casing wear technology, SPE 27532 presented at the SPE/IADC Drilling Conference, Dallas, Texas, February 15–18, 1994.
[205] G. Poss, R. Hall Jr, Subsea drilling riser wear: A case history, SPE 29392 presented at the SPE/IADC Drilling Conference, Amsterdam, The Netherlands, February 28–March 2, 1995.
[206] R. Hall Jr, K.P. Malloy, Contact pressure threshold: An important new aspect of casing wear, SPE 94300 presented at the SPE Production Operations Symposium, Oklahoma City, Oklahoma, April 16–19, 2005.
[207] American Petroleum Institute, Casing Wear Tests, 1st ed., API, Washington, D.C., 2015, API Standard 7CW.
[208] S.M. Selby, Standard Mathematical Tables, fifteenth ed., The Chemical Rubber Company, Cleveland, 1967.
[209] R.M. Bowen, Introduction to Continuum Mechanics for Engineers, revised ed., Dover Publications, Inc., Mineola, New York, 2007.
[210] L.A. Segel, Mathematics Applied to Continuum Mechanics, Macmillan Publishing Company, Inc., New York, 1977.
[211] H.L. Taylor, C.M. Mason, A systematic approach to well surveying calculations, SPE Journal 12 (6) (1972) 474–488.
[212] S. Sawaryn, J. Thorogood, A compendium of directional calculations based on the minimum curvature method, SPE Drilling and Completion 20 (1) (2005) 24–36.
[213] P. Peška, M.D. Zoback, Compressive and tensile failure of inclined wellbores and determination of in situ stress and rock strength, Journal of Geophysical Research 100 (B7) (1995) 12791–12811.
[214] C. Fairhurst, Stress estimation in rock: a brief history and review, International Journal of Rock Mechanics & Mining Sciences 40 (2003) 957–973.
[215] T. Kristiansen, Drilling wellbore stability in the compacting and subsiding Valhall field, SPE Drilling & Completion 22 (4) (2007) 277–295.

INDEX

A

AFE, *see* Annular pressure build-up
Air gap, 413
American Petroleum Institute, 192, 199, 200, 204, 208, 210, 213, 218, 227, 228, 230, 233, 235, 243, 245–248, 252–255, 257, 259–262, 268, 270, 451, 527
Annular fluid expansion, *see* Annular pressure build-up
Annular pressure build-up, 354, 459–461, 463–470, 473
  as a low-probability, high-consequence event, 459, 461, 463
  design principles, 463
    all shoes are closed, 463, 468
    every annulus must stand alone, 464
    use a safety factor multiplier, 465
    use the hottest temperature, 464
    use the proper initial conditions, 465
  mitigation, 463, 465, 466, 468, 471
    annulus boundary flexibility, 468
    annulus fluid properties, 466
    annulus temperature change, 471
    designer fluids, 466
    foam spacer, 467, 470
    formation fracture, 468
    rupture disks, 468, 470
    syntactic foam, 470, 471
    vacuum-insulated tubing, *see* Vacuum-insulated tubing
  non-linear fluid behavior, 461
  sources, 460
Annulus fluid heat-up, *see* Annular pressure build-up
APB, *see* Annular pressure build-up
API, *see* American Petroleum Institute
Archimedes' principle, 275, 276, 326
Artificial lift, 430
Associative operation, 496
Axial force, 280, 284, 318, 442
Axial load, 28, 29, 31, 100, 122, 197, 198, 204, 208, 217, 225–229, 260, 274, 277, 278, 285, 287, 288, 298–300, 304, 315–318, 321, 325, 326, 328–331, 333, 334, 337, 338, 440, 442, 444–447, 450–454, 457
  distribution, 337
  example problem, 325
Axial stress, 315, 316
Axial traction, 197, 315, 316
Axial yield, 337, 338

B

Barlow equation, 199, 200
Barrier envelope, 372
Bauschinger effect, 157, 159, 193
  defined, 159
Beam equations for tube, 126
  contact force, 147
Bending, 122, 141, 197, 273, 276, 277, 280, 281, 283, 290, 293, 298, 299, 301, 307, 456
  moment, 299, 302
  stiffness, 146
Bending stress, 298, 308, 456, 457
  due to column buckling, 273, 312, 315, 453, 456
Blowout preventer, 4, 412
BOP, *see* Blowout preventer
Bottomhole pressure, 337
BTC, *see* Threaded connections, types, API buttress thread casing
Buckling
  bifurcation, 219, 220, 222, 235
  column, *see* Column stability
  snap-through, 219–221, 223, 241, 242
Buoyancy factor, 277, 290

C

CAL, *see* Threaded connections, qualification and testing, connection application level
Casing
  intermediate, *see* Intermediate casing
  production, *see* Production casing
  surface, *see* Surface casing
Casing seat selection, 395, 398
  bottom-up method, 21, 415–421

chemical sensitivity, *see* Rock, deficiencies as a structure, chemical sensitivity
mobile formation, 20, 415
regulatory requirements, 20, 415
riser margin, *see* Riser margin
top-down method, 21, 417, 421–423
Casing wear, 307, 430, 474, 475, 479
contact force per length, 475, 476
design work flow, 482
drill ahead through buckled casing, 273, 481
effect on external pressure resistance, 242, 480
effect on internal pressure resistance, 213, 480
governing equations, 474
residence length, 475
wear factor, 474–476
defined, 474
wear volume and wall loss, 478
Cauchy deformation tensor, 40, 41, 44
defined, 41
Cauchy stress tensor, 75, 77, 83, 113–116, 157, 160, 201
CEE, *see* Threaded connections, qualification and testing, connection evaluation envelope
Cement, 236, 397, 456, 467, 471
and APB mitigation, 466
between concentric casings, 238–242
float fails, 356
initial condition for casing, 354
plug bumps, 354–356
role in external fluid scenario, 375
sheath, 236, 240, 337, 375, 430, 431
thickening time, 354
top of cement, 365, 367, 370, 371, 440, 444–448, 452, 453, 468, 470
effect on APB design, 463, 464
Characteristic equation, 507
Characteristic value, *see* Eigenvalue
Characteristic vector, *see* Eigenvector
Coefficient of linear thermal stress
isotropic scalar, 119
tensor, 118
Collapse resistance, 181, 204, 215–222, 225, 228, 229, 233, 239, 242, 273, 289, 315, 325, 337, 338, 377, 389, 457, 469, 480
analogy to column buckling, 215
API average, 222, 225, 227, 228
API collapse modes, 224, 230, 231
elastic collapse mode, 218, 222, 225–231, 233
plastic collapse mode, 218, 225–232
transition collapse mode, 228, 230–233
yield collapse mode, 218, 222, 225, 227, 229–232
API minimum, 218, 227, 228, 451
design summary, 30
modeling, 222
non-uniform loading, 215, 235–240
concentric casing, 238, 240–242
design guidelines, 240
importance of wall thickness, 237
point loading, 236
thick-walled casing, 237, 238, 240, 242
uniform loading, 215, 228
example problem, 231
Column pressure
ideal gas, 343
real gas, 345
Column stability, 122, 141, 273, 275, 277, 278, 285, 442
buckling check for hydrostatic-set packer, 334
critical buckling force, 284, 285
elastic buckling, 216
plastic buckling, 204, 216
post-buckled configuration, 293, 308
helical buckling, 283, 284, 288, 293, 305, 307, 308, 310, 312, 313, 319, 320, 453
lock-up, 284
sinusoidal buckling, 283, 284, 293, 305, 307, 308, 310, 319, 320
undesirable consequences, 273
Commutative operation, 486, 488, 495
Completion fluid
defined, 339
Compressibility
fluid, 460
Compressibility factor, 346
defined, 345
Conservation of mass, 130, 131
Conservation of momentum, 128, 130, 131
Control surface, 128–130, 132
defined, 128
Control volume, 128–130, 132, 133, 135, 138
defined, 128
Coordinate system, 144, 515, 516
Cartesian, 33, 34, 36, 58, 73, 108, 187, 515–518
curvilinear, 50
cylindrical, 33, 34, 36, 50, 51, 53, 56, 67, 69, 73, 74, 84, 93, 108, 111, 123, 124, 187, 345, 439, 500, 502, 515

defined, 50
global material, 34–38, 41–47, 50, 51, 53, 57, 73, 77, 83, 94, 113, 128, 132, 148, 160, 202, 277, 308, 320, 500, 502, 515–519, 521
polar, 51
rectangular, *see* Cartesian, 84
spatial, 34–36, 38, 41–47, 51, 53, 67, 70, 73, 75, 77, 78, 83, 93, 108, 114, 127, 132, 133, 160, 202, 308, 439, 515, 516
Corrosion
external, 430
Critical buckling force, 293, 307, 310
curved wellbore, 305
inclined wellbore, 304
summary, 307
vertical wellbore, 299, 448
Cross-flow, 396
CSS, *see* Cyclic Steam Stimulation
Curvature
due to buckling, 273, 309
wellbore, 273
Cyclic loading, 159
Cyclic Steam Stimulation, 267

D

Datum
rotary kelly bushing, 399
Deformation, 38, 77, 117, 122, 143
elastic, 117
isotropic, 117
example problem, 39, 42, 43, 46
plastic, 117
Deformation gradient, 33, 36, 44, 77, 117
cylindrical coordinates, 53
defined, 36
example problem, 38
Depleted reservoir, 363, 405
Design
by hand, 337
casing seat determination, 20, 438
deterministic, 337
importance of triaxial yield, 337
input data, 19
probabilistic, 403
sizing, 21, 439
Design equation, 192, 198, 199, 208, 210, 213, 227, 338, 385, 387, 388
Design factor, 337, 385, 386, 455
conventional, 388
collapse, 389, 390
collapse example problem, 390
triaxial yield, 388, 389
defined, 385
table of typical values, 29
Determinant, *see* Second order tensor, invariants, I_3
Differential sticking, 20, 404, 405, 407
described, 396
Differential sticking limit, 404–406
Displacement, 33, 47, 57, 70, 144
defined, 35
Displacement gradient, 47, 144
Distributive operation, 488, 490, 496
Divergence theorem, *see* Gauss theorem
Drilling fluid, 341, 363, 369, 378–380, 395–397, 412
column pressure, 341
incompressible constituents, 342
incompressible solids, 342
single fluid with no solids, 342
single incompressible fluid, 343
degraded, 363
density, 369, 395, 396, 398–401, 403, 405–407, 409, 410, 412, 414–423, 431, 438, 520–523
acceptable range, 20, 21, 402–404, 407, 410–414, 416, 417, 420–422, 521, 524
defined, 398
Drilling riser, 412
Ductile rupture, 160, 197, 200, 201, 204, 205, 208, 210, 469
design summary, 30
example problem, 210
Dyad, *see* Tensor product

E

ECD, *see* Equivalent circulating density
Effective force, 131, 141, 208, 273, 274, 276–278, 283–285, 287, 292, 293, 305–307, 312, 334, 440, 442, 443, 448
derivative, 141
equivalent system, 274, 276
explained, 141, 277
extending known solutions, 281
generalized, 141
neutral point, 284, 286, 287, 290, 312, 320
defined, 284
Effective stress, 174–176, 195, 204
neutral point, 298
Effective weight, 277, 288, 289, 305–307

neutral buoyancy, 289
Eigenvalue, 45, 507
Eigenvector, 45, 507
Elastic behavior, 151, 157
Elastic stiffness tensor, 118
Energy method, 294, 299
conservative system, 295, 296
external work, 294, 310
heat, 294
internal energy, 294, 298, 310
due to axial force, 298, 300, 310
due to bending, 299, 310
internal work, 294
kinetic energy, 294, 298
potential energy, 295, 296, 300
principle of stationary potential energy, 295
variational solution
kinetic boundary conditions, 301
natural boundary conditions, 302
Engineering stress, *see* Piola-Kirchhoff stress tensor, first kind
Epsilon-delta identity, 492
Equilibrium, 122, 123, 293–298, 300–302
defined, 294
neutral stability, 298
stable, 293, 295–298
example problem, 296
unstable, 298
Equilibrium equations, *see* Stress, equations of motion
Equivalent circulating density, 410, 411
Euler buckling load, 277, 278, 281
Euler column
example problem, 282
Eulerian strain tensor, 33, 38–40, 44, 46, 47, 57, 67, 75, 187
cylindrical coordinates, 67, 68, 70
defined, 44
Example tubingless design, 437
axial force distribution, 444
axial force distribution above cement top, 445
axial force distribution below cement top, 446
axial force distribution when buckling above cement top, 448
comments, 456
length change, 440
preliminary calculations, 439
problem statement, 437
safety factors, 451
Expandable tubulars, 30, 213, 431
External pressure, 19, 23–25, 27, 30, 122, 141, 177–179, 181, 197, 199, 210, 215, 217, 220–223, 228, 241, 274, 275, 290, 323, 334, 337, 349
change, 28, 315, 317, 318, 323, 325, 329, 332, 337
differential, 24, 451, 456
distribution, 25, 26, 31, 338, 350–353, 356, 358, 360, 362, 365, 367, 370–374, 376, 377, 379, 381, 382, 384–387, 456
effect on column stability, 274, 275, 280
External pressure resistance, *see* Collapse resistance

F

Filter cake, 396, 404
First law of thermodynamics, 294
Floating casing string, 287
Fluid gradient, 337
Force, 77–79, 85, 86, 276–278, 285, 286
and mass, 8
body, 77–80, 85–88, 97, 110
contact, 77–80
external, 77, 79
gravitational, 77
intensity, 77, 79
internal, 79, 80
Force vector, *see* Traction, designation as force vector
Formation compaction, 397
Fourier's inequality, 294, 295
Fracture pressure, 365, 397, 404, 431
gradient, 20, 401–406, 412, 415, 438
defined, 399
Fracture toughness, 197
Free body diagram, 274, 315
Frenet-Serret formulas, 509, 511
curvature, 509, 511–513
example problem, 511
radius of curvature, 509, 511
torsion, 511
Friction, 284, 288, 349, 350, 352

G

Gas constants, 15
Gauss theorem, 130, 132, 340
Green deformation tensor, 40, 43–45
defined, 41
example problem, 42

I

Inelastic behavior, *see* Yield, post-yield behavior
Inflow performance relation, 428, 429
Initial condition, 26, 28, 29, 321, 328, 332, 349, 352, 442, 444, 447, 456
  design, 337
Initial state, *see* Load case, initial condition
Intermediate casing, 337
  sizing, 430
Internal pressure, 19, 23–25, 27, 122, 141, 177, 179, 180, 182, 183, 193, 197, 199, 200, 215, 228, 229, 274, 290, 323, 327, 330, 334, 337, 338, 437, 440, 441, 456
  change, 28, 315, 317, 318, 323, 325, 329, 330, 332, 337
  differential, 24, 456
  distribution, 25, 26, 31, 338, 350–353, 356, 358, 360, 362, 365, 367, 370–374, 376, 377, 379, 381, 382, 384–387, 456
  effect on column stability, 274, 275, 281
  effect on testing, 292
Internal pressure resistance, 181, 197, 199, 204, 213, 215, 242, 273, 315, 469, 480
  capped end, 198
  design summary, 30
  no axial force, no external pressure, 199
IPR, *see* Inflow performance relation

J

Jacobian
  defined, 49

K

Kick intensity
  defined, 423
Kick tolerance, 21, 422–426
  calculation, 424
    comparison of volumes, 426
    influx height, 423–425
    influx volume, 425
  defined, 423
  example problem, 426
Kronecker delta, 35, 53, 492

L

Lagrangian strain tensor, 33, 38–40, 42–44, 46, 47, 67, 75
  cylindrical coordinates, 50, 54, 57
  defined, 42
  example problem, 43
Lamé constants, 119
Lamé equations, 73, 125, 185, 200
Langrangian strain tensor, 67
Lateral buckling, *see* Column stability, post-buckled configuration, sinusoidal buckling
Length change, 29, 316, 318, 319, 322–324, 327–334, 440, 442, 444–446
  and related axial force, 315–317, 327, 330, 331
  due to column buckling, 273
  sources, 316, 442, 444
    ballooning, 28, 317, 323, 325, 329, 332, 443
    buckling, 28, 308, 319, 320, 324, 440, 443, 449–451
    self-weight, 321, 324
    shoulder, 28, 318, 324–326, 329, 333, 440, 443, 447
    temperature, 28, 317, 323, 443, 448
  stretch calculation example, 322
Levi-Civita symbol, 491
Limit state, 30, 151, 153, 161, 186, 260, 455
Limit state equation, 117, 184, 192, 197, 198, 204, 208, 212, 227, 235, 242, 387
Linear coefficient of thermal expansion
  defined, 122
Liner, 338
  defined, 5
  effect on pressure test, 364, 366
Liner hanger, 431
Load case, 23, 24, 26, 28, 29, 31, 32, 439, 440, 442, 447, 449, 454, 455
  casing
    drill ahead, 25, 370
    initial condition, 25, 354, 356, 444
    initial condition example problem, 355, 444
    overpull, 25, 349, 351
    pre-installation, 349
    pressure test, 25, 365
    running in hole, 25, 349, 350
  defined, 337
  initial condition, 351, 352
    annular pressure build-up, 354
    conventional design, 354
  production casing
    packer leak, 25, 382
    pressure test, 369
    riser margin, 381
    tubing leak, 25, 369, 371
  production tubing

annulus pressure test, 26, 383, 384
evacuation, 26, 384, 387, 437
initial condition, 26, 355, 358, 360, 362
injection, 26, 373, 437
overpull, 26, 351, 353
pre-installation, 350
pressure test, 26, 372, 437
production, 26, 373, 374, 437
production from long term shut-in, 26, 383, 385
pump in to kill well, 26, 375, 376
running in hole, 26, 350, 352
safety valve leak, 26, 383, 386
shut-in, 26, 375, 377
surface and intermediate casing
drill ahead, 369
lost circulation, 25, 378, 379
lost circulation example problem, 380
pressure test, 364
riser margin, 25, 381
well control, 25, 364, 367
tubingless design example, 440–448, 450–453, 455–457
Logarithmic strain tensor, 33, 38, 40, 44–47, 57, 75, 160–162, 201
cylindrical coordinates, 73
axisymmetric deformation, 74
generalized plane strain, 74
generalized plane strain, axisymmetric, 74
defined, 45
example problem, 45
Lost circulation, 397
LTC, *see* Threaded connections, types, API long round thread casing

M

Mass
and force, *see* Force, and mass
Material derivative
defined, 129
Material force, *see* Force
Mean sea level, 412
Measured depth, 317
Minimum internal yield pressure, 199, 200, 337, 338, 364
MIYP, *see* Minimum internal yield pressure
ML, *see* Mudline
Mohr-Coulomb failure model, 408–411, 520, 521
Mohr's circle, 111, 112
Moment, 77, 81, 87–89
Moment of inertia, 82
MSL, *see* Mean sea level
Mudline, 412
Multiple completion, 430

N

Necking
defined, 157
Notation, 16
direct, 16, 486
index, 16, 486
example problem, 511
Numerical analysis, 245

O

Ovality
defined, 224
manufactured, 220, 221, 241
measured, 224
Overpull, 349, 351

P

Packer, 273, 281, 437
hydraulic-set, 327, 330, 333, 357, 360
example problem, 327
hydrostatic-set, 331, 334, 359, 362
example problem, 331
mechanically-set, 357
open hole, 397
setting pressure, 327, 329, 331, 333, 334
Packer fluid
defined, 339
PBR, *see* Polished bore receptacle
Permeability, 396
Permutation symbol, *see* Levi-Civita symbol
Piola-Kirchhoff stress tensor, 113, 116
first kind, 113–116
example problem, 114, 157
infinitesimal deformation, 116, 516
second kind, 115
Planar isotropy, 118
Plastic behavior, *see* Yield, post-yield behavior
Poisson's ratio, 120, 157, 218, 317
Polished bore receptacle, 233, 273, 464
collapse, 233
Polytetrafluoroethylene, 261–263
POOH, *see* Pull out of hole
Pore pressure, 354, 378, 396, 398, 400, 404–406, 411, 412, 431

external fluid for casing load cases, 363
gradient, 20, 399–406, 412, 413, 415, 438
defined, 399
Position, 33
current, *see* spatial
material, 33
original, *see* material
spatial, 34
Post buckling
curved wellbore, 313
inclined wellbore, 312
vertical wellbore, 308
Pressure
distribution, 339
external, *see* External pressure
flowing, 348
hydrostatic, 339
internal, *see* Internal pressure
Principle of virtual work, 295
Production casing, 337, 362, 437, 462, 463, 471
sizing, 429
Production tubing, 337, 363, 437
sizing, 428
PTFE, *see* polytetrafluoroethylene
Pull out of hole, 349, 403
Pullout, *see* Threaded connections, joint strength, jumpout

R

Right-hand rule, 490
Rigid body motion, 33
RIH, *see* Run in hole
Riser margin, 20, 381, 412, 414
defined, 412
RKB, *see* Rotary kelly bushing
ROB, *see* Rotate off bottom
Rock
deficiencies as a structure, 395
chemical sensitivity, 20, 398, 415
permeability, 396
weakness, 20, 397, 415
fracture, 397
sandstone, 396
shale, 396
Rotary kelly bushing, 338
Rotate off bottom, 349
Rotation, 38
defined, 33
example problem, 39, 42, 43, 46
Run in hole, 288, 349, 350, 403

S

Safety factor, 385
conventional, 388
axial, 452, 457
collapse, 389, 390, 451, 452, 457
triaxial yield, 389, 452–454, 456
defined, 385
radial, 390–392, 439
extension, 393, 394
extension to multiple limit states, 393
extension to non-radial load lines, 393
triaxial yield example problem, 392
Safety margin
defined, 385
SAGD, *see* Steam Assisted Gravity Drainage
Salt
creep, 235, 236, 239, 240, 397
Scab liner
defined, 6
Scalar, 485
Sea water, 412
Secant modulus, 159
defined, 153
Second order tensor, 77, 494
addition, 494
contraction
defined, 495
coordinate transformation, 502
example problem, 84, 503
inverse, 503
coordinate transformation matrix
defined, 503
eigenvectors, 507
identity
defined, 37
scalar invariants, 505, 508
I_1, 505
I_2, 505
I_3, 506
scalar multiplication, 495, 496
symmetric
defined, 494
tensor contraction product, 495
transpose, 497
defined, 494
Self energizing seal, 264, 265
Shock load, 99

dropped tubular, 108
Soft string model, 349, 476, 478
Specific volume
defined, 343
SSSV, *see* Subsurface safety valve
Standardization, 430
STC, *see* Threaded connections, types, API short round thread casing
Steam Assisted Gravity Drainage, 267
Strain, 33, 39, 75, 77, 117, 118, 120, 121, 125
area change, 47, 50, 58, 113
axisymmetric, 33, 64, 71
beam
derived, 143
middle surface, 145
choosing a strain tensor, 75
generalized plane strain, 65, 71, 122, 123
axisymmetric, 66, 72
axisymmetric, infinitesimal, 66, 72
infinitesimal, 33, 40, 47, 57, 70, 100, 122, 143–145, 187, 188
axisymmetric, 65, 71, 123
physical interpretation, 58
physical interpretation (extension), 58, 60, 61
physical interpretation (shear), 61–64
plane strain, 66, 72, 123, 125
relating definitions, 46
volume change, 47, 48, 57, 58, 70
Stress, 75, 77, 79, 83–86, 117, 118, 120, 125, 132, 137, 191, 273
axisymmetric, 113, 122
basic concepts, 77
components, 83–85, 87, 94
sign convention, 83, 84
deviatoric, 167, 191
defined, 167
equations of motion, 86, 87, 97, 123
tube cross section, 122
hydrostatic, 162–164, 172, 178
mean, 162, 167
defined, 162
plane stress, 111
principal, 162–171, 515, 516, 518, 520–523
defined, 89
Stretch ratio, 47
defined, 44
Subsea wellhead, 338
Subsurface safety valve, 383
Surface casing, 337
sizing, 430
Surface pressure, 337
Surge margin, 403, 404, 407, 413, 414
Swab margin, 403, 404, 407, 413, 414
Swab pressure, 423

T

Tangent modulus, 159
defined, 153
TAP, *see* Annular pressure build-up
Temperature, 23, 25, 31, 117, 118, 317, 322, 325, 337, 455, 456
change, 28, 122, 315–317, 323, 325, 337
distribution, 25, 26, 322, 350–353, 356, 358, 360, 362, 365, 367, 370–374, 376, 377, 379, 381, 382, 384–387
geostatic, 355
unit conversion, 15
Tensor
first order, *see* Vector
zeroth order, *see* Scalar
Tensor and matrix operations, 497
Tensor product, 495
Threaded connections, 30, 245, 318, 321, 325, 438, 452, 454, 457, 462–464, 470–473, 481
compression joint efficiency, 250, 251, 260
critical cross-sectional area, 252, 253, 255, 256
elements, 246
external pressure resistance, 266
flush internal profile, 266
internal pressure resistance, 260, 266
joint strength, 252, 253, 255, 260, 337
defined, 252
jumpout, 254, 257–259
lead
defined, 247
pitch
defined, 247
pitch diameter, 247
defined, 247
pitch line
defined, 247
qualification and testing, 30, 267, 292, 452, 463
connection application level, 268
connection evaluation envelope, 267, 268
Series A test, 268
Series B test, 268
Series C test, 268
test load envelope, 268

seal, 245, 261
  assembly, 264
  coating, 263
  contact stress profile, 264
  galling, 263
  metal-to-metal, 245, 247, 249–252, 261–267
  seal ring, 245, 248, 249, 251, 261, 262
  surface roughness, 263
  thread lubricant, 245, 261
stab flank
  defined, 247
taper
  defined, 247
tension joint efficiency, 250, 251, 254–257
  defined, 253
thread crest
  defined, 246
thread form, 245
  API buttress, 247, 248, 254, 259, 262
  API round thread, 248, 251, 254, 256, 257, 259, 261, 262
  hook thread, 259
  negative load flank, 249–251, 259, 260
  negative stab flank, 249–251, 260
  wedge thread, 260
thread height
  defined, 247
thread load flank
  defined, 247
thread root
  defined, 246
thread taper
  defined, 266
torque shoulder, 245, 247, 249–252, 267
torsional resistance, 266
types, 247
  API buttress thread casing, 247, 248, 257, 259, 261
  API casing, 247, 253
  API EUE tubing, 251, 254
  API extreme-line, 254
  API IJ tubing, 254
  API long round thread casing, 247
  API NUE tubing, 247, 254
  API short round thread casing, 247
  flush integral, 250, 481
  non-flush integral, 249, 481
  threaded and coupled, 249
  two-step tubing and work string, 252
  upsetting, 251, 256
Tieback, 363, 364
  defined, 6
TLE, *see* Threaded connections, qualification and testing, test load envelope
TOC, *see* Cement, top of cement
Torque-turn graph, 264
Trace, *see* Second order tensor, invariants, I_1
Traction, 77, 80–83, 86
  average, 79–83
  defined, 78
  designation as force vector, 79
  example problem, 81
  local, 80, 81, 83, 85
    from stress tensor, 85, 108, 110
Translation, 38
  defined, 33
  example problem, 38, 42, 43, 45
Trapped annulus pressure, *see* Annular pressured build-up
Triaxial compression test, 407, 408
Trip in, *see* Run in hole
Trip out, *see* Pull out of hole
True force, *see* Force
True stress, *see* Cauchy stress tensor
Tubing
  production, *see* Production tubing
Tubing flow performance, 429
Tubingless completion, 437
  defined, 357
Tubular sizing, 428
  example problem, 432
Tubular types, 2
  by function, 2
    conductor casing, 3
    intermediate casing, 4
    production casing, 4
    production tubing, 5
    surface casing, 3
  by interval, 5
    liner, 5
    long string, 5
    scab liner, 6
    tieback, 6

U

Ultimate stress, 30, 155, 208, 252
Uncertainty, 337, 403–405
Unit conversion

acceleration, 10
area, 8
curvature, 11
dry volume, 9
force, 12
length, 8
mass, 12
mass density, 12
pressure, 13
pressure gradient, 14
temperature, 14
velocity, 10
volumetric flow rate, 11
wet volume, 9
Unit systems, 7
Unit vector, 41, 163, 164, 299
base, 41, 50–52, 54, 67, 133, 148, 163, 165, 517, 518
defined, 36
dependence on Θ, 52
binormal, 509–513
normal, 78, 509, 510, 512, 513
of direction, 44
surface, 129, 132
tangent, 509, 510, 512, 513

V

Vacuum-insulated tubing, 471, 472
mechanical design, 471
thermal design, 472, 473
Vector, 485
addition, 486, 487
component, 485, 486
coordinate transformation, 498
example problem, 500
inverse, 499
coordinate transformation matrix
defined, 499
cross product, 490
distributive, 490
example problem, 492, 493
scalar multiplication, 491
dot product, 55, 68, 69, 114, 487, 495
commutative, 488
distributive, 488
example problem, 83, 488, 489
scalar multiplication, 488
dotproduct, 489
inner product, *see* Vector, dot product
scalar multiplication, 487
shifter tensor, 35, 36
transpose, 494, 496
Vertical depth, 317
VIT, *see* Vacuum-insulated tubing
VME stress, *see* Yield, von Mises yield criterion, von Mises equivalent stress

W

Wash-over operation, 430
Water depth, 413
Well control, 364, 396
Wellbore
low side of hole, 515
Wellbore pressure, 405, 412, 413
gradient, 412
Wellbore stability, 20, 398, 406, 407, 411, 412
defined, 406
equations for stress, 515
Wellbore trajectory, 509, 511, 512
azimuth, 512
inclination, 511
measured depth, 511
Minimum Curvature model, 512–514
example problem, 511
survey station, 511–514
tortuosity, 293
Work, 294, 295, 297, 298

Y

Yield, 117, 122, 151, 154, 156–163, 165, 166, 168, 169, 171, 173, 175, 176, 178, 179, 182–184, 186, 189, 191–195, 197, 198, 200, 207, 218, 222, 273, 338, 452, 480
anisotropic, 193–195
design summary, 30
multiple dimensions, 184, 186, 197, 198, 207
design equation, 184, 186
pi-plane, 163–165, 171, 172, 175
post-yield behavior, 117, 151, 156–159, 186, 187, 189, 190
flow rule, 189
hardening law, 167, 190
isotropic hardening, 191, 194, 203, 212
kinematic hardening, 193, 195
loading, 187, 188
neutral loading, 188
plastic strain, 157, 160, 161, 187–192, 194
unloading, 188
work-hardening, 156, 189, 233, 234, 238

strain space, 151
stress space, 151, 156, 165, 167
Tresca yield criterion, 169, 171–173, 189, 207, 237
uniaxial, 204
  0.2% offset, 154
  API definition, 154, 452
  Ludwik's model, 160, 162
  Needleman's model, 159, 160, 233, 234
  stress-strain curve, 120, 151–157, 159–161, 169, 171, 187, 188, 191–193, 215, 223, 299
von Mises yield criterion, 162, 166, 167, 169, 172–176, 178, 179, 181, 186, 191–195, 203, 207, 229
  expression with axial stress, 176, 179
  expression with axial stress and internal pressure, 176, 177
  expression with effective stress, 174–176, 182
  simple expression, 179, 180, 182, 183
  von Mises equivalent stress, 181, 200, 452
with bending, 183
without bending, 173
Yield stress, 30, 153–159, 161, 166, 169, 171, 182–184, 191, 193–195, 217, 218, 228, 229, 234, 238, 252, 337, 451, 455
Yield surface, 188–191, 193–195, 456
Young's modulus, 218
  defined, 152

ELEMENTS OF OIL AND GAS WELL TUBULAR DESIGN

P.D. PATTILLO

Elements of Oil and Gas Well Tubular Design offers insight into the complexities of oil well casing and tubing design. The book's intent is to be sufficiently detailed on the tubular-oriented application of the principles of solid mechanics while at the same time providing readers with key equations pertinent to design. It addresses the fundamentals of tubular design theory, bridging the gap between theory and field operation. Filled with derivations and detailed solutions to well design examples, *Elements of Oil and Gas Well Tubular Design* provides the well designer with sound engineering principles applicable to today's oil and gas wells.

Key Features

- Understand engineering mechanics for oil well casing and tubing design with emphasis on derivation, limitations, and application of fundamental equations
- Grasp well tubular design from one unified source with underlying concepts of stress, strain, and material constitution
- Quantify practice with detailed well design worked examples amenable to quality check with commercial software

About the Author

Phillip Pattillo, PhD, currently works on a contract basis in Houston, Texas. He retired as a Distinguished Advisor in Exploration and Production Technology after over 40 years of service for BP America. Phillip was active in API/ISO Subcommittee 5 with multiple leadership roles including that of US Representative and document editor to ISO TC 67 / SC 5 / WG 2b, whose purview includes the fundamental equations for rating oil country tubulars. He was awarded the SPE Drilling Engineering Award in 2009, SPE Paper of the Year, and awarded for his service by the API Executive Committee on Standardization. Phillip has written numerous conference and journal papers. He earned a BS in Mechanical Engineering from Louisiana State University, an MS in Engineering Science from Louisiana State University, and an MS and PhD, both in Engineering Science from the University of Notre Dame.

Related Titles

Byrom, *Casing and Liners for Drilling and Completion, Second Edition,* 978-0-12-800570-5
Lyons, Plisga and Lorenz, *Standard Handbook of Petroleum and Natural Gas Engineering, Third Edition,* 978-0-12-383846-9
Renpu, *Advanced Well Completion Engineering, Third Edition,* 978-0-12-385868-9
Bellarby, *Well Completion Design,* 978-0-444-53210-7

Engineering/Energy

ISBN 978-0-12-811769-9
9 780128 117699

ELSEVIER

Gulf Professional Publishing
An imprint of Elsevier
elsevier.com/books-and-journals